NASA
Technical Memorandum 4186

AVSCOM
Technical Report 88-A-003

Rotor Systems Research Aircraft Risk-Reduction Shake Test

J. Brent Wellman
Aeroflightdynamics Directorate
USAARTA-AVSCOM
Ames Research Center
Moffett Field, California

Accession For
NTIS GRA&I ☒
DTIC TAB ☐
Unannounced ☐
Justification
By
Distribution/
Availability Codes
Avail and/or
Dist Special
A-1

QUALITY INSPECTED 4

DTIC
ELECTE
AUG 31 1990
S D
E

NASA
National Aeronautics and
Space Administration
Office of Management
Scientific and Technical
Information Division
1990

DISTRIBUTION STATEMENT A
Approved for public release;
Distribution Unlimited

SUMMARY

A shake test and an extensive analysis of results were performed to evaluate the possibility of and the method for dynamically calibrating the Rotor Systems Research Aircraft (RSRA). The RSRA airframe was subjected to known vibratory loads in several degrees of freedom and the responses of many aircraft transducers were recorded. Analysis of the transducer responses using the technique of Dynamic Force Determination showed that the RSRA, when used as a dynamic measurement system, could predict, a posteriori, an excitation force in a single axis to an accuracy of about 5% and sometimes better. As the analysis was broadened to include multiple degrees of freedom for the excitation force, the predictive ability of the measurement system degraded to about 20%, with the error occasionally reaching 100%. The poor performance of the measurement system is explained by the nonlinear response of the RSRA to vibratory forces and the inadequacy of the particular method used in accounting for this nonlinearity. The RSRA shake test has revealed areas of concern for an RSRA dynamic calibration, and has pointed out weaknesses in the force-determination method. Suggestions are made to extend the method to nonlinear systems both by using a force-determination variant and by approaching the problem using a totally different model of the airframe response.

INTRODUCTION

The NASA/Army Rotor Systems Research Aircraft (RSRA) is a flying test bed for in-flight investigation and verification of new helicopter rotor system concepts and technologies (fig. 1). It is designed specifically to provide research information similar to that obtained from wind-tunnel testing of rotors, but its data are unique because they are obtained in flight. A complete description of the aircraft is given by Hall and Merrill (ref. 1).

The RSRA is unique among rotorcraft in that it possesses a rotor-loads balance system consisting of seven load cells mounted beneath the main transmission; the load cells are designed to detect and measure forces induced by the rotor system on the rotor shaft. The geometry of this force-measuring system (fig. 2) is such that vertical, lateral, and longitudinal loads can be measured, as well as moments about the pitch, roll, and torque axes. In addition, the transmission housing, transmission frame, fuselage, and wings are equipped with accelerometers, and the main-rotor shaft is equipped with strain gauges.

One of the primary research goals of the RSRA is to measure static and dynamic loads imposed by rotor systems on the RSRA rotor shaft. Such measurements will provide the rotorcraft community with a national facility for testing new rotors and rotor systems concepts. The static calibration of the RSRA balance system is described by Acree (ref. 2) and will not be treated here. The method of a dynamic calibration of RSRA was the subject of a study conducted at NASA Ames Research Center by the Rotorcraft Flight Investigations Branch.

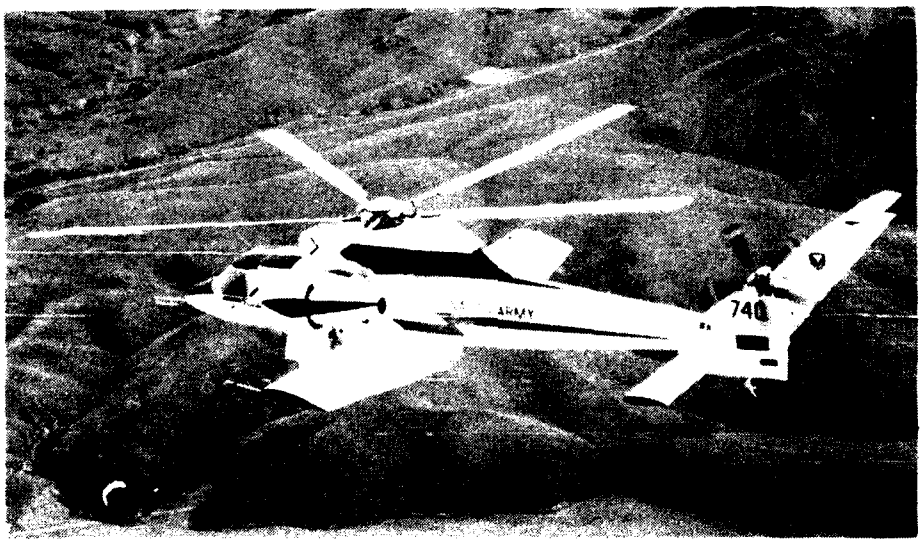

Figure 1.– Rotor Systems Research Aircraft.

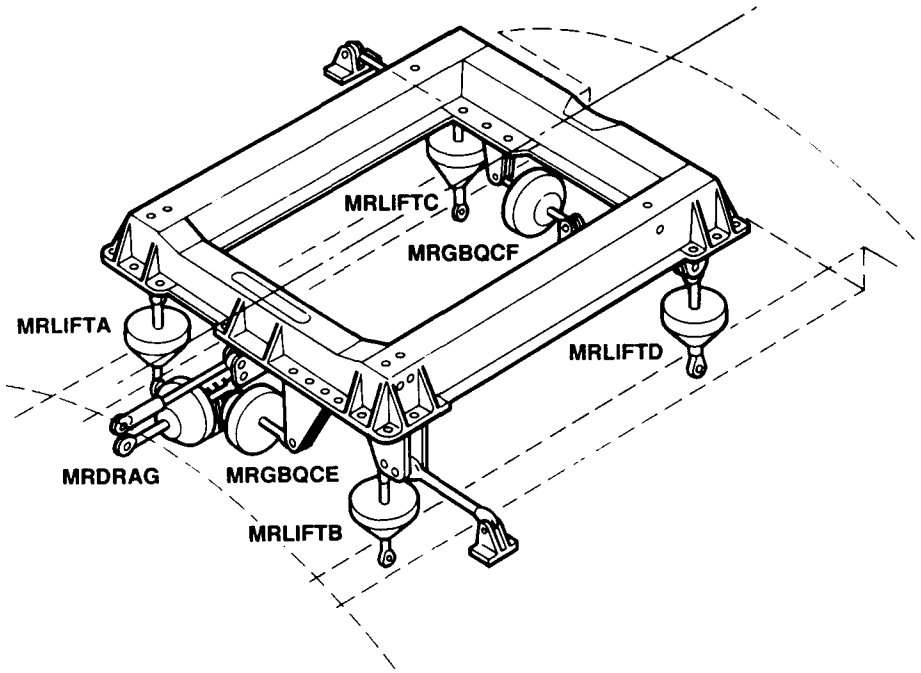

Figure 2.– Main-rotor load-measurement system.

It will be necessary to conduct a lengthy, and costly, dynamic calibration of the RSRA loads-measurement system to provide the RSRA with the capability to measure in-flight vibratory loads. This calibration will require the application of a series of known vibratory loads on the aircraft and the measurement of the aircraft structural response to those loads. The resulting data may then be correlated statistically to yield dynamic calibration matrices.

A risk-reduction shake test was conducted to define the validity and acceptability of the proposed vibratory-load measurement technique, called Dynamic Force Determination. This document presents results of the test, interprets the results in terms of RSRA airframe dynamics, and discusses directions for further work to evaluate the potential for dynamic load measurement with the RSRA. The appendix provides detailed results for all conditions of the test.

SYMBOLS

$[A]^T$	matrix transpose of A
$[A]^+$	matrix pseudoinverse of A
C	calibration factor
c_n	nth coefficient of a polynomial
F_i	force amplitude in the ith degree of freedom
F_i'	predicted force amplitude in the ith degree of freedom
F_m	complex force of master shaker
F_s	complex force of slave shaker
H_{ji}	transfer function of the jth transducer response to the ith degree of freedom of the inputs
i,j,k	indices
Im(z)	imaginary part of z
n	number of test runs for a given load direction
Re(z)	real part of z
R_j	response of the jth transducer
ε_i	normalized error in the ith degree of freedom
ξ	error radius of predicted force

Σ summation

ϕ phase angle

ω frequency

BACKGROUND

The RSRA force-measurement system consists of seven load cells mounted at the base of the transmission as shown in figure 2. Its application to the measurement of static loads is discussed in detail by Burks (ref. 3) and Acree (ref. 4).

For the purposes of force measurement, a hub-centered, nonrotating coordinate system is used (fig. 3). Load-cell outputs may be transformed into static loads in this frame of reference by using a calibration matrix whose coefficients are determined by statistical regression techniques on calibration data obtained from ground testing. A similar technique may be used in principle to measure simple sinusoidal excitation at a single frequency. The method, known as Dynamic Force Determination, uses transfer function data to establish a complex calibration matrix, which may then be used to transform transducer amplitude and phase data into force amplitudes in any given coordinate system. A more detailed explanation is provided in a later section.

A number of extra transducers were added for this test to allow more accurate determination of the forces. Twenty-eight transducers were used in an attempt to find the best combination of sensors for a hybrid force-measurement system. The transducers were divided into three "sets":

1. Set 1: Load cells of the static force measurement system

2. Set 2: Accelerometers mounted in orthogonal groups of three on the transmission case and force-measuring system frame

3. Set 3: Accelerometers mounted on the airframe

Details of the location, type, and orientation of these transducers are given in table 1, and illustrated in figures 2, 4, and 5.

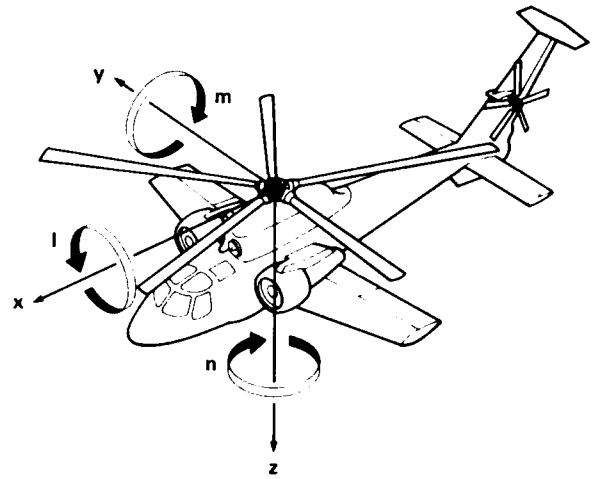

Figure 3.– RSRA rotor-axis system.

These sensors, in various combinations, were evaluated for their ability, as sets, to allow accurate determination of the applied vibratory load in five coordinate axes, as well as in a multiple-axis shaking mode. For this purpose the three transducer groups were combined to form five "cases":

1. Case 1: Static load cells alone

2. Case 2: Static load cells plus the transmission accelerometers

3. Case 3: Static load cells plus the airframe accelerometers

4. Case 4: Airframe accelerometers alone

5. Case 5: All load cells and accelerometers

The mathematical techniques presented below were used to evaluate each case as a potential dynamic load measurement system.

Vibratory steady-state loads on a generalized dynamic system at any particular frequency may be determined by applying a linear transformation to the complex response, assuming system linearity. In generic terms,

$$\begin{Bmatrix}\text{Force}\\ \text{input}\end{Bmatrix} = \begin{bmatrix}\text{Some quality}\\ \text{of the structure}\end{bmatrix} \times \begin{Bmatrix}\text{Structural}\\ \text{response}\end{Bmatrix} \qquad (1)$$

TABLE 1.– TRANSDUCER LOCATIONS

Mnemonic	Type[a]	Set[b]	Location	Orientation
MRDRAG	L/C	1	Drag load cell	Aft
MRLIFTA	L/C	1	Left fwd. load cell	Up
MRLIFTB	L/C	1	Right fwd. load cell	Up
MRLIFTC	L/C	1	Left aft load cell	Up
MRLIFTD	L/C	1	Right aft load cell	Up
MRGBQCE	L/C	1	Fwd. torque load cell	Left
MRGBQCF	L/C	1	Aft torque load cell	Right
LOMGB	Acc	2	Atop main gearbox casing	Fwd
LMGB	Acc	2	Atop main gearbox casing	Left
VMGB	Acc	2	Atop main gearbox casing	Up
XMRFBPV	Acc	2	Fwd transmission frame	Up
XMRFBPL	Acc	2	Fwd transmission frame	Left
XMRFBPLO	Acc	2	Aft transmission frame	Left
STA56NV	Acc	3	Station 56, centerline	Up
STA56NL	Acc	3	Station 56, centerline	Left
VWGTPRT	Acc	3	Right wing tip	Up
VWGTPLT	Acc	3	Left wing tip	Up
LIGB	Acc	3	Base of vertical tail	Left
VIGB	Acc	3	Base of vertical tail	Up
LATTPYLN	Acc	3	Top of vertical tail	Left
VTTPYLON	Acc	3	Top of vertical tail	Up
XMRFLV	Acc	3	Under left fwd. trans. frm.	Up
XMRFRV	Acc	3	Under right fwd. trans. frm	Up
S222FLRV	Acc	3	Station 222, floor, right	Up
S222FLLV	Acc	3	Station 222, floor, left	Up
S450FLV	Acc	3	Station 450, floor, c.l.	Up
S450FLL	Acc	3	Station 450, floor, c. l.	Left
S450OVRL	Acc	3	Station 450, top, c. l.	Left

[a]L/C = load cell; Acc = accelerometer.
[b]Set = number as described in text: 1 = baseline load cells; 2 = transmission accelerometers; 3 = fuselage accelerometers.

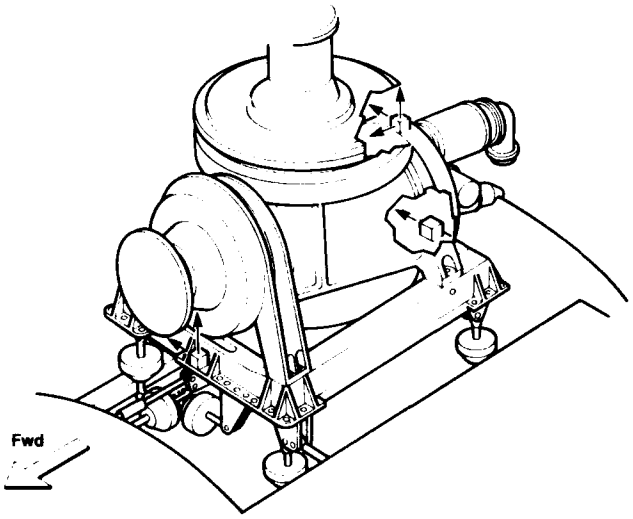

Figure 4.– Transmission accelerometer locations.

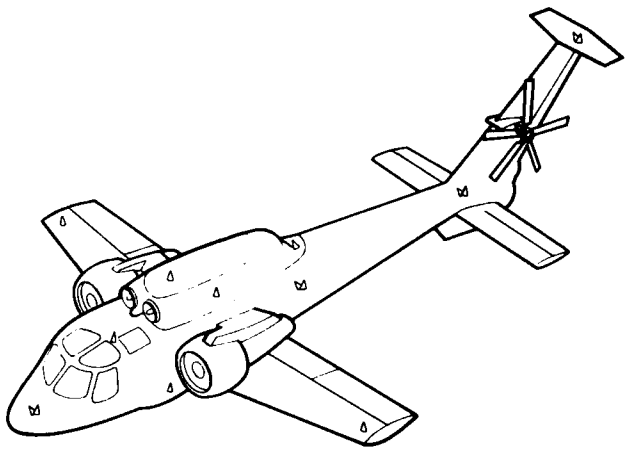

Figure 5.– Airframe accelerometer locations.

For example ,

$$\{F_i\} = [C] \ \{R_j\} \tag{2}$$

where $\{F_i\}$ is a vector of time-independent amplitudes of the forcing function describing the structural force input:

$$f(t) = F_i \, e^{i\omega t} = F_i \cos(\omega t + \phi) \tag{3}$$

and [C] is a matrix representation of the modal response model of the structure. In this respect, the structure is treated as a black box problem, in which the behavior is inferred from input-output measurements.

An approach to the formation of the [C] matrix is to use transfer functions of the transducers as matrix elements. For such purposes, a transfer function may be defined as

$$H_{ji} = R_j / F_i \tag{4}$$

if the system is assumed linear.

In the frequency domain, all quantities in equation (3) are complex, so that

$$[H_{ji}] \ \{F_i\} = \{R_j\} \tag{5}$$

which indicates the implied vector nature of the complex quantities, and in which

$$[H_{ji}] = \begin{bmatrix} Re(H_{ji}) & -Im(H_{ji}) \\ Im(H_{ji}) & Re(H_{ji}) \end{bmatrix} \tag{6}$$

For such a simple one-degree-of-freedom (DOF) system it is easy to see that

$$[C] = [H_{ji}]^{-1} \tag{7}$$

If this idea is extended to six degrees of freedom, a minimum of six responses must be recorded for each input to determine all six inputs. Equations (5) and (7) hold, and

$$\{F_i\} = \begin{Bmatrix} Re(F_1) \\ Im(F_1) \\ \cdot \\ \cdot \\ Re(F_6) \\ Im(F_6) \end{Bmatrix} \tag{8}$$

a column vector of order $2 \times$ DOF, and

$$[H] = \begin{bmatrix} [H_{11}] & \cdot & \cdot & [H_{16}] \\ \cdot & \cdot & & \cdot \\ \cdot & & \cdot & \cdot \\ [H_{61}] & \cdot & \cdot & [H_{66}] \end{bmatrix} \tag{9}$$

The [H] matrix is in this case a 6×6 square array of 2×2 arrays.

Unfortunately, equations (2), (5), and (7) are not useful in an engineering sense because they exhibit sensitivity to errors in the measurements of the elements of $[H_{ji}]$. If the [H] matrix is inverted, along with any errors in the measurement of its elements, it may yield physical information that is meaningless. The effects of such an inversion are insidious because they are independent of how well-conditioned [H] is. This is a serious problem, but it may be alleviated by the utilization of redundancy, as related by Bartlett and Flannelly (ref. 5). Redundancy is achieved by allowing the row space of the response to be larger than the column space of the input forcing function. In practice this may be achieved by using a large number of transducers relative to the number of degrees of freedom of the input.

If a redundant response space is used, then [H] is rectangular, being of dimension $12 \times (2n)$, where n is the number of transducers, and is in general singular and cannot be inverted. To transform [H] into [C] we use the following:

$$[C] = \{[H]^T \ [H]\}^{-1} [H]^T = [H]^+ \tag{10}$$

which is the pseudoinverse first introduced by Moore (ref. 6). The pseudoinverse may be shown to be a least-squares solution to the redundant transformation. Now equation (2) becomes

$$\{F_i\} = [H_{ji}]^+ \{R_j\} \tag{11}$$

In principle, this approach should give the elements of F_i to an arbitrarily high degree of accuracy, assuming linear responses of both the RSRA structure and the transducers. In practice, however, the accuracy is limited by the large number of transducers required for a relatively small gain in accuracy, and by the mathematical stiffness and ill-conditioning of the system as the ratio of transducers to input DOFs increases.

The concept of Dynamic Force Determination may be extended to cover inputs other than sinusoids by allowing the input force F_i to be a function of ω:

$$\{F_i(\omega)\} = [H_{ji}(\omega)]^+ \{R_j(\omega)\} \tag{12}$$

Figure 6 shows $H_{ji}(\omega)$ for a hypothetical ideally linear structure plotted versus ω and F_i. In practice, if the calibration matrix $[H_{ji}]^+$ is known discretely for a large number of frequencies distributed over some bandwidth, then the input vector $\{F_i\}$ may be input discretely into equation (12) over the frequency band to reconstruct $\{F_i(\omega)\}$, a spectrum of the input excitation. The proposed process of dynamic calibration is the determination of a suitably large number of such discrete calibration matrices, as determined from $\{R_j(\omega)\}$ data taken in a shake test, to cover the frequency band of interest.

The actual response of the RSRA airframe was not expected to be truly linear because of the effects of mechanical clearances (such as those around rivets) and of breakout friction in the joints connecting the transmission to the load cells. These affect the transmission of vibration from the input excitation point to the response transducer, resulting in a transfer function that is itself a function of the input force. The effect, called ankylosis, is such that H_{ji} is not constant with respect to input force, but

$$H_{ji} = \partial R_j / \partial F_i = f(F_i) \neq R_j / F_i \tag{13}$$

The effect was expected to be more noticeable at low force levels than at high force levels. The expected effect of ankylosis on data for an otherwise linear airframe is shown in figure 7. At low force levels, the frictional breakout forces and rivet clearances have a significant effect on the response. As force levels are increased, however, these effects drop off relative to the applied force so that the transducer R_j shows a net nonlinear transfer function with respect to F_i.

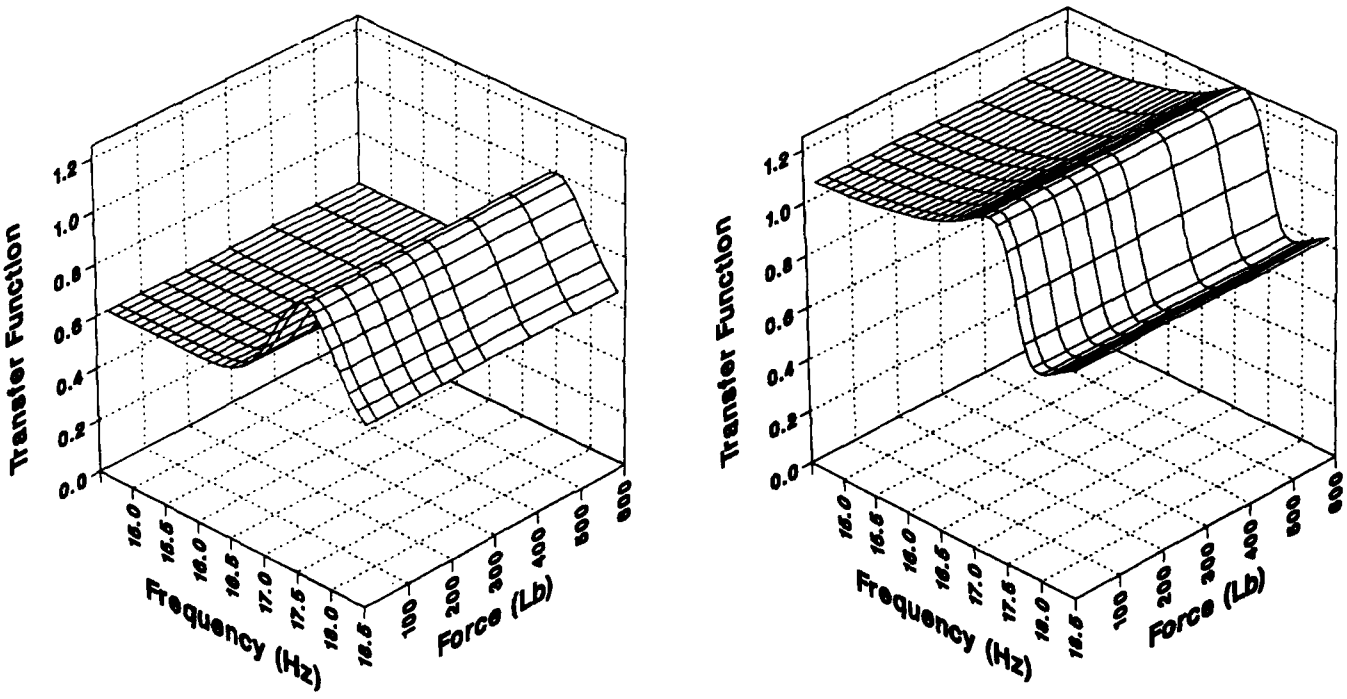

Figure 6.– Transfer function of hypothetical linear structure. (a) Real; (b) imaginary.

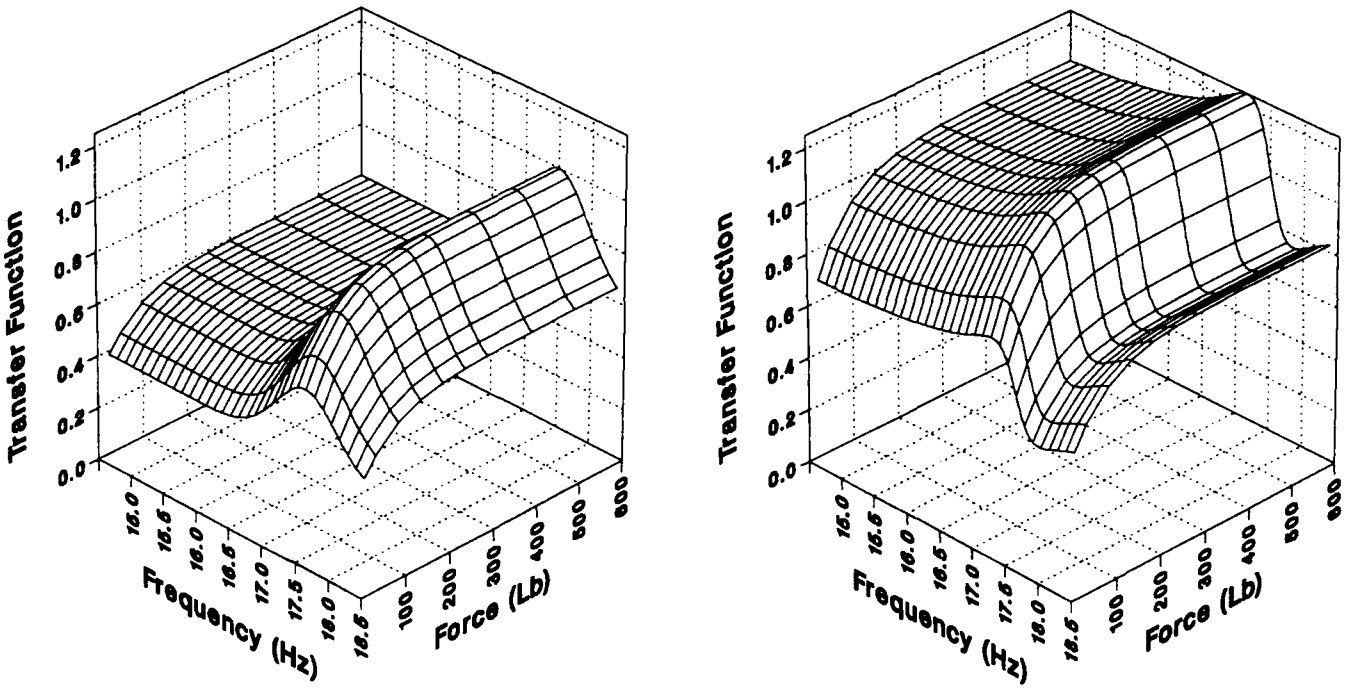

Figure 7.– Effect of ankylosis on transfer function data. (a) Real; (b) imaginary.

At high force levels, this source of nonlinearity is ameliorated and the response becomes more nearly linear with respect to the applied force. The transfer function H_{ji} therefore approaches some constant value asymptotically as force level is increased. This asymptote may be used as an estimate of H_{ji}, in which case this source of nonlinearity is, in effect, ignored. If ankylosis is indeed small, the use of the asymptote is justified.

To find asymptotes for each transducer for each degree of freedom, it was required to take data at numerous force levels and to then find the best fit of those data to some asymptotic curve. The curve chosen was

$$H_{ji} = c_0 + \frac{c_1}{F_i} \tag{14}$$

This curve was chosen for no other reason than that it was a curve that had the required property of approaching a horizontal line $y = c_0$ for large F_i. The constants c_0 and c_1 are determined by least-squares statistical analysis of bivariate data (i.e., ordered pairs of force and transfer function). Additionally, the horizontal line

$$H_{ji} = c_2 \tag{15}$$

was used as an alternate fit. The constant c_2 represents the best approximation of the data that neg'ects the dependence of ankylosis on force level. This approach consists of the taking of a simple statistical mean on the univariate transfer function data. The least-squares approaches of equations (14) and (15) are shown in figure 8. Equation (11) may then be used with statistically determined c_0 or c_2 estimates for H_{ji} to build matrix [C].

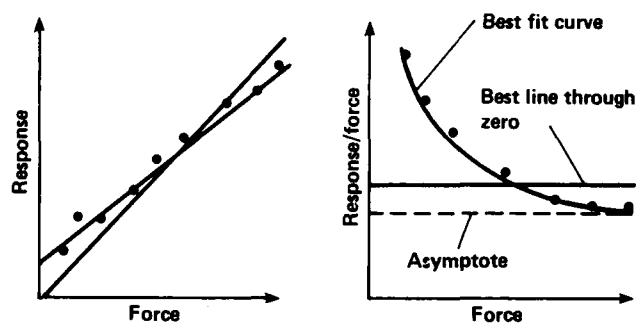

Figure 8.– Curve-fit approaches.

For the purpose of this test, nonlinear mass, stiffness, and damping effects were not modeled. If the mass or stiffness matrices for the structure contain elements that are functions of the applied excitation, then modal frequencies are also, in general, functions of applied excitation. The expected effect of this phenomenon, if present, is shown in figure 9. Note that the constant-frequency lines in the vicinity of this hypothetical nonlinear mode vary with force in a manner that is not easily modeled by

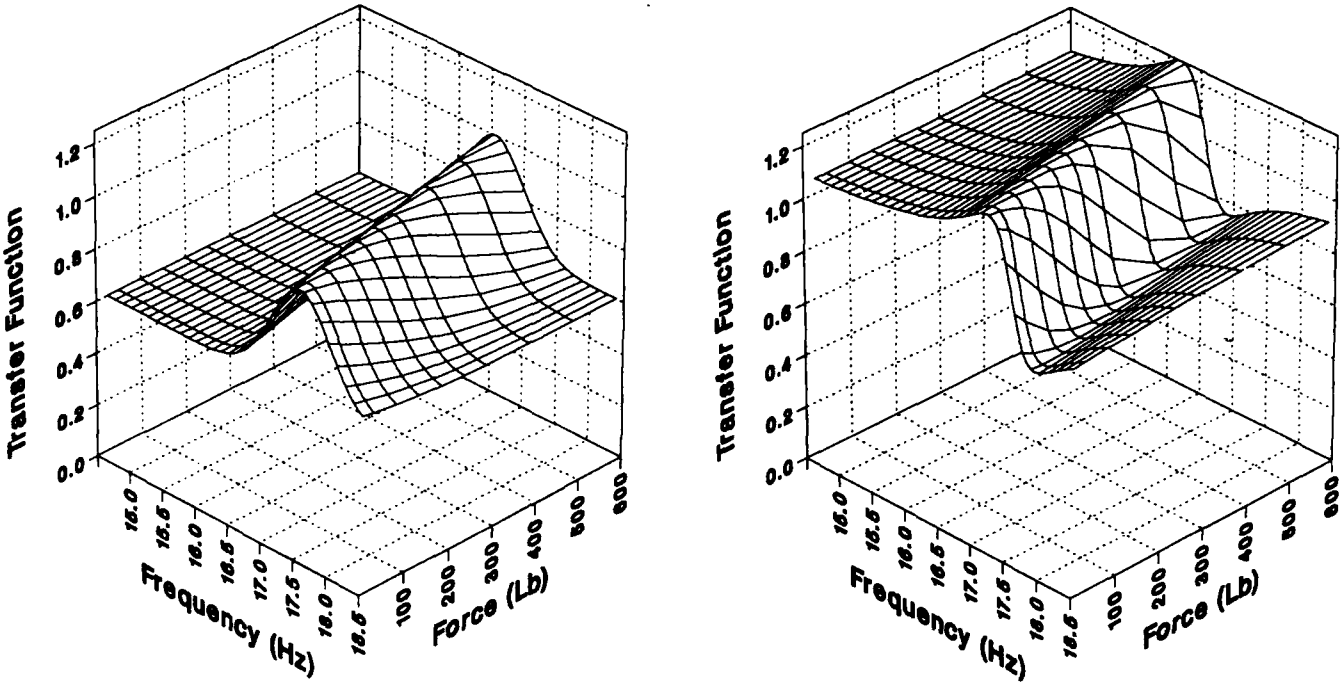

Figure 9.– Effect of frequency shift on transfer function. (a) Real; (b) imaginary.

the scheme given above, whereas constant-frequency lines not close to the drifting peak are relatively well behaved. Consequently, at frequencies close to such modes, c_0 and c_2 values, if indiscriminately used as values for H_{ji} in matrix [C], should result in large errors when applied to the input data.

DESCRIPTION OF TEST

The RSRA was tested in the compound configuration with the rudder, lower and upper horizontal stabilizers, wing and auxiliary engines, and pylons in place. It was prepared for the test by removing the rotor and rotor hub and replacing them with a specially designed aircraft support adapter. The adapter was designed to match the mass and inertial properties of the rotor head. The fuel system was drained and preserved, and the T-58 engines were replaced with scrap engines of the same model. Substitutes for the TF-34 auxiliary engines were not available, necessitating a daily period of motoring for each engine, to preserve the bearings and seals. Extra accelerometers were added to the transmission and airframe.

The aircraft was suspended indoors from a large movable crane (fig. 10). The suspension system included a soft bungee bundle to provide a free-free environment simulating flight. A safety cable with a factor of safety of 6 was used to back up the bungees. Hydraulic power was supplied to the aircraft, thus allowing the wing to be moved to a flight attitude and the landing gear to be retracted. The cabin door had to be removed because of heat buildup from instrumentation, thereby preventing a totally faithful re-creation of the flight configuration of the aircraft.

Excitation was provided by a two-axis hydraulic inertial shaker mounted on the aircraft support adapter (fig. 11). The mount provided for longitudinal, lateral, vertical, roll, and pitch excitation, as well as a combination of lateral, longitudinal, and vertical shears (fig. 12). Because of structural limitations of the main transmission, vertical moments (i.e., torques) were not applied.

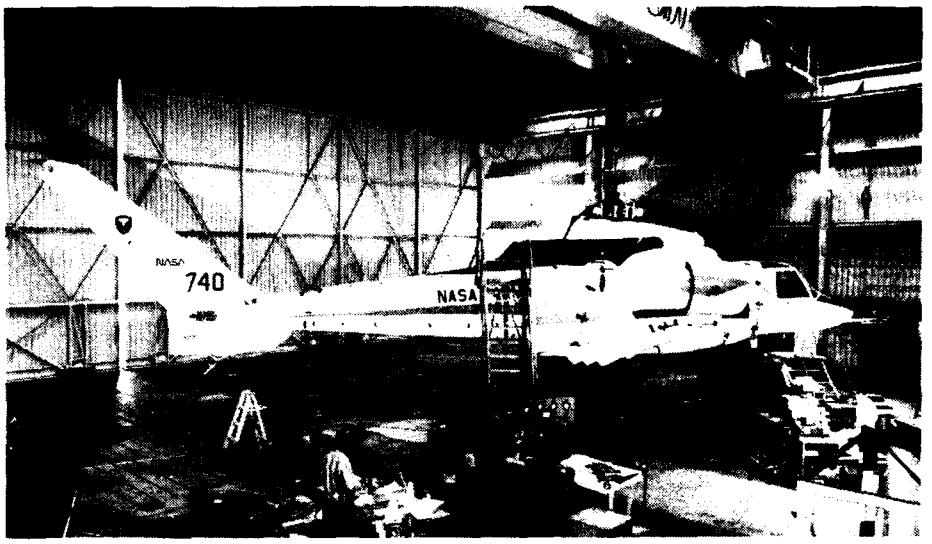

Figure 10.– RSRA in shake test facility.

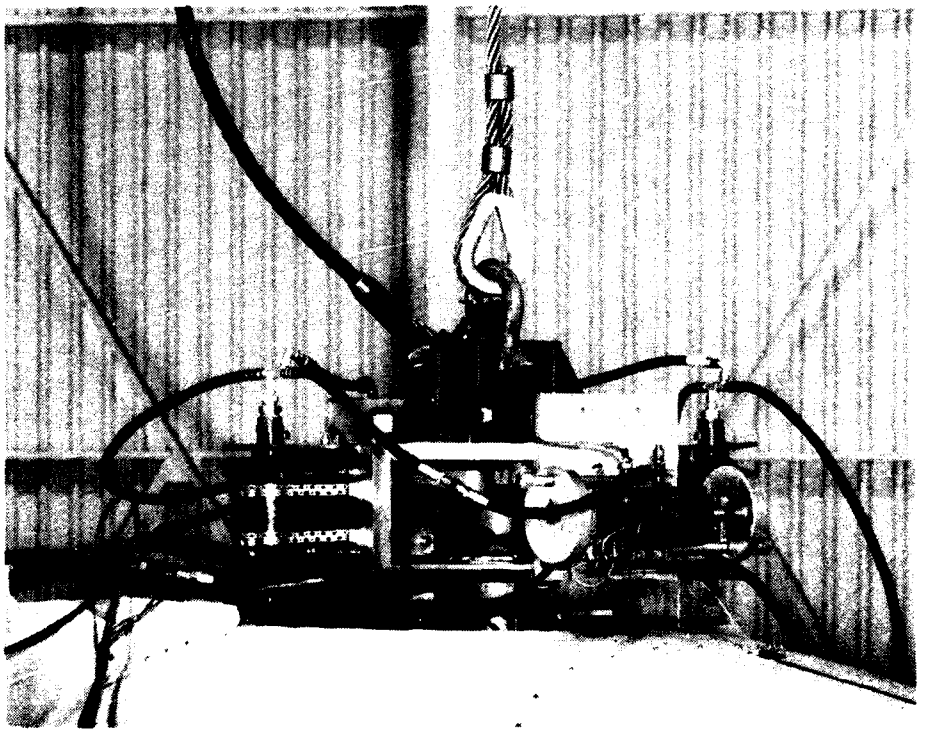

Figure 11.– Hydraulic inertial shaker for hub excitation.

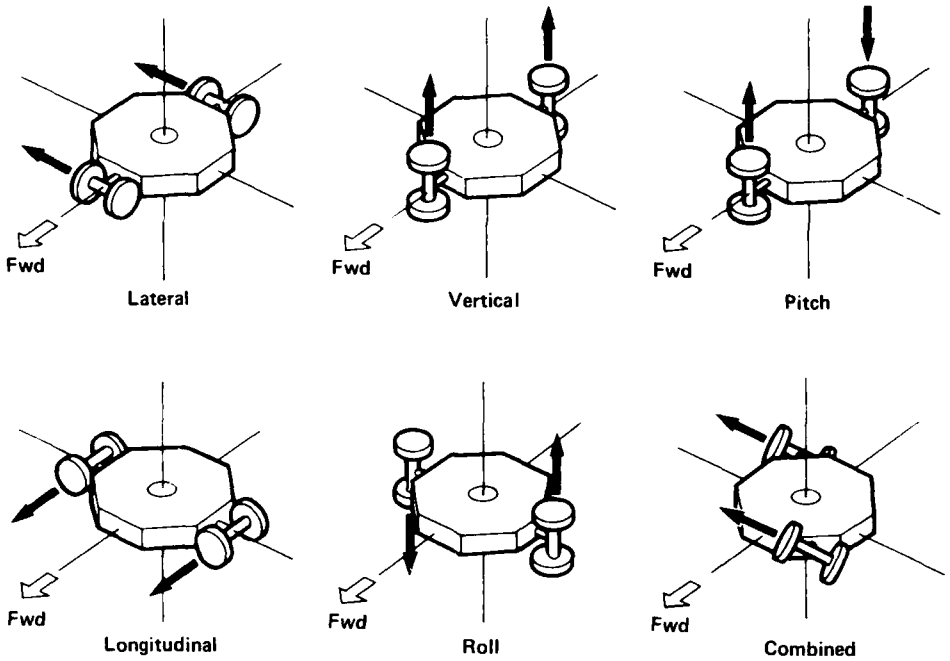

Figure 12.– Shaker configurations.

The locations of the 28 aircraft transducers used are shown in figures 2, 4, and 5. The transducers are given by their mnemonics in table 1, which shows the transducer types, locations, and orientations. The specific selection of the 28 transducers was intended to evaluate the various proposed approaches for the measurement of dynamic forces at the rotor hub. The load-measurement system load cells alone (fig. 2) were chosen to evaluate the possibility of using the static system to measure hub dynamic loads. Two orthogonal groups of three accelerometers each (fig. 4) were also added to evaluate the addition of transmission and load-system inertial properties into the measurement approach. Airframe accelerometers (fig. 5) were selected to evaluate force determination without the use of the static load system and to gather modal data on the RSRA airframe. Before each test, the shaker and lower support assembly were moved into the proper configuration for the particular axis to be excited. Figure 12 shows the various configurations.

During each test, the aircraft was lifted from the floor of the test bay, and the landing gear was retracted; the wing was placed at an angle of incidence of 10°, which is typical of that used in flight. The tail landing gear was loosely constrained with nylon line to prevent large amplitude movements of the tailcone and empennage (which could damage either the equipment or the aircraft).

Structural limitation studies were first made in each of the axes to determine acceptable test limits to follow. These studies were conducted by exciting the rotor shaft at a low force level (typically 50 lb (222.4 N)) at frequencies in the range of 3 to 60 Hz. The responses of critical structural parameters were monitored in real time by using a computer-controlled digital structural analyzer. Additionally, the effect of bandwidth on the transfer function was studied around a center frequency of 16 Hz. It was found that 4 Hz provided an adequate bandwidth for the study of research rotors. The current S-61 rotor has a 5/rev frequency of 16.9 Hz; the Sikorsky UH-60 has a 4/rev frequency of 17.1 Hz, and the Boeing-Vertol 360 rotor has a 4/rev frequency of 17.6.

The shakers were controlled by a digital signal generator whose output frequency could be controlled by microcomputer. The computer was programmed to conduct a logarithmic sweep of the frequency band at a rate that would allow the RSRA airframe to reach steady-state response at any given frequency. During each test, the time-responses of all transducers were recorded on magnetic tape, using the Piloted Aircraft Data System (PADS) in the RSRA. These tapes were then removed from the aircraft and processed off-line, as described below.

The time records of each transducer and the master shaker were input to a commercial structural analyzer, which performed a fast Fourier transform (FFT) on the signals and produced a least-squares estimate of the complex transfer function. This transfer function was then displayed on the screen as a plot of

transducer-response/shaker-force versus frequency. The data to create the plot, in the form of 256 real-imaginary pairs, were transferred to a microcomputer that had been programmed to interrogate the analyzer and record the data it received back onto a digital tape cartridge. Each transducer produced a file of measurements for each degree of freedom for each transducer at each force level tested.

Using commercially available software, the microcomputer transmitted the reduced data to a mainframe computer, for processing and permanent storage. Mainframe post-processing was divided into four steps: (1) data correction; (2) determination of slopes and asymptotes by least-squares; (3) production of calibration matrices; and (4) comparison of "predicted" excitation to actual excitation.

The transfer function data were computed relative to twice the master shaker force. The slave shaker was not, however, perfectly in phase with the master (a lag of up to about 6°), nor did the force match perfectly. To account for this effect, the real and imaginary parts of these transfer function data were multiplied by the complex factor $(F_m + F_s)/(2 \times F_m) = (1 + F_s/F_m)/2$. To extract slave-cylinder data, a transfer function was taken of the slave cylinder versus the master cylinder for each load level and excitation axis (shaker inaccuracy was found to be a function of both). These F_s/F_m data were transmitted to the mainframe computer in the same manner as the transducer transfer-function data. A mainframe program then read the F_s/F_m data and applied the proper corrections to the corresponding transducer data.

The factors c_0, c_1, and c_2 from equations (13) and (14) were determined from transformed least-squares formulas where

$$c_0 = \frac{\left[\left(\sum_{k=1}^{n} \frac{1}{F_{ik}^2} \times \sum_{k=1}^{n} H_{jik}\right) - \left(\sum_{k=1}^{n} \frac{1}{F_{ik}} \times \sum_{k=1}^{n} \frac{H_{jik}}{F_{ik}}\right)\right]}{\left[n \times \sum_{k=1}^{n} \frac{1}{F_{ik}^2} - \left(\sum_{k=1}^{n} \frac{1}{F_{ik}}\right)^2\right]} \tag{16}$$

$$c_1 = \frac{\left[\left(n \times \sum_{k=1}^{n} \frac{H_{jik}}{F_{ik}}\right) - \left(\sum_{k=1}^{n} \frac{1}{F_{ik}} \times \sum_{k=1}^{n} H_{jik}\right)\right]}{\left[n \times \sum_{k=1}^{n} \frac{1}{F_{ik}^2} - \left(\sum_{k=1}^{n} \frac{1}{F_{ik}}\right)^2\right]} \tag{17}$$

$$c_2 = \frac{\sum_{k=1}^{n} \frac{H_{jik}}{F_{ik}}}{\sum_{k=1}^{n} \frac{1}{F_{ik}^2}} \tag{18}$$

in which k is an index of experiments (different force levels), and all arithmetic is complex. The coefficients c_0 and c_2 for each transducer (index j) and degree of freedom (index i) were computed for 256 frequency intervals over the range of 14.5 Hz to 18.5 Hz. Each coefficient was then weighted by normalizing it to the full-scale value of the corresponding transducer to prevent ill-conditioning of the transfer matrices.

For each set of sensors used (i.e., for each case), two calibration matrices were formed, one using c_0 as the estimate for H_{ji}, the other using c_2. Each such matrix was pseudoinverted to produce a candidate calibration matrix for each frequency interval. These matrices were then multiplied by normalized transducer transfer function data to produce a normalized prediction of the input vector (a vector of order 10 containing real and imaginary parts for the five input degrees of freedom). This was then compared with the ideal normalized vectors as given in table 2.

An "error radius," $\xi(\omega)$, was defined as an ad hoc measure of goodness-of-fit for the matrices. It is defined as the square root of the sum of the squares of all errors in the 10-dimensional measurement space:

TABLE 2.– IDEAL NORMALIZED INPUT VECTOR

Input DOF	X		Y		Z		L		M	
	Re	Im	Re	Im	Re	Im	Re	Im	Re	Im
Longitudinal	1	0	0	0	0	0	0	0	0	0
Lateral	0	0	1	0	0	0	0	0	0	0
Vertical	0	0	0	0	1	0	0	0	0	0
Roll	0	0	0	0	0	0	1	0	0	0
Pitch	0	0	0	0	0	0	0	0	1	0
Combined	0.612	0	0.612	0	0.5	0	0	0	0	0

$$\xi(\omega) = \sqrt{\sum_{i=1}^{10} \varepsilon_i^2} \tag{19}$$

where

$$\varepsilon_i = \frac{F_i'(\omega) - F_i(\omega)}{|F(\omega)|} \tag{20}$$

The term error radius arises because its value represents the magnitude of a vector from the actual force vector to the measured force vector in a space of dimension 10. Since the single DOF data were used to make the calibration matrices in the first place, the error radius represents only (1) computational errors, such as roundoff error; (2) mathematical uncertainty resulting from ill-conditioning and stiffness; and (3) nonlinear behavior of the physical system.

Measurement uncertainties do not show up in the error radii except for those generated from the multi-axis input data, which were not used to make the calibration matrices. Therefore, differences in the error radii between the multi-axis and single-axis data sets give a rough measure of the effects of nonlinearities in the structure versus inaccuracies in the transducer data.

RESULTS

The corrected transfer functions of the individual transducers at different excitation levels were plotted in a three-dimensional format to present an integrated representation of the response of each transducer to shaker excitation. Each transfer function appears on the plot as a wavy or jagged line connecting the 256 data points in the test-frequency interval. Each transfer-function curve is connected to the corresponding point in the neighboring curve to form constant-frequency curves in the y-z plane, giving the appearance of a surface. On such a plot, gross nonlinearities show up very prominently. Force-dependent nonlinearities (such as ankylosis) would appear as shown previously in figure 7, and frequency-dependent nonlinearities (such as nonlinear modes) would appear as shown in figure 9.

The data exhibited the expected nonlinear behavior described above in many cases, as may be seen in the typical test data shown in figure 13. The real and imaginary parts of measured transfer-function data were plotted against the input shaker force. Curves of the form (eq. (14))

$$H_{ji} = c_0 + \frac{c_1}{F_i}$$

and (eq. (15))

$$H_{ji} = c_2$$

were fitted to the data as shown above. It may be seen here that the explanation and modeling of the nonlinear behavior given above is at least reasonable in this case. The transfer function plots for the 28 transducers are given in the appendix. They are grouped by force direction and ordered by transducer as in table 1.

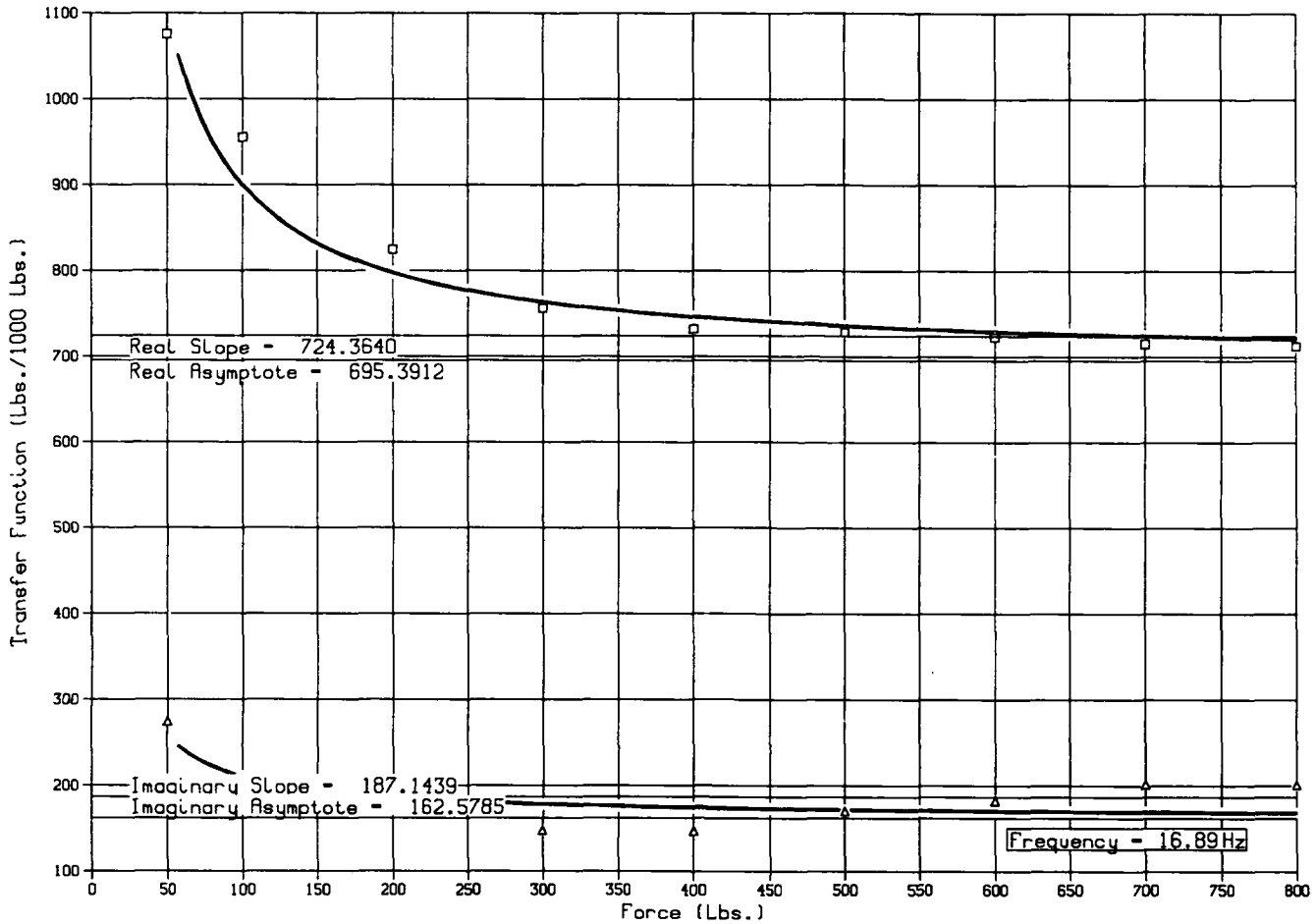

Figure 13.– Asymptote plot: MRLIFTB response to lateral forcing.

The transfer function plots for the load cells (MRDRAG through MRGBQCF) show that the load cells give fairly linear responses in the range of about 17 through 18.5 Hz, as evidenced by the fairly smooth and level contours of the plots in this region. At the low end of the frequency scale, however, a force-dependent nonlinearity is seen in the form of a saddle-shaped feature centered on about 200 lb (890 N). This feature is seen to a greater or lesser degree in all the load cells and at different values of the transfer function (given in the plots as lb/1000 lb of excitation). It is, therefore, not believed to be associated with the load cells themselves, but with the transmission and mounting system.

The plots for the transmission accelerometers (LOMGB through XMRFPLO) show some of the same features as those for the load cells. The saddle structure noted earlier is seen in these plots as well, also centered on 200 lb, though in some cases (XMRFBPLO as an example), the feature is inverted to form a hump. As general observations, note the following.

1. The accelerometer response (shown in g's/1000 lb of excitation) is low, probably because of the large mass of RSRA, relative to the excitation levels allowable for this test.

2. The vertical accelerometers exhibit very good linearity in the range from 16.5 to 18.5 Hz.

3. Accelerometers with low response show reduced linearity/repeatability. Transducer noise becomes significant because of a mismatch (intentional, to simulate flight hardware) of accelerometer range and measured acceleration. Transducer noise shows up as jaggedness in the plot and is most pronounced for low force inputs.

4. The accelerometers that have a high enough response to be reliable give plots with striking similarity to load-cell plots for load cells of similar orientation (e.g., compare XMRFBPV and MRLIFTC or compare LOMGB and MRDRAG).

The results support the hypothesis that the main gearbox and frame assembly respond as a rigid body relative to the response of the fuselage (as explained below).

The 15 airframe accelerometers must be examined with their locations, relative to the point of excitation, in mind. Accelerometers directly below the transmission, XMRFRV and XMRFLV, show similar responses to the transmission load cells and accelerometers. Accelerometers at the airframe extremes, such as VWGTPRT or VWGTPLT on the wings, or LATTPYLN or VTTPYLON atop the vertical tail, show responses dominated by airframe structural dynamics and bear little resemblance to the transmission transducers. Note especially, the structural mode at 17.5 Hz, which is absent from transmission and wing responses. Intermediate accelerometers, such as S222FLRV or S450FLV, show a response between these extremes. These observations support the expected conclusion that the fuselage is more flexible and behaves less like a rigid body than does the transmission.

The "local modes" seen in the transfer function plots for LATTPYLN and VTTPYLON are worthy of note. Modal analysis holds that all modes of vibration are global properties of a structure and exist everywhere in the structure, but in this case the responses of all the other transducers are negligibly small and the mode may be thought of as localized in the tail pylon. Fabunmi (ref. 7) has shown that the accuracy of the force-determination method is limited when one mode dominates the response of a structure (i.e., at or near the natural frequency of the dominating mode).

Furthermore, these modes exhibit nonlinear behavior. Note that the constant-frequency lines near the classical mode in LATTPYLN are far from level; they rise and fall as the mode shifts in frequency with increasing force input. These effects are difficult to model, since they do not affect each constant-frequency cross section in the same manner, and are not accounted for at all using Dynamic Force Determination.

Calculated error radii for cases 1 through 5, for use of c_2 coefficients, are shown in figures 14 through 18. The individual transducer plots are presented in the appendix. Case 5 (fig. 18) represents the best performance of the measurement system for all five input axes. Each data point represents the magnitude difference between predicted force and actual force normalized to 100% of the nominal applied force. Each of the first five curves for each case represents the accuracy of the method for a particular degree of freedom and reveals only how well the calibration matrices were able to "predict" the statistical data that generated them, as explained above. The exception to this is the "combined," or multi-axis, load data, which represent data outside this statistical universe.

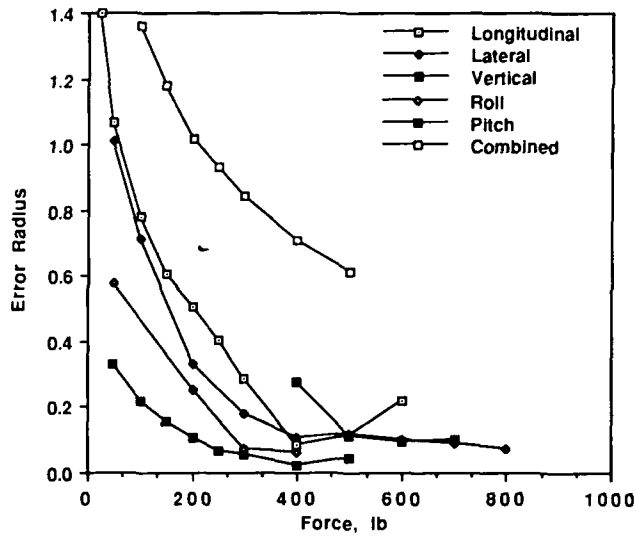

Figure 14.– System error radius: Case 1, load cells only.

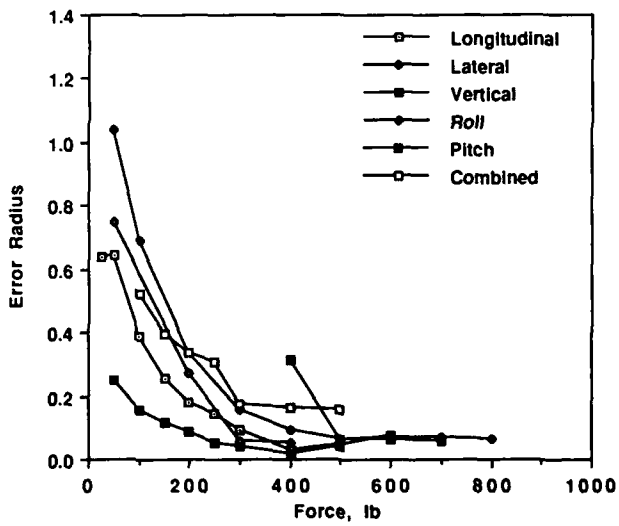

Figure 15.– System error radius: Case 2, load cells and gearbox accelerometers.

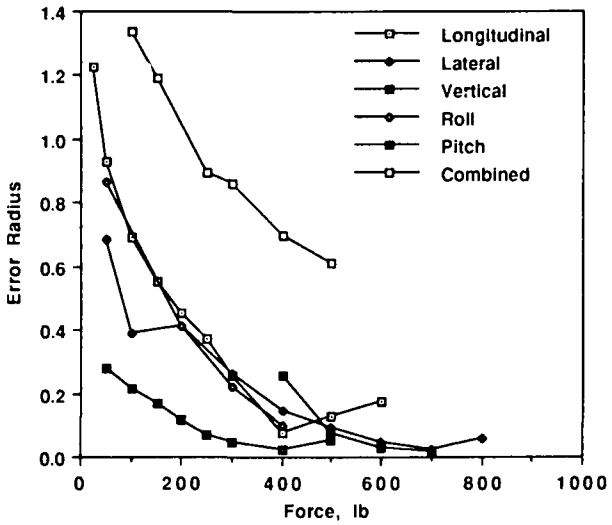

Figure 16.– System error radius: Case 3, load cells and airframe accelerometers.

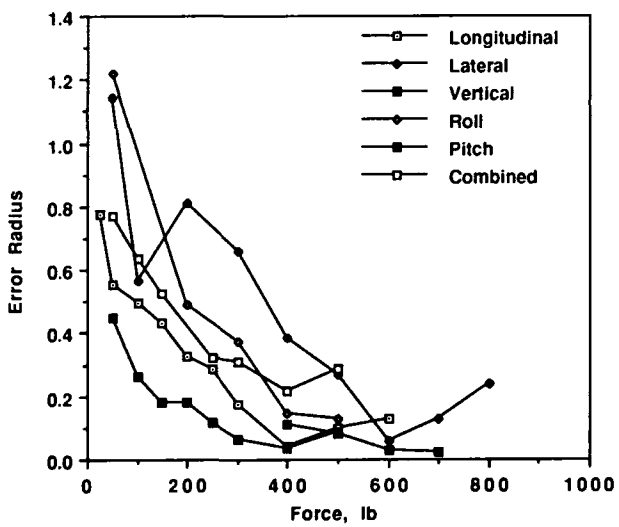

Figure 17.– System error radius: Case 4, airframe accelerometers alone.

The predictions are least accurate at low force levels, but begin to level out at 200-300-lb input force (lb-ft for moments). Here the ankylosis effect diminishes. Beyond this point each curve has a minimum in the 400- to 700-lb range. This is thought to be an artifact of the model for obtaining H_{ji} coefficients, and not to represent some "ideal" force level for the system.

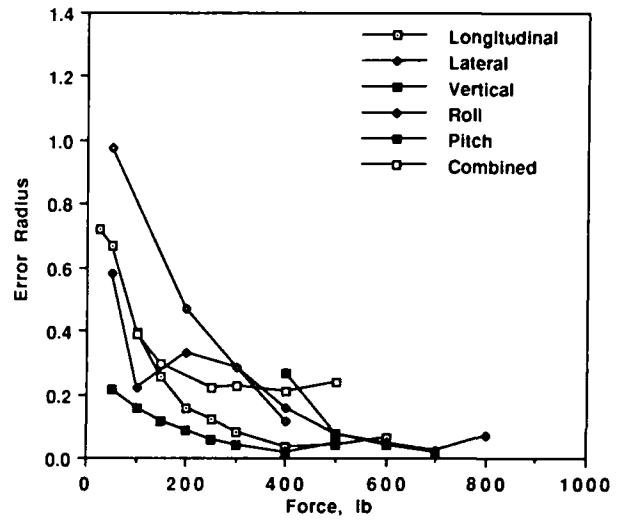

Figure 18.– System error radius: Case 5, all transducers.

CONCLUSIONS

It seems clear from the size of the error radii that a full-scale dynamic calibration using Dynamic Force Determination would only result in a vibratory measurement capability with at best a 5% accuracy. This limit is imposed by the RSRA airframe and by the method used. The best accuracy achieved with data not used to form calibration matrices was of the order of 20%. This is the best accuracy that can be reasonably expected with the configuration tested here. This is far less than the accuracy expected of a research tool.

A dynamic calibration is not ruled out altogether, if the method is accurate enough to reliably reduce the error radii to under 5% of measured force or if a different measurement or analysis technique is identified and used. There is hope on both fronts.

The Dynamic Force Determination used here was based on a linear model of airframe response. The method may be extended to a nonlinear model by using coefficients from a curve fit of transducer data and applying them to a predictor-corrector numerical algorithm, in which the linear model already developed becomes the force predictor for the nonlinear force corrector. Development of such a model could extend the accuracy to lower force levels. It is uncertain at this time whether the approach would exhibit enough numerical stability to be reliable in all cases, and whether the increased computer time required would be justified by the results.

Work along different lines, using a nonlinear model of load-cell deflection angles and parameter estimation techniques on time-domain data has been done and was reported by others.

REFERENCES

1. Hall, G. W.; and Merrill , R. K.: Flight Testing the Rotor Systems Research Aircraft (RSRA). NASA TM-85852, 1983.

2. Acree, C. W., Jr.: Performance of the Rotor Systems Research Aircraft Calibrated Rotor Loads Measurement System. Presented at the 38th Annual National Forum of the American Helicopter Society, May 1982, pp. 461-473.

3. Burks, J. S.: Rotor Systems Research Aircraft (RSRA)—Rotor Force and Moment Measurement System. AIAA Paper 81-2516, Las Vegas, Nev., Nov. 1981.

4. Acree, C. W., Jr.: Results of the First Complete Static Calibration of the RSRA Rotor-Load-Measurement System. NASA TP-2327, 1984.

5. Bartlett, F. D., Jr.; and Flannelly, W. G.: Model Verification of Force Determination for Measuring Vibratory Loads of Rotors on Helicopters. AHS J., vol. 24, no. 2, Apr. 1979, pp. 10-18.

6. Moore, E. H.: General Analysis, Part I. American Philosophical Society, Philadelphia, 1935.

7. Fabunmi, J. A.: Modal Constraints on Structural Dynamic Force Determination. AHS J., vol. 30, no. 4, Oct. 1985, pp. 48-54.

APPENDIX

Graphs that represent the responses of 28 transducers in the RSRA to excitation in five degrees of freedom at the rotor head and one coupled excitation in three axes (multi-axis mode) are presented at the end of this report. The explanation of the axes in these "transducer-response" plots is given in the main body of the report in the Results section. They are ordered by transducer as shown in table 1 and grouped by force direction.

The author gratefully acknowledges the fine work contributed by Cathie M. Jacobson in processing the data and producing the graphs.

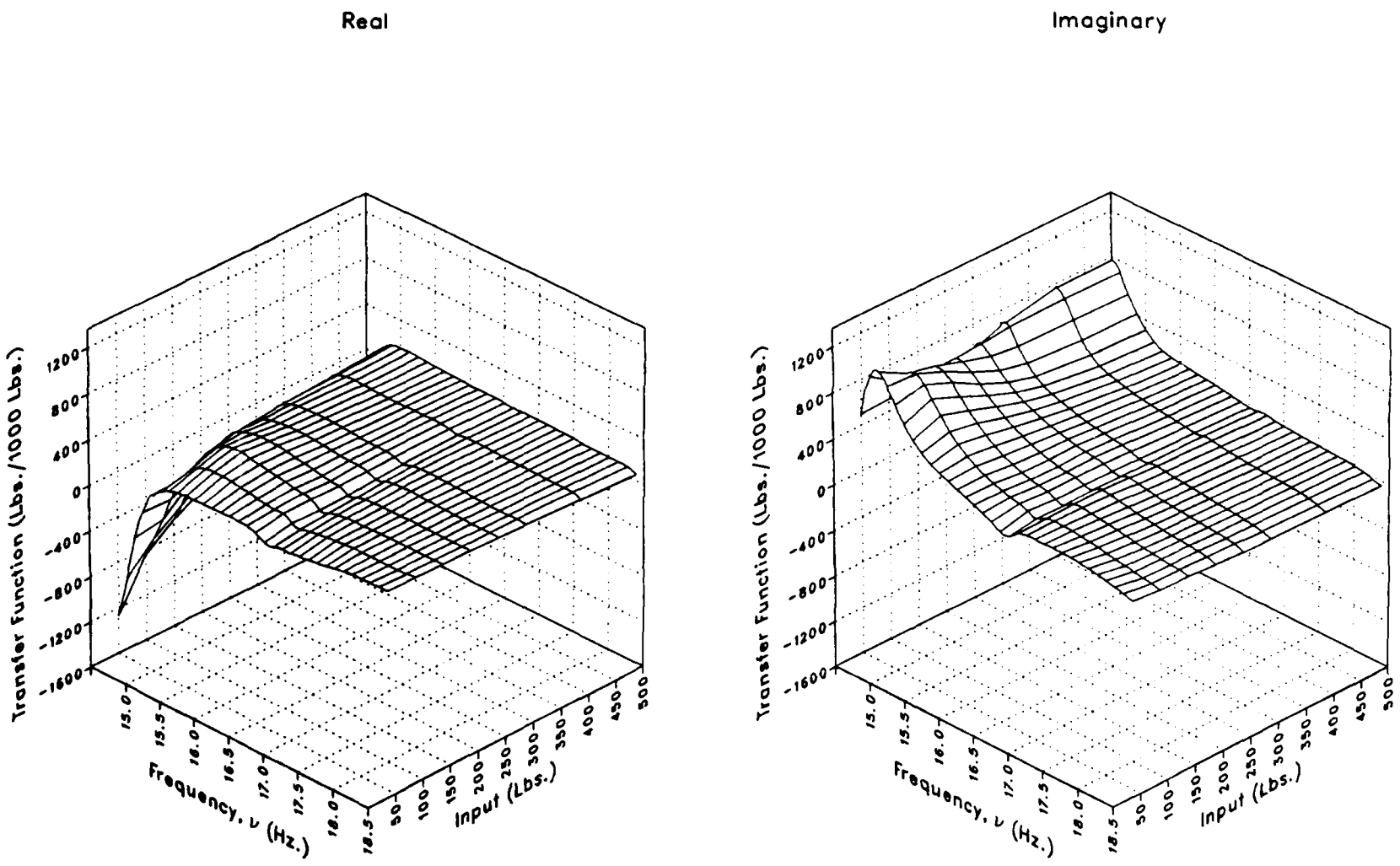

(a) MRDRAG

Figure 1.– Vertical forcing.

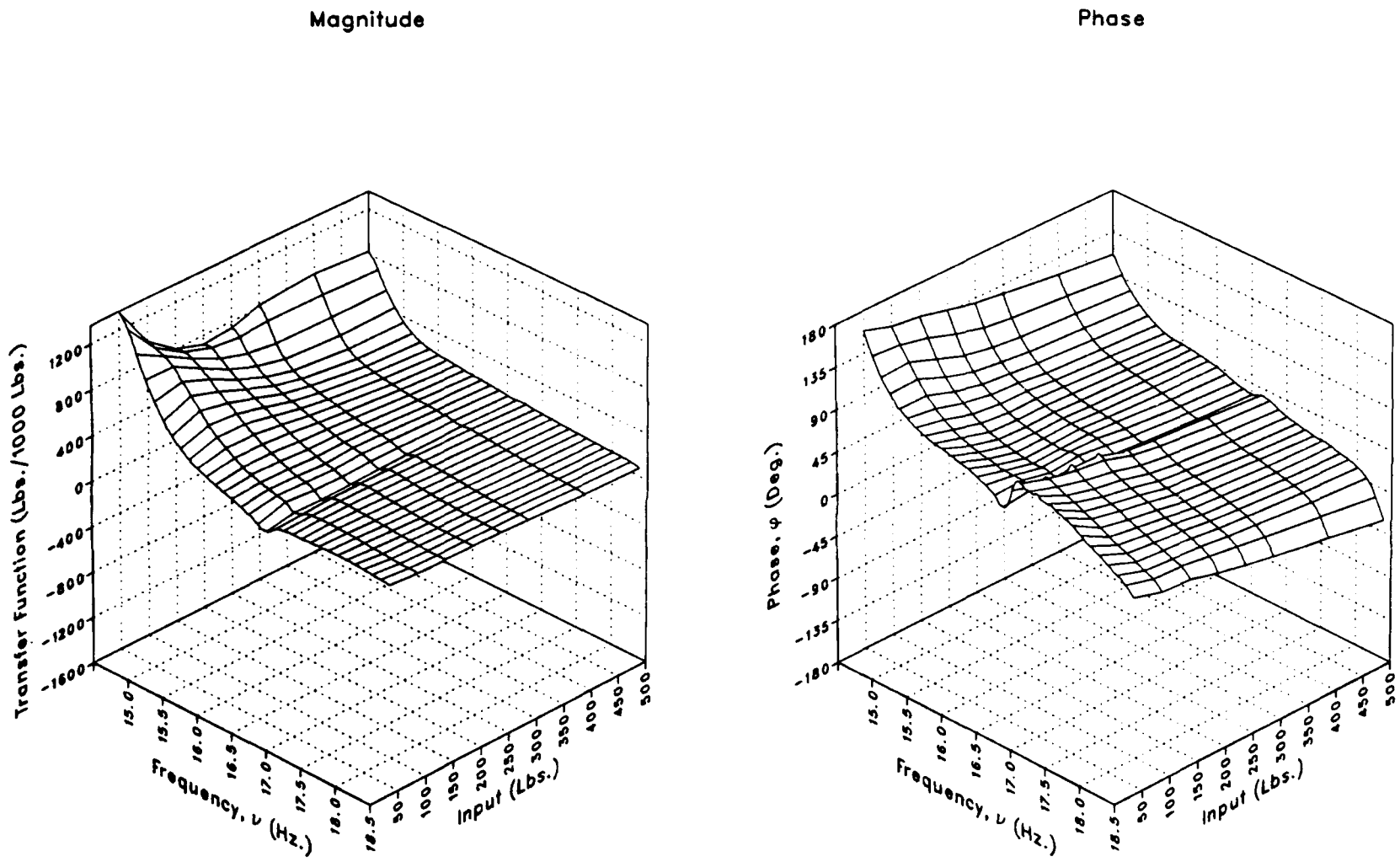

(a) MRDRAG Concluded.

Figure 1.– Continued.

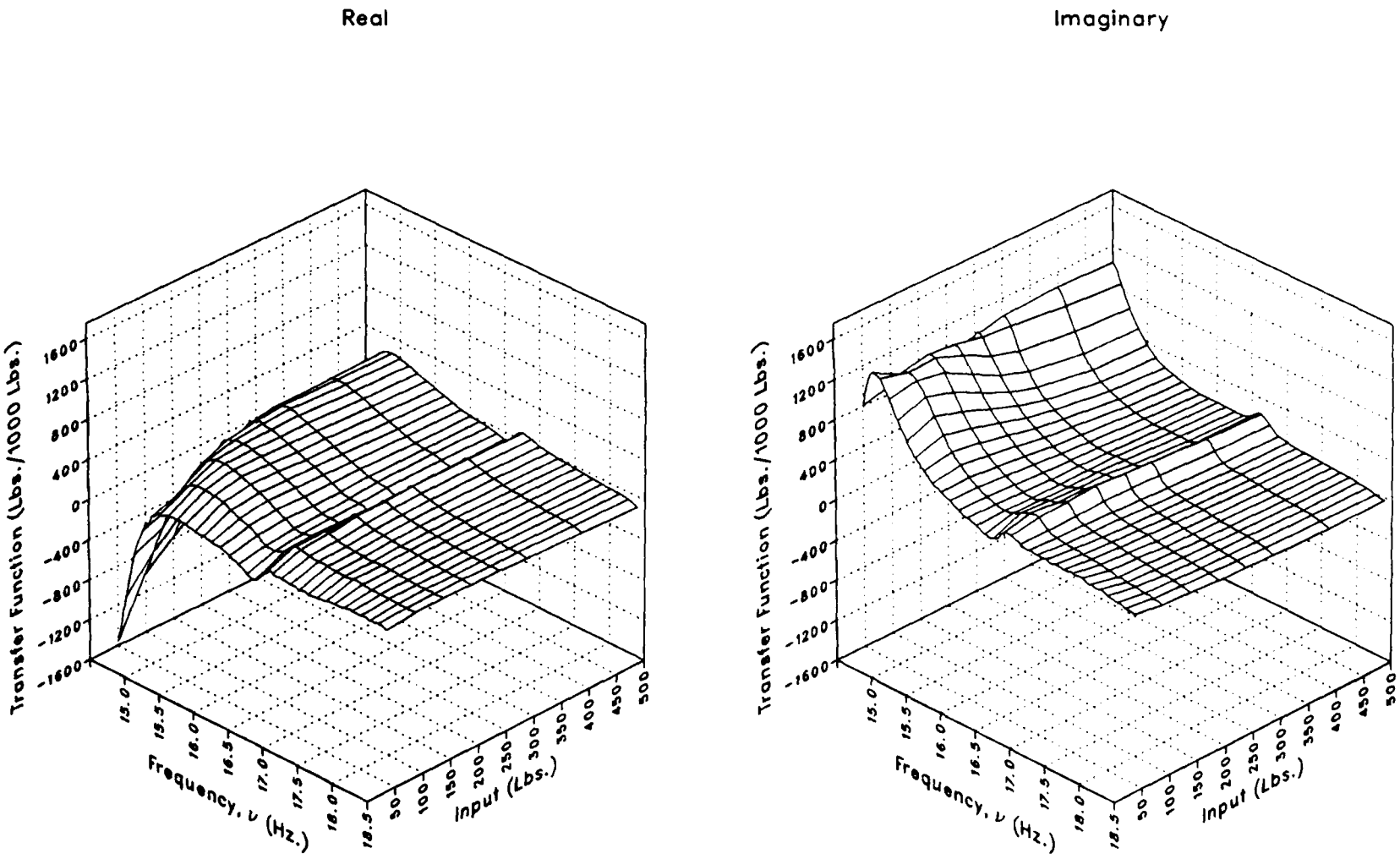

(b) MRLIFTA

Figure 1.– Continued.

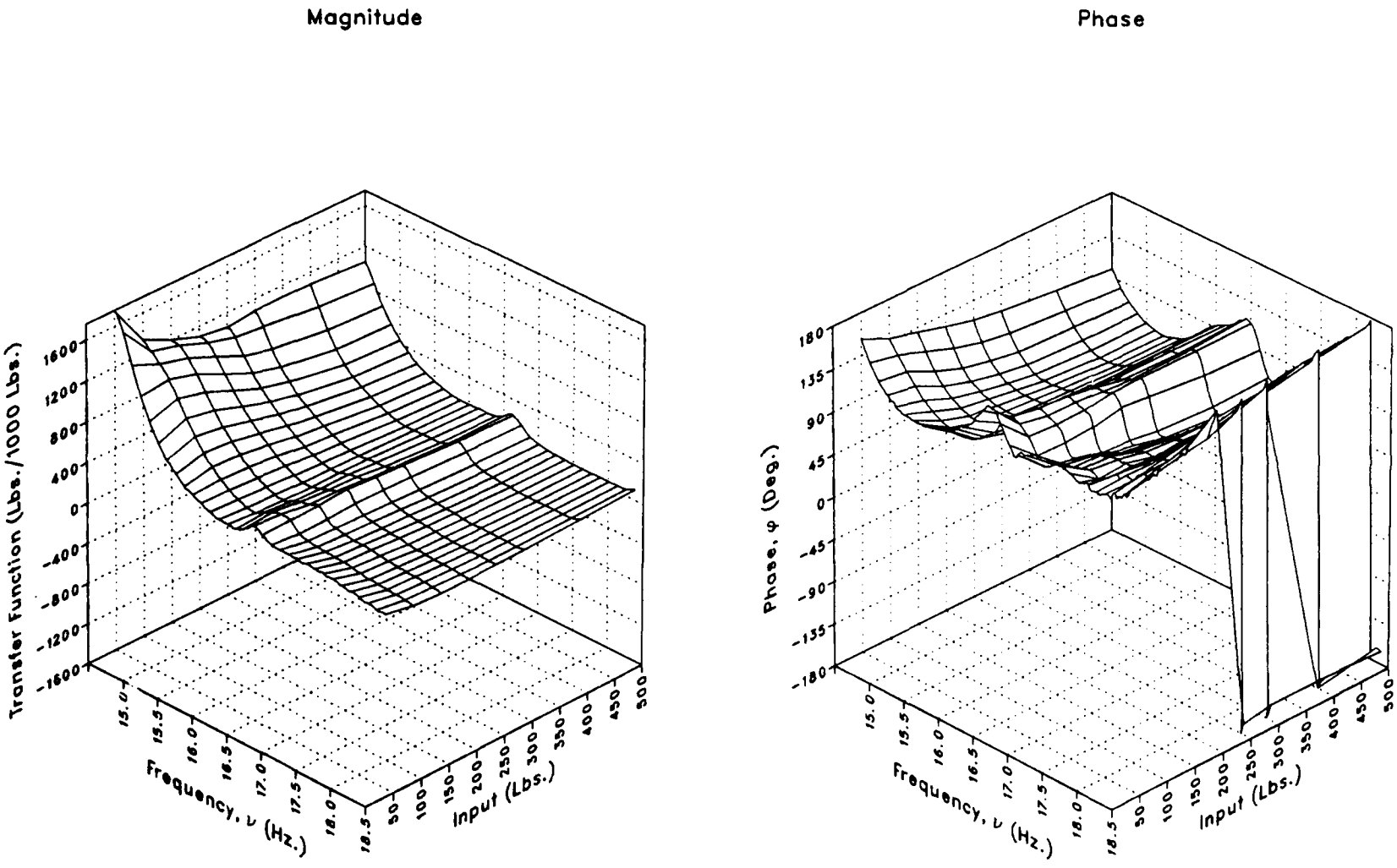

(b) MRLIFTA Concluded.

Figure 1.– Continued.

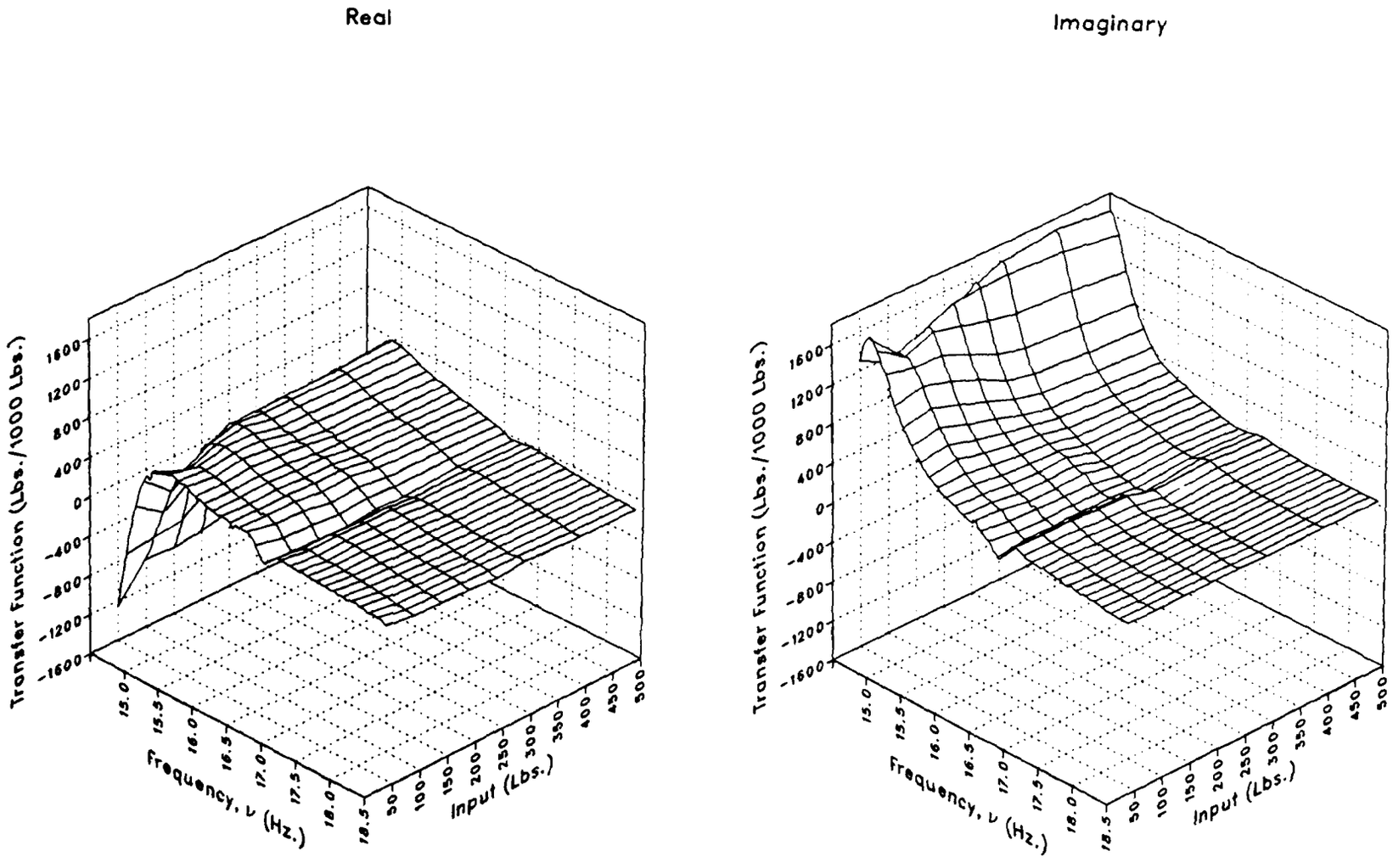

(c) MRLIFTB

Figure 1.– Continued.

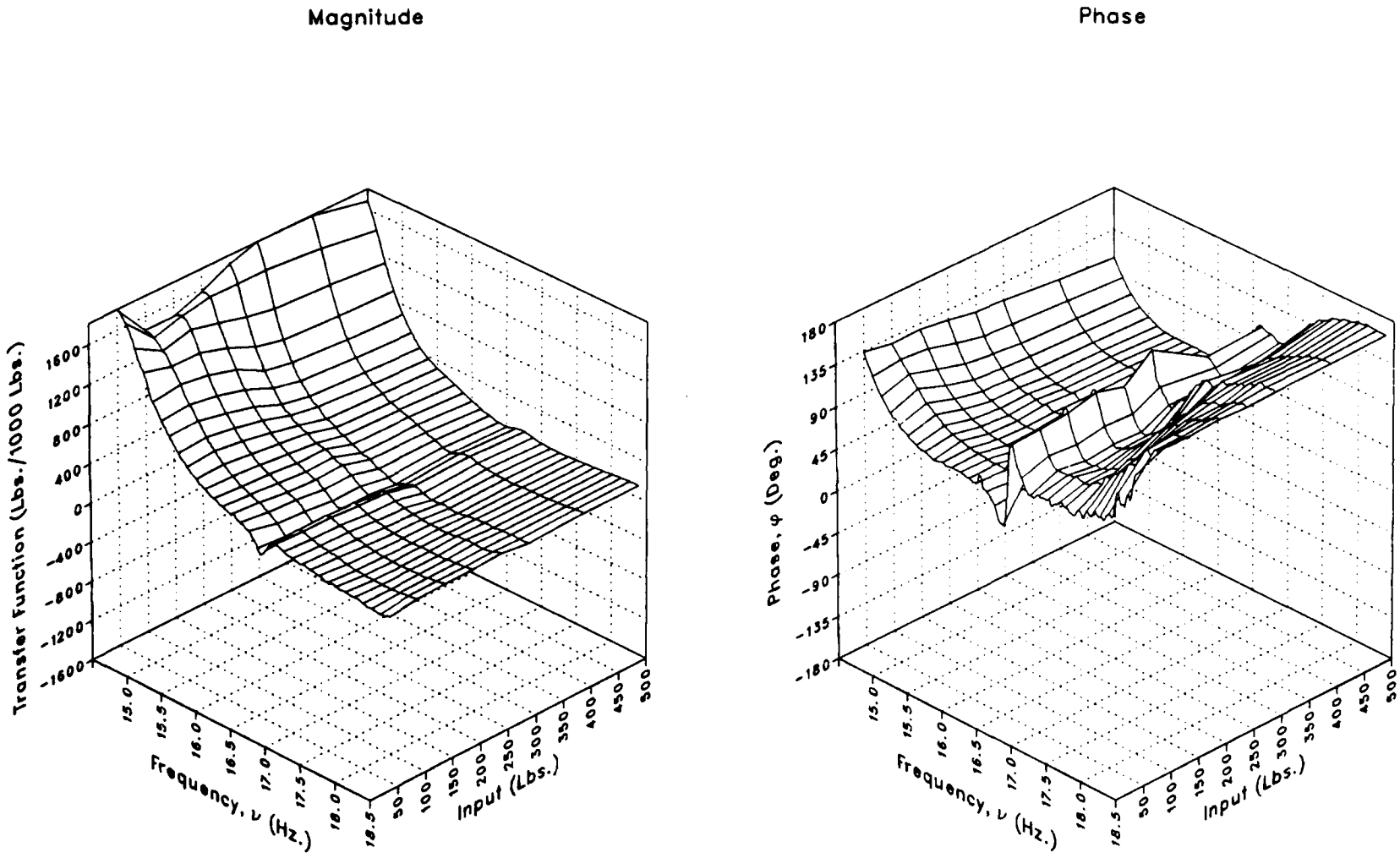

(c) MRLIFTB Concluded.

Figure 1.– Continued.

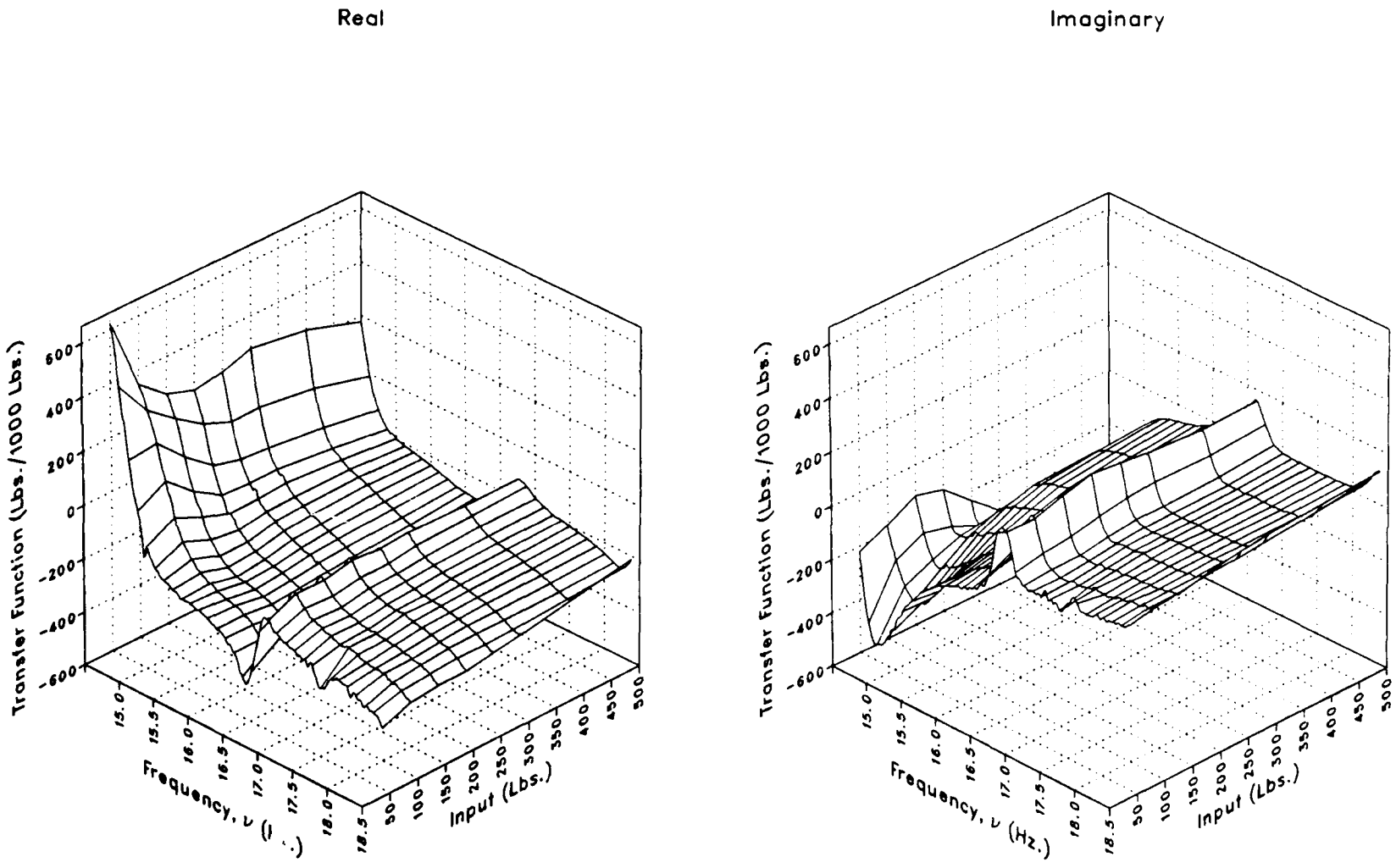

(d) MRLIFTC

Figure 1.– Continued.

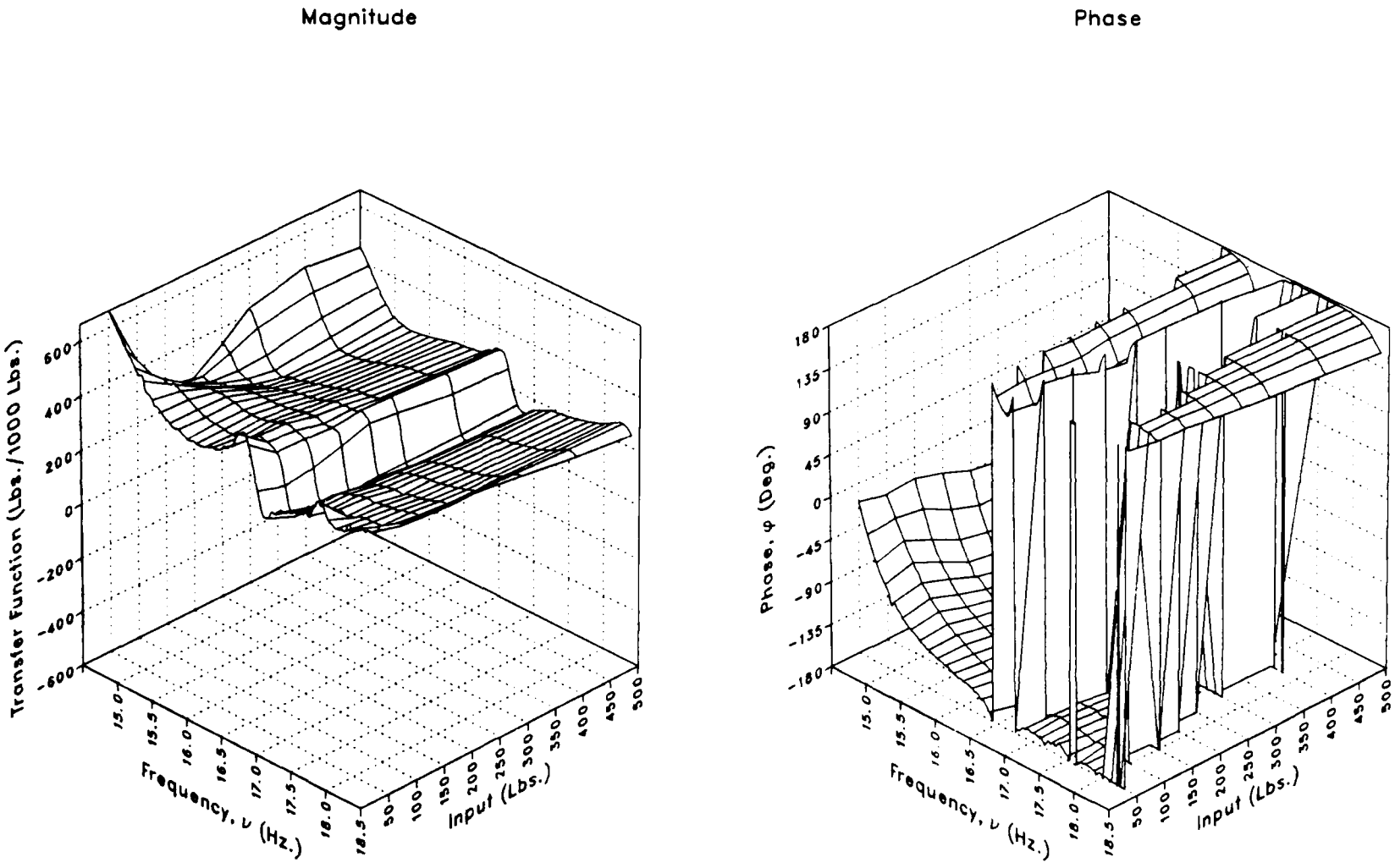

(d) MRLIFTC Concluded.

Figure 1.– Continued.

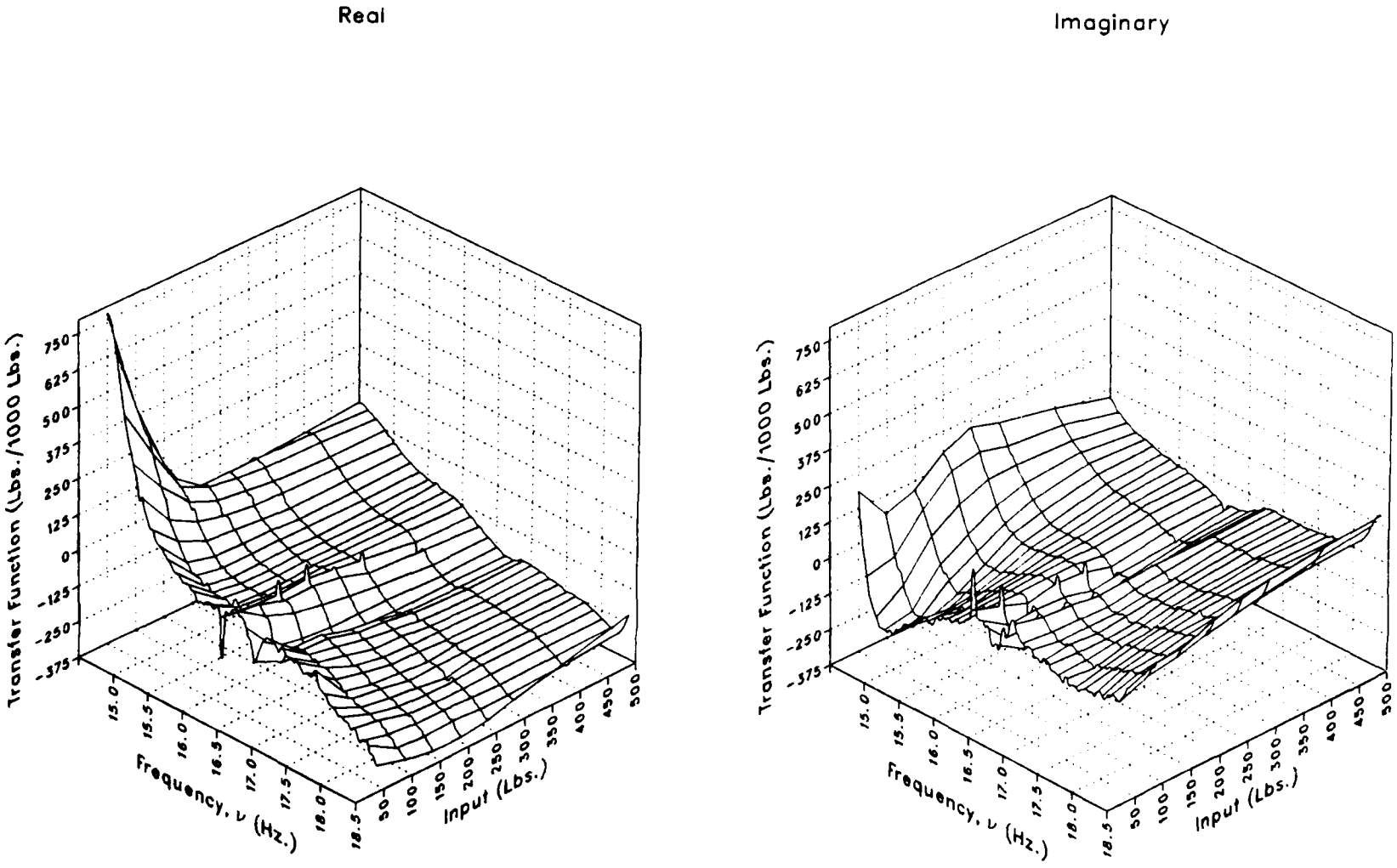

(e) MRLIFTD

Figure 1.– Continued.

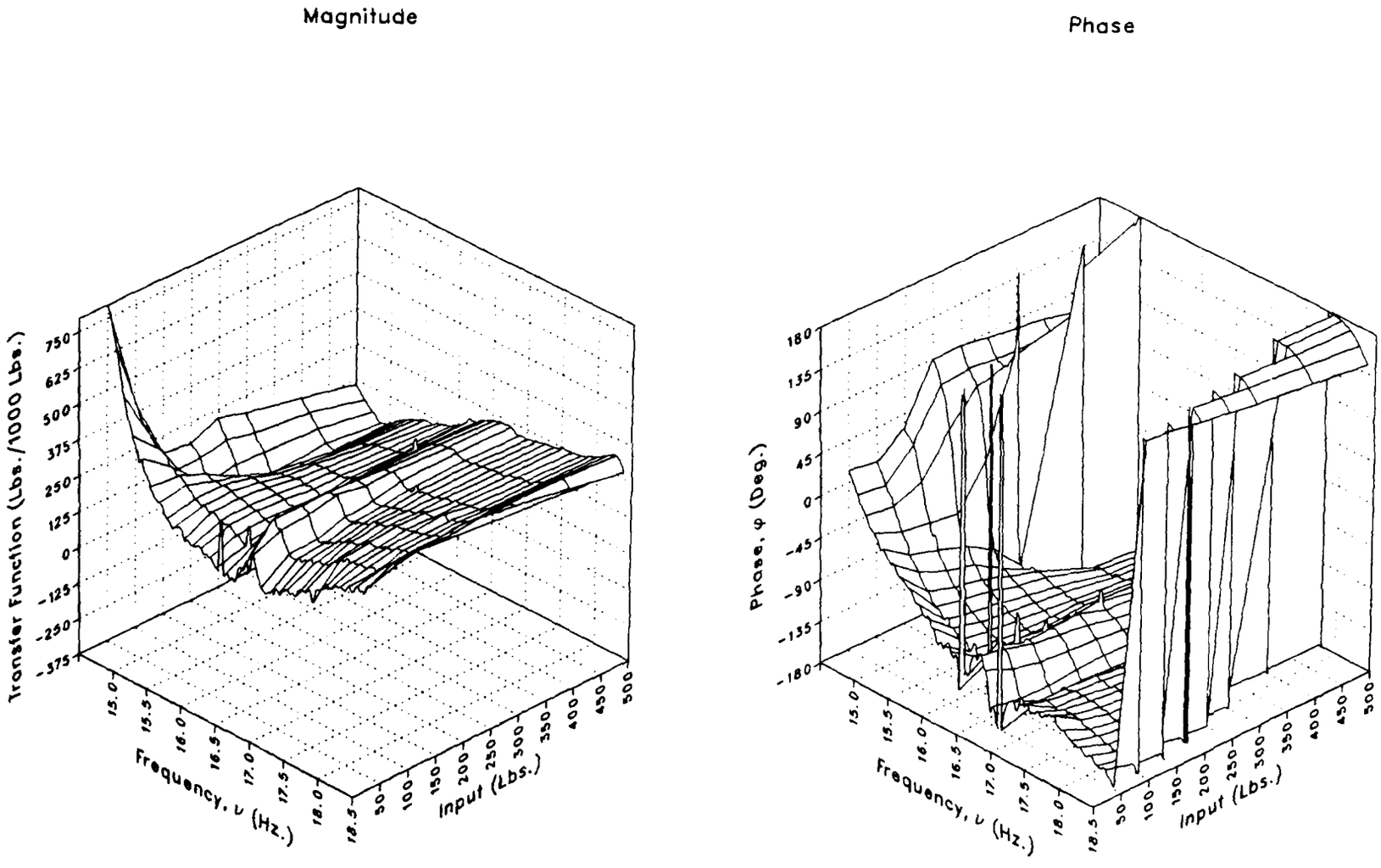

(e) MRLIFTD Concluded.

Figure 1.– Continued.

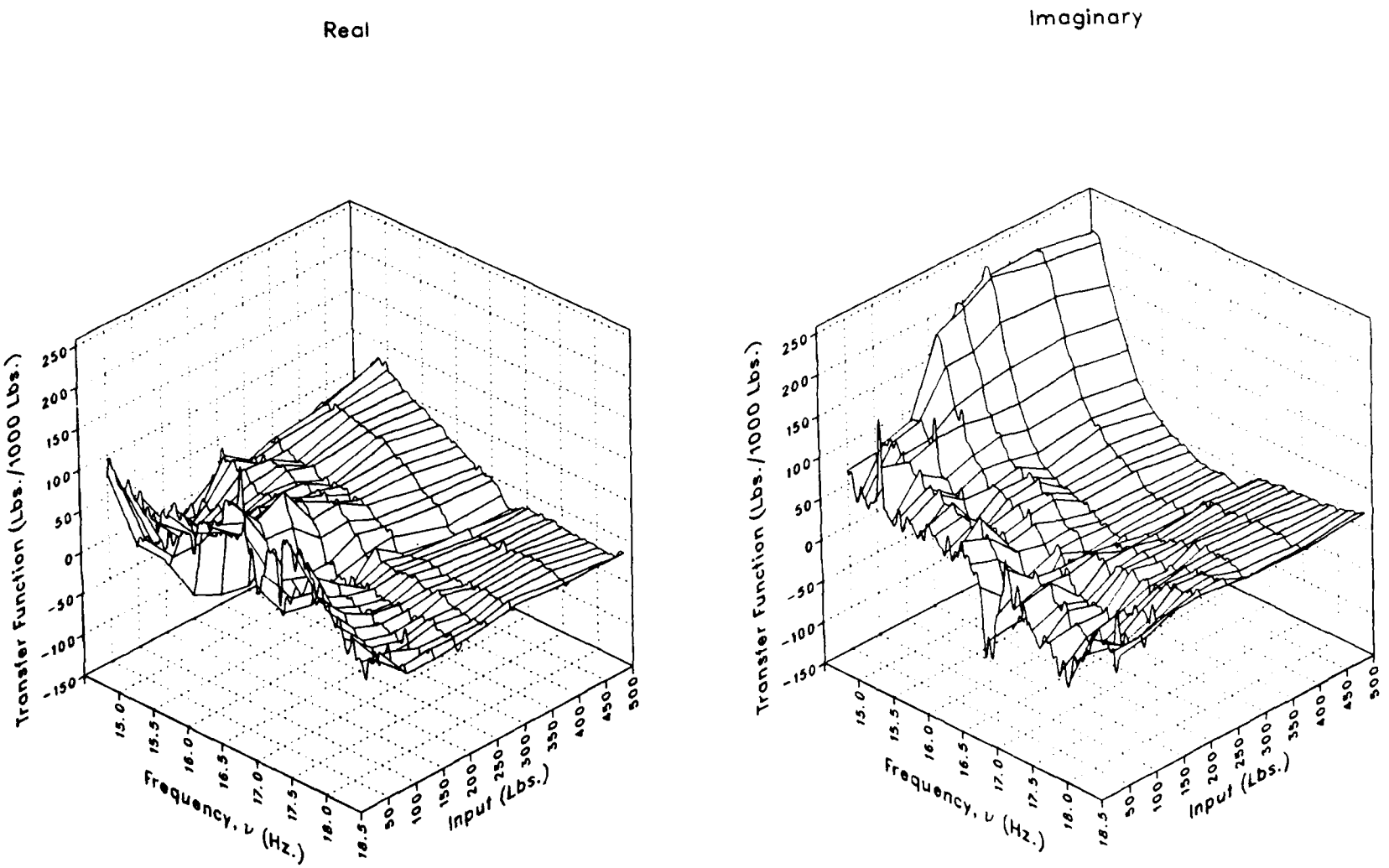

(f) MRGBQCE

Figure 1.– Continued.

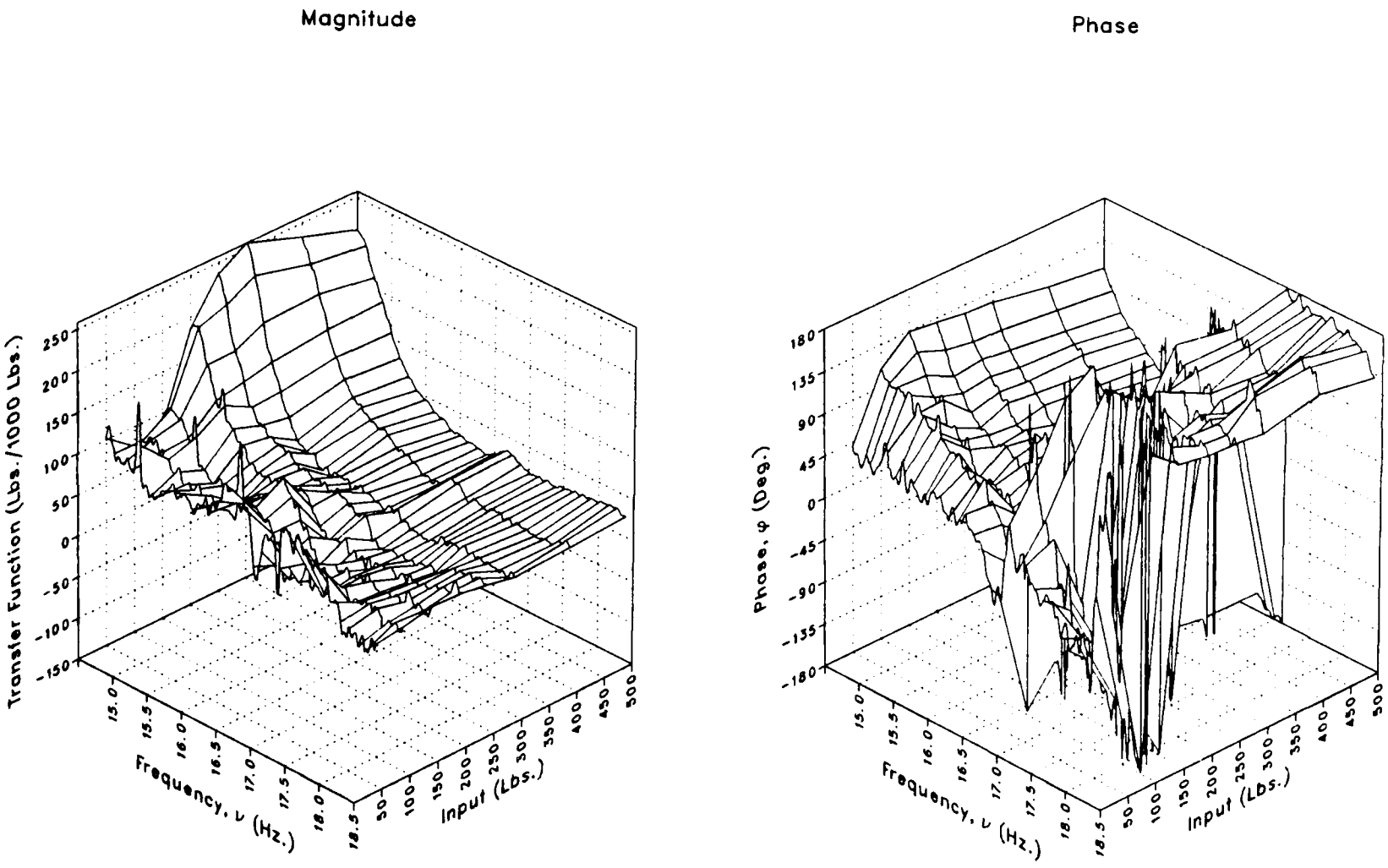

(f) MRGBQCE Concluded.

Figure 1.– Continued.

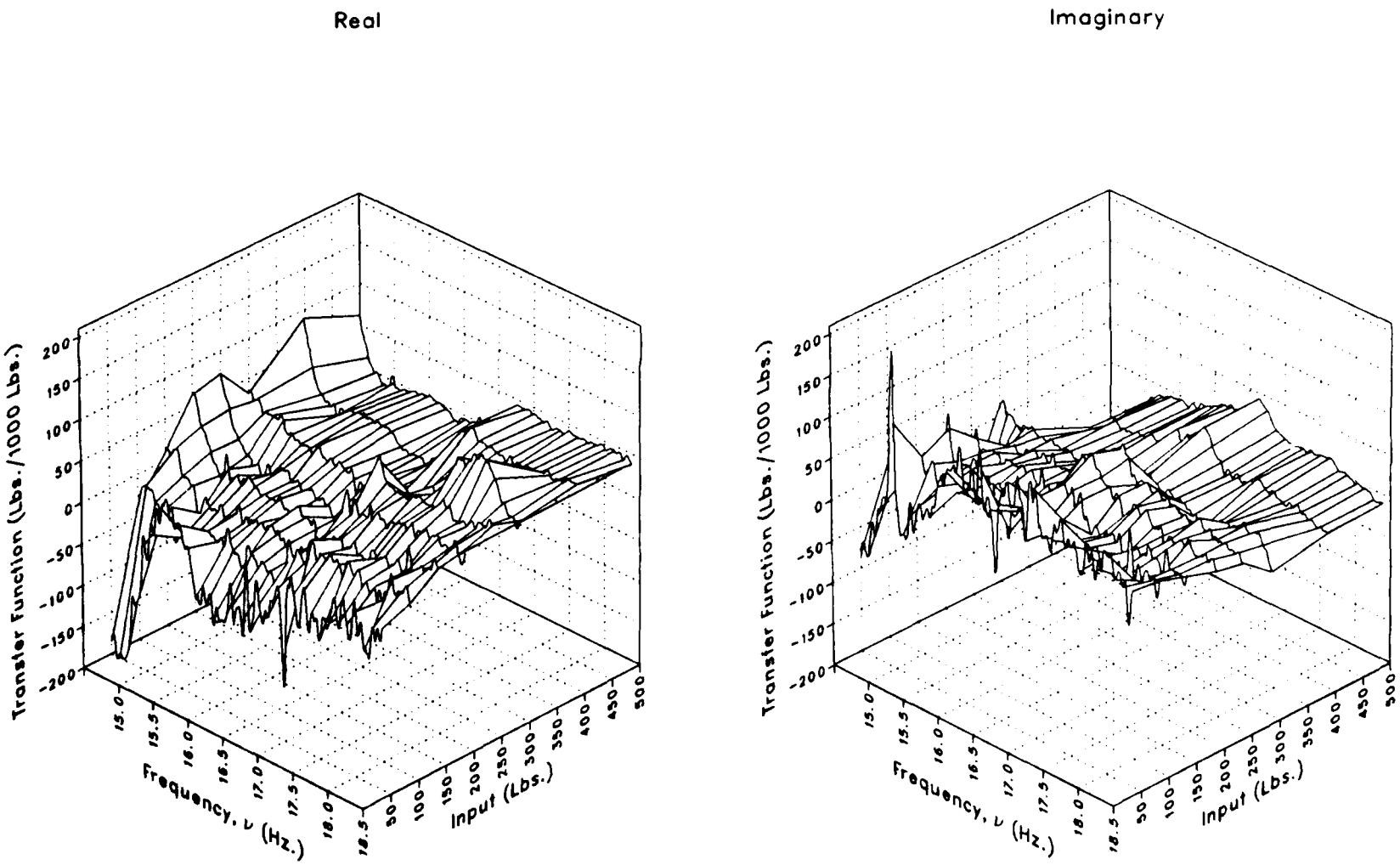

(g) MRGBQCF

Figure 1.– Continued.

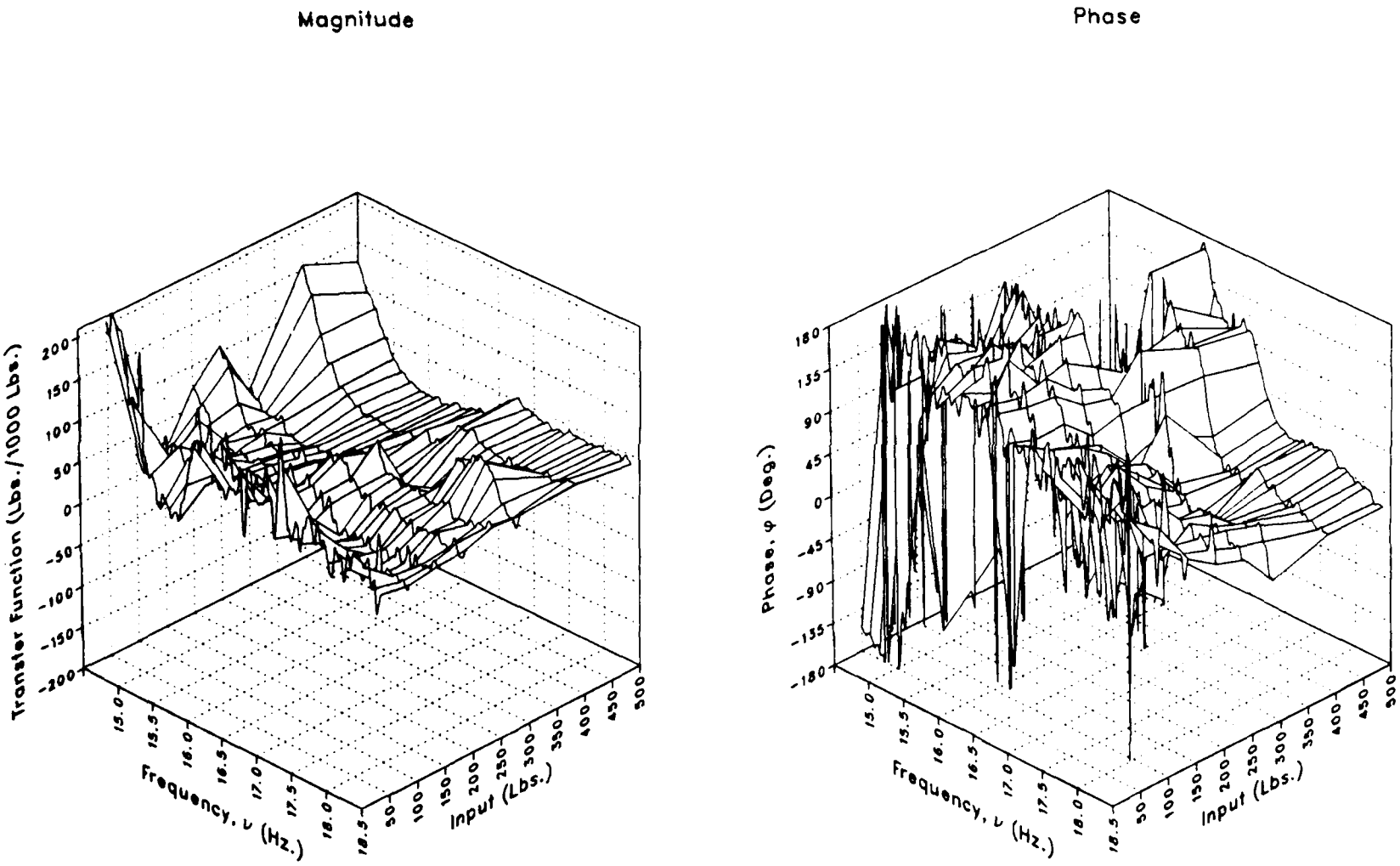

(g) MRGBQCF Concluded.

Figure 1.– Continued.

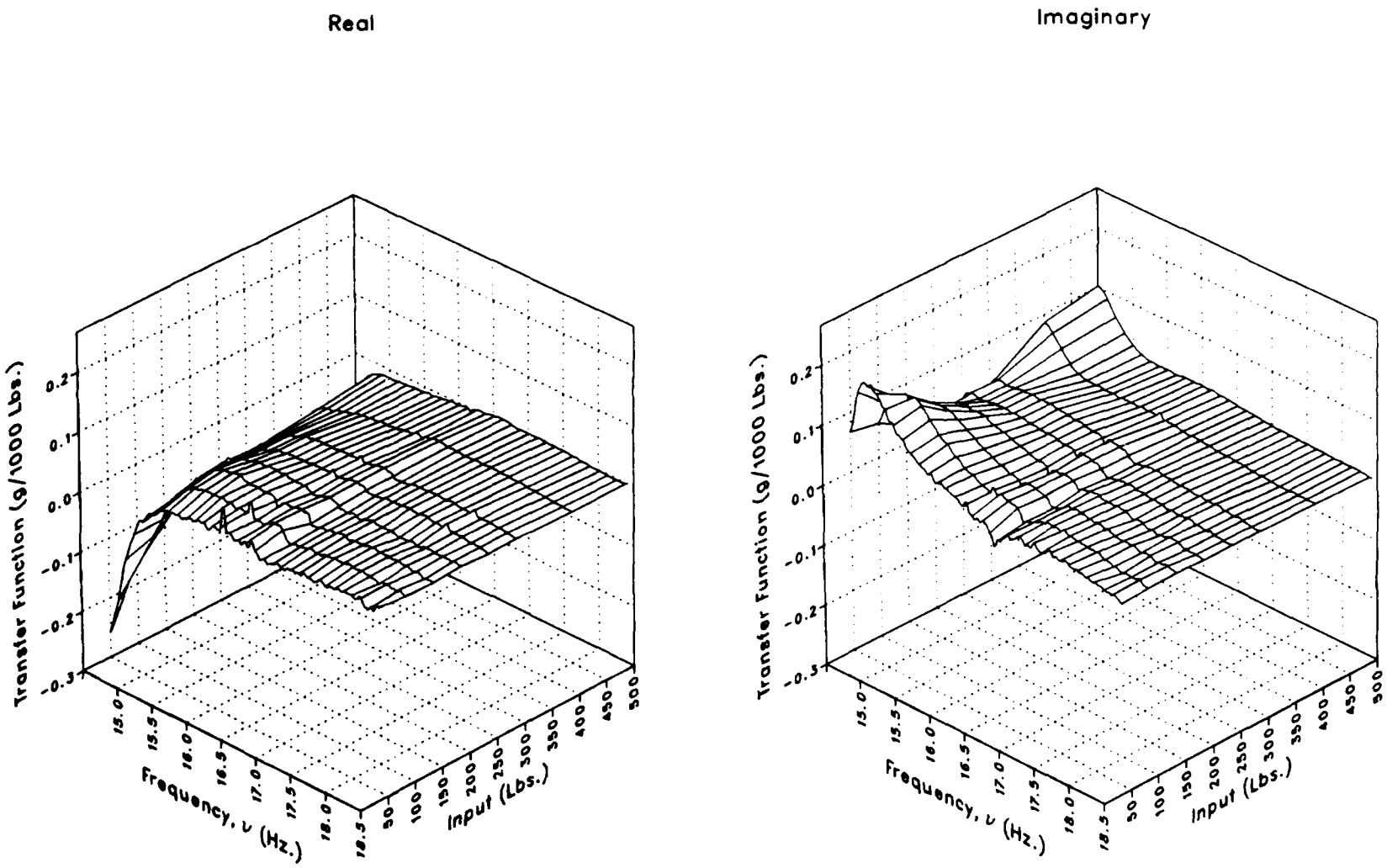

(h) LOMGB

Figure 1.– Continued.

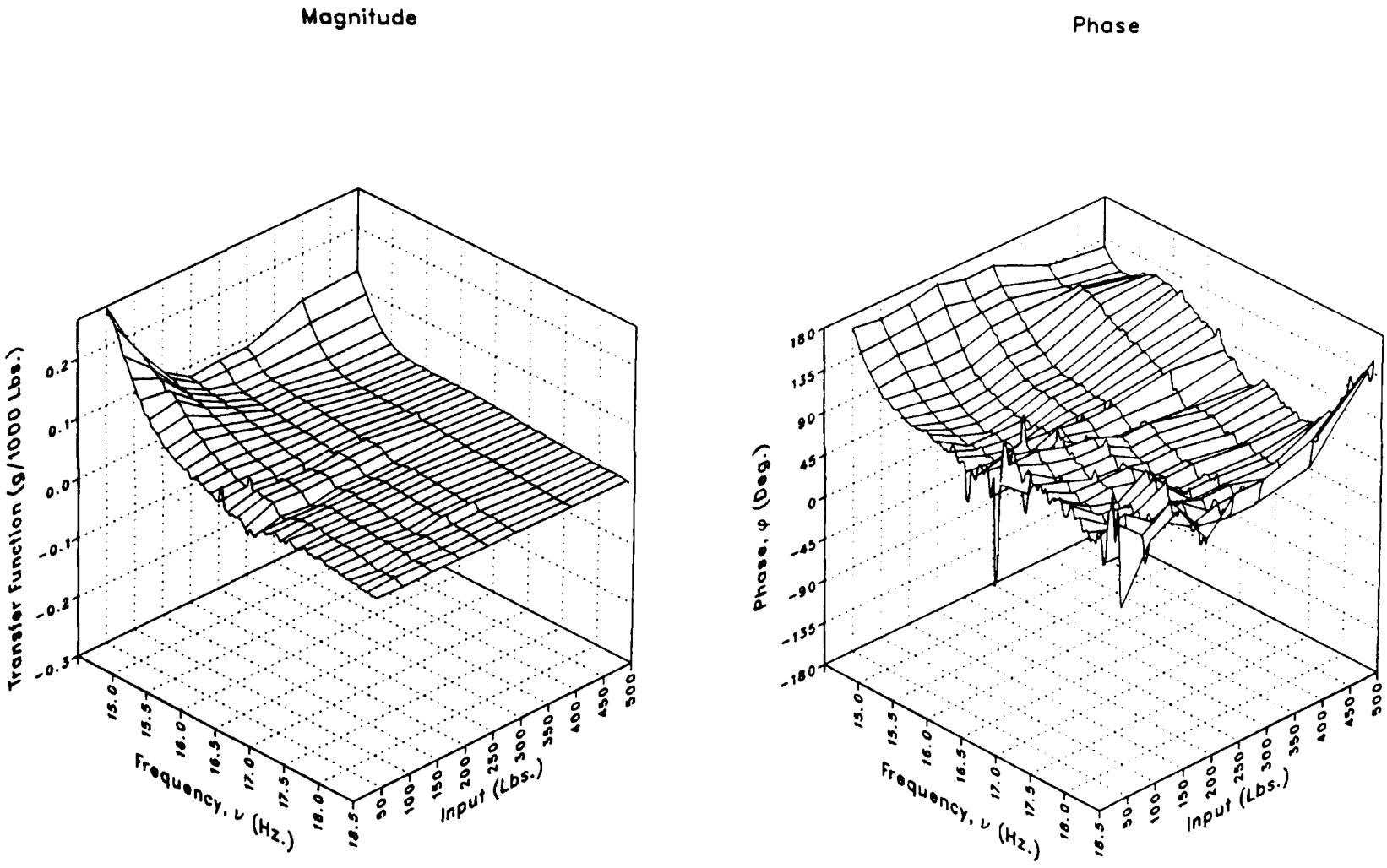

(h) LOMGB Concluded.

Figure 1.– Continued.

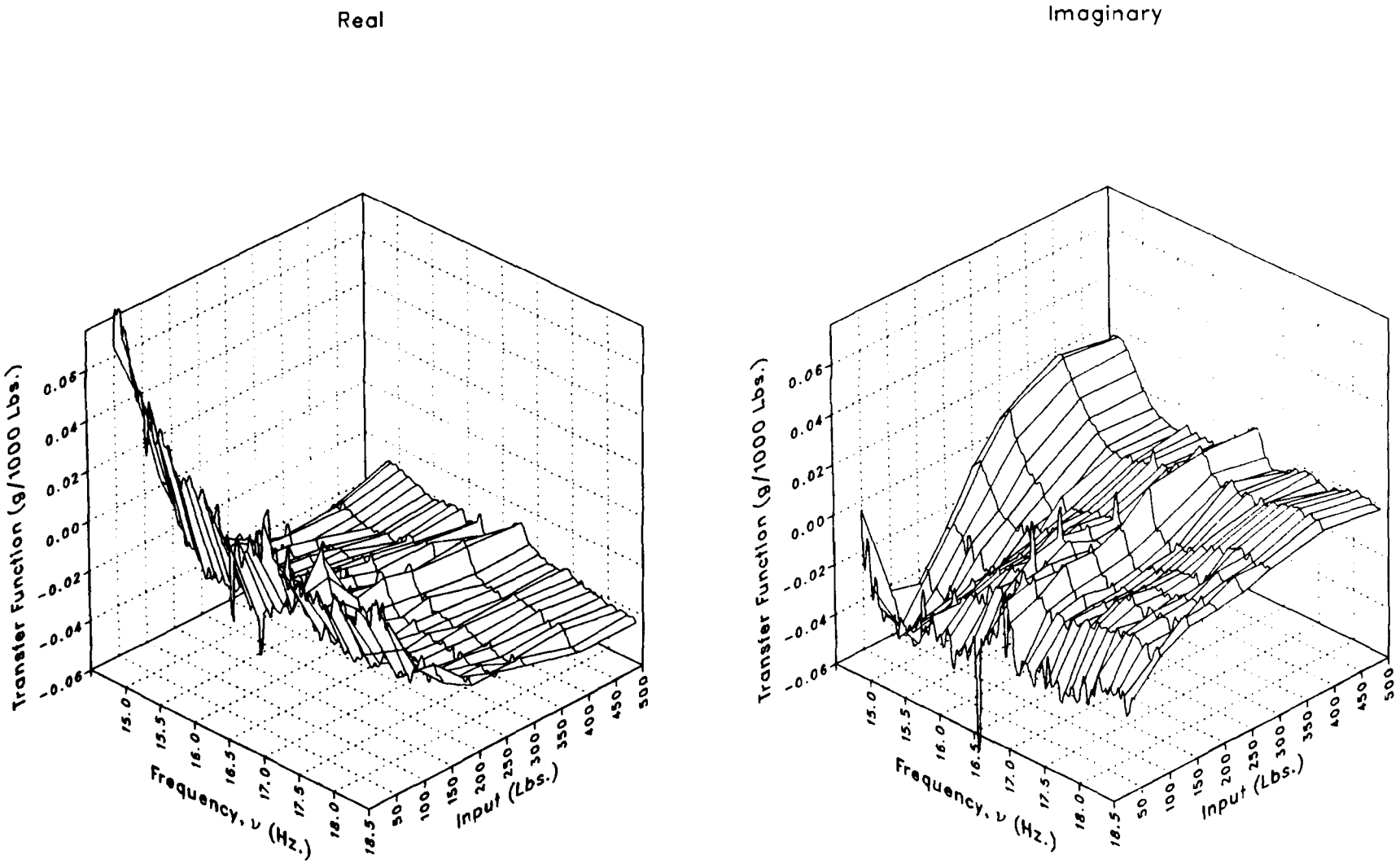

(i) LMGB

Figure 1.– Continued.

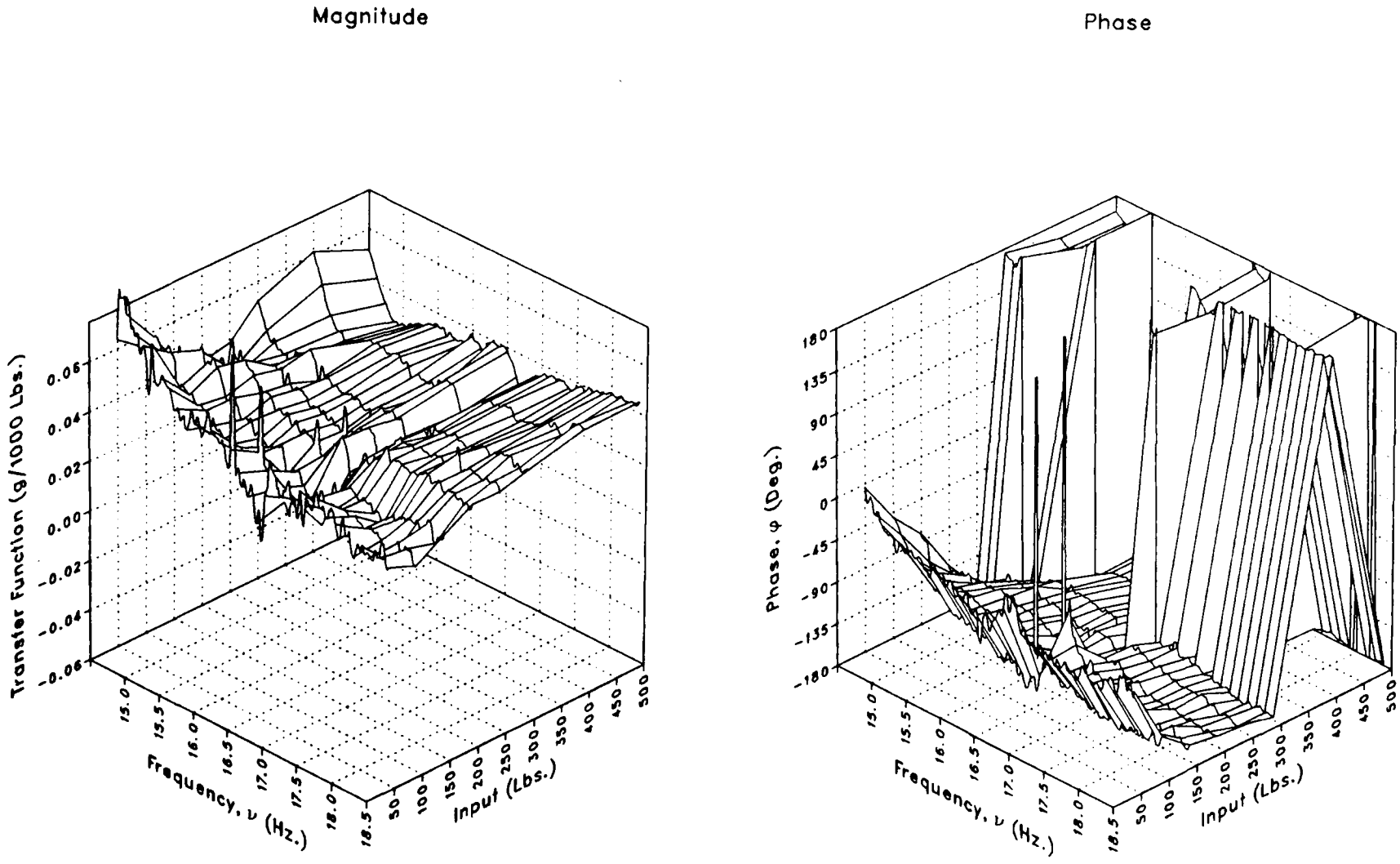

(i) LMGB Concluded.

Figure 1.– Continued.

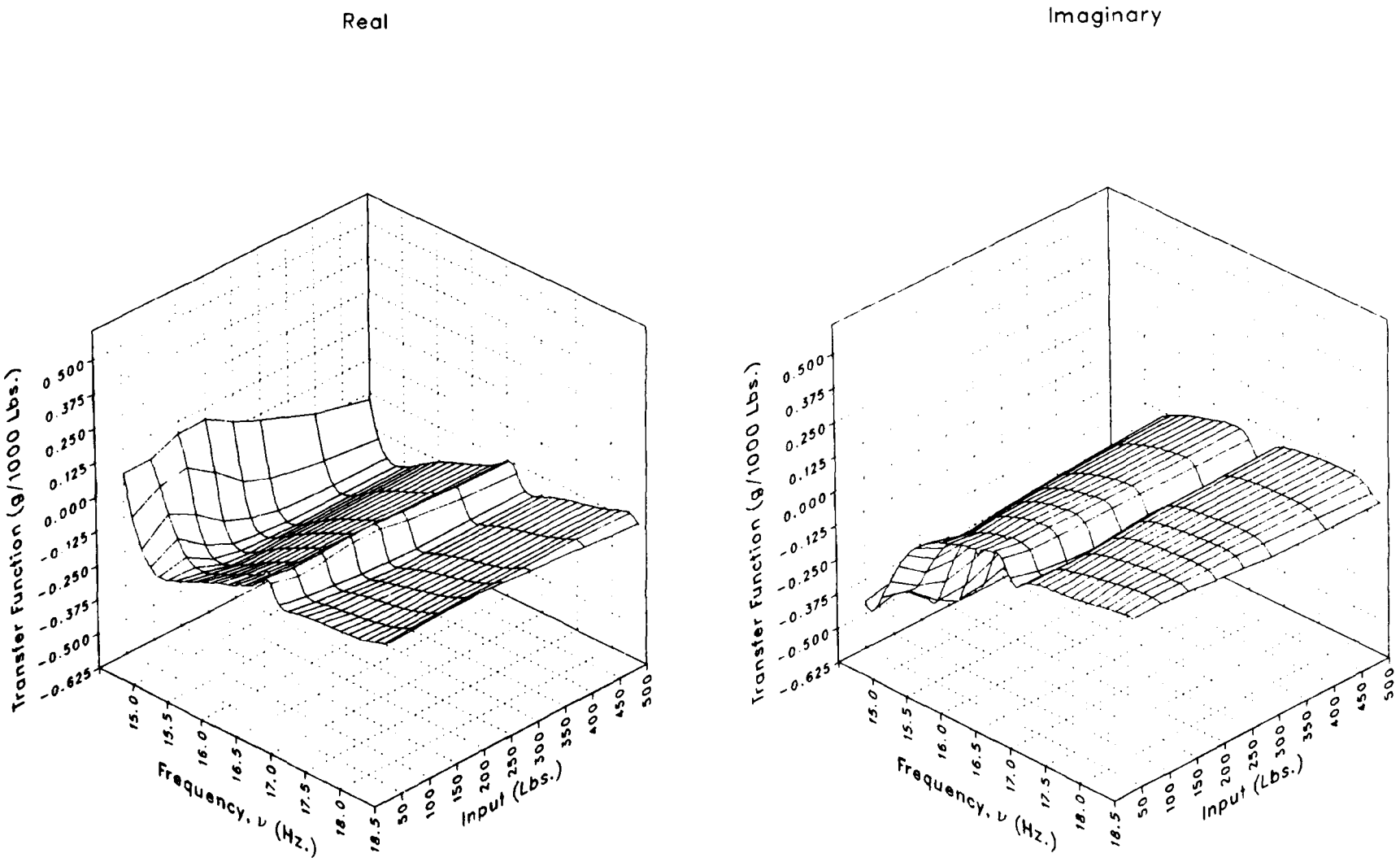

(j) VMGB

Figure 1.– Continued.

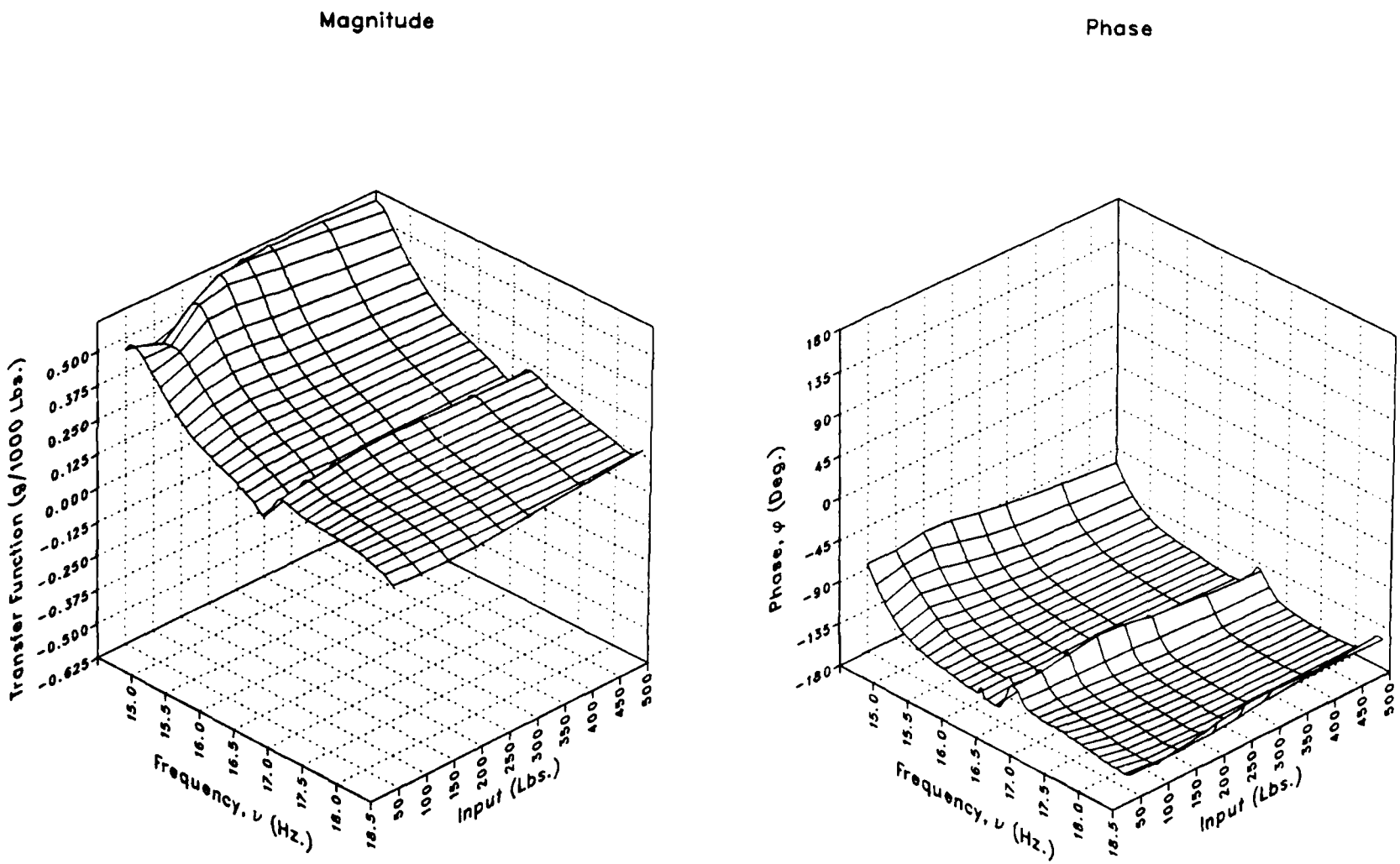

(j) VMGB Concluded.

Figure 1.– Continued.

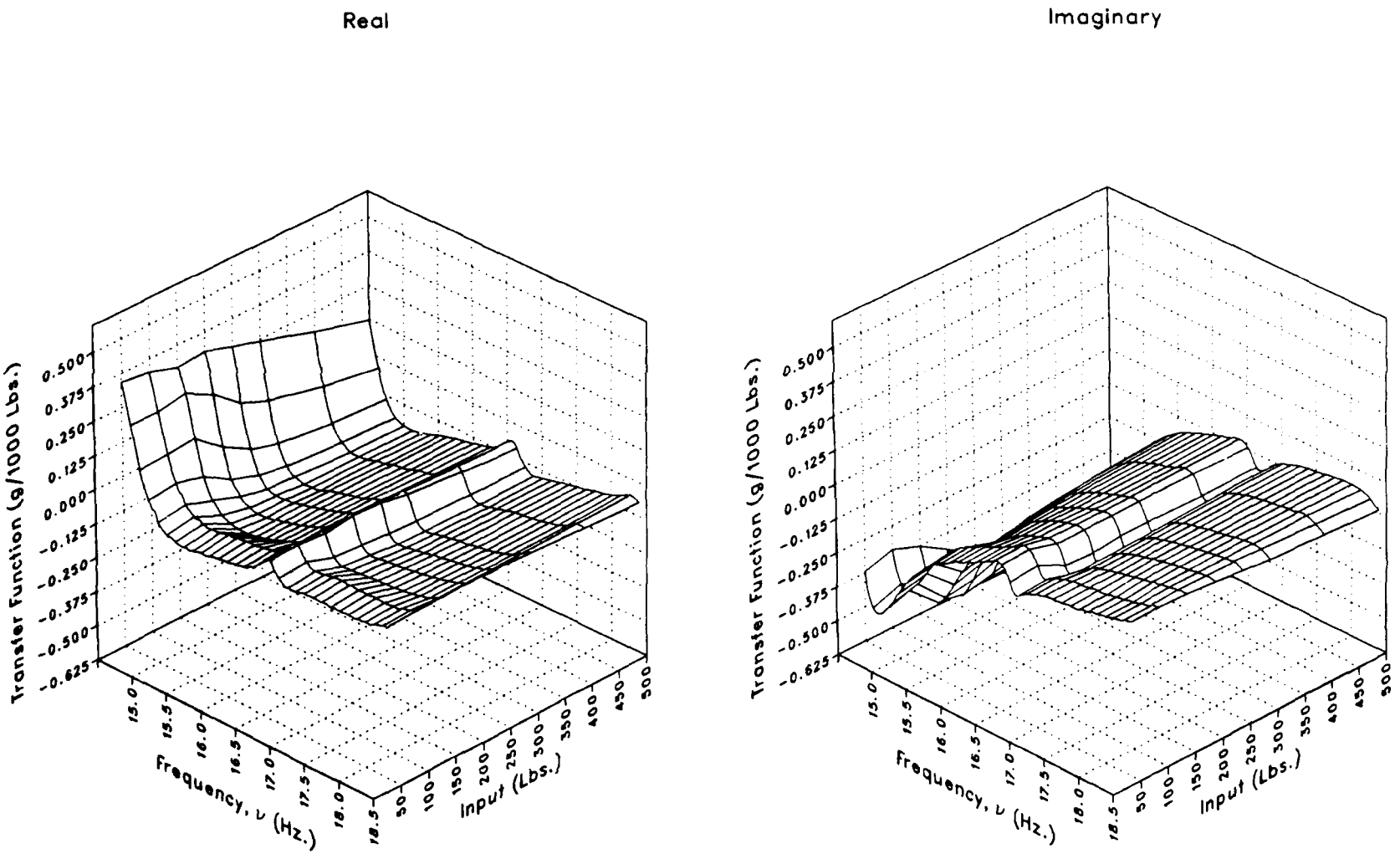

(k) XMRFBPV

Figure 1.– Continued.

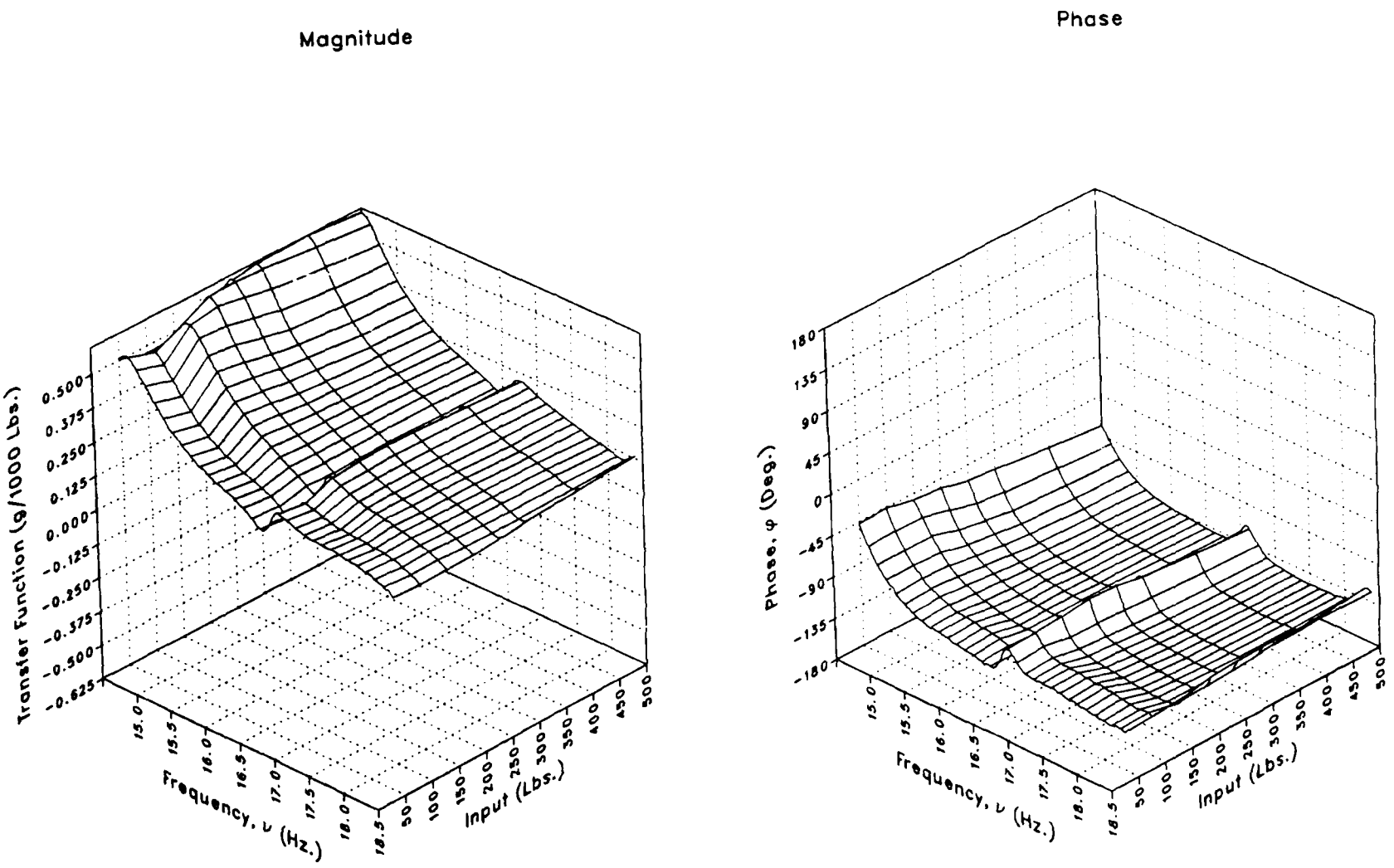

(k) XMRFBPV Concluded.

Figure 1.– Continued.

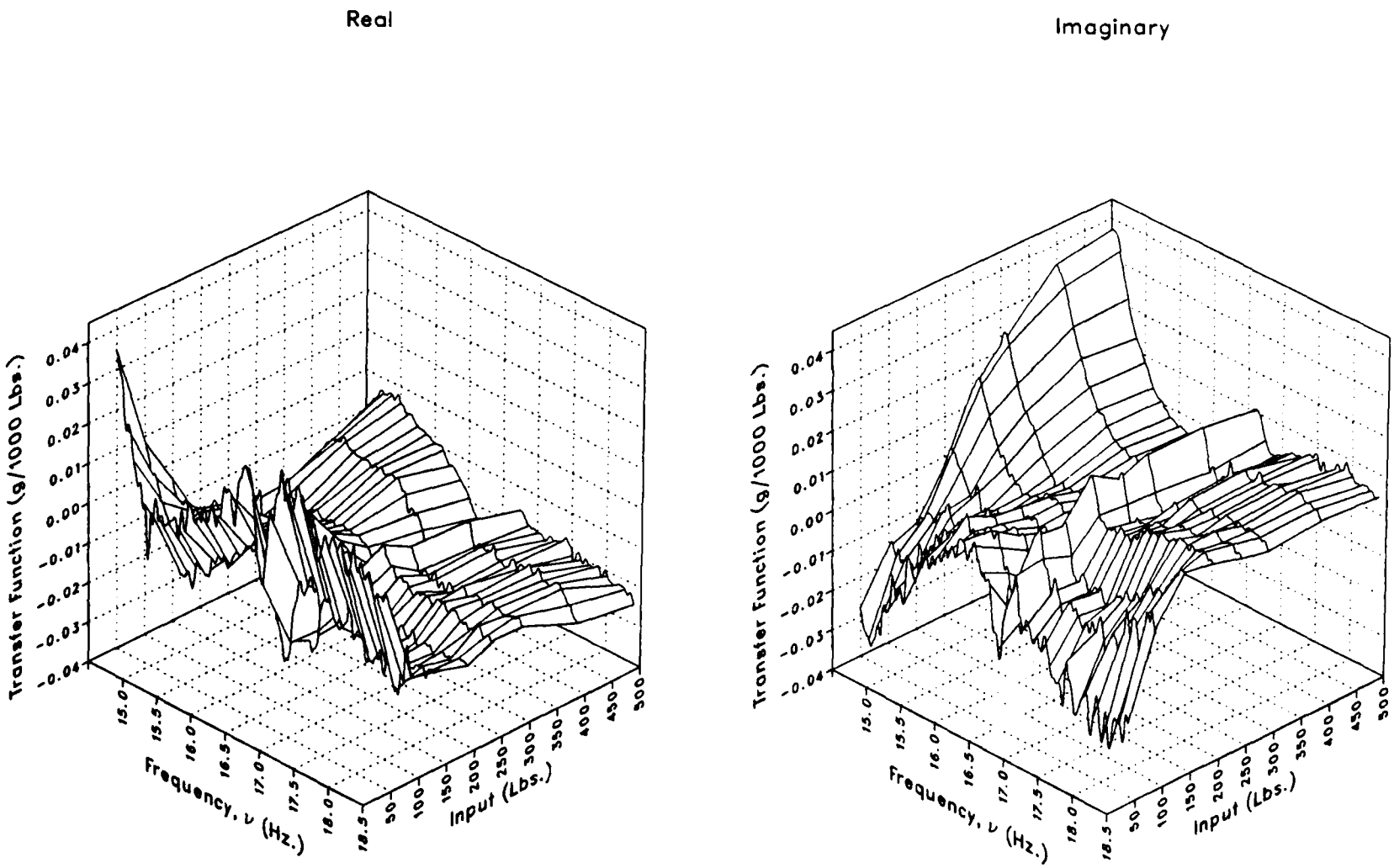

(l) XMRFBPL

Figure 1.– Continued.

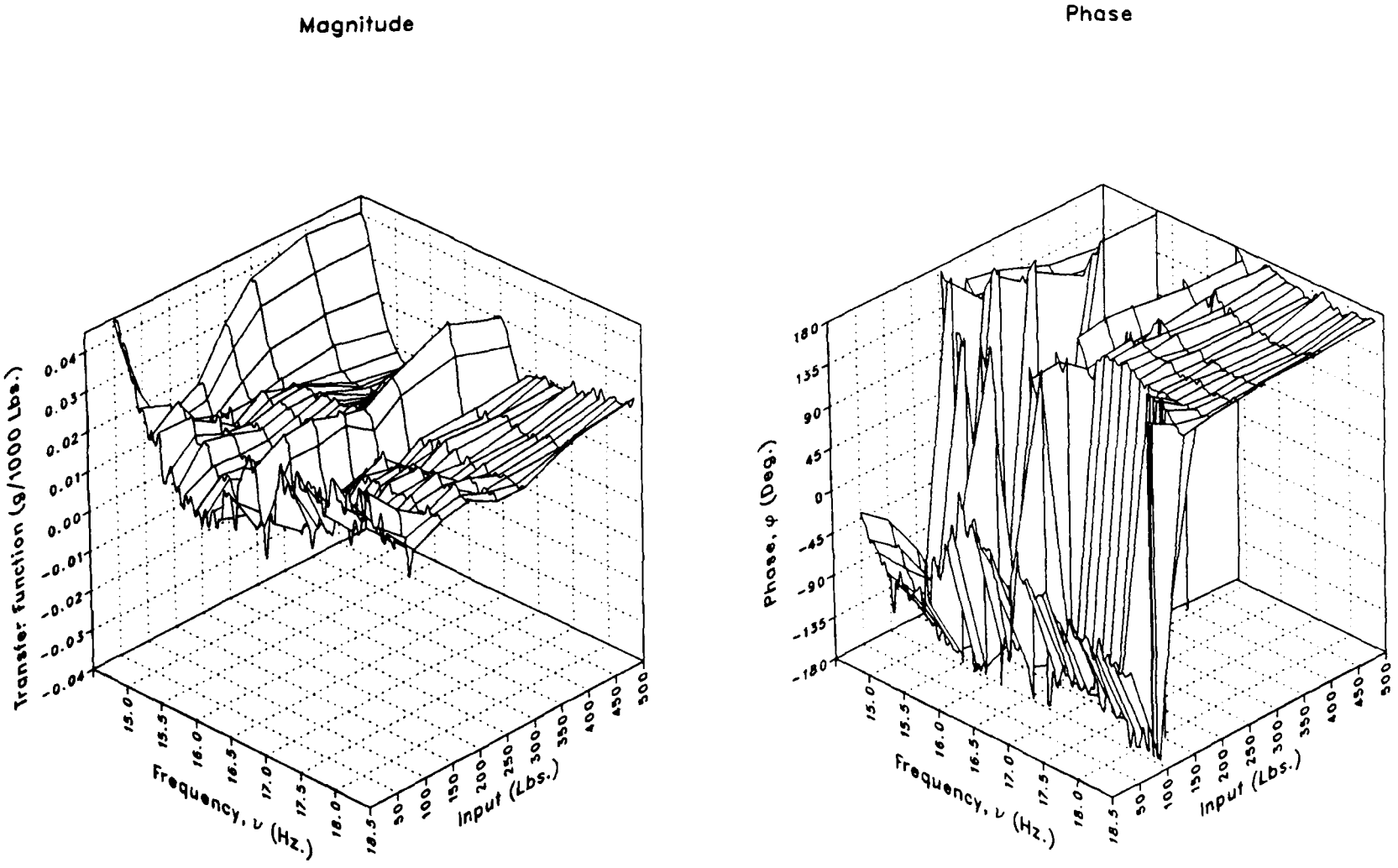

(l) XMRFBPL Concluded.

Figure 1.– Continued.

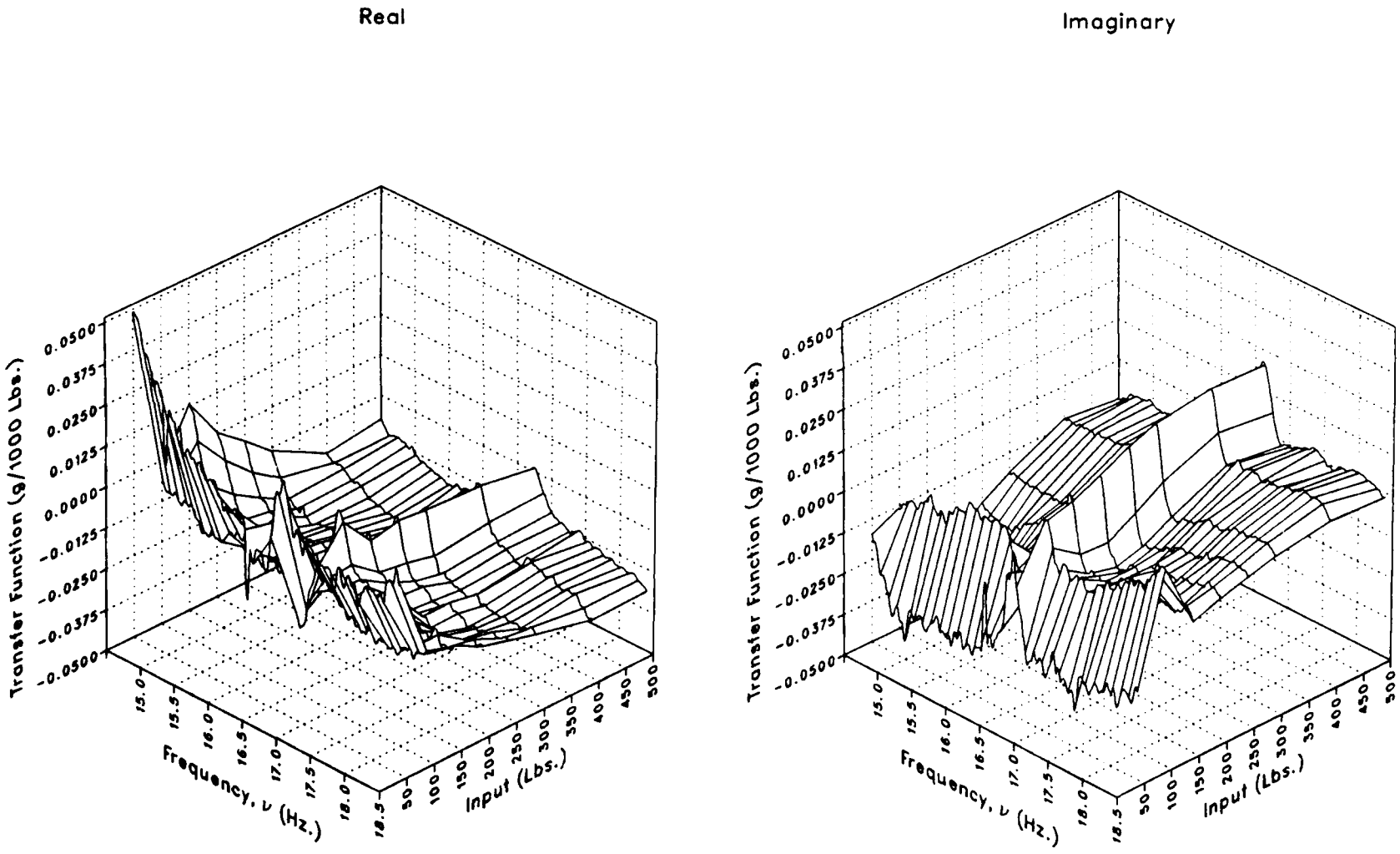

(m) XMRFBPLO

Figure 1.– Continued.

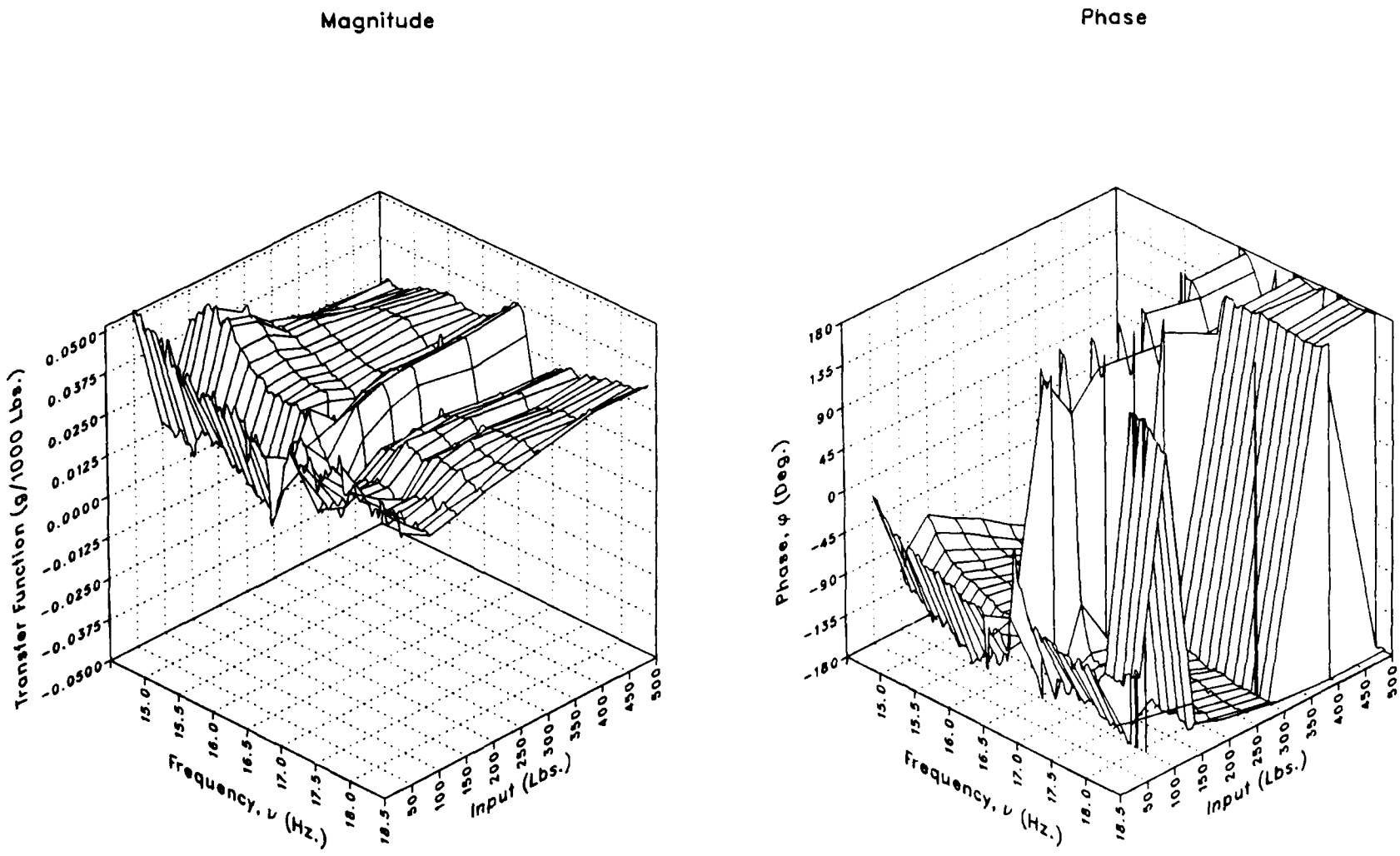

(m) XMRFBPLO Concluded.

Figure 1.– Continued.

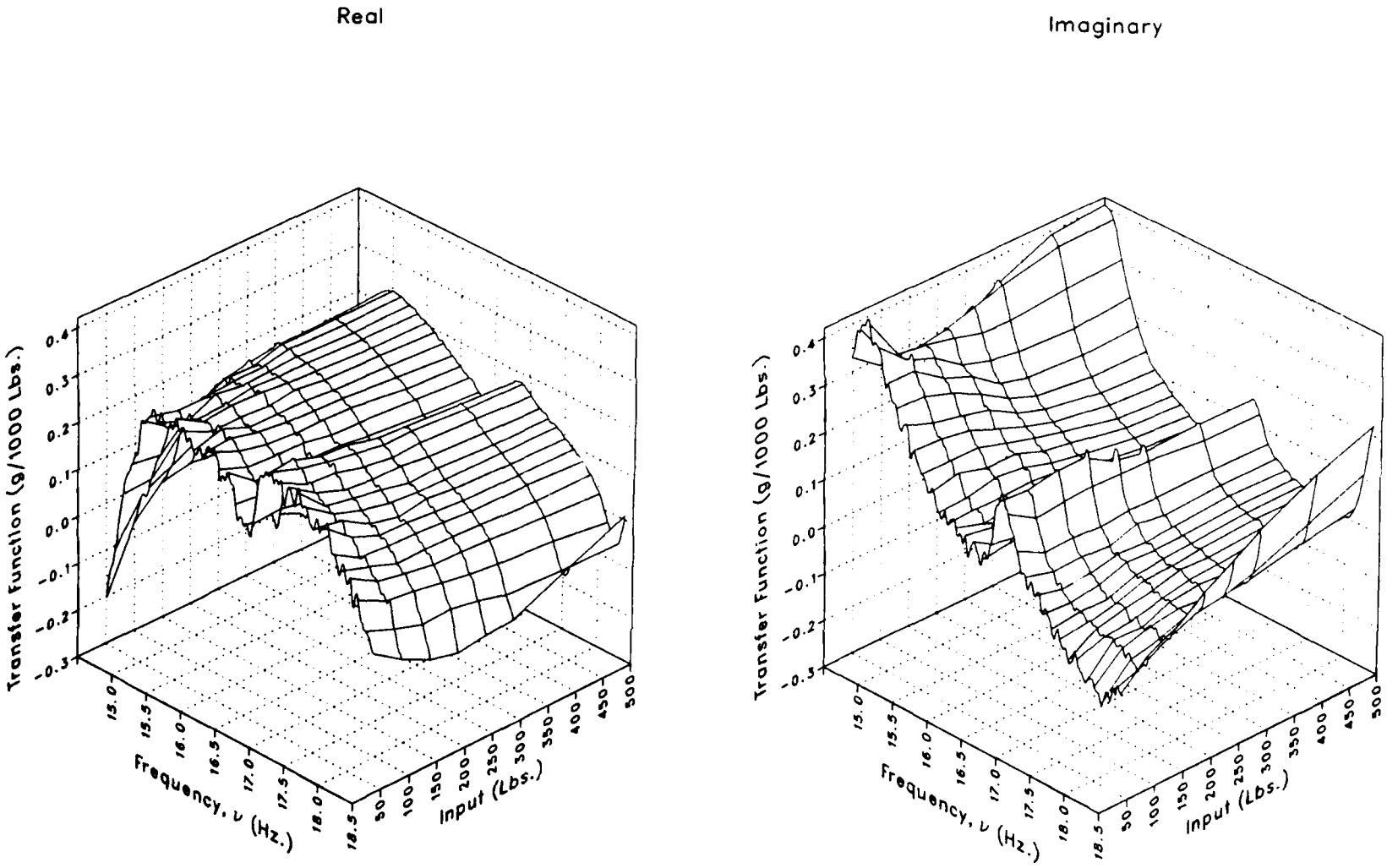

(n) STA56NV

Figure 1.– Continued.

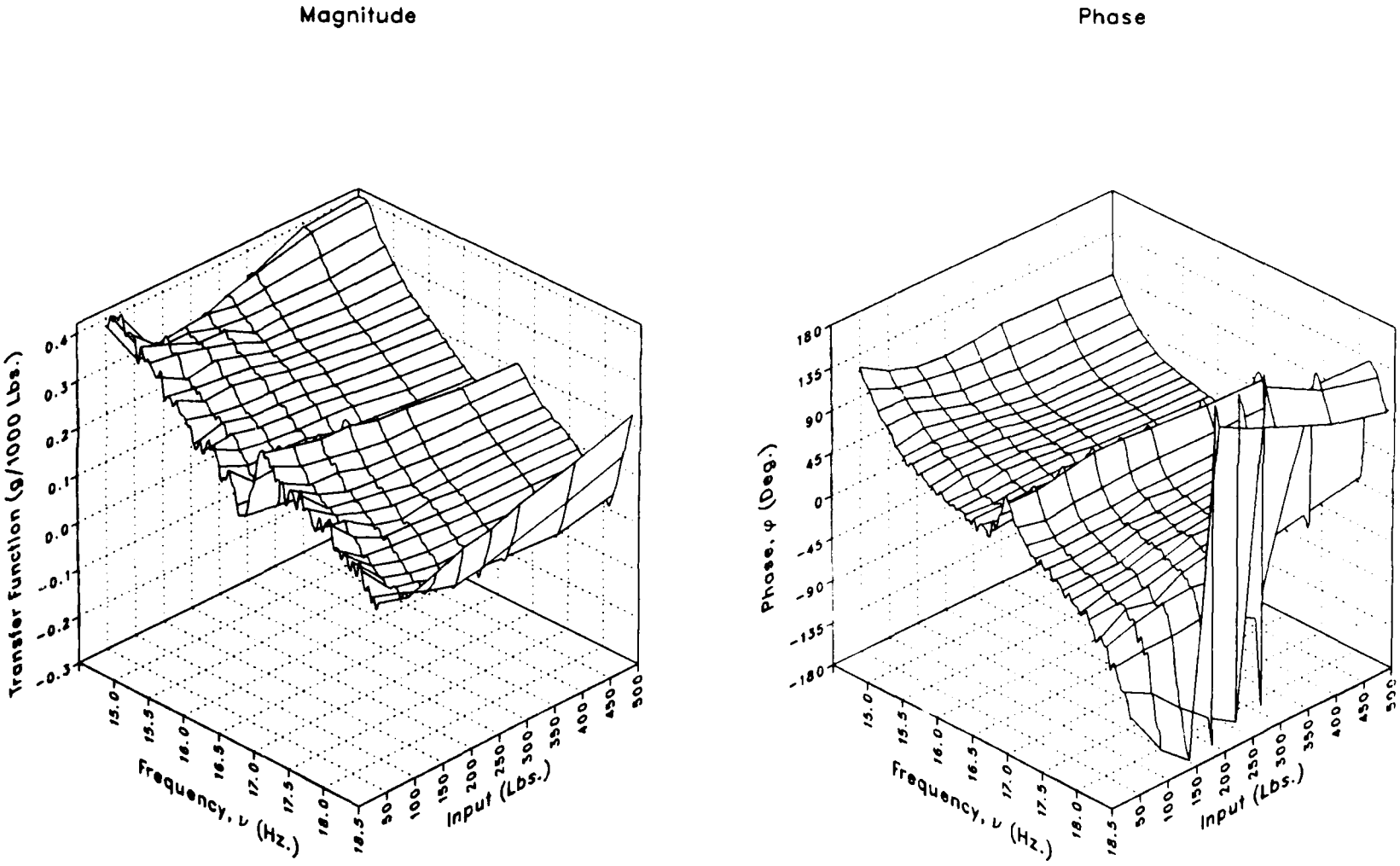

(n) STA56NV Concluded.

Figure 1.– Continued.

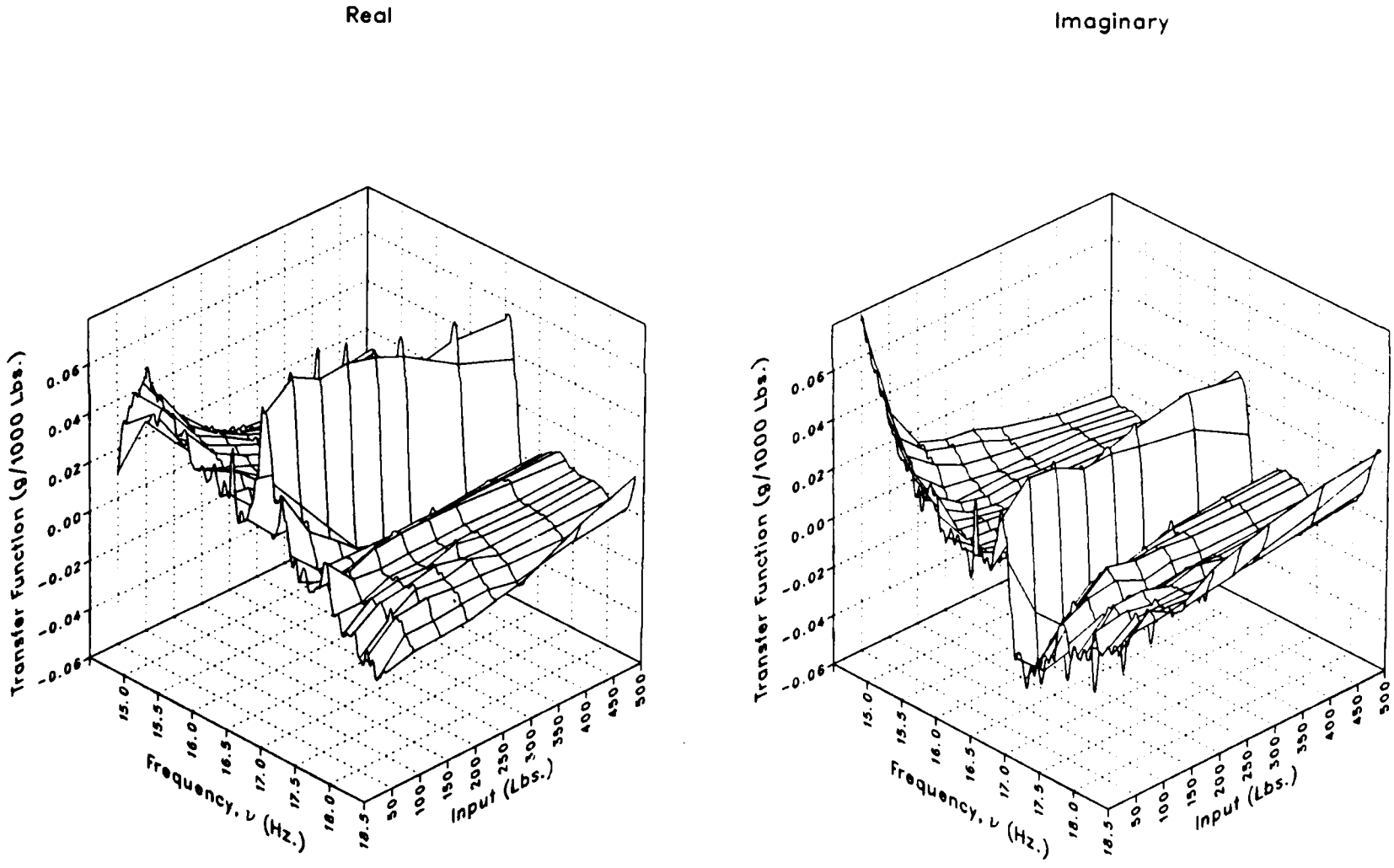

(o) STA56NL

Figure 1.– Continued.

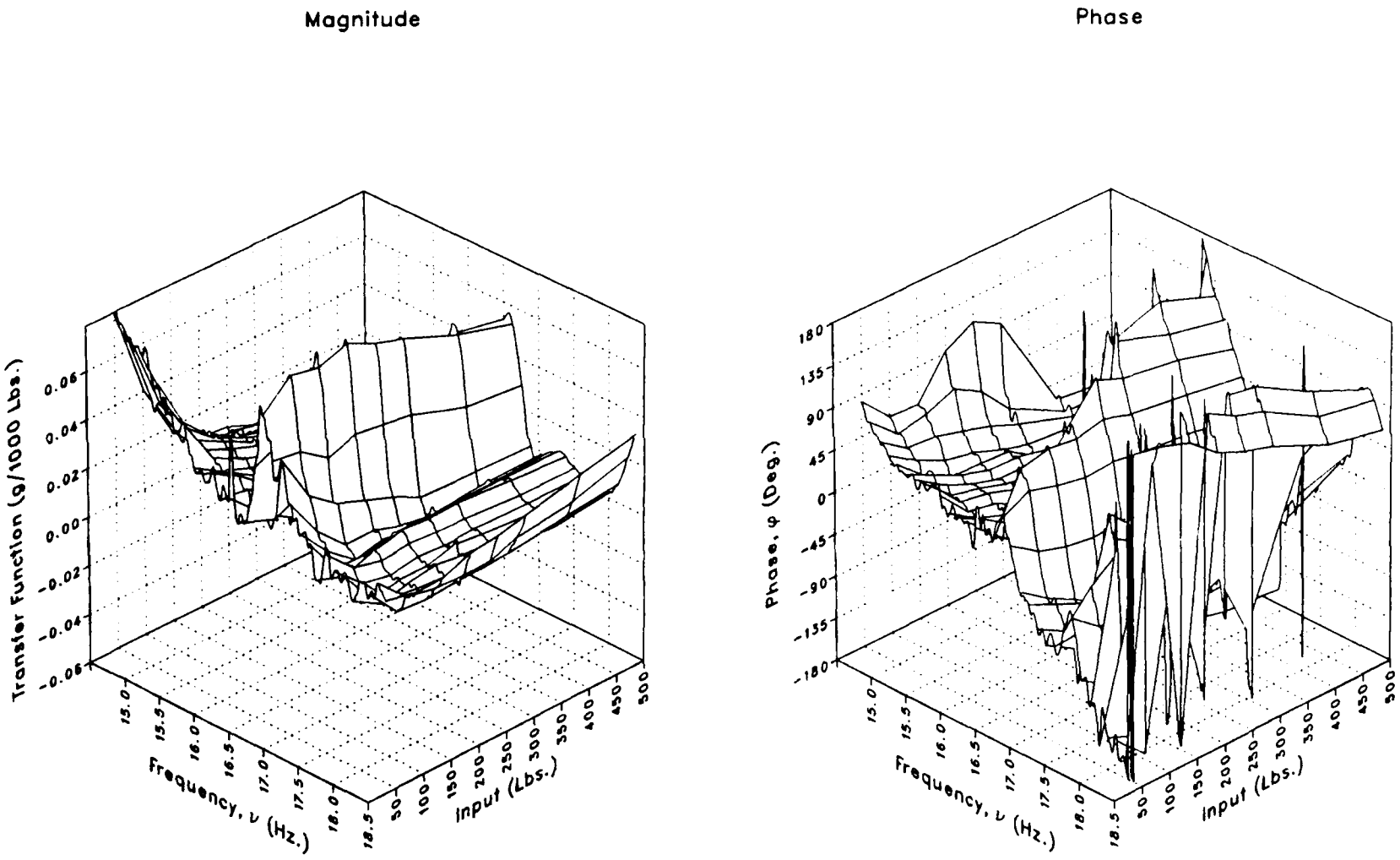

(o) STA56NL Concluded.

Figure 1.– Continued.

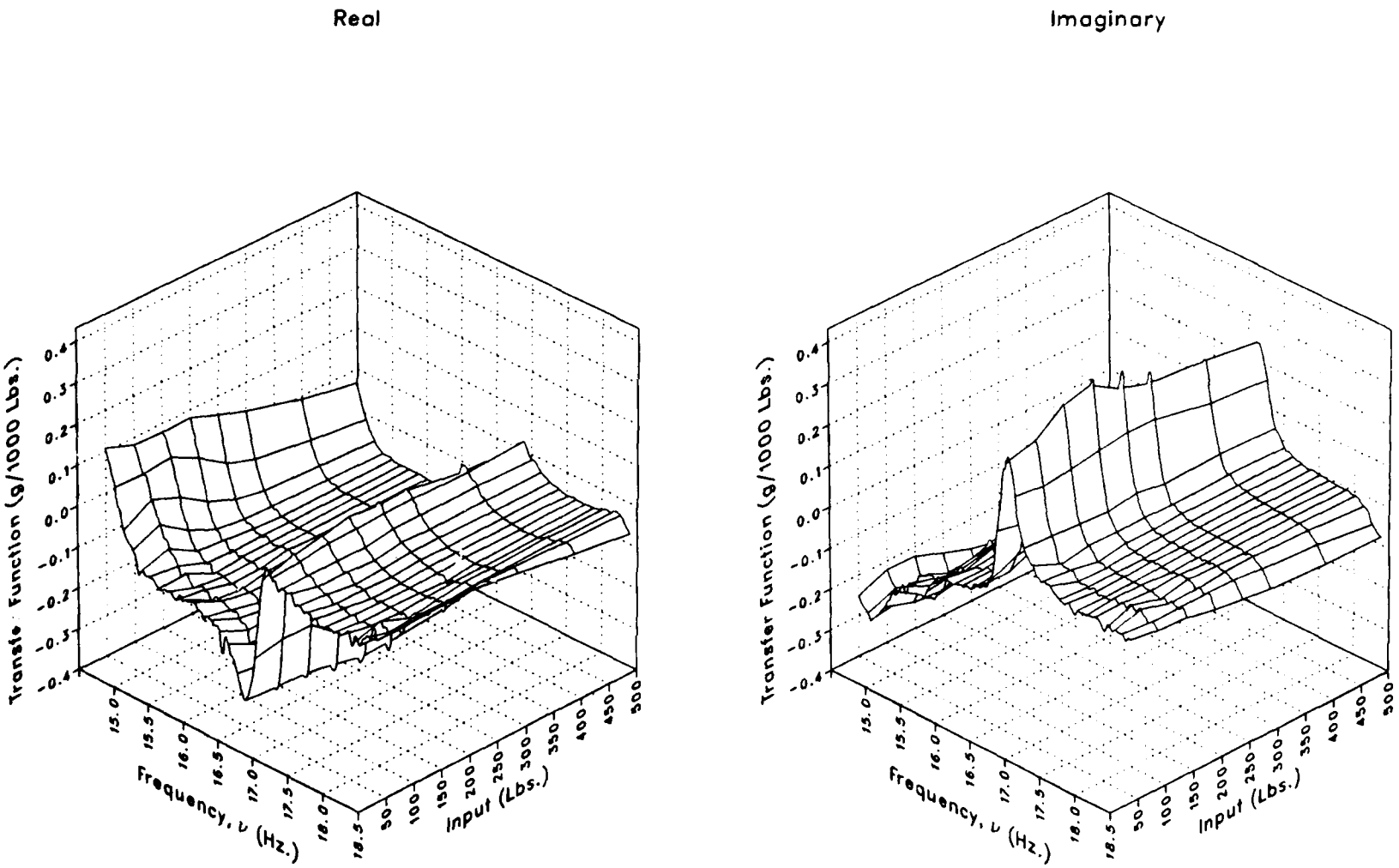

(p) VWGTPRT

Figure 1.– Continued.

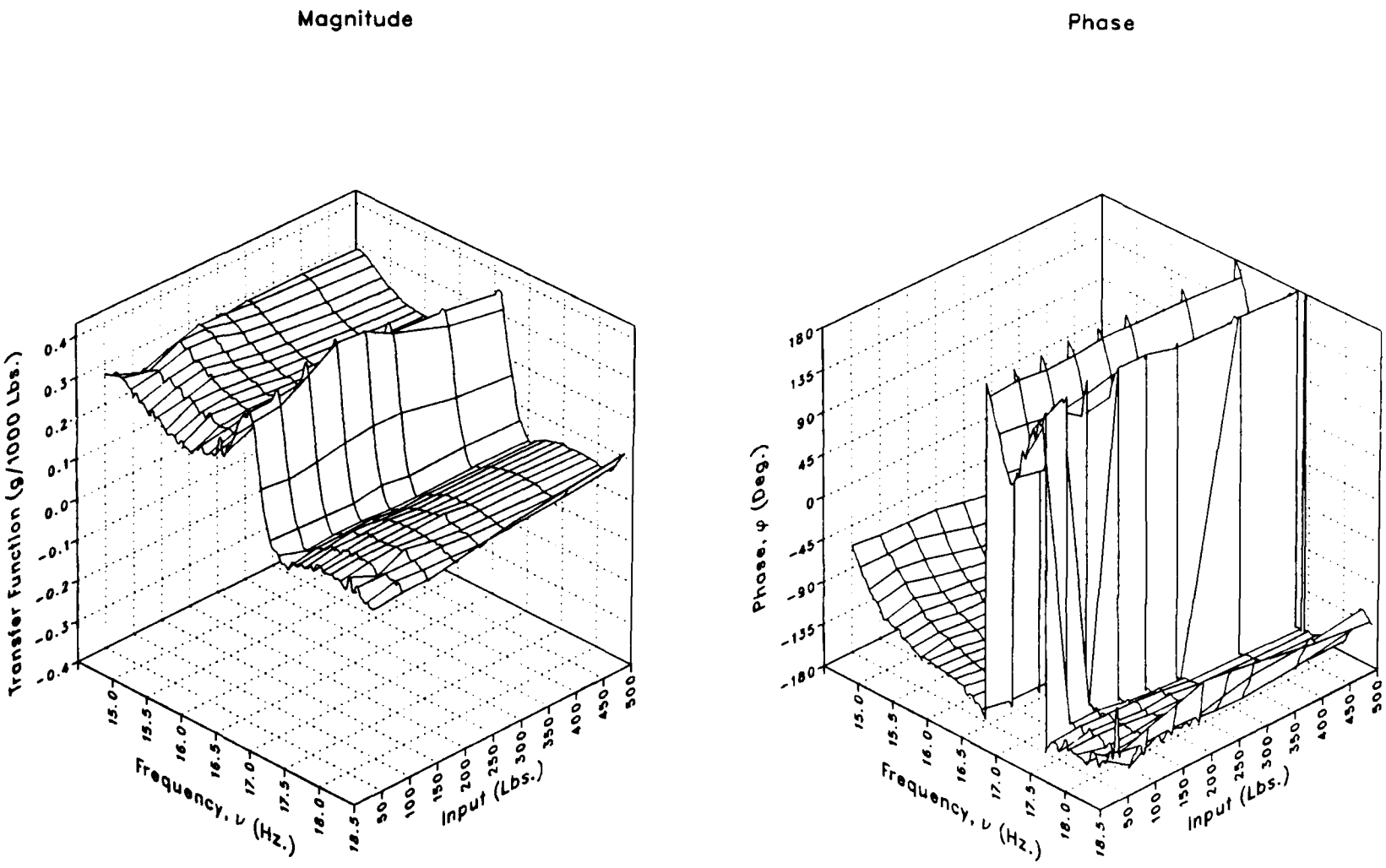

(p) VWGTPRT Concluded.

Figure 1.– Continued.

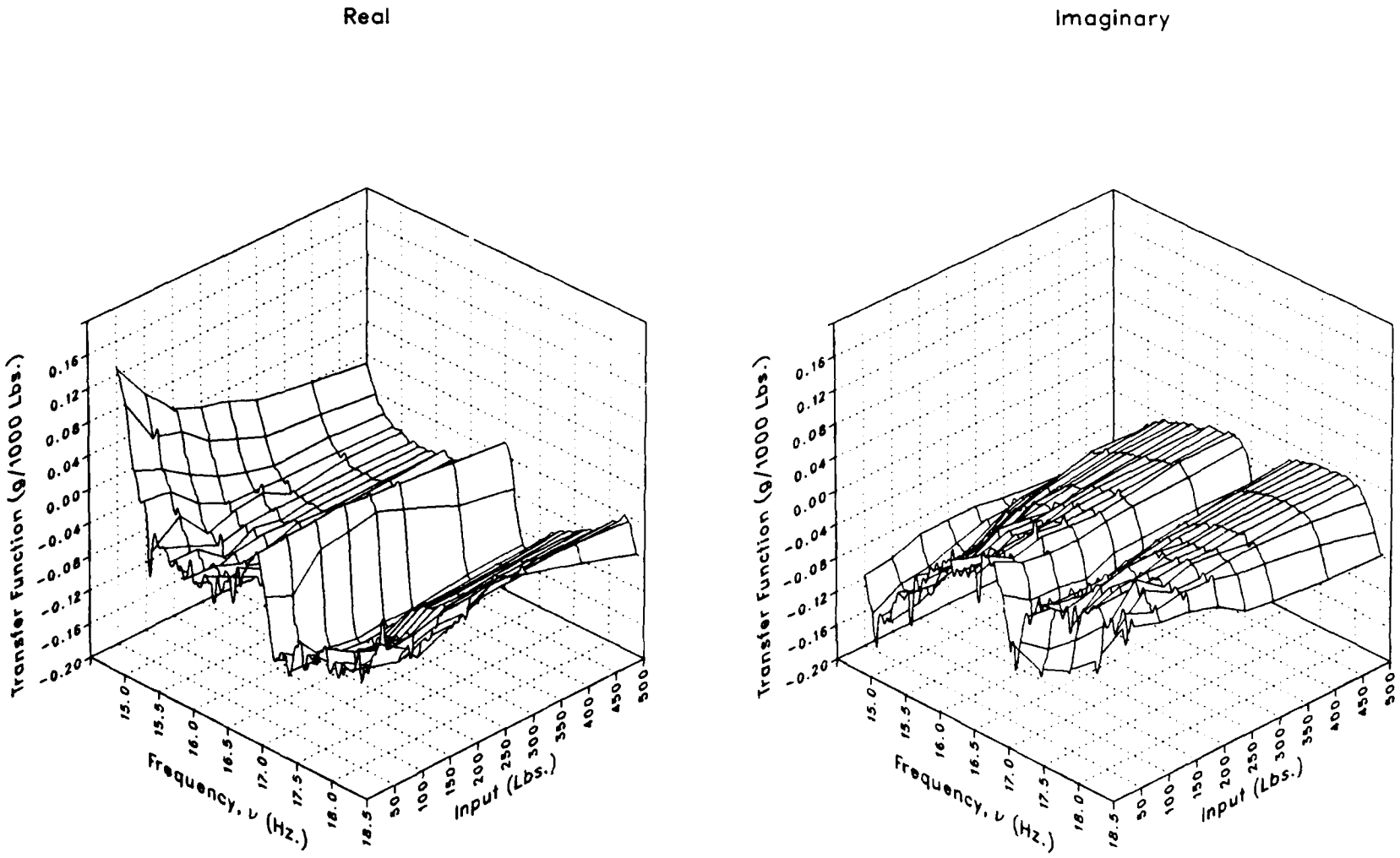

(q) VWGTPLT

Figure 1.– Continued.

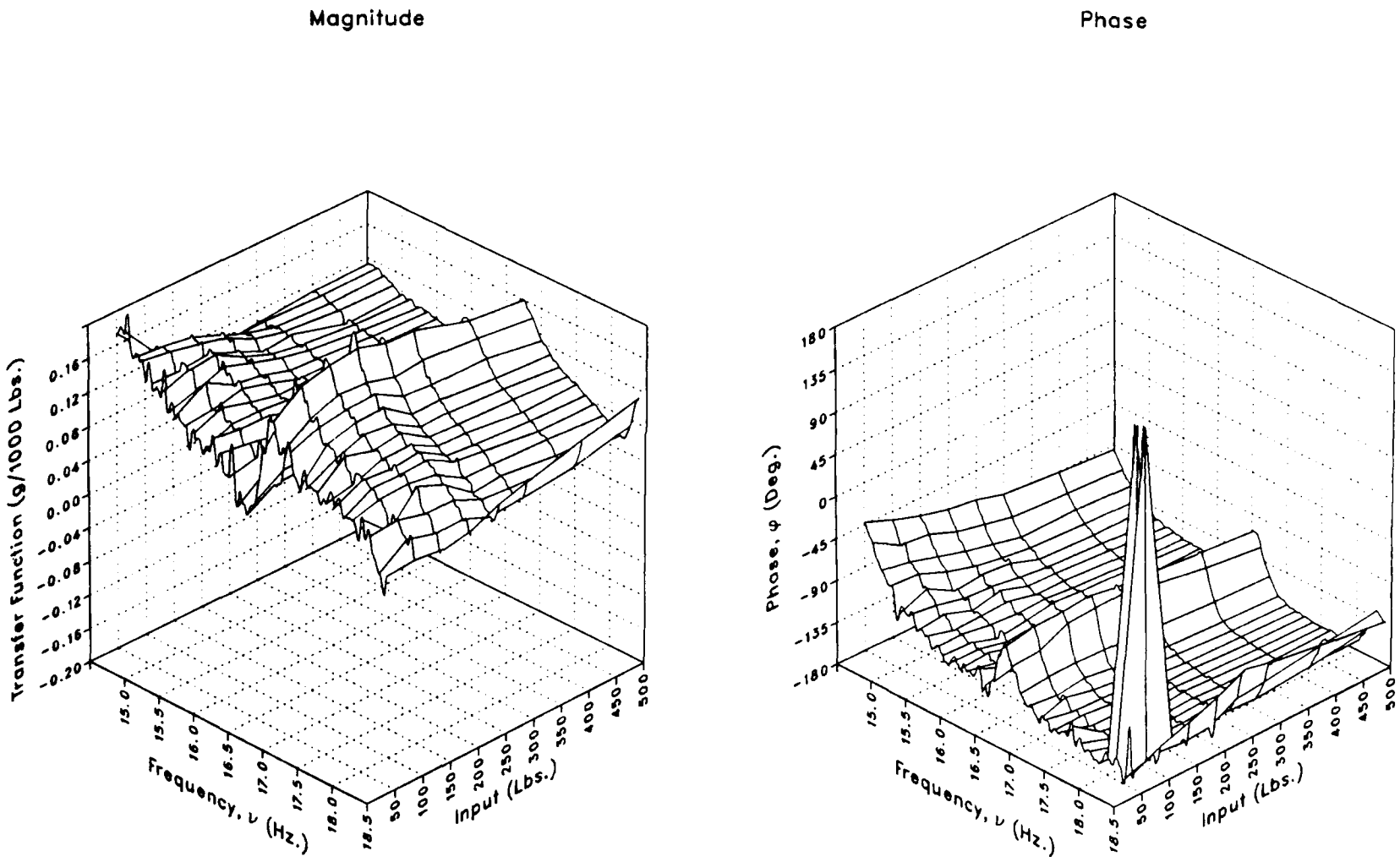

(q) VWGTPLT Concluded.

Figure 1.– Continued.

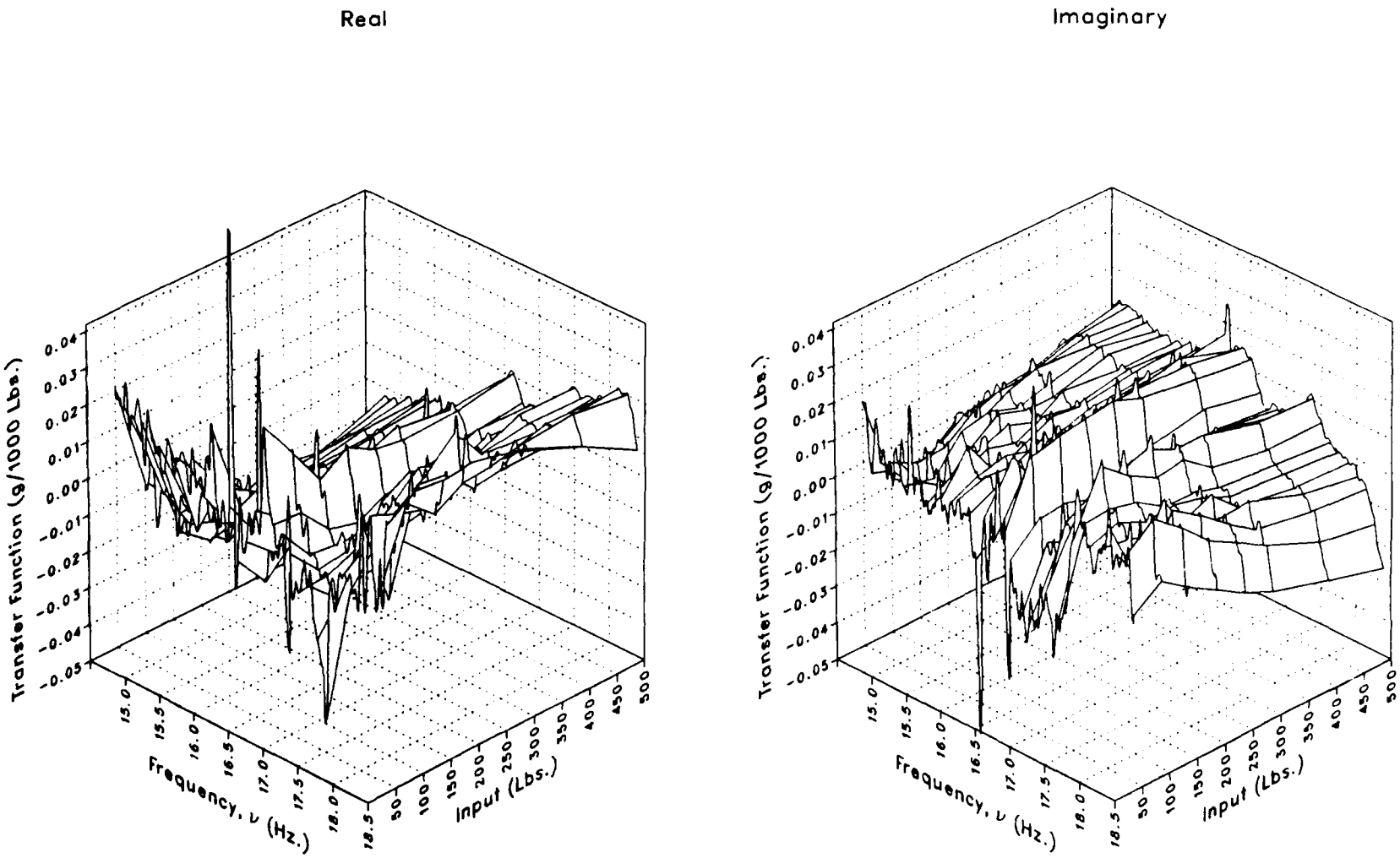

(r) LIGB

Figure 1.– Continued.

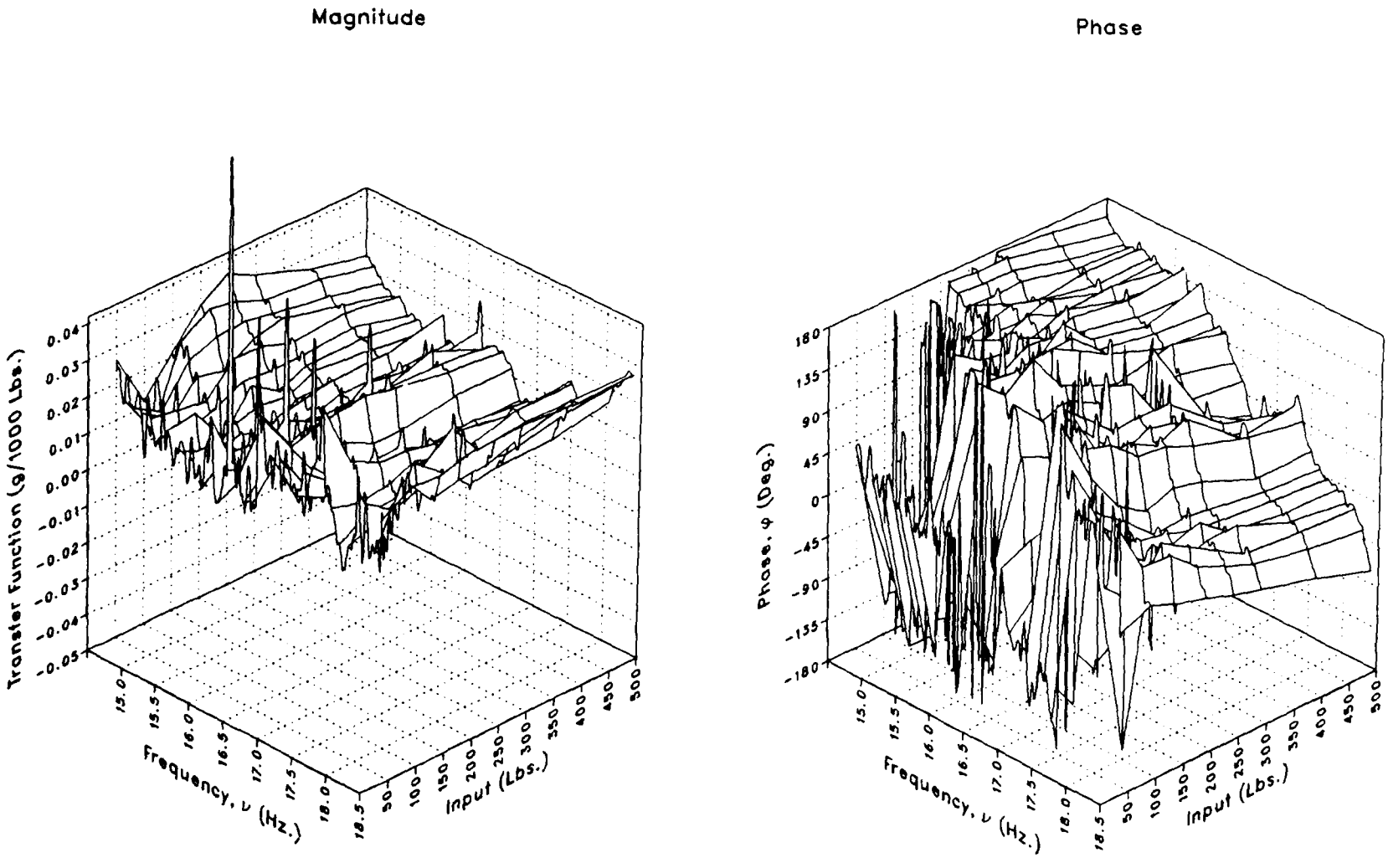

(r) LIGB Concluded.

Figure 1.– Continued.

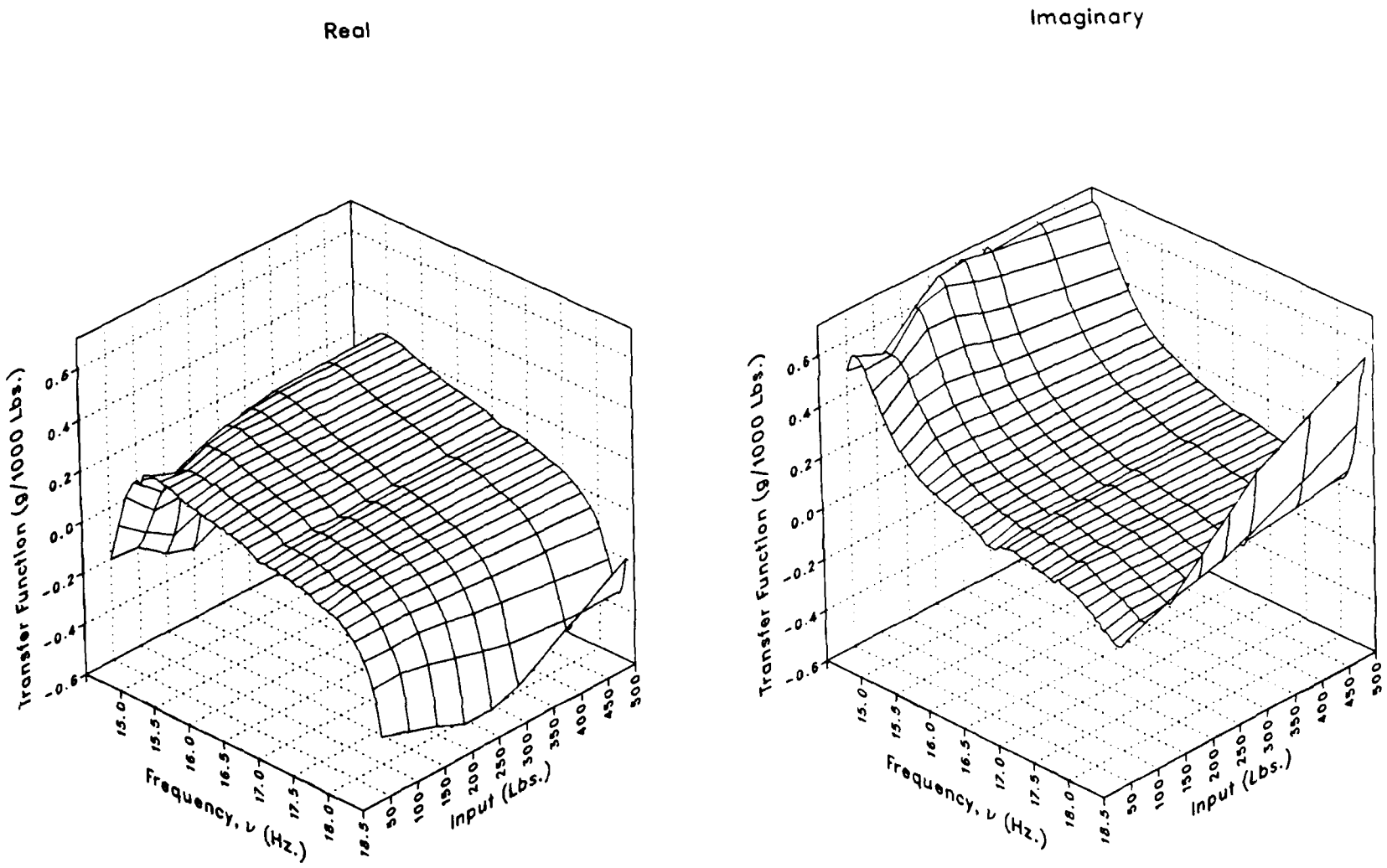

(s) VIGB

Figure 1.– Continued.

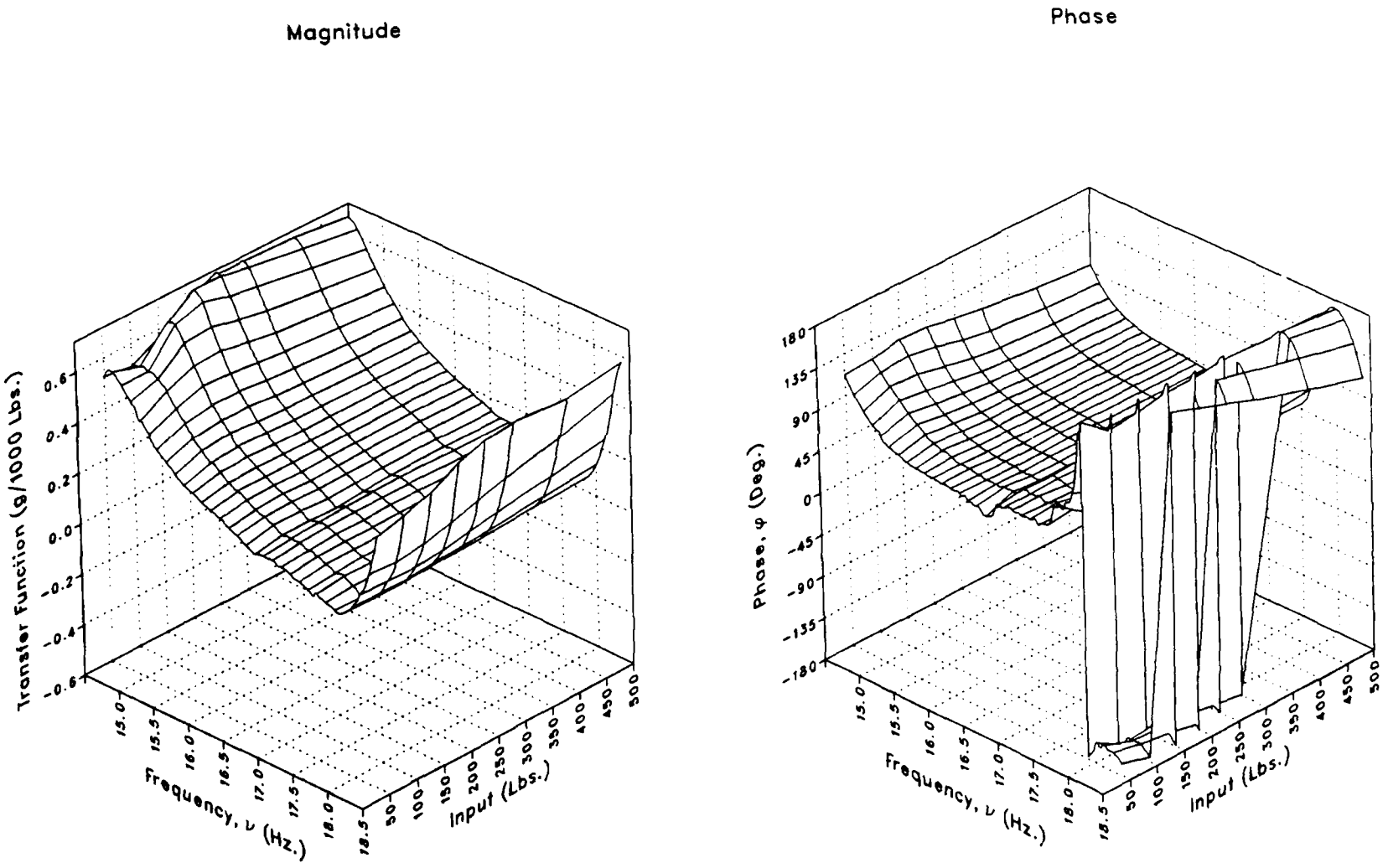

(s) VIGB Concluded.

Figure 1.– Continued.

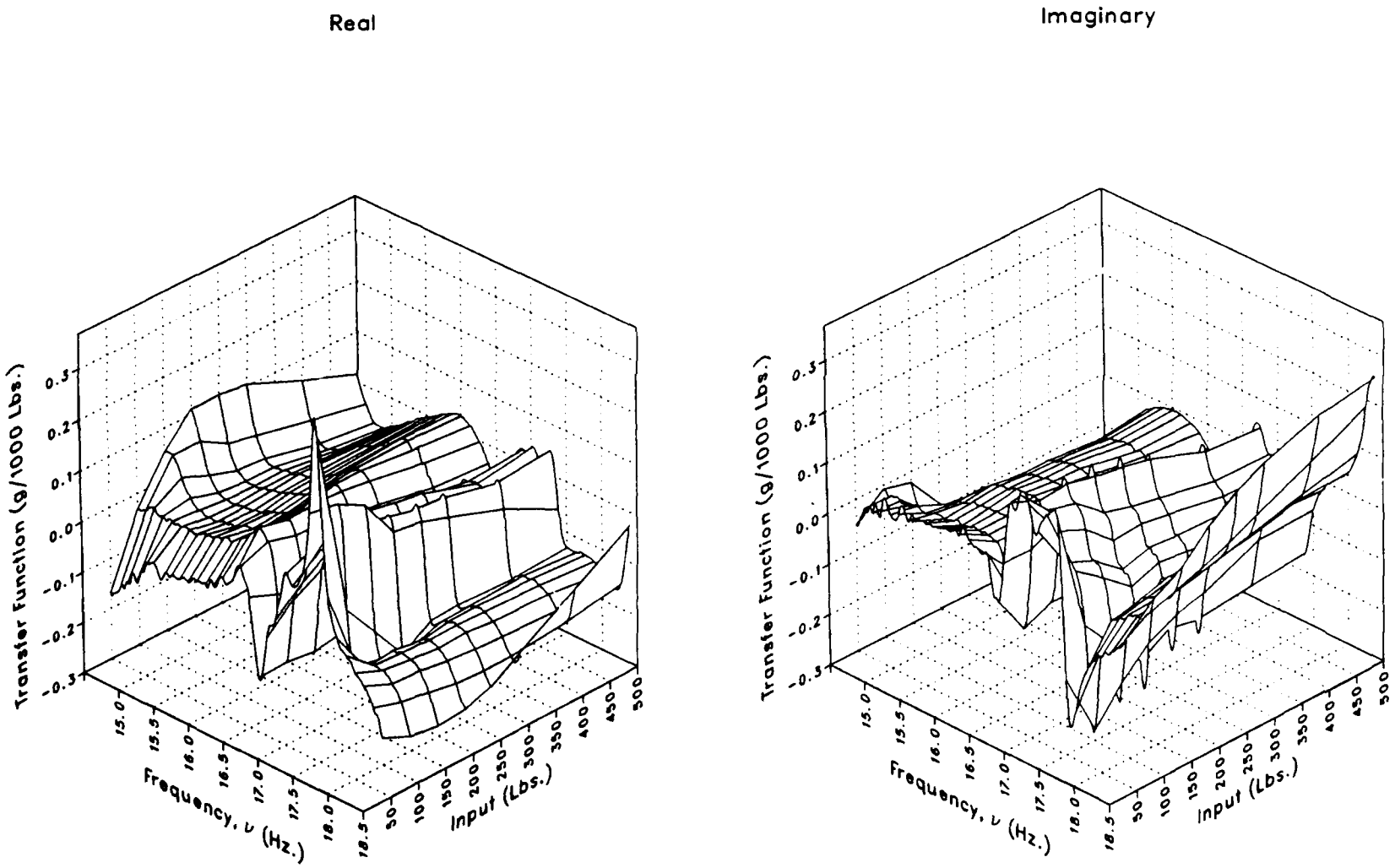

(t) LATTPYLN

Figure 1.– Continued.

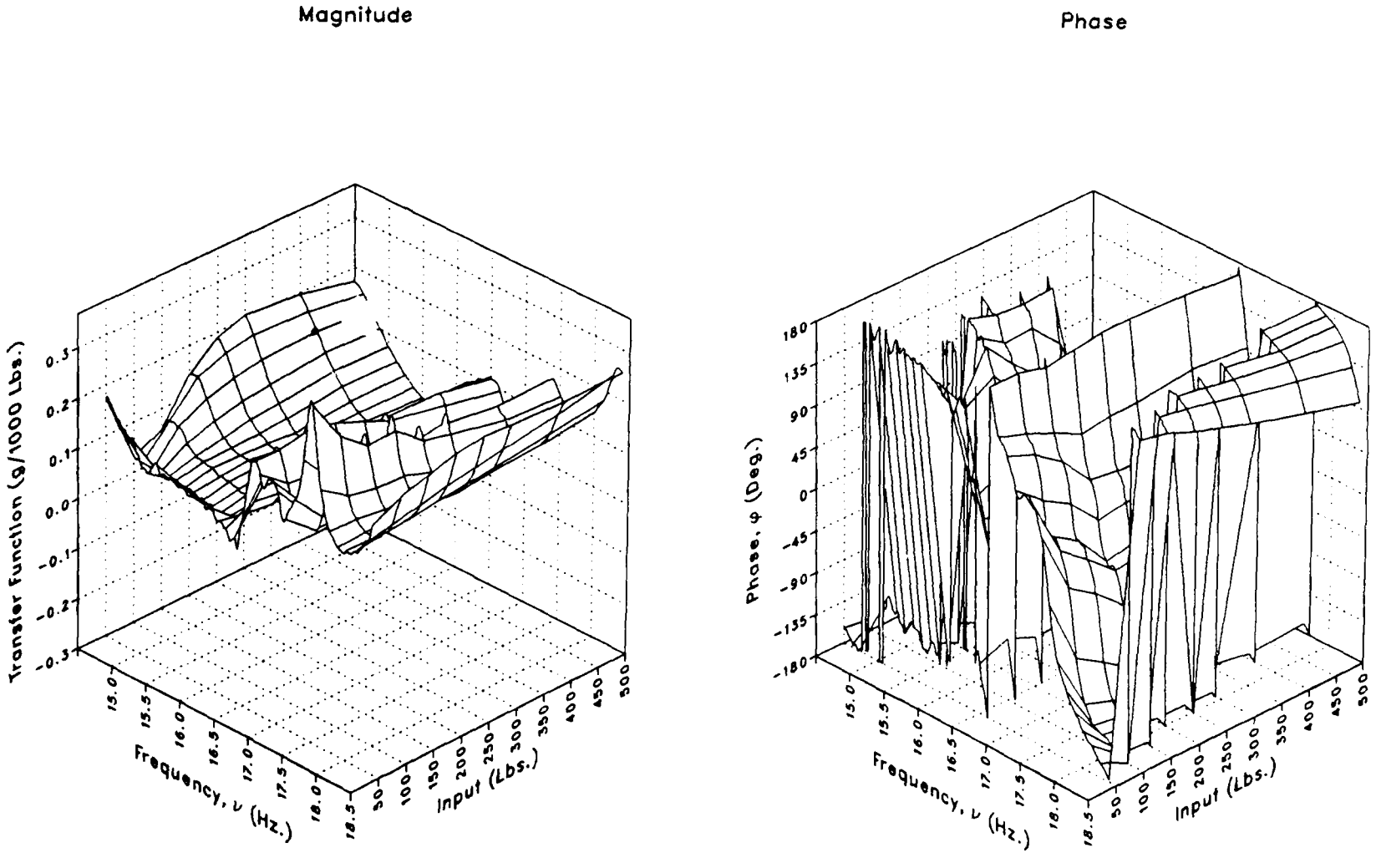

(t) LATTPYLN Concluded.

Figure 1.– Continued.

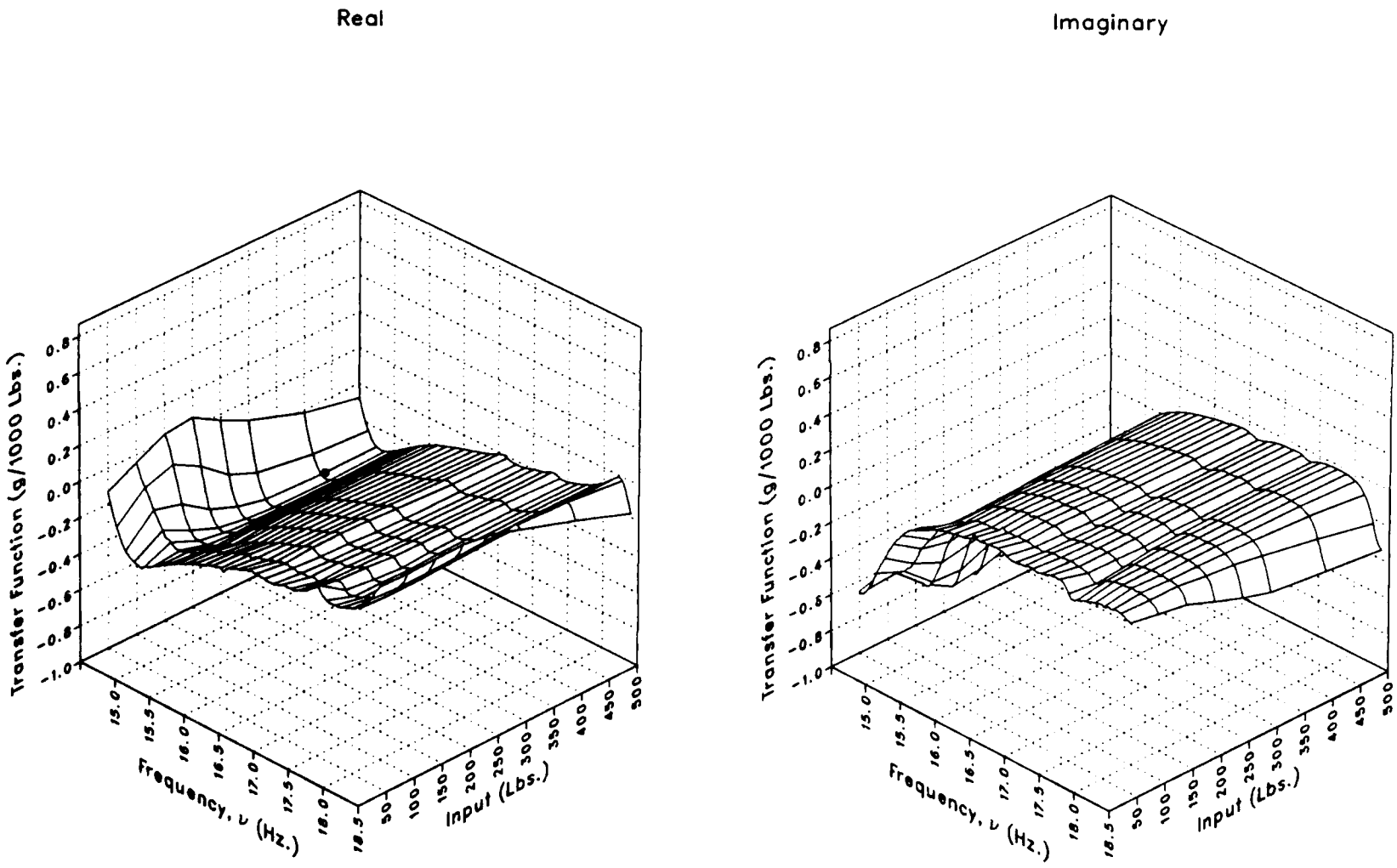

(u) VTTPYLON

Figure 1.– Continued.

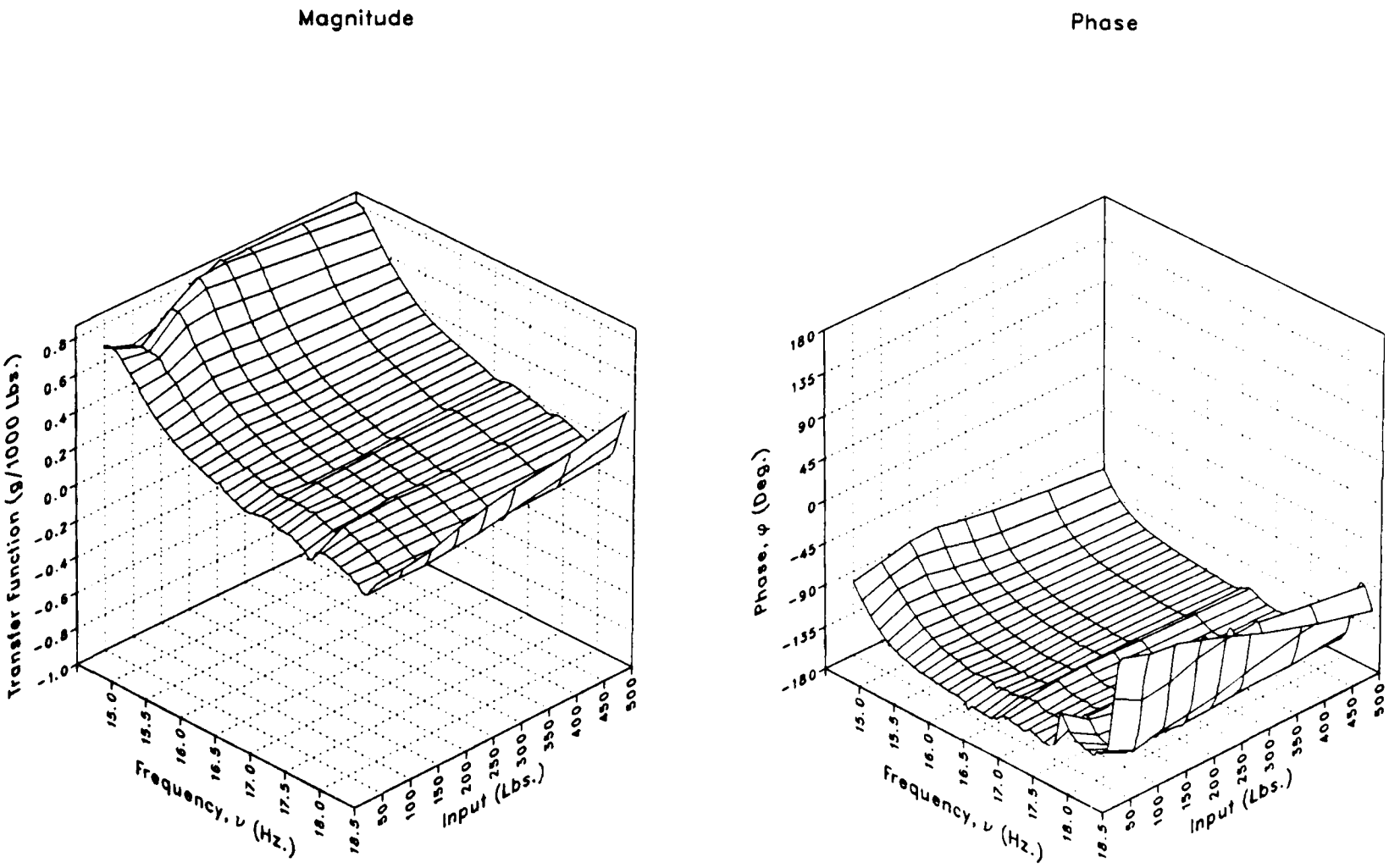

(u) VTTPYLON Concluded.

Figure 1.– Continued.

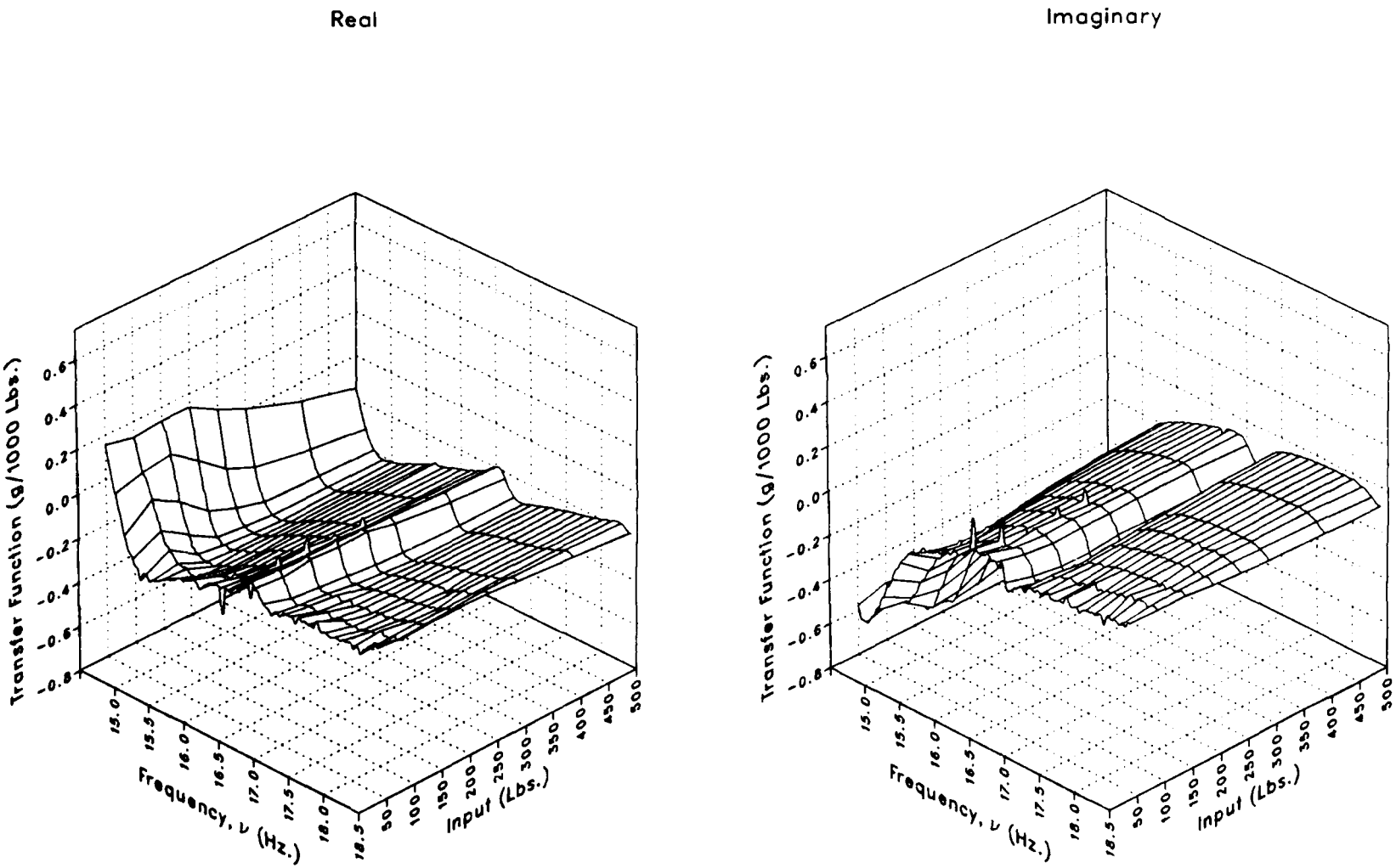

(v) XMRFLV

Figure 1.– Continued.

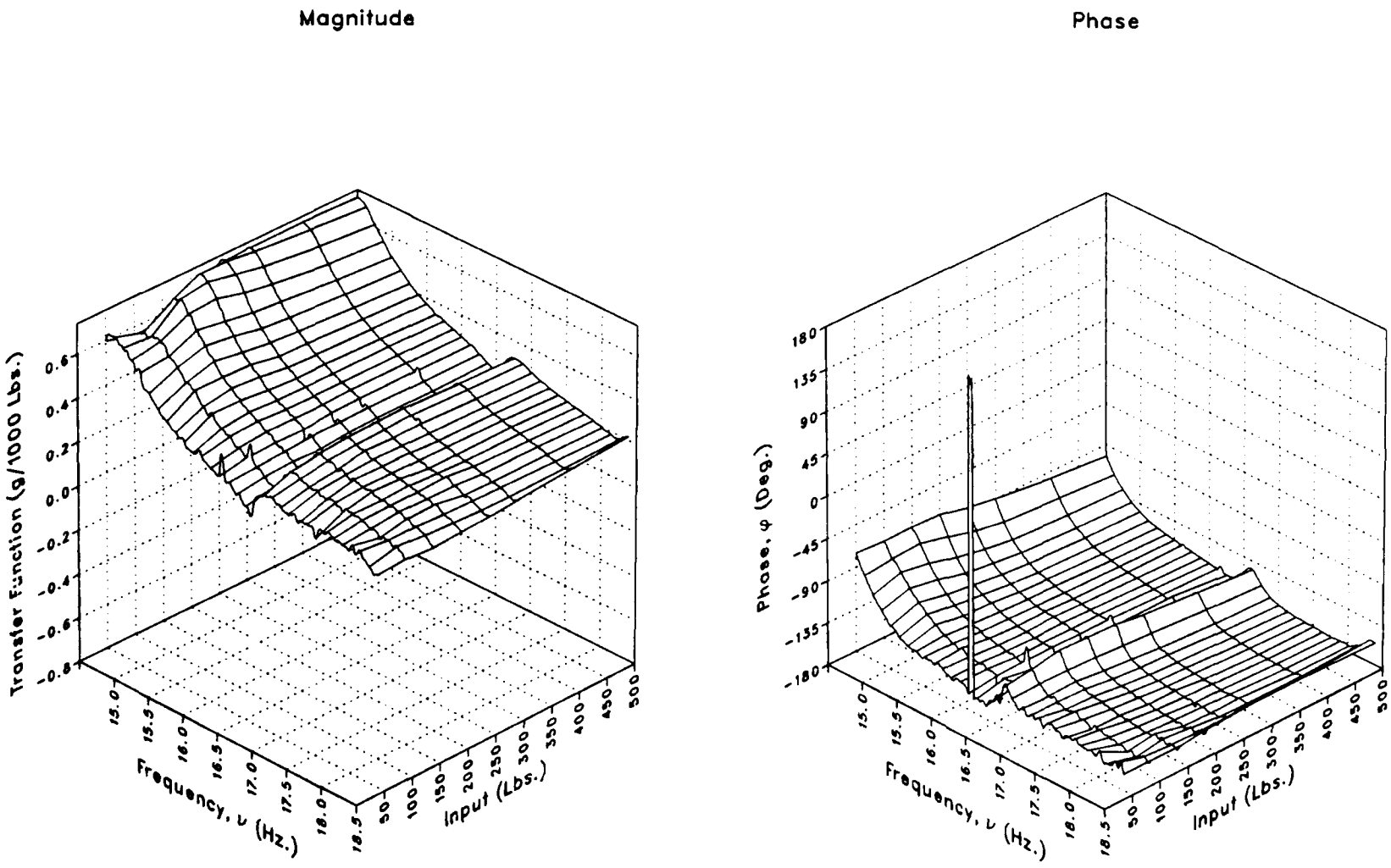

(v) XMRFLV Concluded.

Figure 1.– Continued.

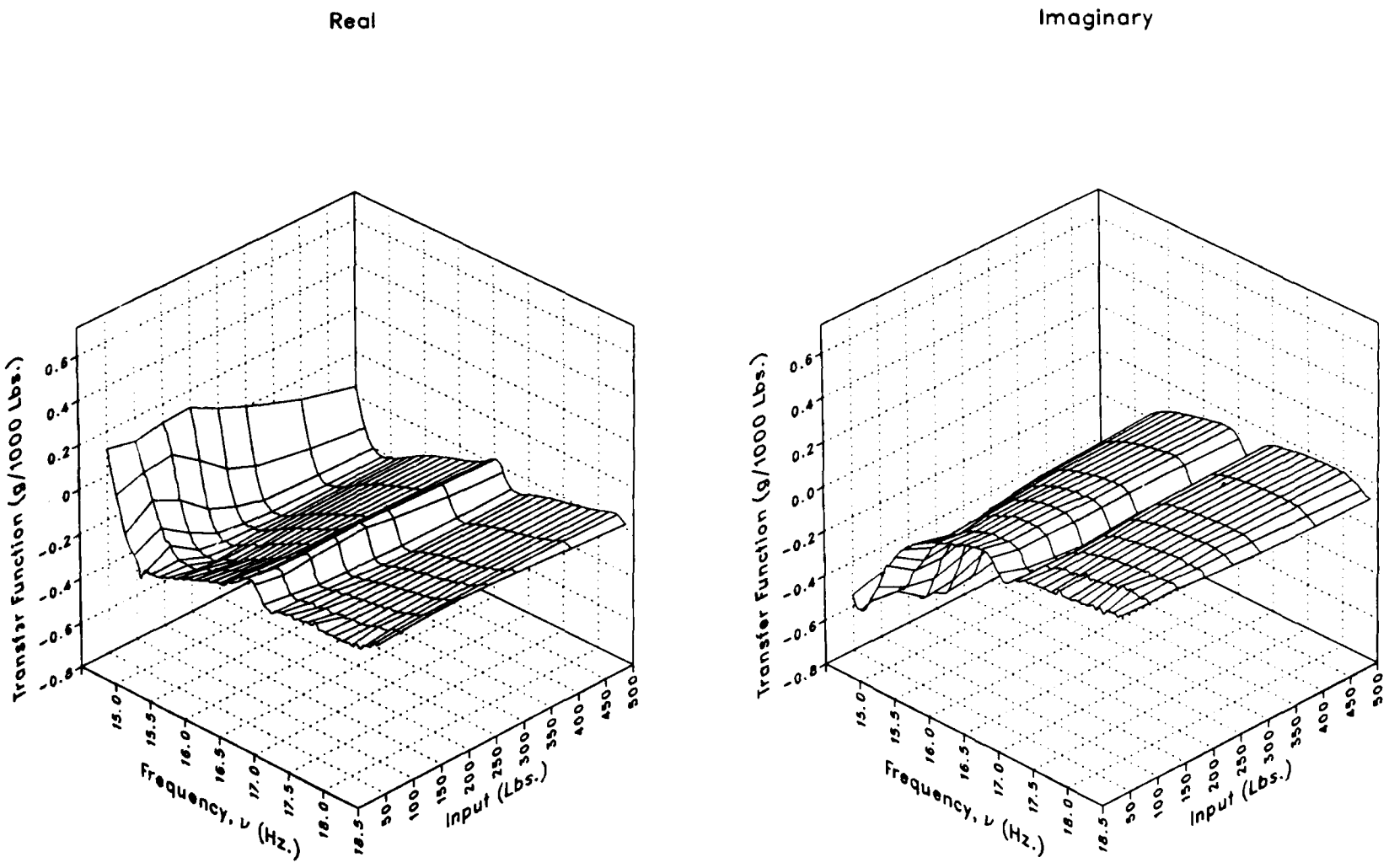

(w) XMRFRV

Figure 1.– Continued.

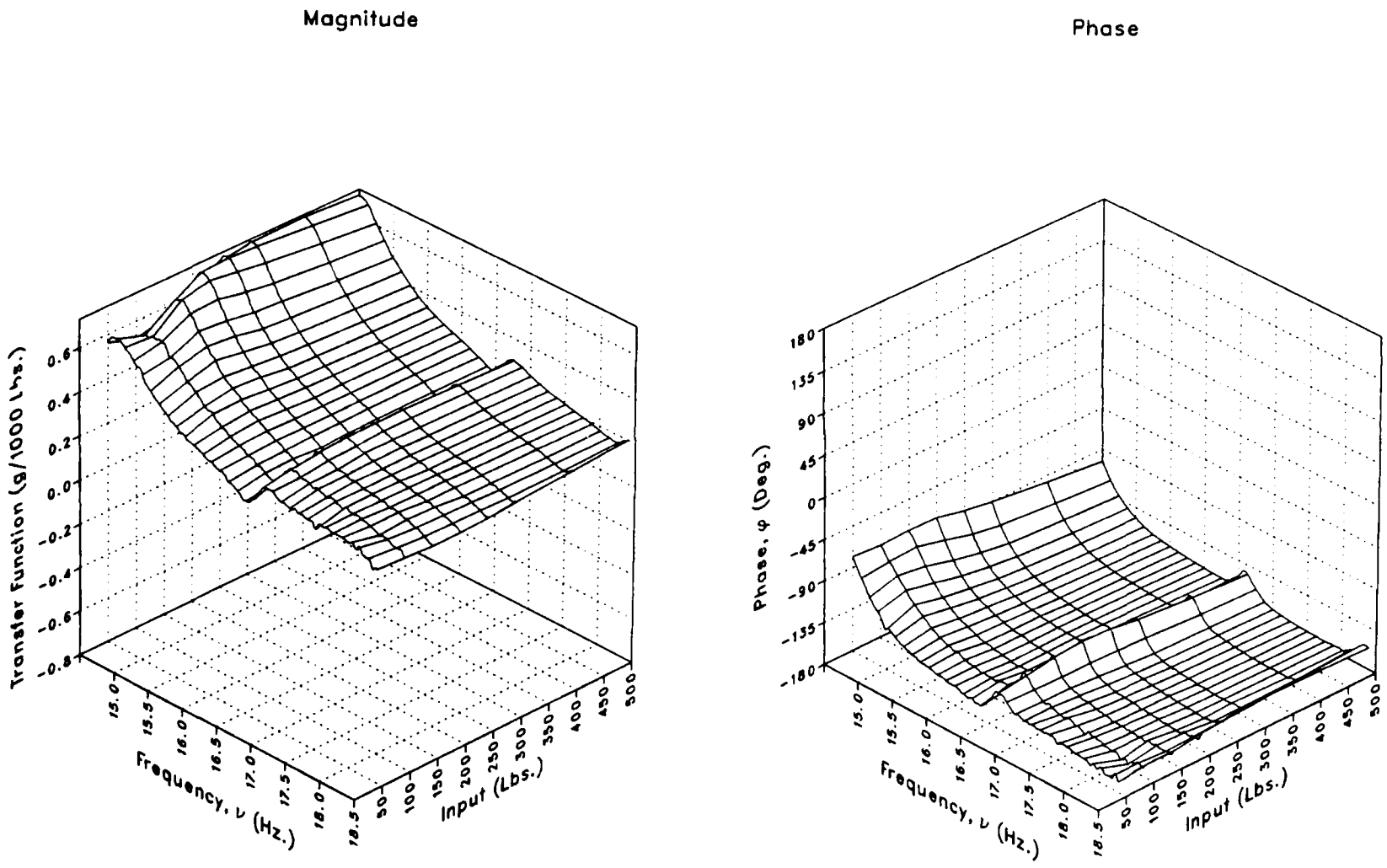

(w) XMRFRV Concluded.

Figure 1.– Continued.

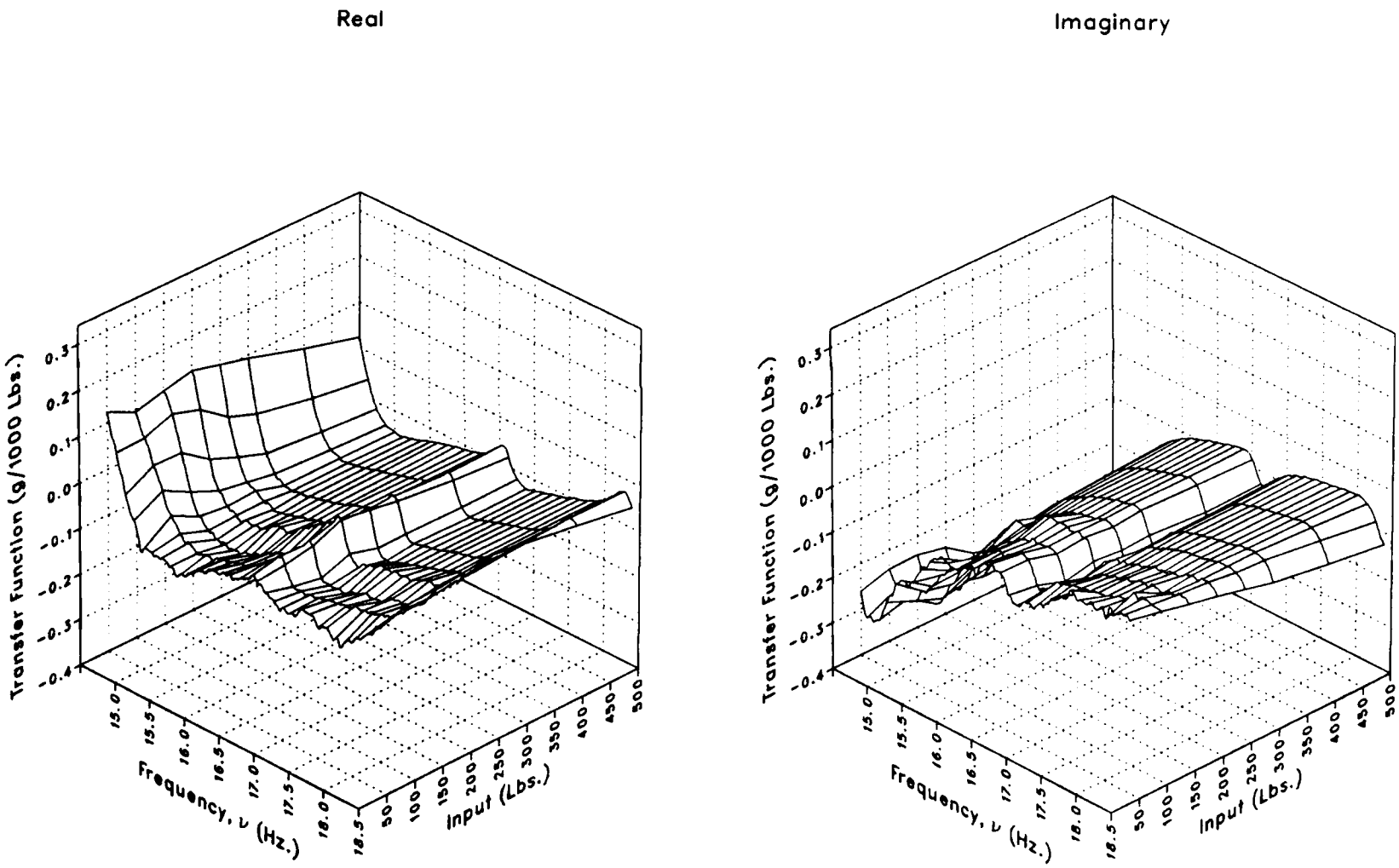

(x) S222FLRV Concluded.

Figure 1.– Continued.

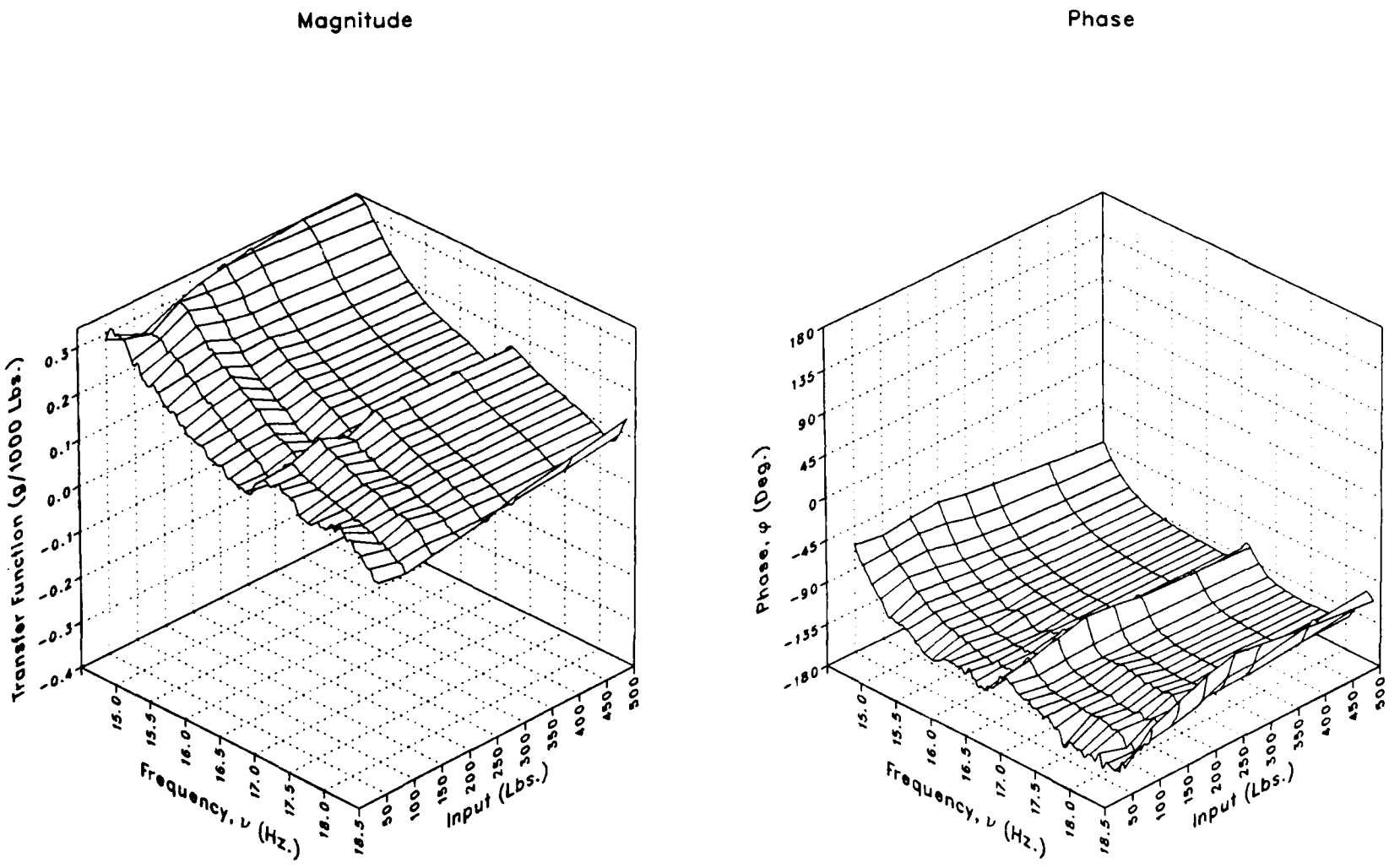

(x) S222FLRV

Figure 1.– Continued.

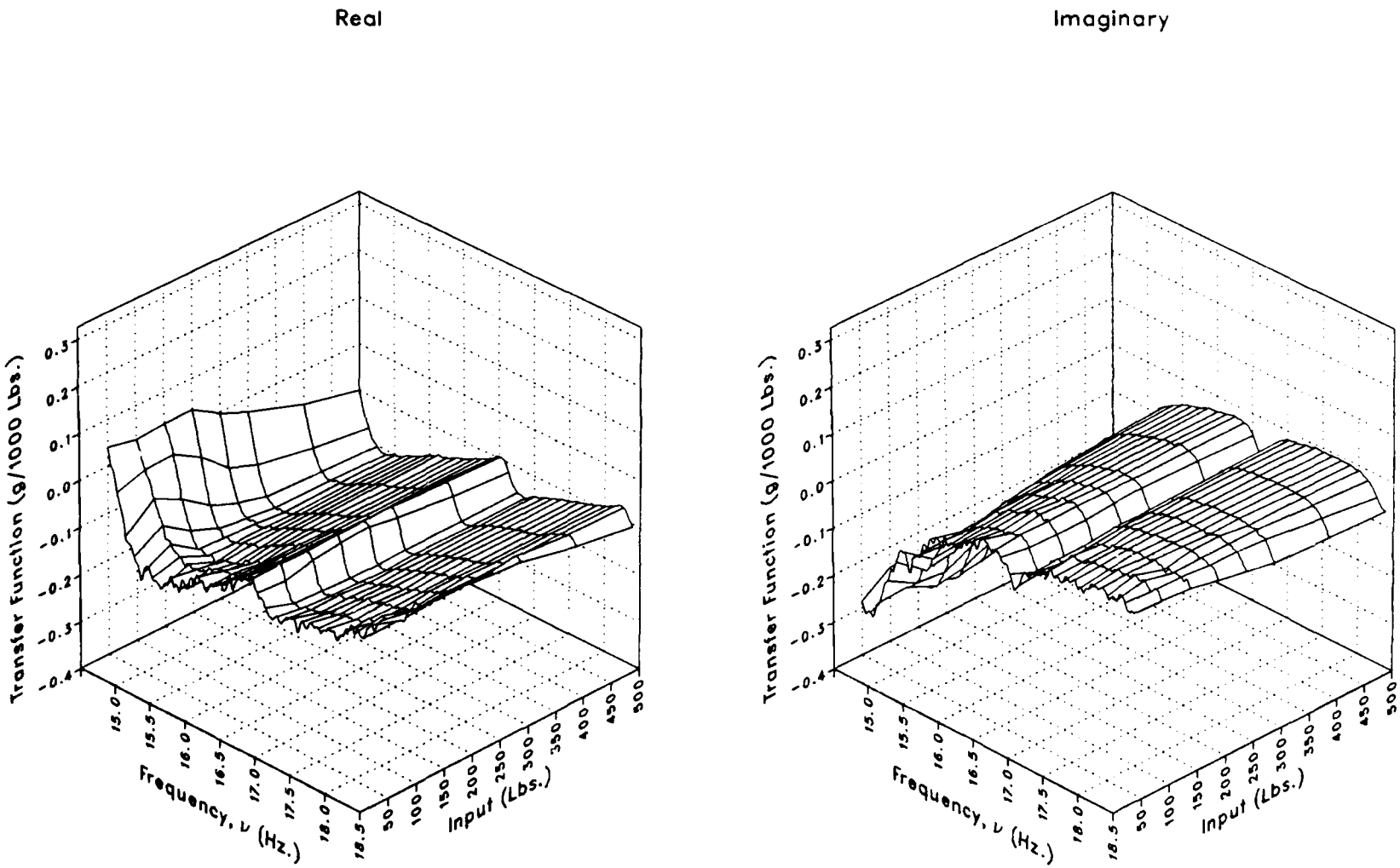

(y) S222FLLV

Figure 1.– Continued.

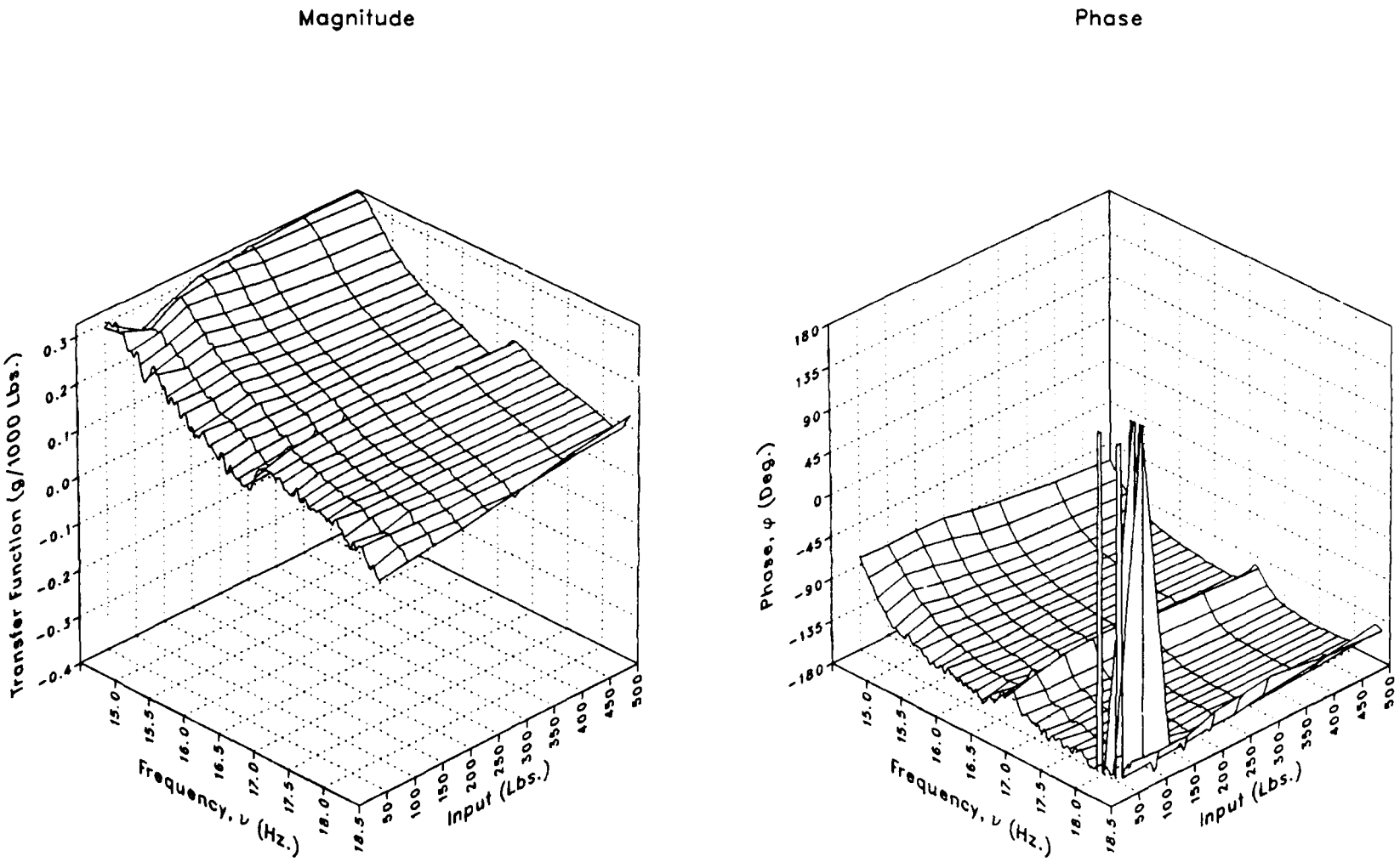

(y) S222FLLV Concluded.

Figure 1.– Continued.

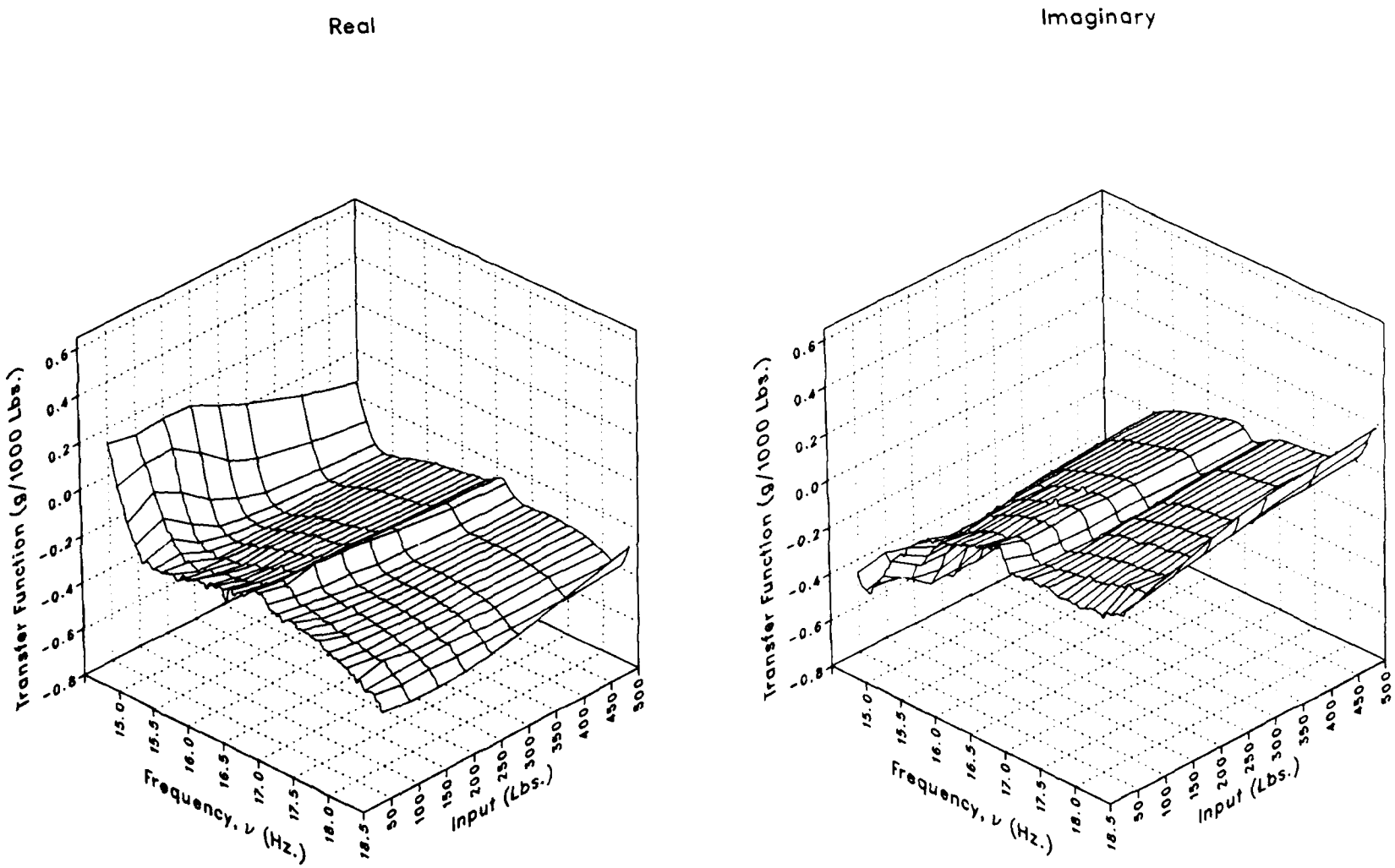

(z) S450FLV

Figure 1.– Continued.

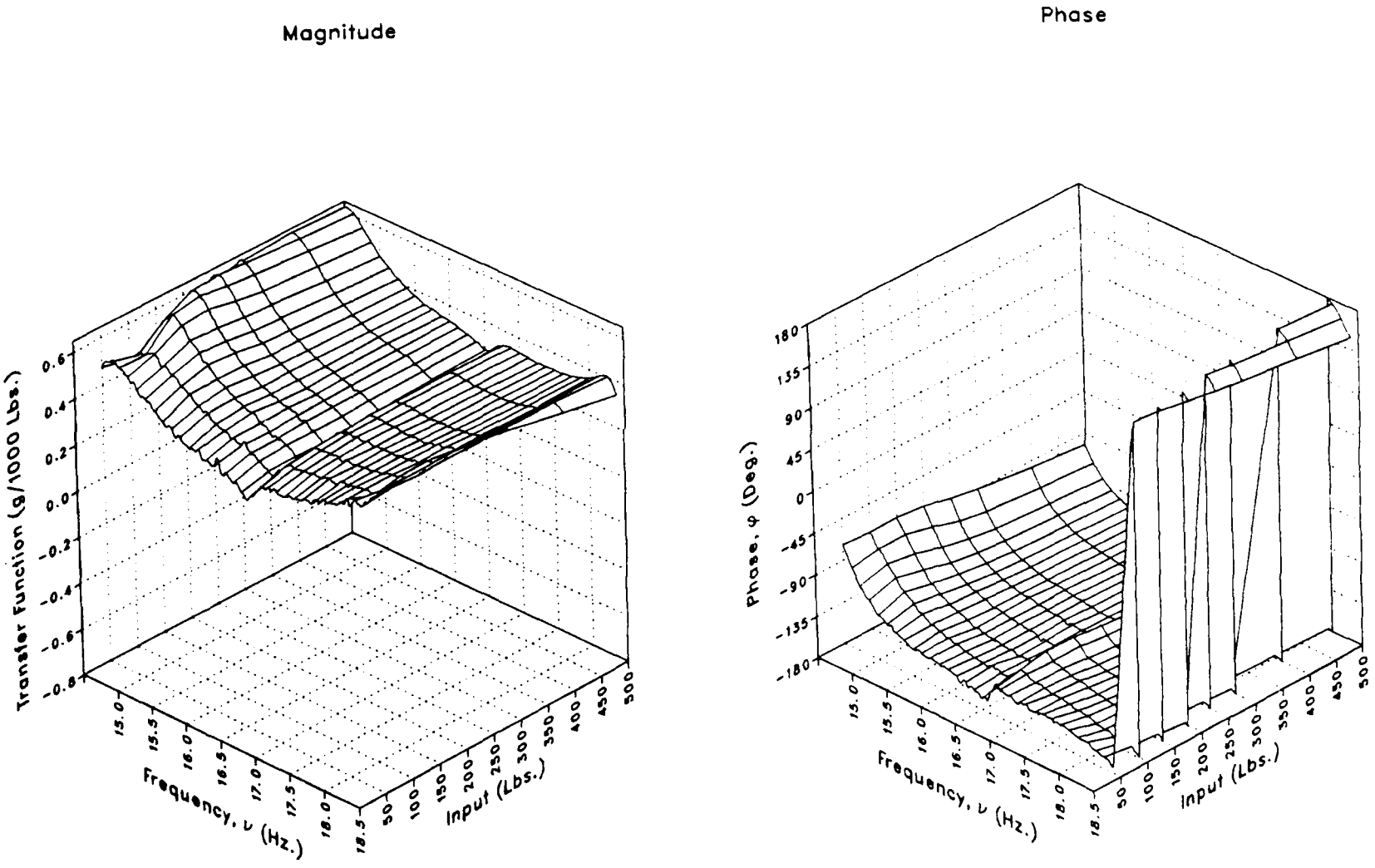

(z) S450FLV Concluded.

Figure 1.– Continued.

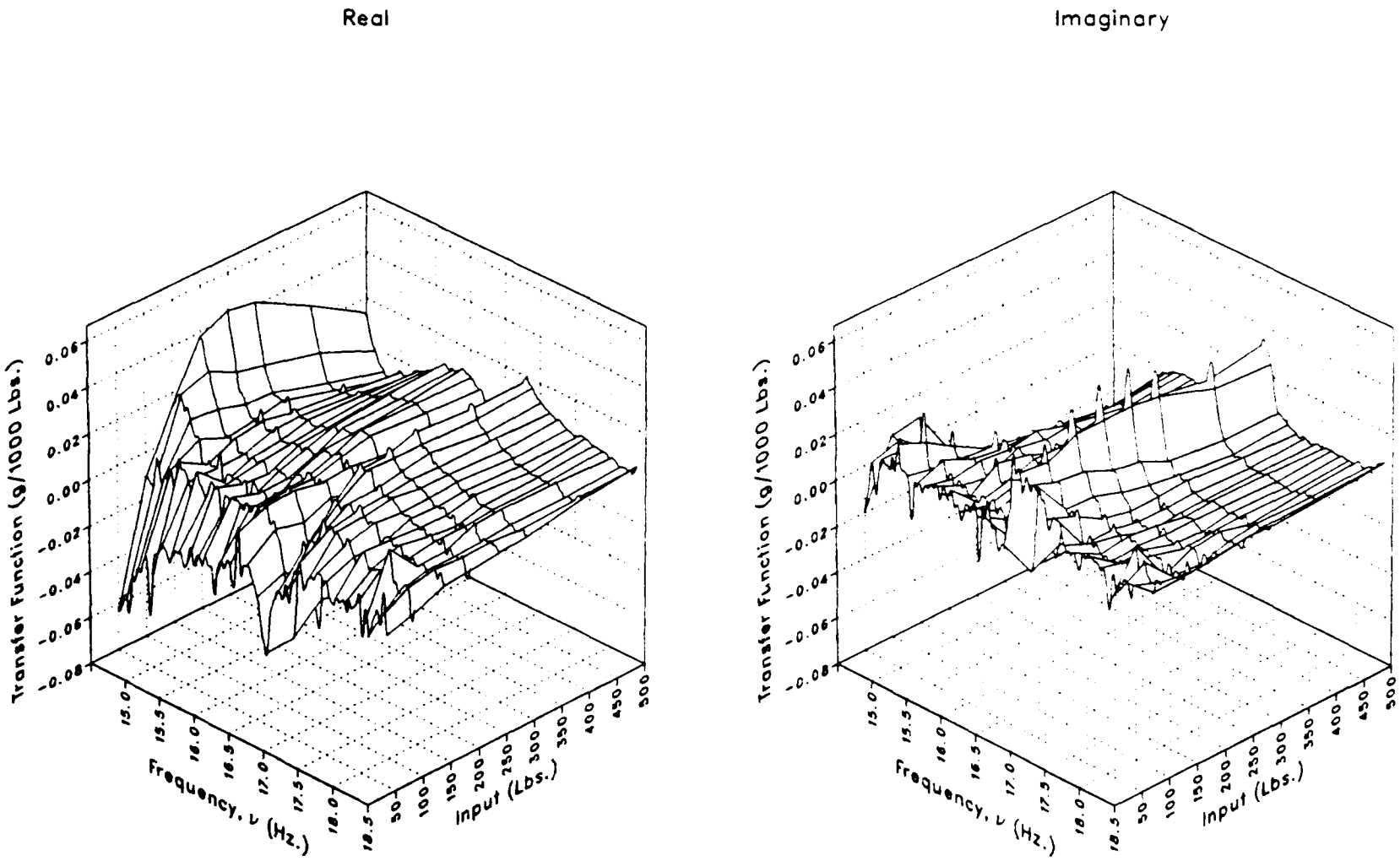

(aa) S450FLL

Figure 1.– Continued.

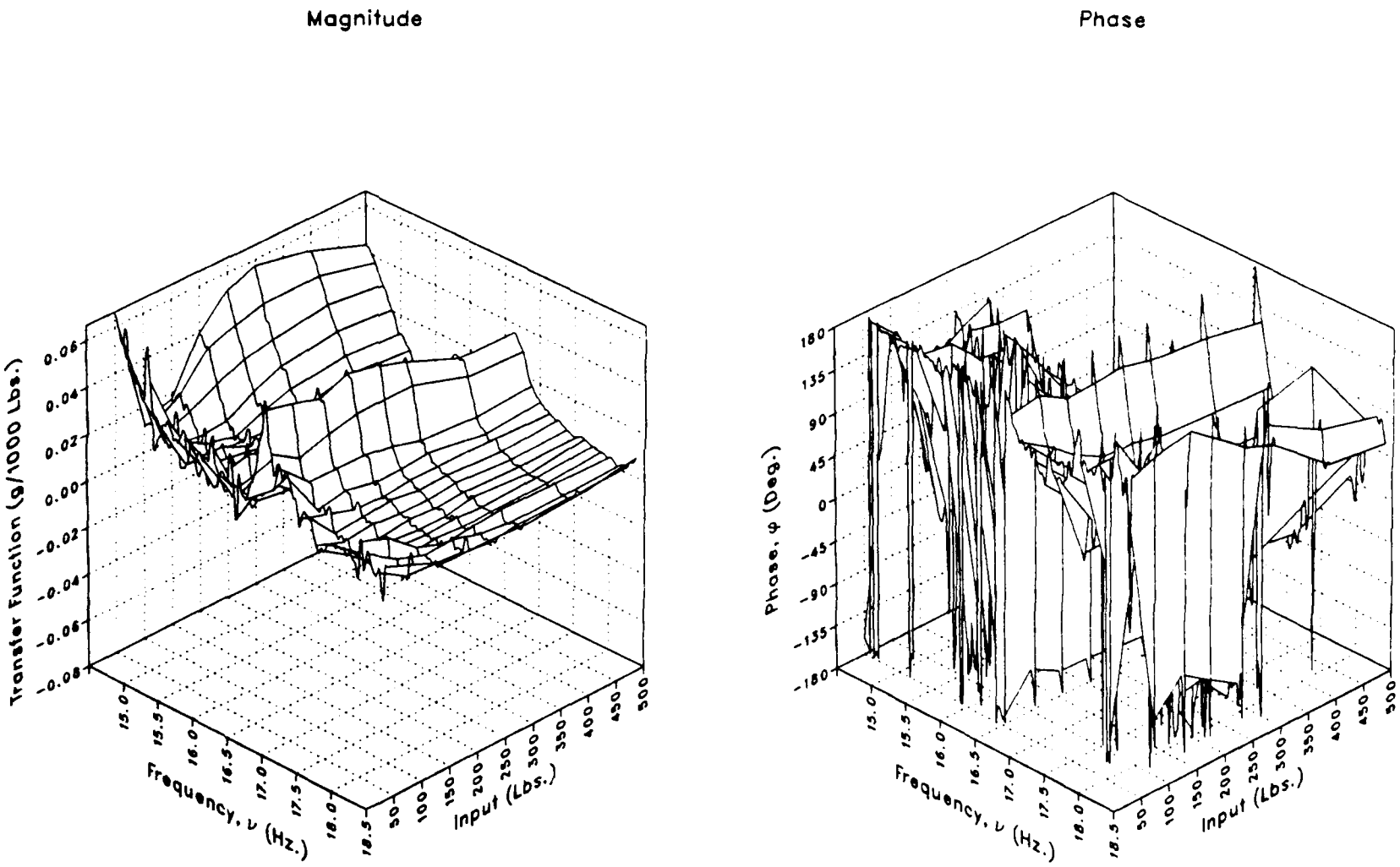

(aa) S450FLL Concluded.

Figure 1.– Continued.

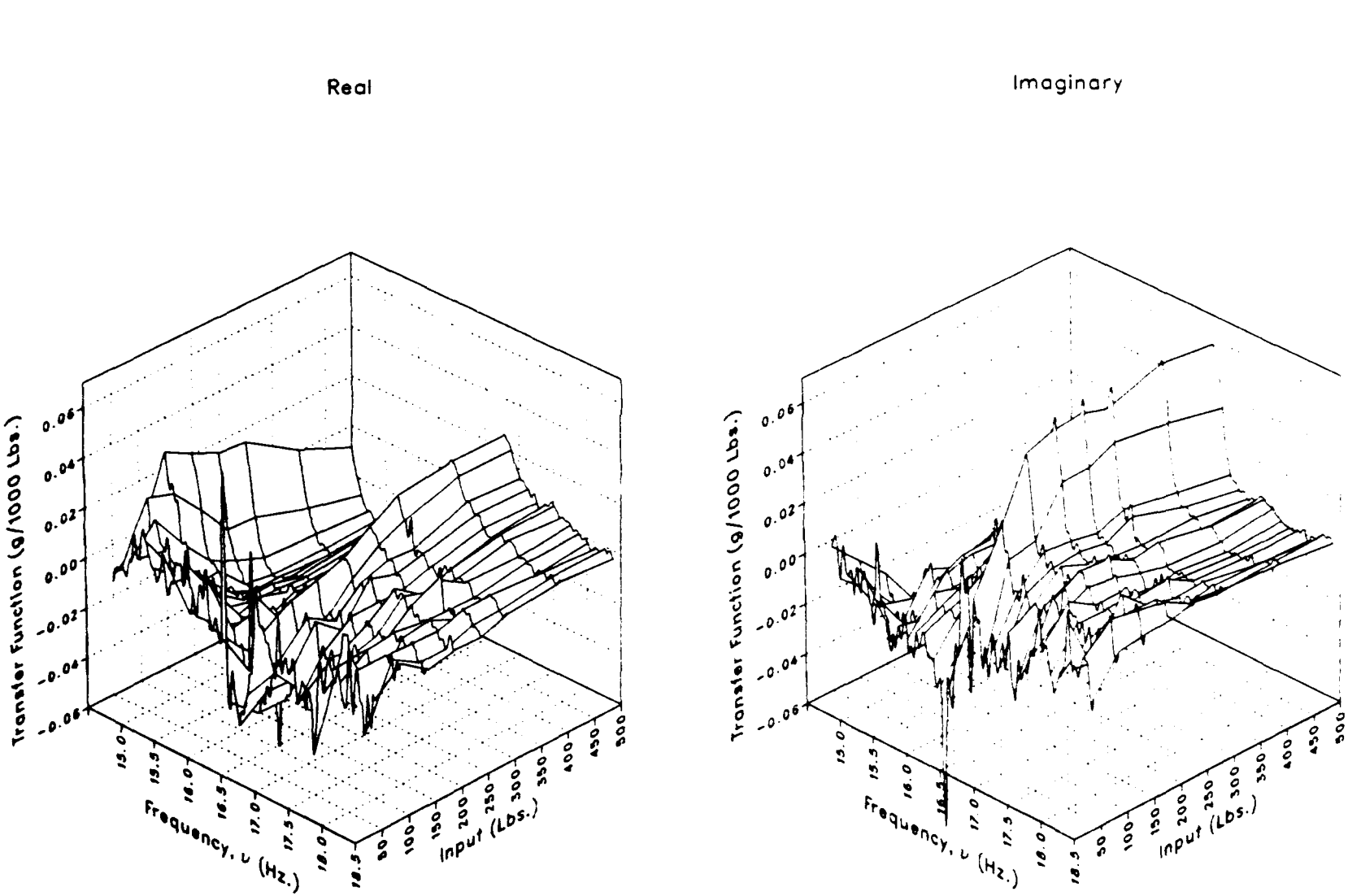

(bb) S450OVRL

Figure 1.– Continued.

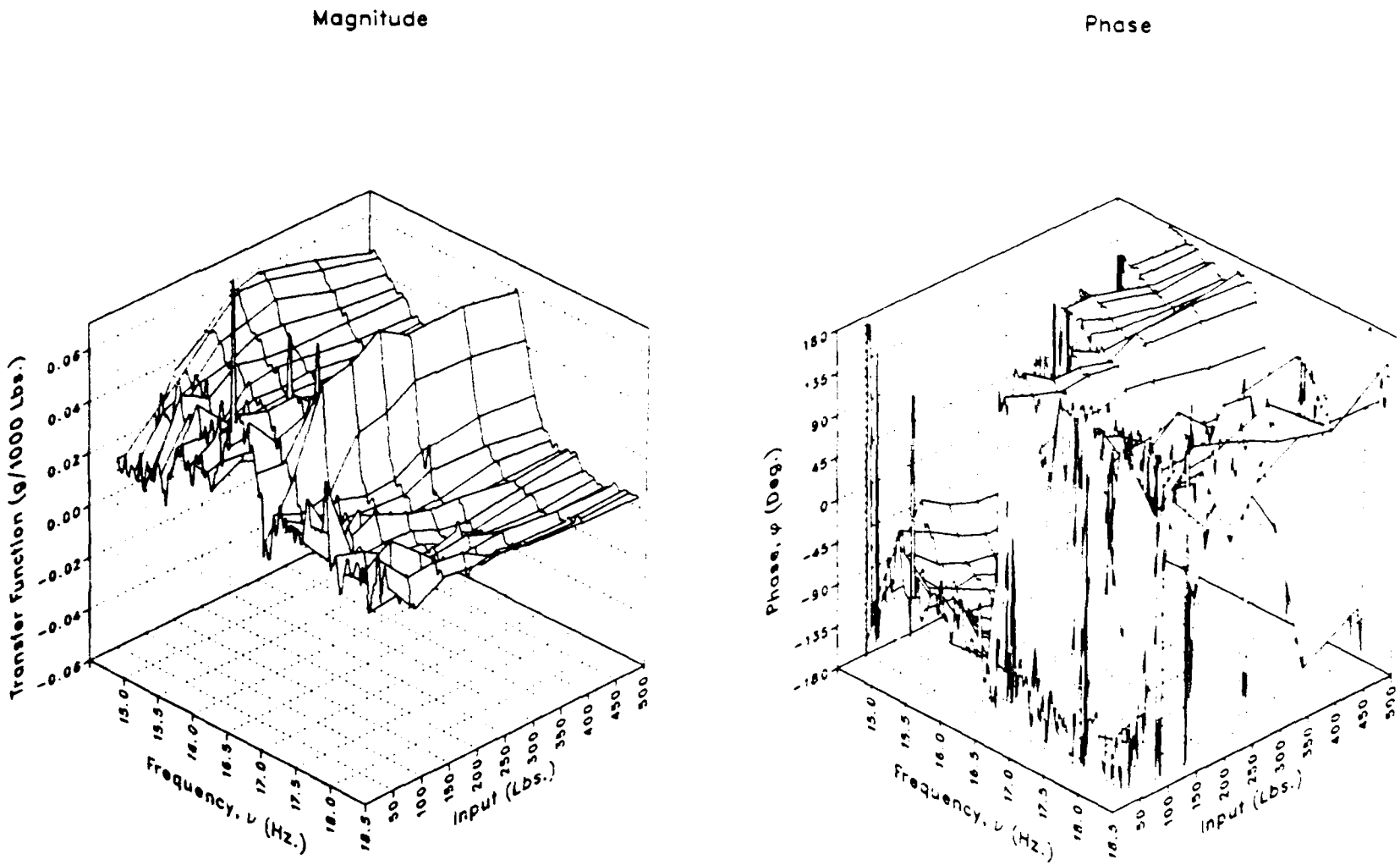

(bb) S450OVRL Concluded.

Figure 1.– Concluded.

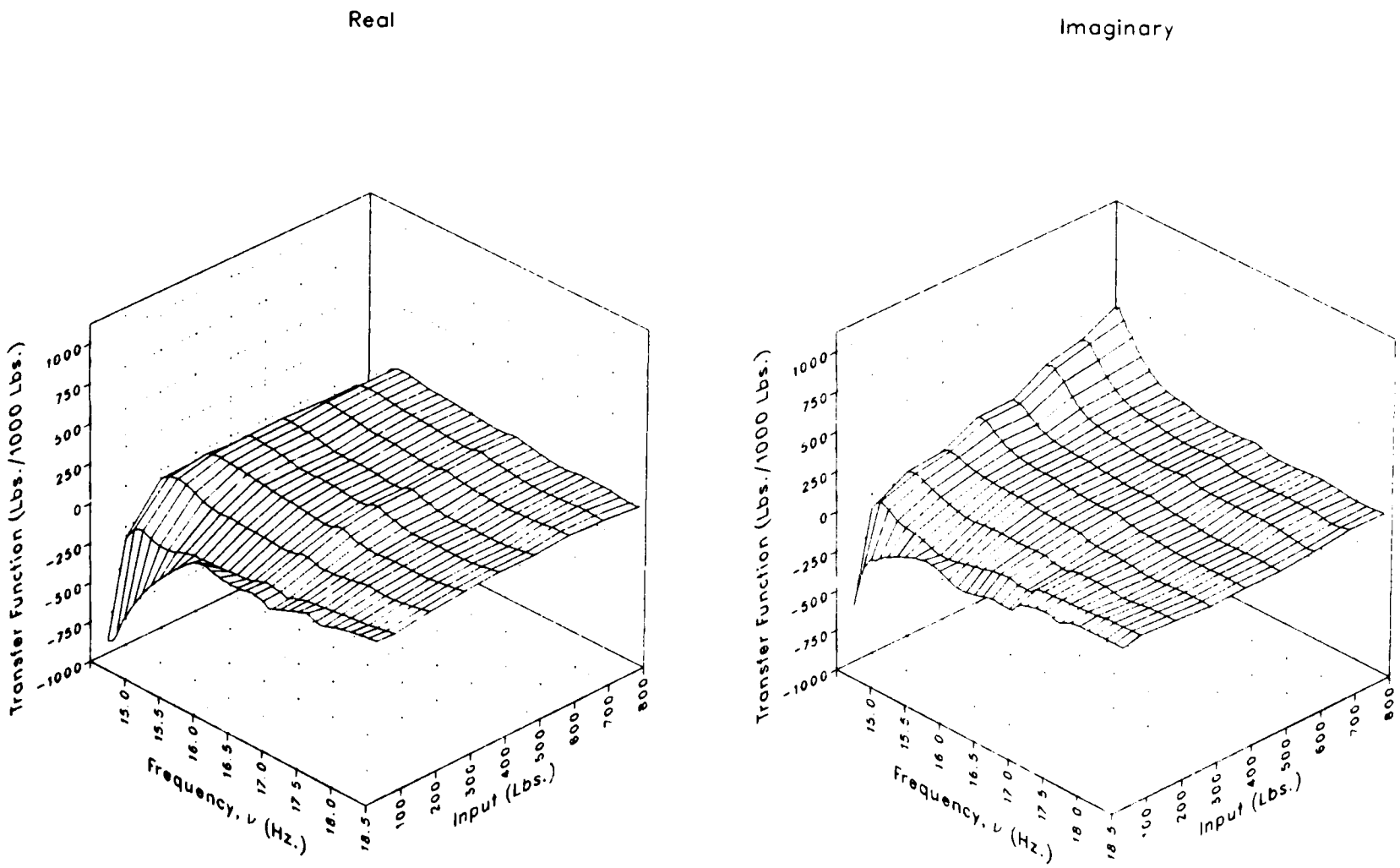

(a) MRDRAG

Figure 2.– Lateral forcing.

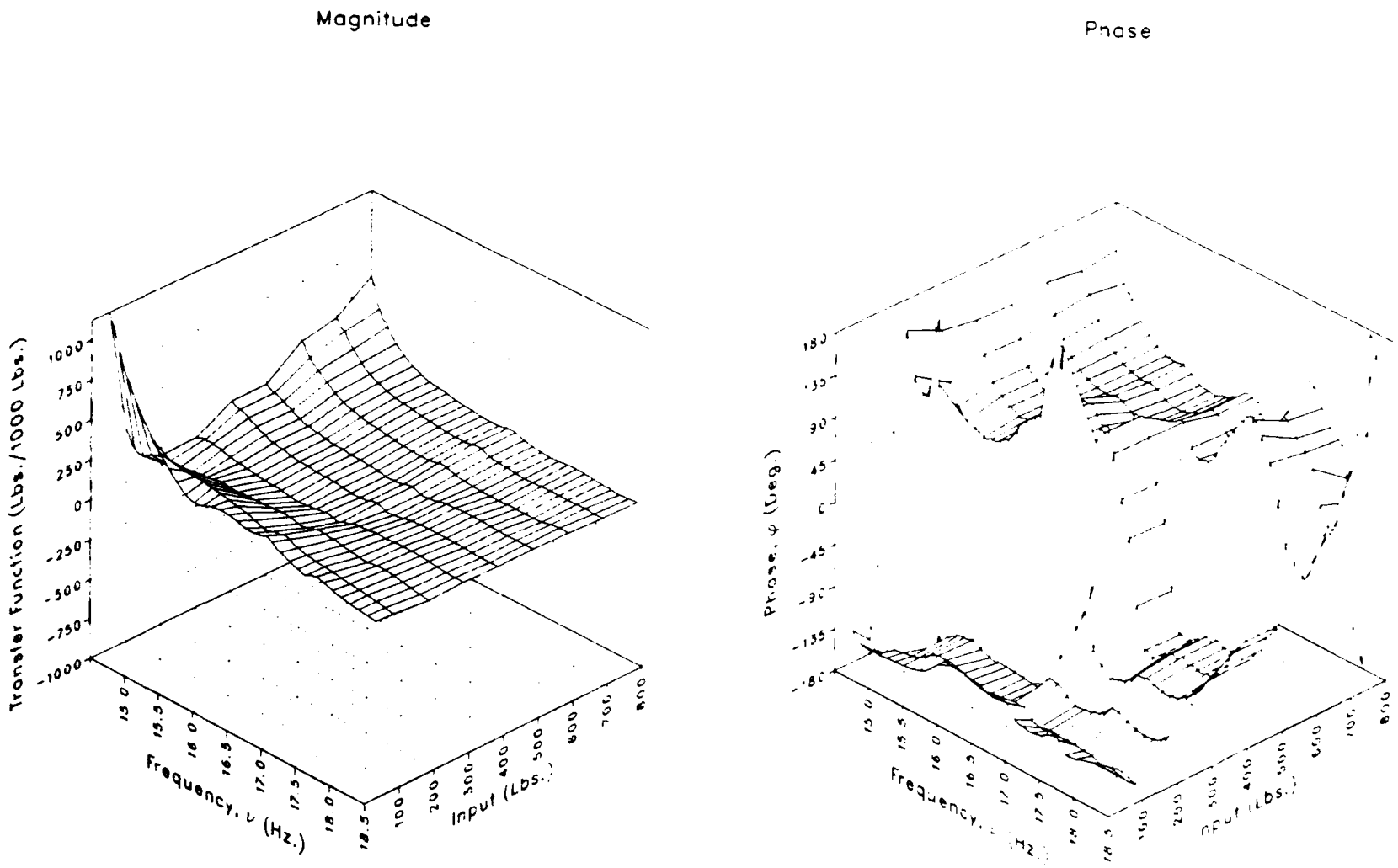

(a) MRDRAG Concluded.

Figure 2.– Continued.

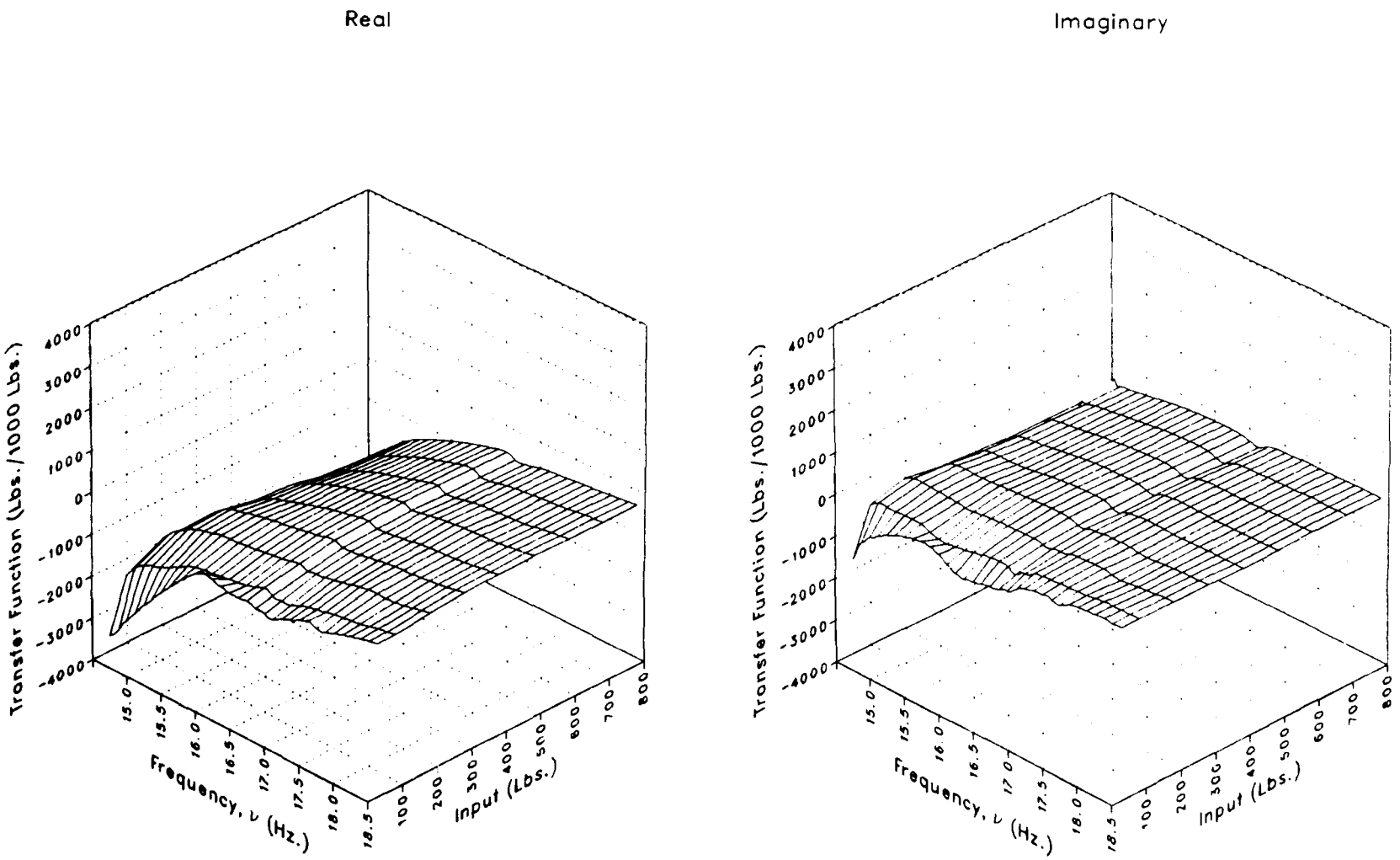

(b) MRLIFTA

Figure 2.– Continued.

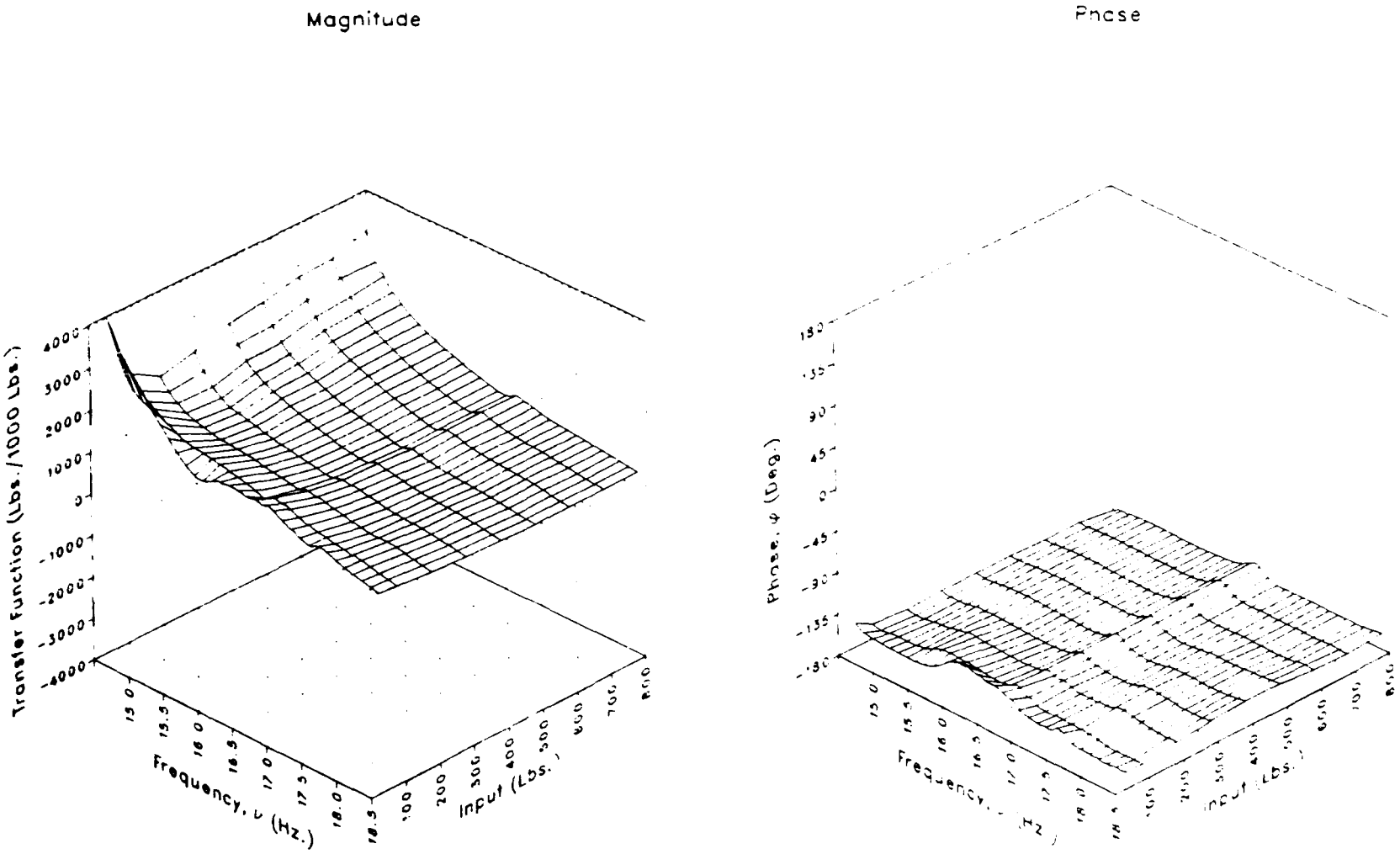

(b) MRLIFTA Concluded.

Figure 2.– Continued.

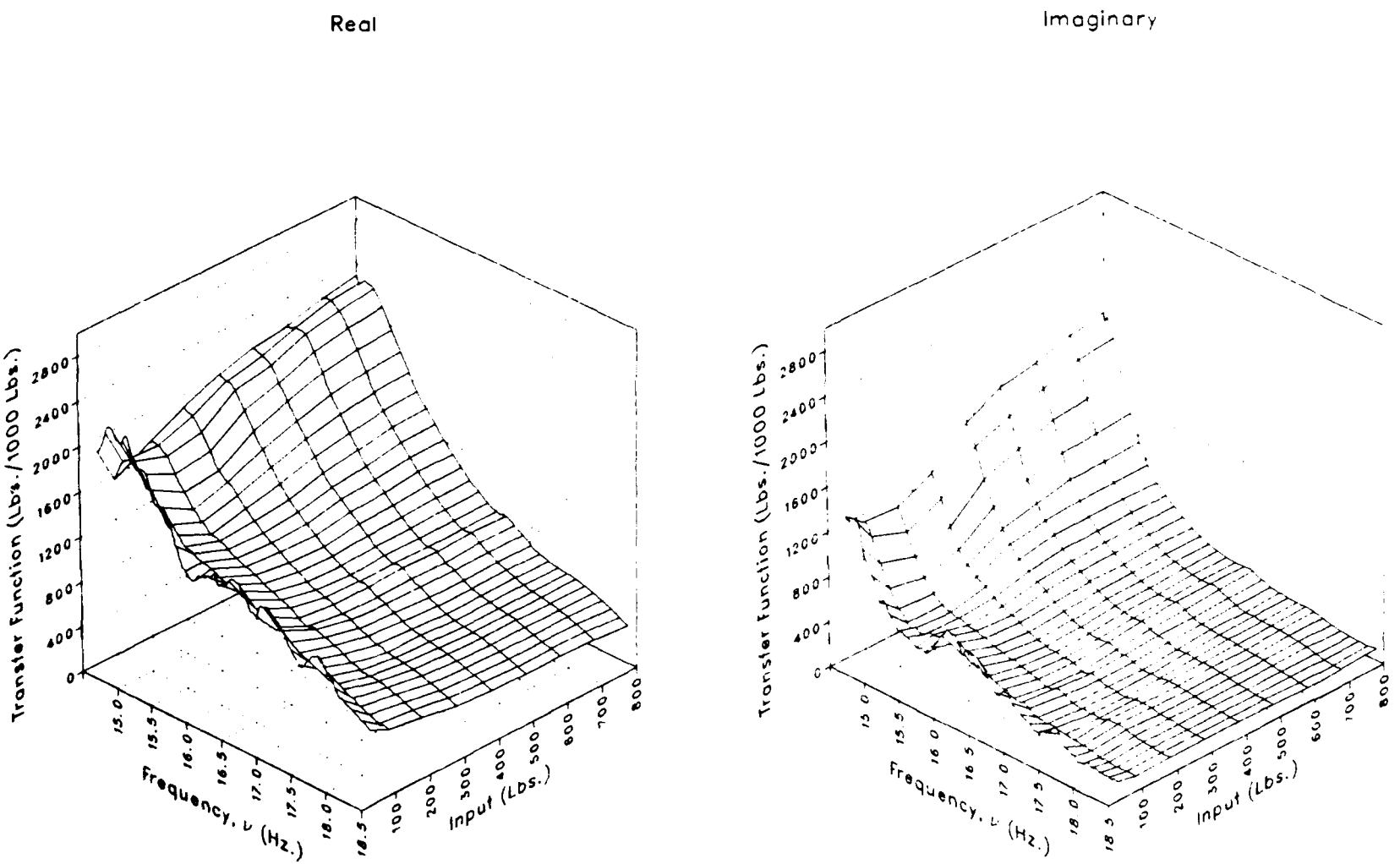

(c) MRLIFTB

Figure 2.– Continued.

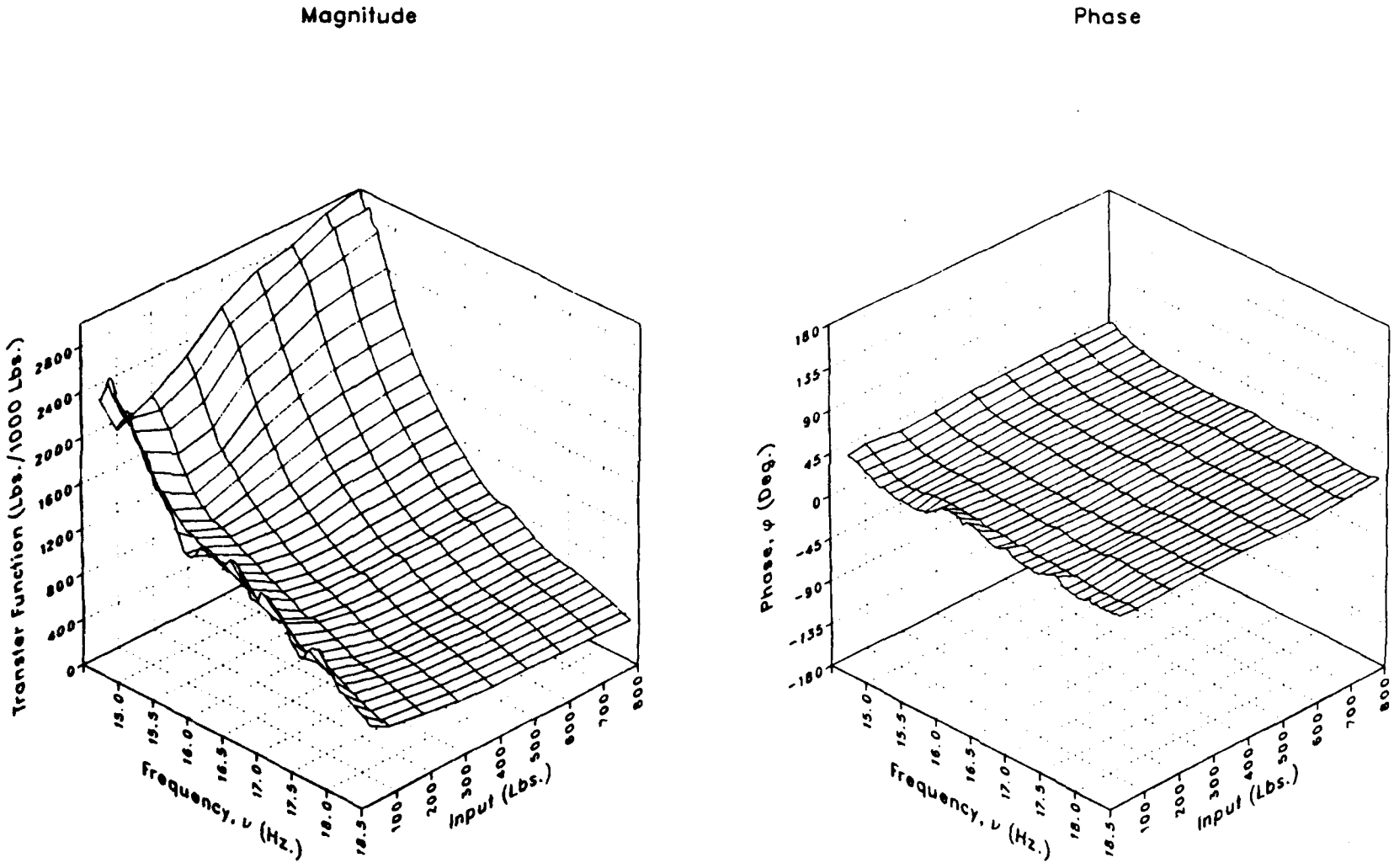

(c) MRLIFTB Concluded.

Figure 2.– Continued.

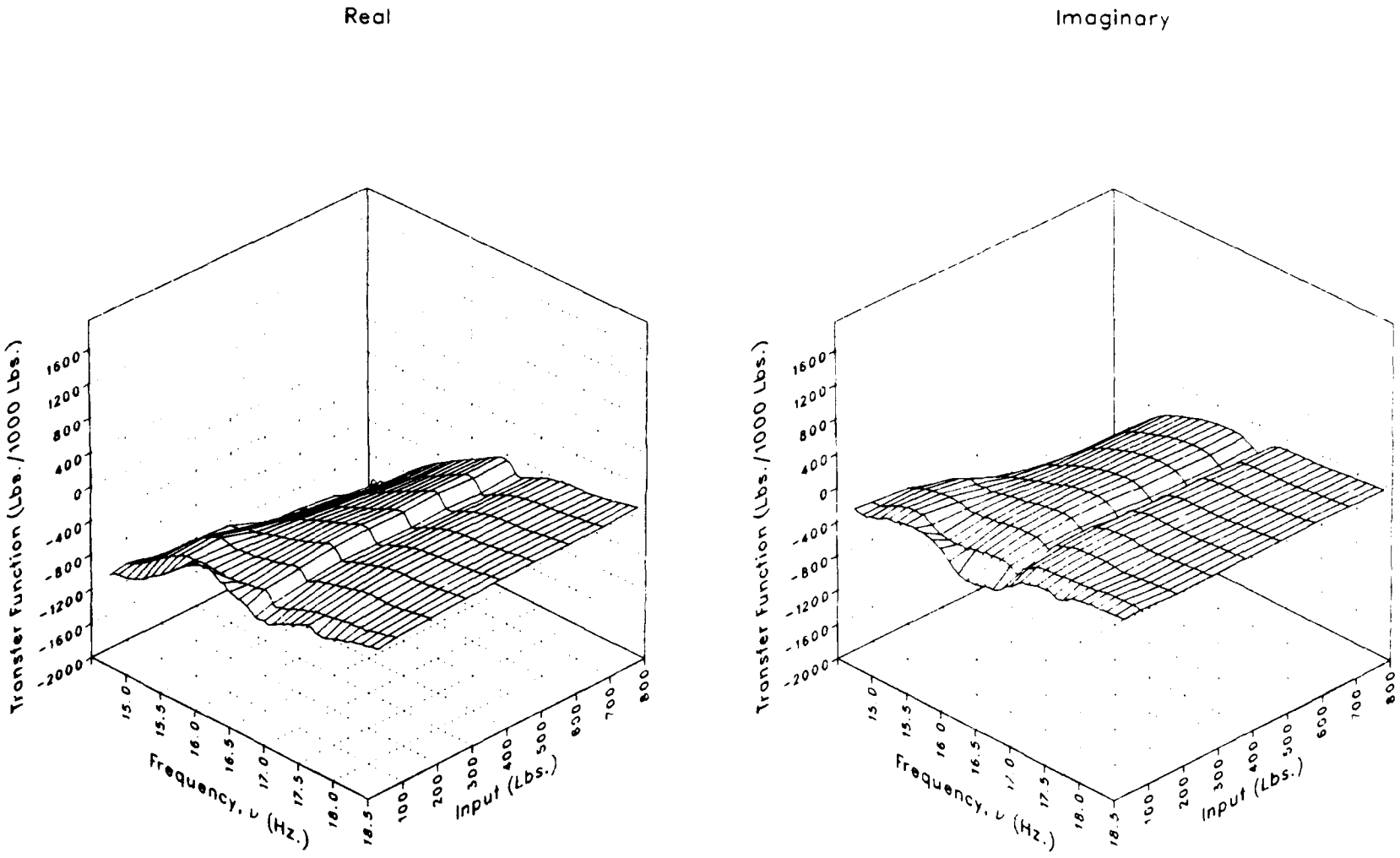

(d) MRLIFTC

Figure 2.– Continued.

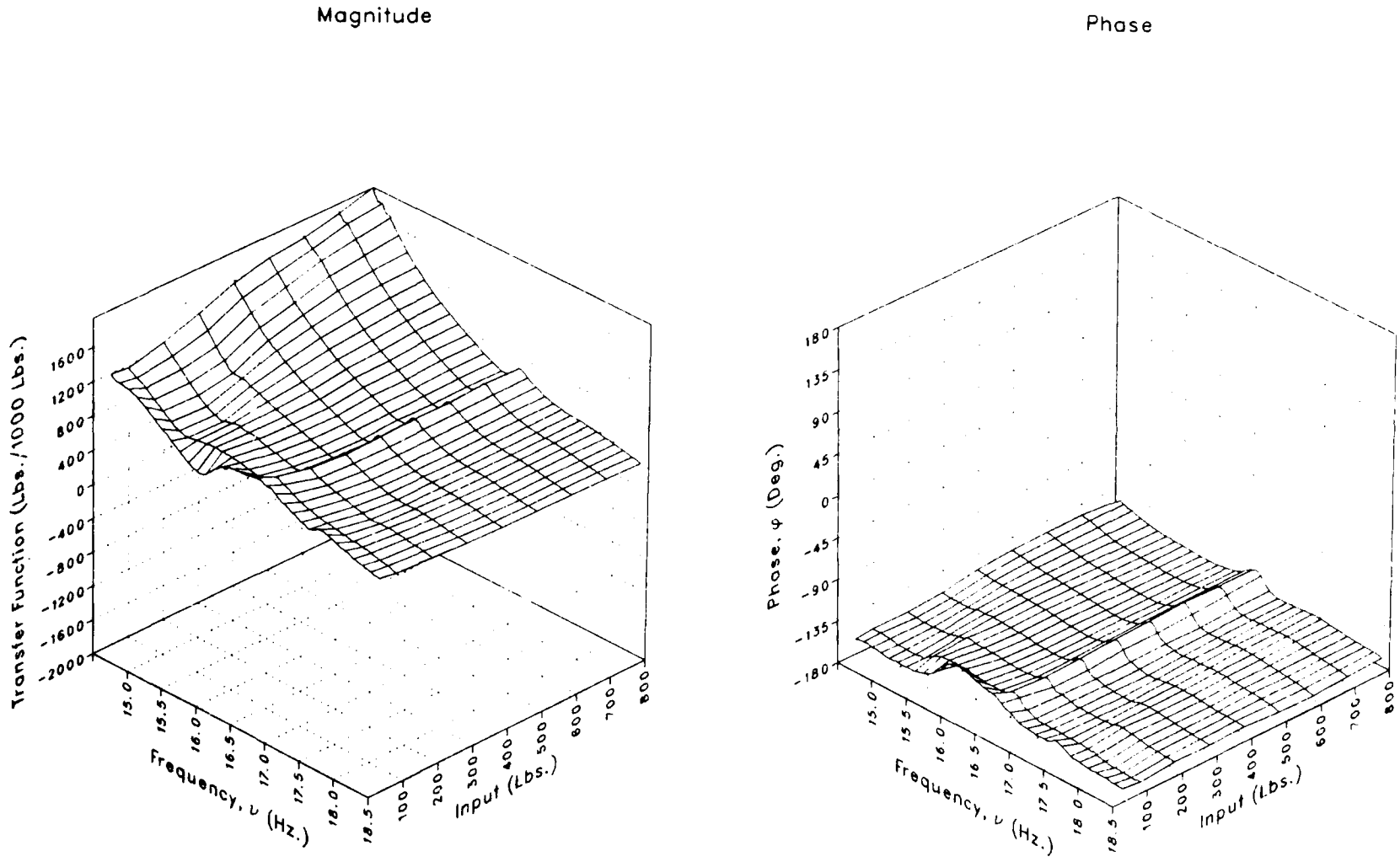

(d) MRLIFTC Concluded.

Figure 2.– Continued.

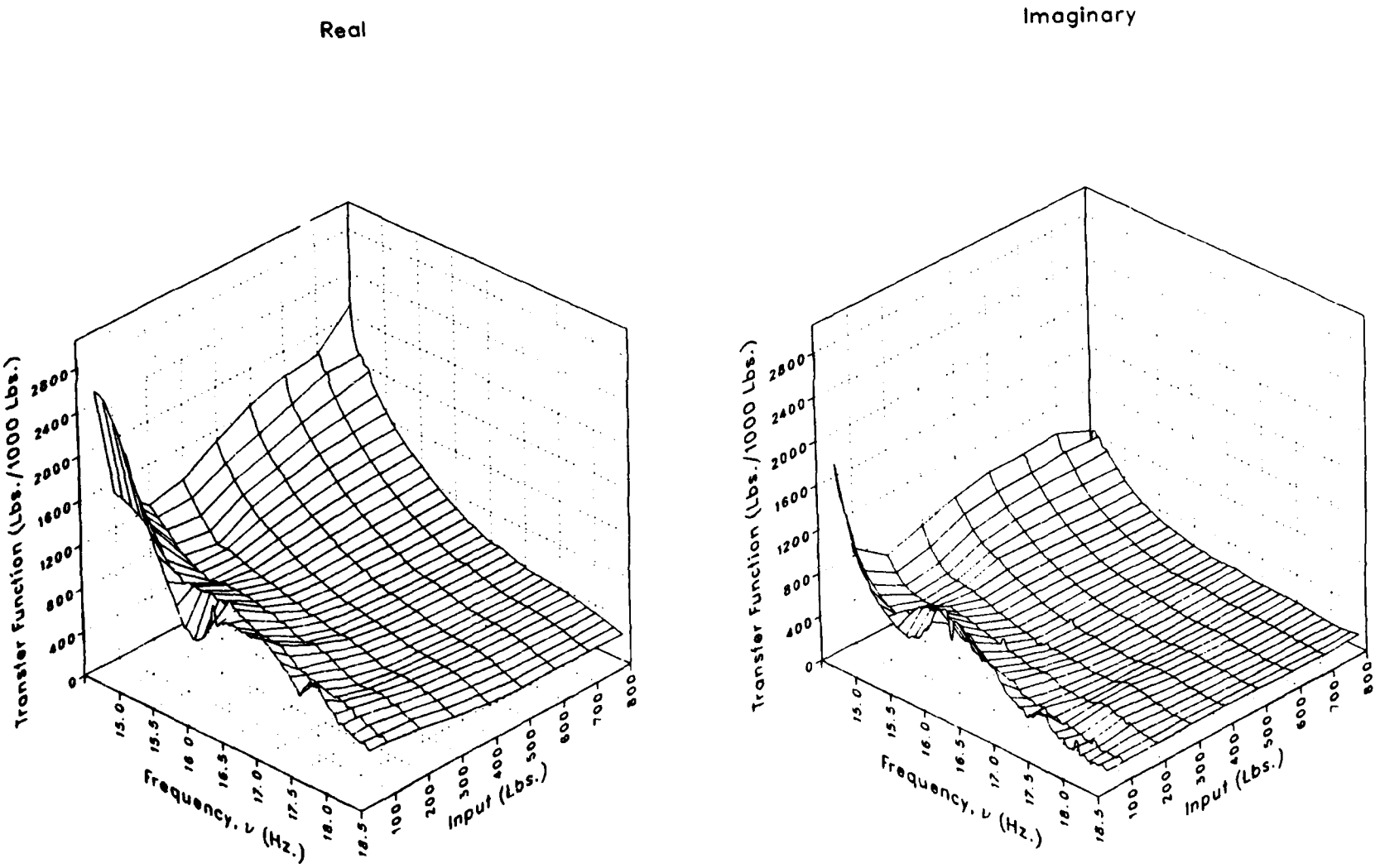

(e) MRLIFTD

Figure 2.– Continued.

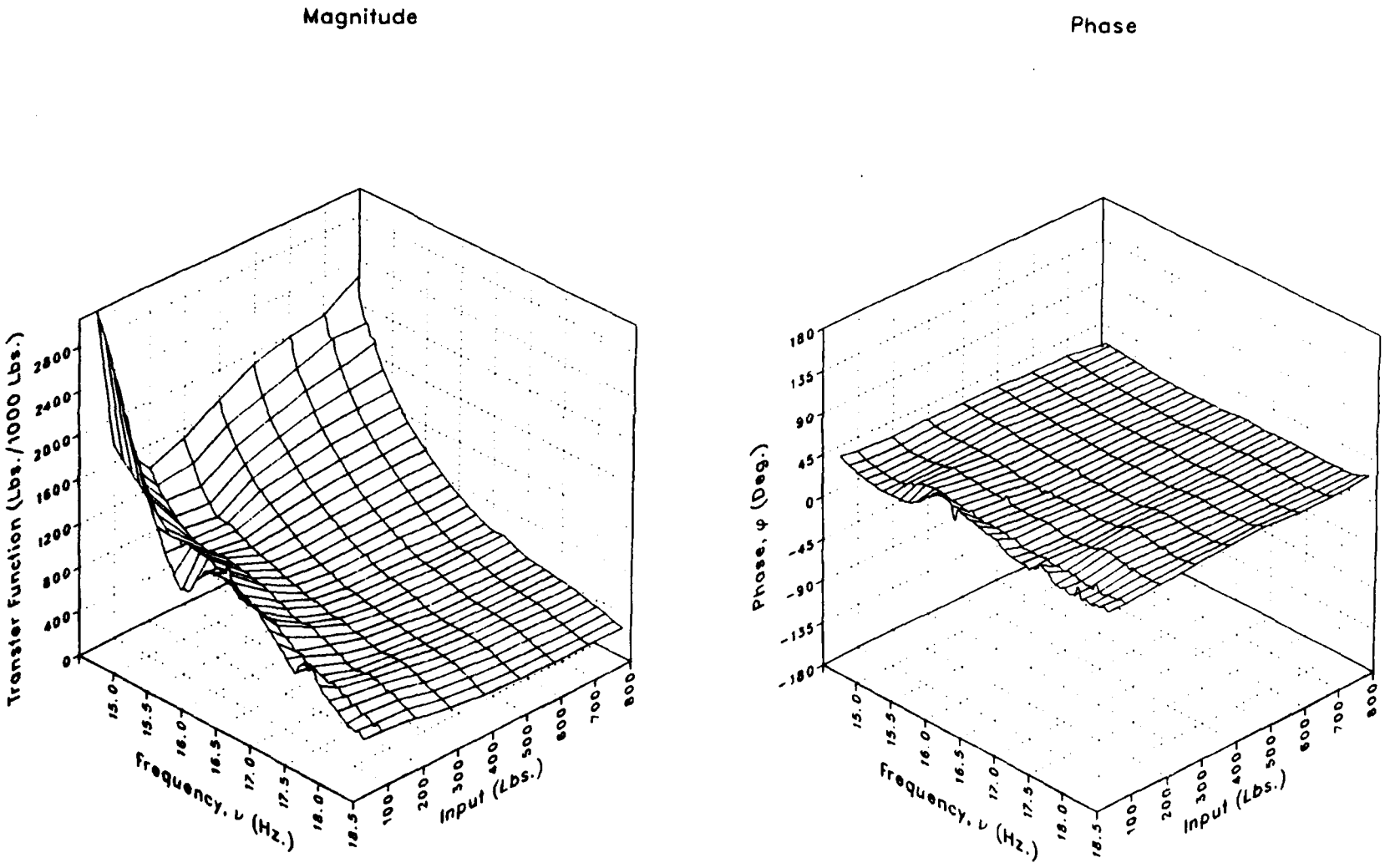

(e) MRLIFTD Concluded.

Figure 2.– Continued.

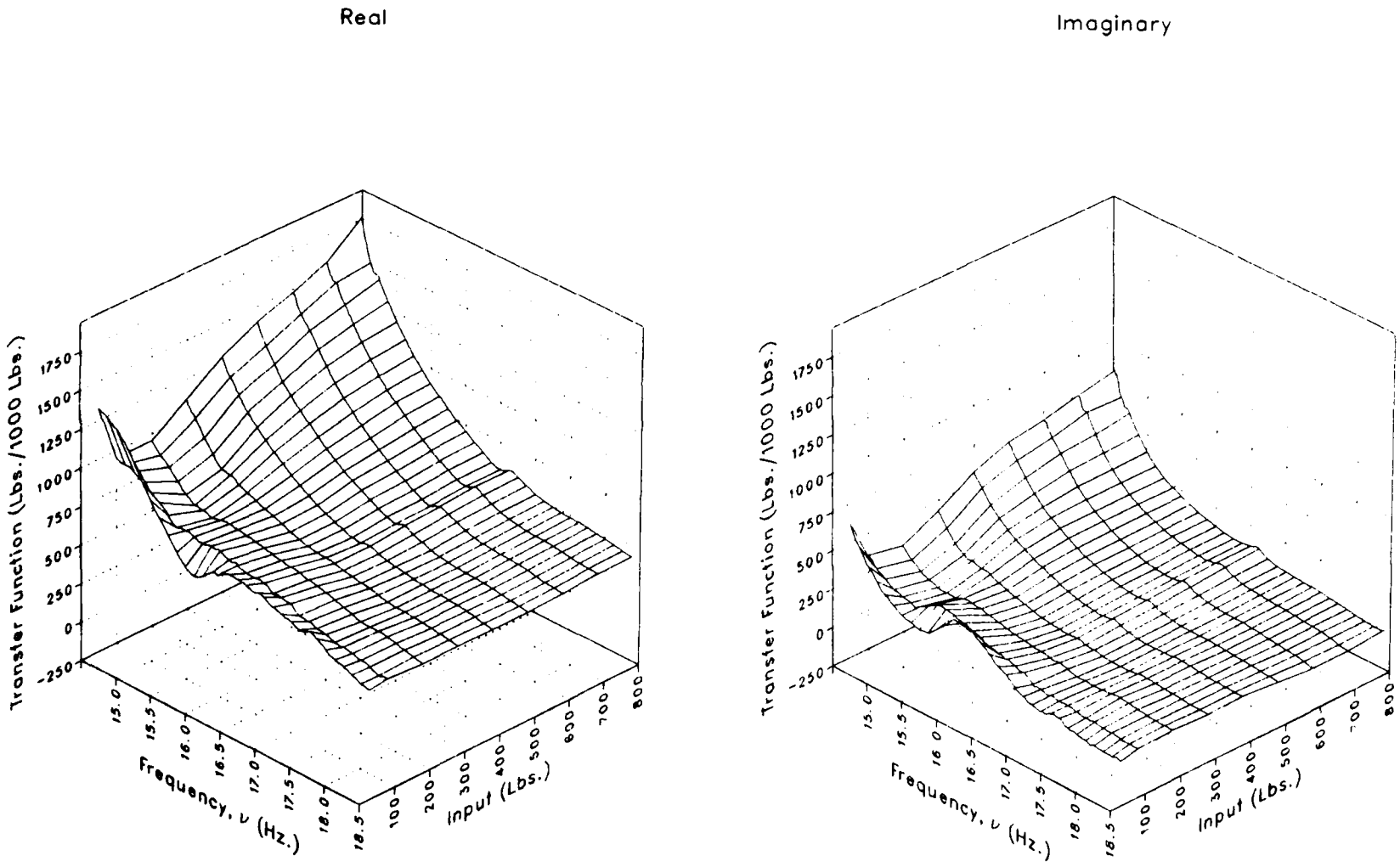

(f) MRGBQCE

Figure 2.– Continued.

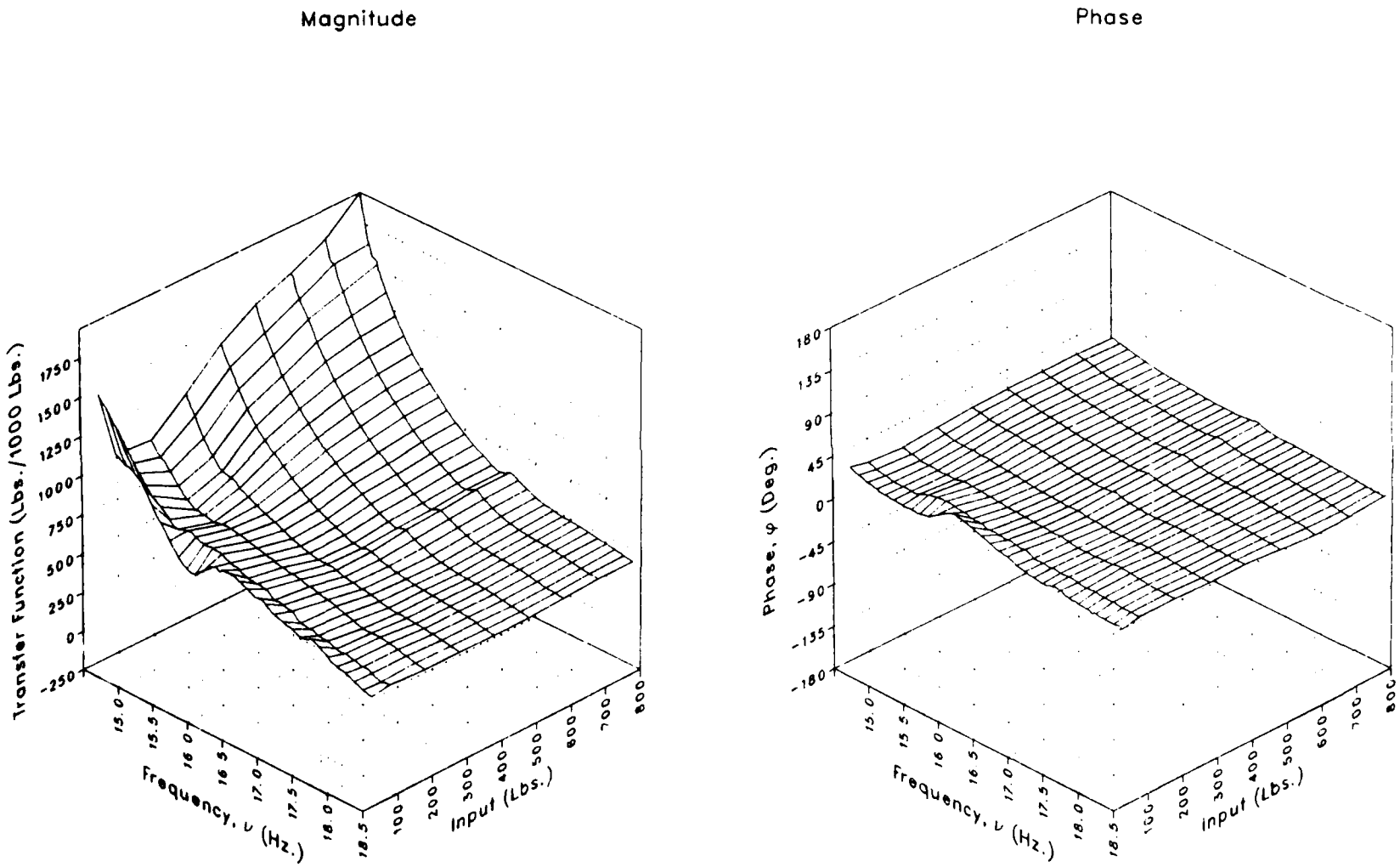

(f) MRGBQCE Concluded.

Figure 2.– Continued.

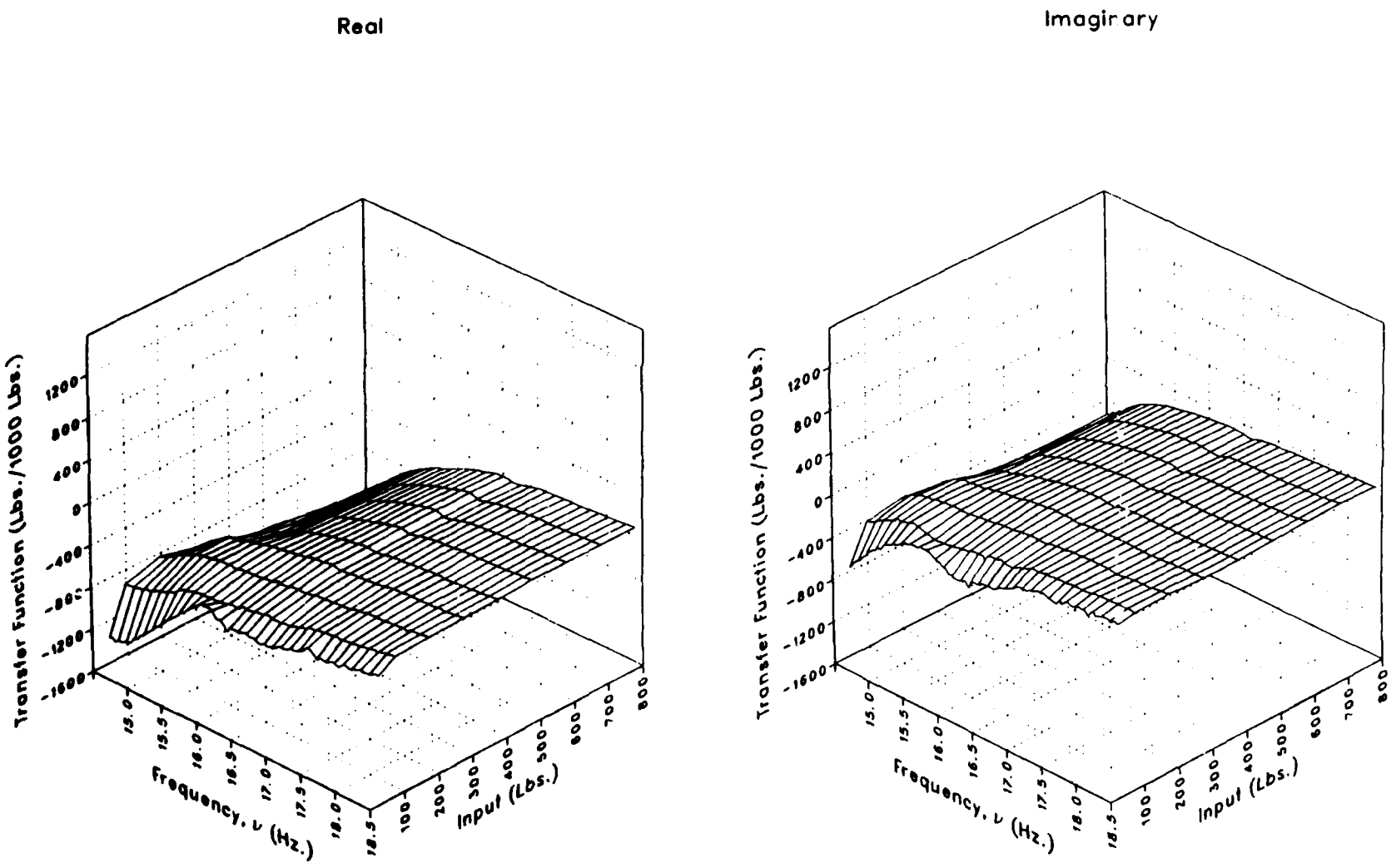

(g) MRGBQCF

Figure 2.– Continued.

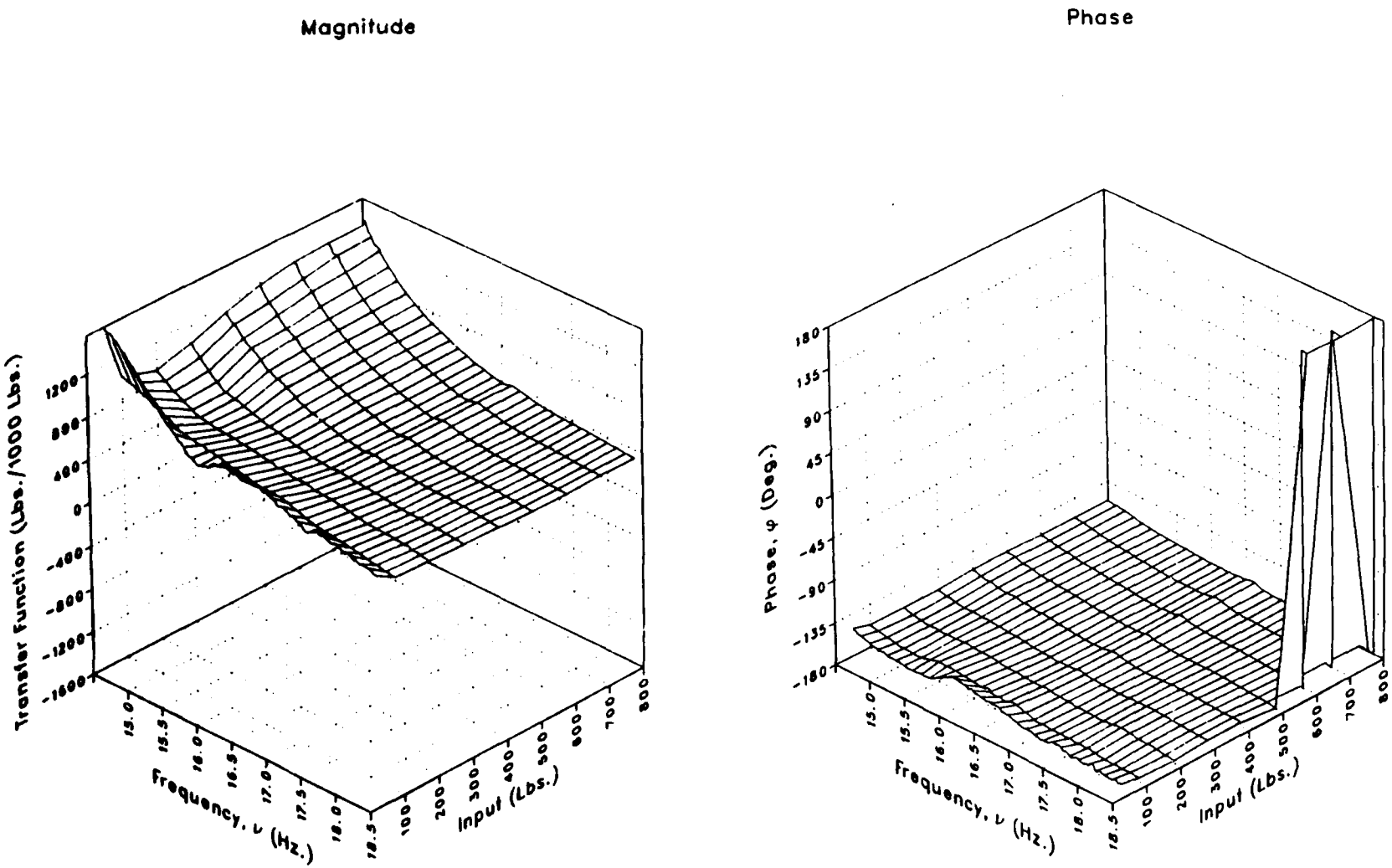

(g) MRGBQCF Concluded.

Figure 2.– Continued.

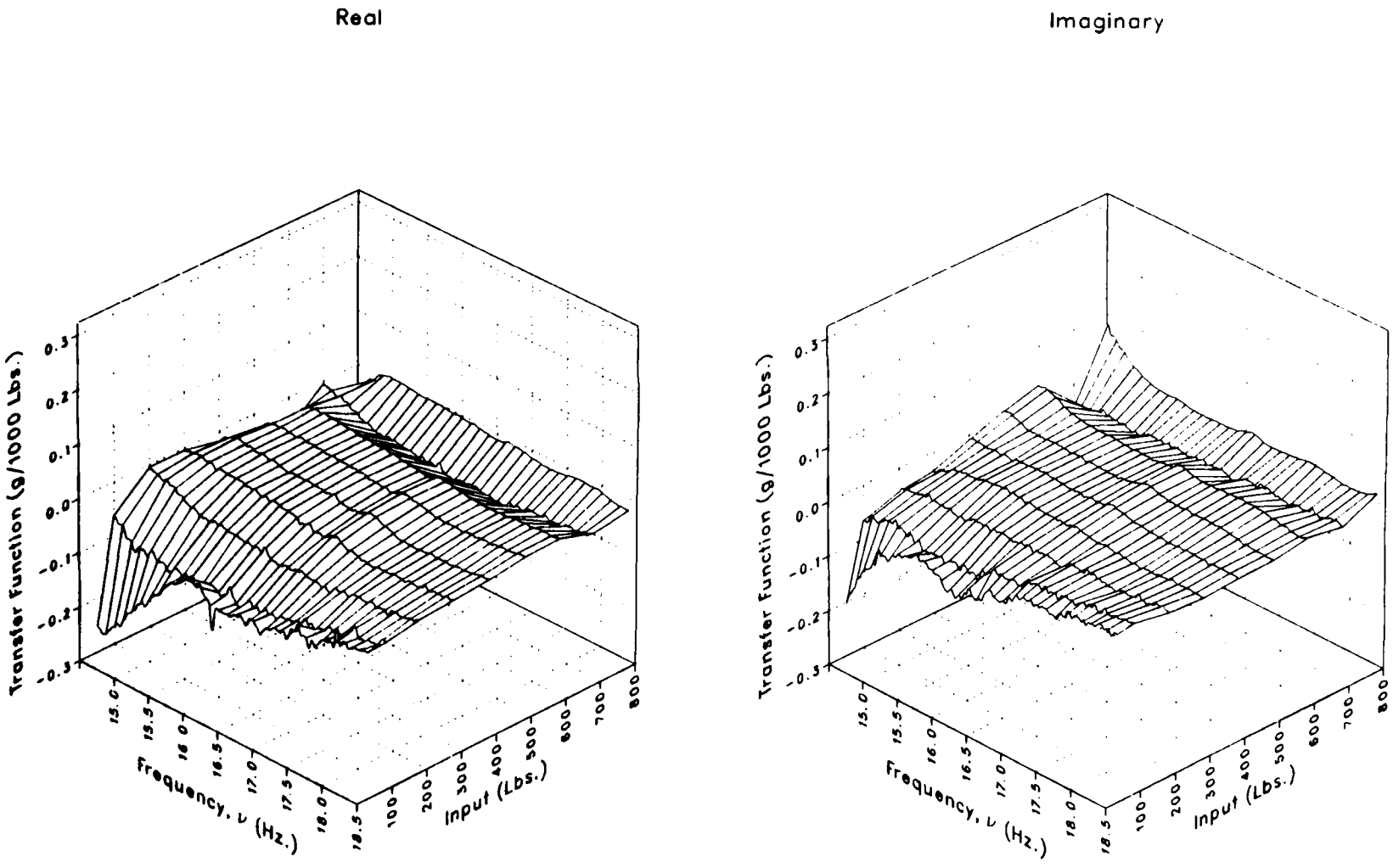

(h) LOMGB

Figure 2.– Continued.

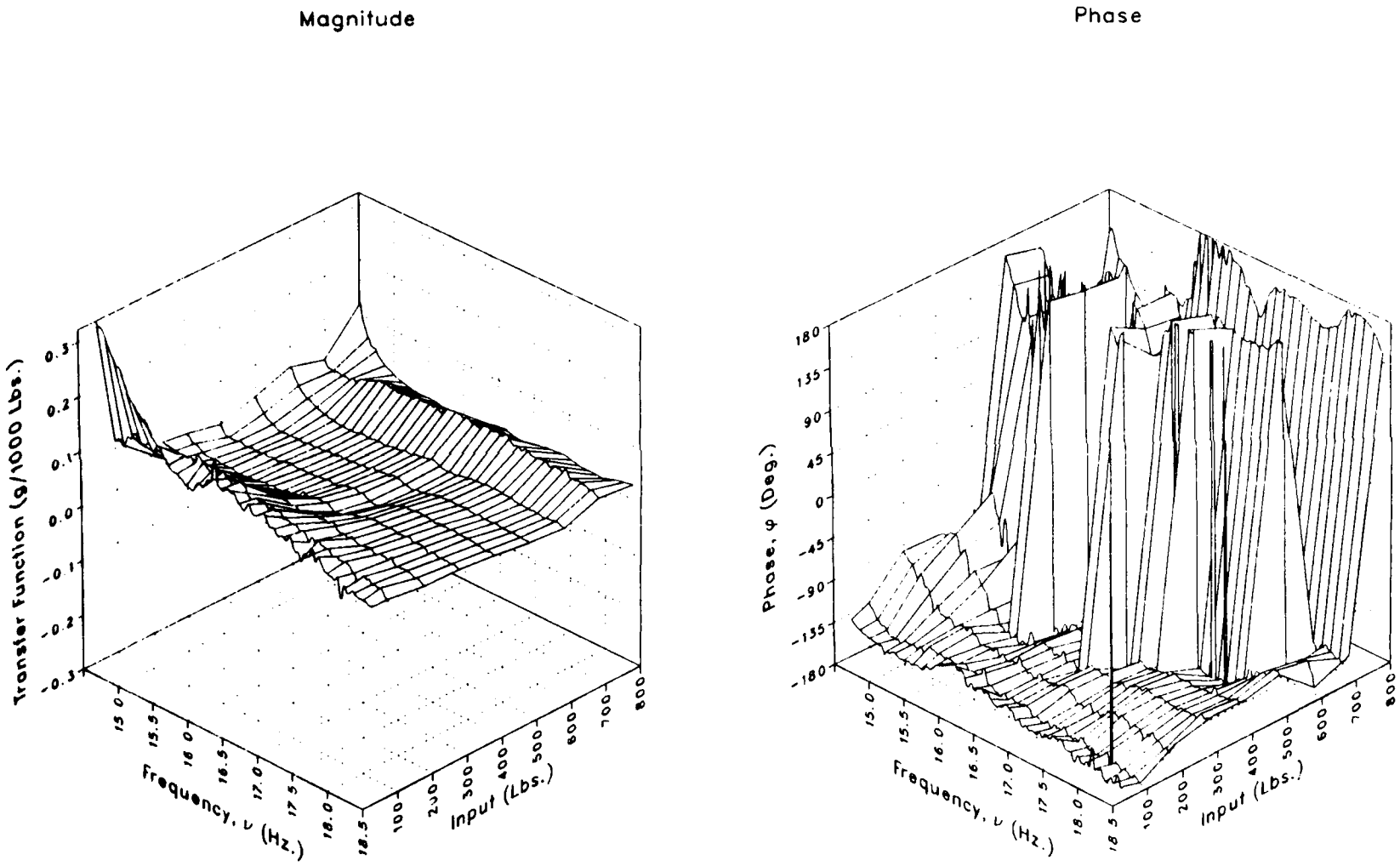

(h) LOMGB Concluded.

Figure 2.– Continued.

Real

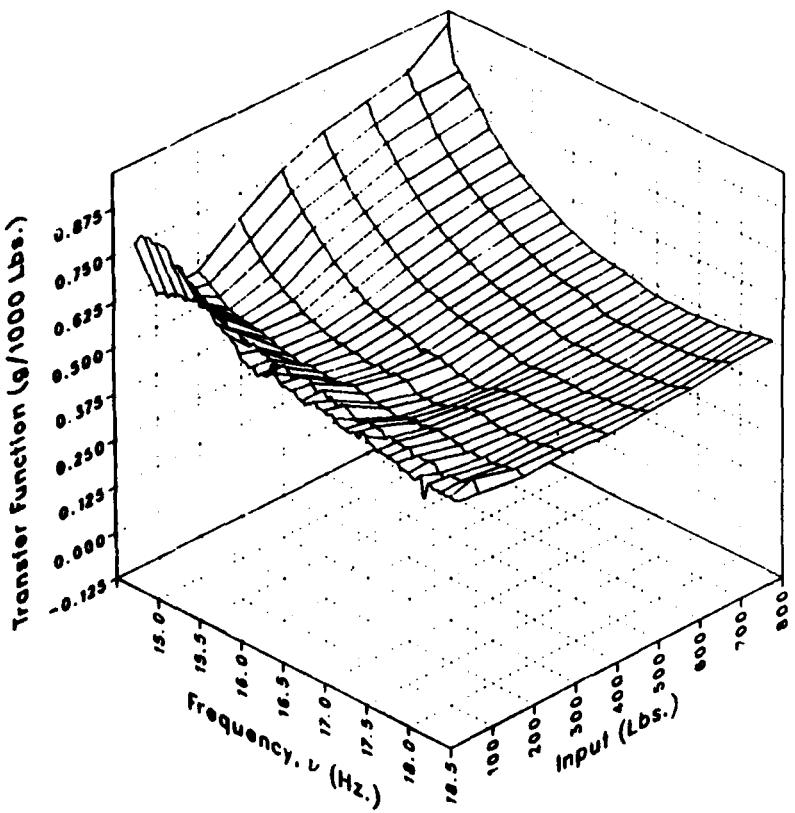

Imaginary

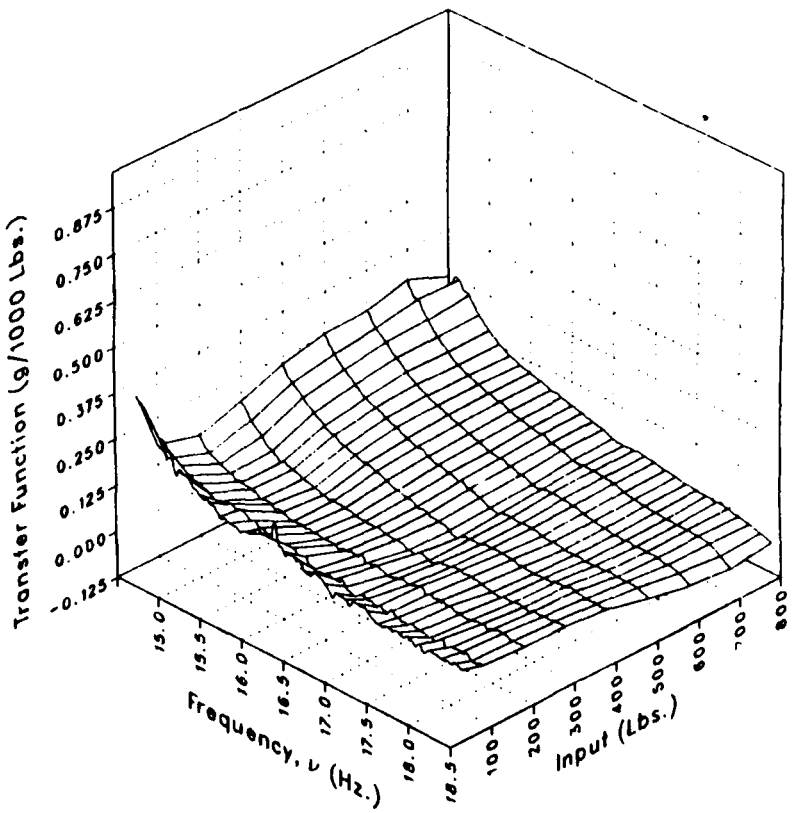

(i) LMGB

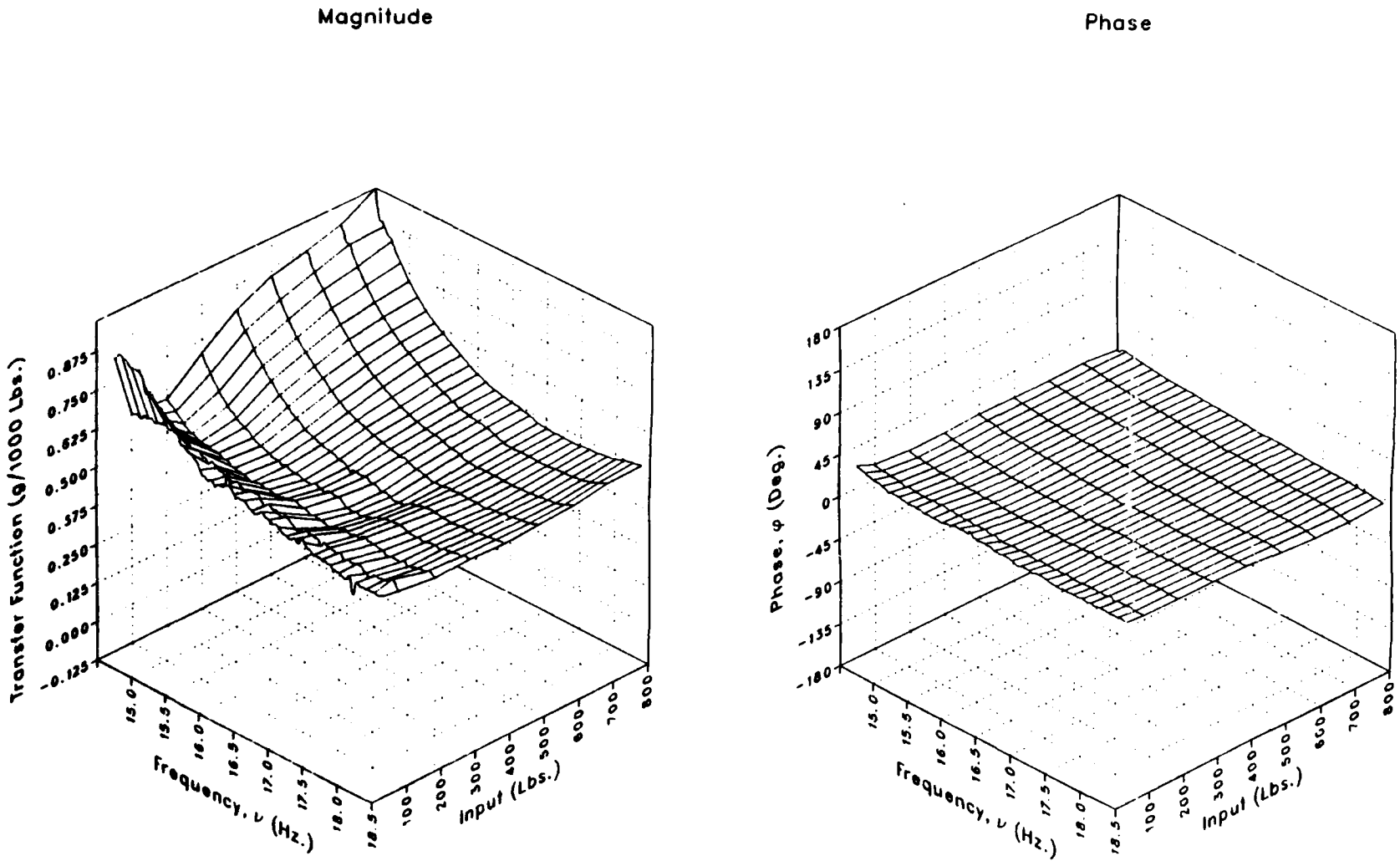

(i) LMGB Concluded.

Figure 2.– Continued.

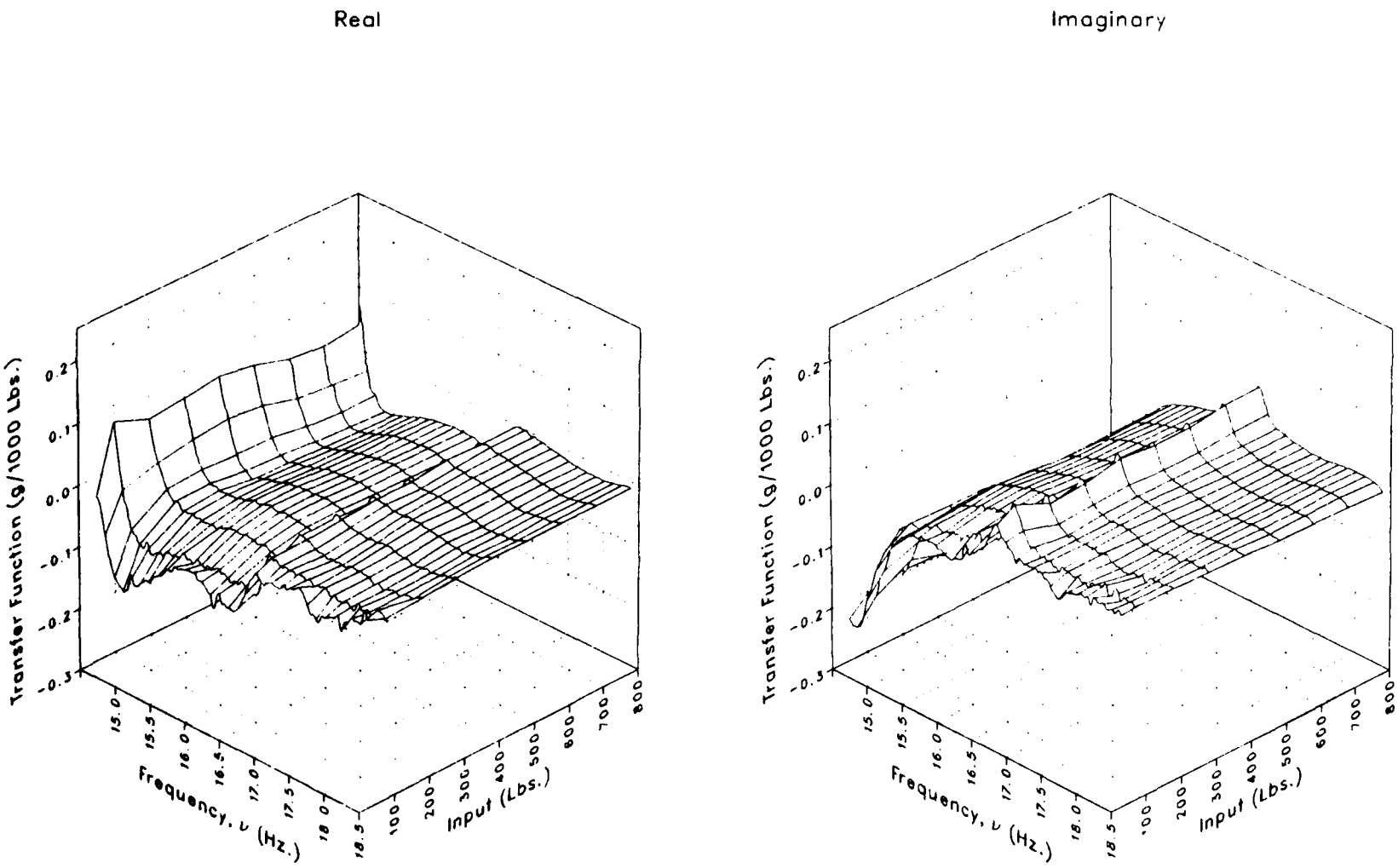

(j) VMGB

Figure 2.– Continued.

Magnitude

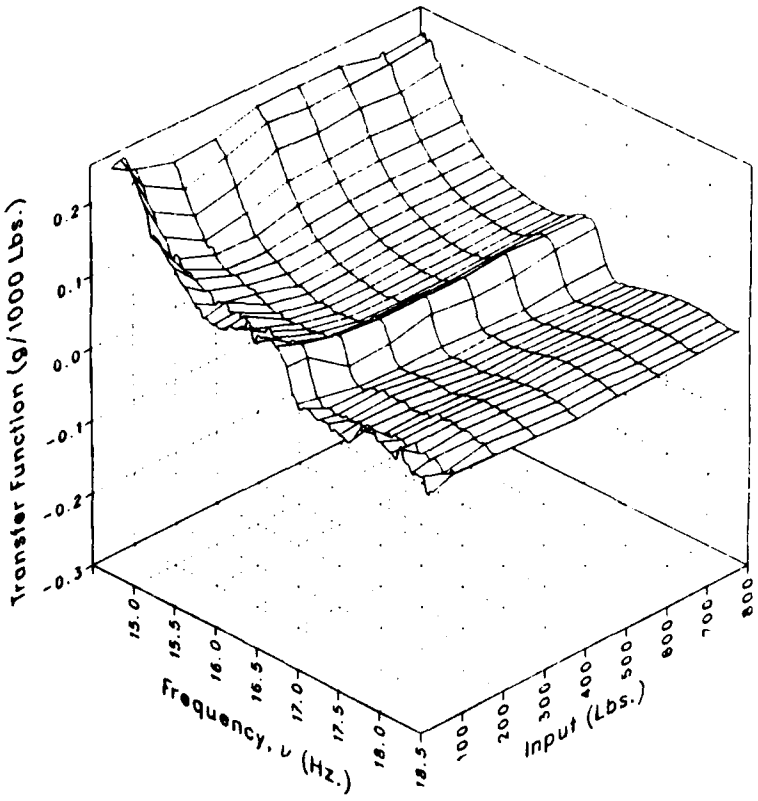

Phase

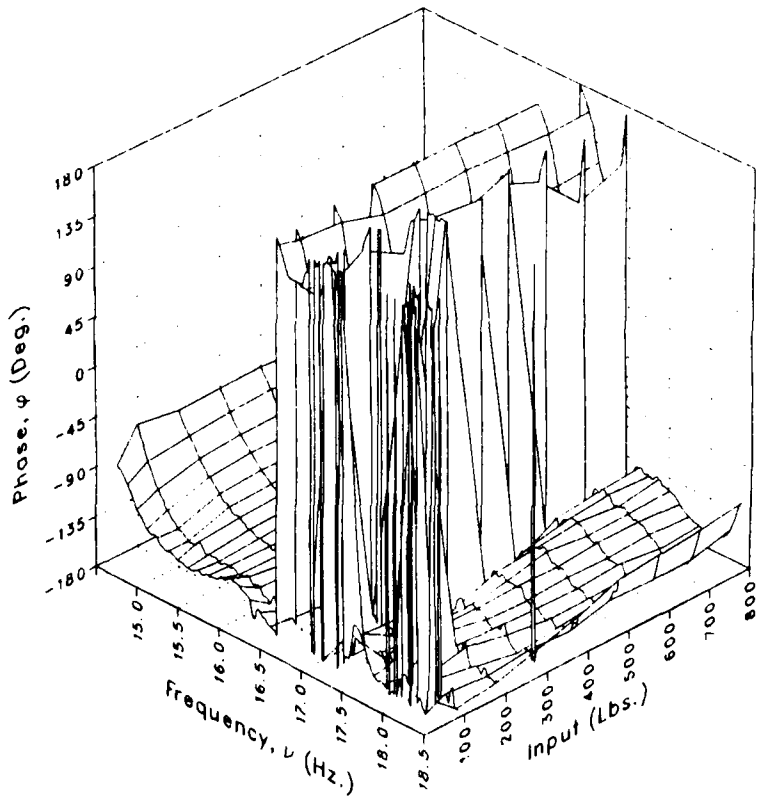

(j) VMGB Concluded.

Figure 2.– Continued.

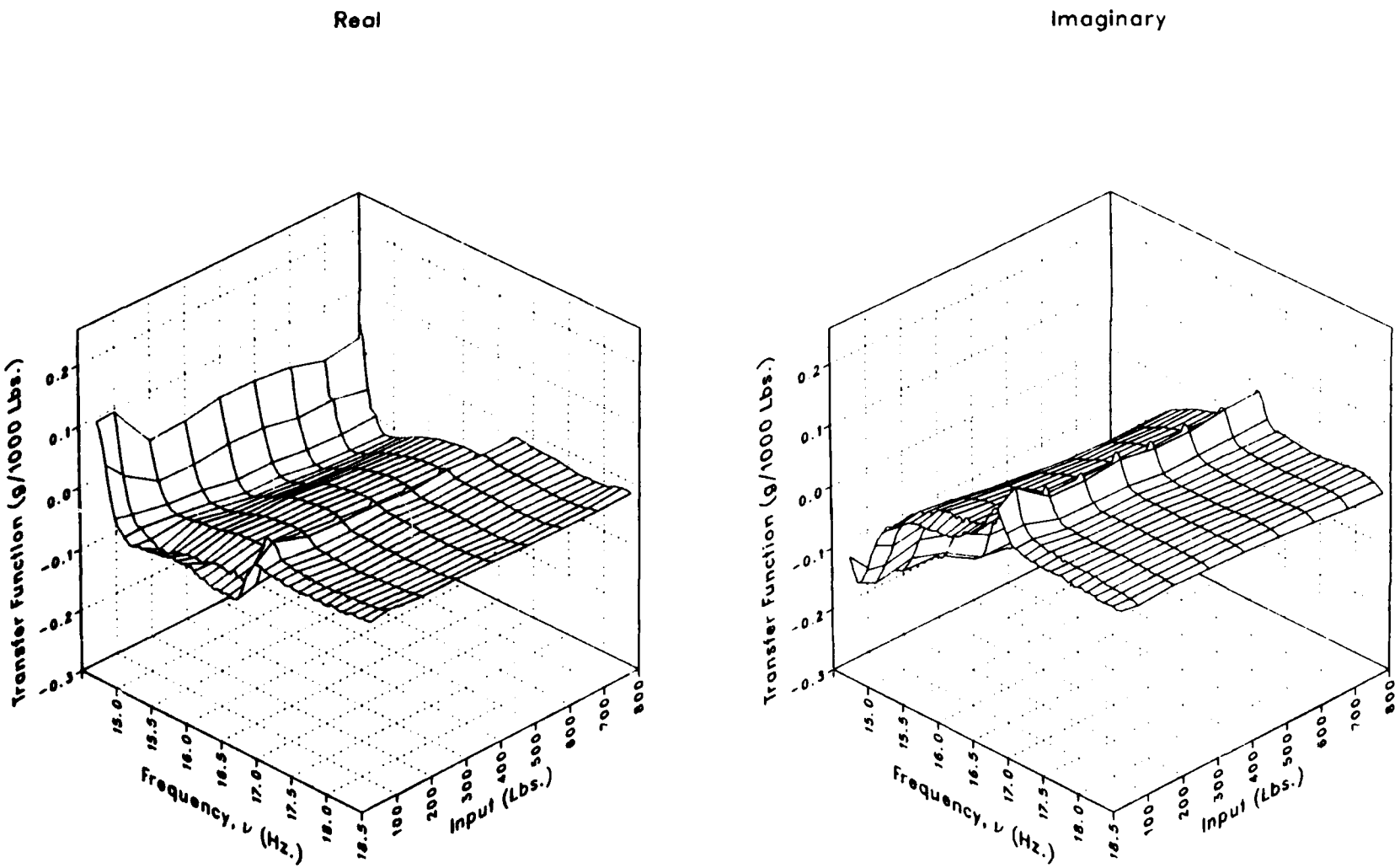

(k) XMRFBPV

Figure 2.– Continued.

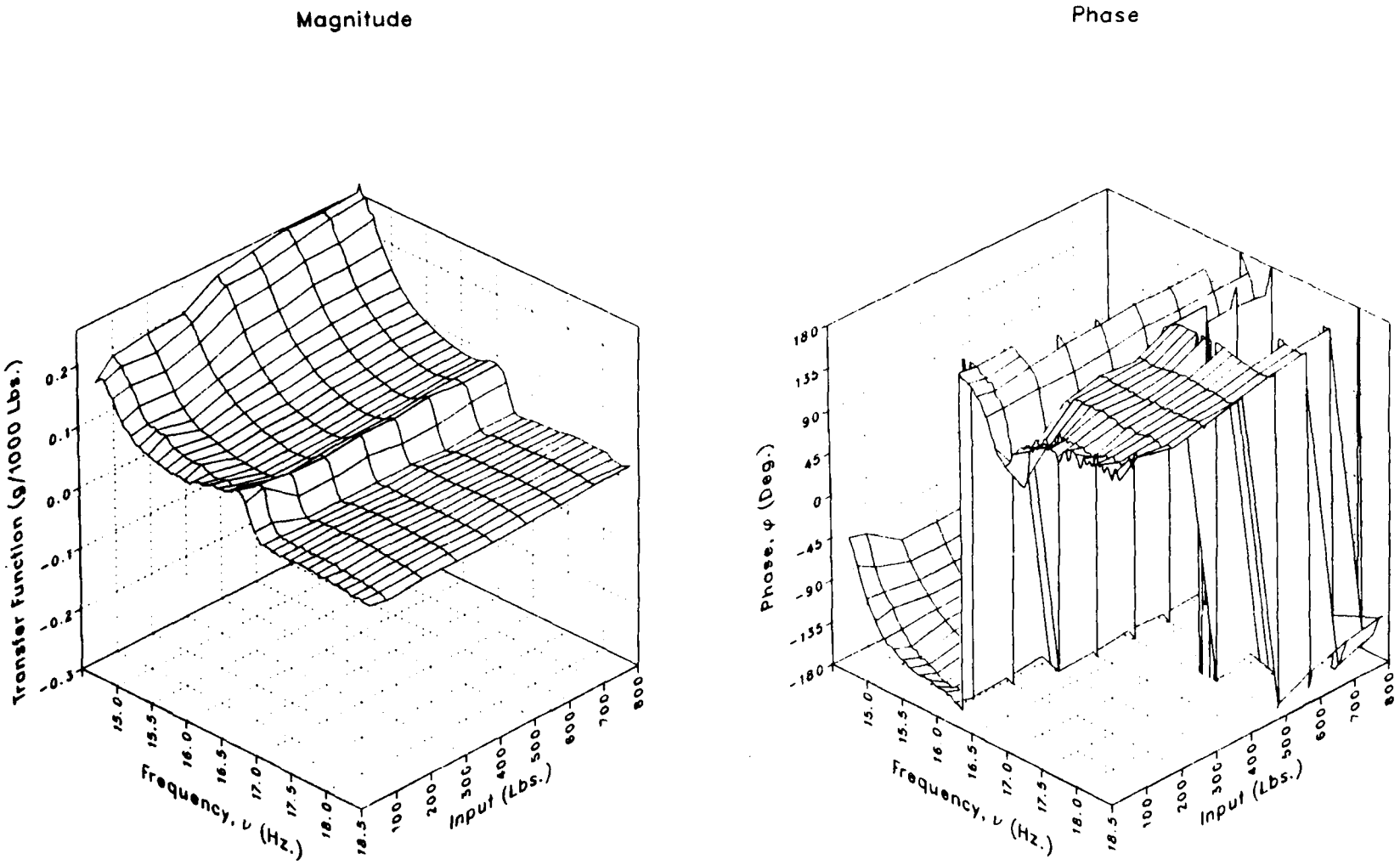

(k) XMRFBPV Concluded.

Figure 2.– Continued.

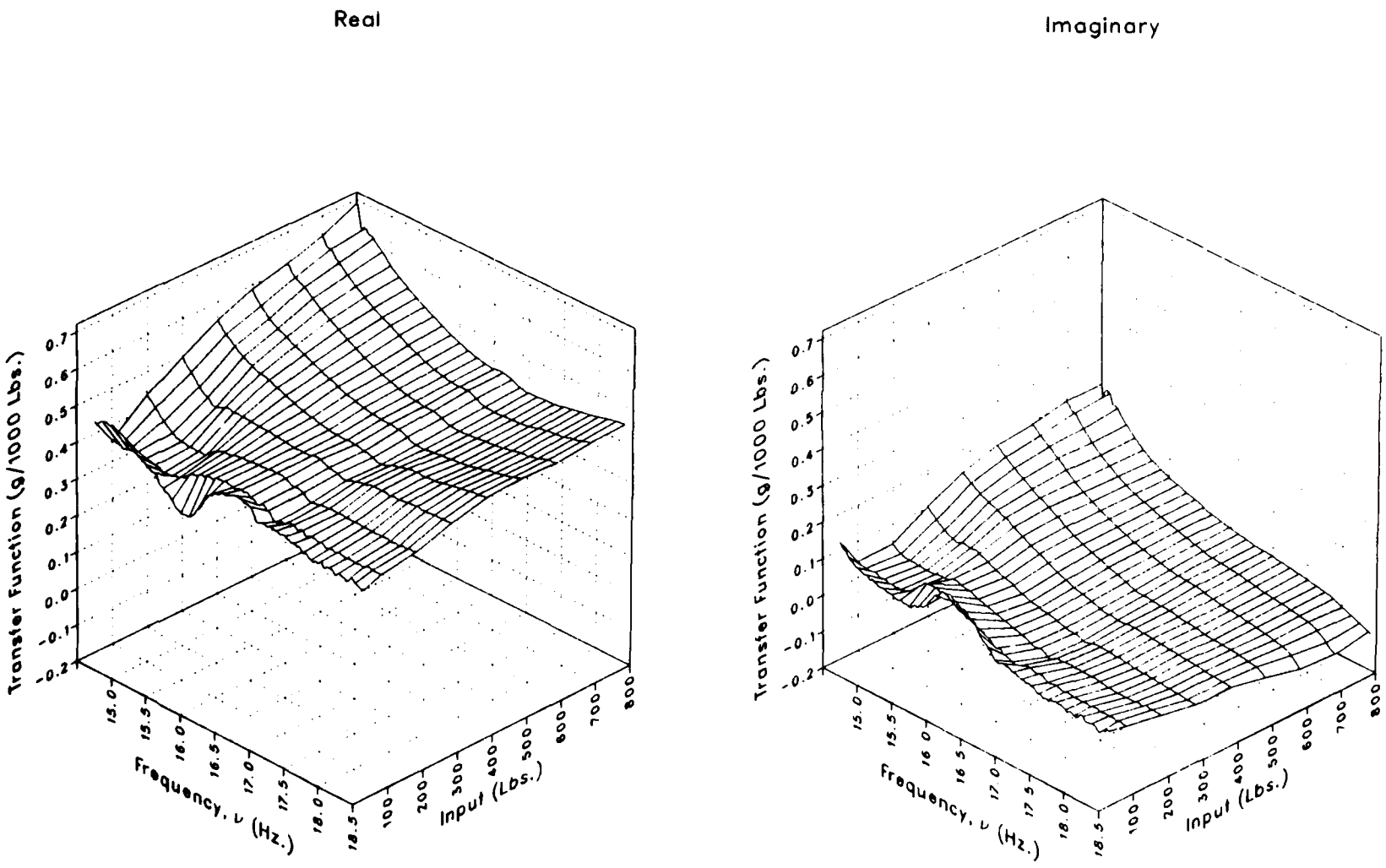

(l) XMRFBPL

Figure 2.– Continued.

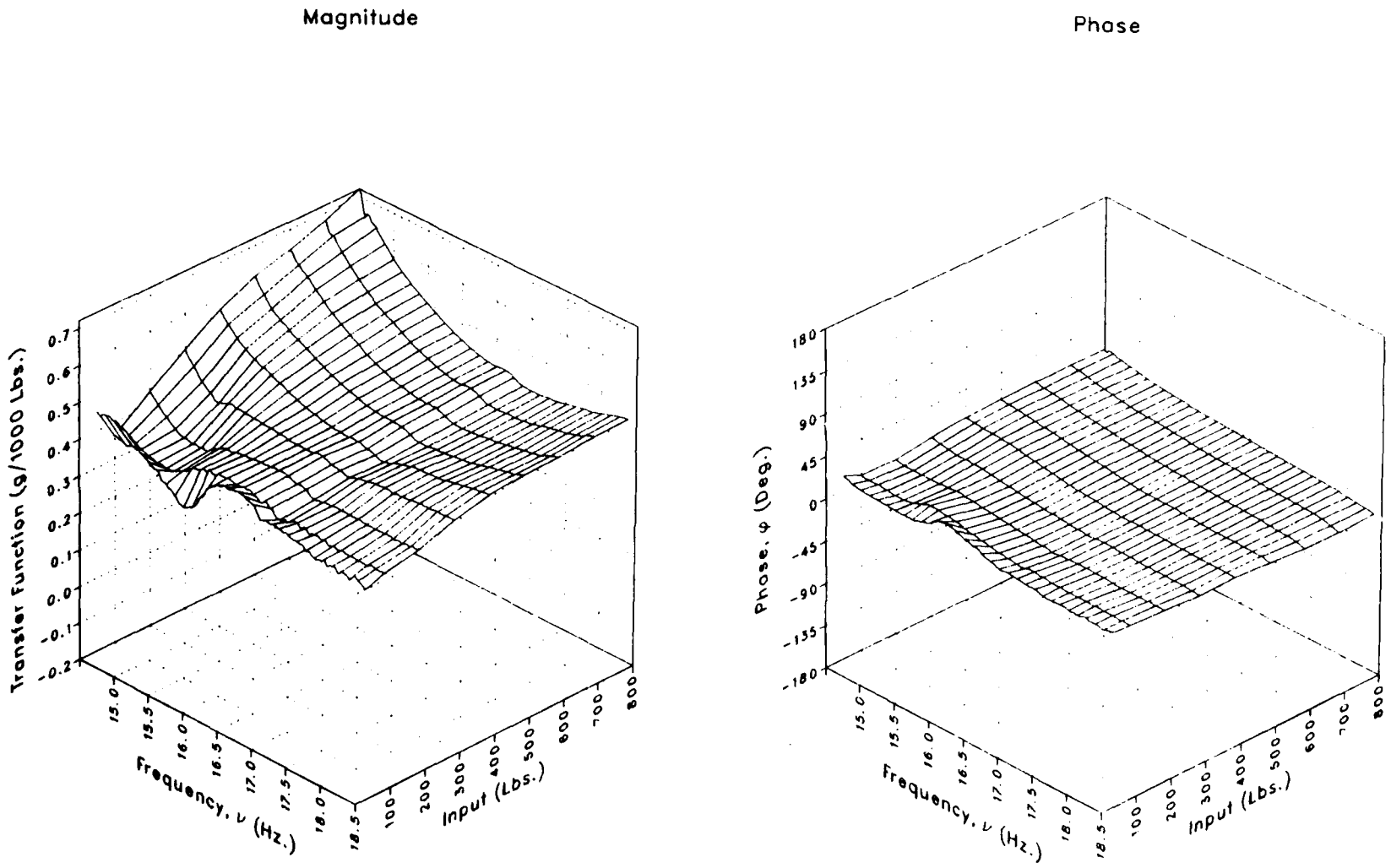

(l) XMRFBPL Concluded.

Figure 2.– Continued.

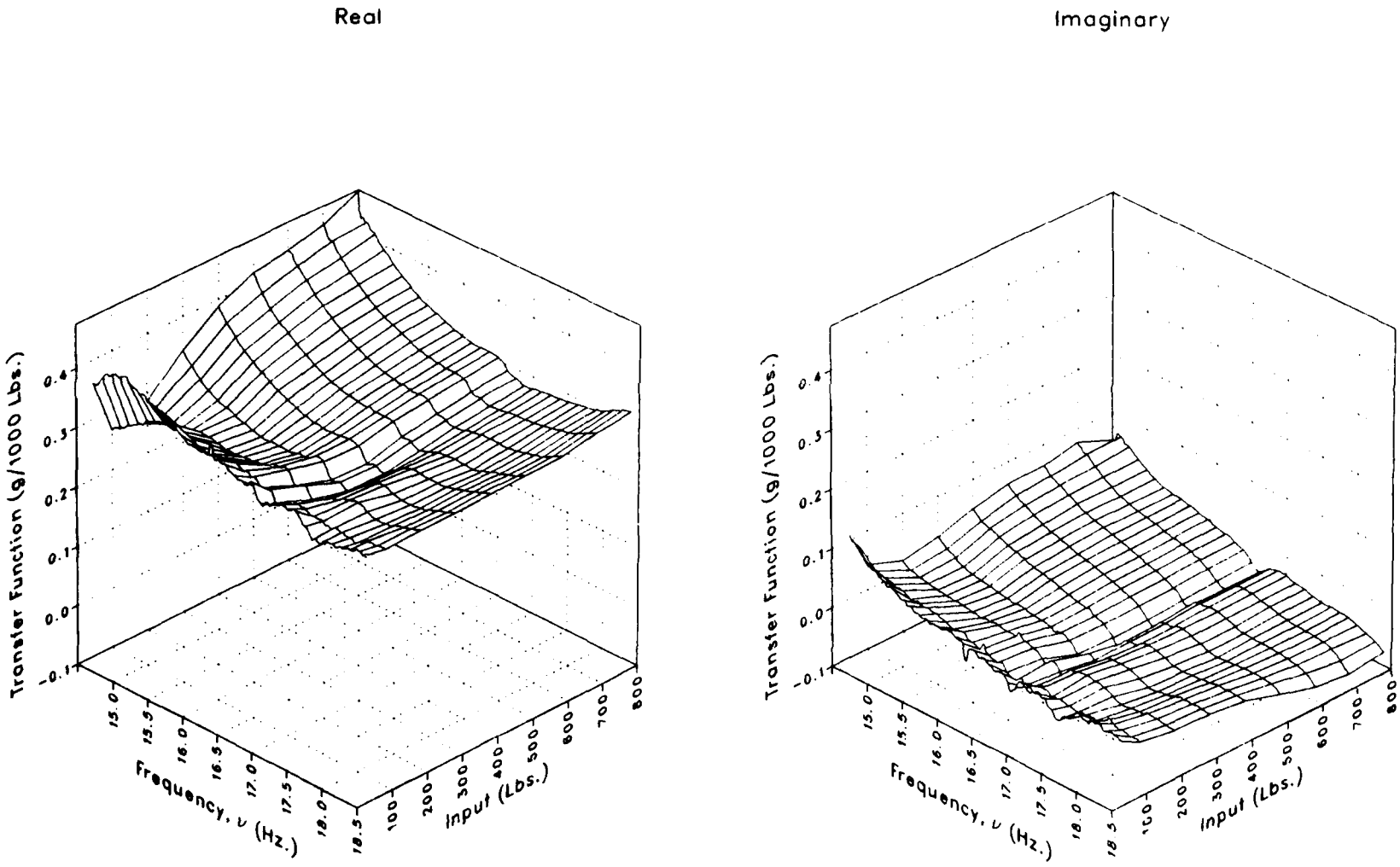

(m) XMRFBPLO

Figure 2.– Continued.

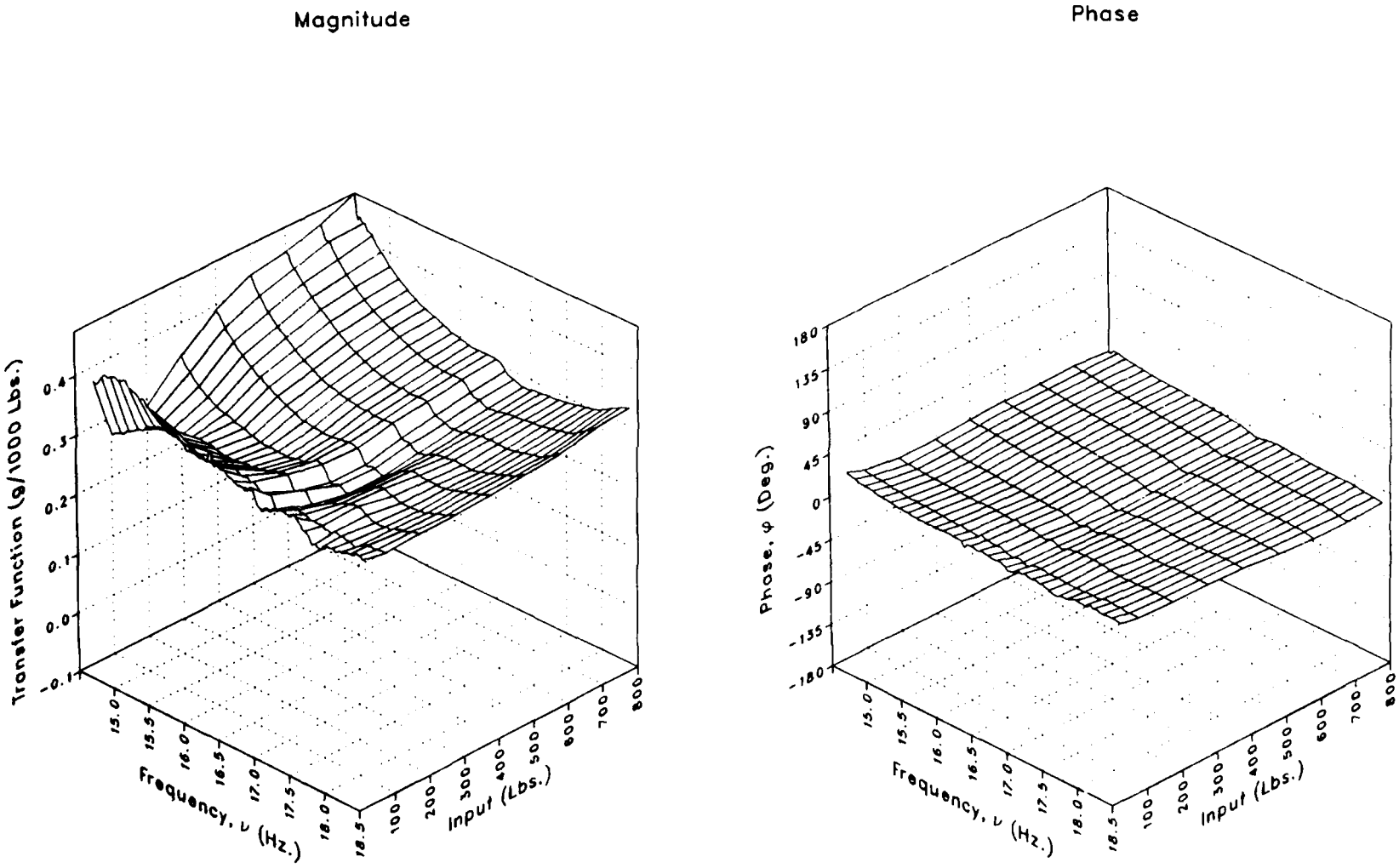

(m) XMRFBPLO Concluded.

Figure 2.– Continued.

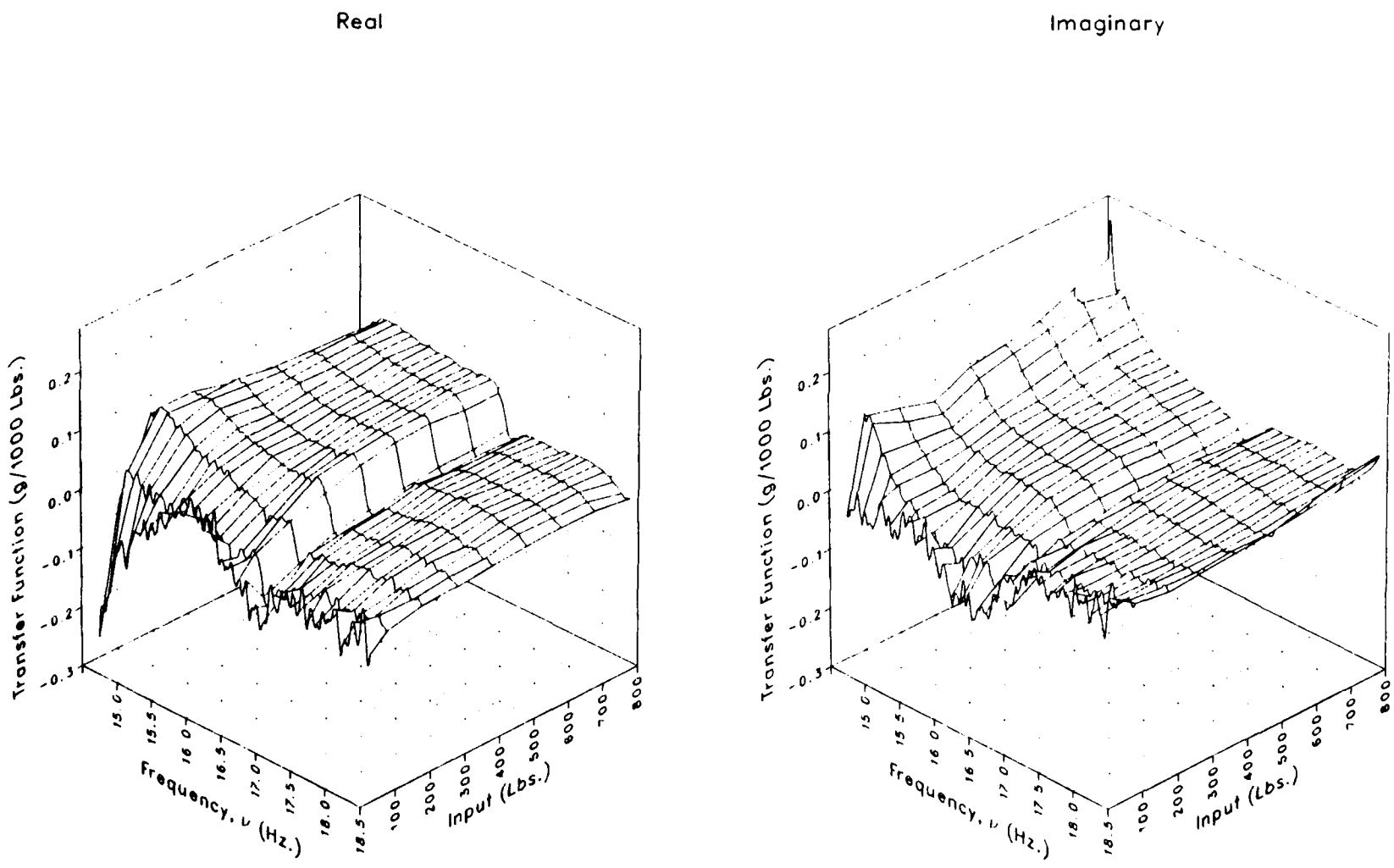

(n) STA56NV

Figure 2.– Continued.

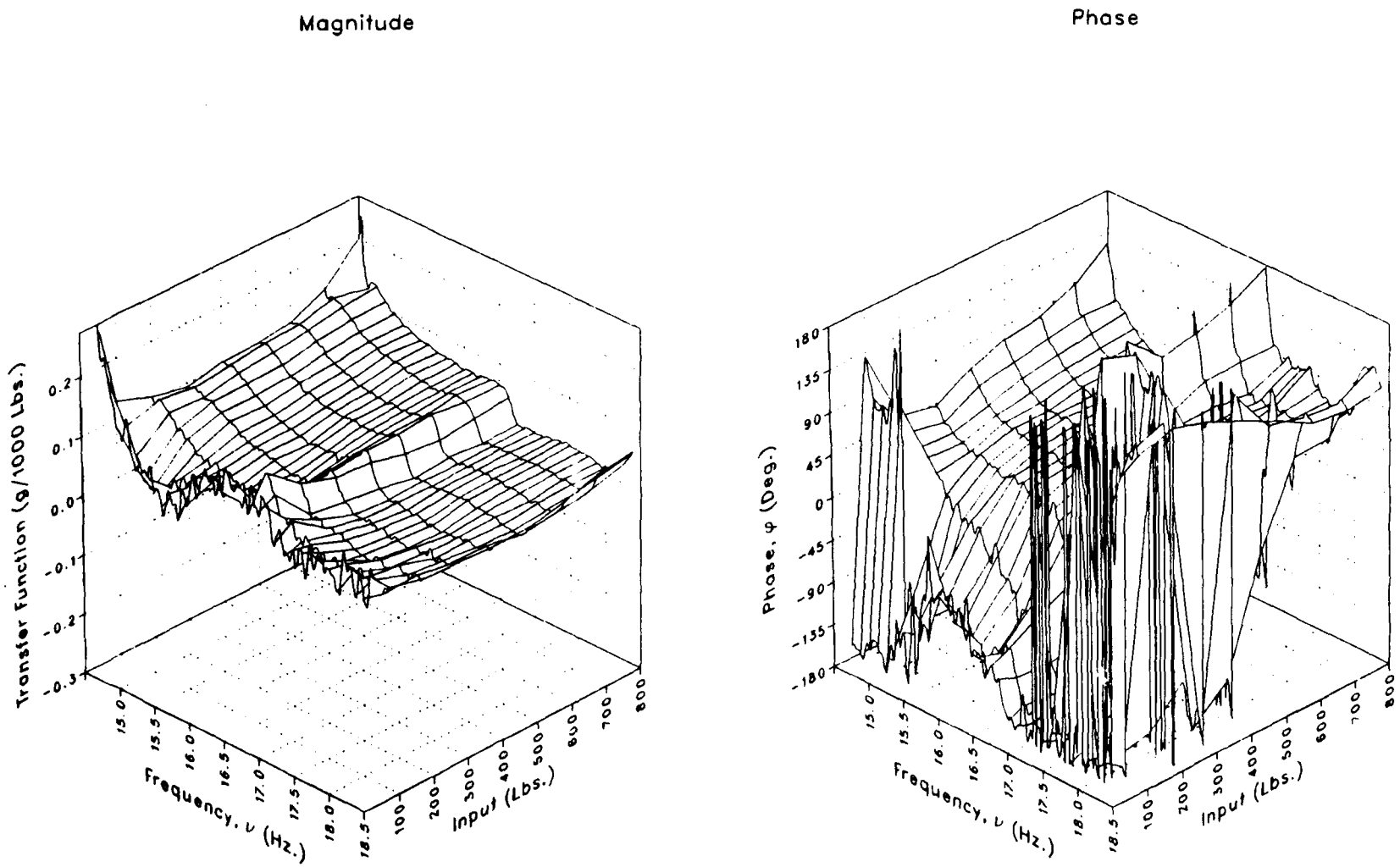

(n) STA56NV Concluded.

Figure 2.– Continued.

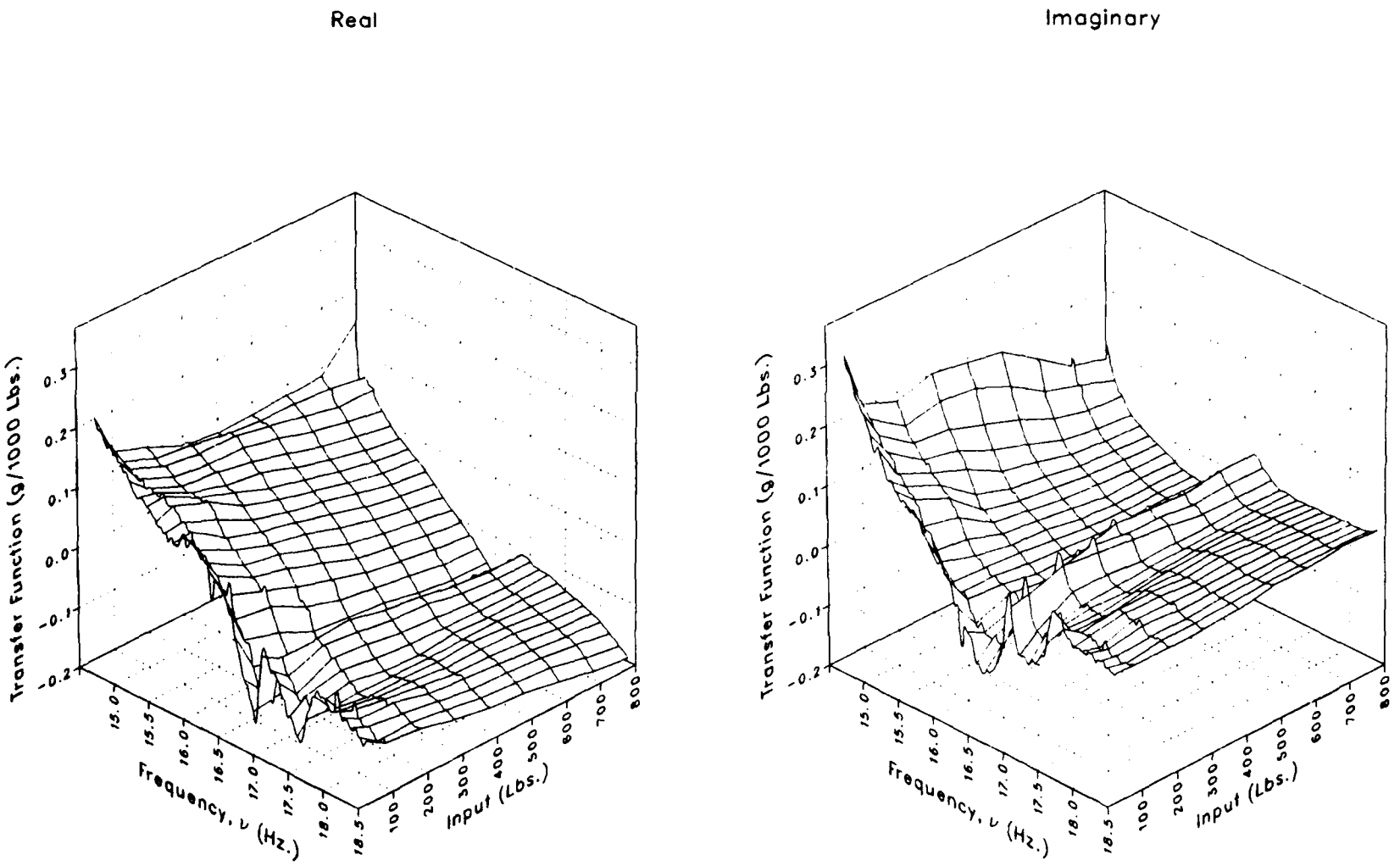

(o) STA56NL

Figure 2.– Continued.

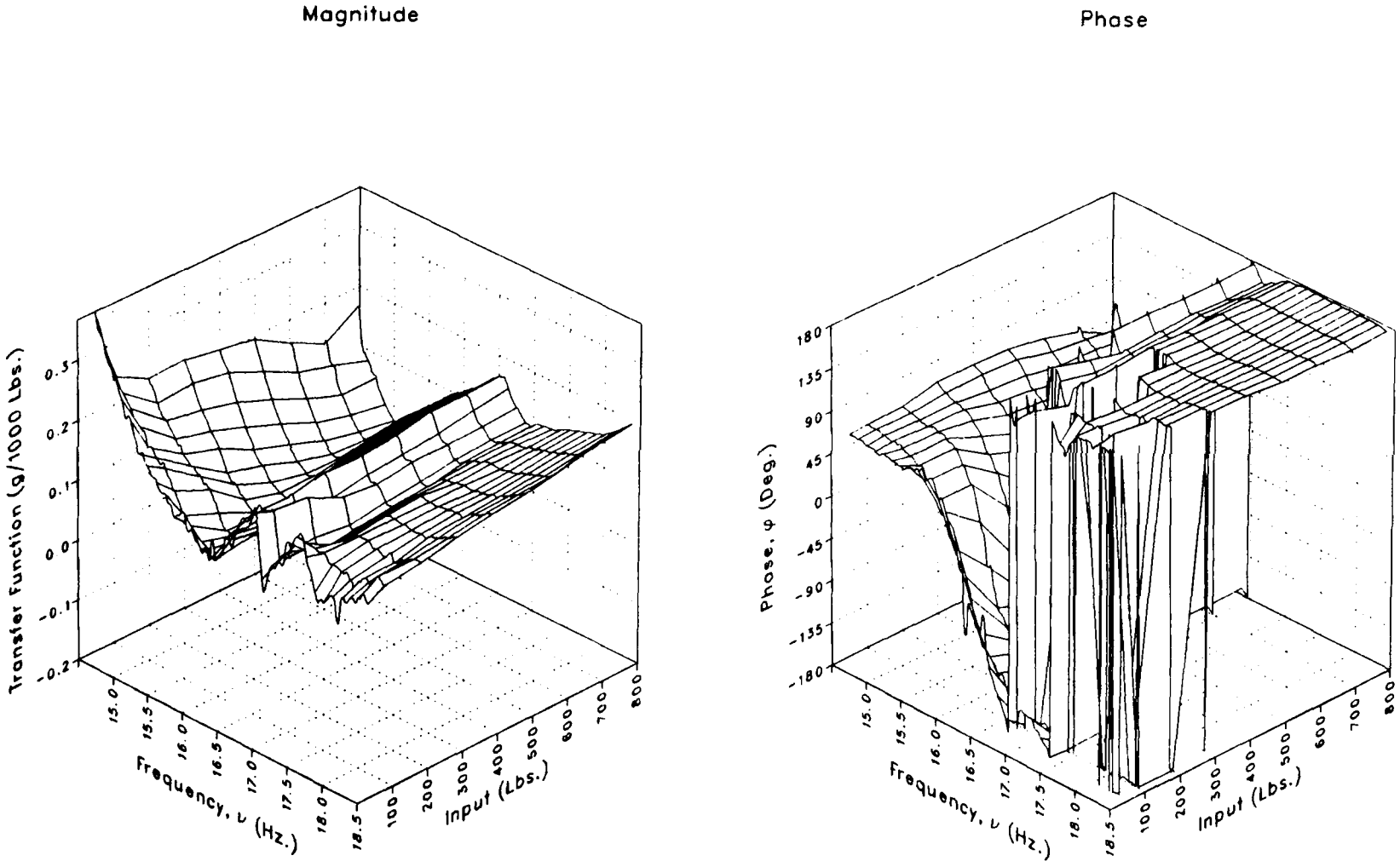

(o) STA56NL Concluded.

Figure 2.– Continued.

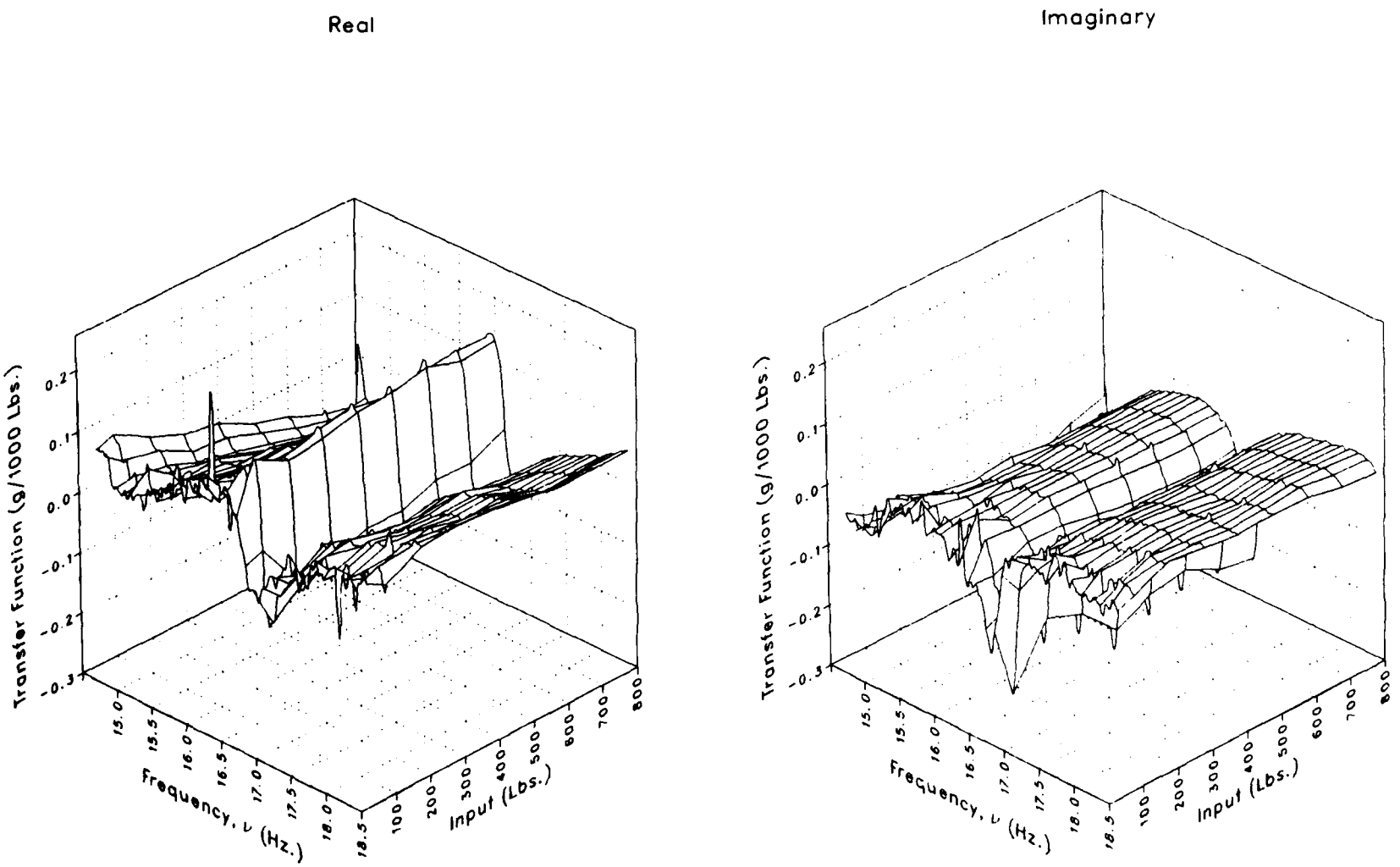

(p) VWGTPRT

Figure 2.– Continued.

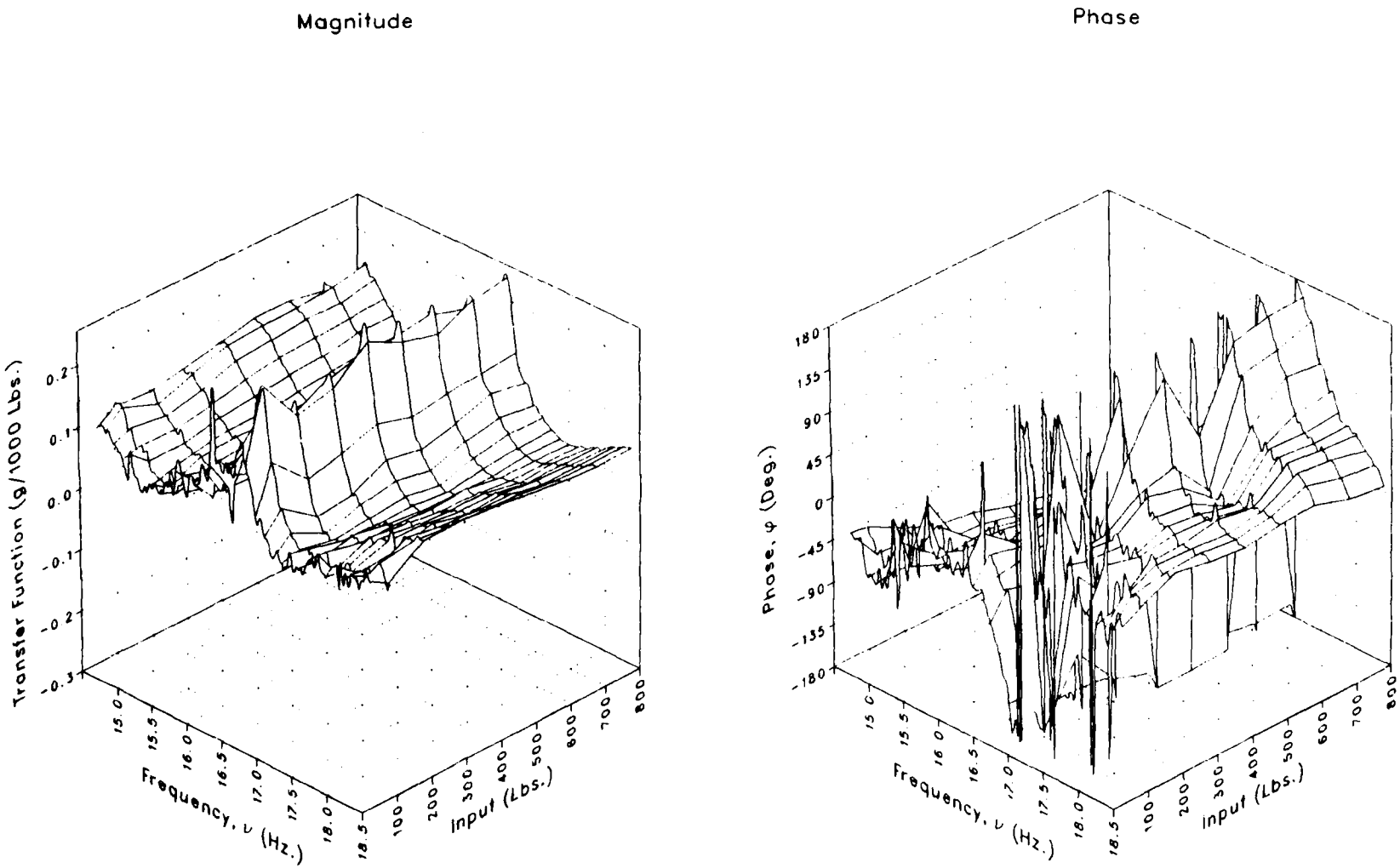

(p) VWGTPRT Concluded.

Figure 2.– Continued.

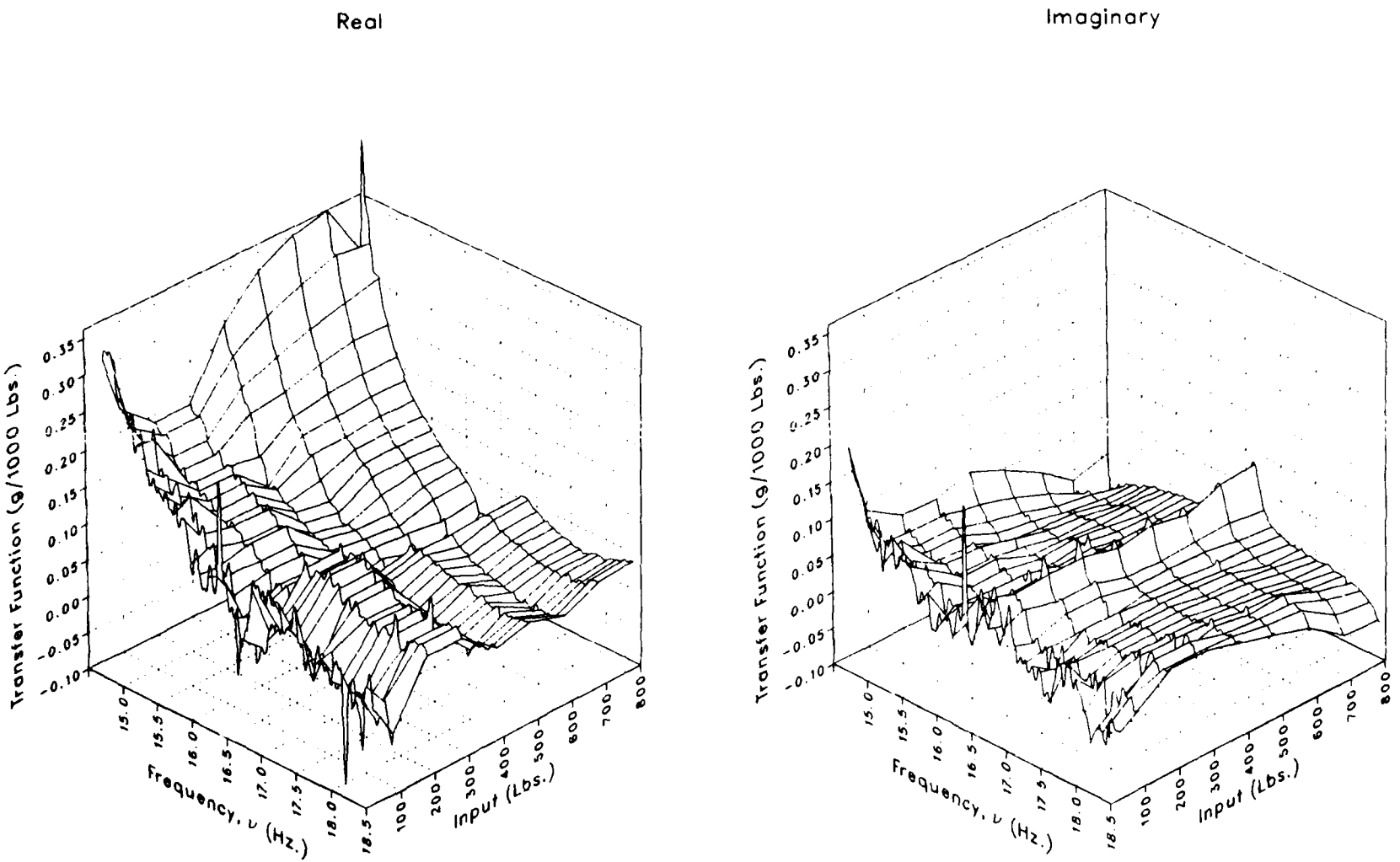

(q) VWGTPLT

Figure 2.– Continued.

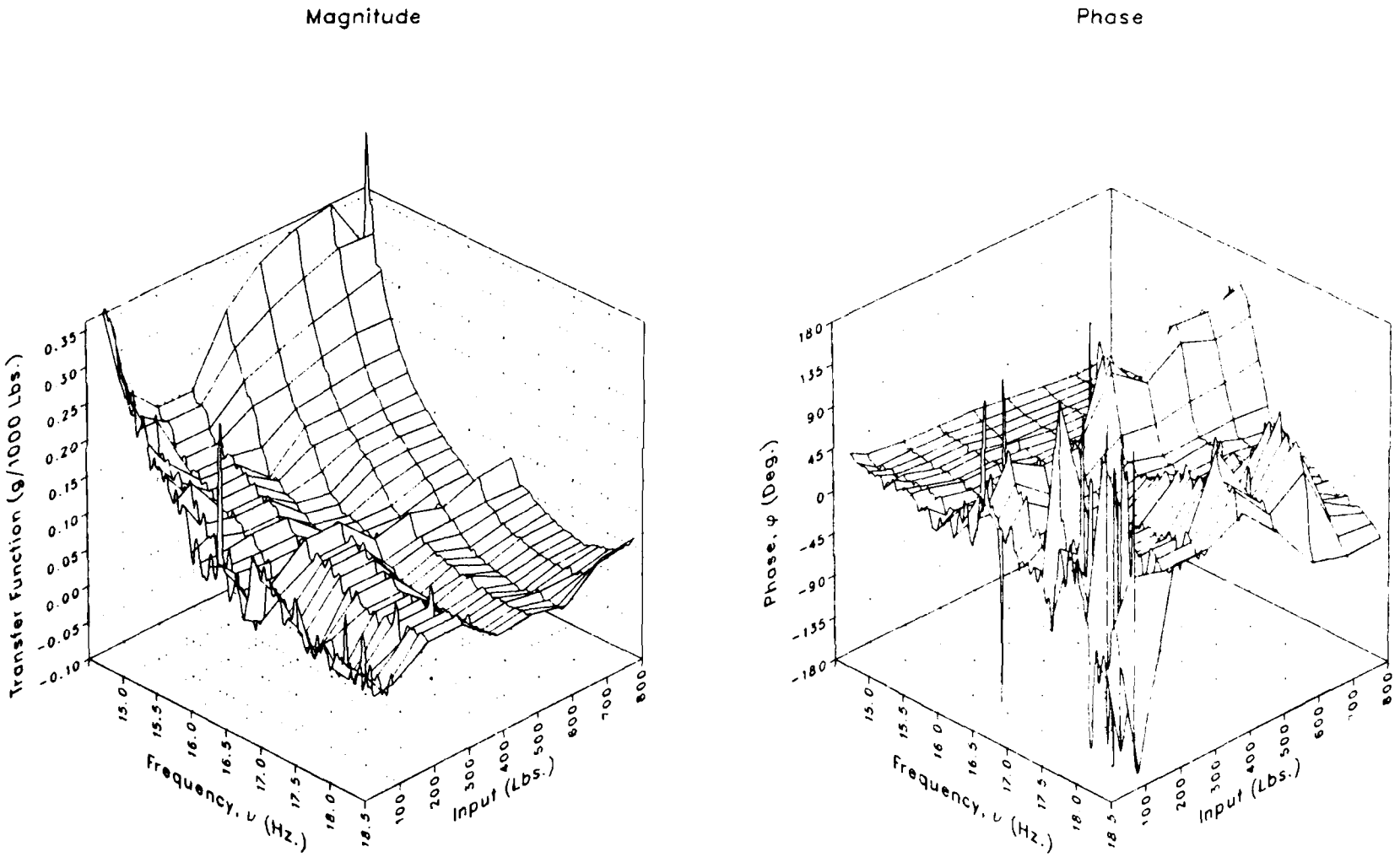

(q) VWGTPLT Concluded.

Figure 2.– Continued.

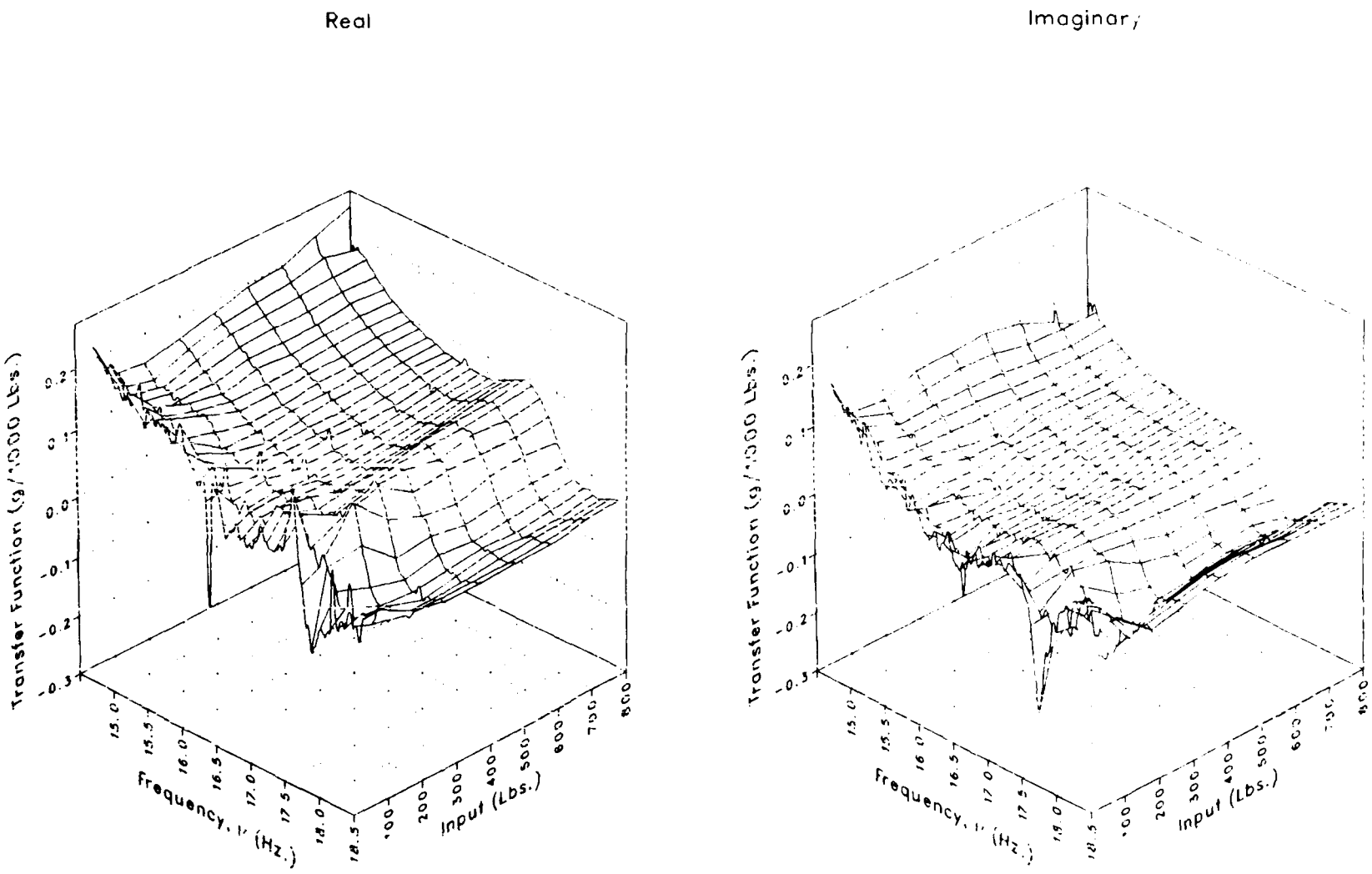

(r) LIGB

Figure 2.– Continued.

Magnitude

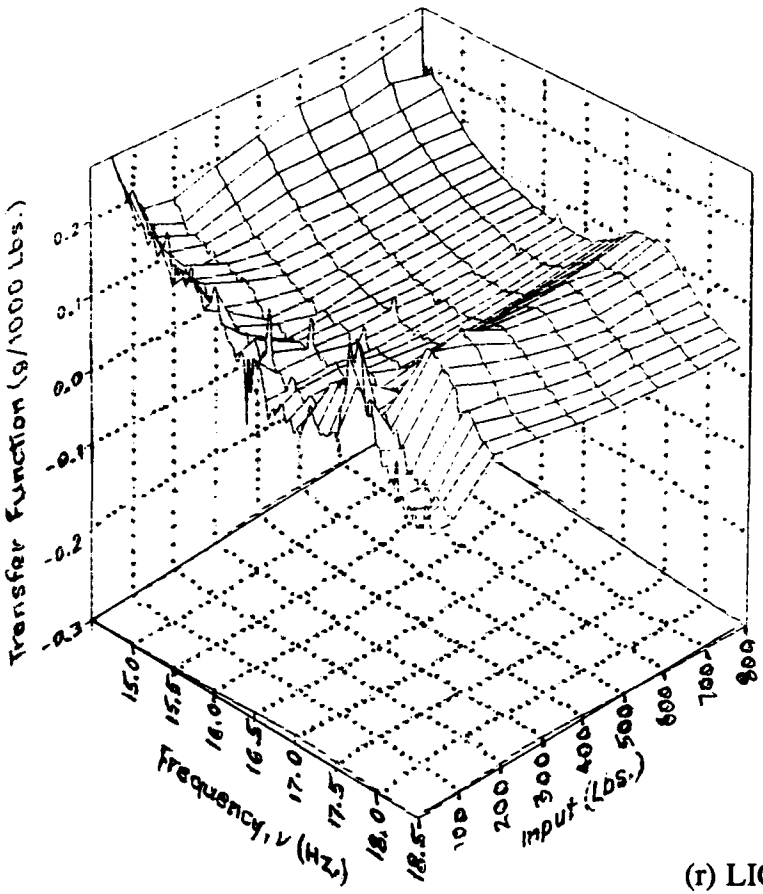

Phase

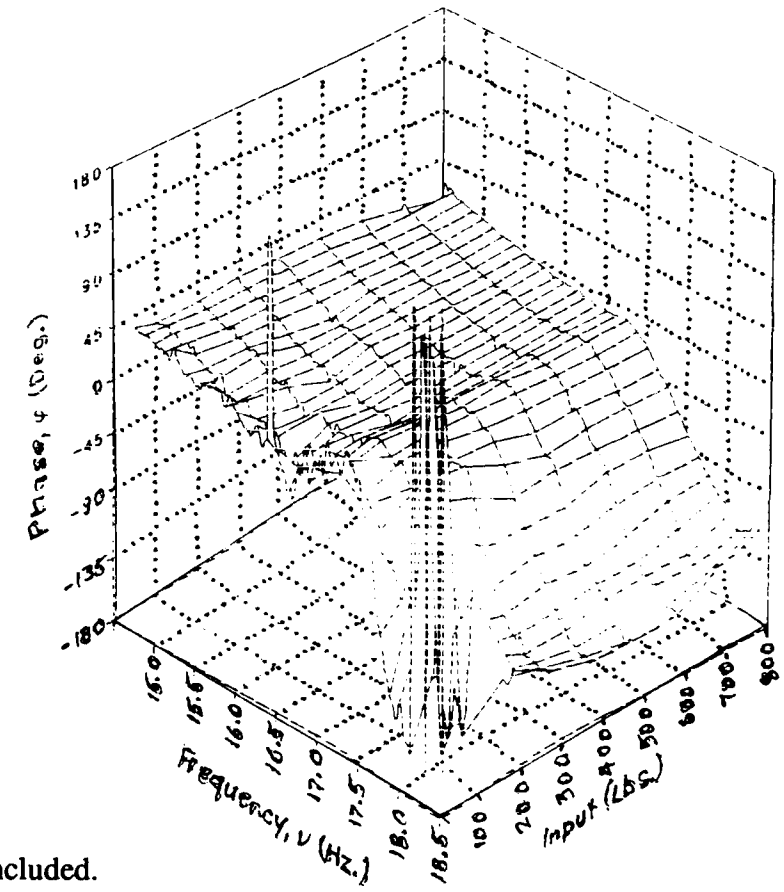

(r) LIGB Concluded.

Figure 2.– Continued.

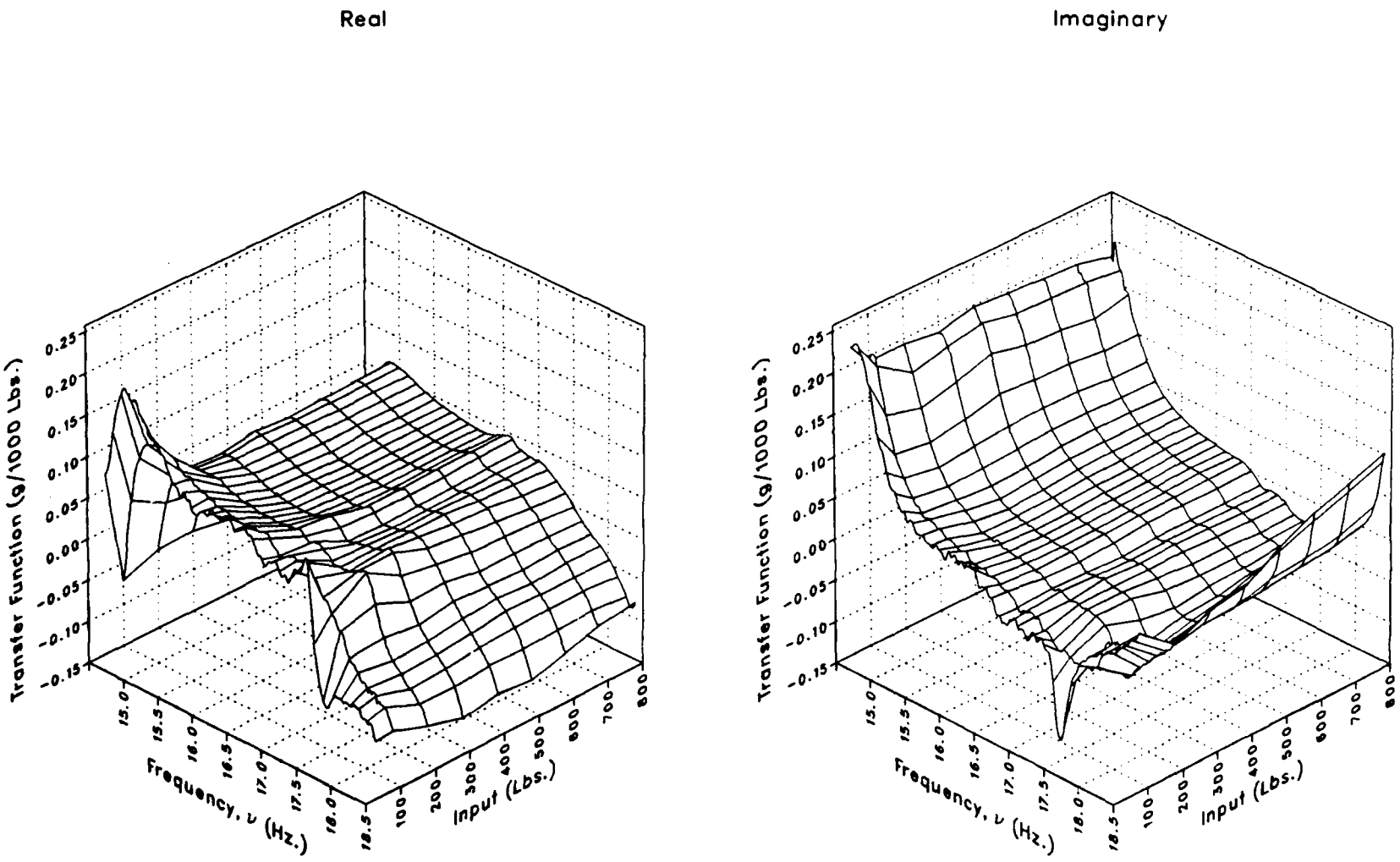

(s) VIGB

Figure 2.– Continued.

Magnitude

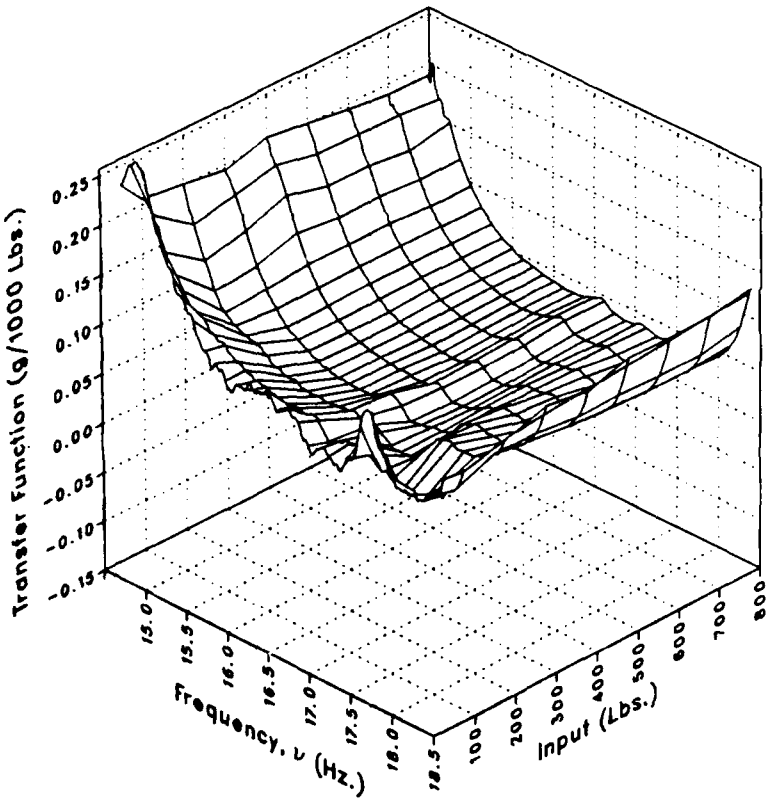

Phase

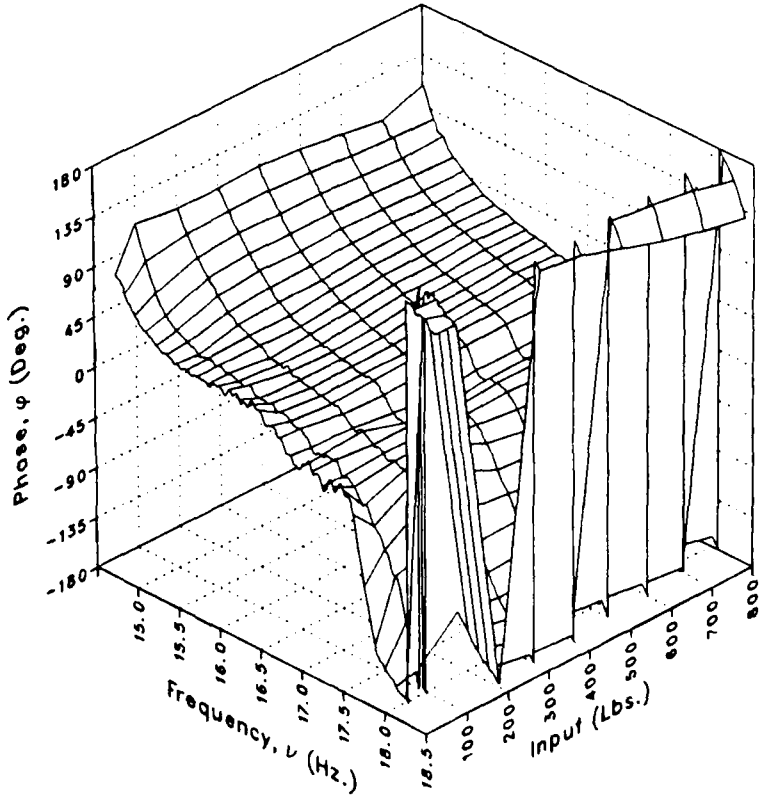

(s) VIGB Concluded.

Figure 2.– Continued.

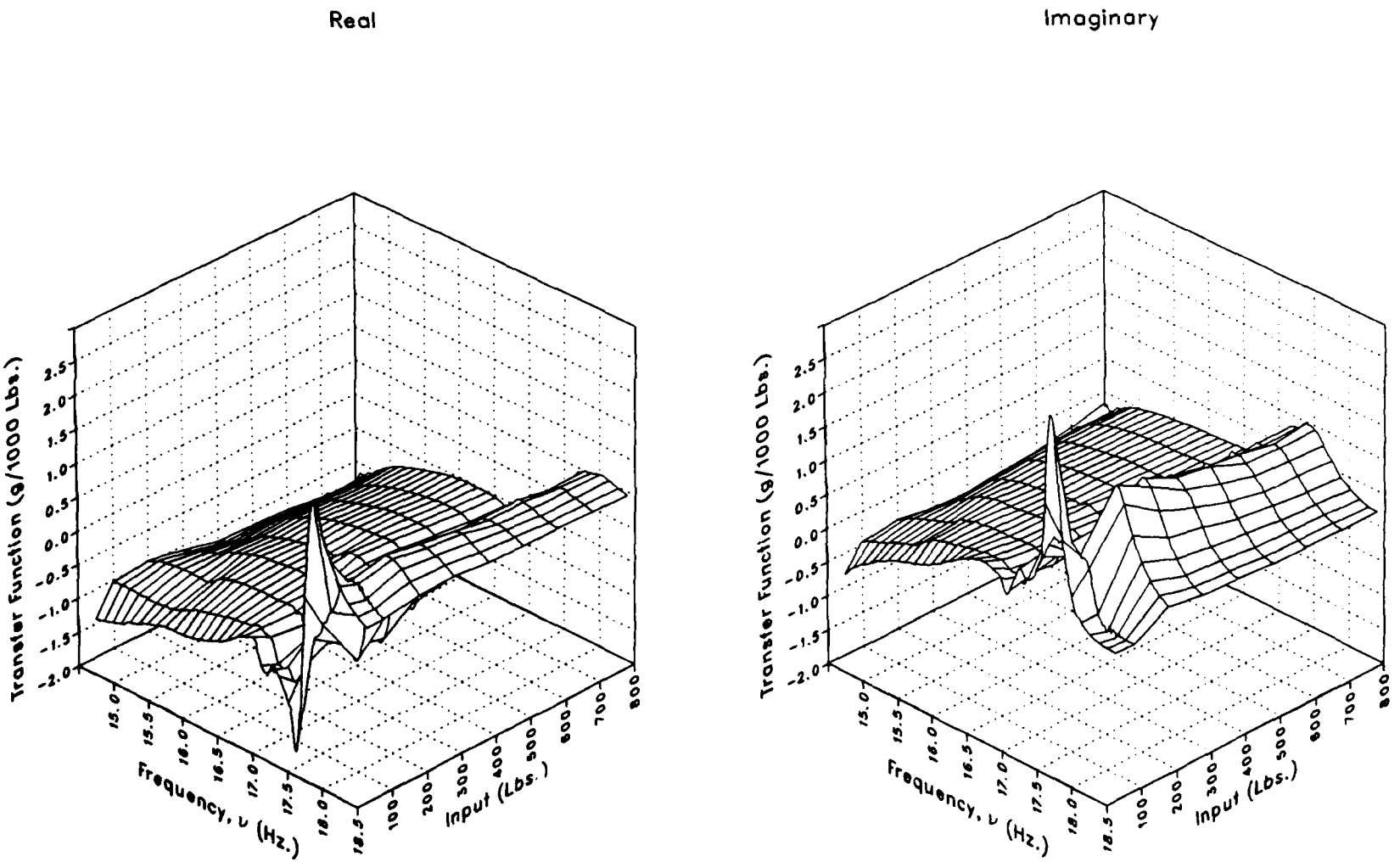

(t) LATTPYLN

Figure 2.– Continued.

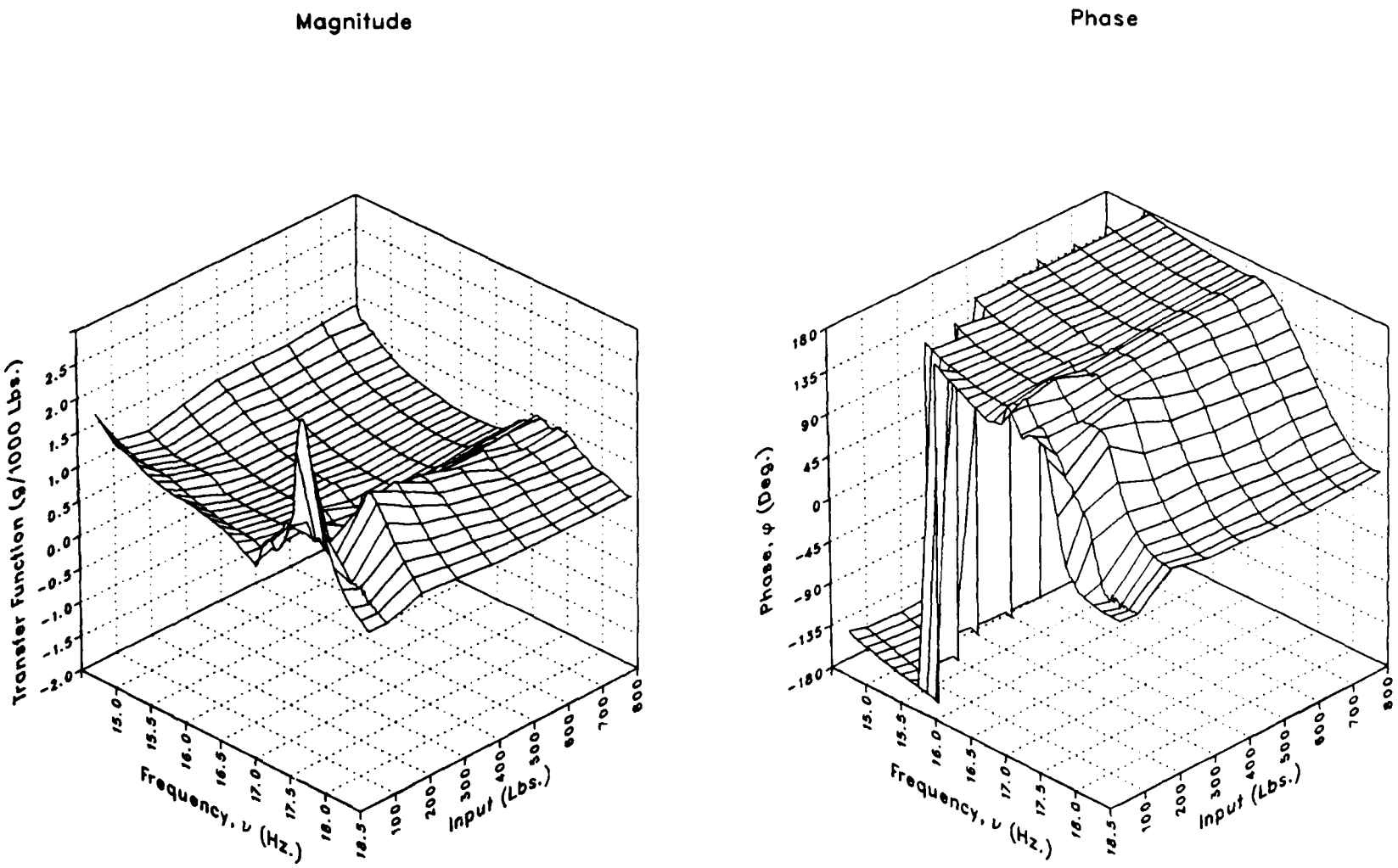

(t) LATTPYLN Concluded.

Figure 2.– Continued.

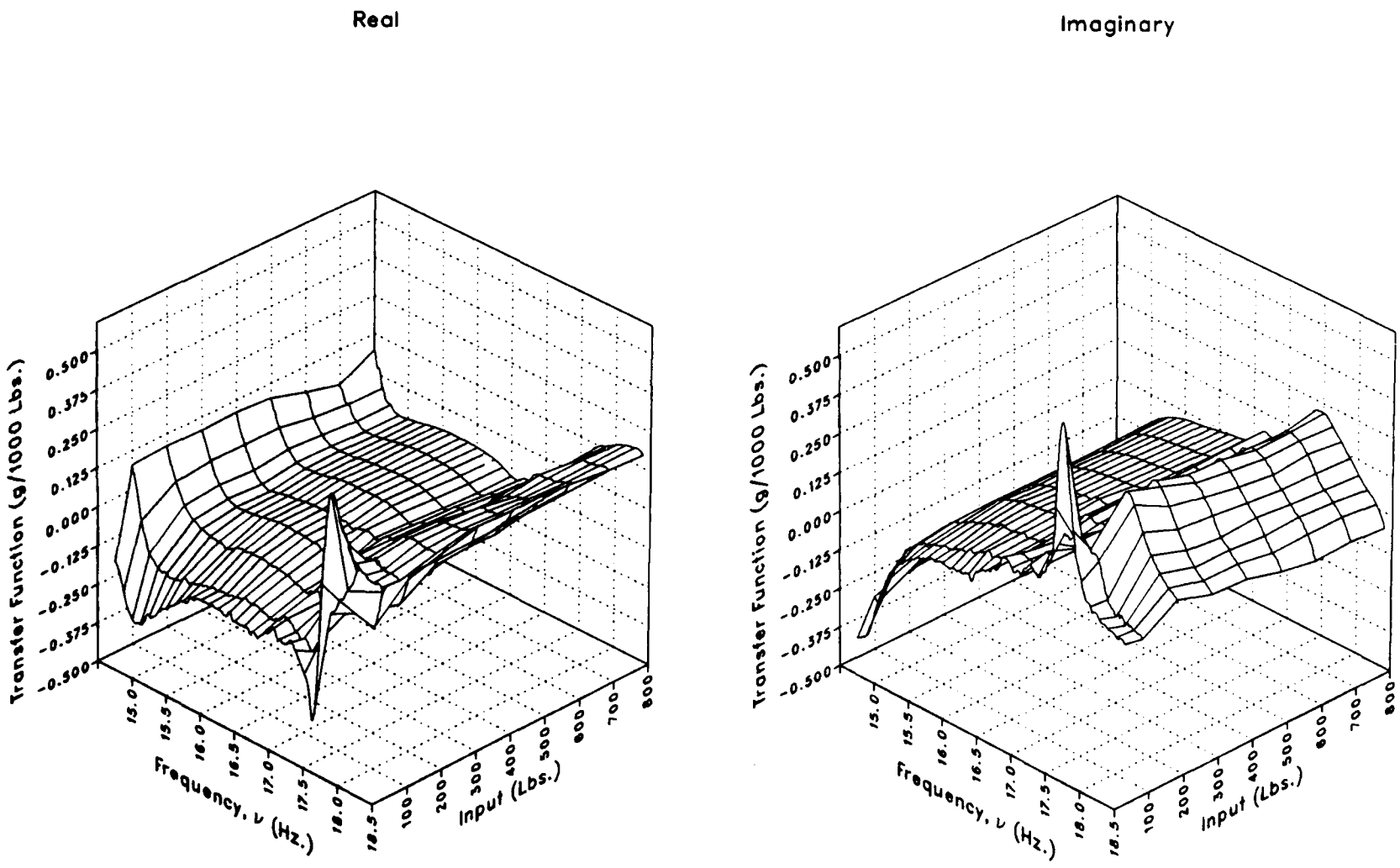

(u) VTTPYLON

Figure 2.– Continued.

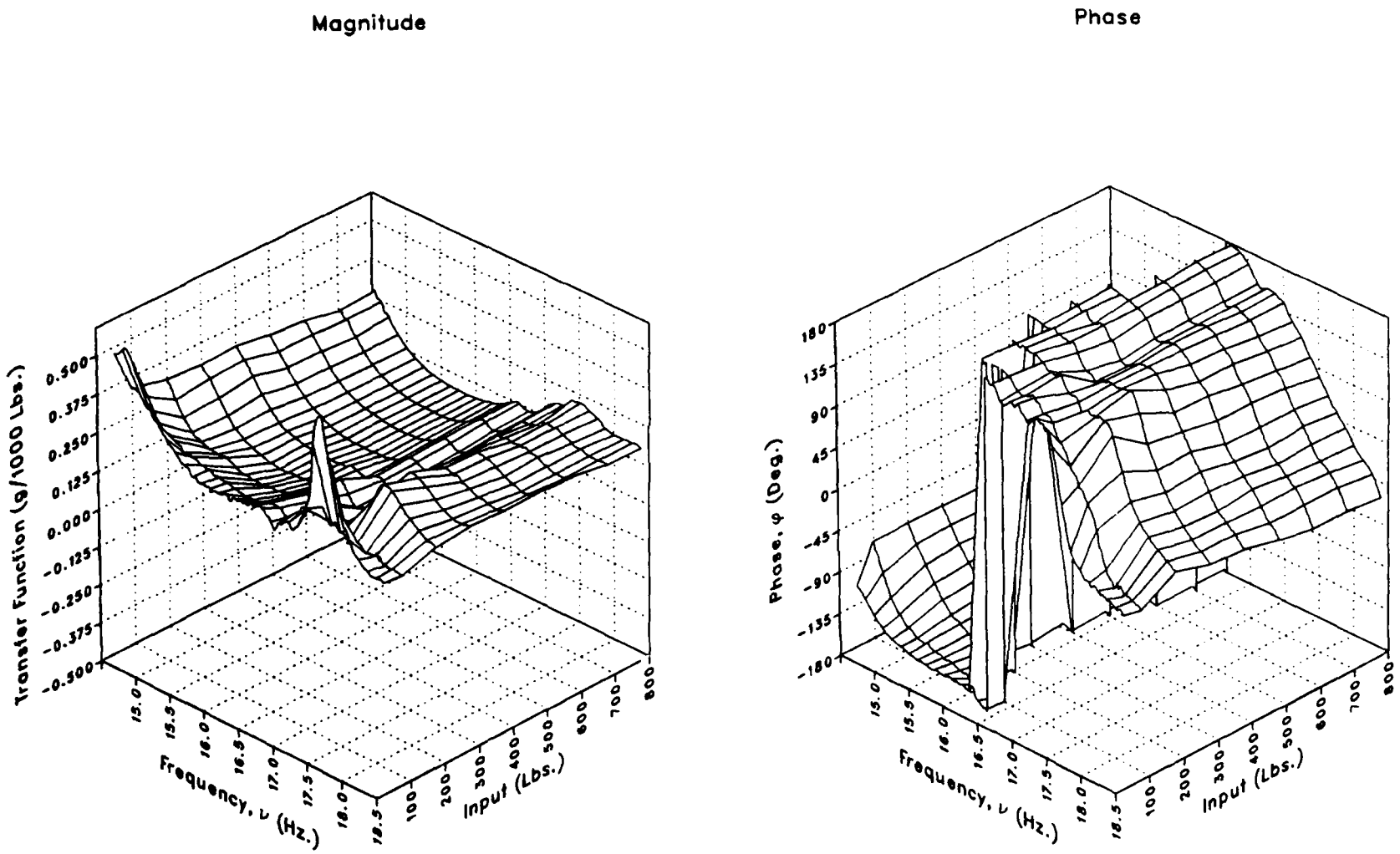

(u) VTTPYLON Concluded.

Figure 2.– Continued.

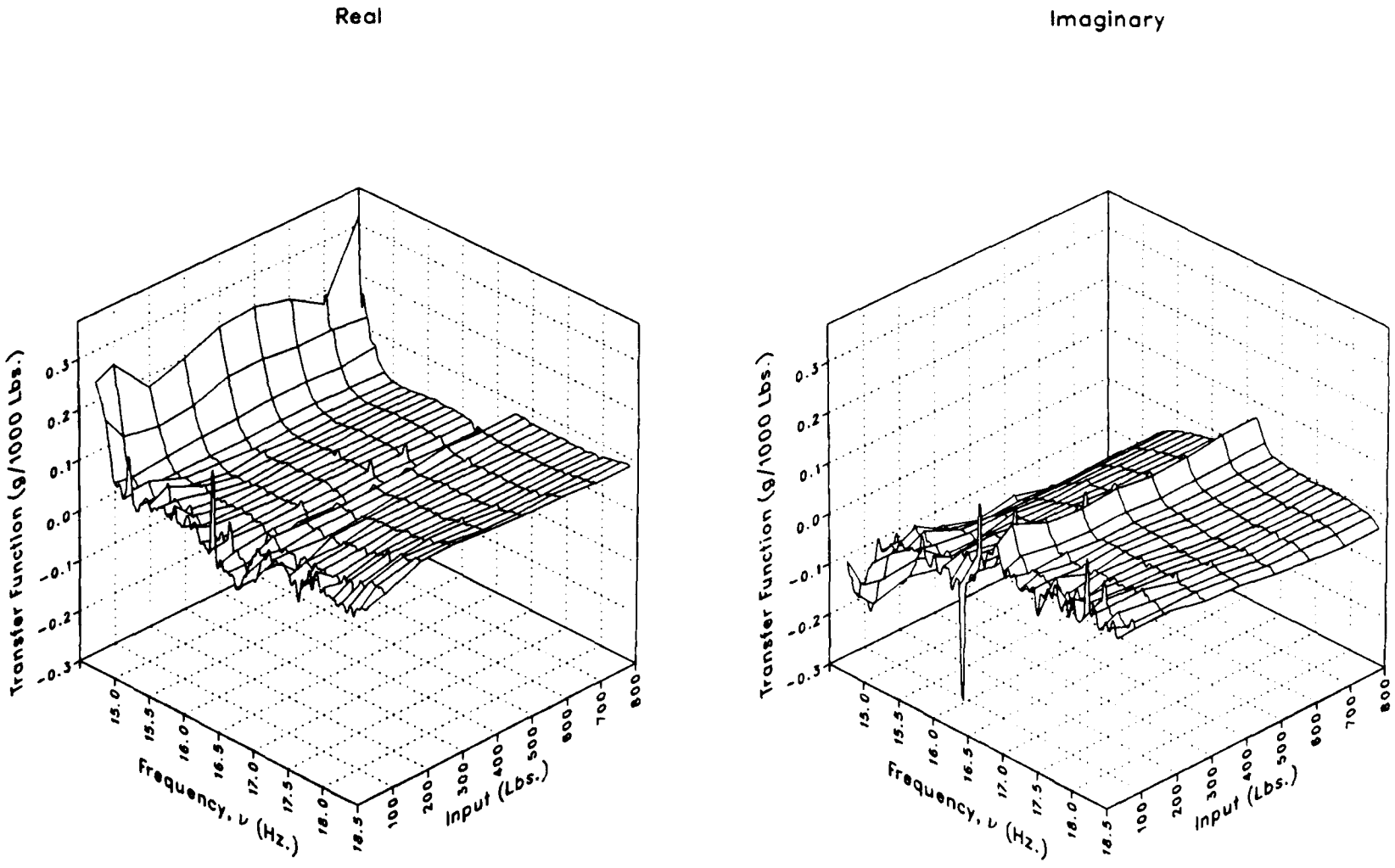

(v) XMRFLV

Figure 2.– Continued.

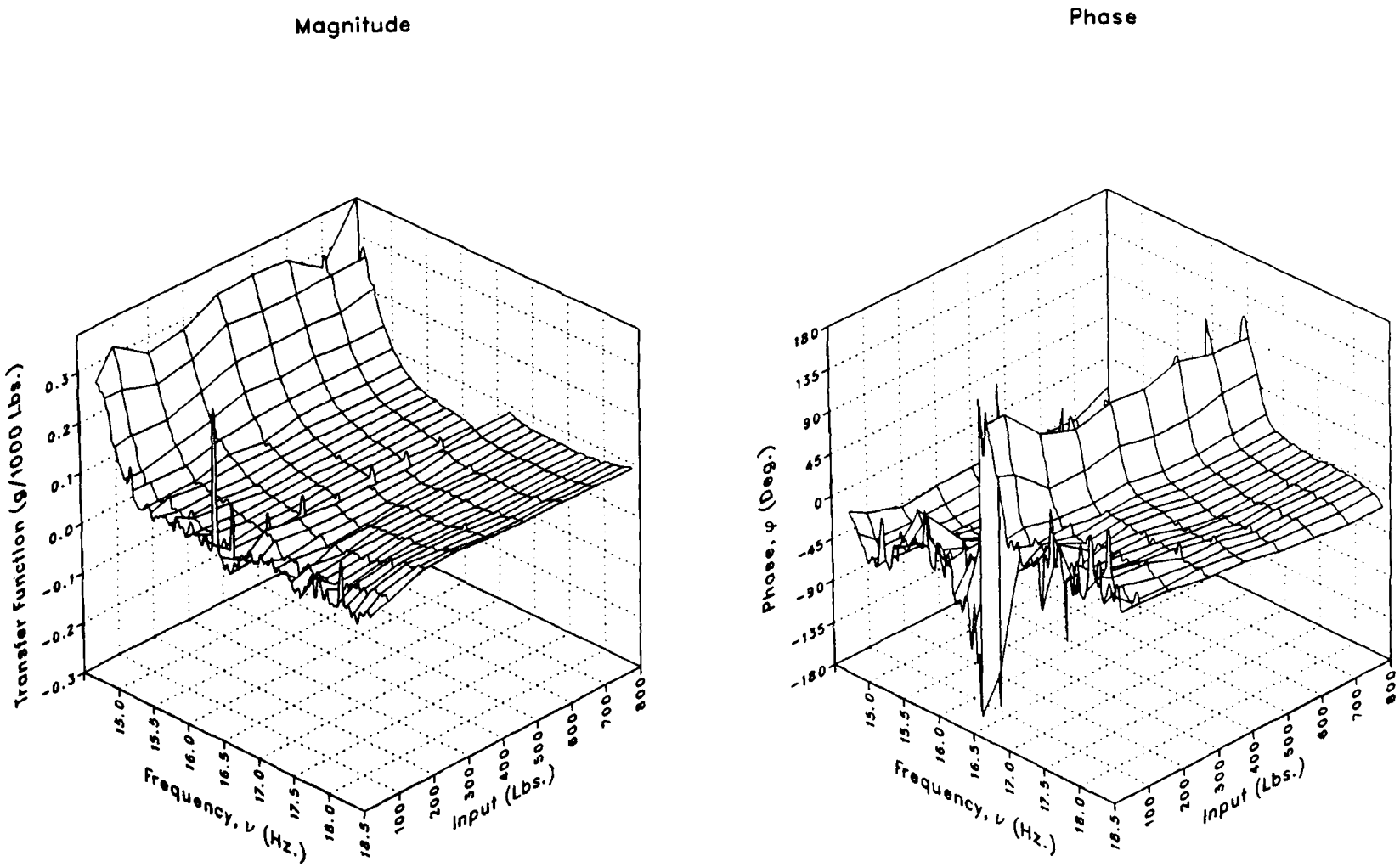

(v) XMRFLV Concluded.

Figure 2.– Continued.

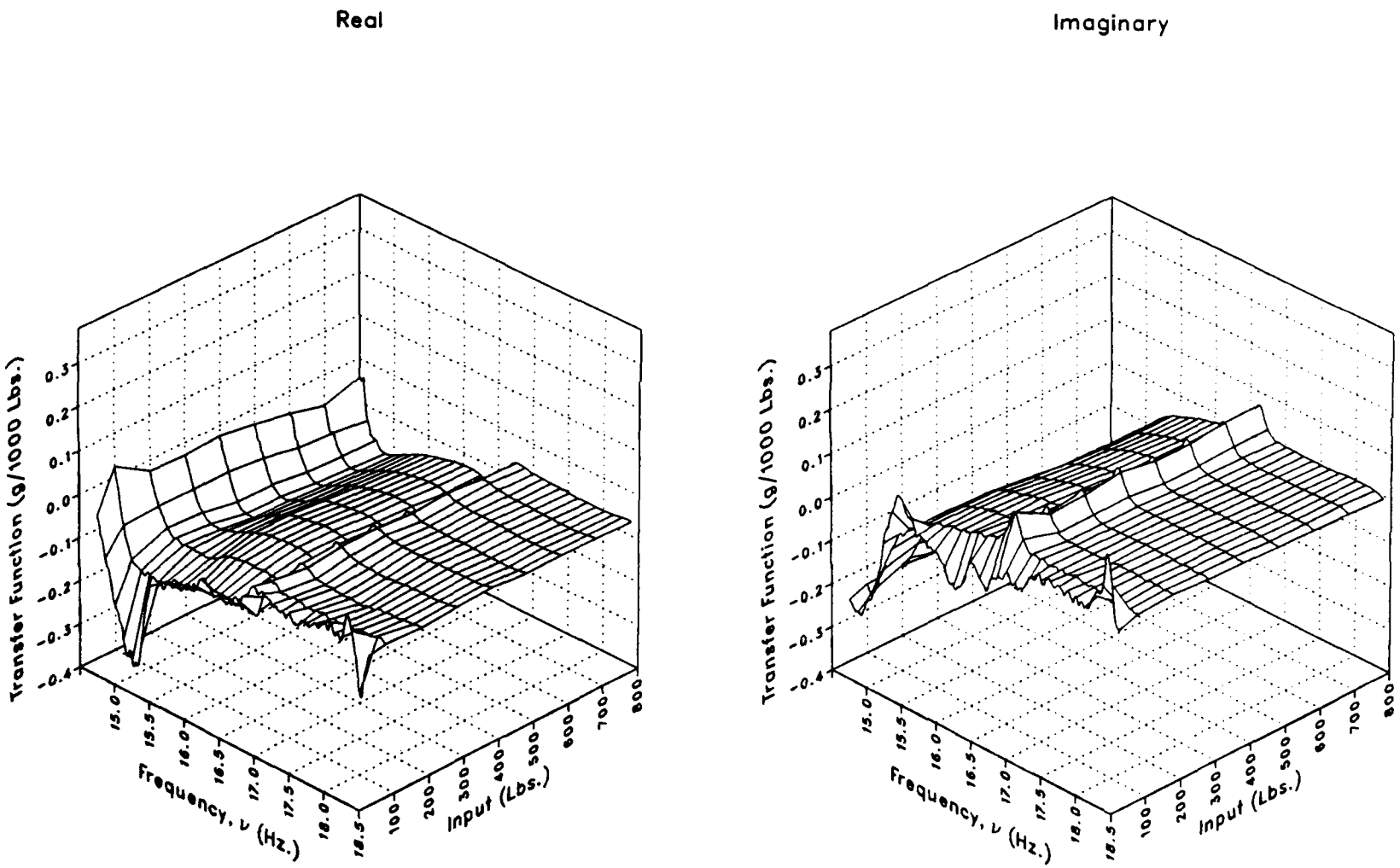

(w) XMRFRV

Figure 2.– Continued.

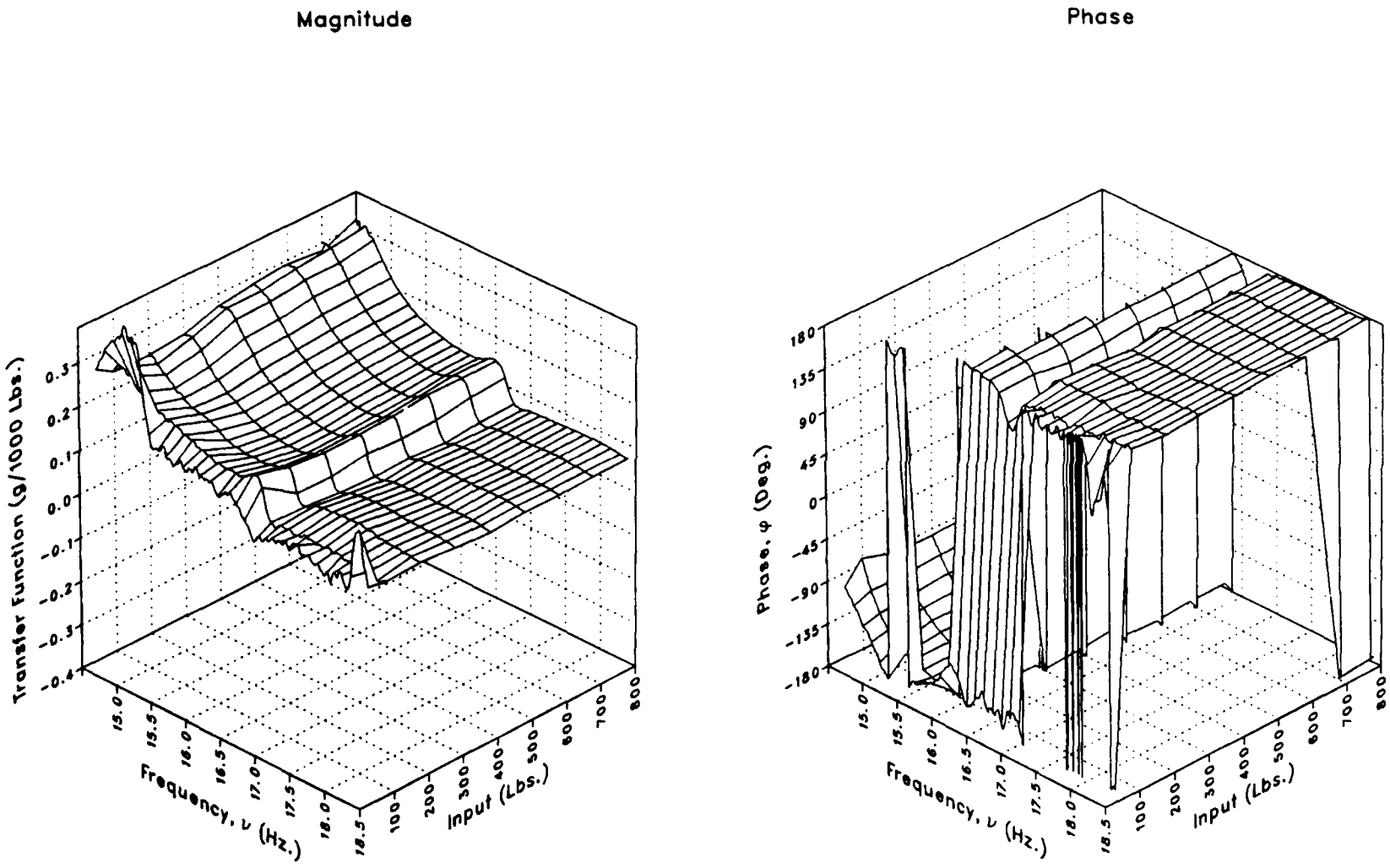

(w) XMRFRV Concluded.

Figure 2.– Continued.

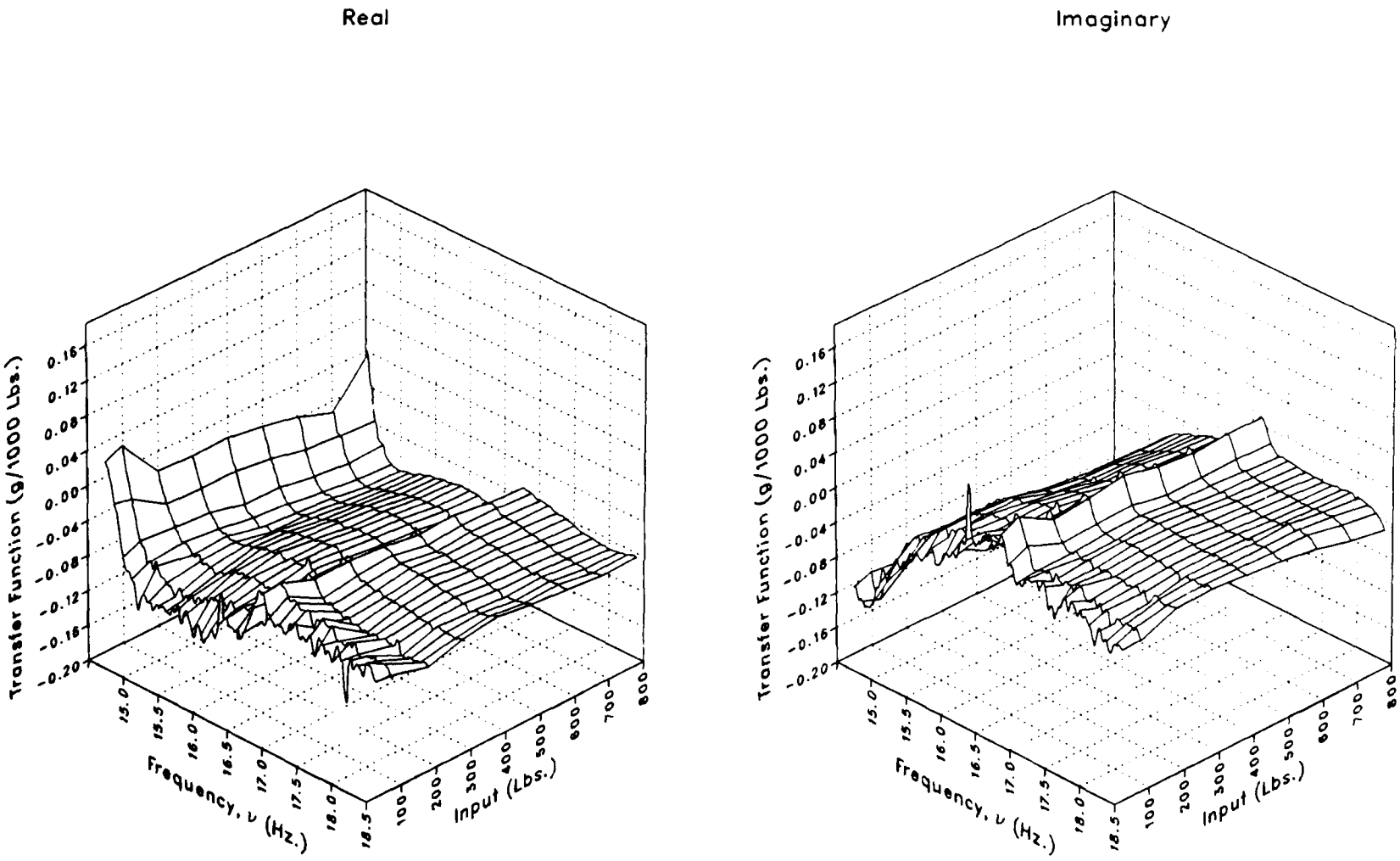

(x) S222FLRV

Figure 2.– Continued.

Magnitude

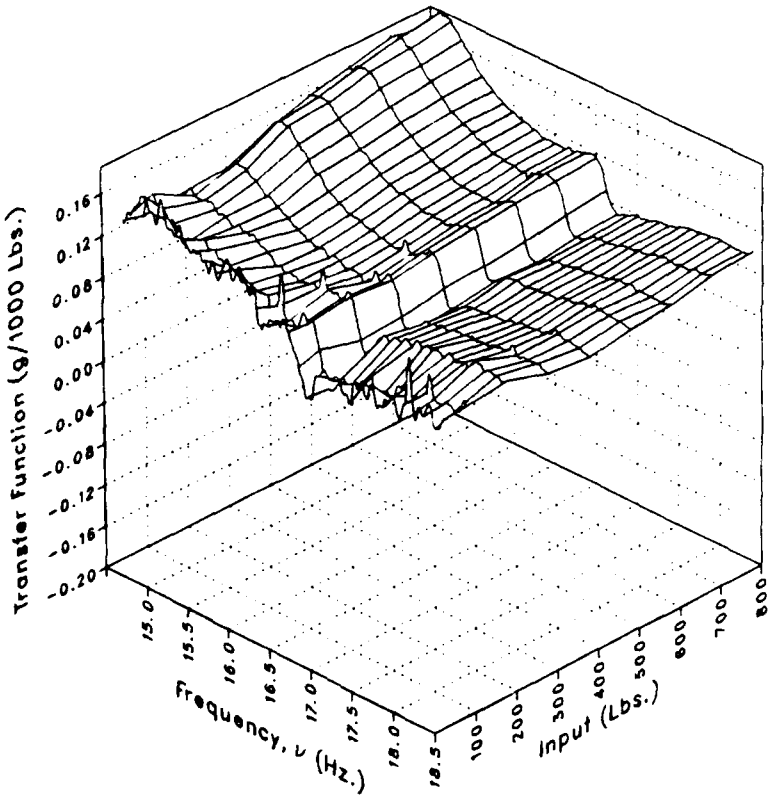

Phase

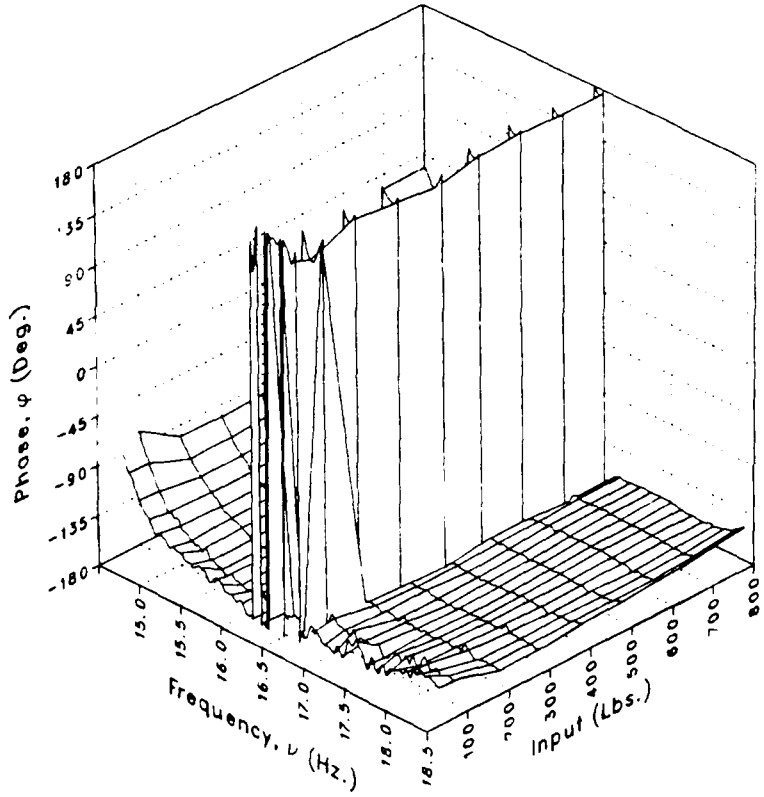

(x) S222FLRV Concluded.

Figure 2.– Continued.

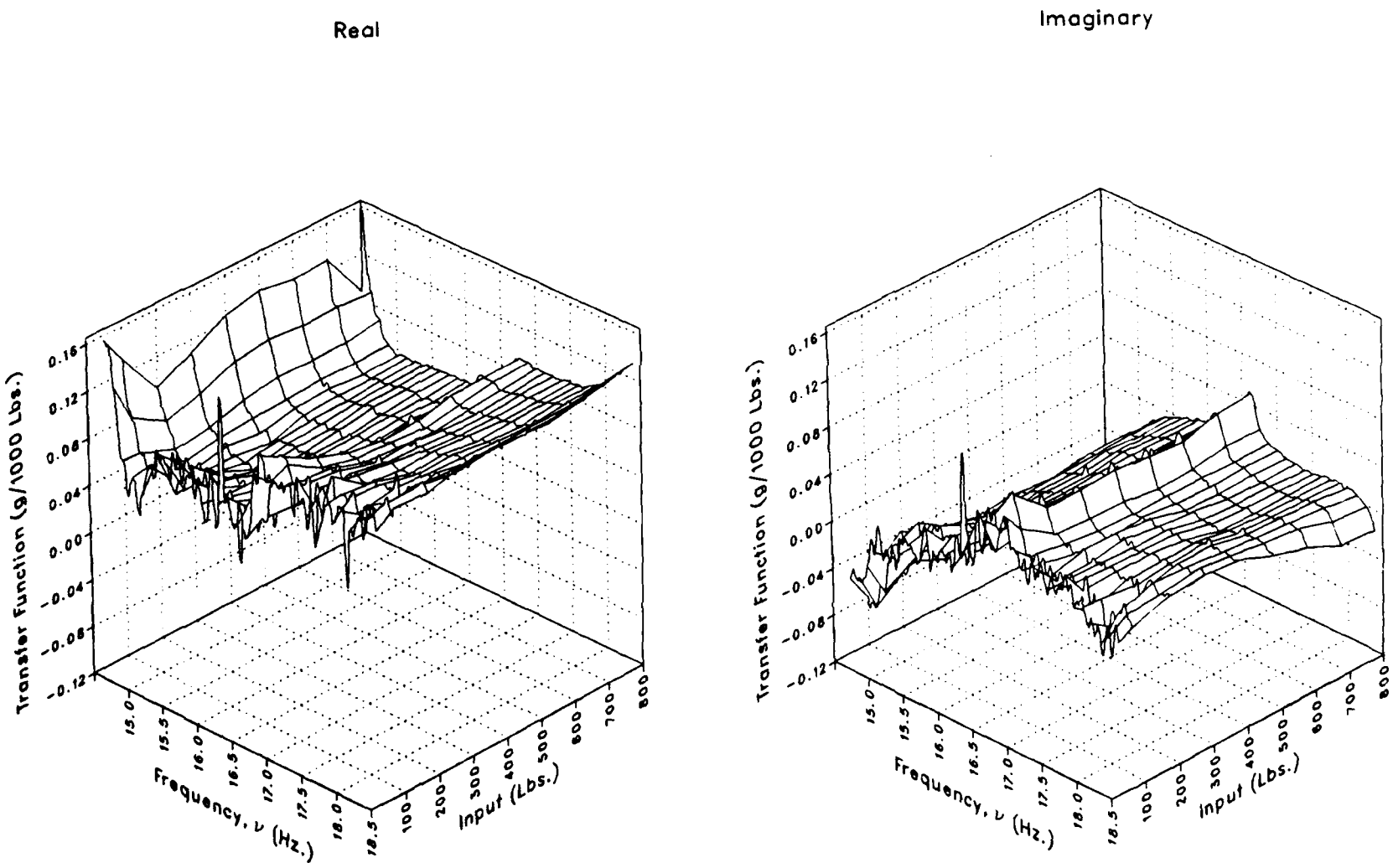

(y) S222FLLV

Figure 2.– Continued.

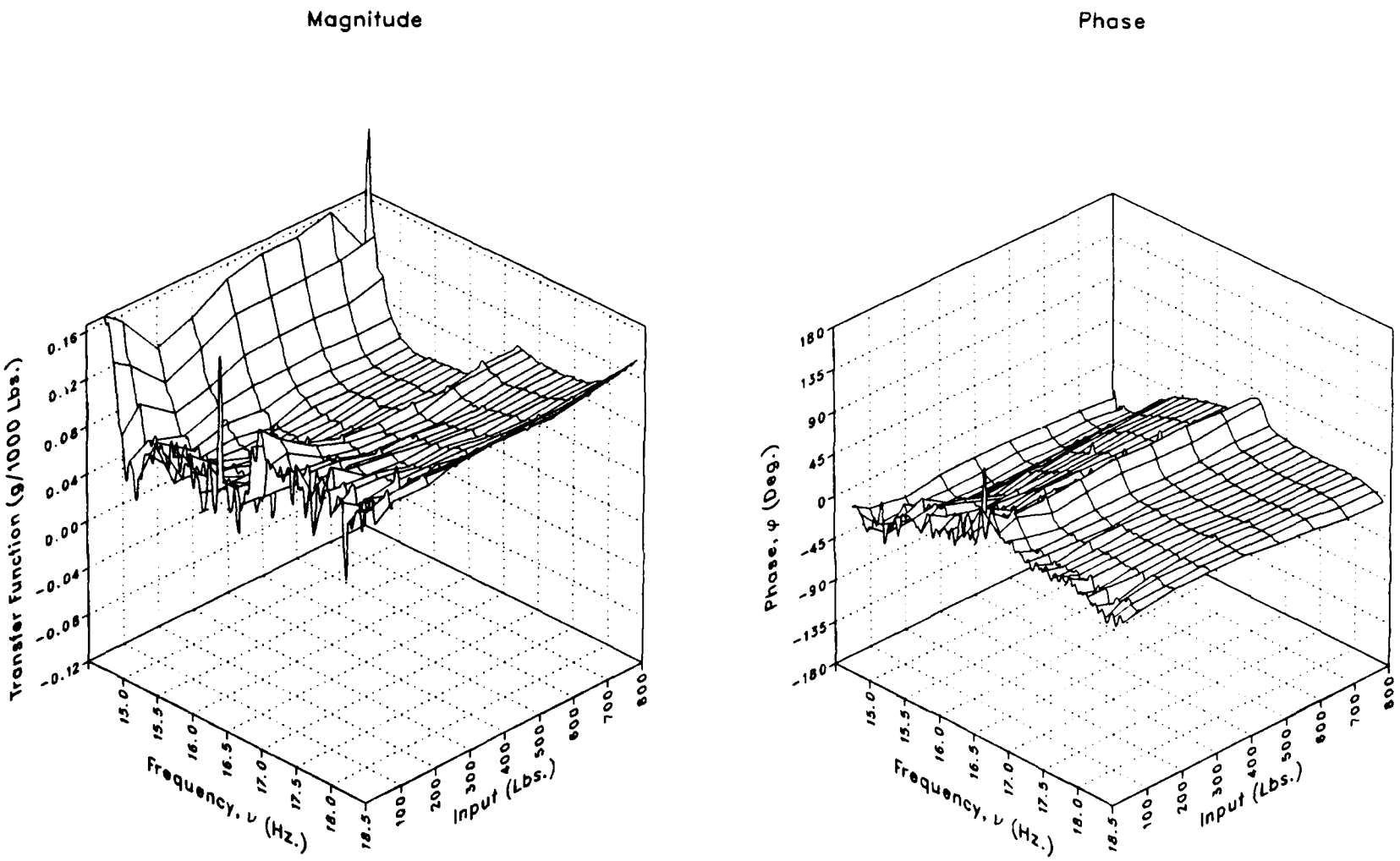

(y) S222FLLV Concluded.

Figure 2.– Continued.

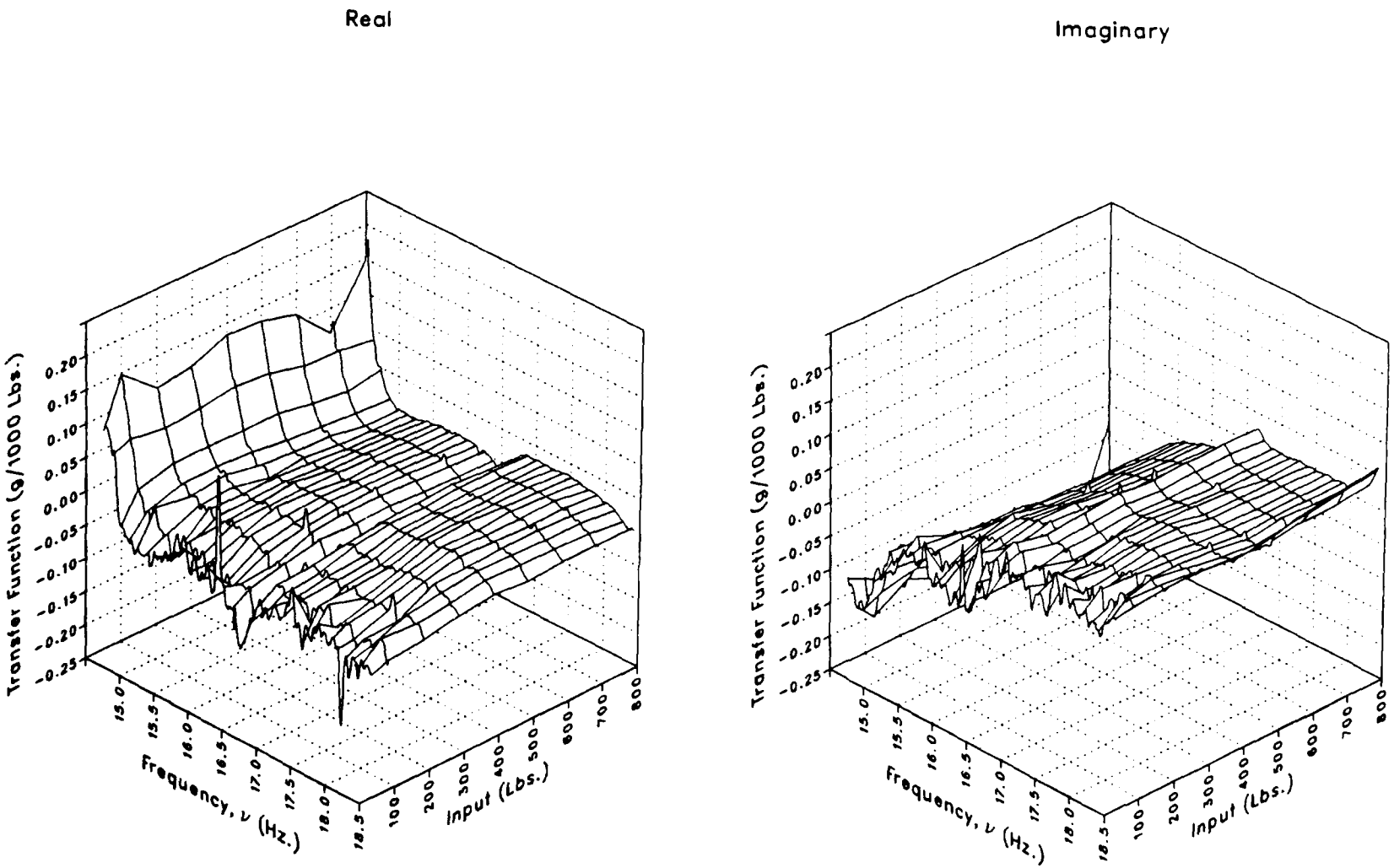

(z) S450FLV

Figure 2.– Continued.

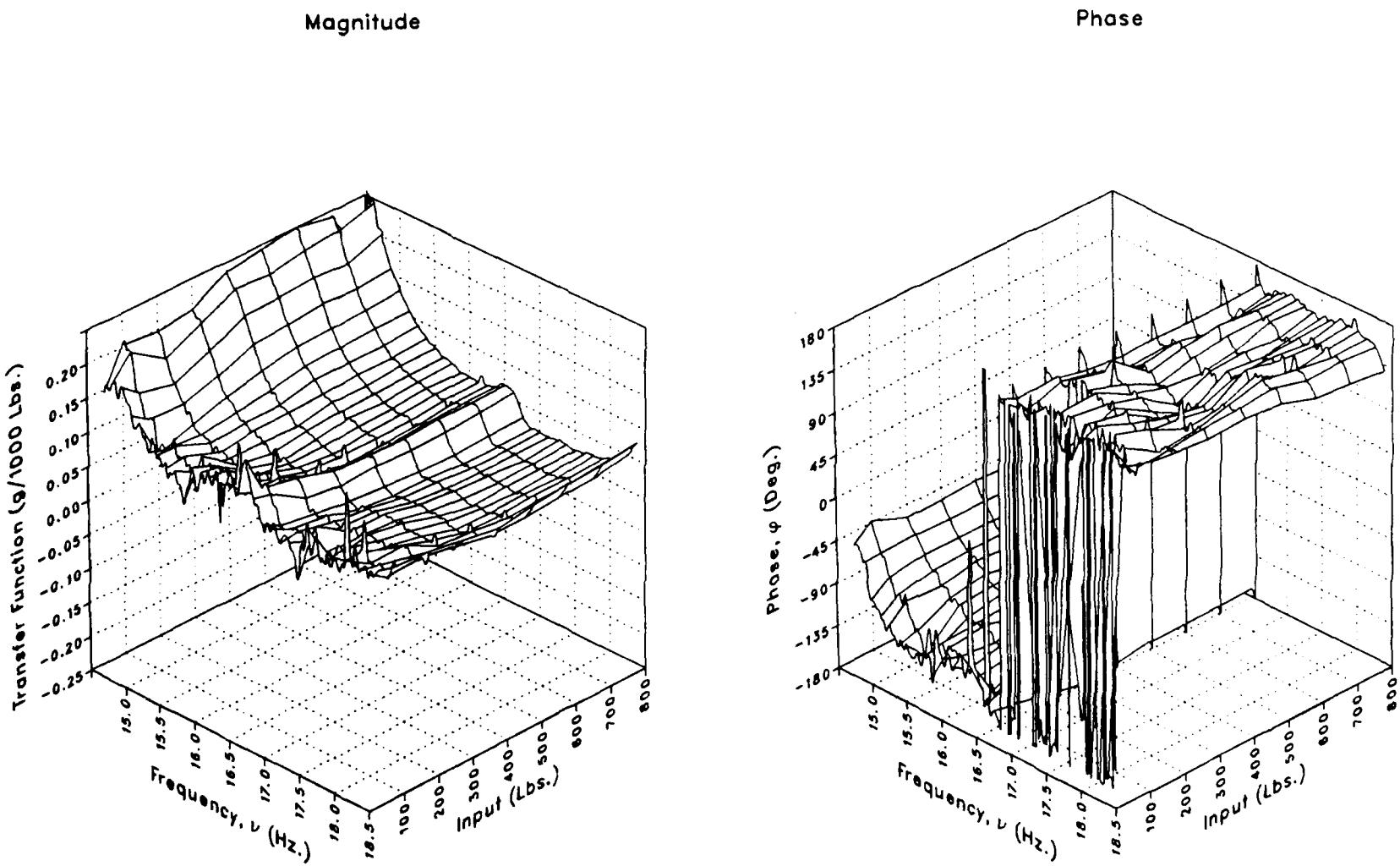

(z) S450FLV Concluded.

Figure 2.– Continued.

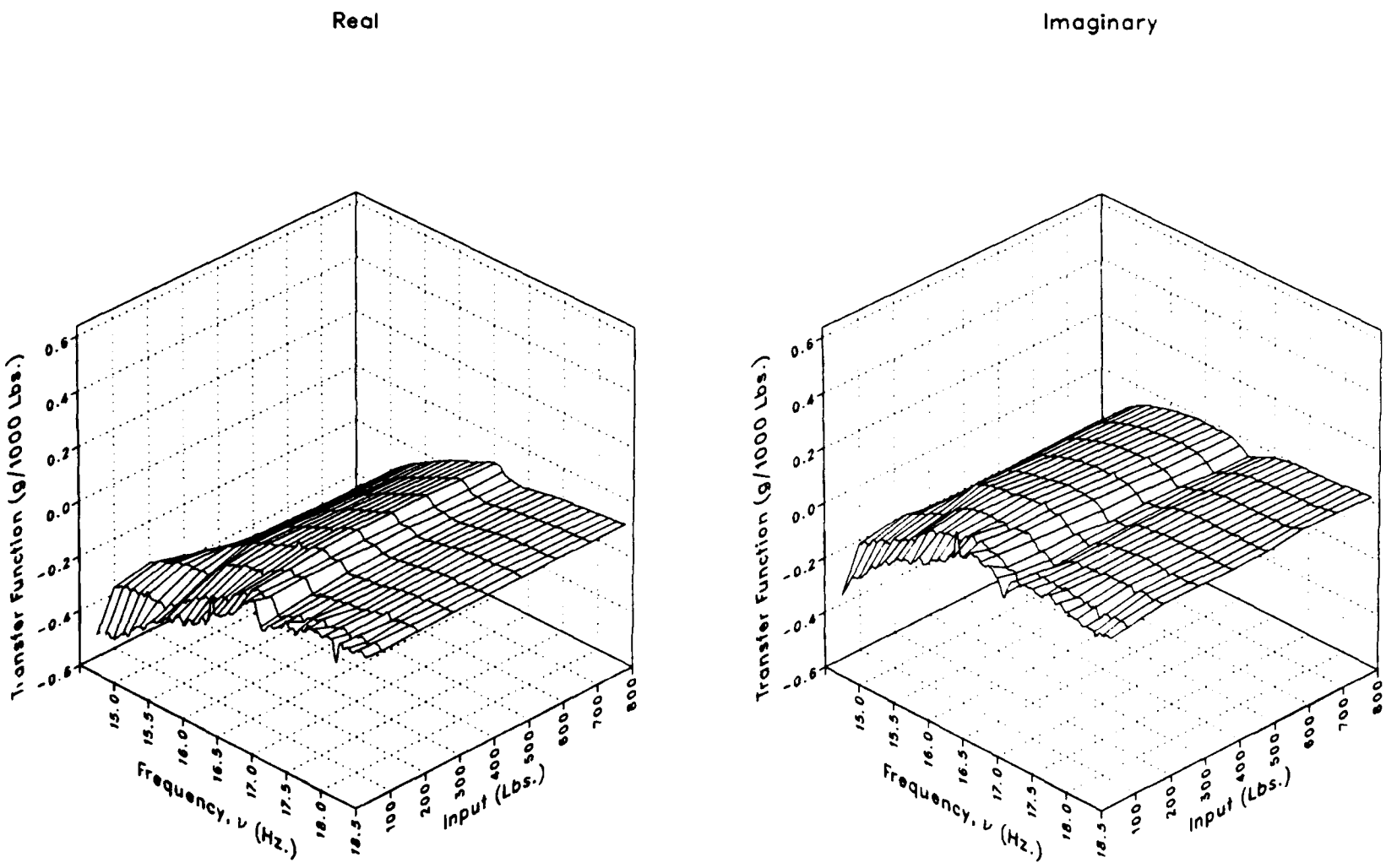

(aa) S450FLL

Figure 2.– Continued.

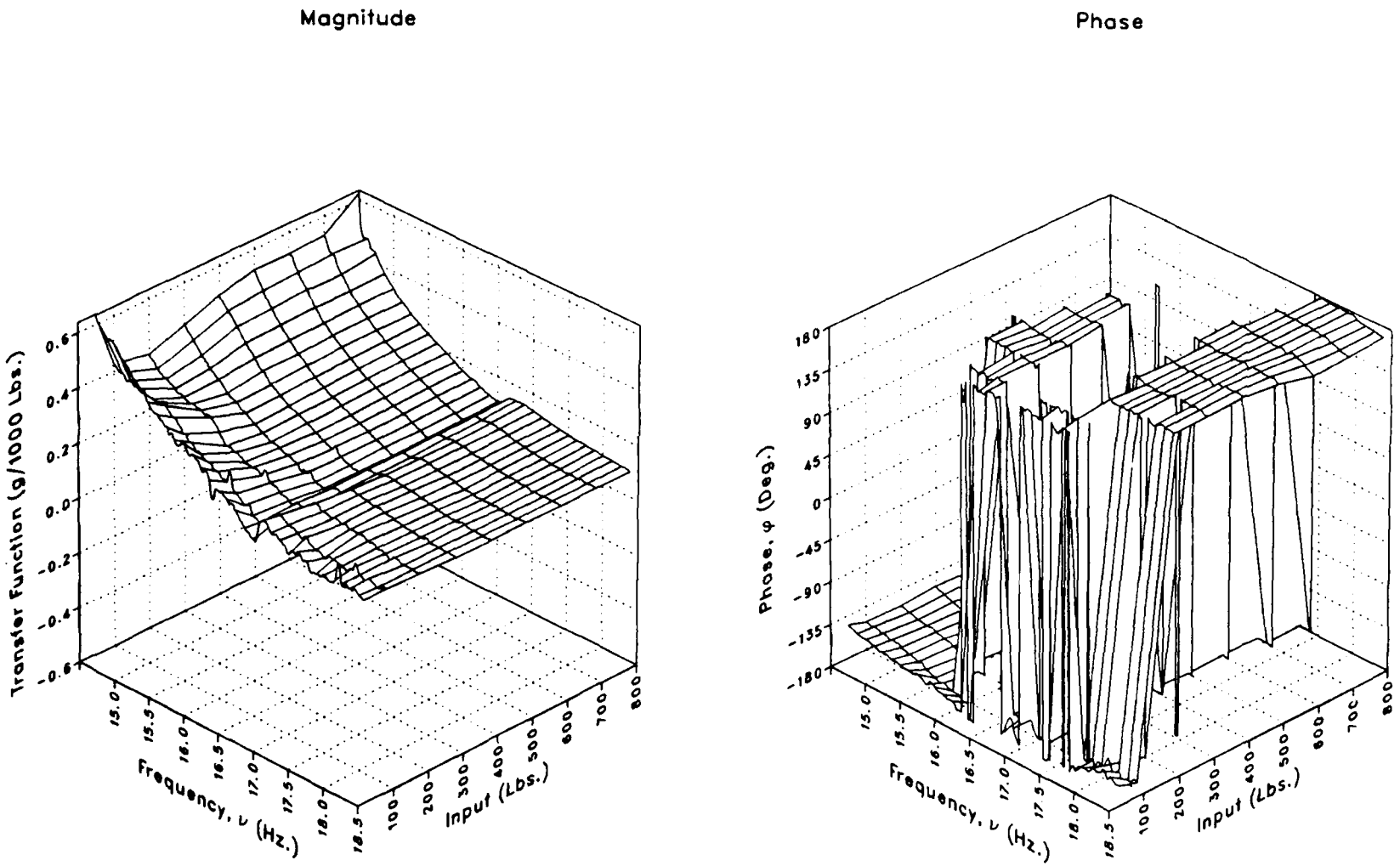

(aa) S450FLL Concluded.

Figure 2.– Continued.

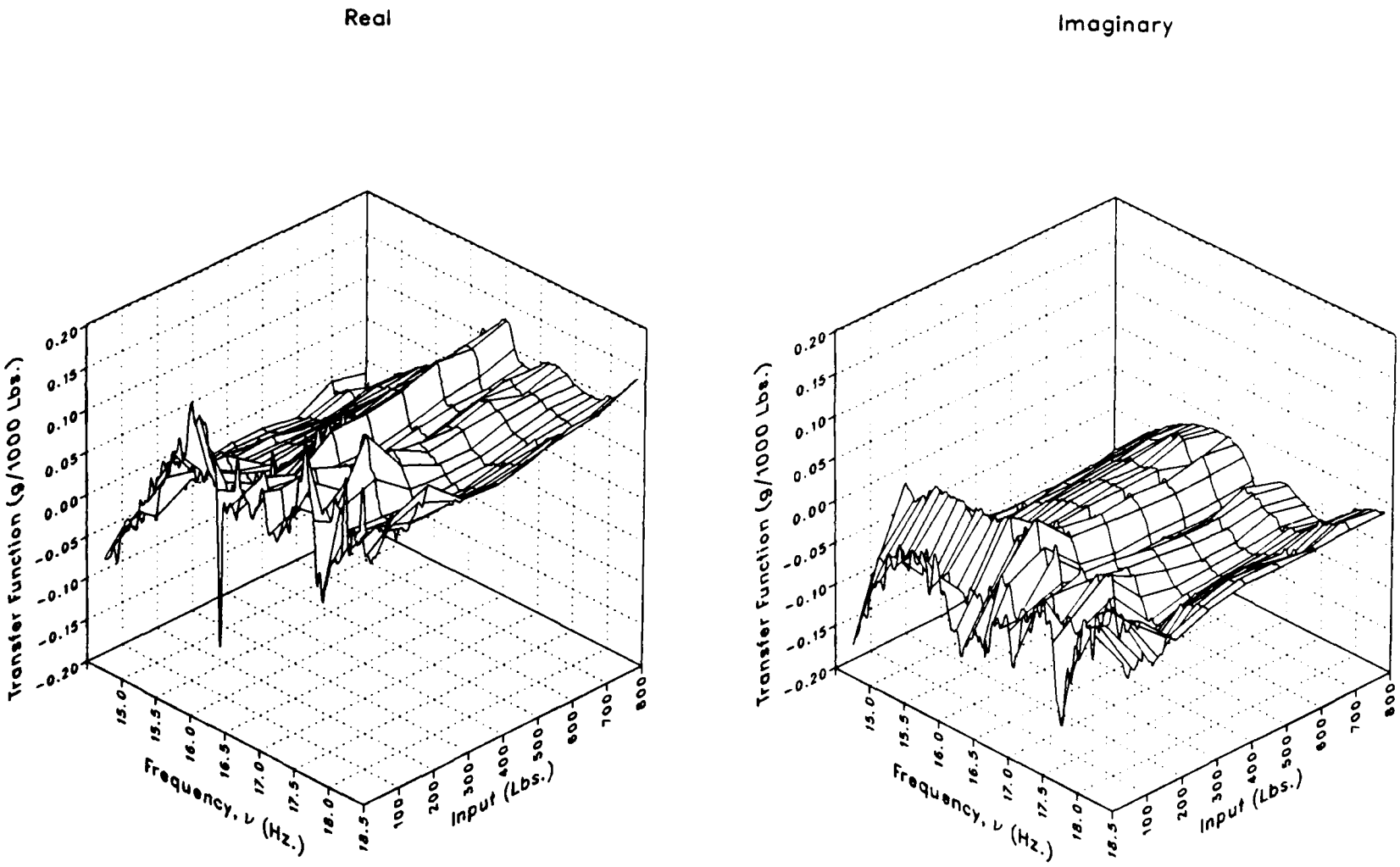

(bb) S450OVRL

Figure 2.– Continued.

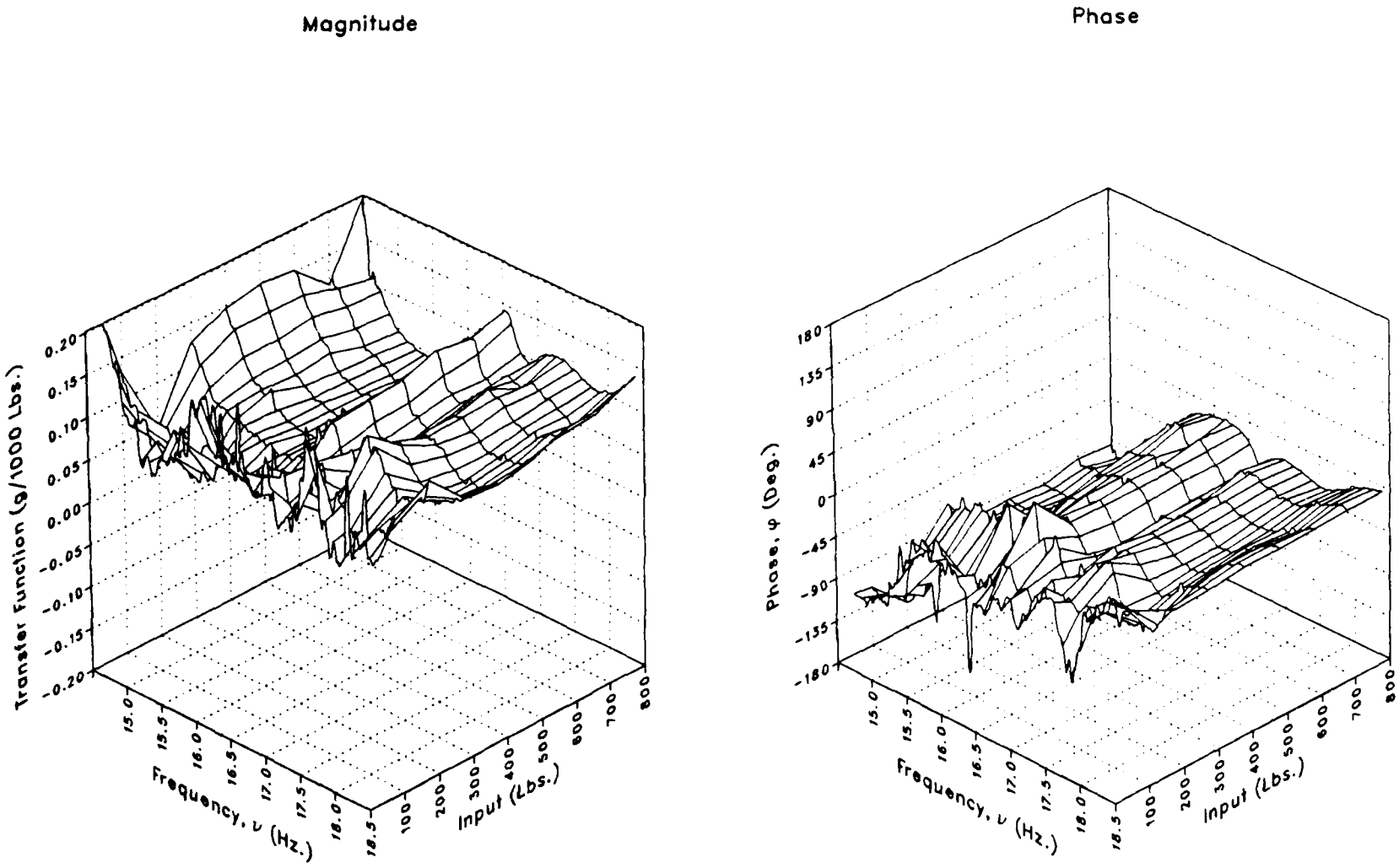

(bb) S450OVRL Concluded.

Figure 2.– Concluded.

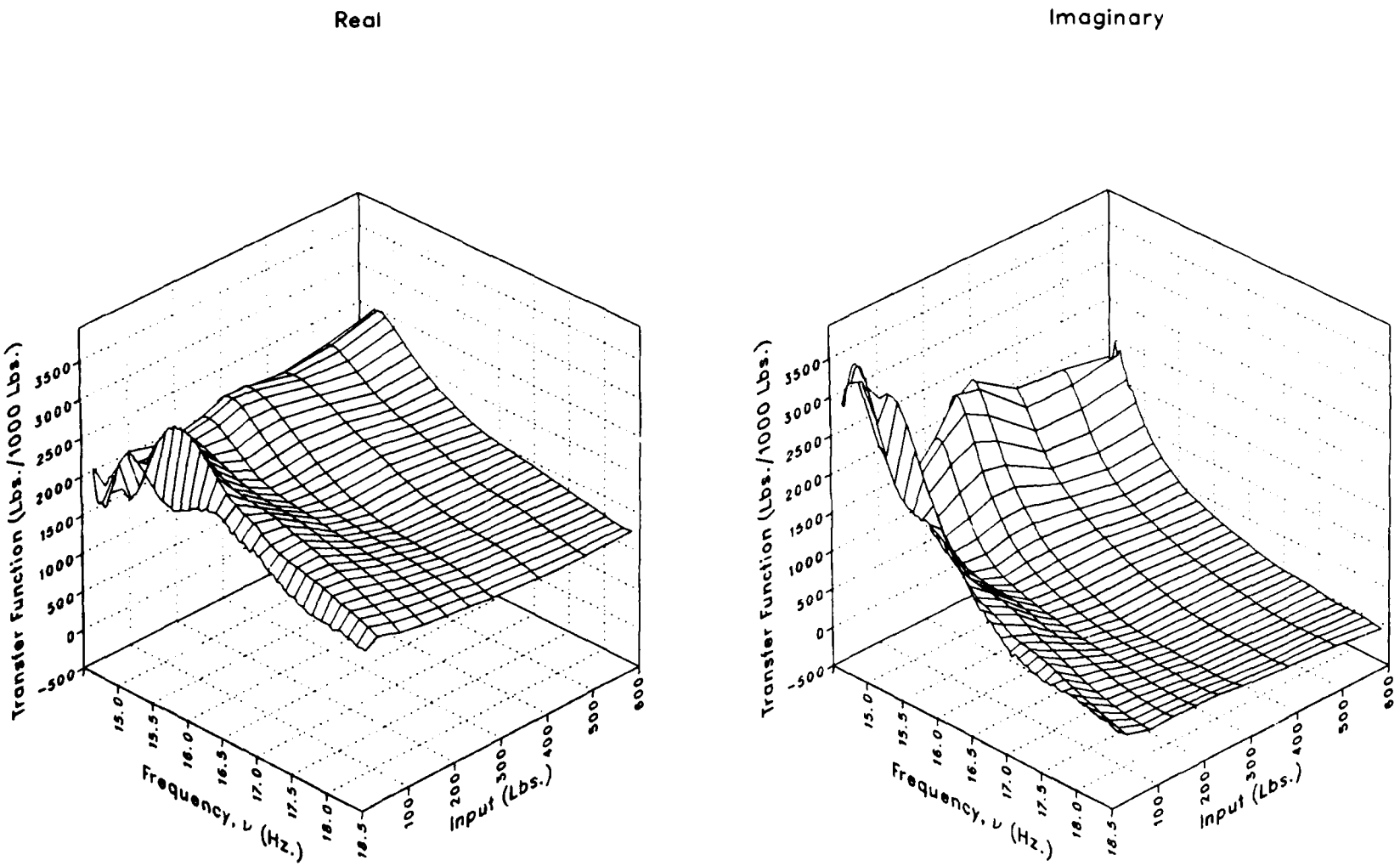

(a) MRDRAG

Figure 3.– Longitudinal forcing.

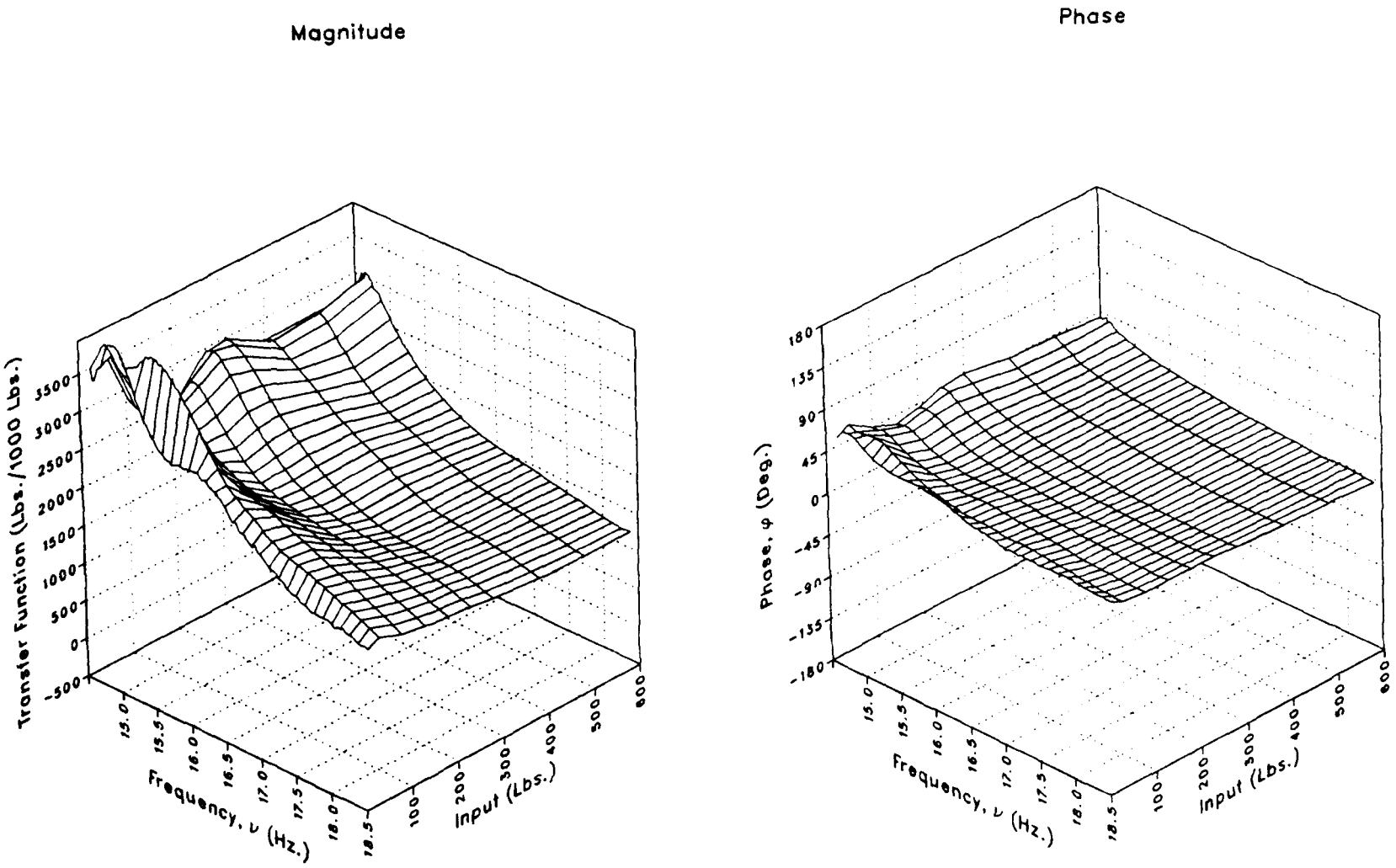

(a) MRDRAG Concluded.

Figure 3.– Continued.

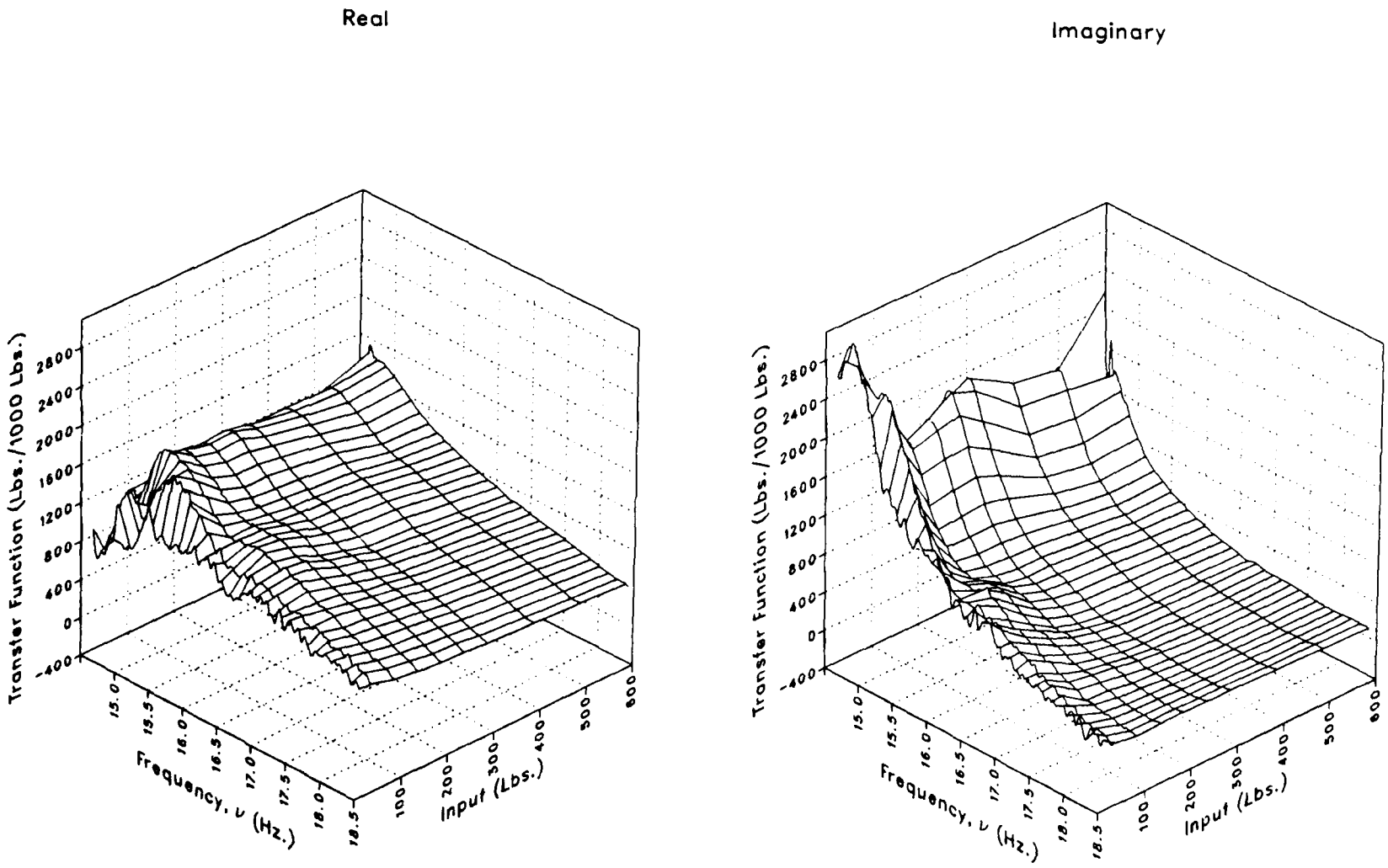

(b) MRLIFTA

Figure 3.– Continued.

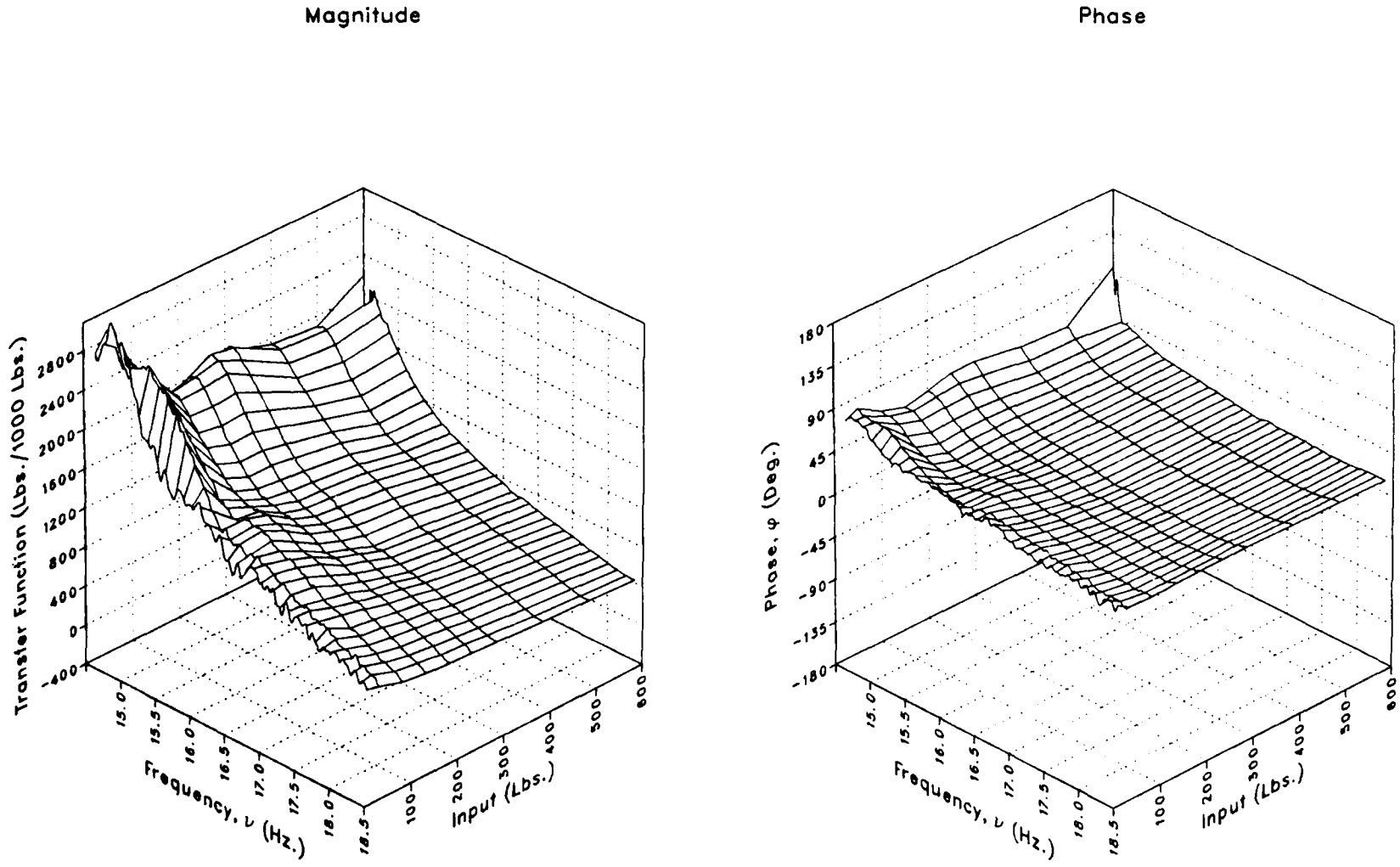

(b) MRLIFTA Concluded.

Figure 3.– Continued.

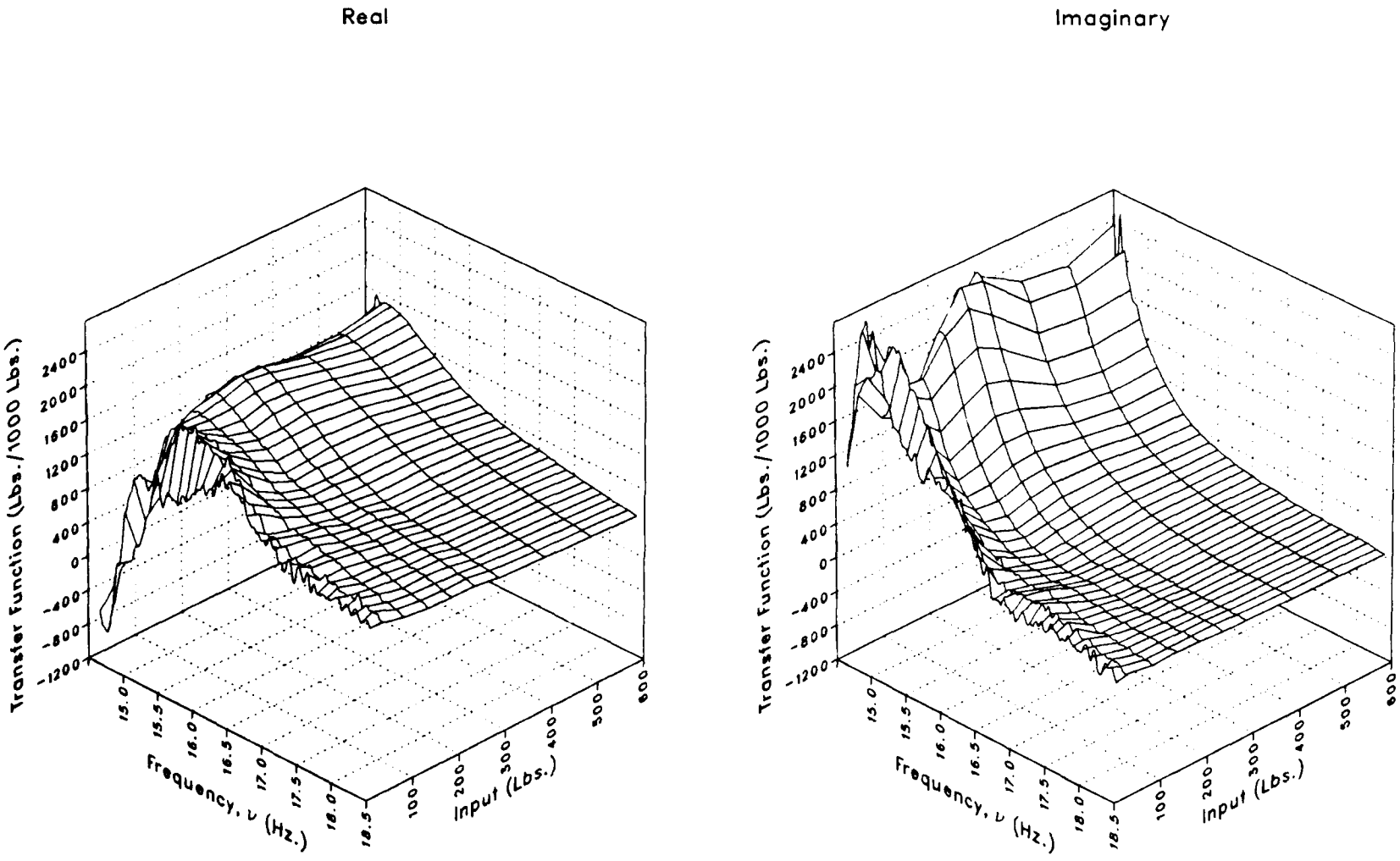

(c) MRLIFTB

Figure 3.– Continued.

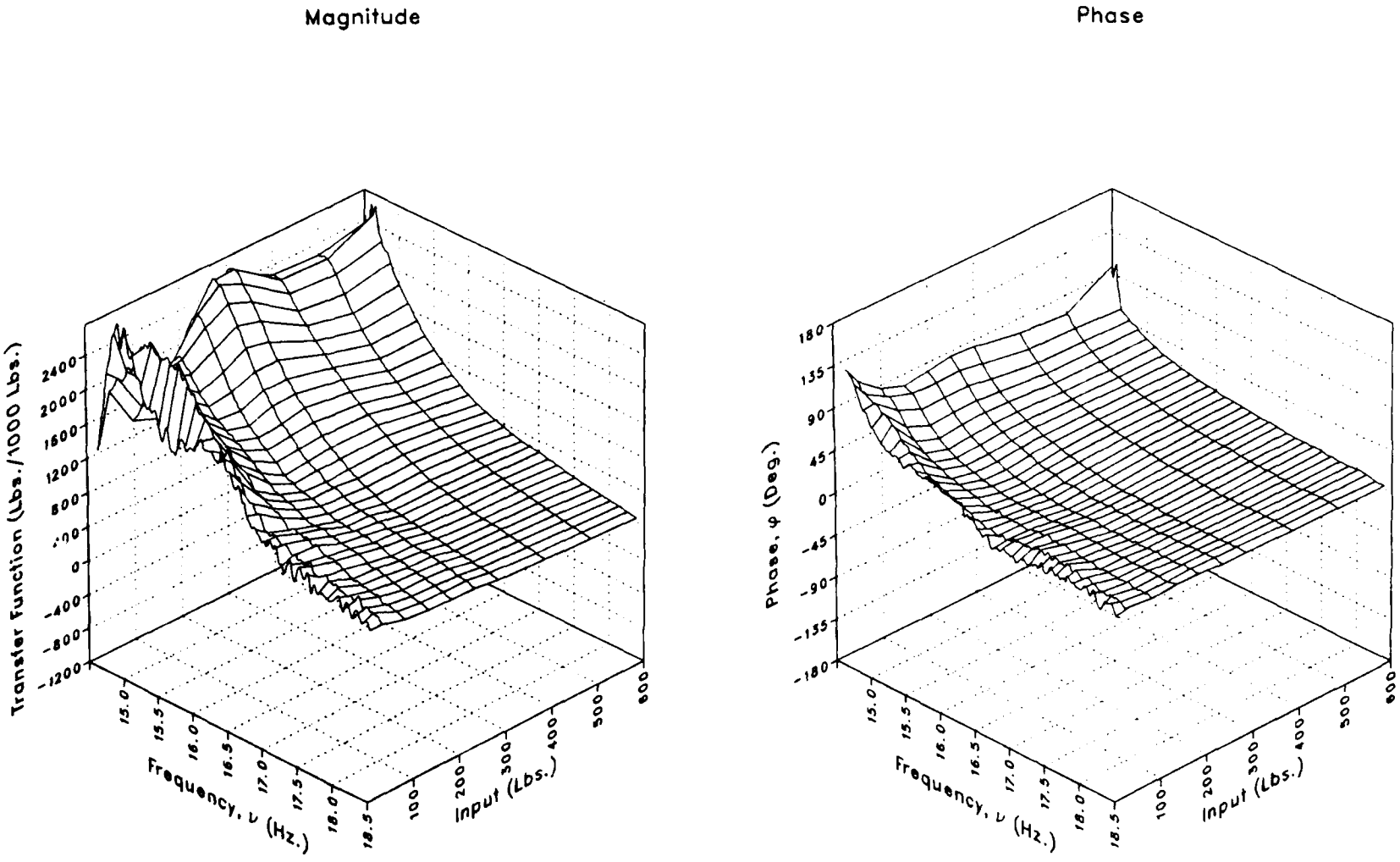

(c) MRLIFTB Concluded.

Figure 3.– Continued.

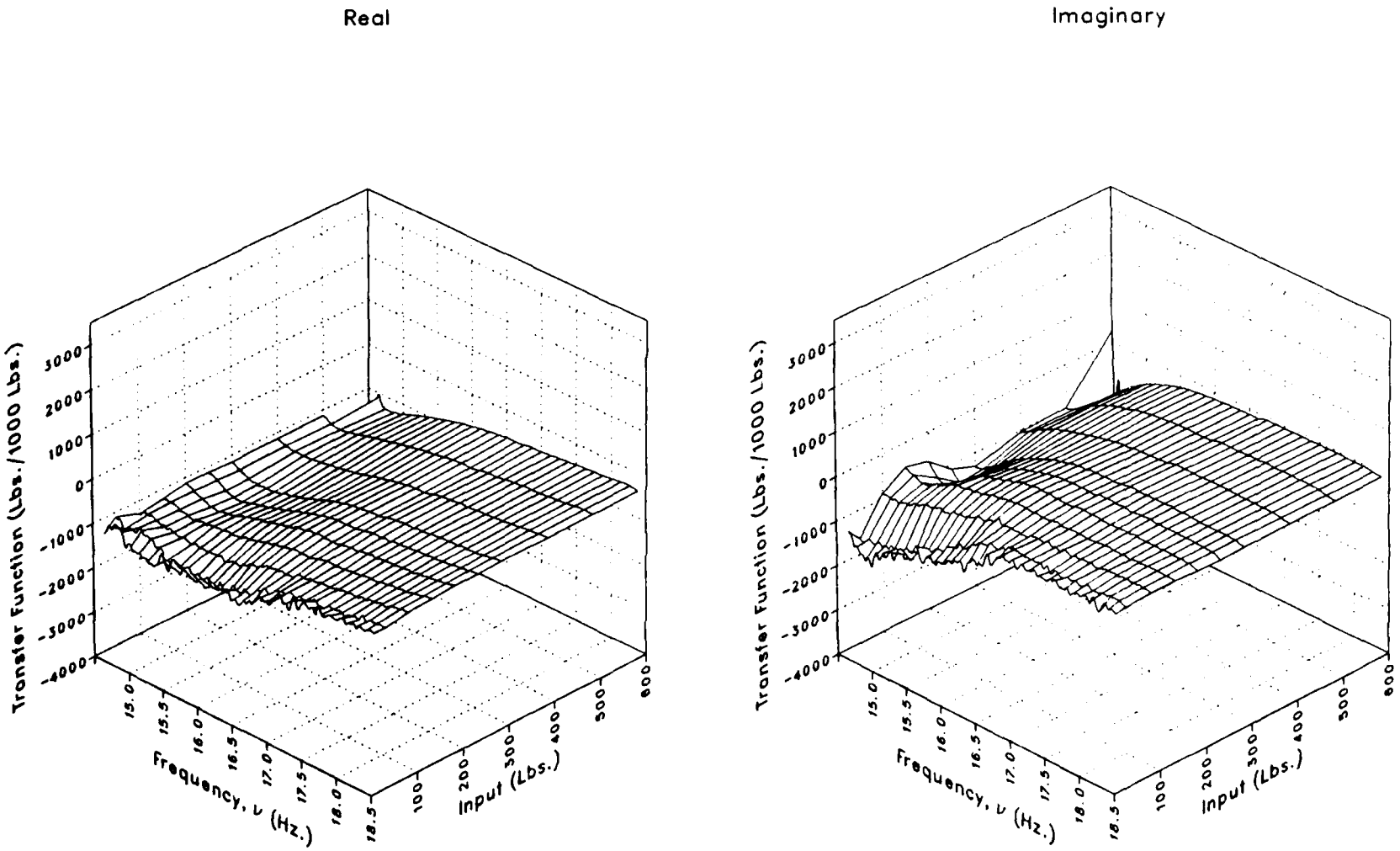

(d) MRLIFTC

Figure 3.– Continued.

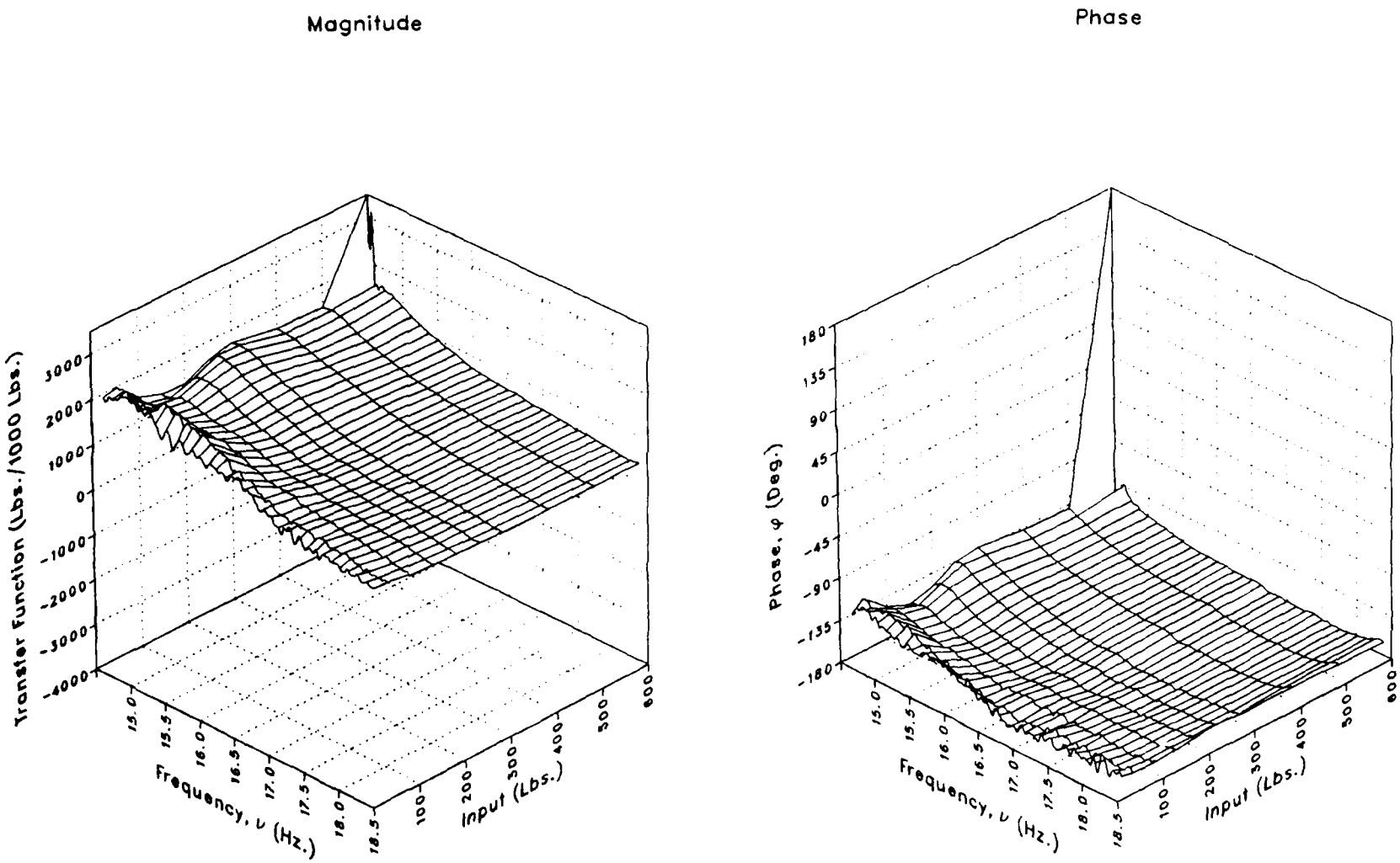

(d) MRLIFTC Concluded.

Figure 3.– Continued.

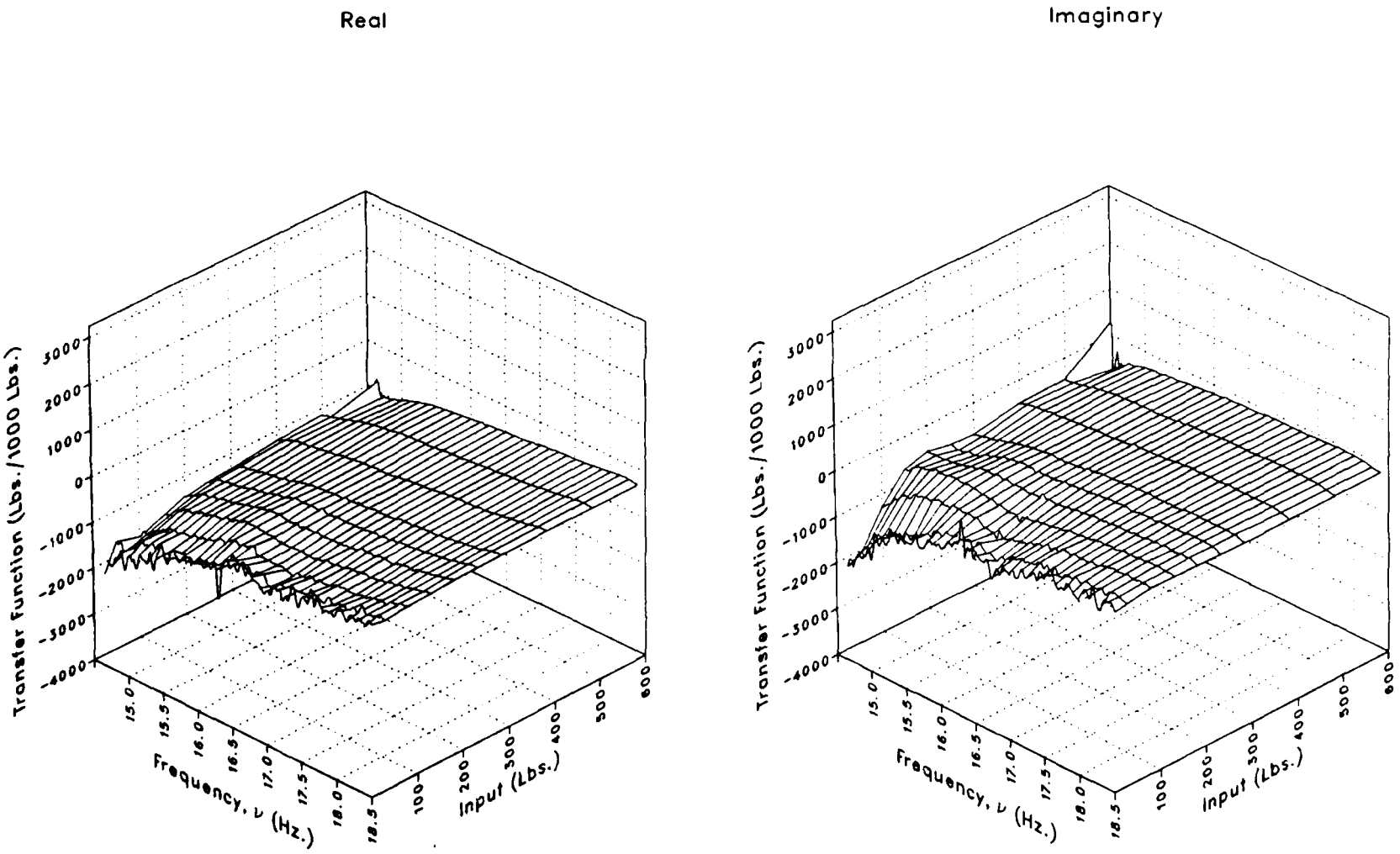

(e) MRLIFTD

Figure 3.– Continued.

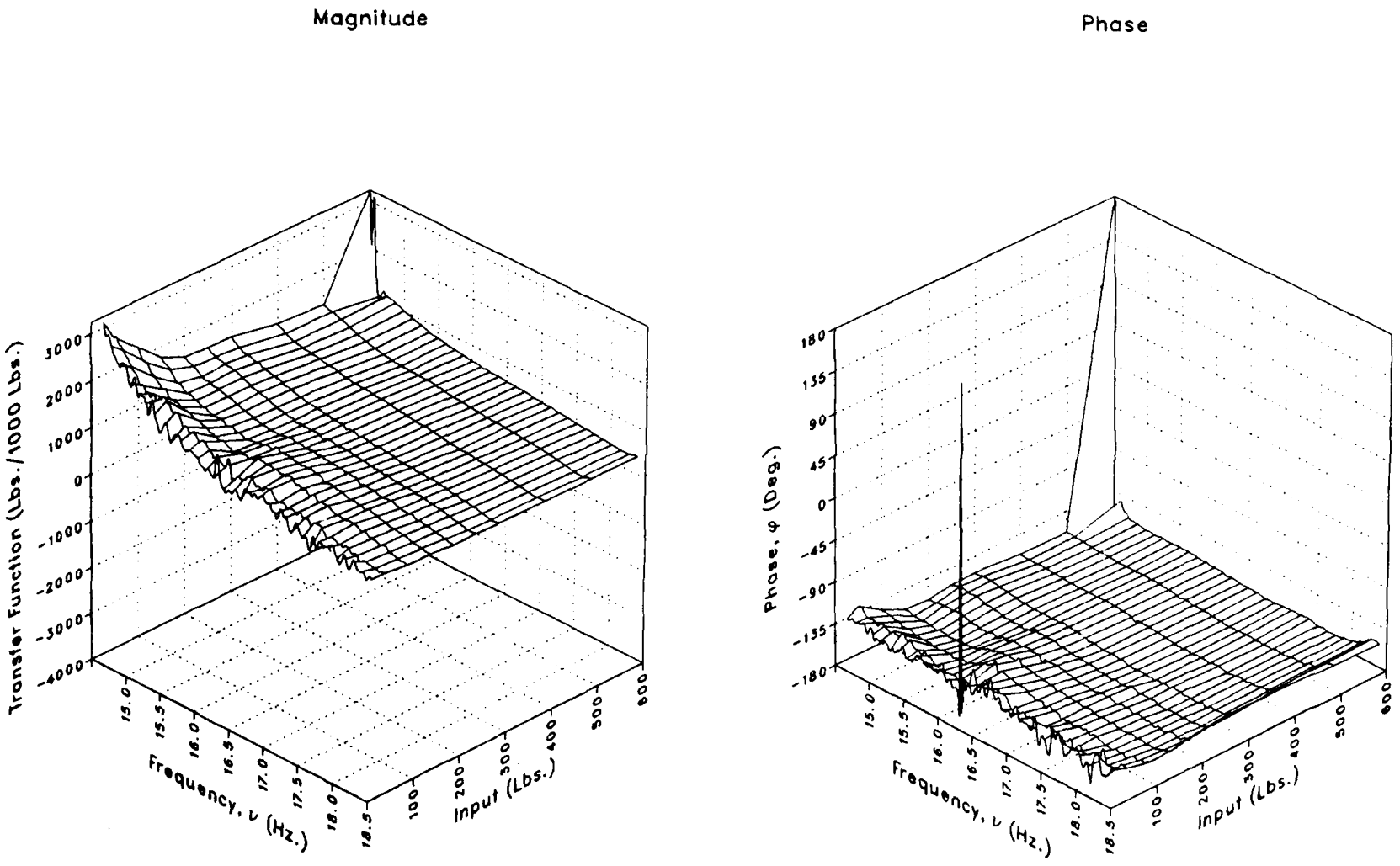

(e) MRLIFTD Concluded.

Figure 3.– Continued.

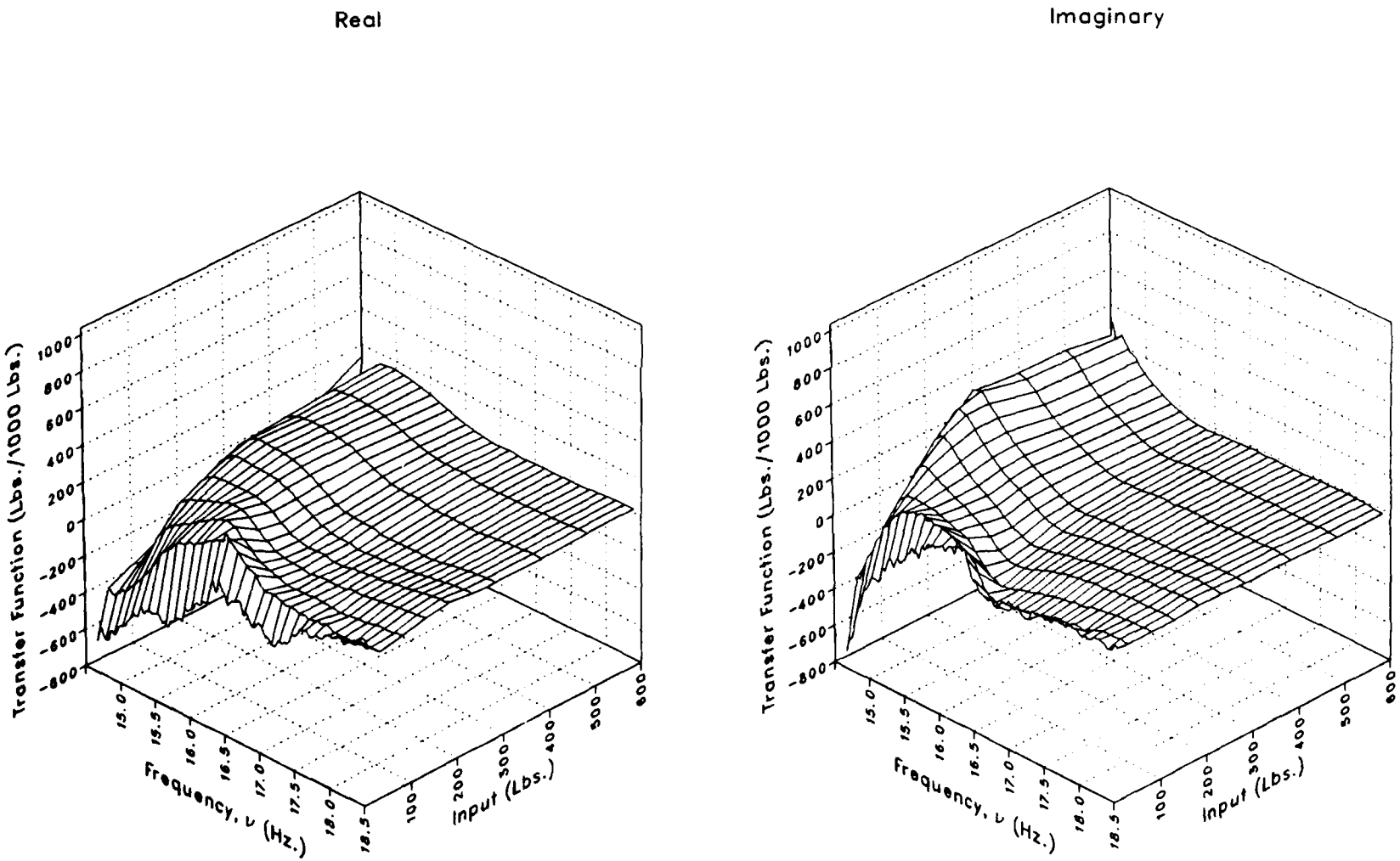

(f) MRGBQCE

Figure 3.– Continued.

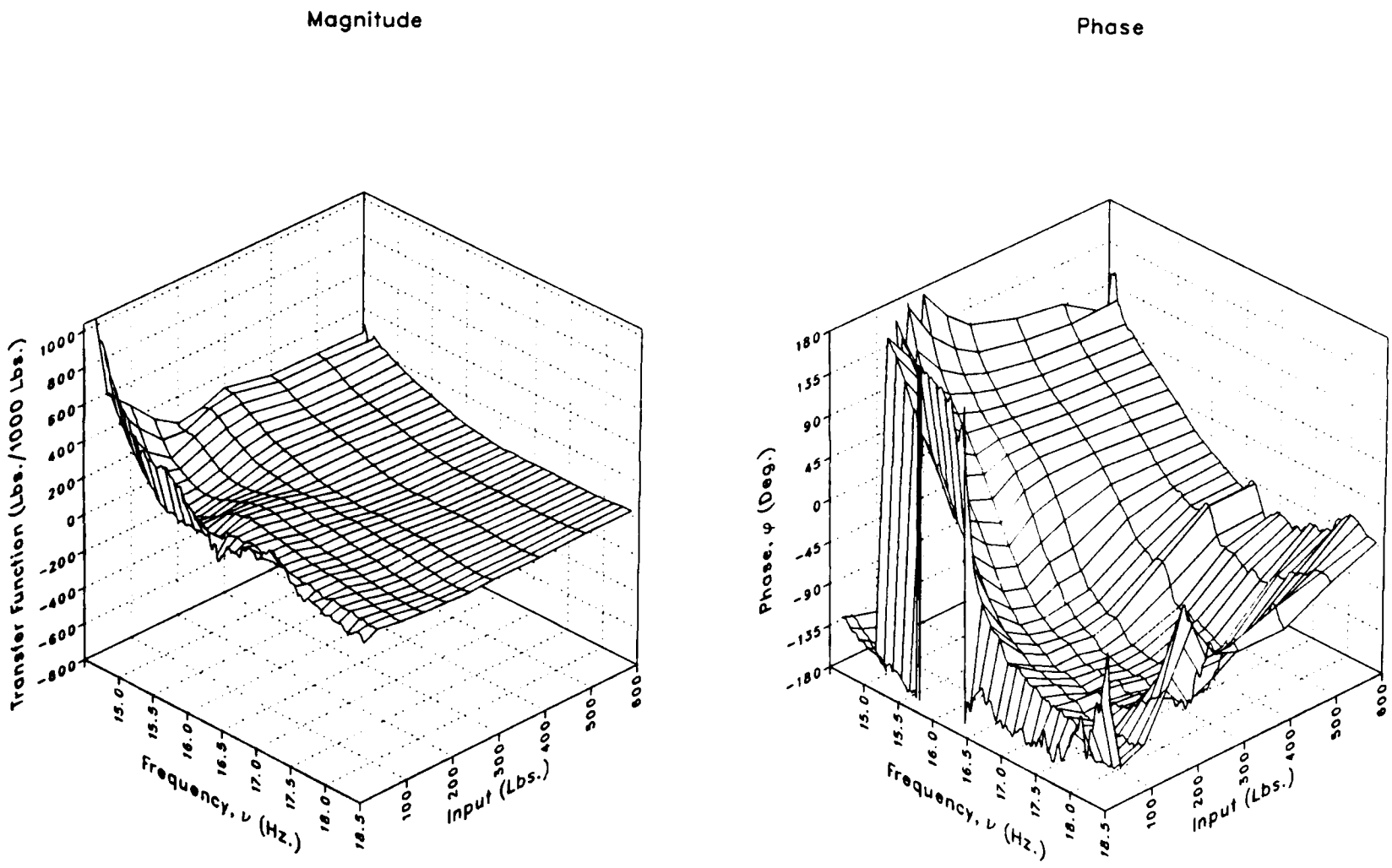

(f) MRGBQCE Concluded.

Figure 3.– Continued.

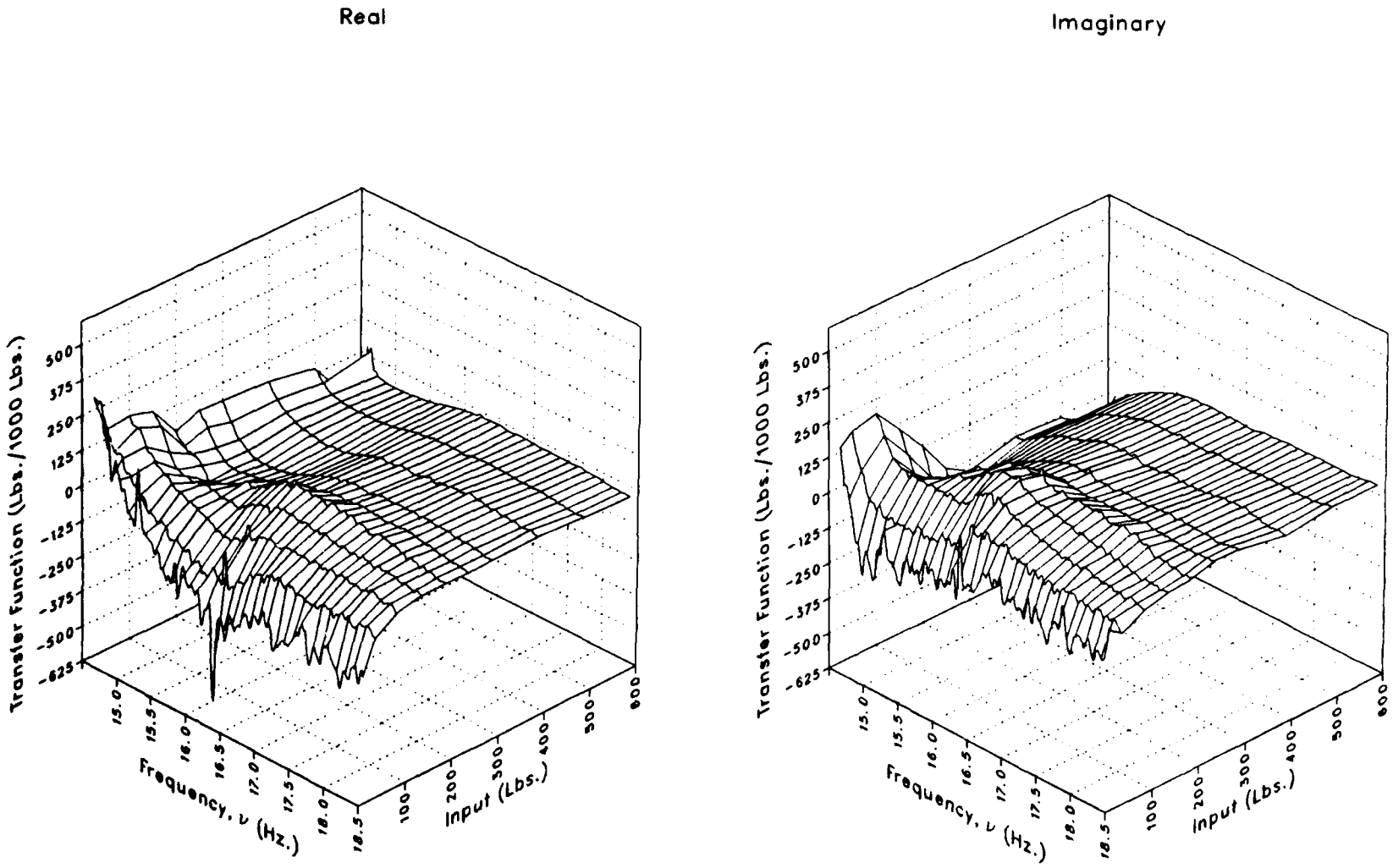

(g) MRGBQCF

Figure 3.– Continued.

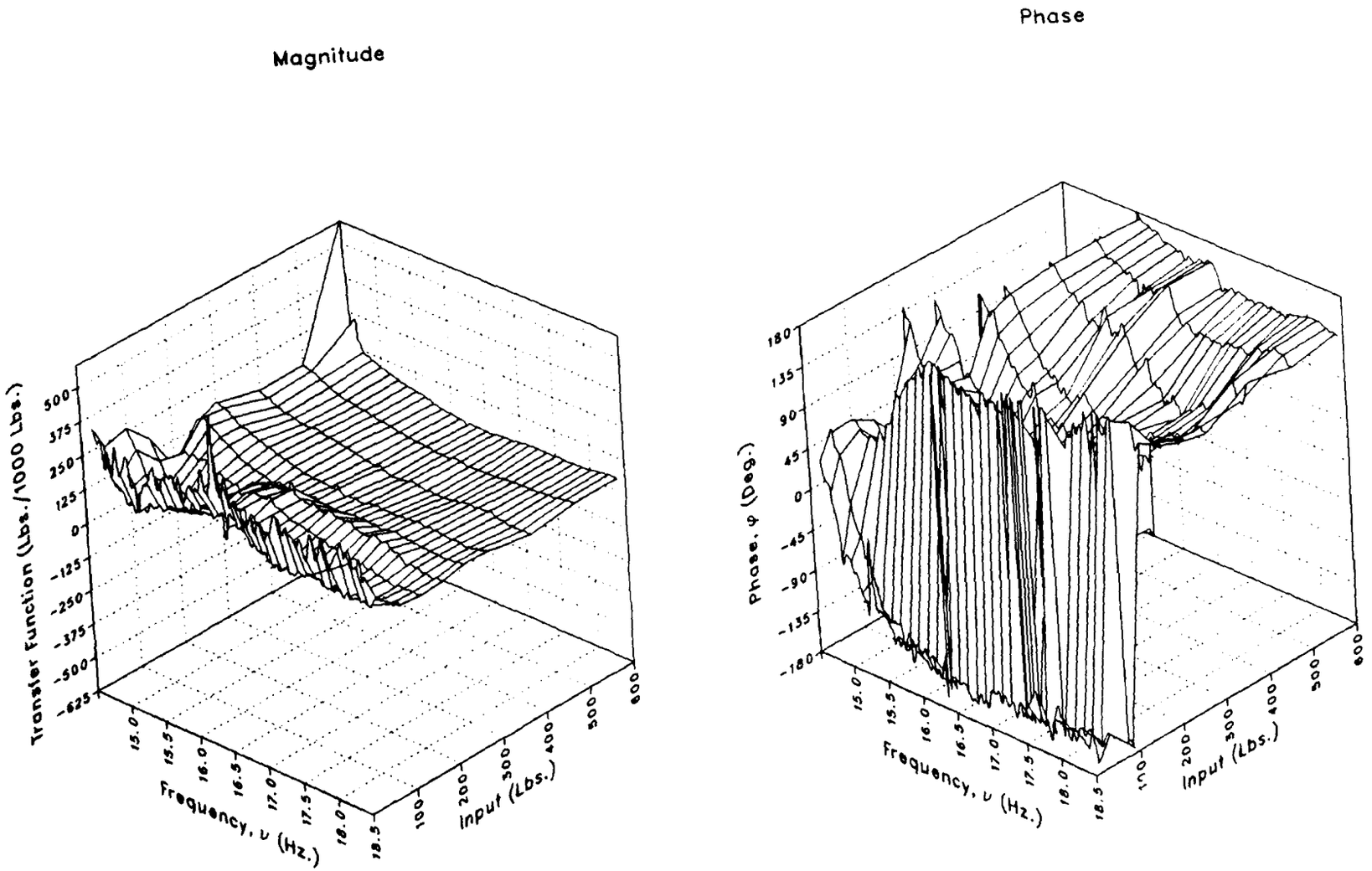

(g) MRGBQCF Concluded.

Figure 3.– Continued.

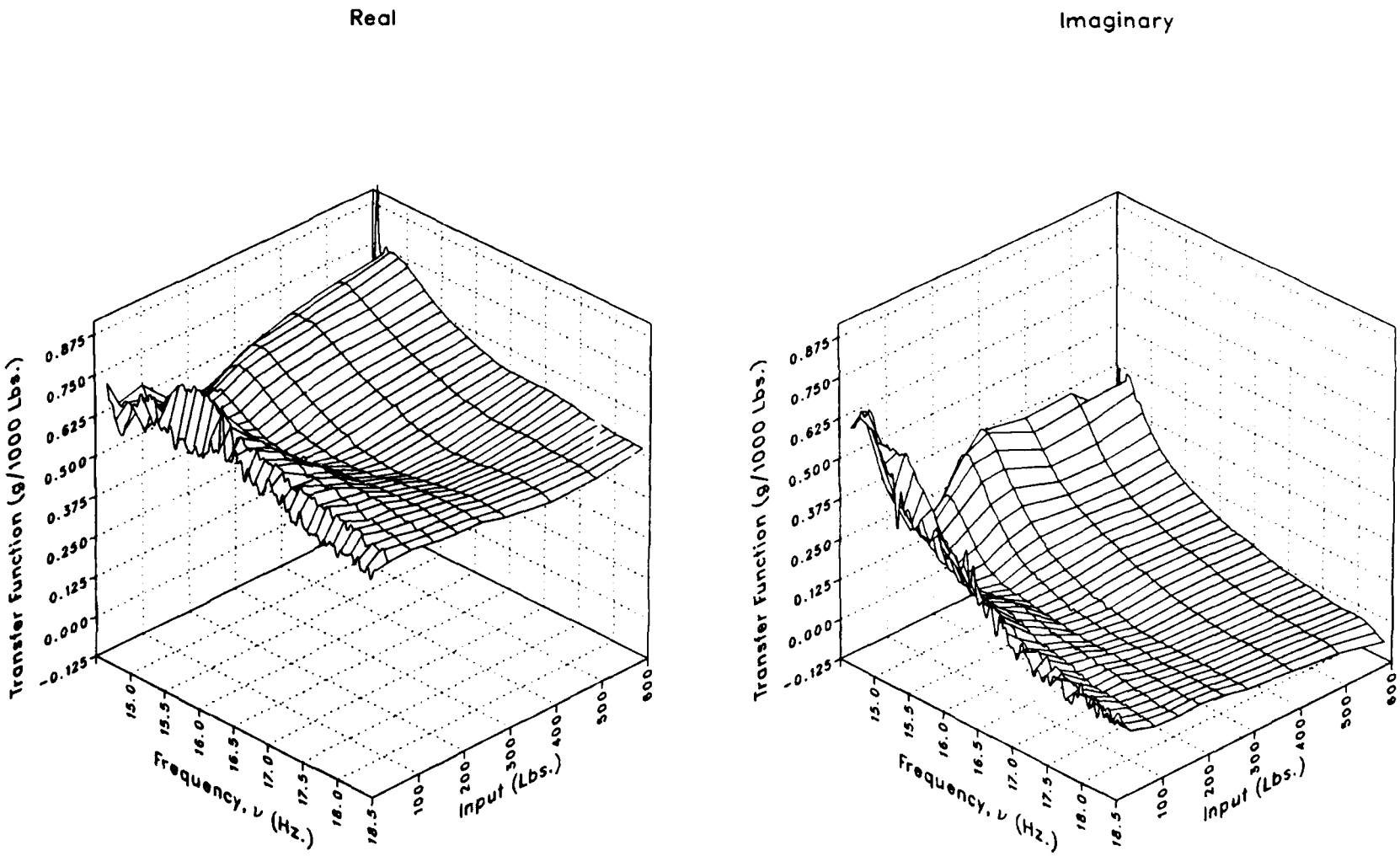

(h) LOMGB

Figure 3.– Continued.

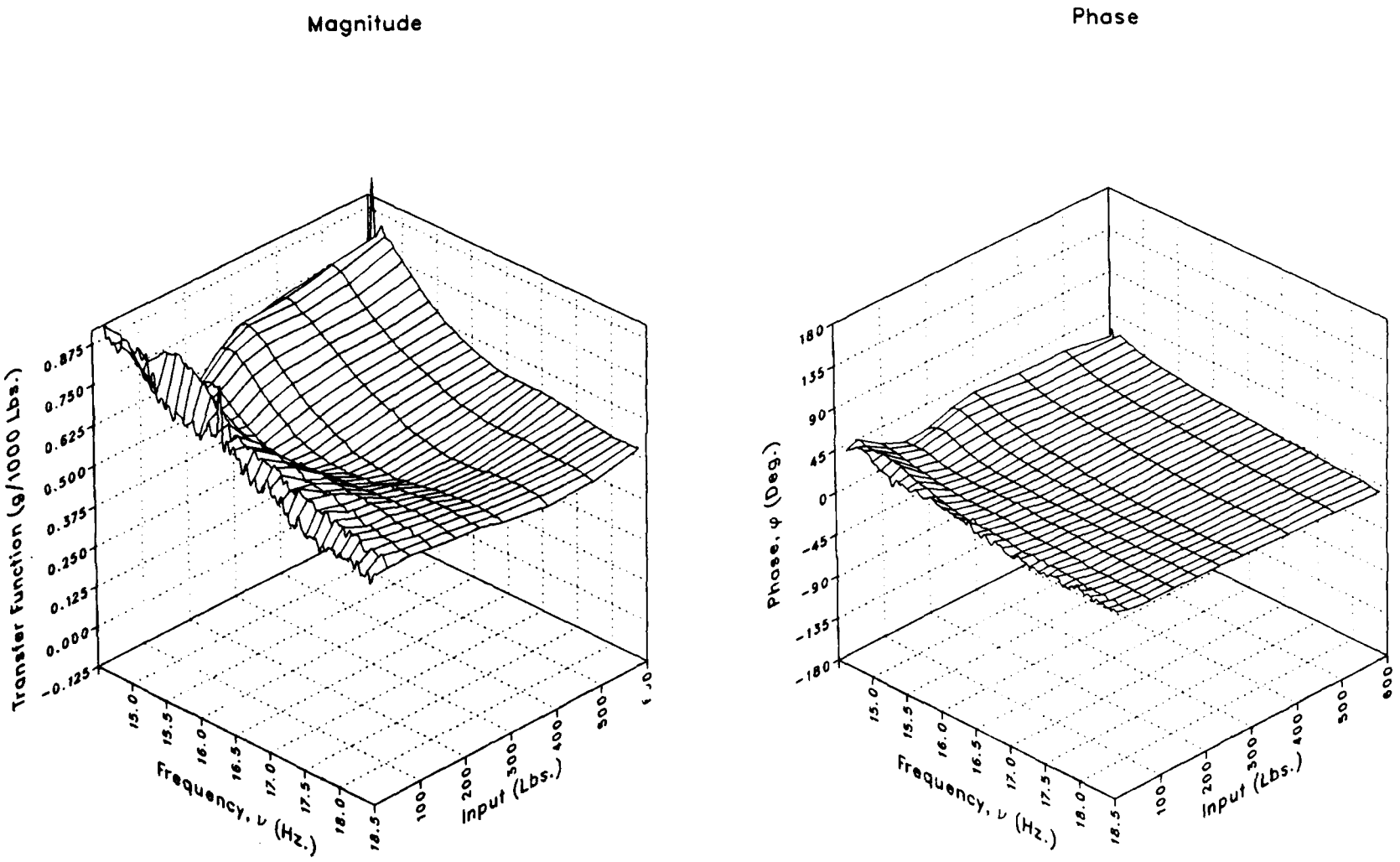

(h) LOMGB Concluded.

Figure 3.– Continued.

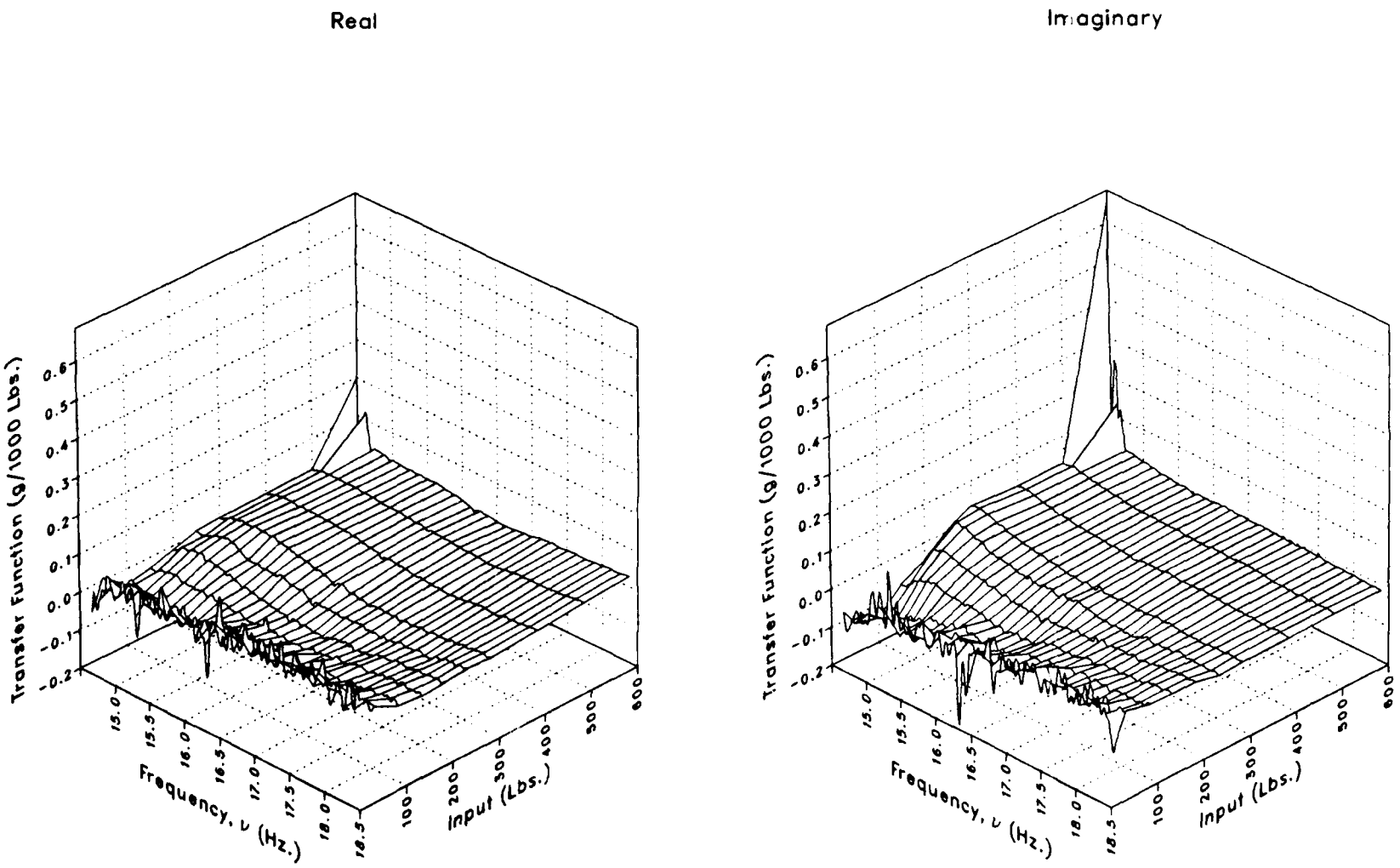

(i) LMGB

Figure 3.– Continued.

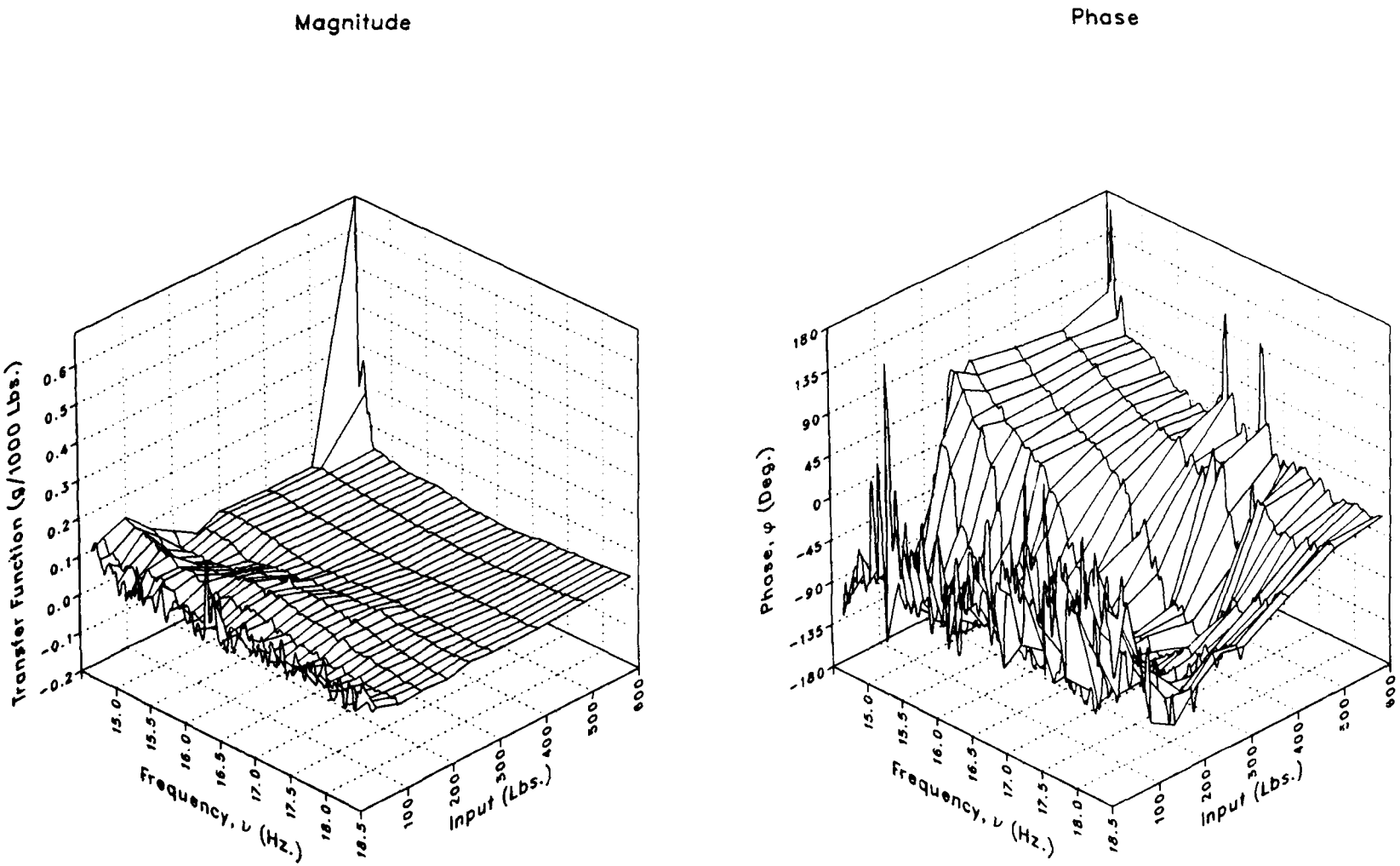

(i) LMGB Concluded.

Figure 3.– Continued.

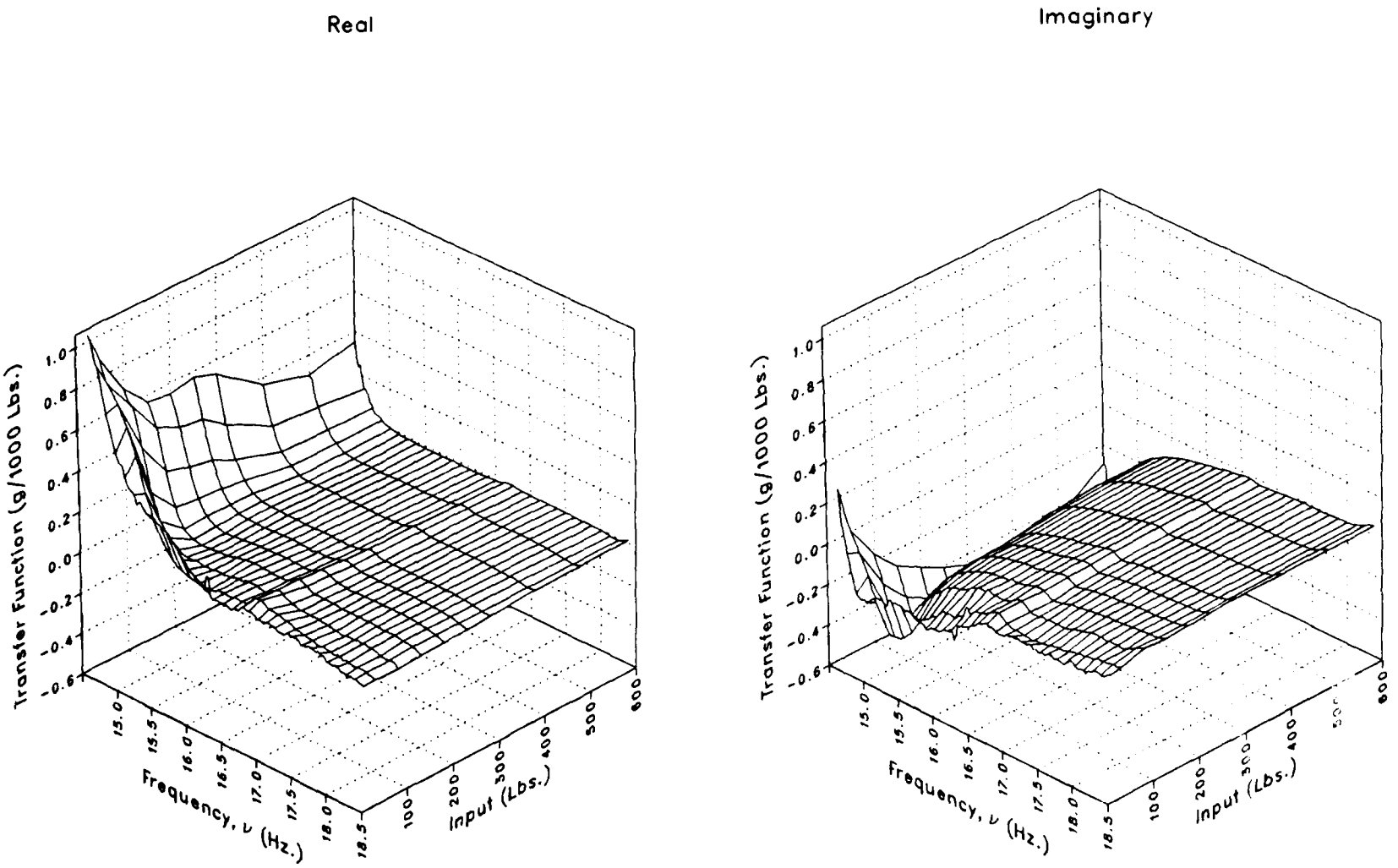

(j) VMGB

Figure 3.– Continued.

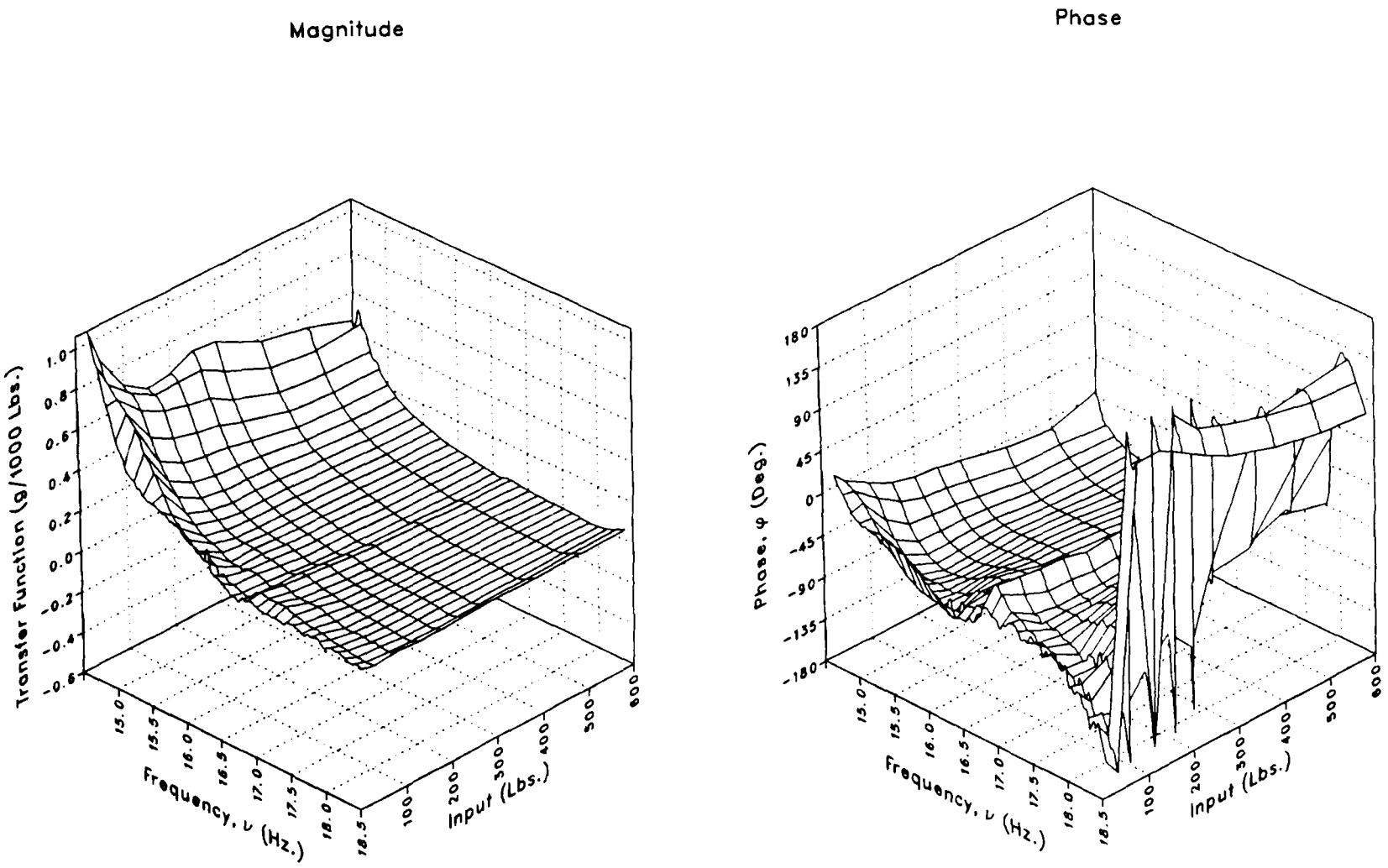

(j) VMGB Concluded.

Figure 3.– Continued.

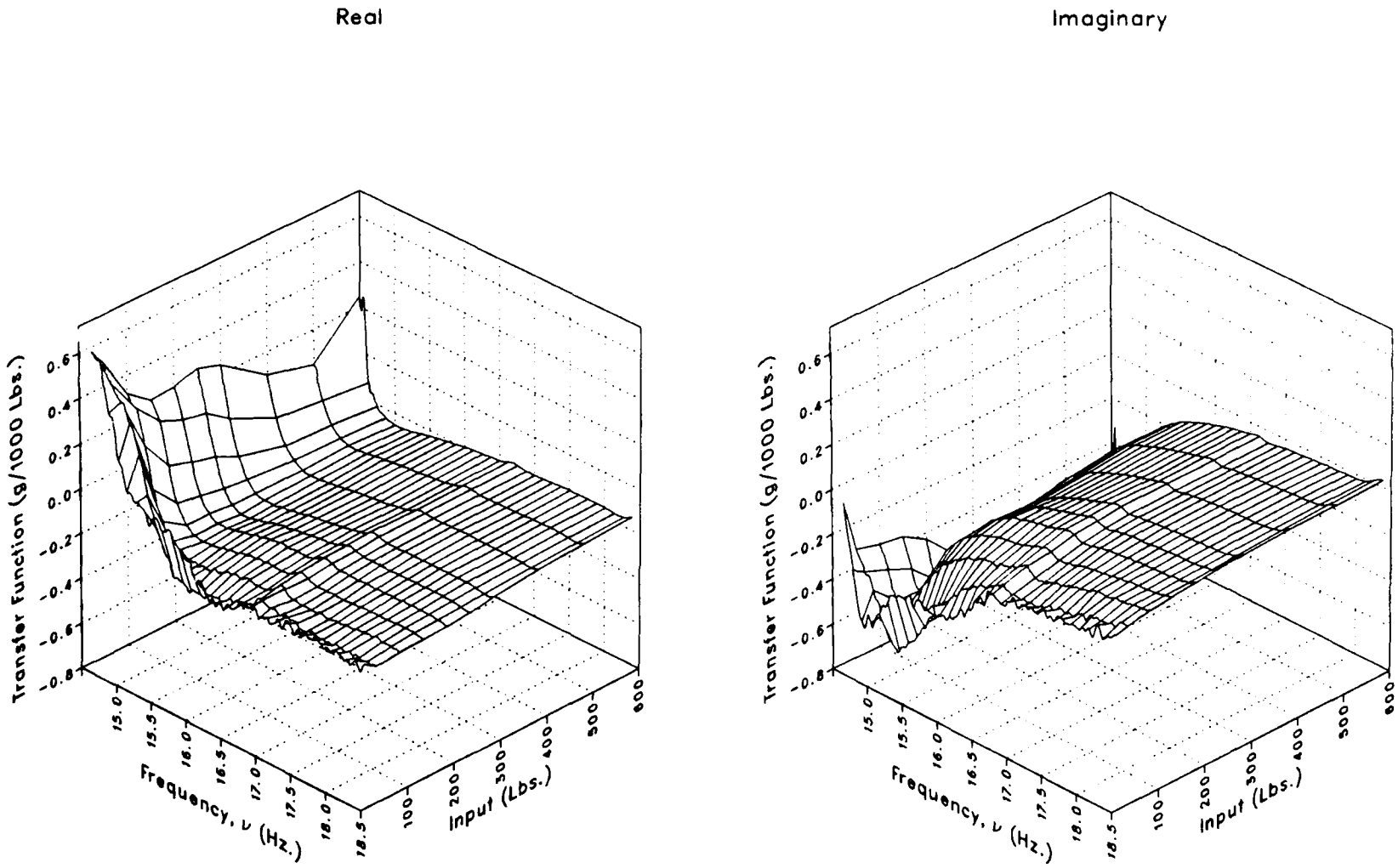

(k) XMRFBPV

Figure 3.– Continued.

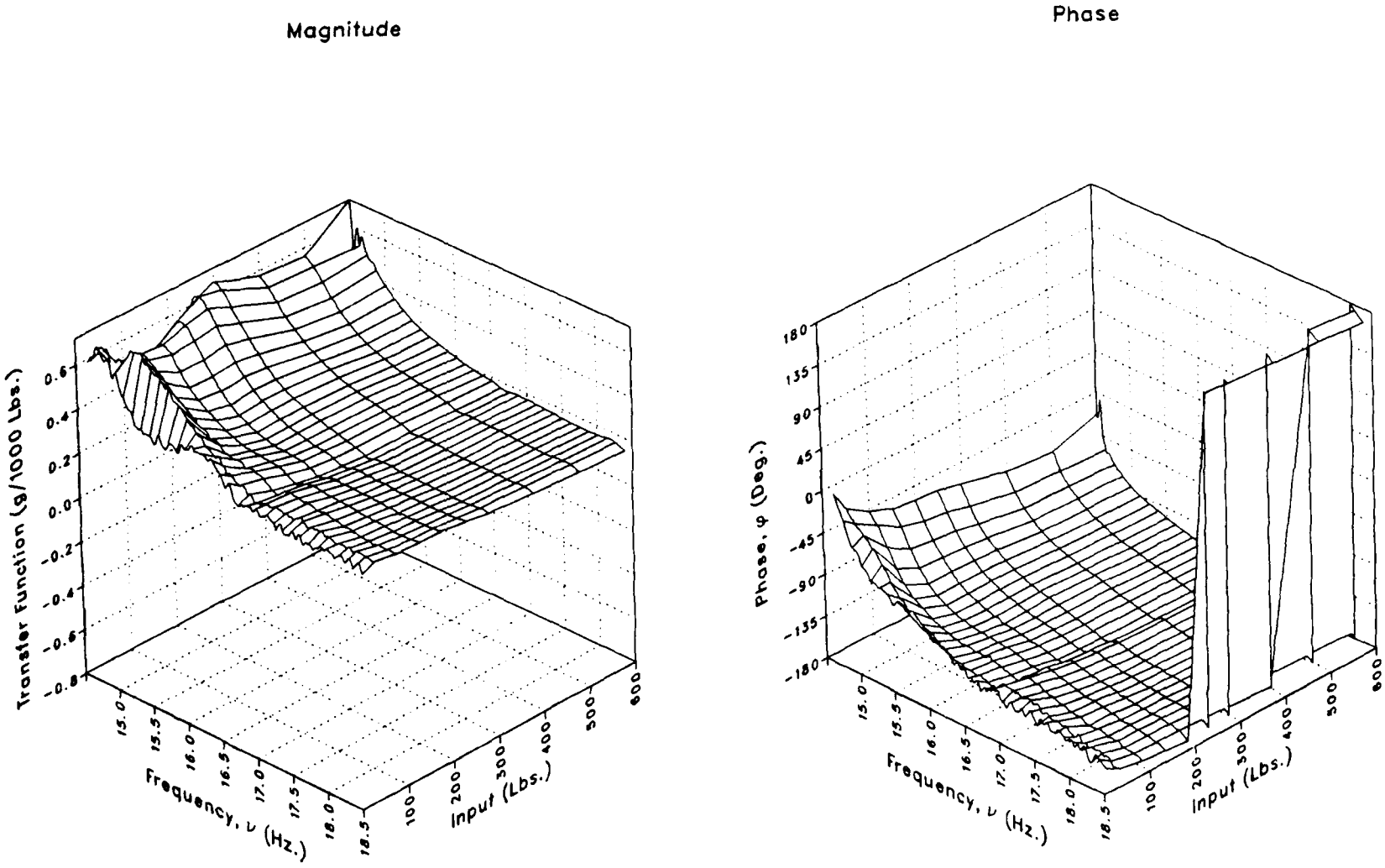

(k) XMRFBPV Concluded.

Figure 3.– Continued.

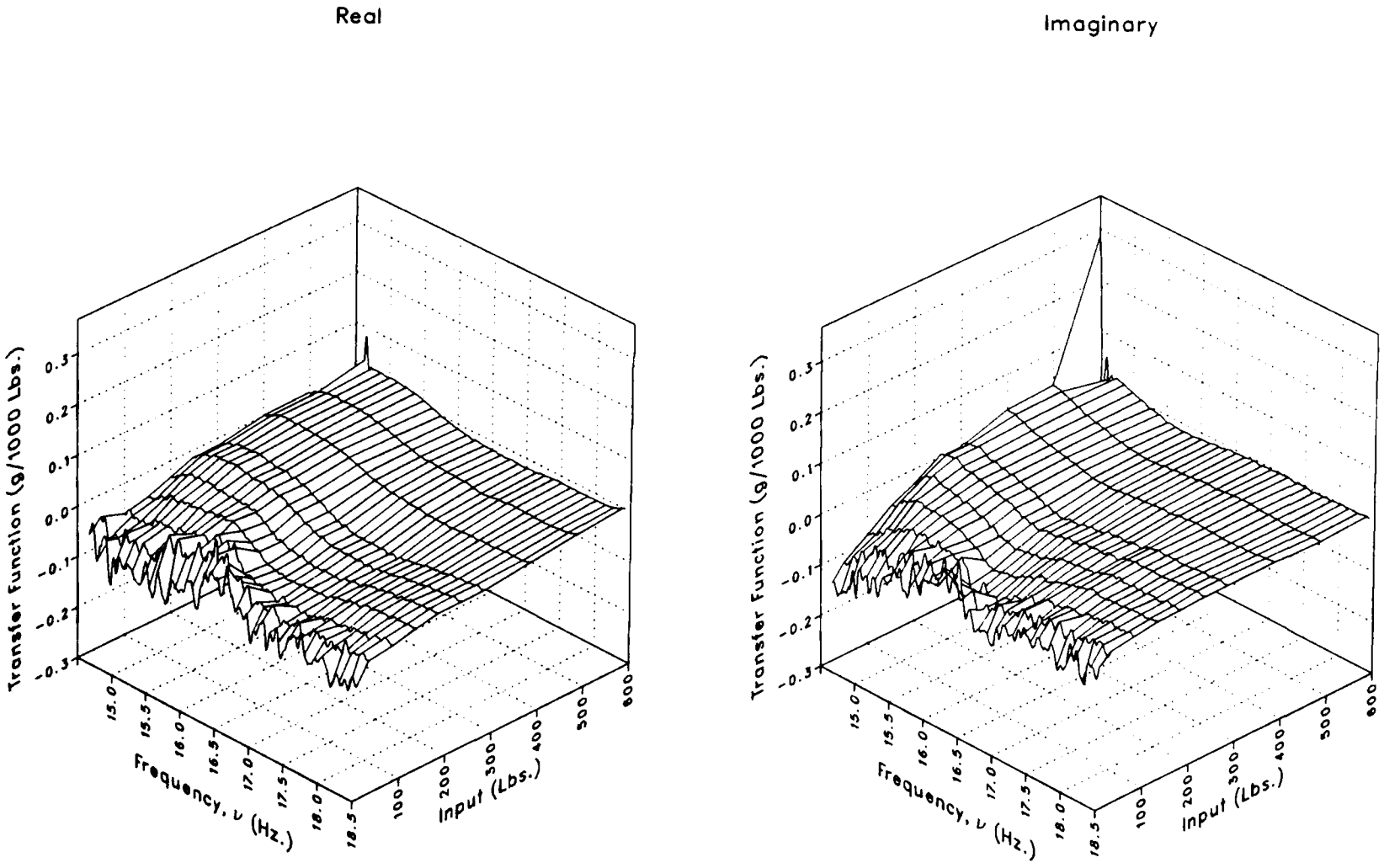

(l) XMRFBPL

Figure 3.– Continued.

Magnitude

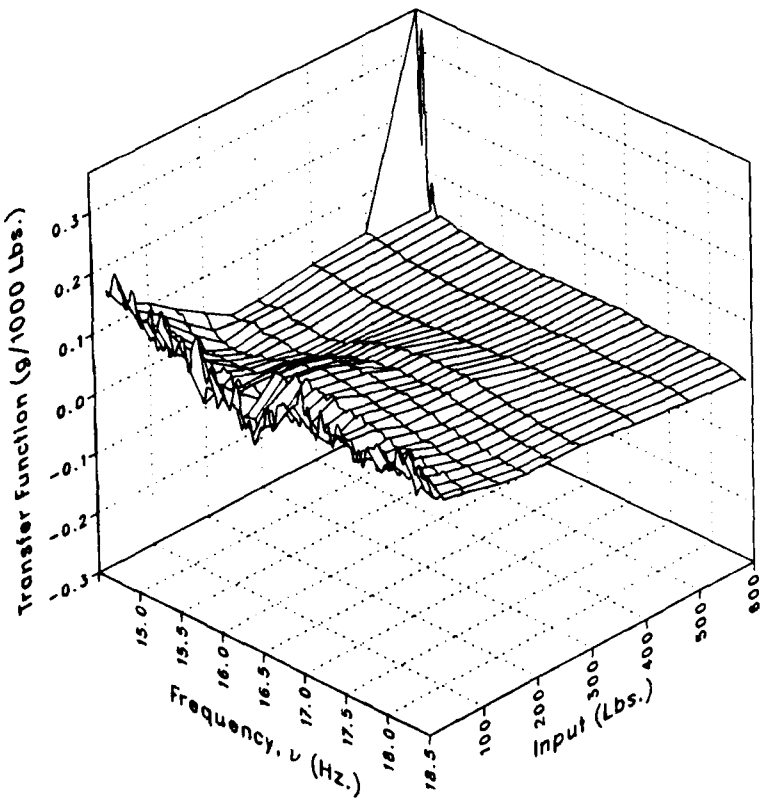

Phase

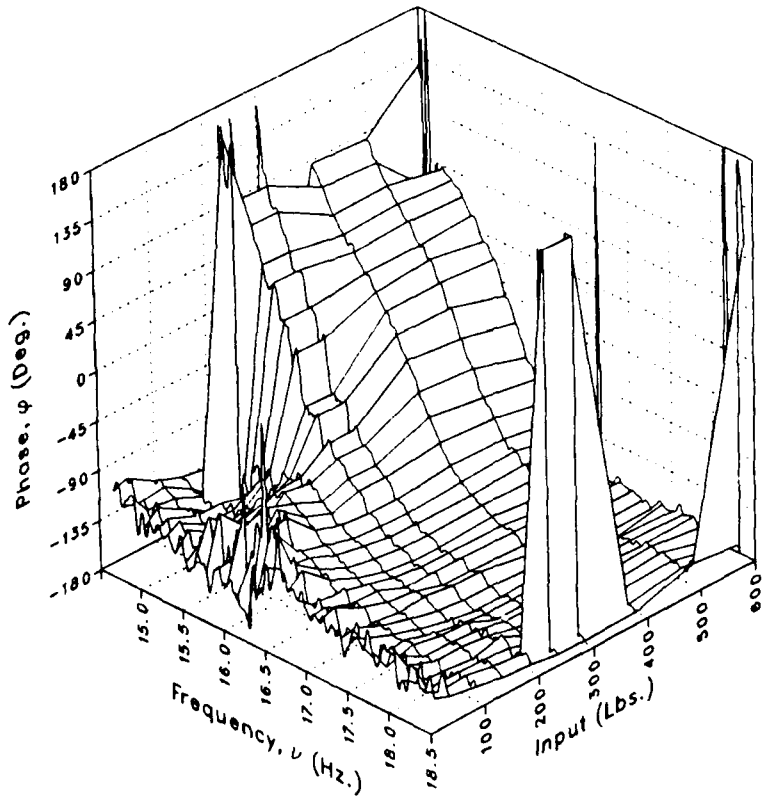

(l) XMRFBPL Concluded.

Figure 3.– Continued.

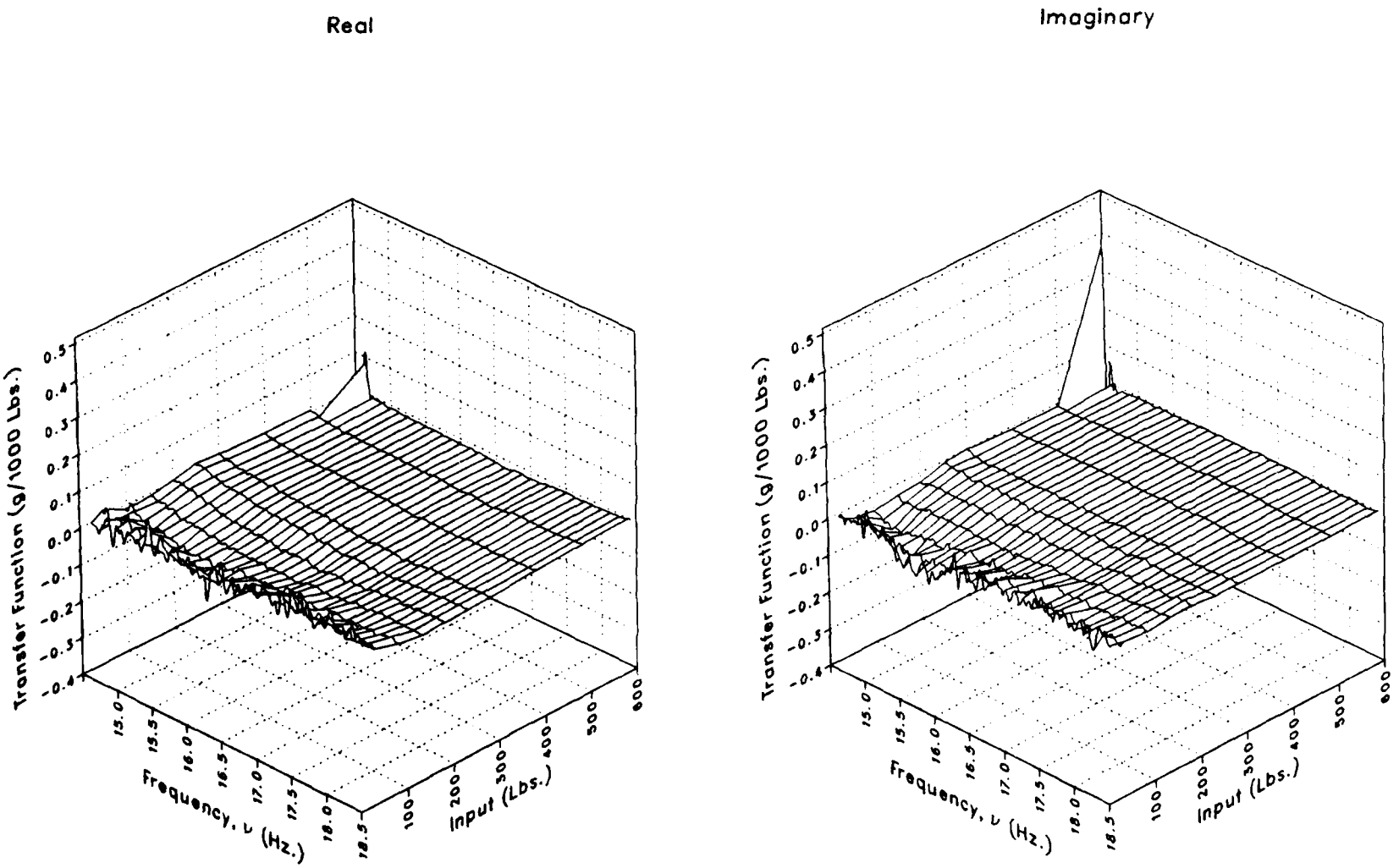

(m) XMRFBPLO

Figure 3.– Continued.

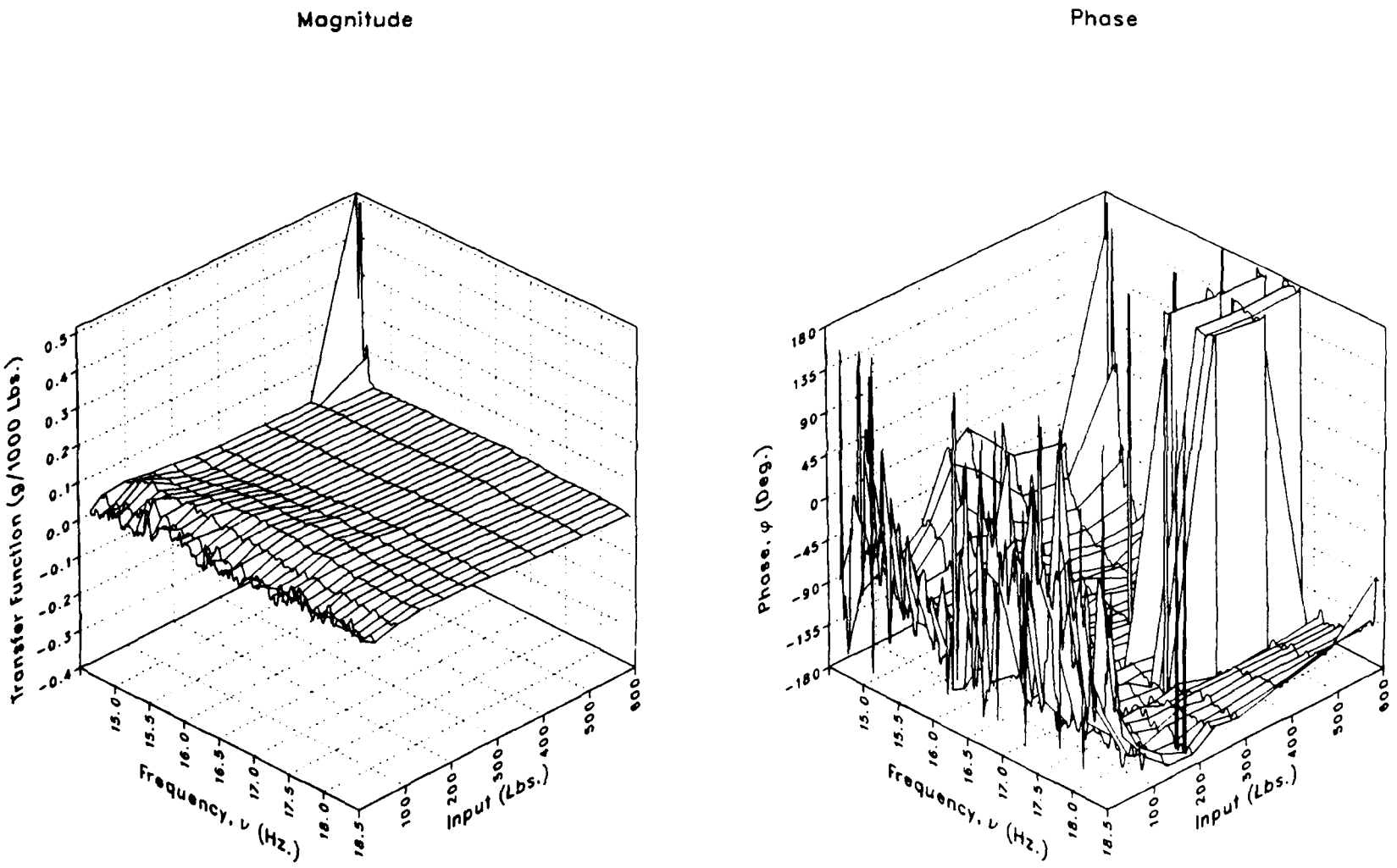

(m) XMRFBPLO Concluded.

Figure 3.– Continued.

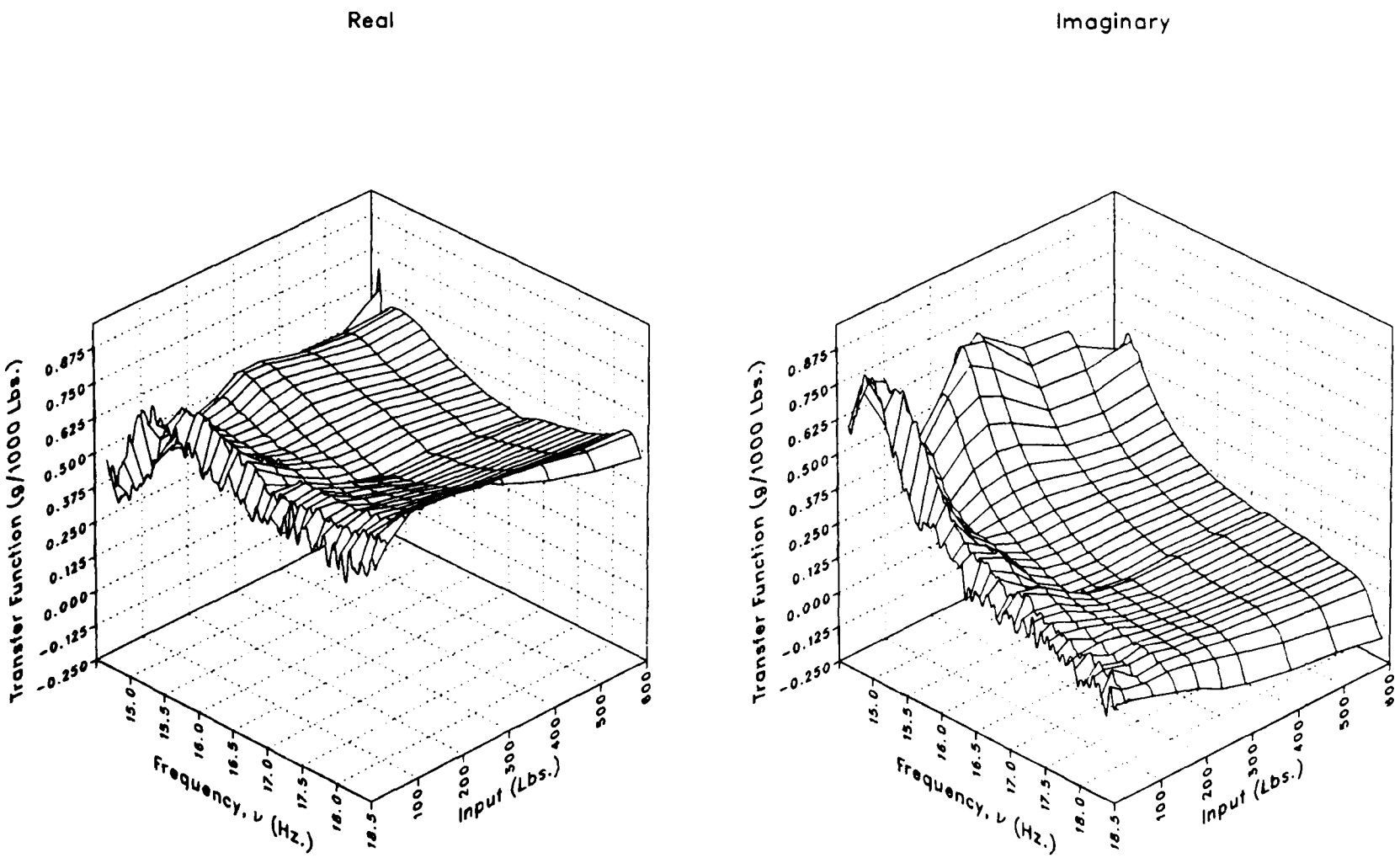

(n) STA56NV

Figure 3.– Continued.

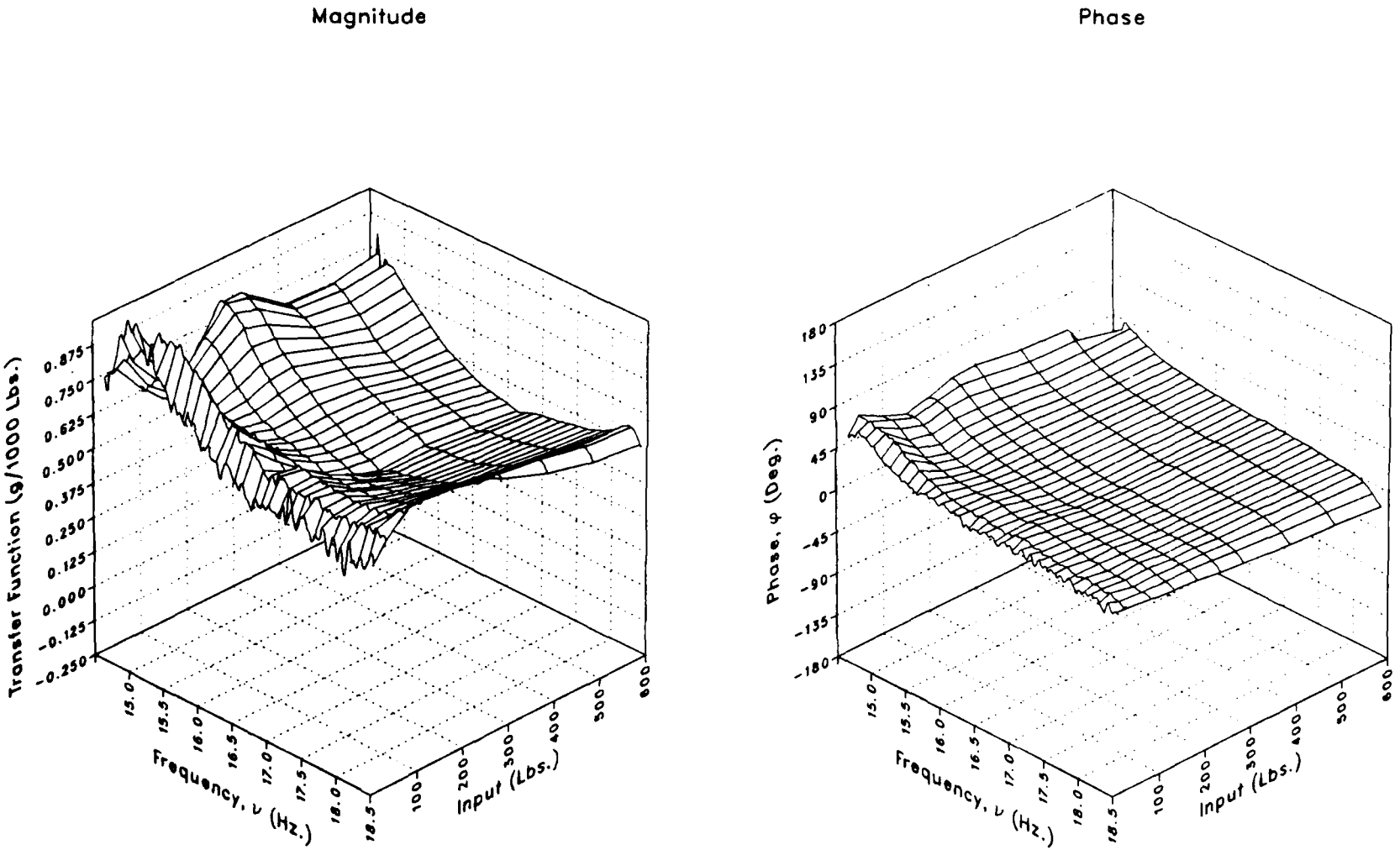

(n) STA56NV Concluded.

Figure 3.– Continued.

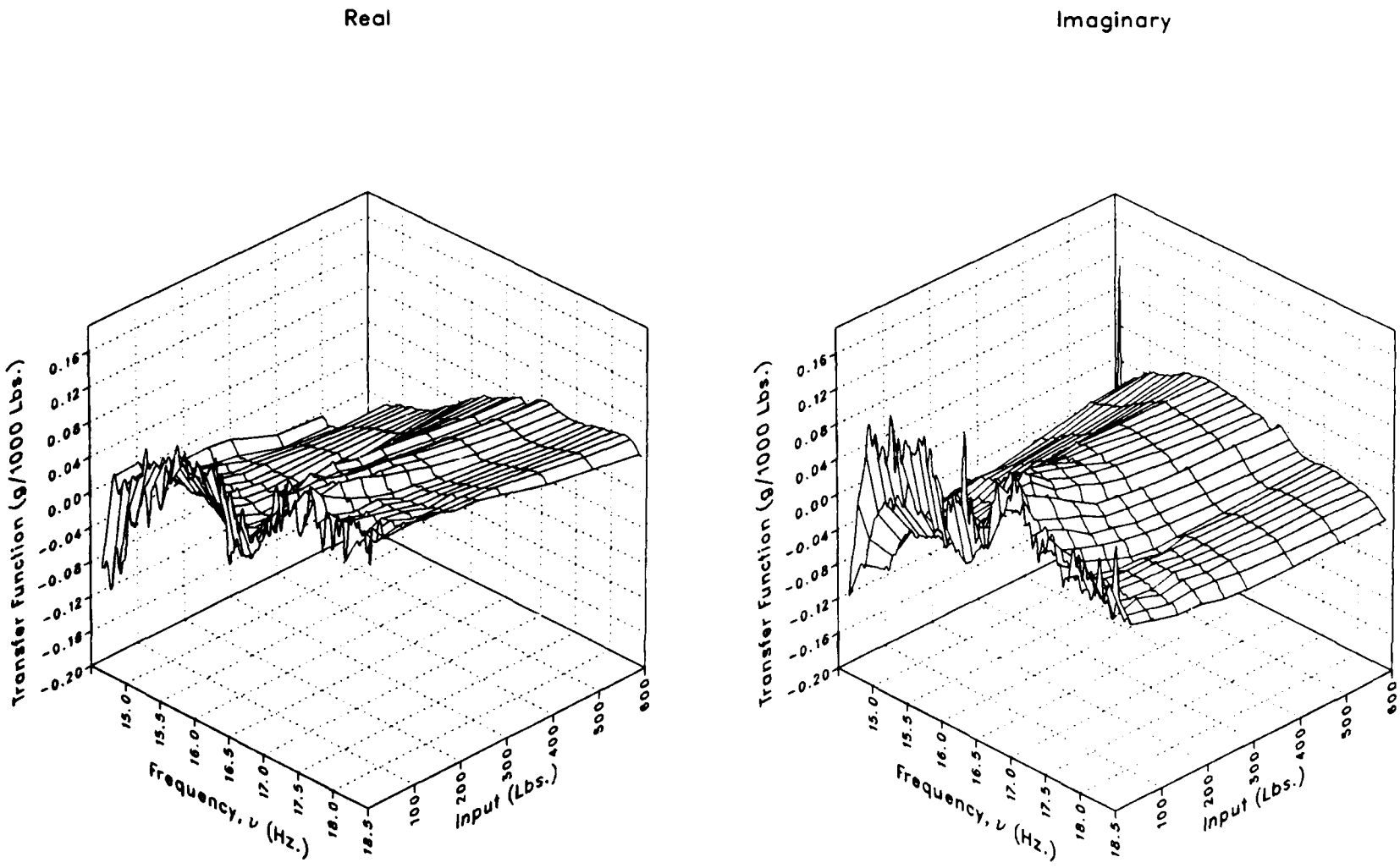

(o) STA56NL

Figure 3.– Continued.

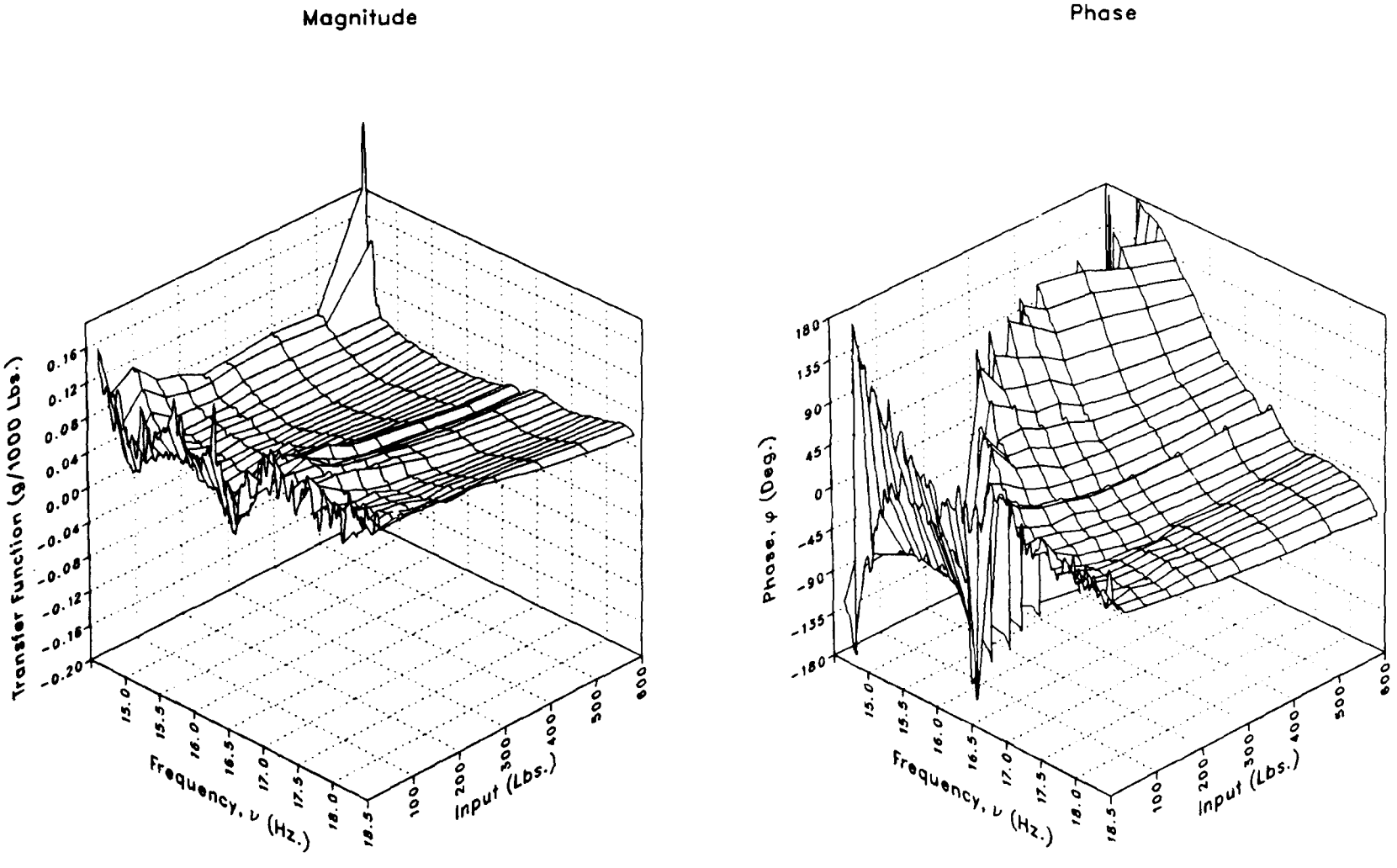

(o) STA56NL Concluded.

Figure 3.– Continued.

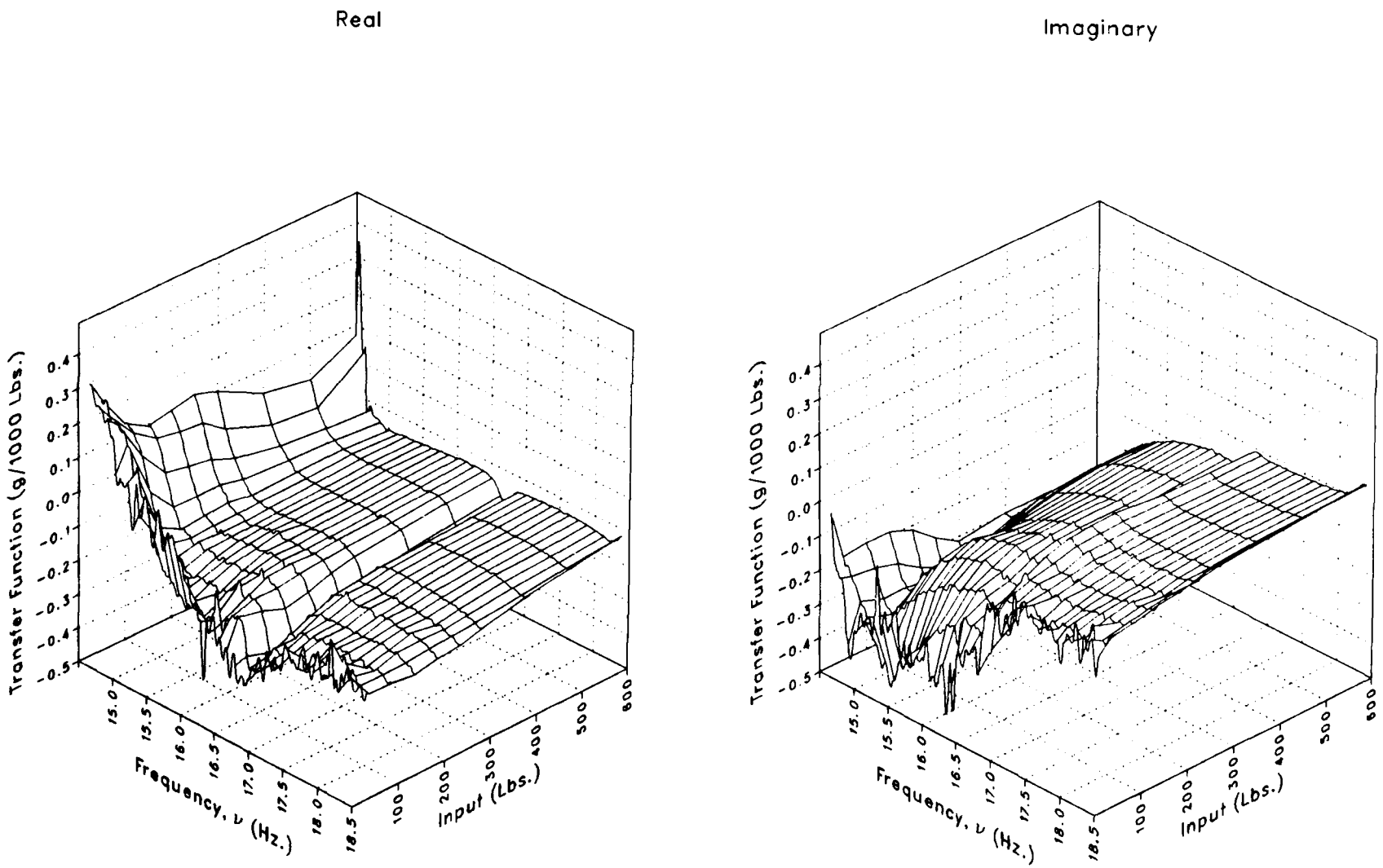

(p) VWGTPRT

Figure 3.– Continued.

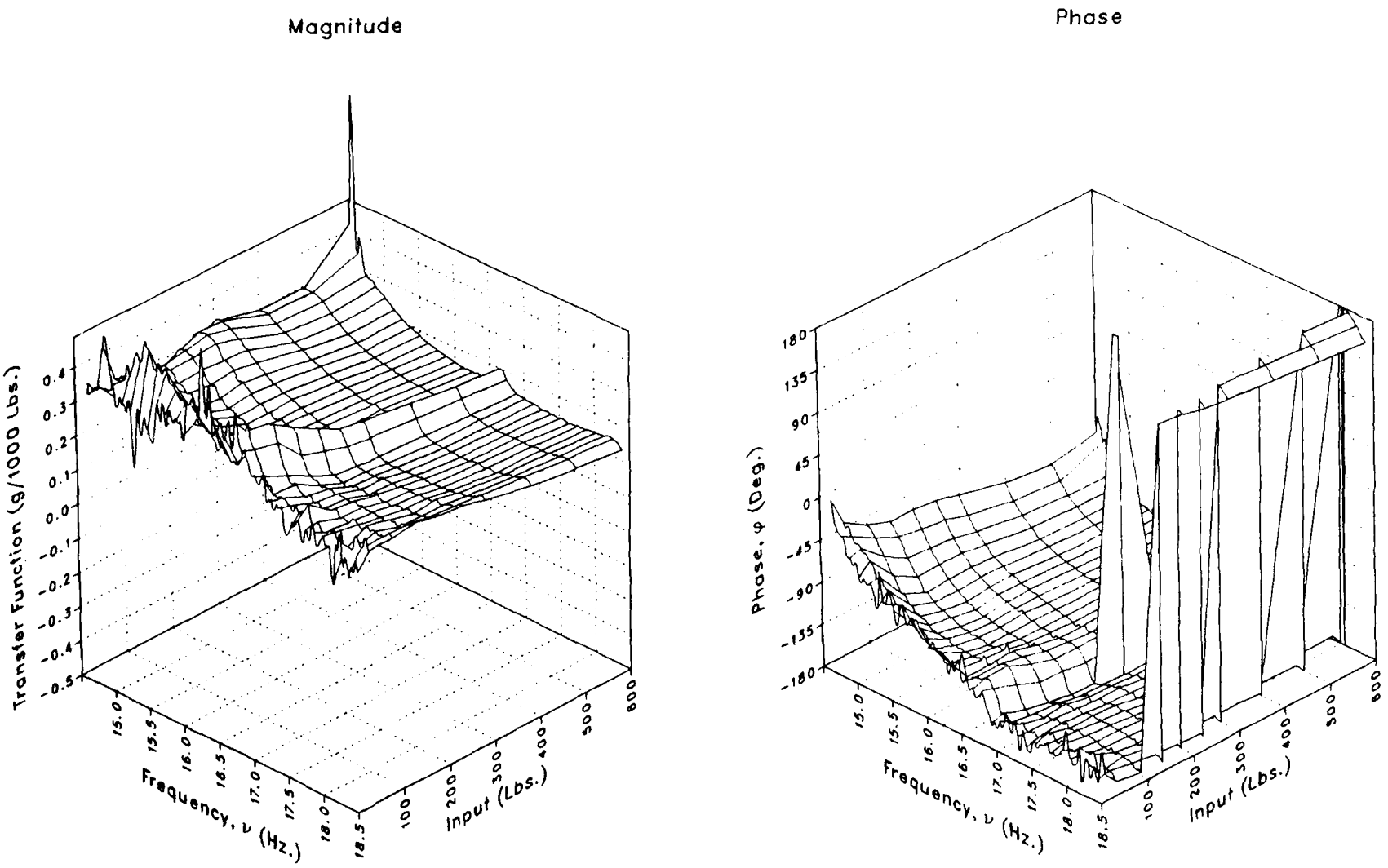

(p) VWGTPRT Concluded.

Figure 3.– Continued.

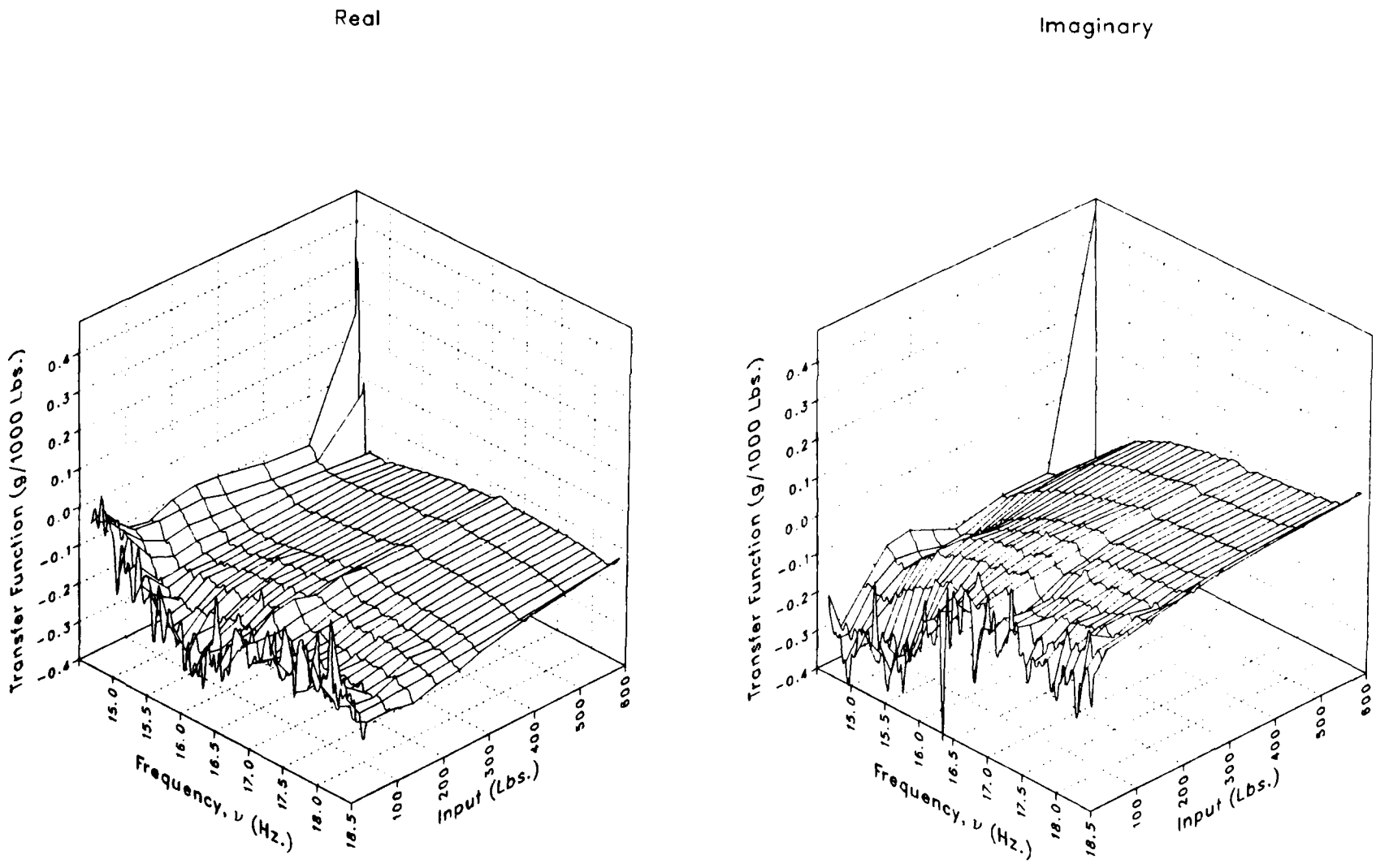

(q) VWGTPLT

Figure 3.– Continued.

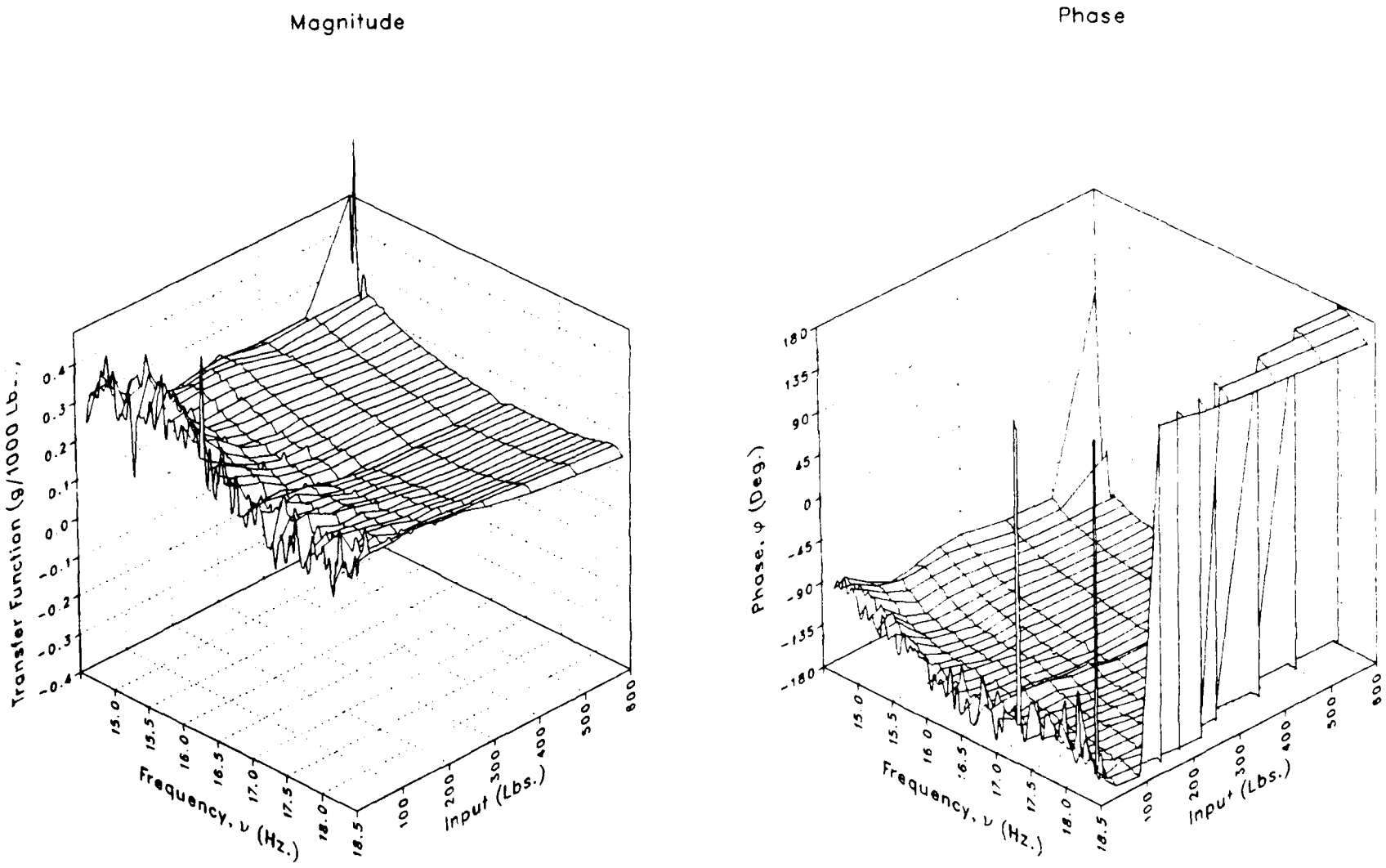

(q) VWGTPLT Concluded.

Figure 3.– Continued.

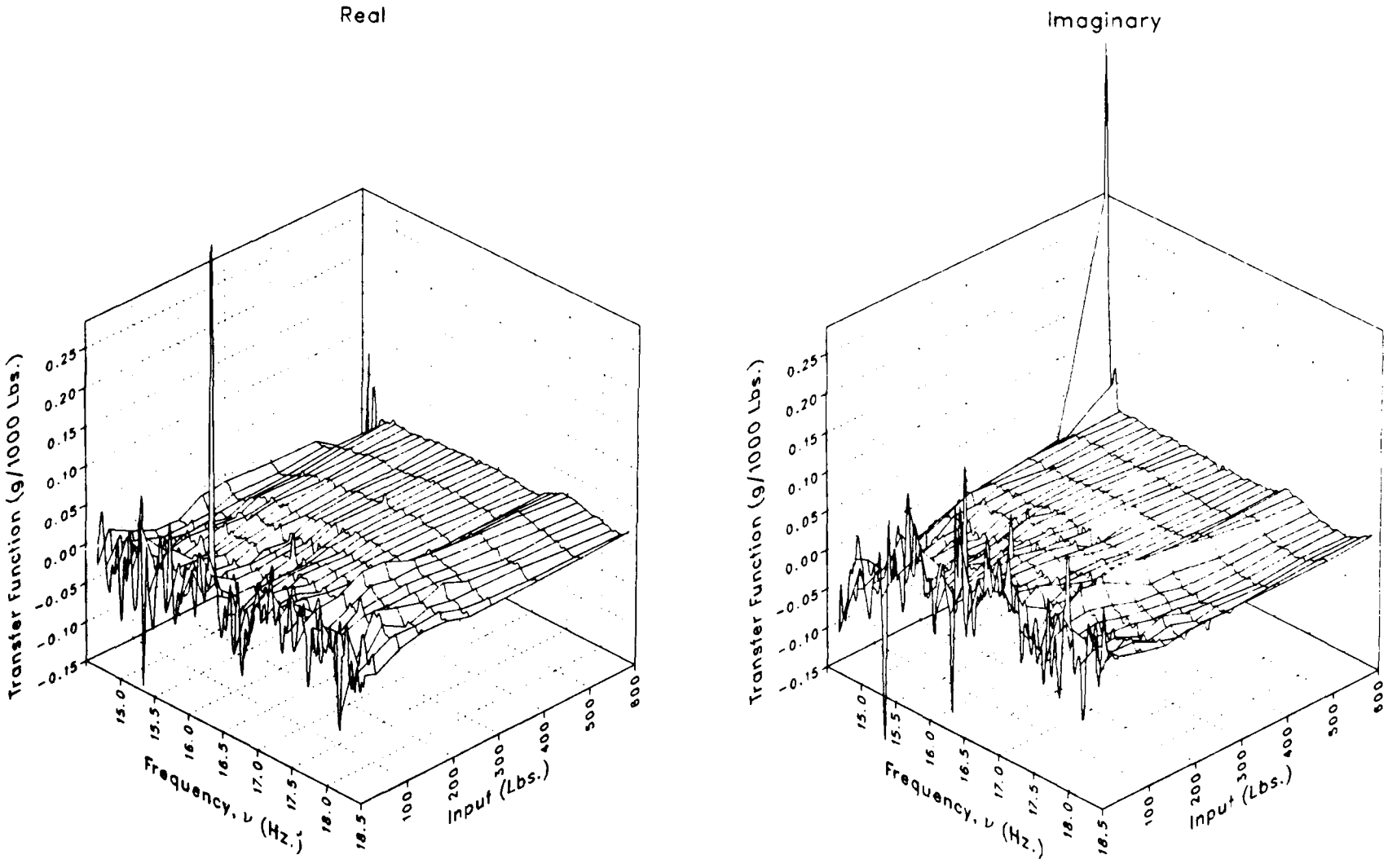

(r) LIGB

Figure 3.– Continued.

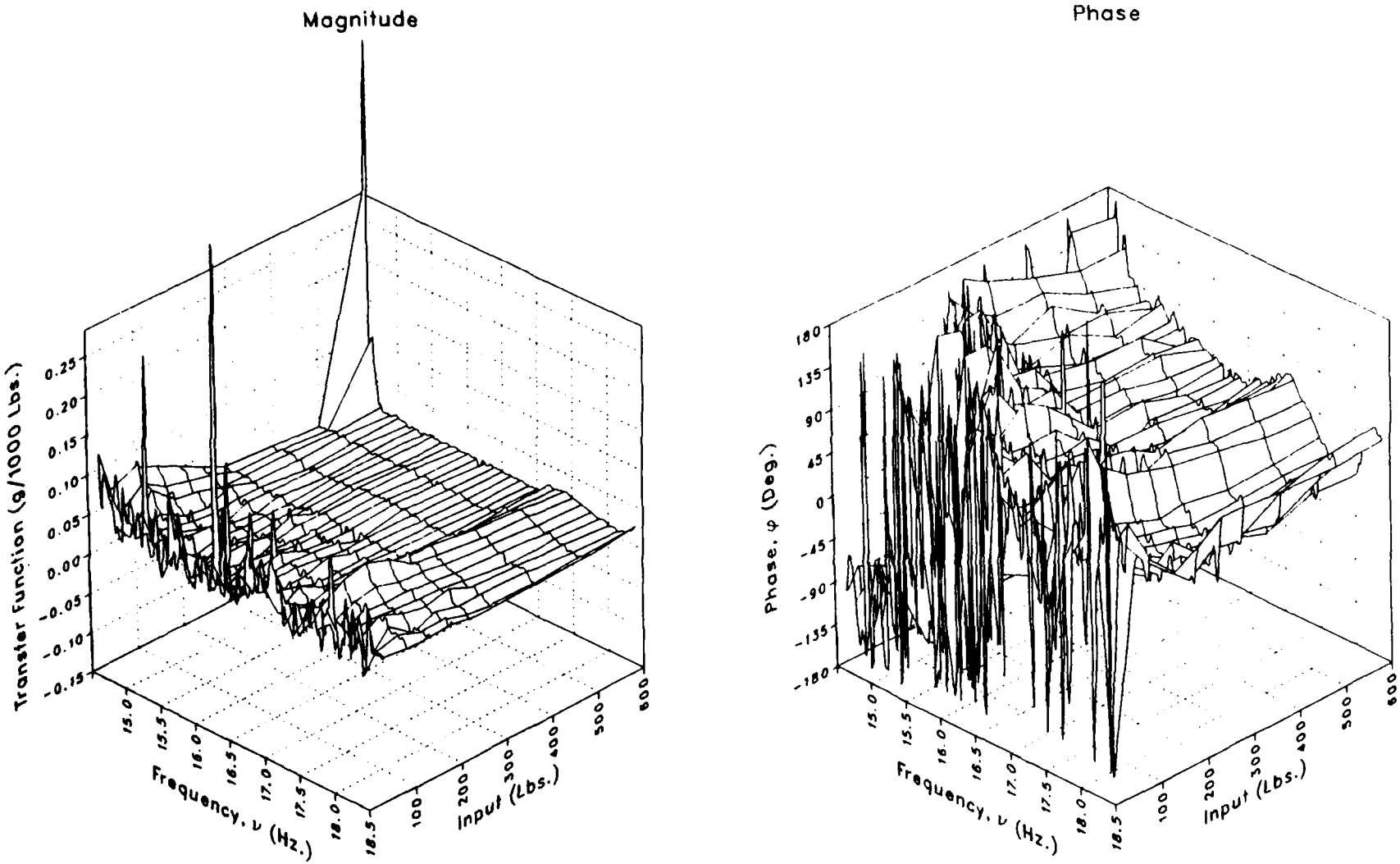

(r) LIGB Concluded.

Figure 3.– Continued.

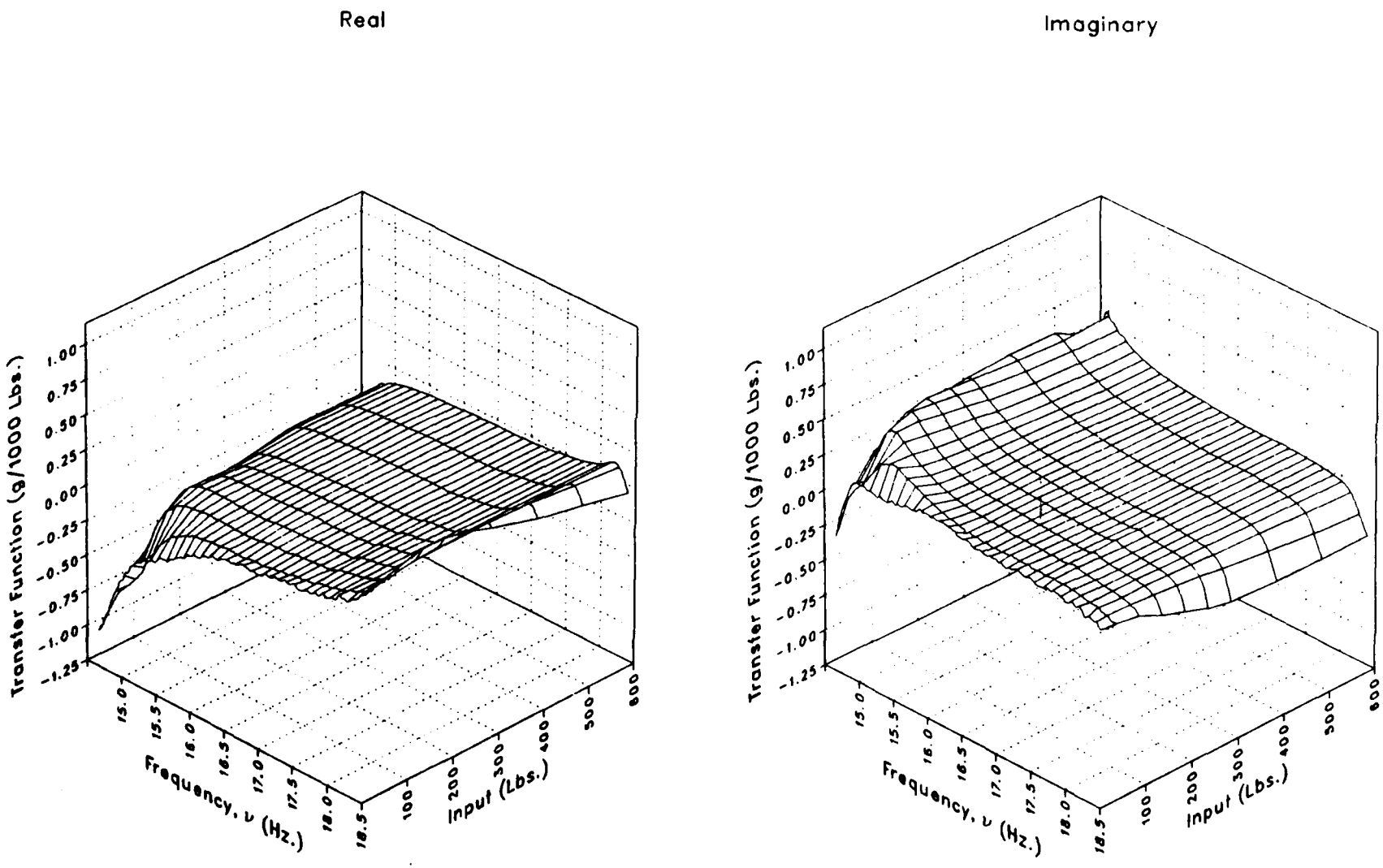

(s) VIGB

Figure 3.– Continued.

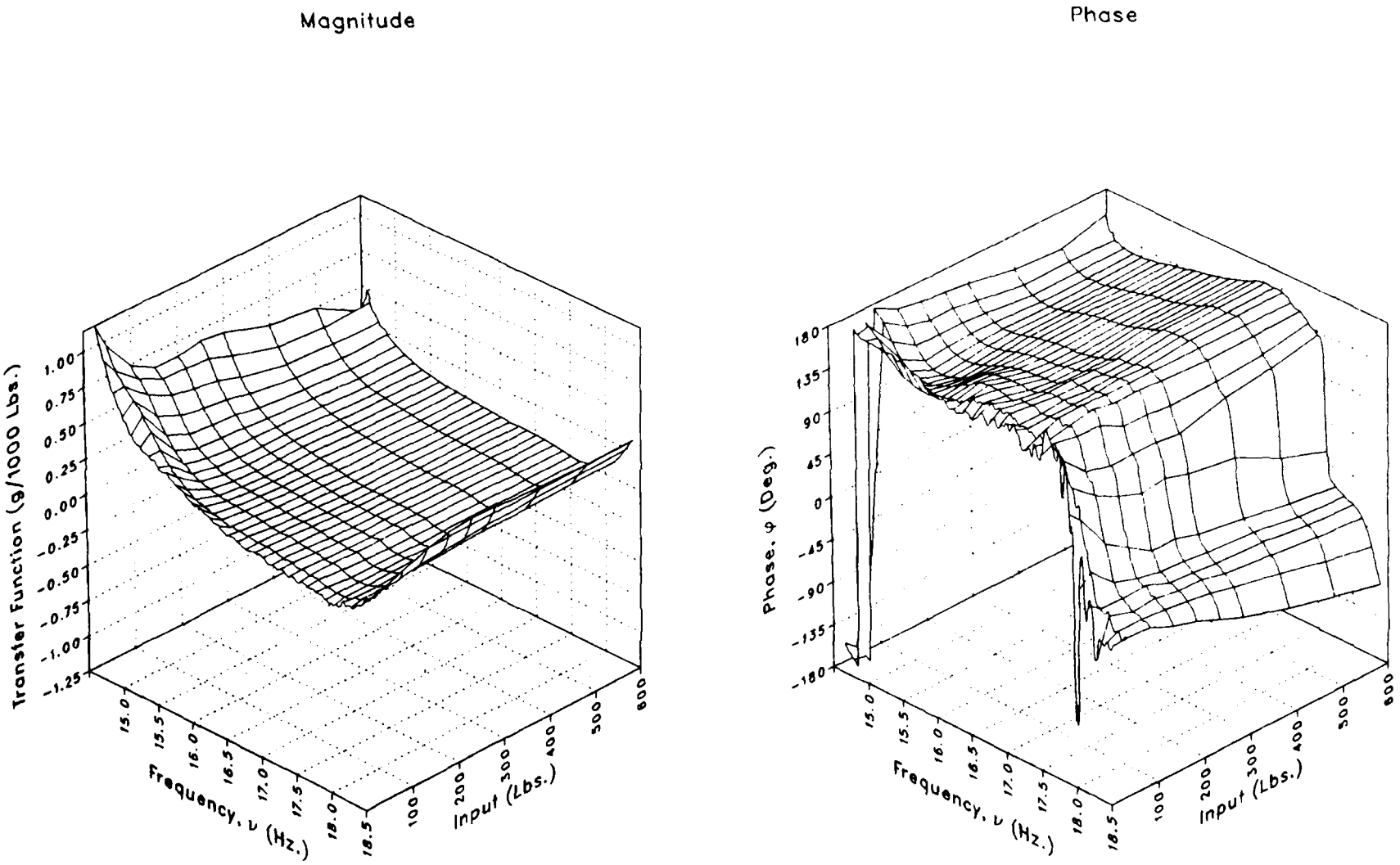

(s) VIGB Concluded.

Figure 3.– Continued.

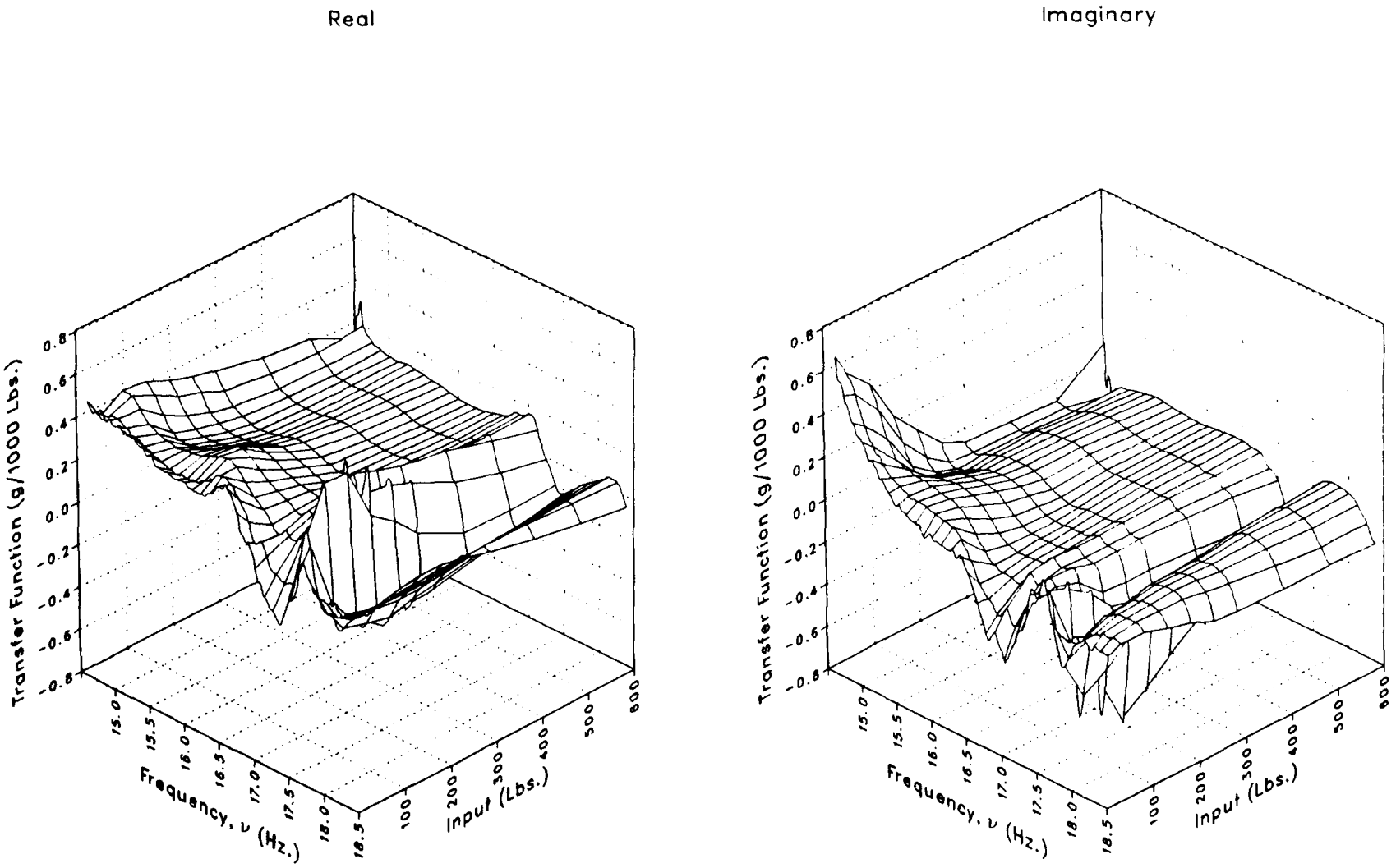

(t) LATTPYLN

Figure 3.– Continued.

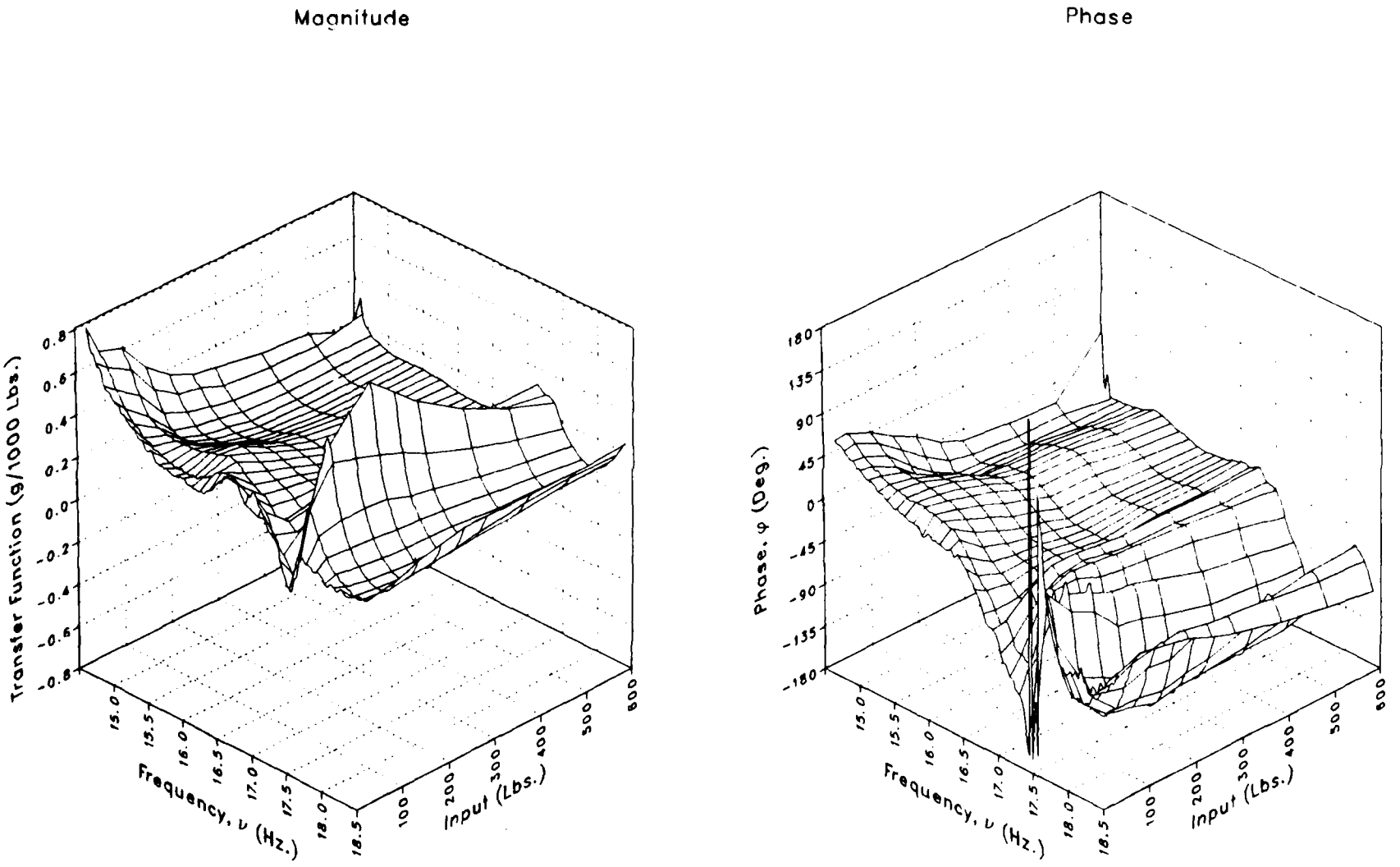

(t) LATTPYLN Concluded.

Figure 3.– Continued.

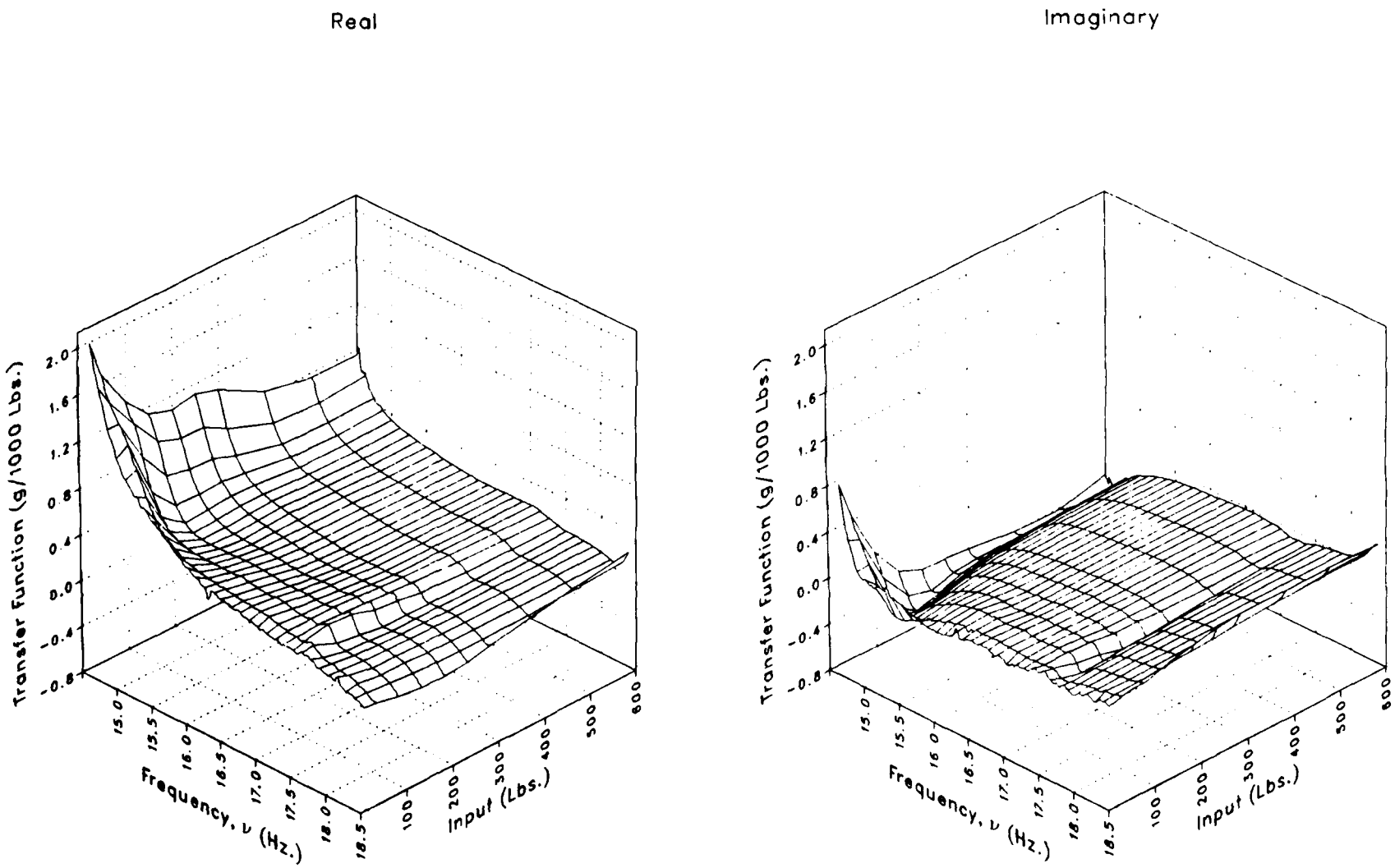

(u) VTTPYLON

Figure 3.– Continued.

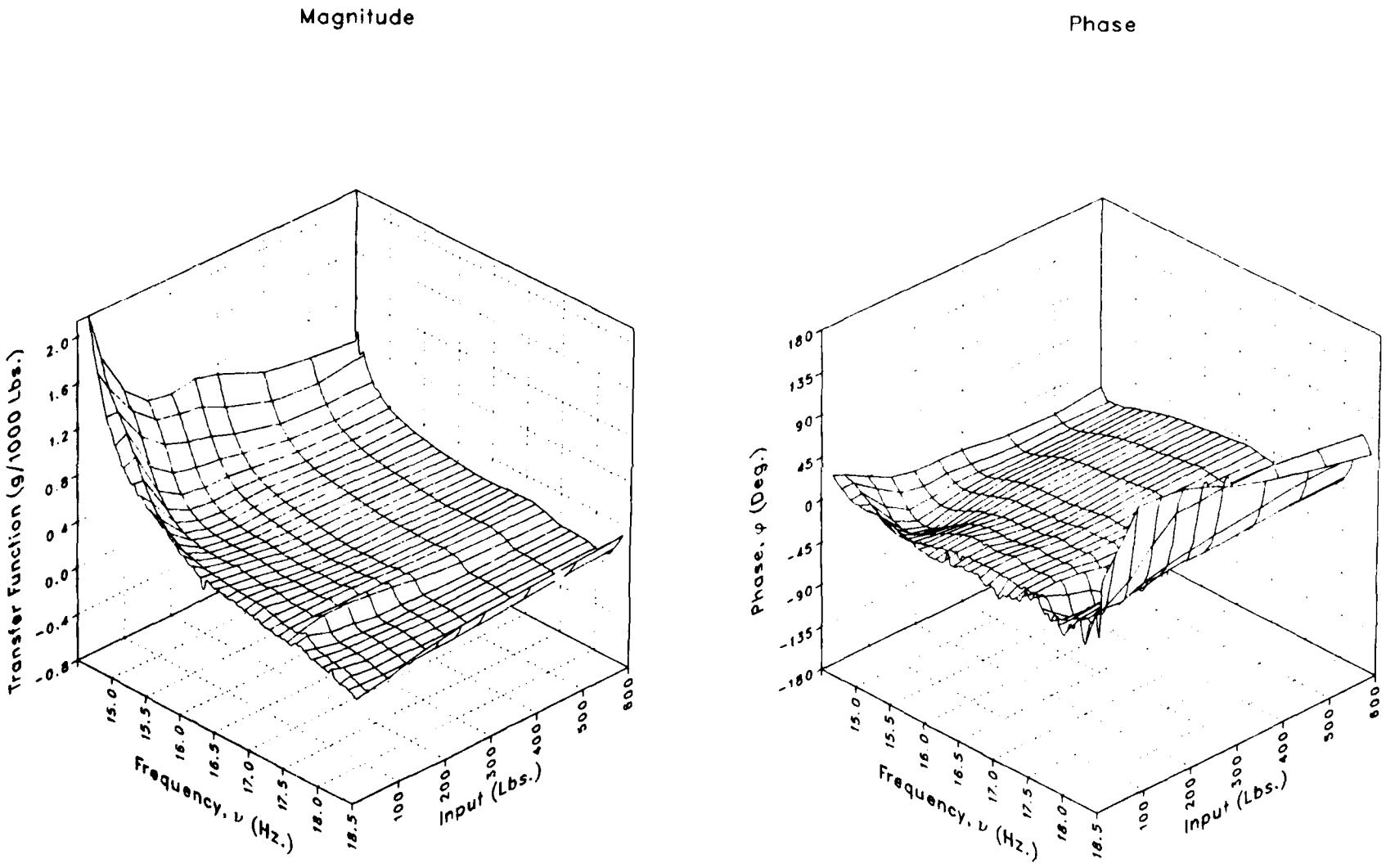

(u) VTTPYLON Concluded.

Figure 3.– Continued.

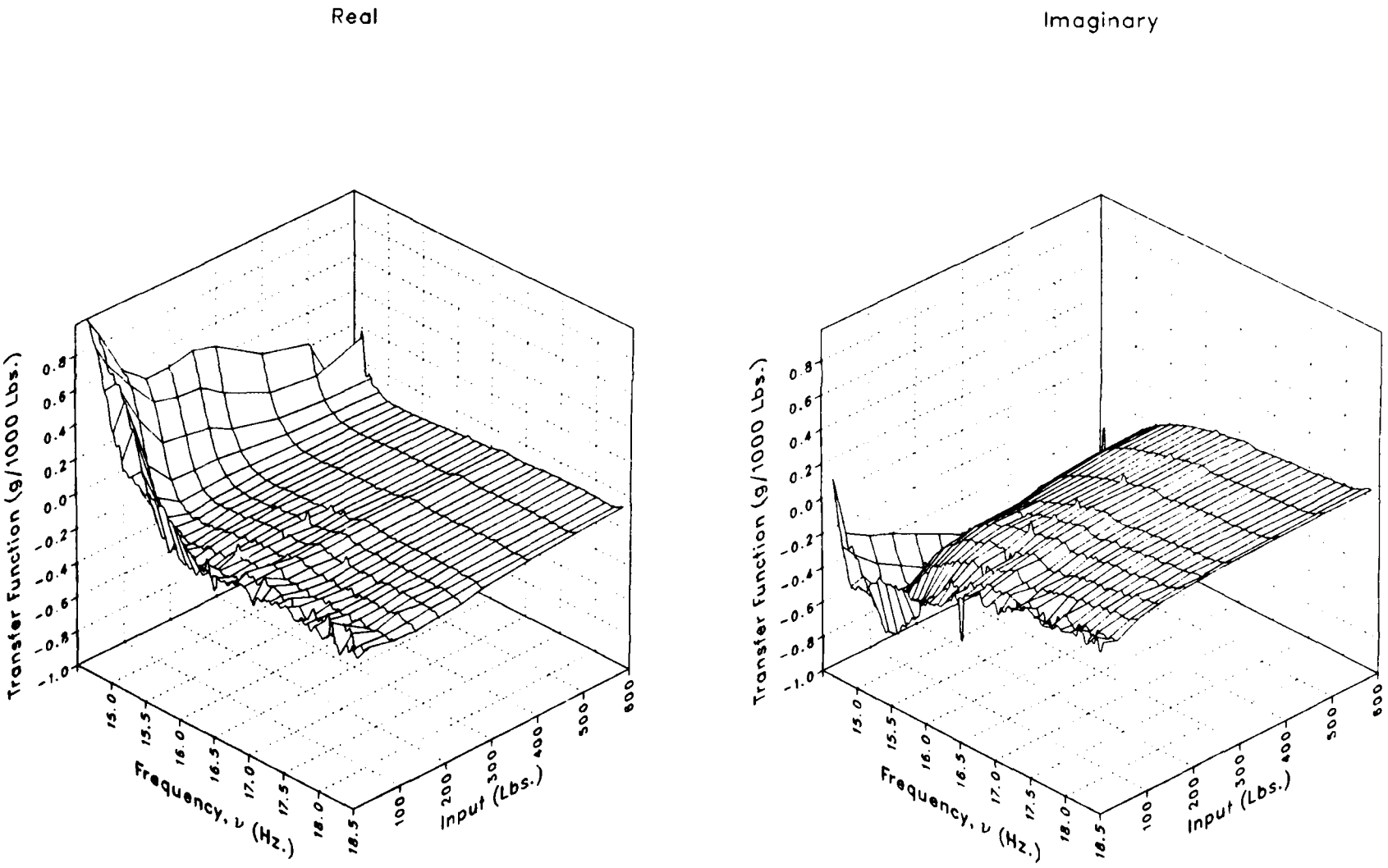

(v) XMRFLV

Figure 3.– Continued.

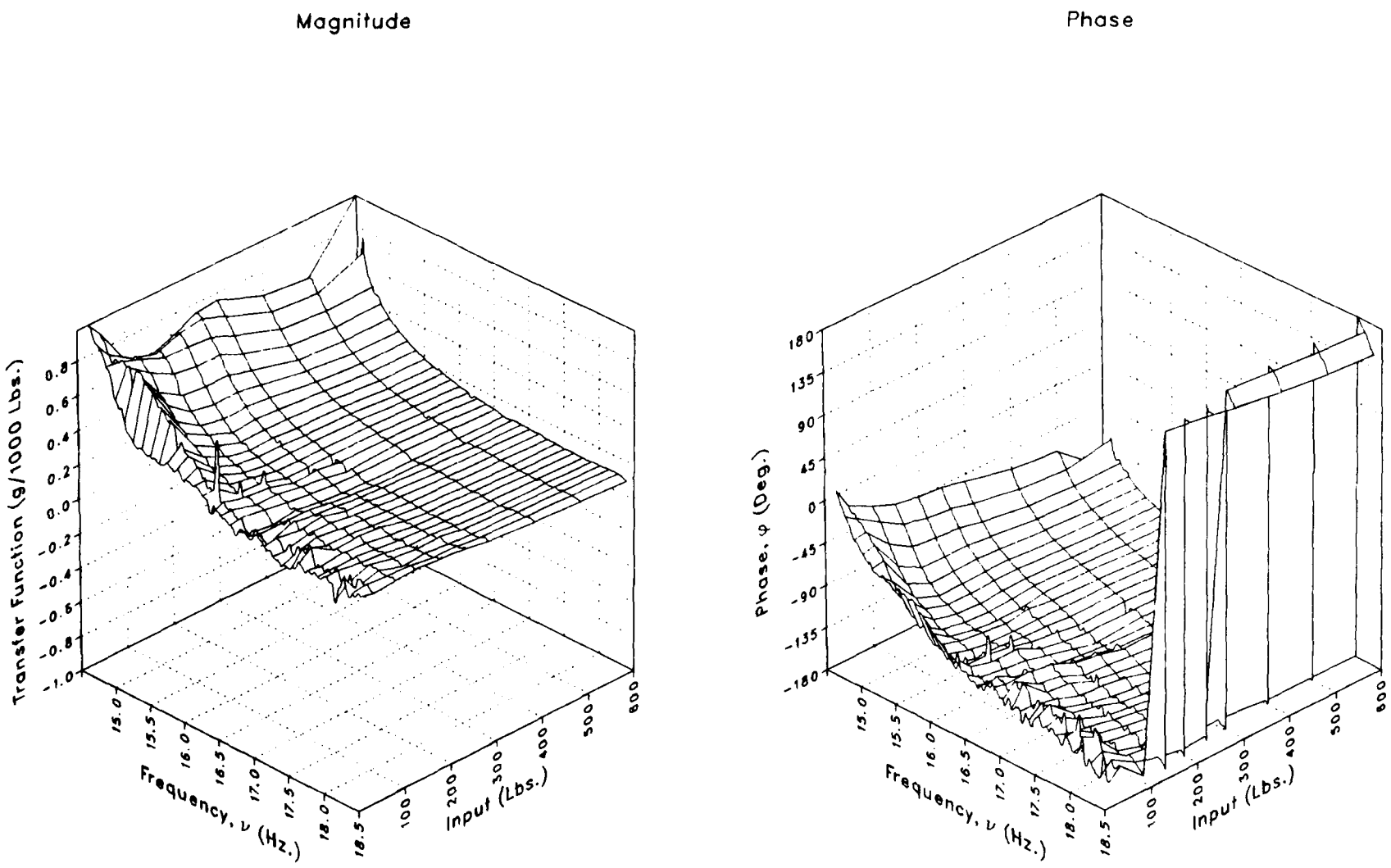

(v) XMRFLV Concluded.

Figure 3.– Continued.

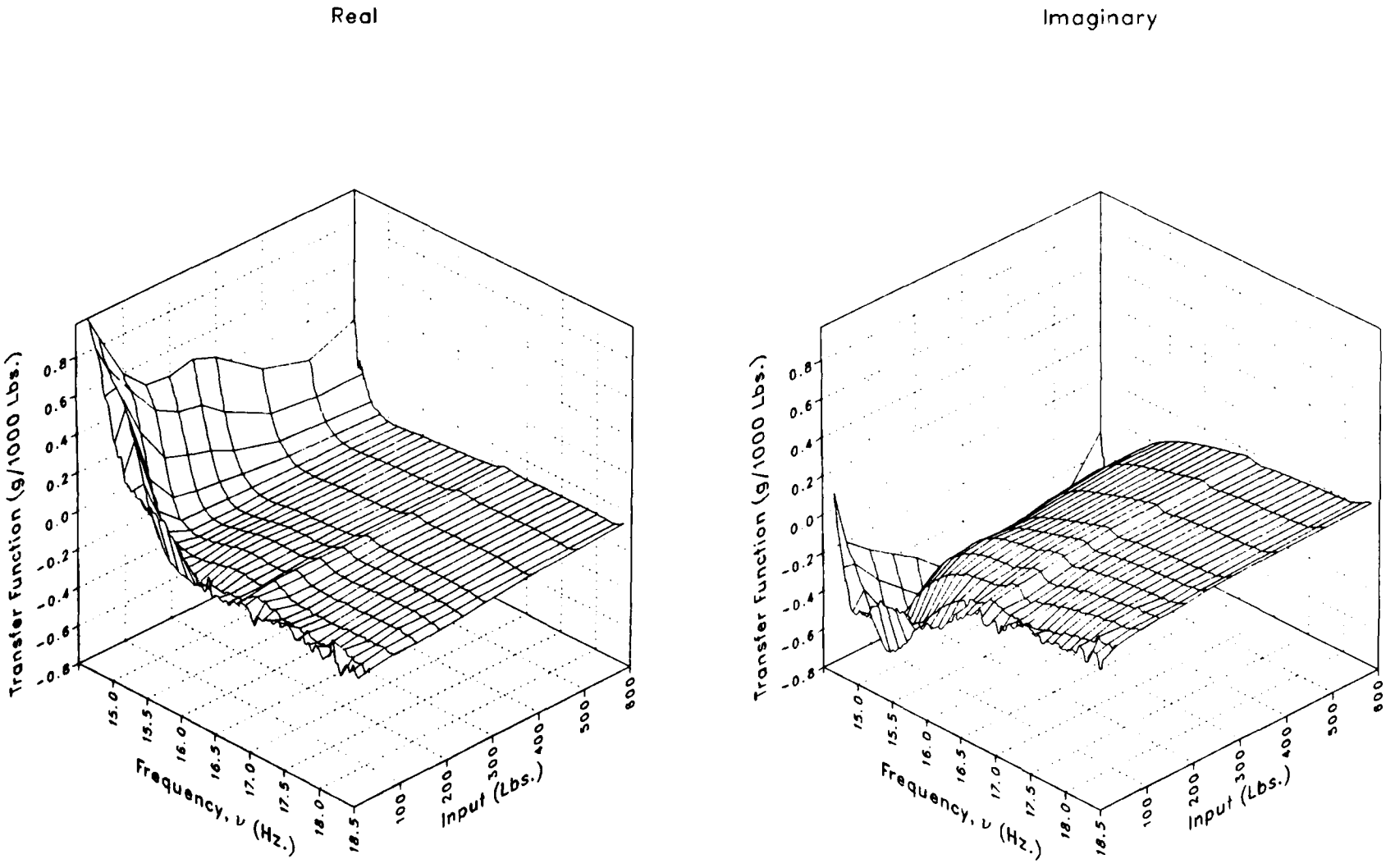

(w) XMRFRV

Figure 3.– Continued.

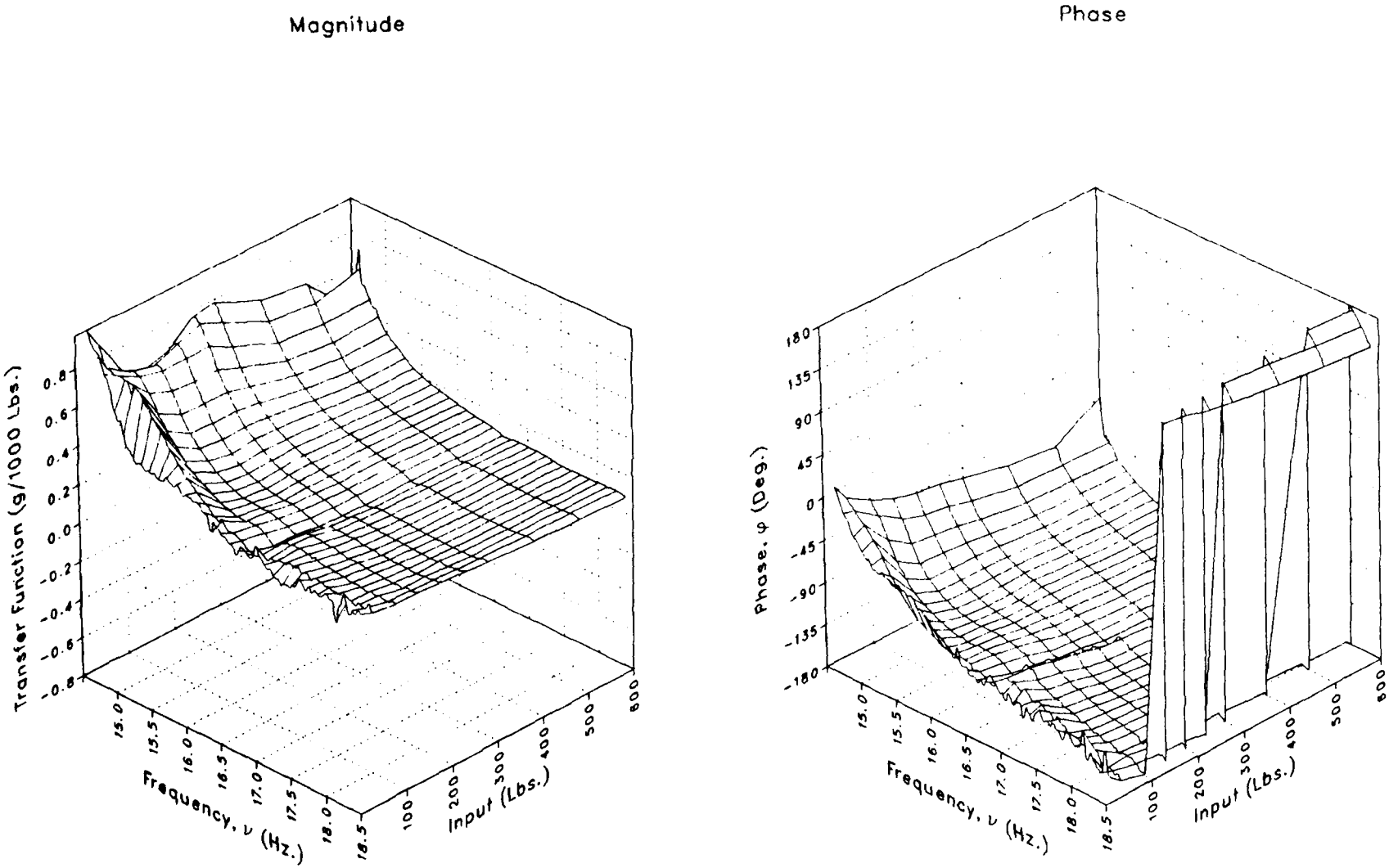

(w) XMRFRV Concluded.

Figure 3.– Continued.

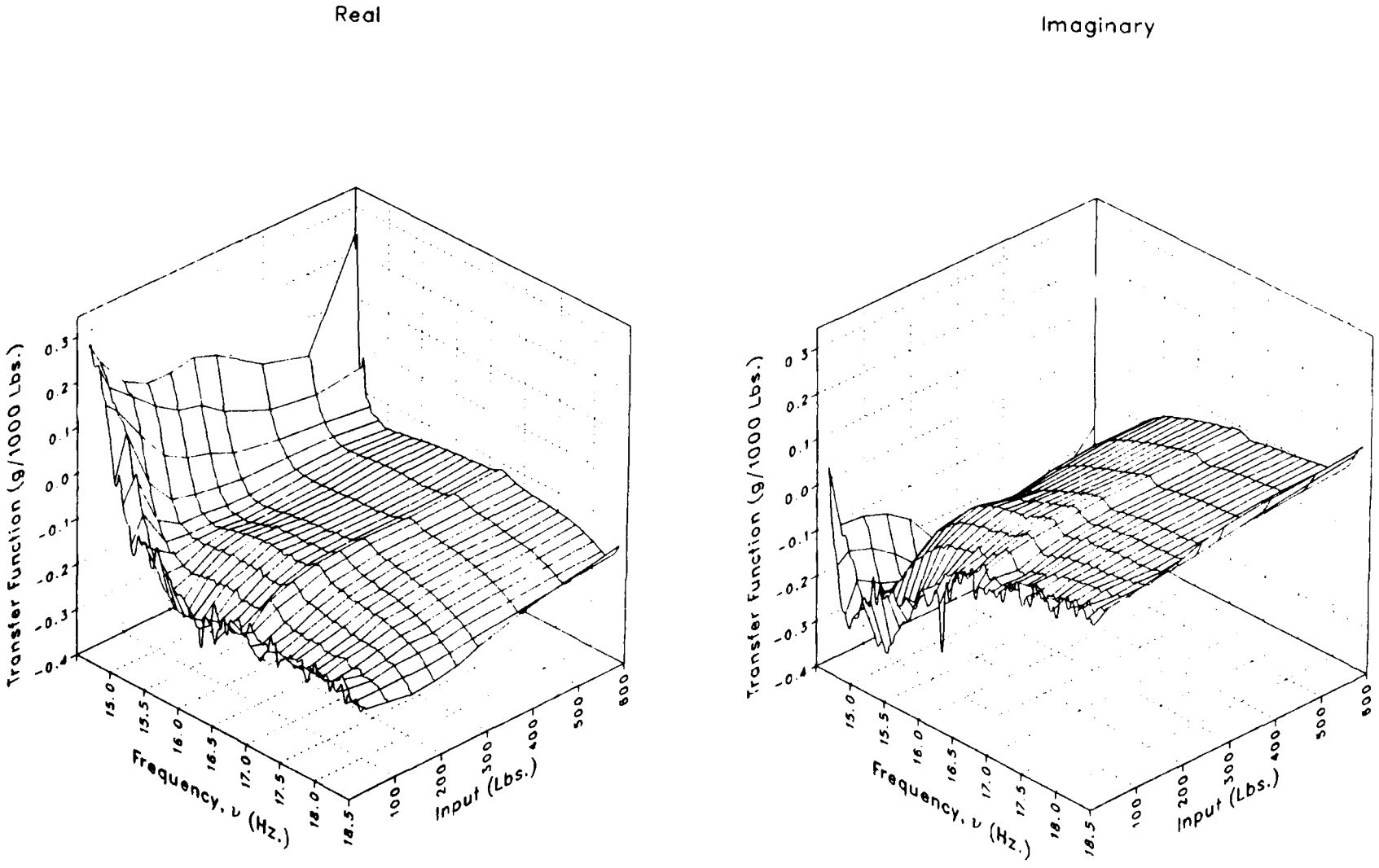

(x) S222FLRV

Figure 3.– Continued.

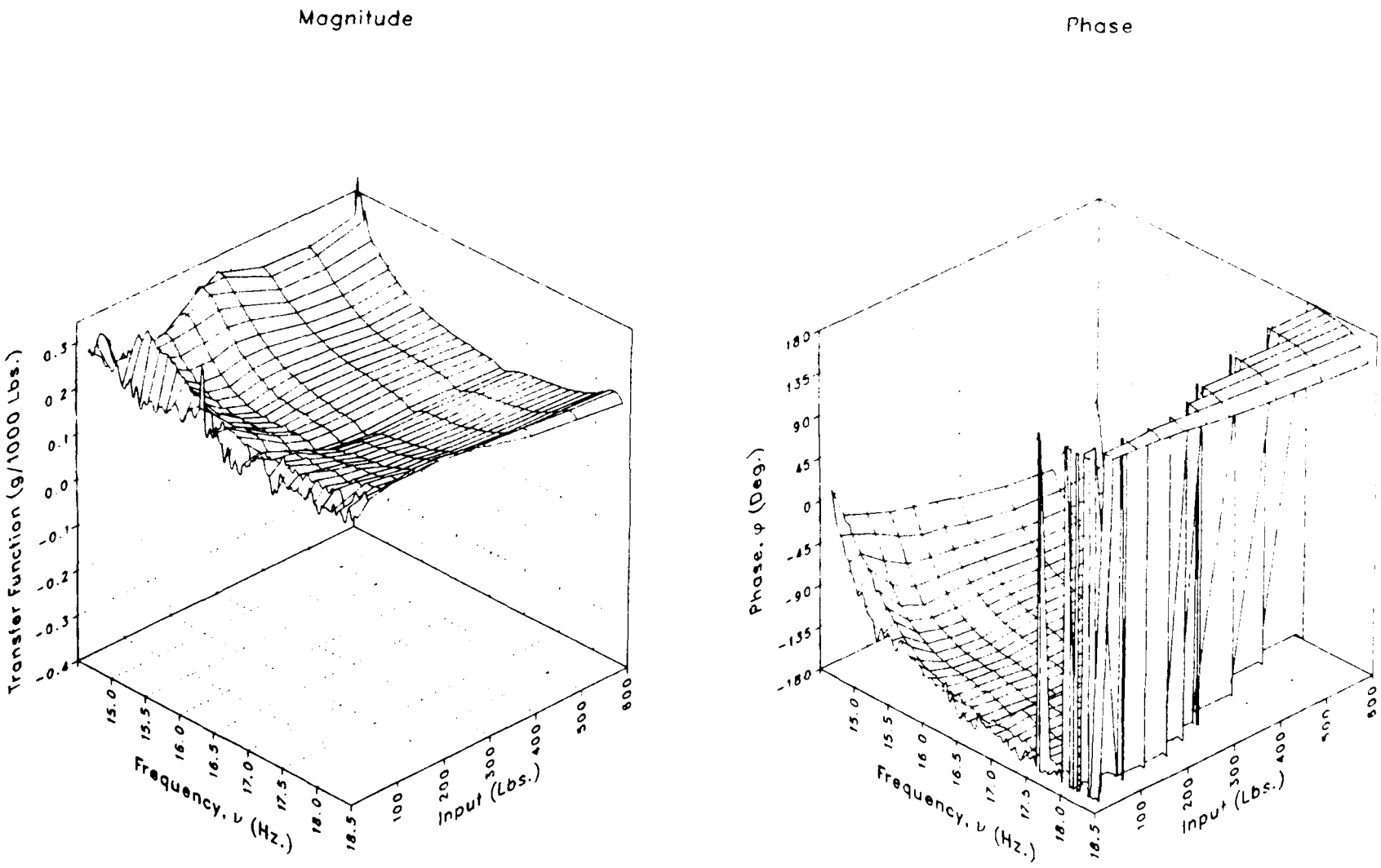

(x) S222FLRV Concluded.

Figure 3.– Continued.

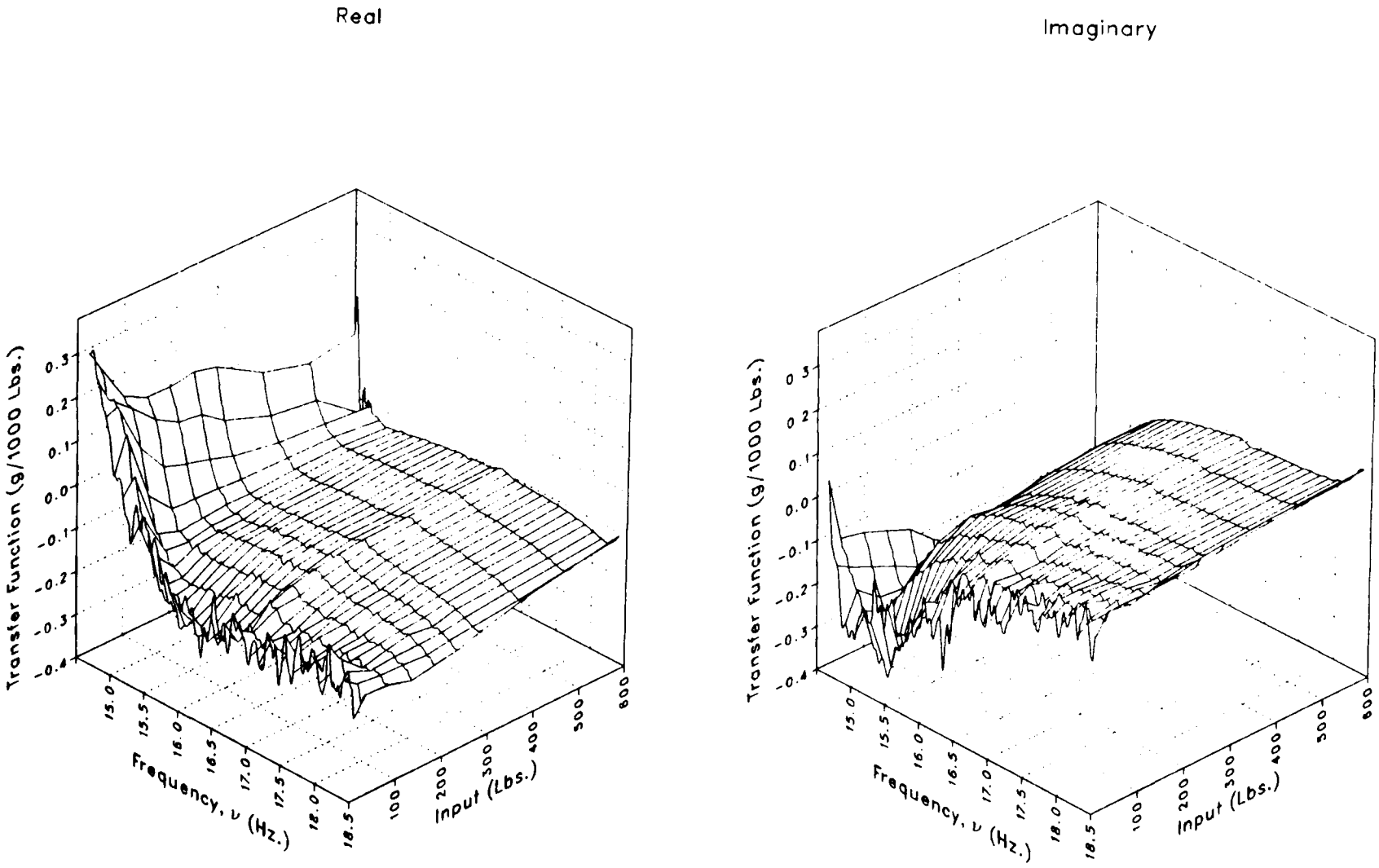

(y) S222FLLV

Figure 3.– Continued.

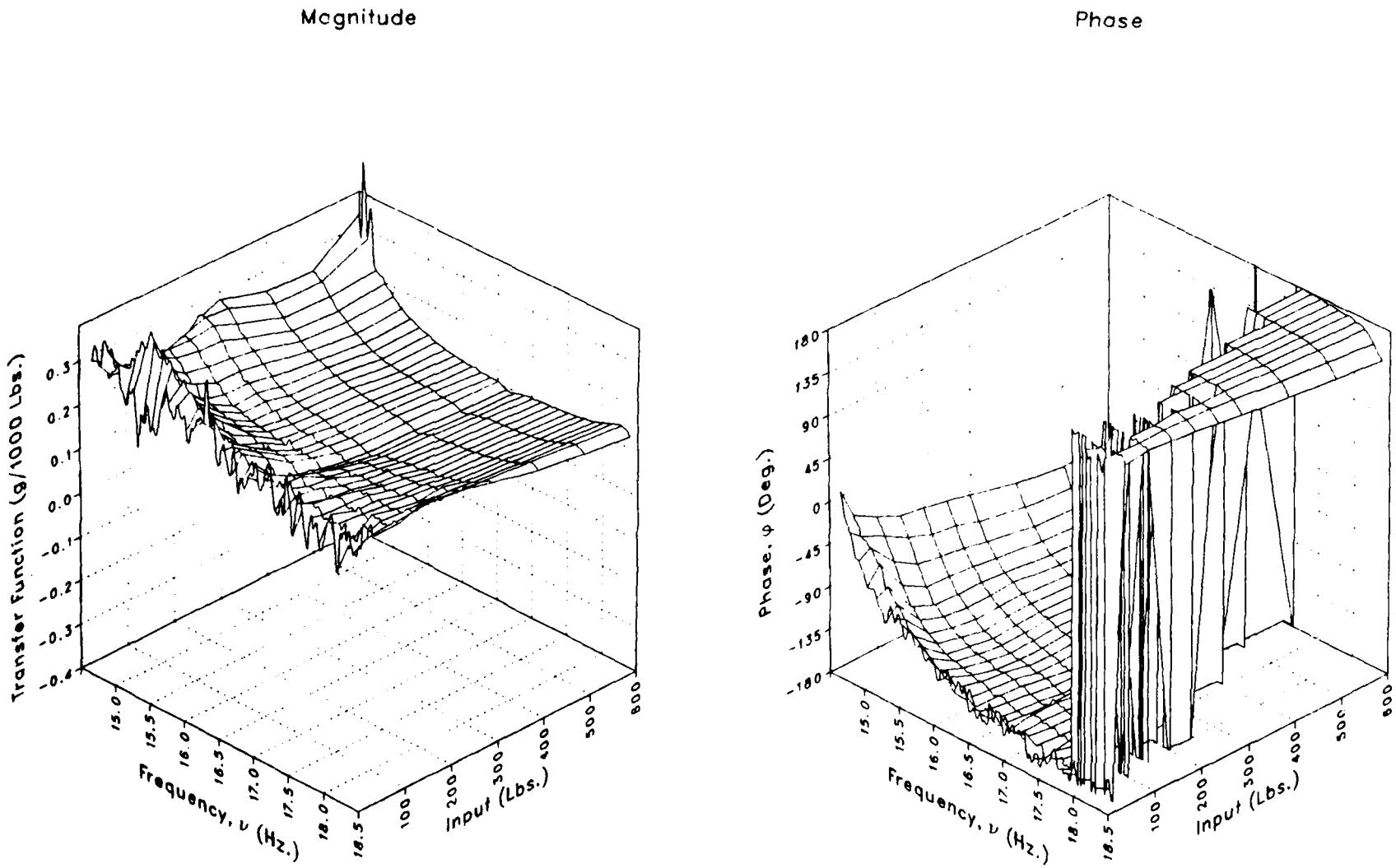

(y) S222FLLV Concluded.

Figure 3.– Continued.

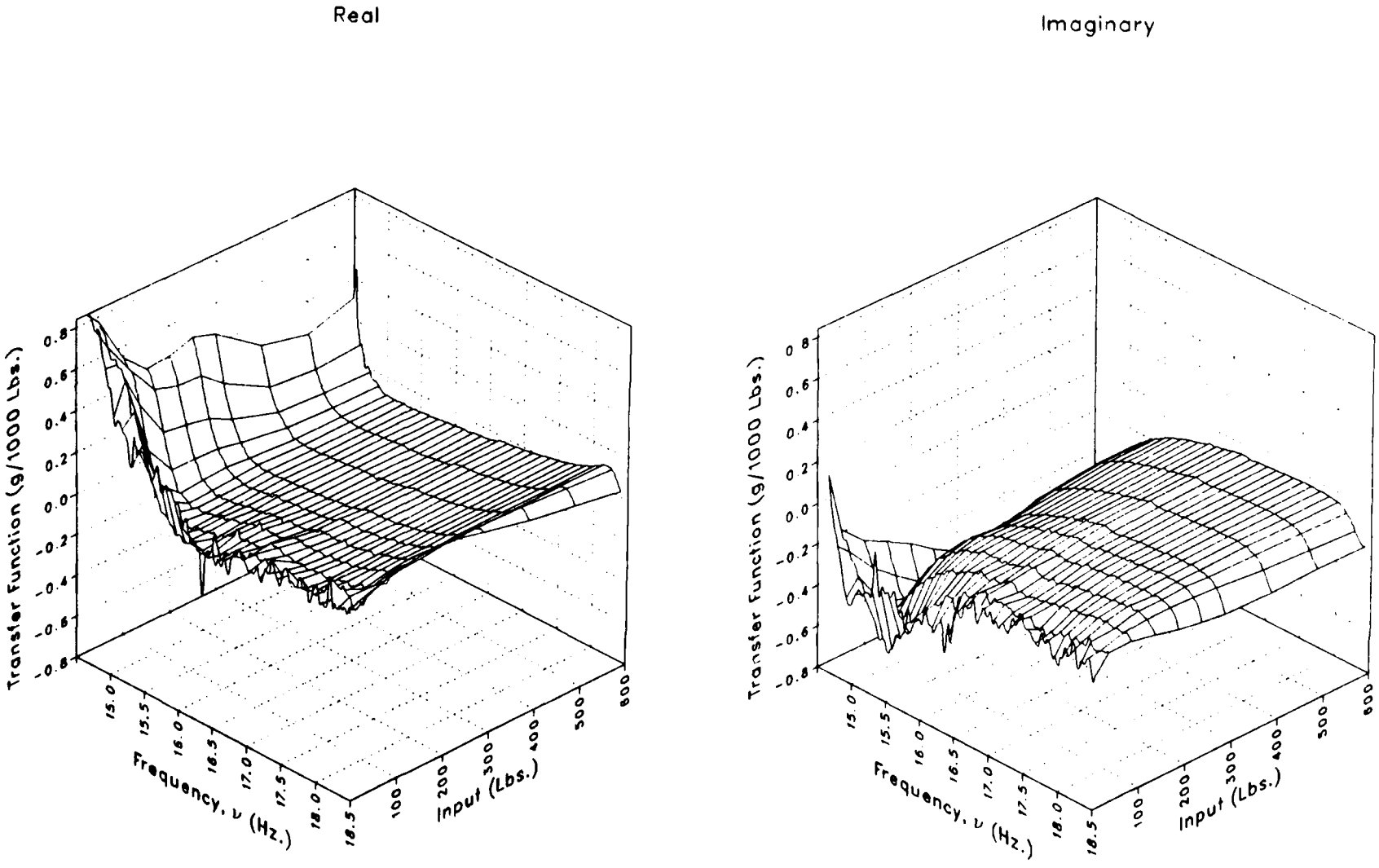

(z) S450FLV

Figure 3.– Continued.

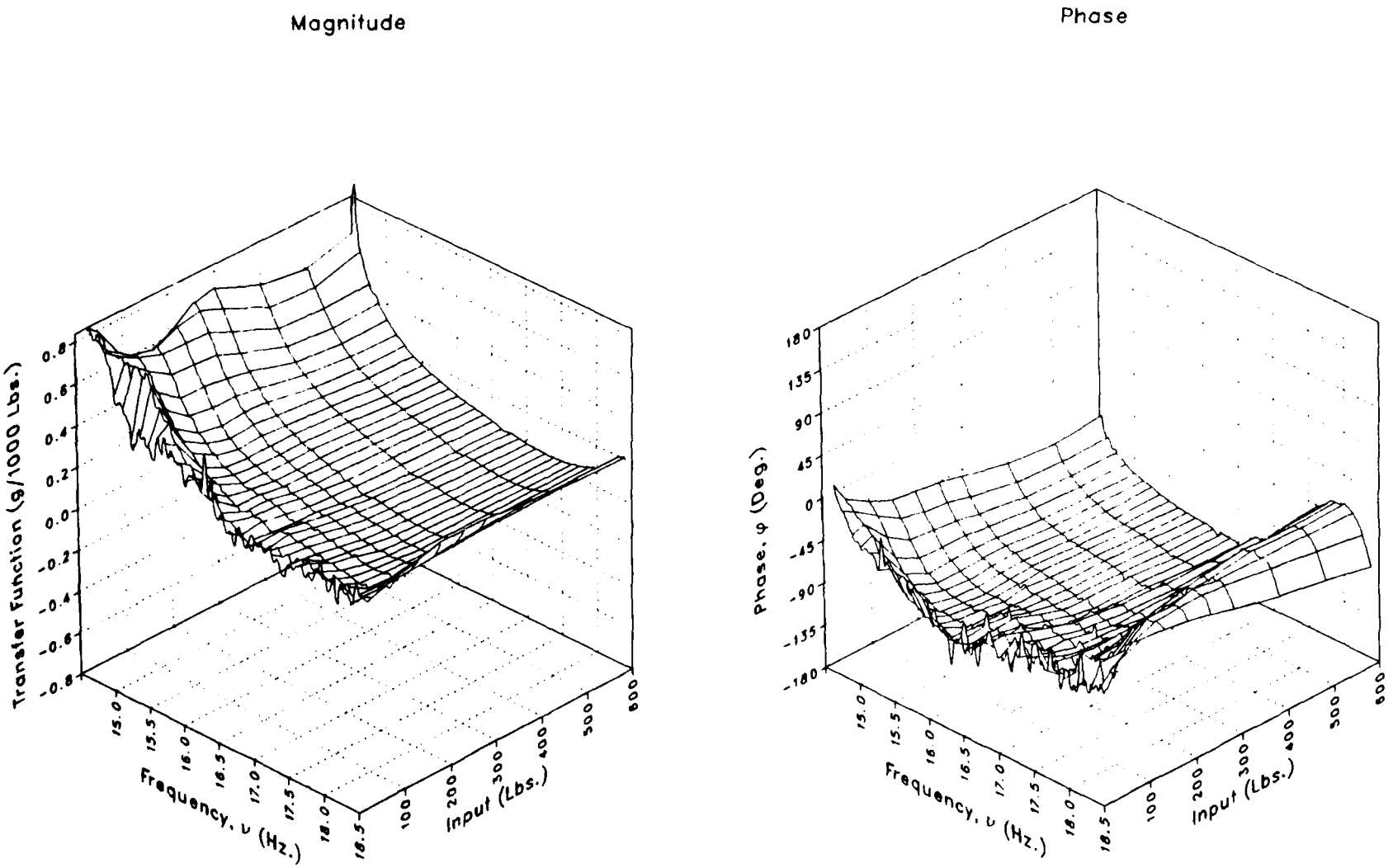

(z) S450FLV Concluded.

Figure 3.– Continued.

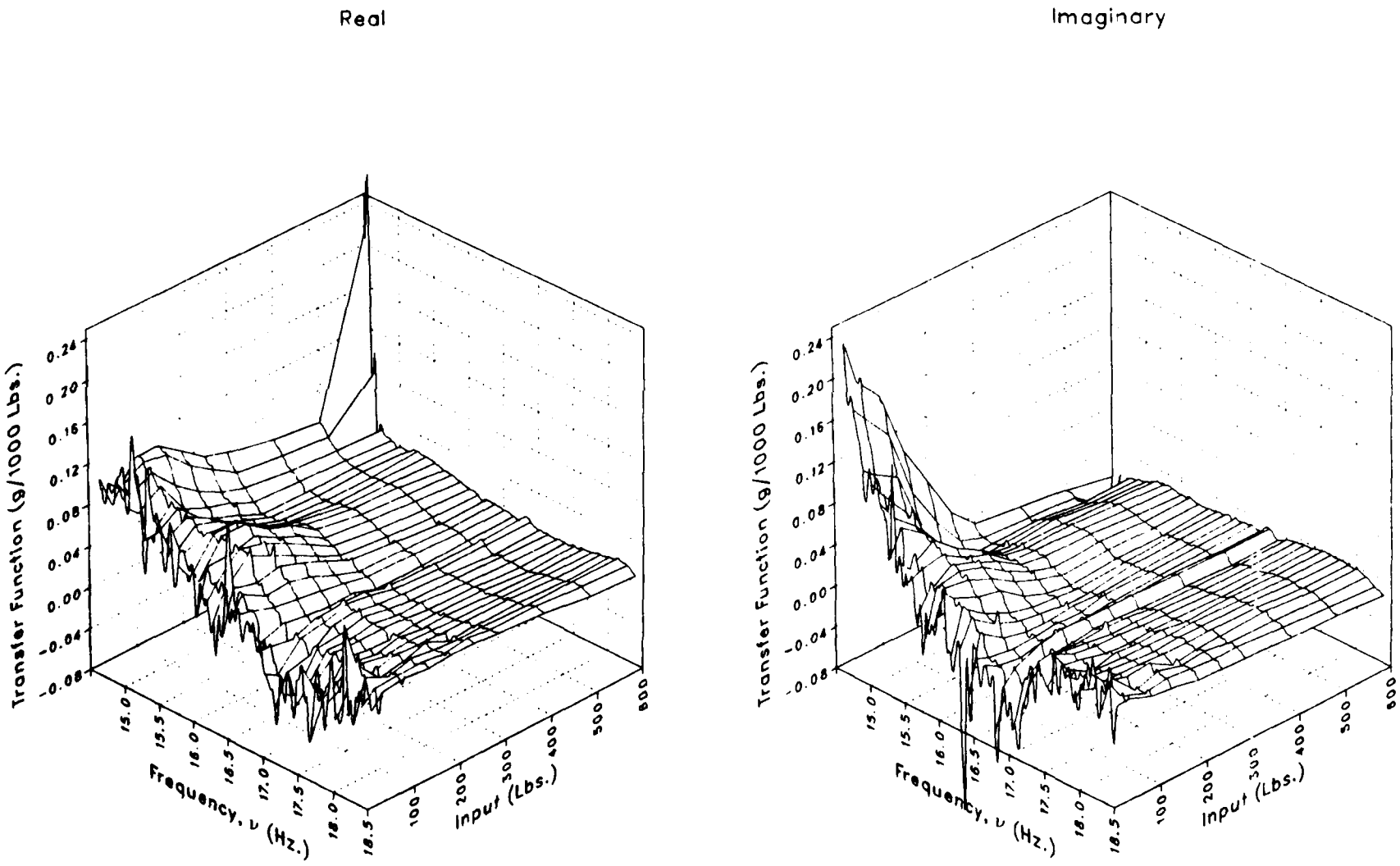

(aa) S450FLL

Figure 3.– Continued.

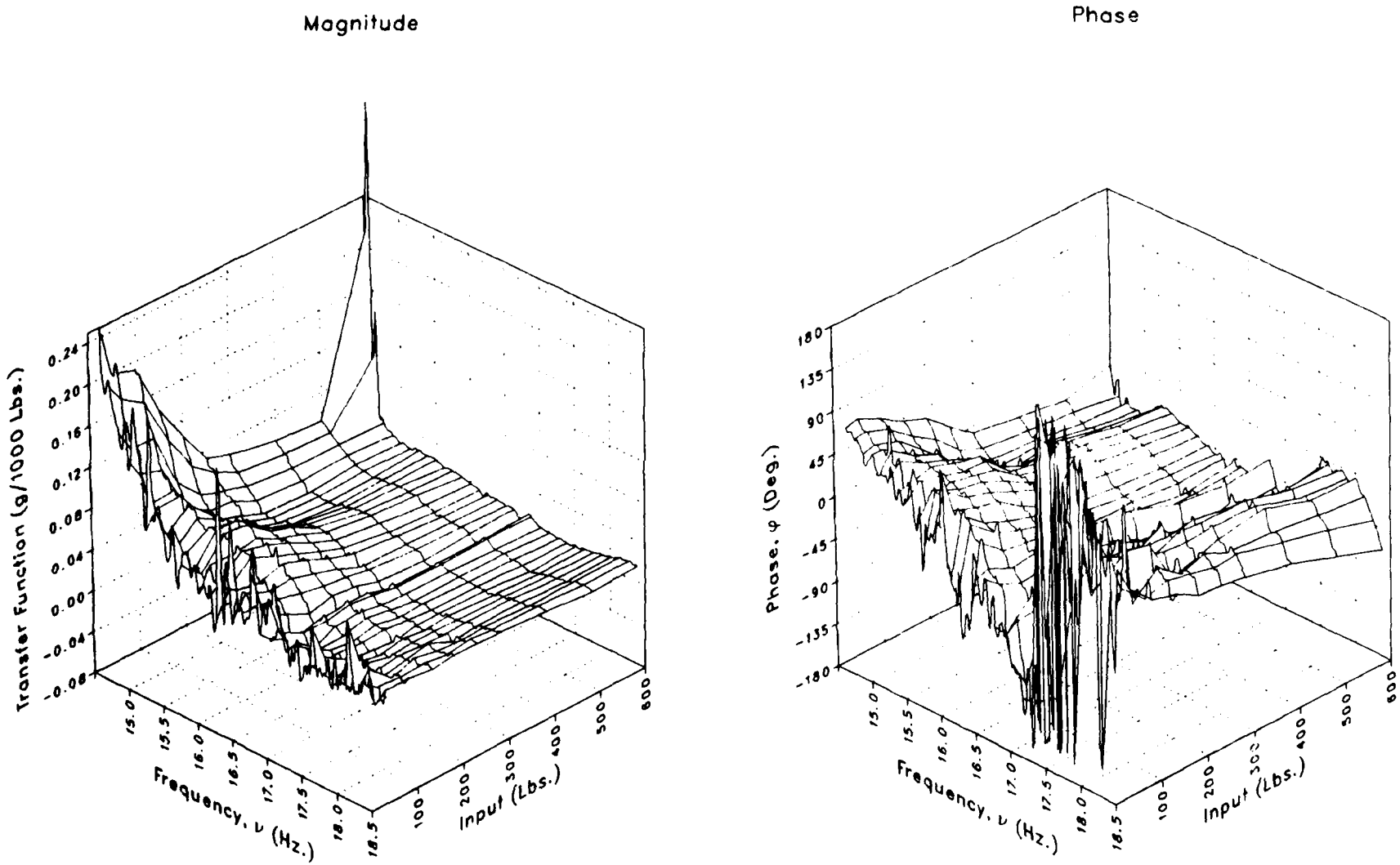

(aa) S450FLL Concluded.

Figure 3.– Continued.

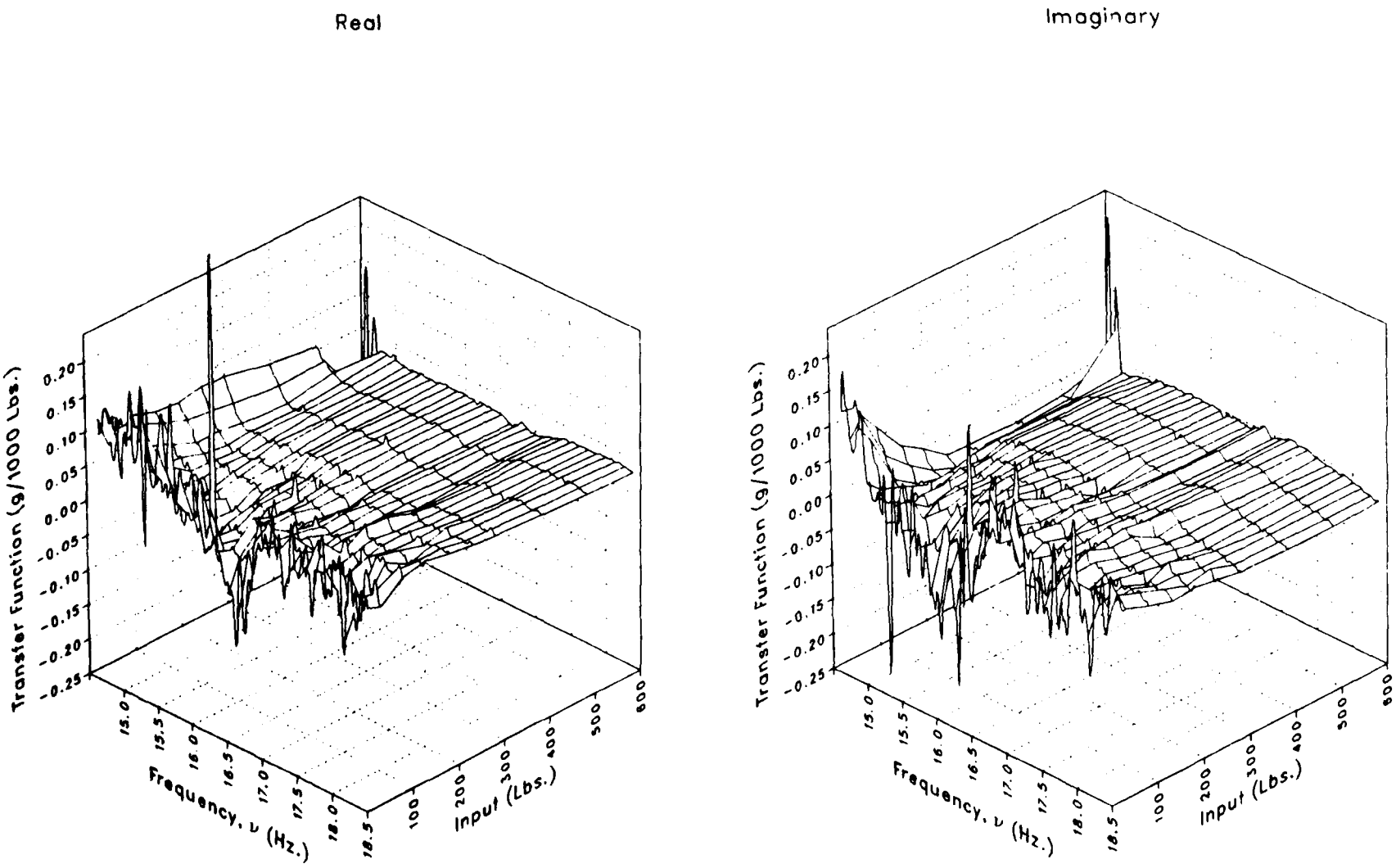

(bb) S450OVRL

Figure 3.– Continued.

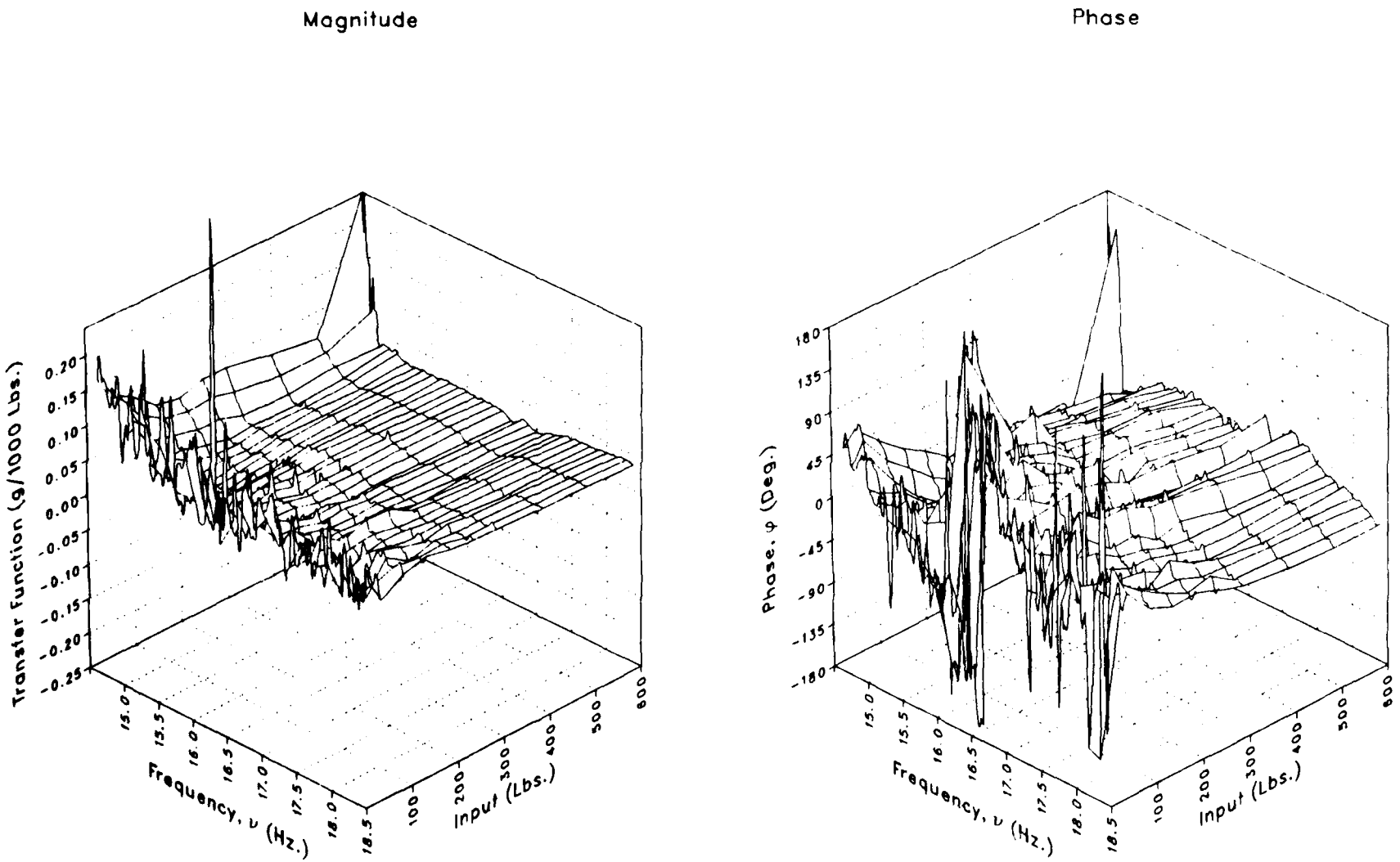

(bb) S450OVRL Concluded.

Figure 3.– Concluded.

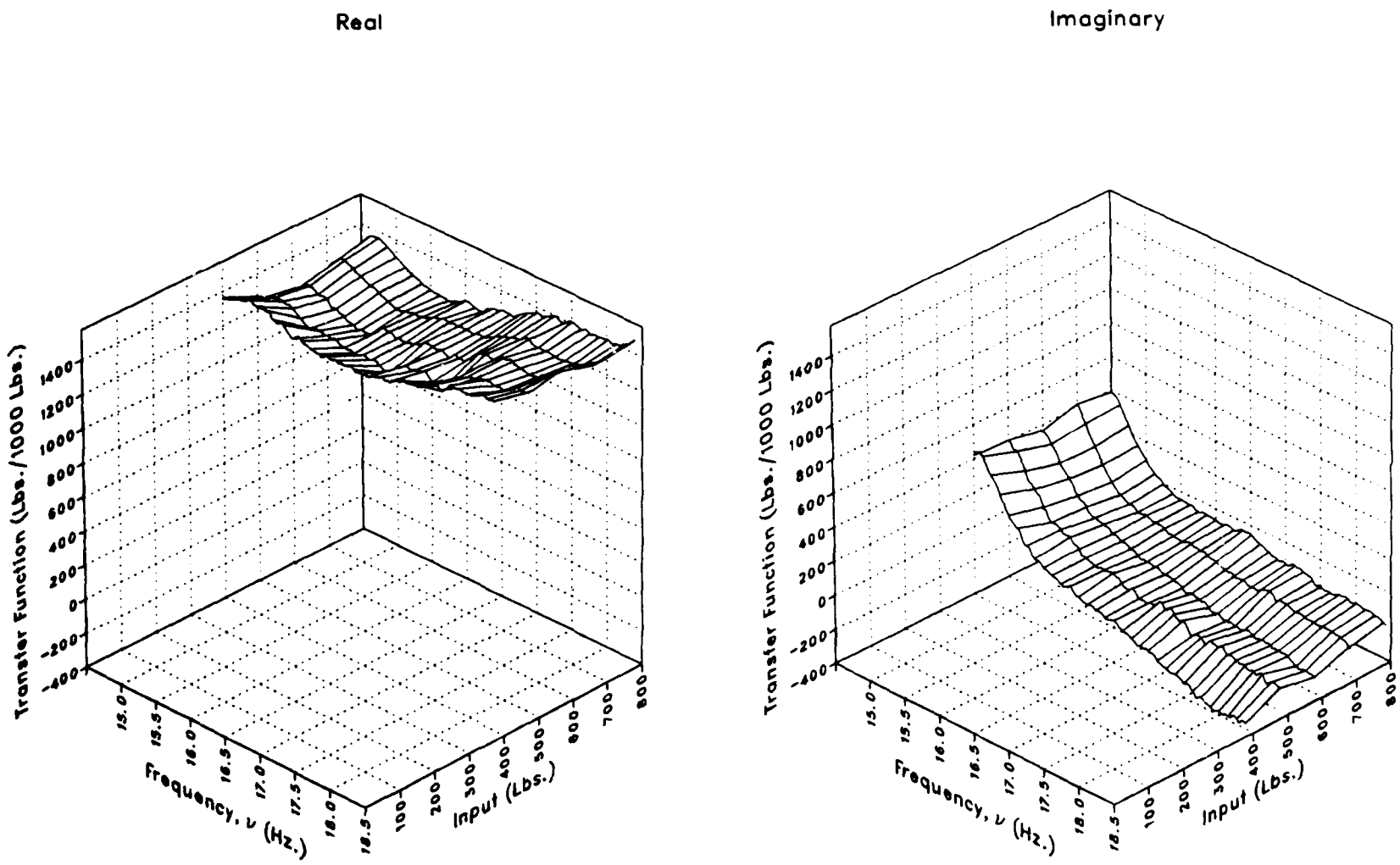

(a) MRDRAG

Figure 4.– Pitch forcing.

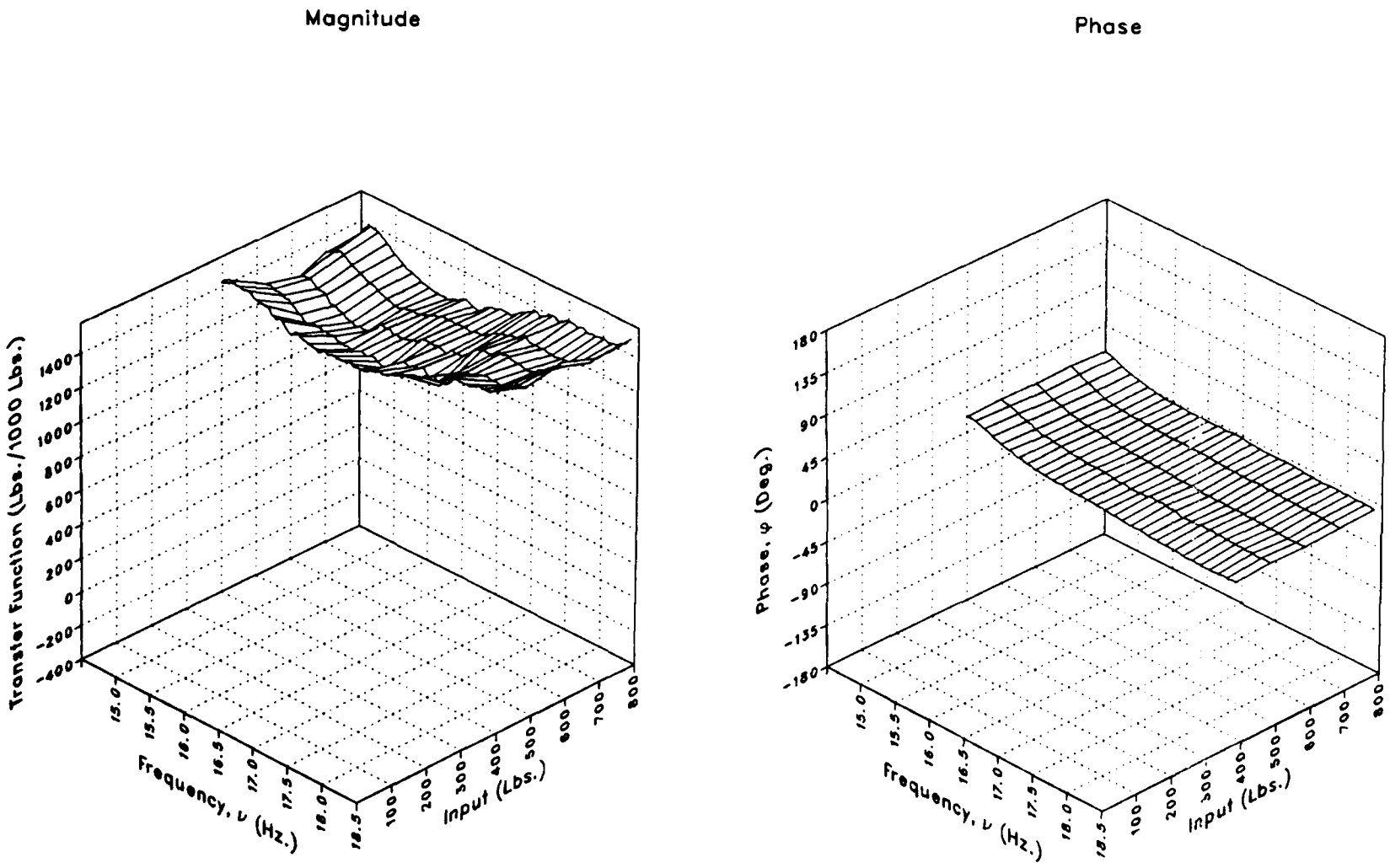

(a) MRDRAG Concluded.

Figure 4.– Continued.

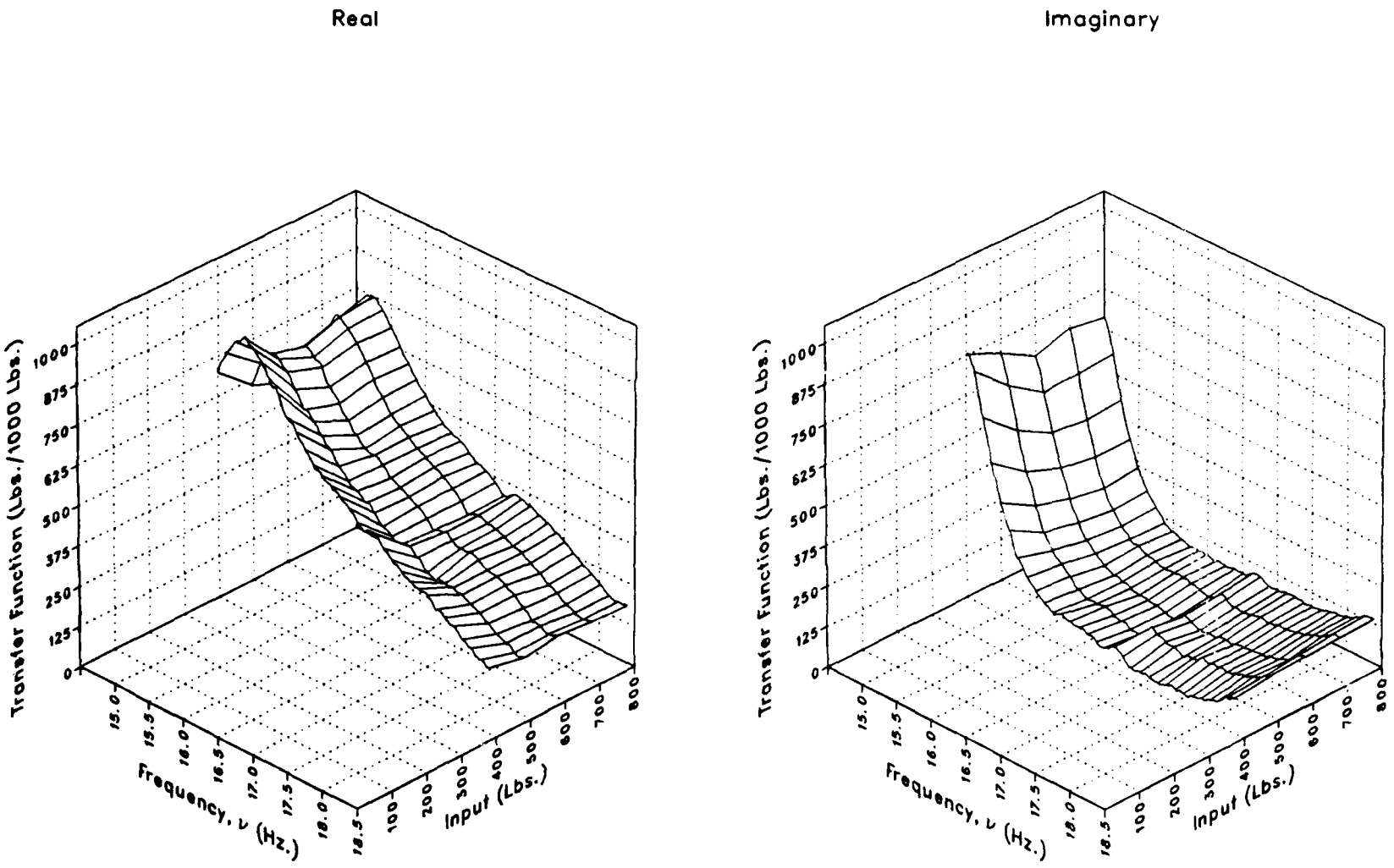

(b) MRLIFTA

Figure 4.– Continued.

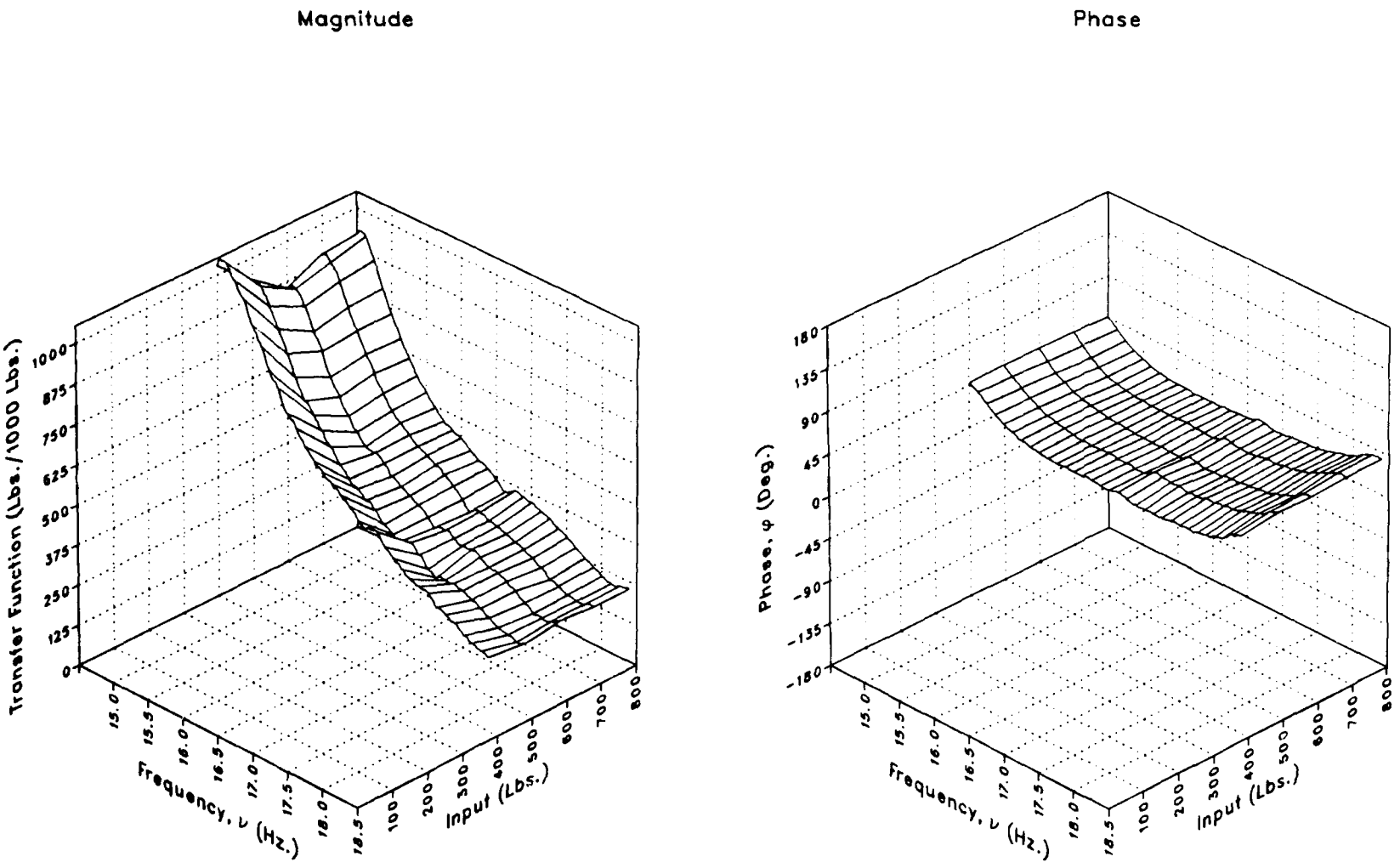

(b) MRLIFTA Concluded.

Figure 4.– Continued.

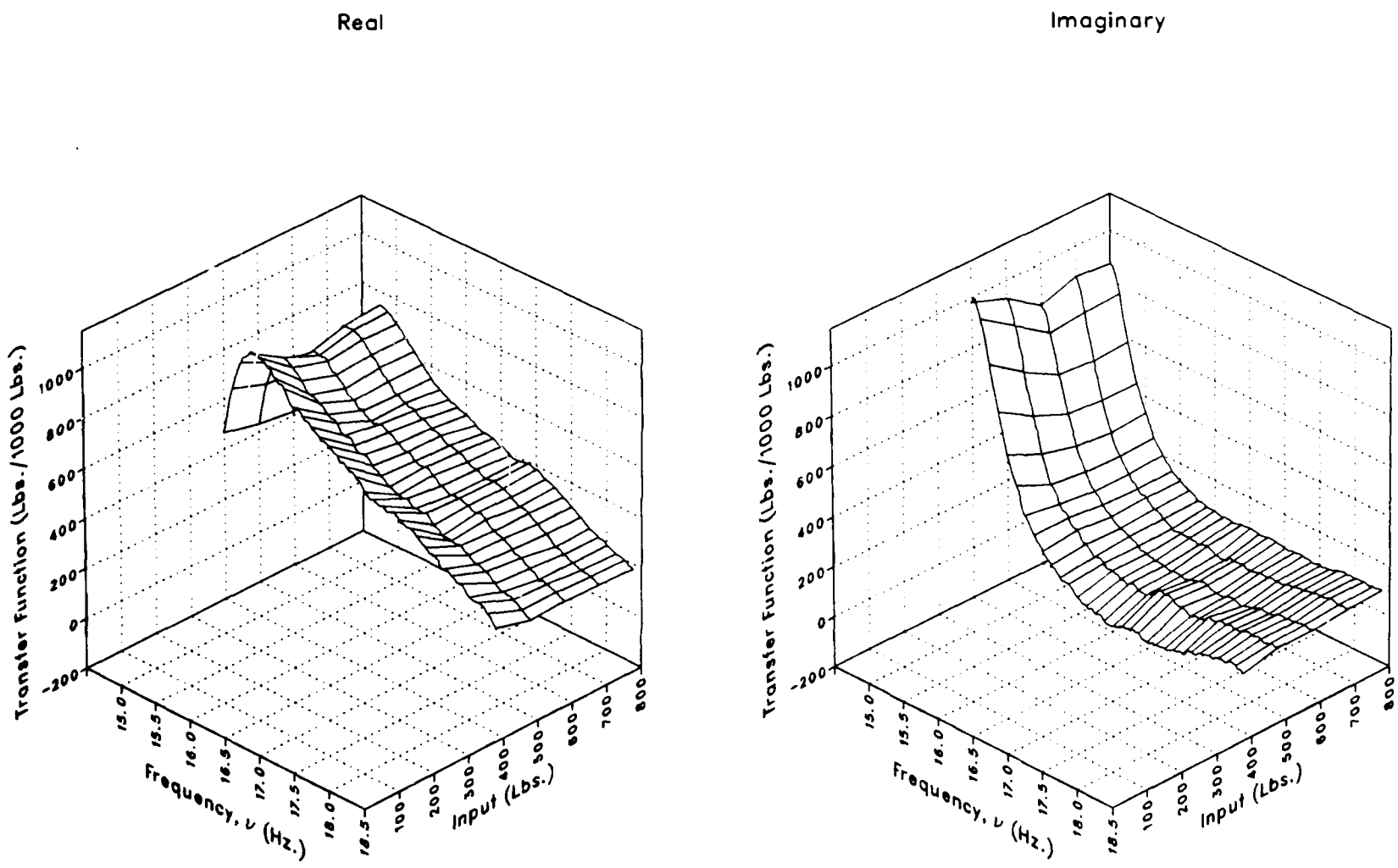

(c) MRLIFTB

Figure 4.– Continued.

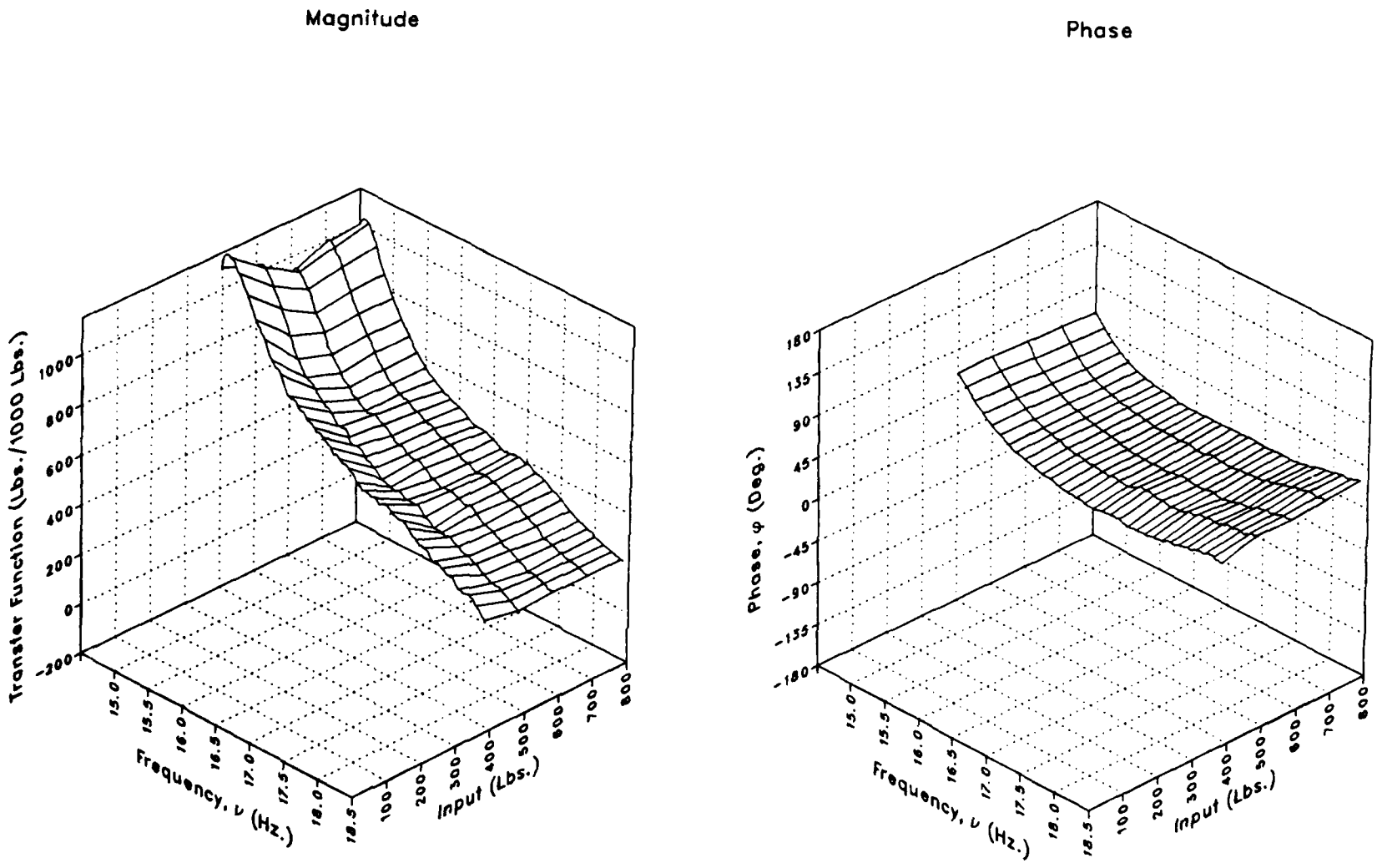

(c) MRLIFTB Concluded.

Figure 4.– Continued.

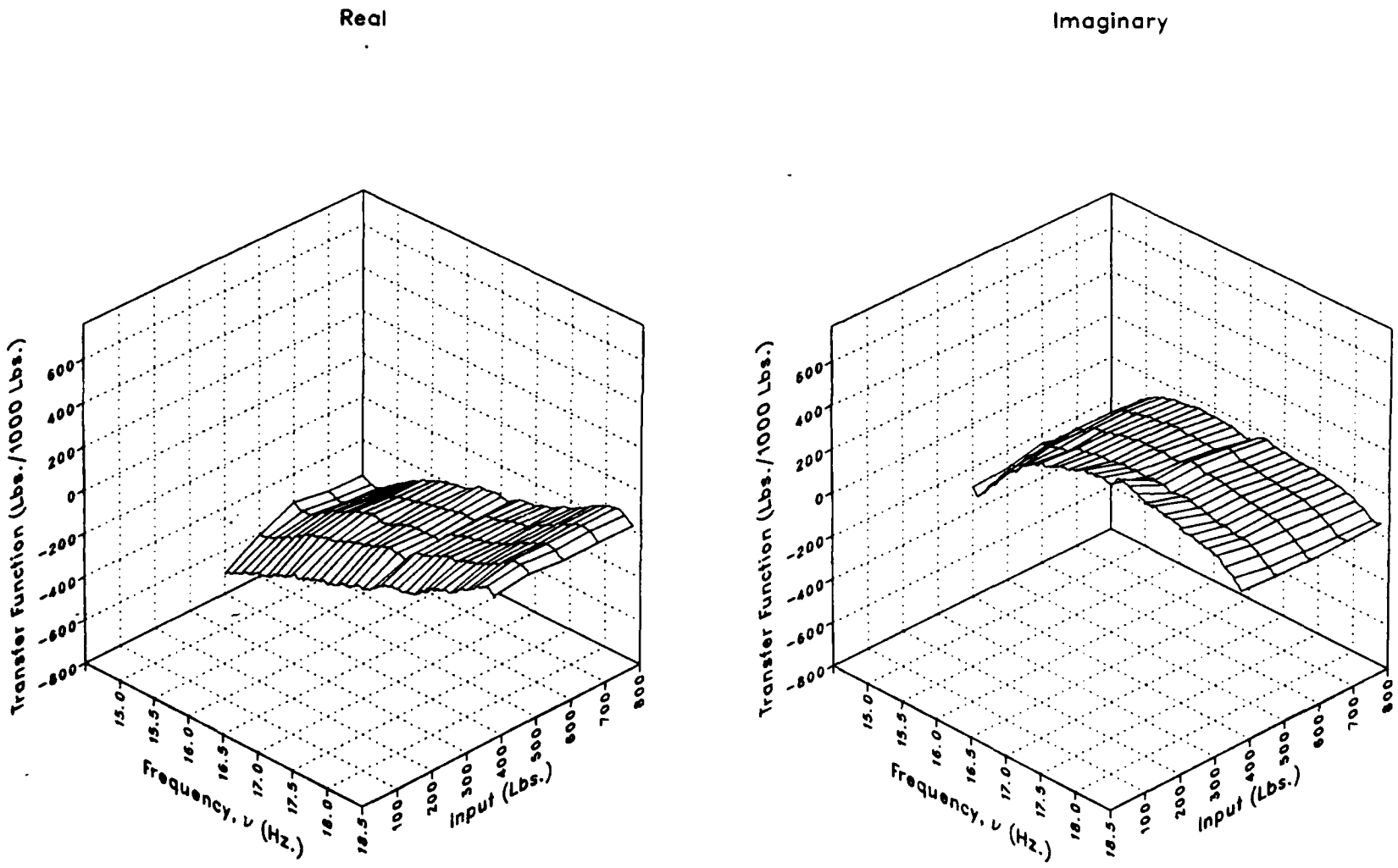

(d) MRLIFTC

Figure 4.– Continued.

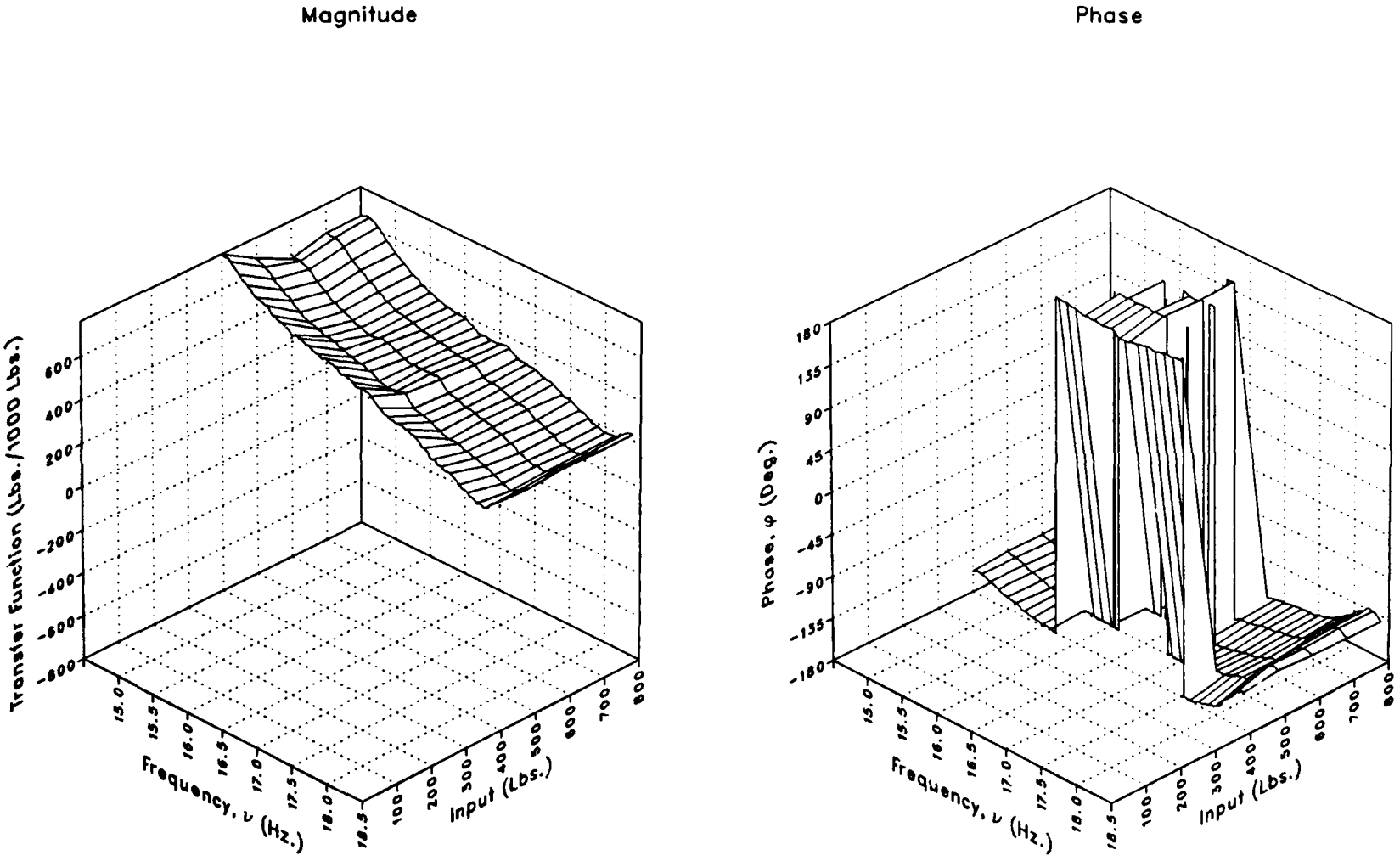

(d) MRLIFTC Concluded.

Figure 4.– Continued.

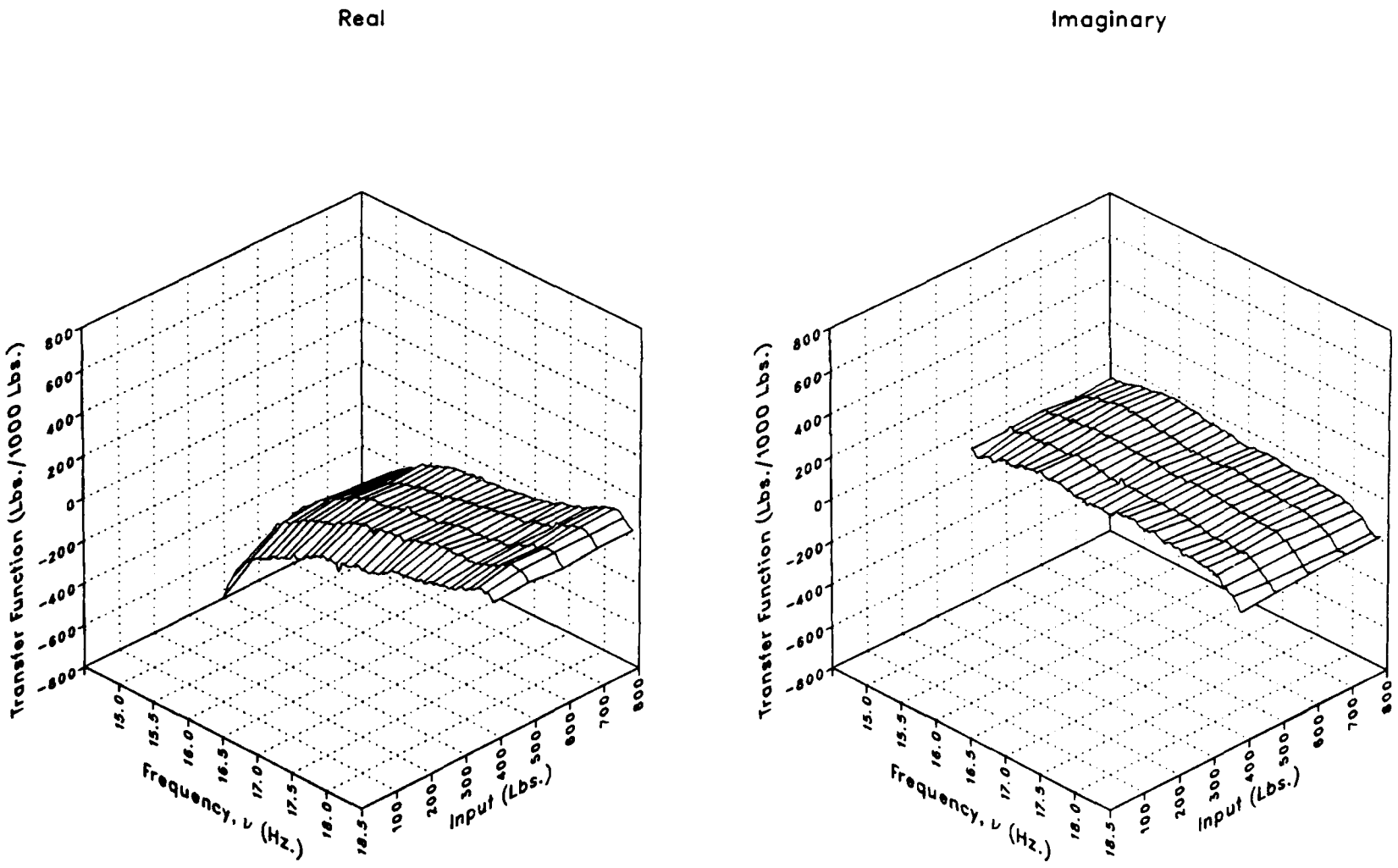

(e) MRLIFTD

Figure 4.– Continued.

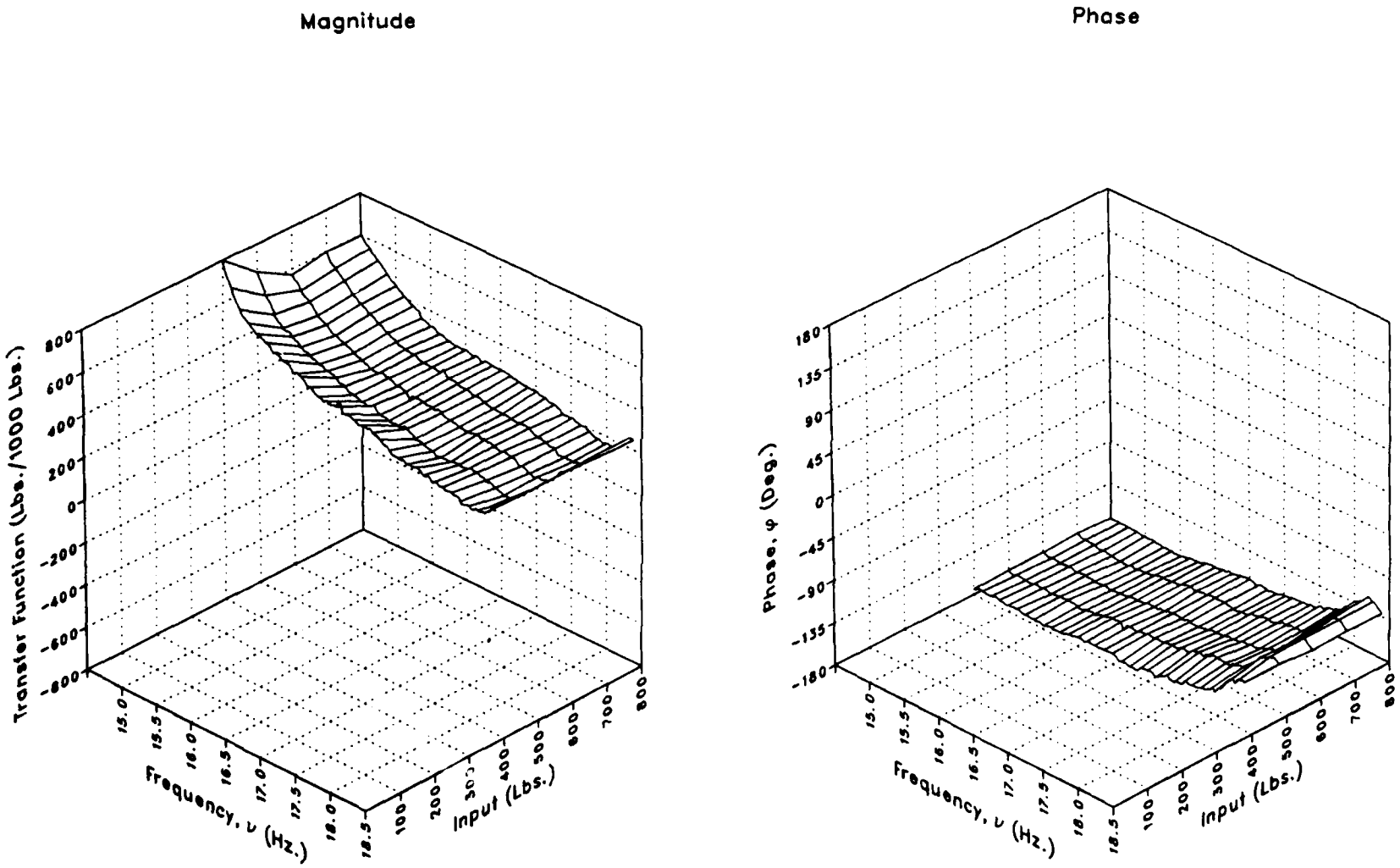

(e) MRLIFTD Concluded.

Figure 4.– Continued.

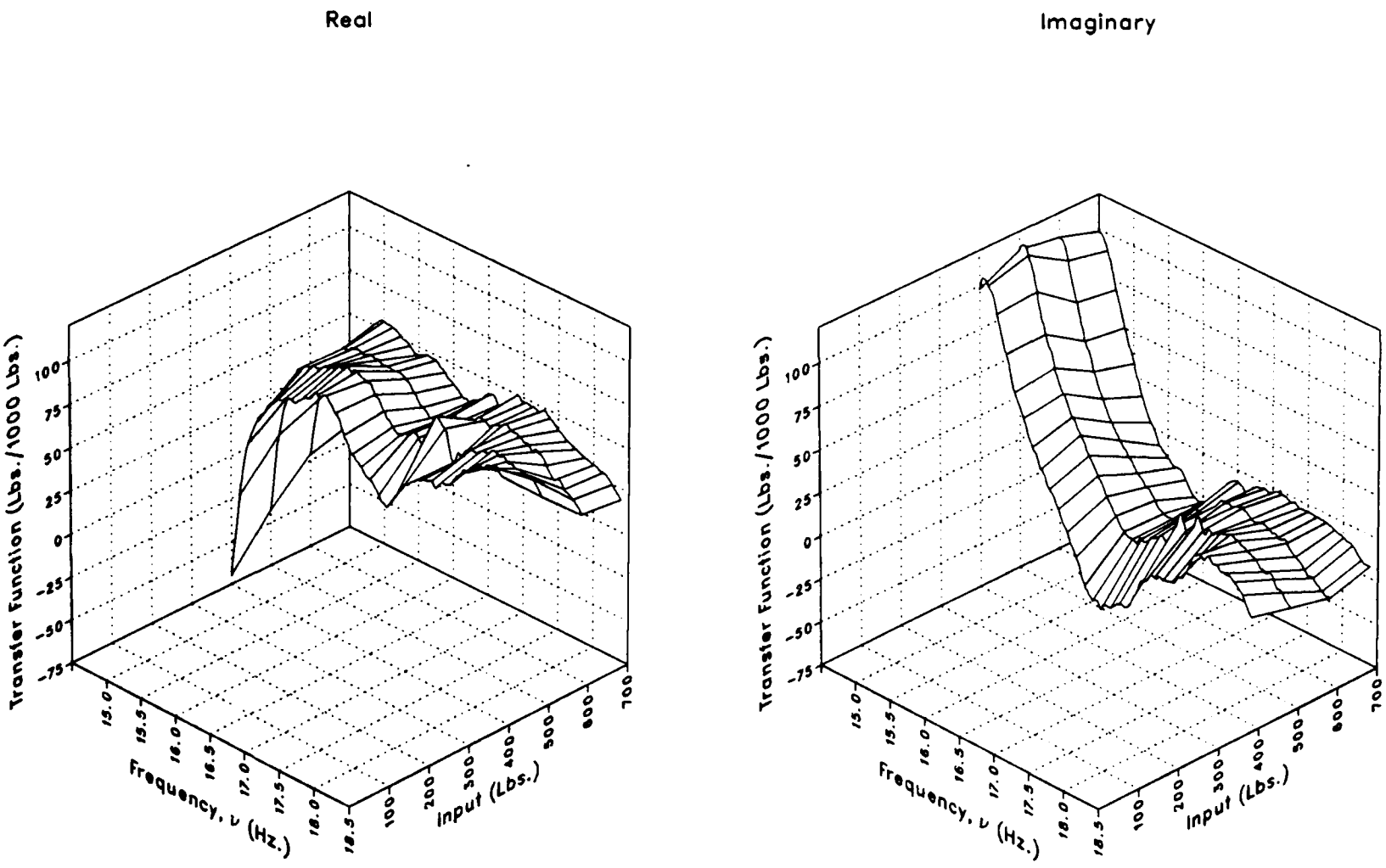

(f) MRGBQCE

Figure 4.– Continued.

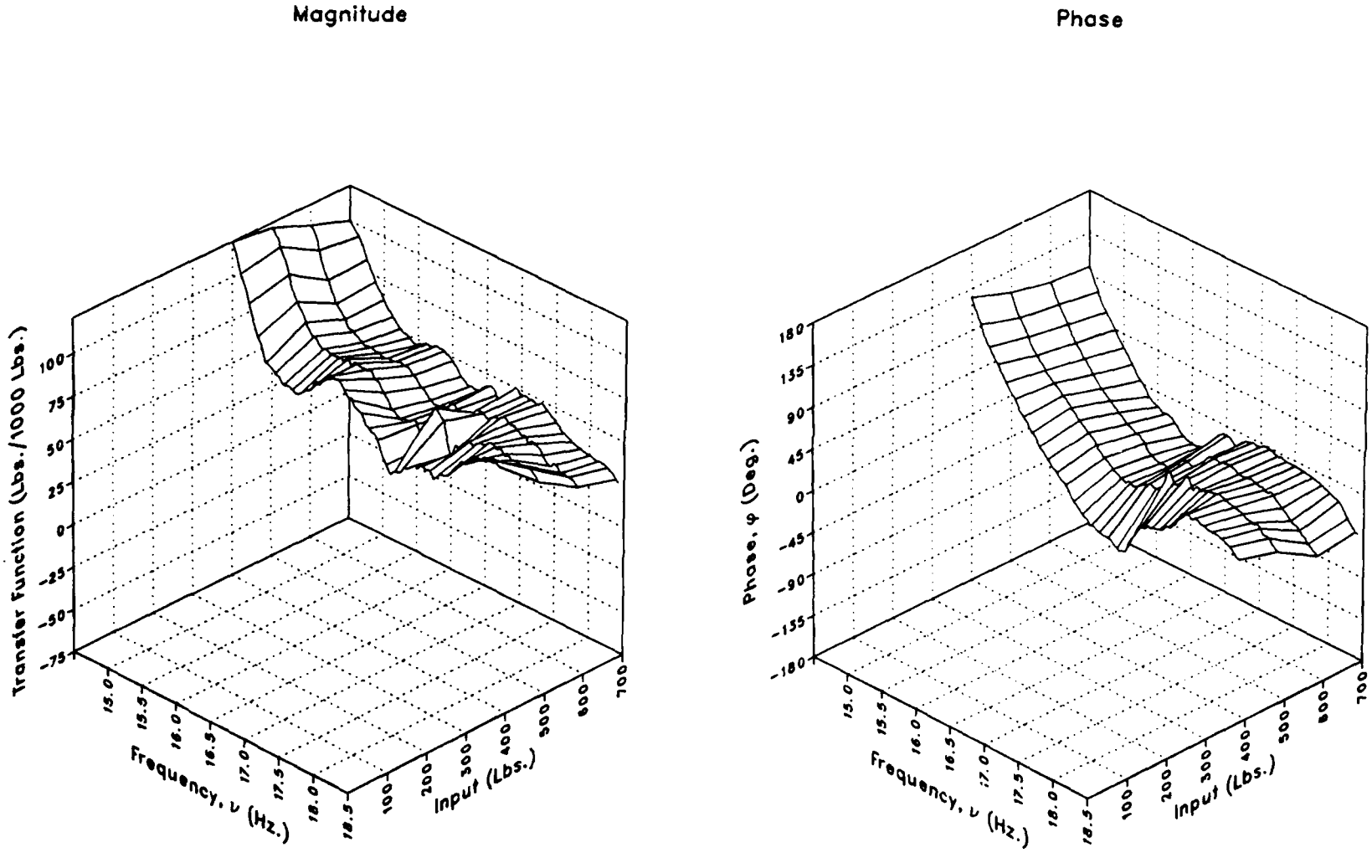

(f) MRGBQCE Concluded.

Figure 4.– Continued.

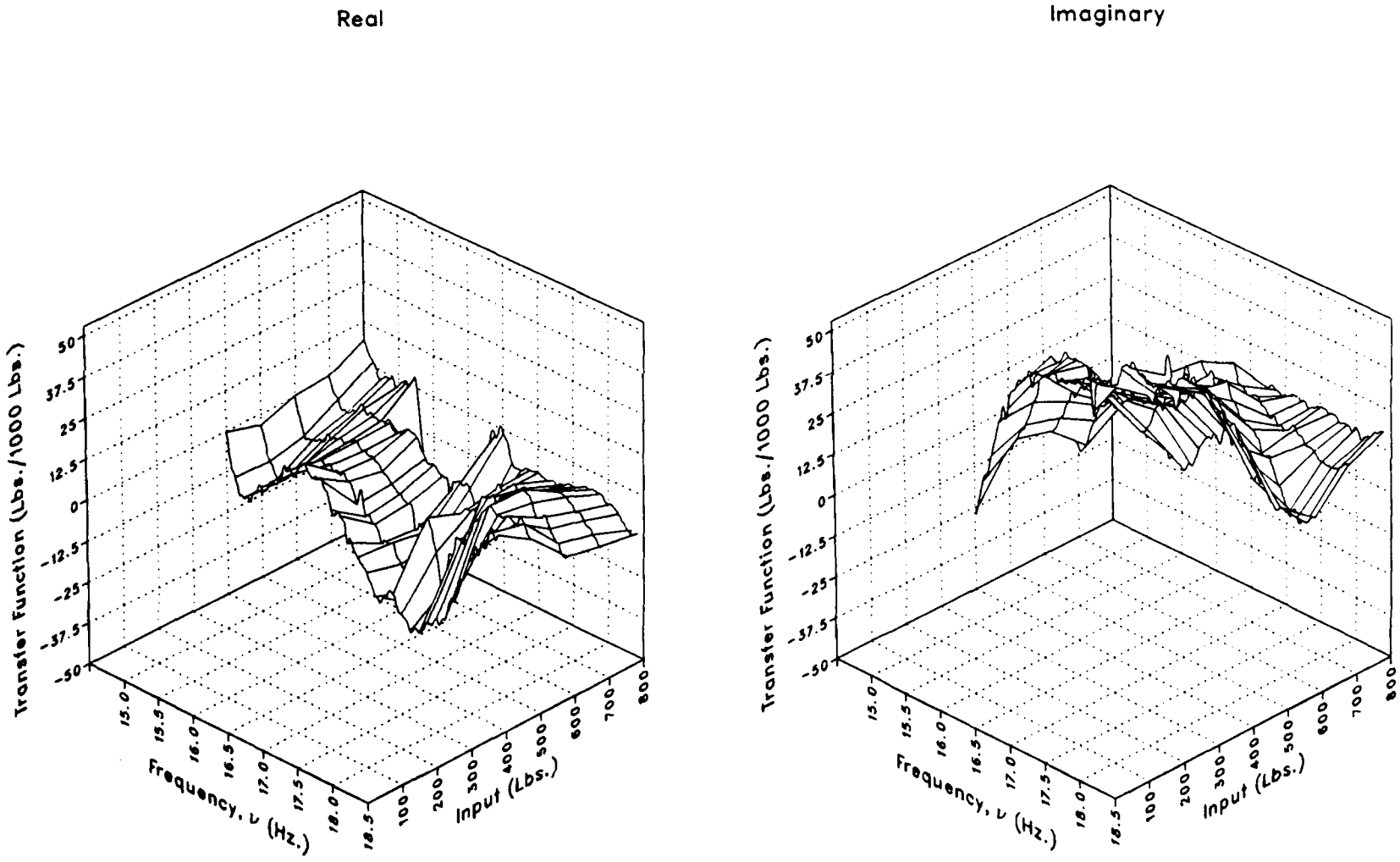

(g) MRGBQCF

Figure 4.– Continued.

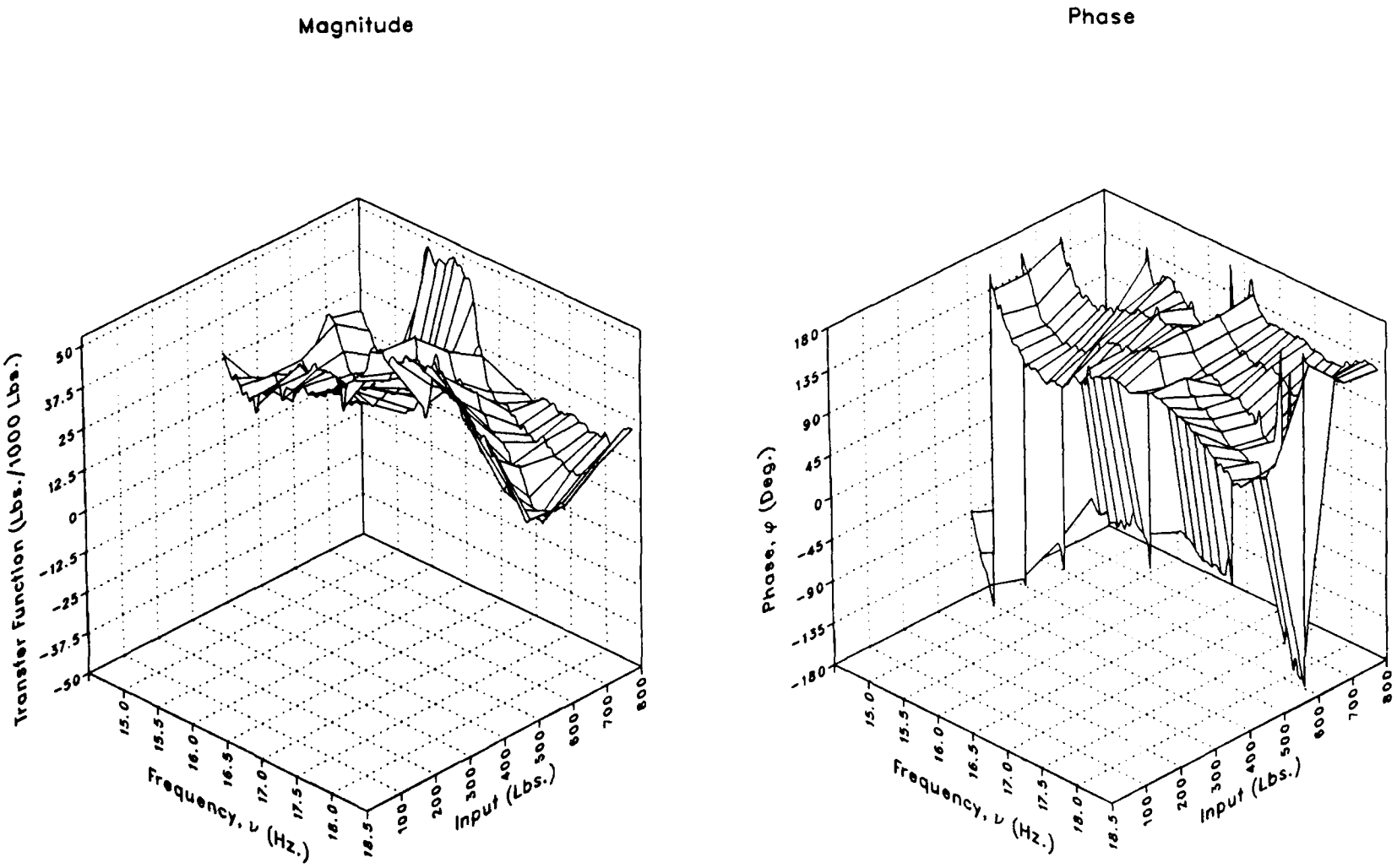

(g) MRGBQCF Concluded.

Figure 4.– Continued.

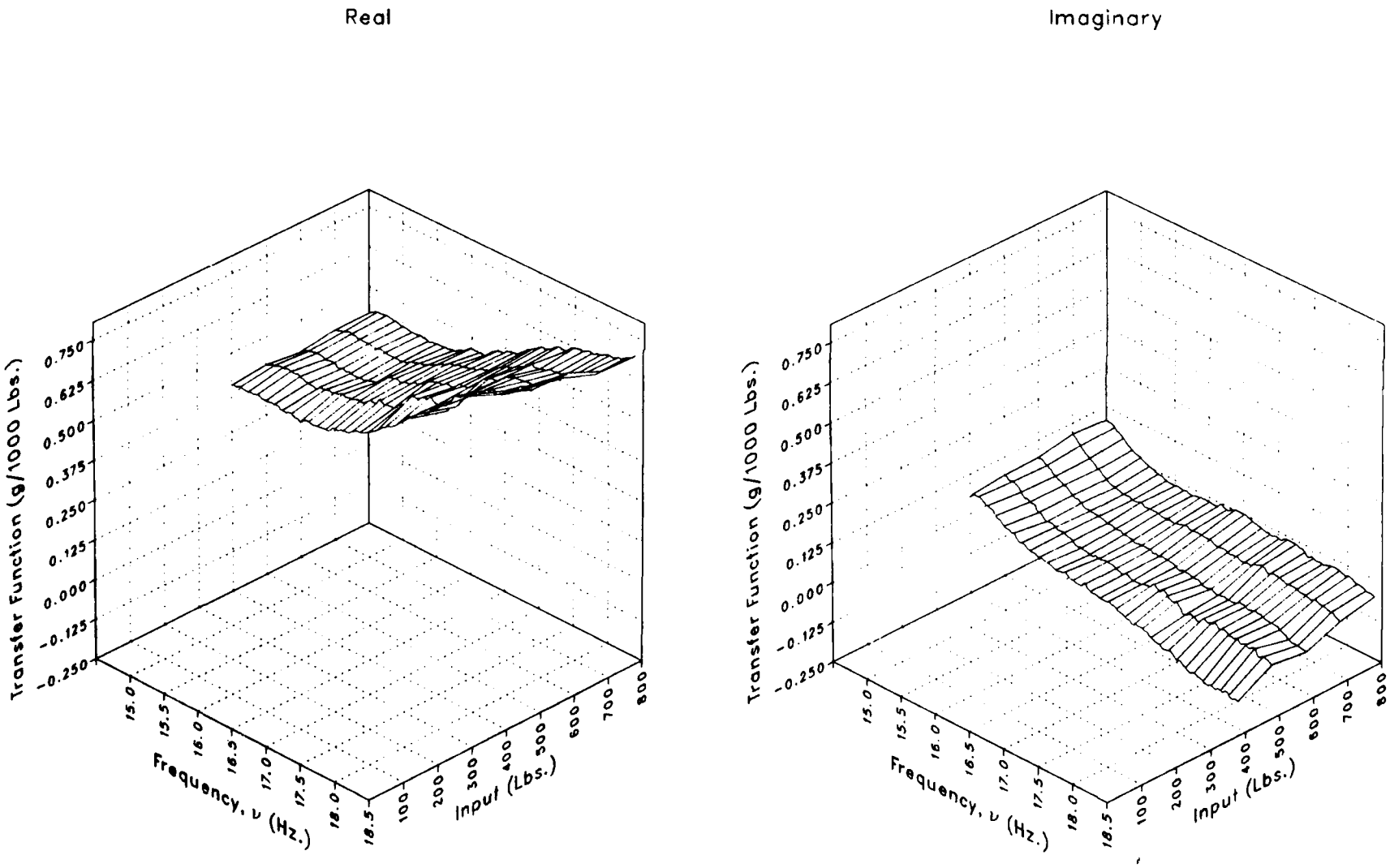

(h) LOMGB

Figure 4.– Continued.

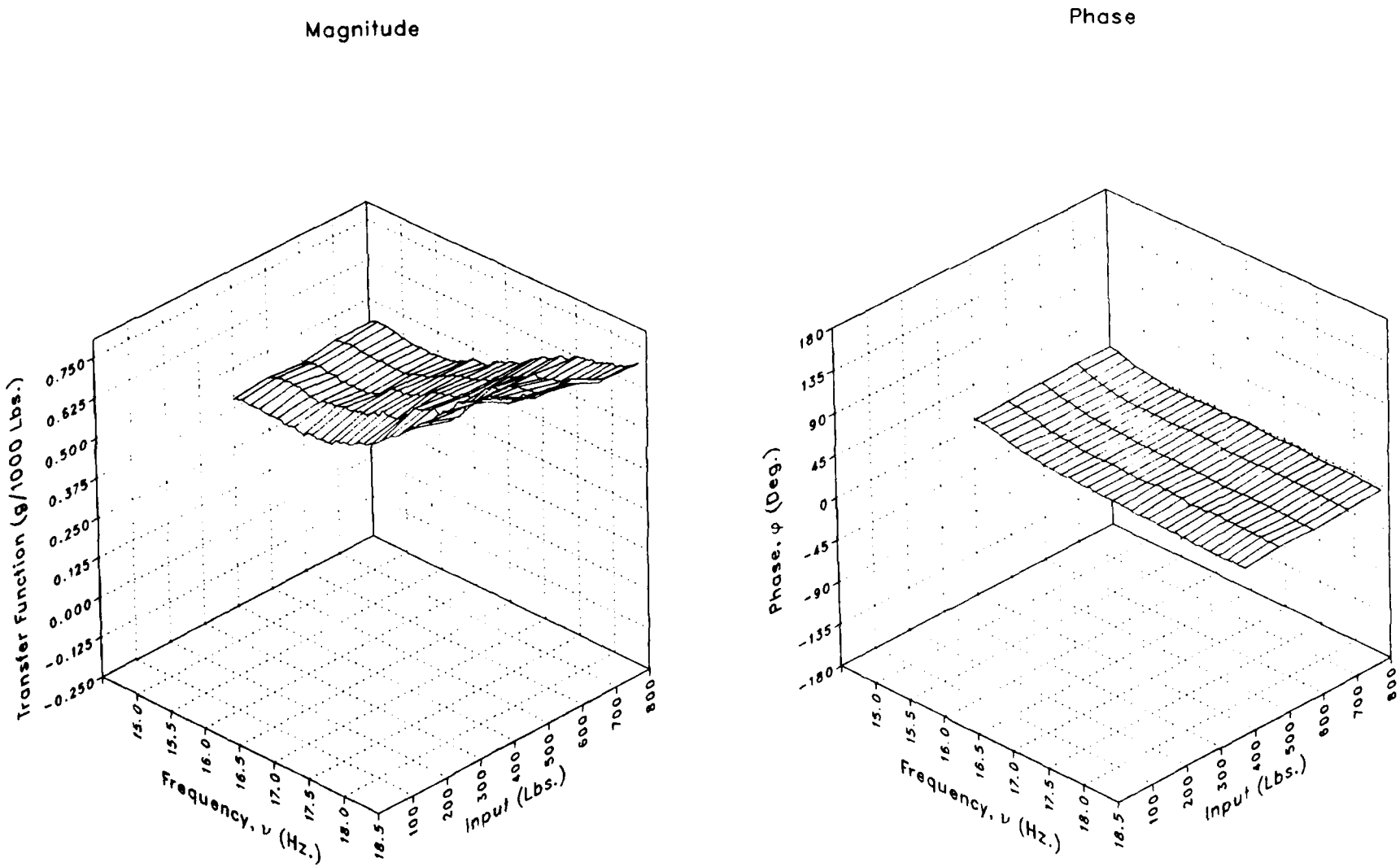

(h) LOMGB Concluded.

Figure 4.– Continued.

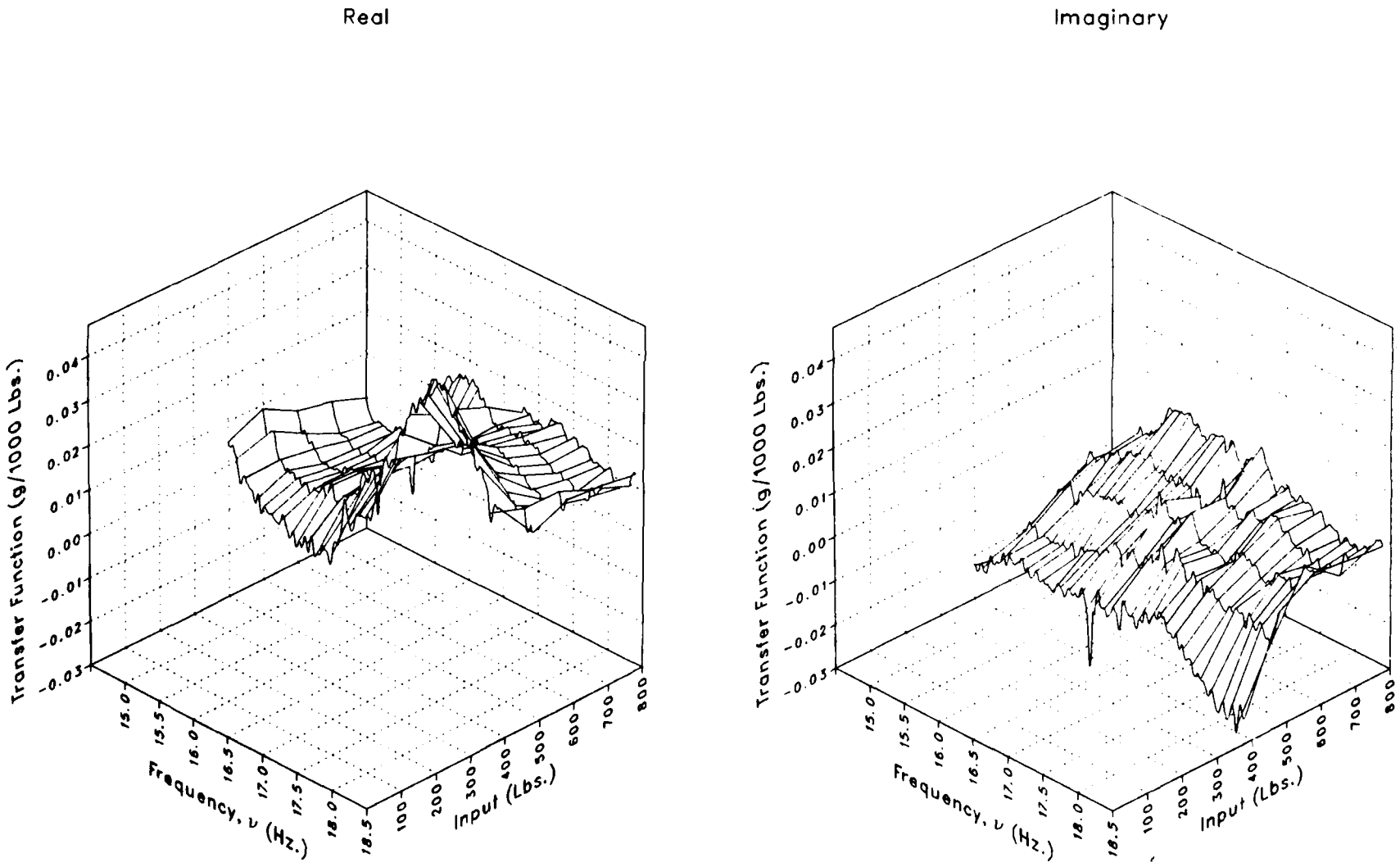

(i) LMGB

Figure 4.– Continued.

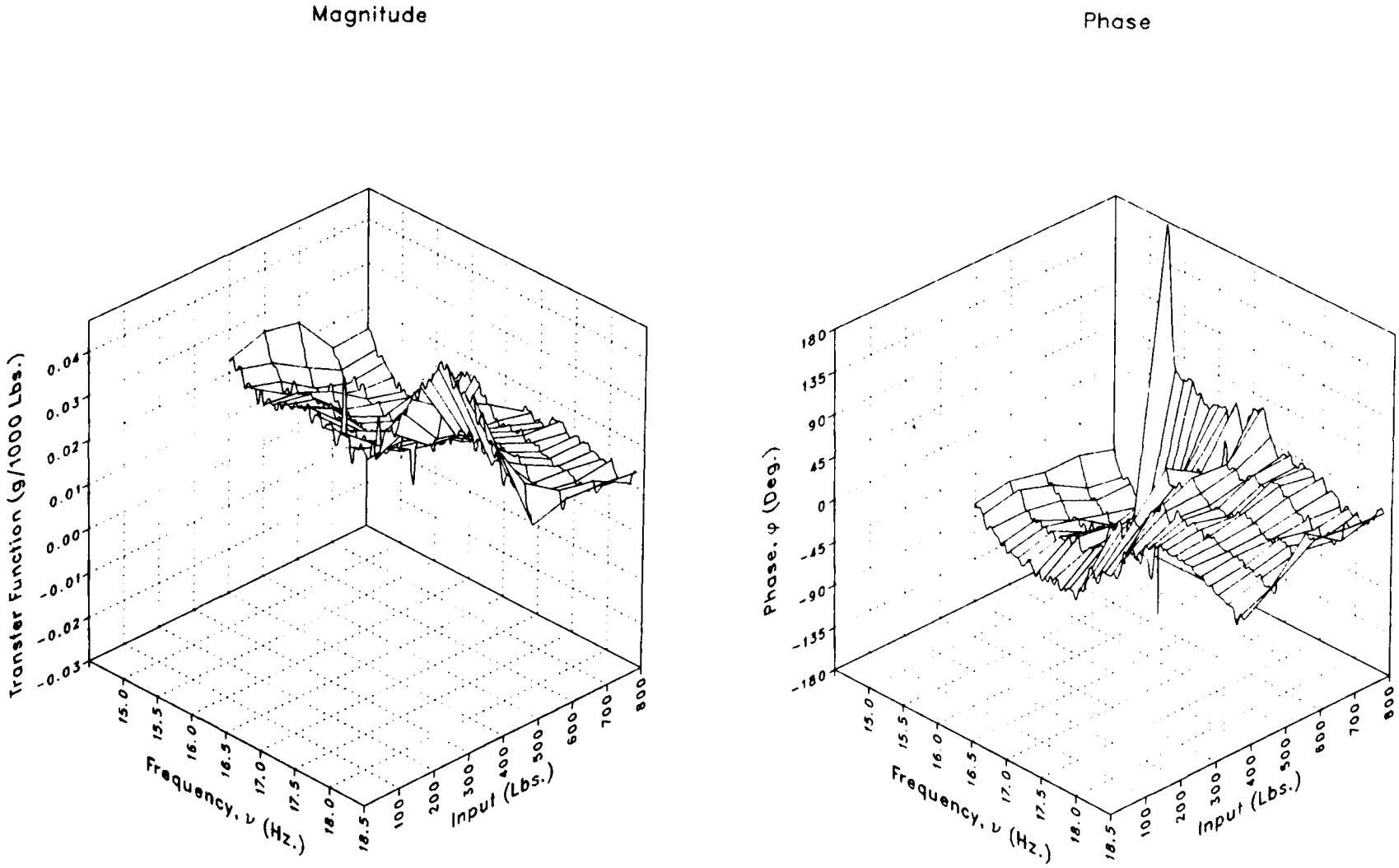

(i) LMGB Concluded.

Figure 4.– Continued.

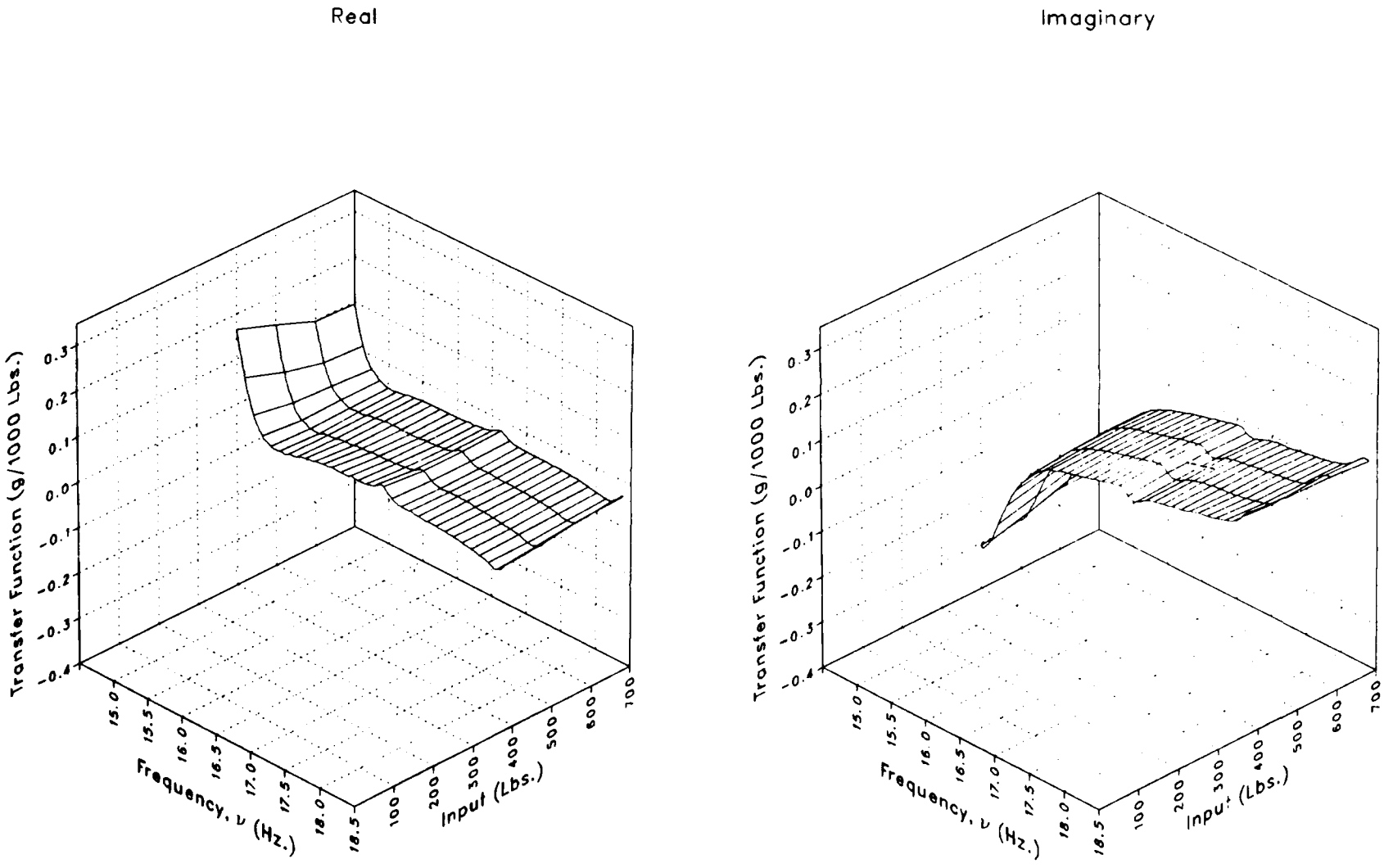

(j) VMGB

Figure 4.– Continued.

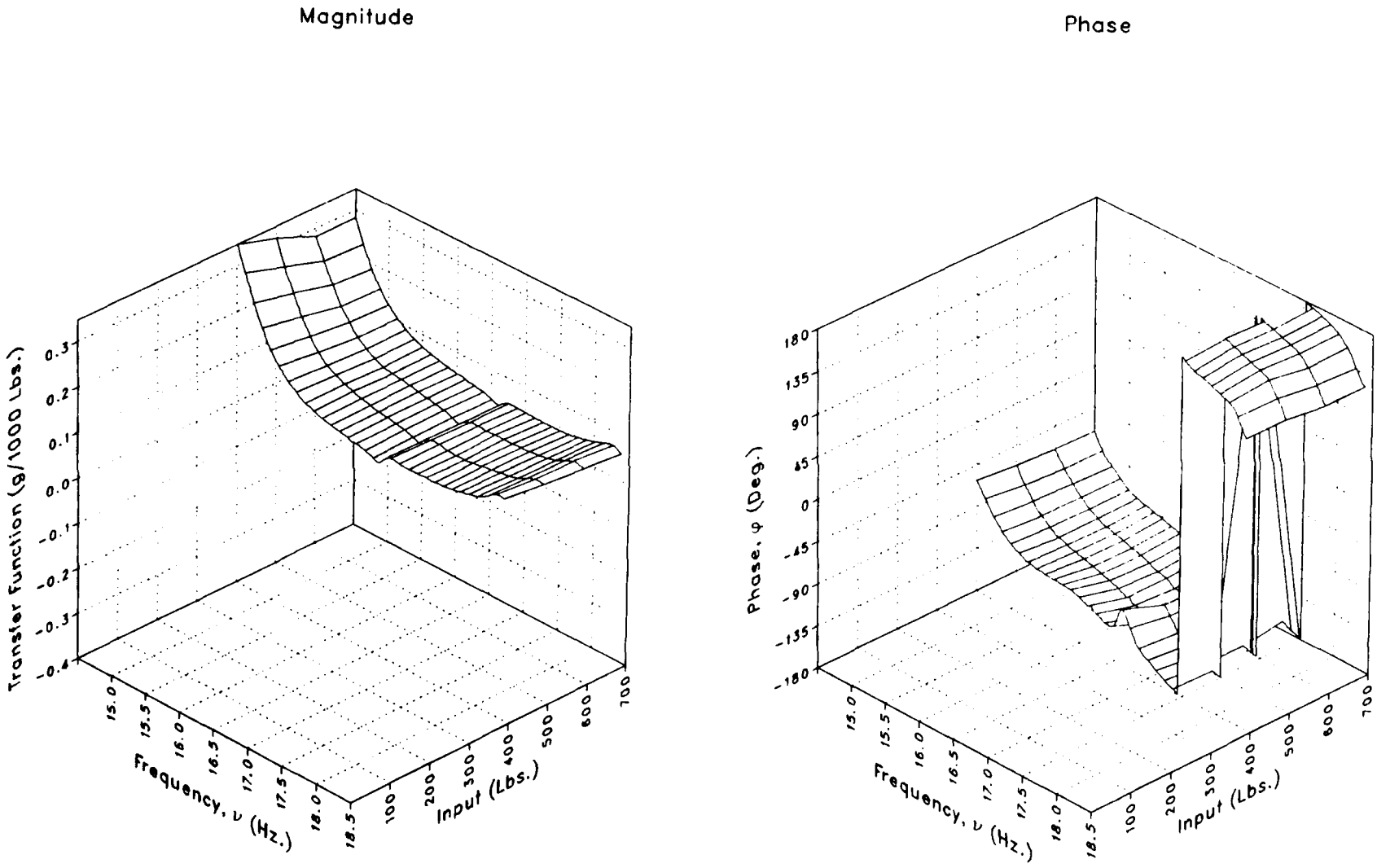

(j) VMGB Concluded.

Figure 4.– Continued.

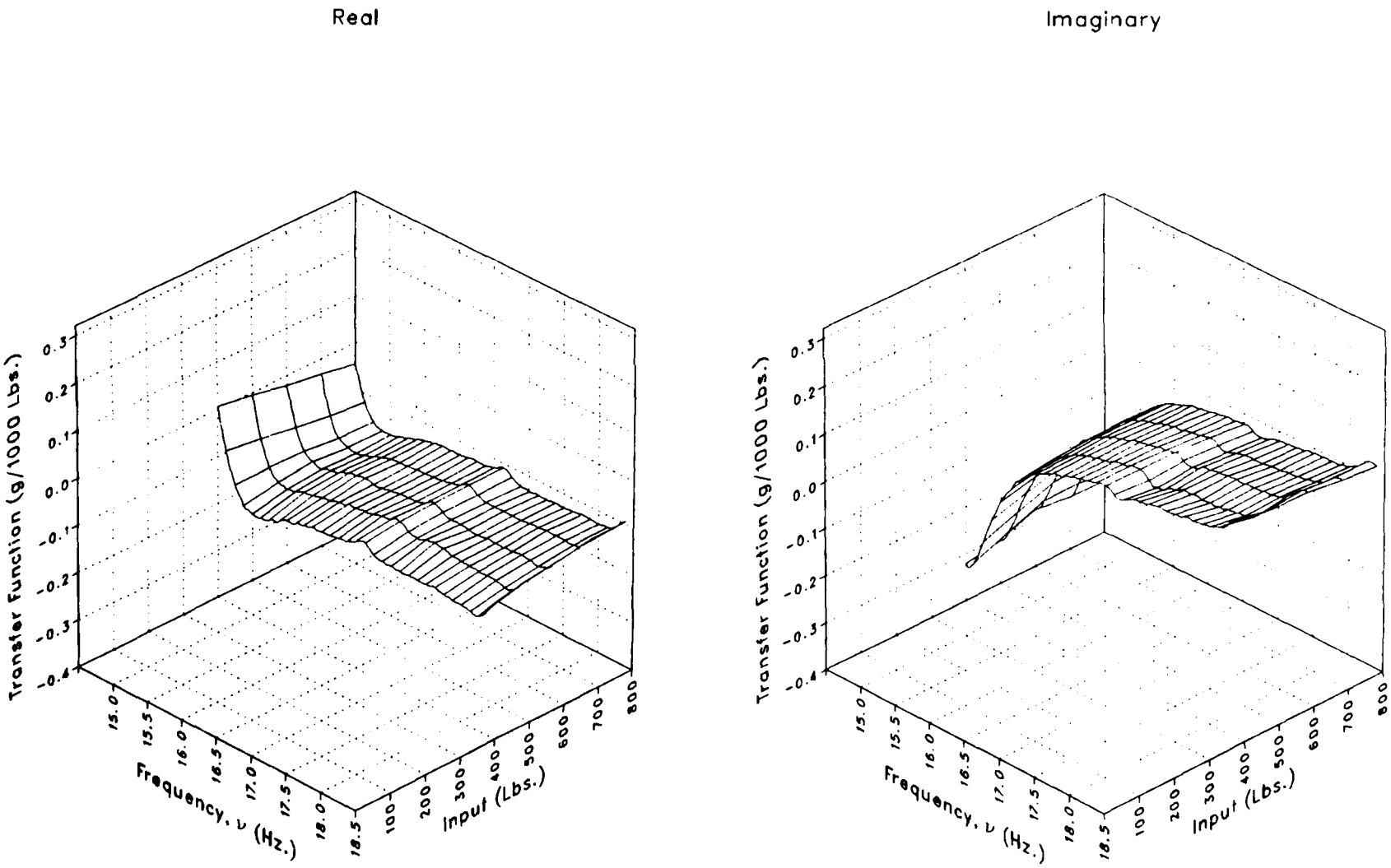

(k) XMRFBPV

Figure 4.– Continued.

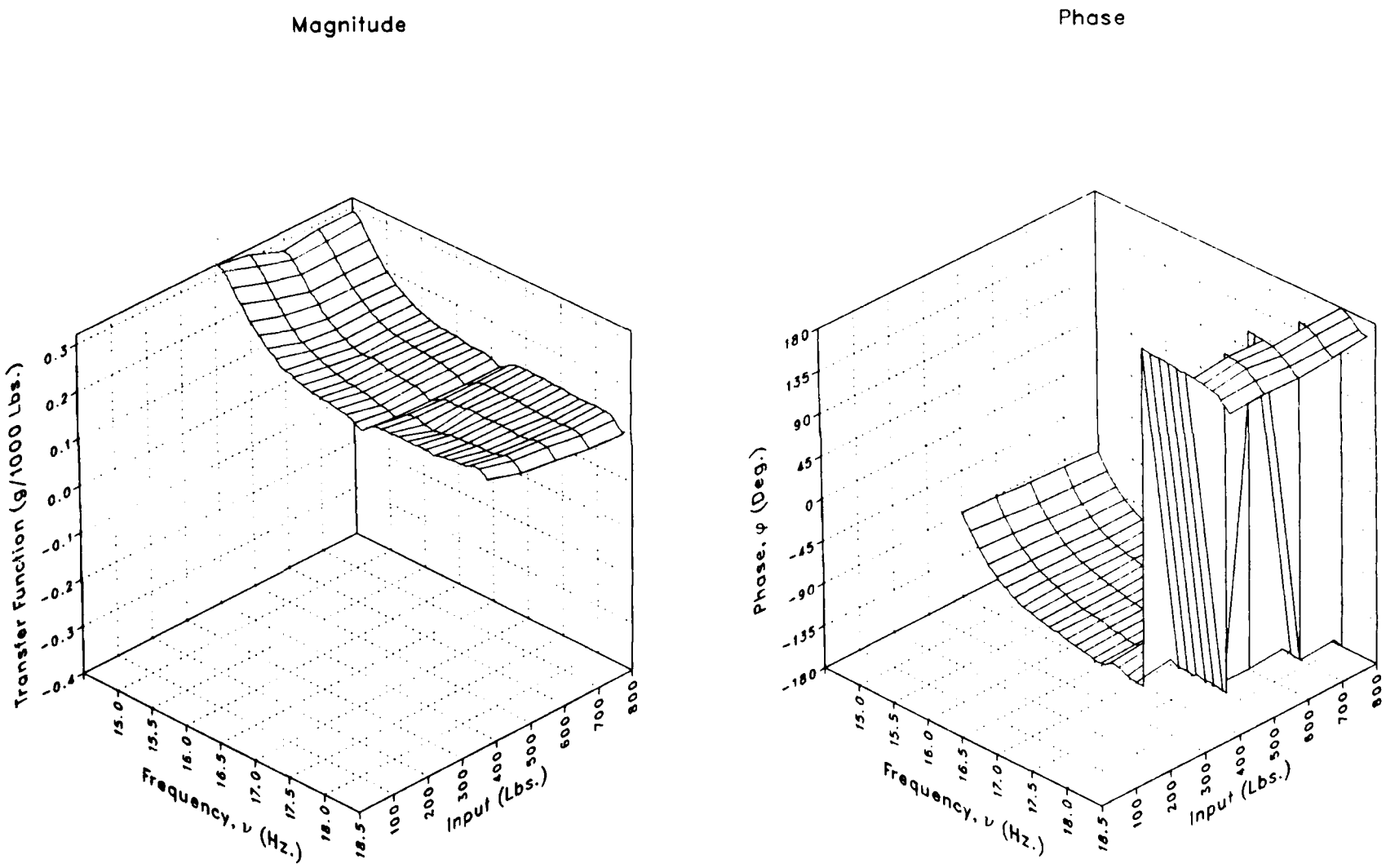

(k) XMRFBPV Concluded.

Figure 4.– Continued.

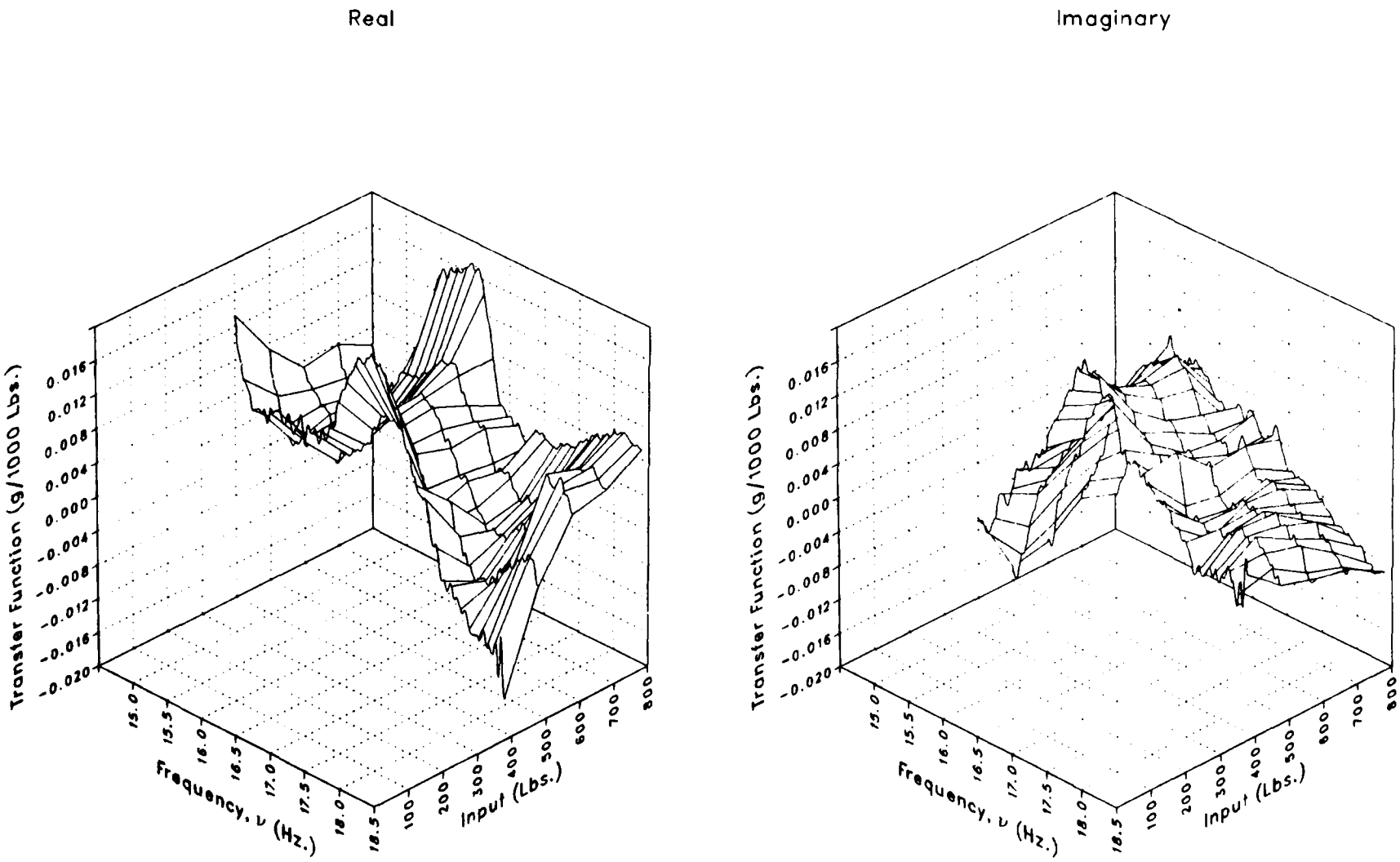

(l) XMRFBPL

Figure 4.– Continued.

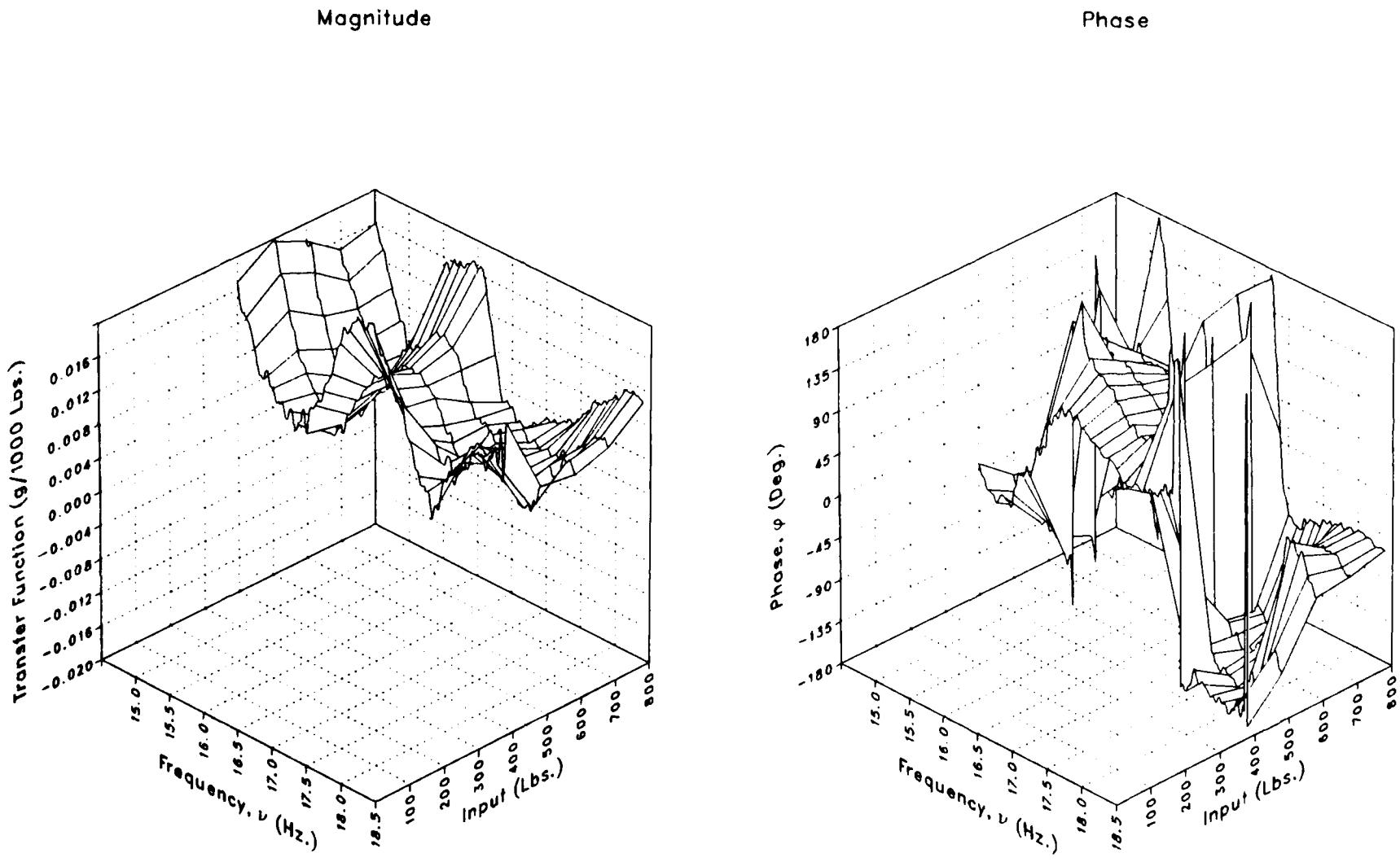

(l) XMRFBPL Concluded.

Figure 4.– Continued.

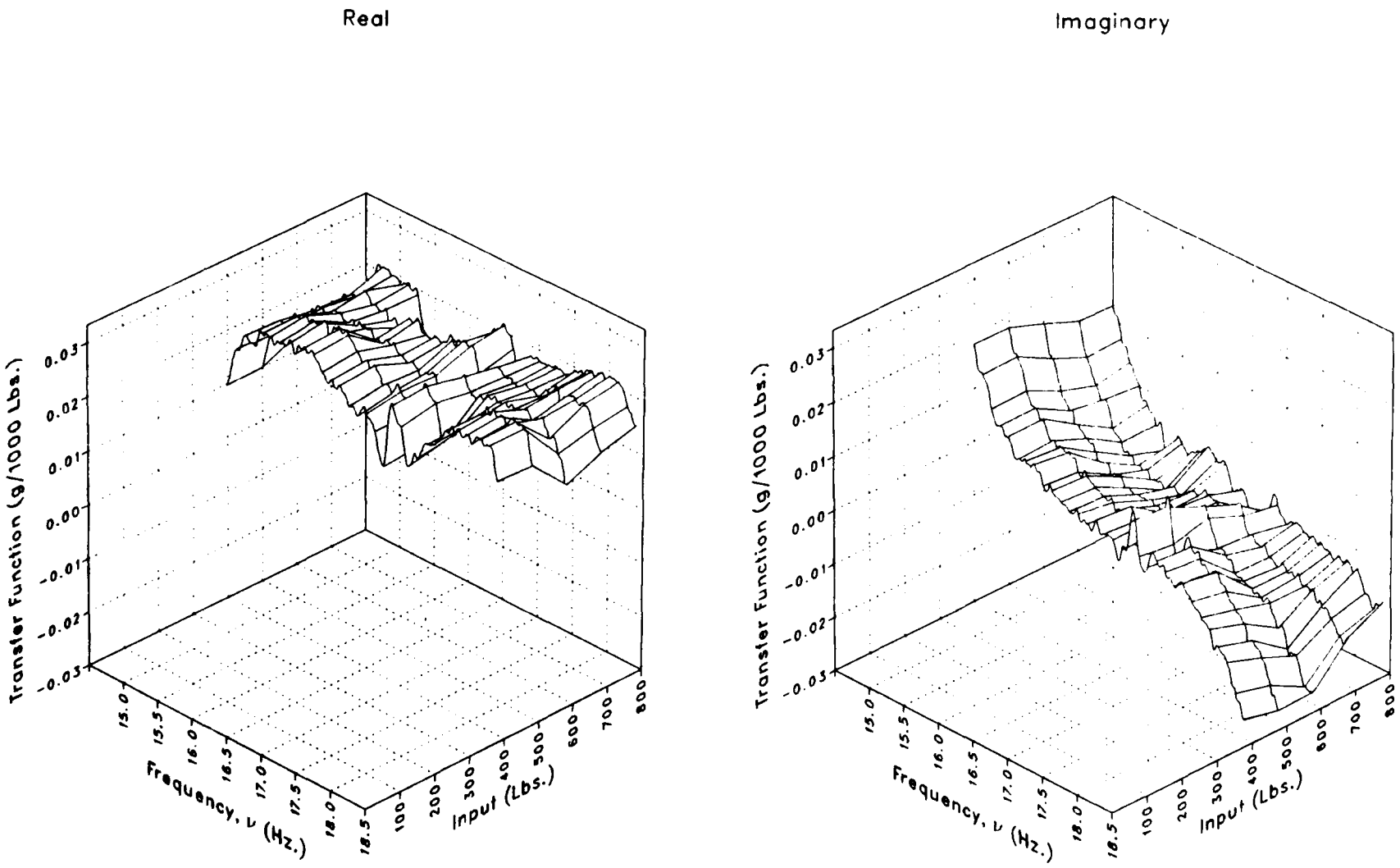

(m) XMRFBPLO

Figure 4.– Continued.

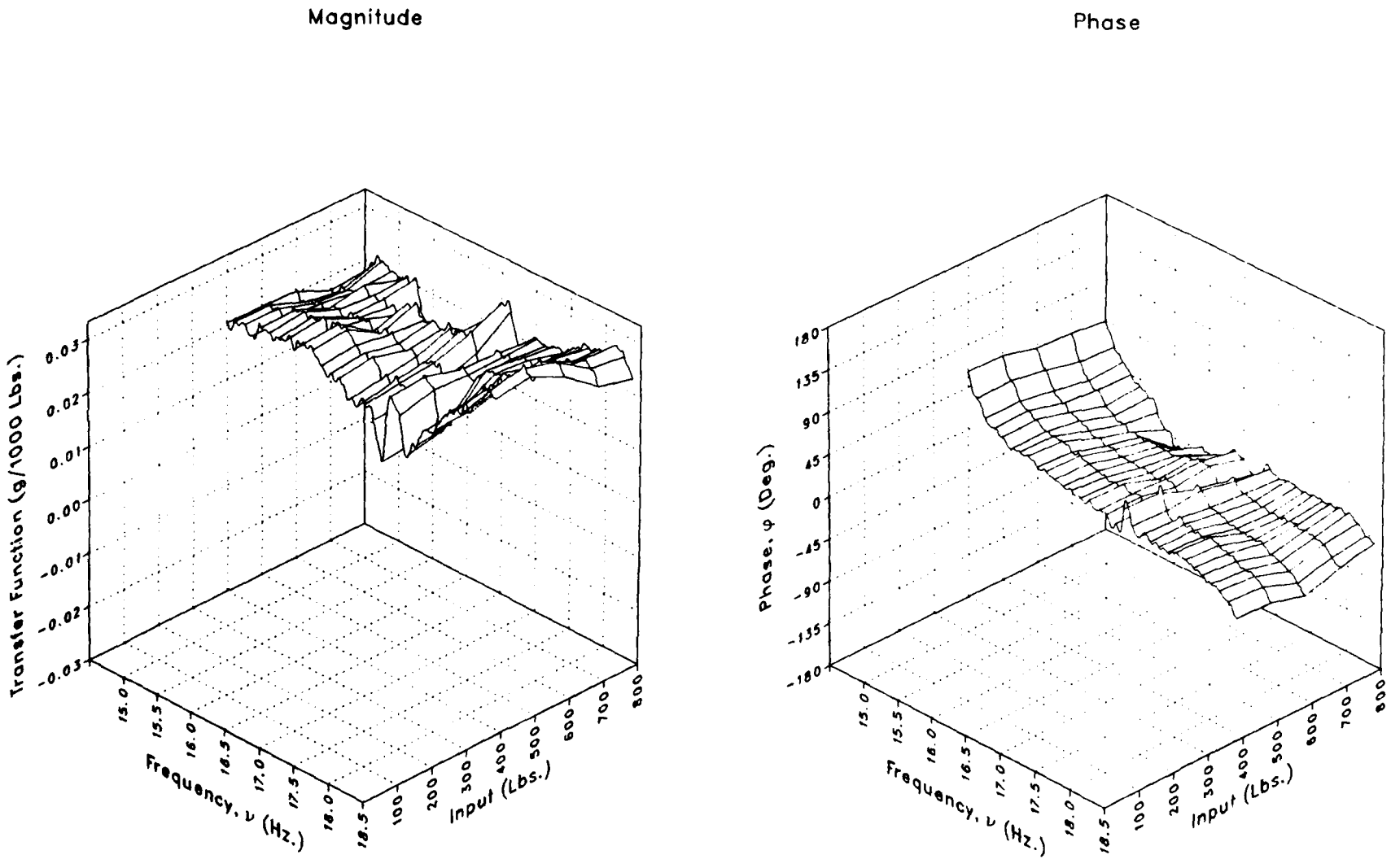

(m) XMRFBPLO Concluded.

Figure 4.– Continued.

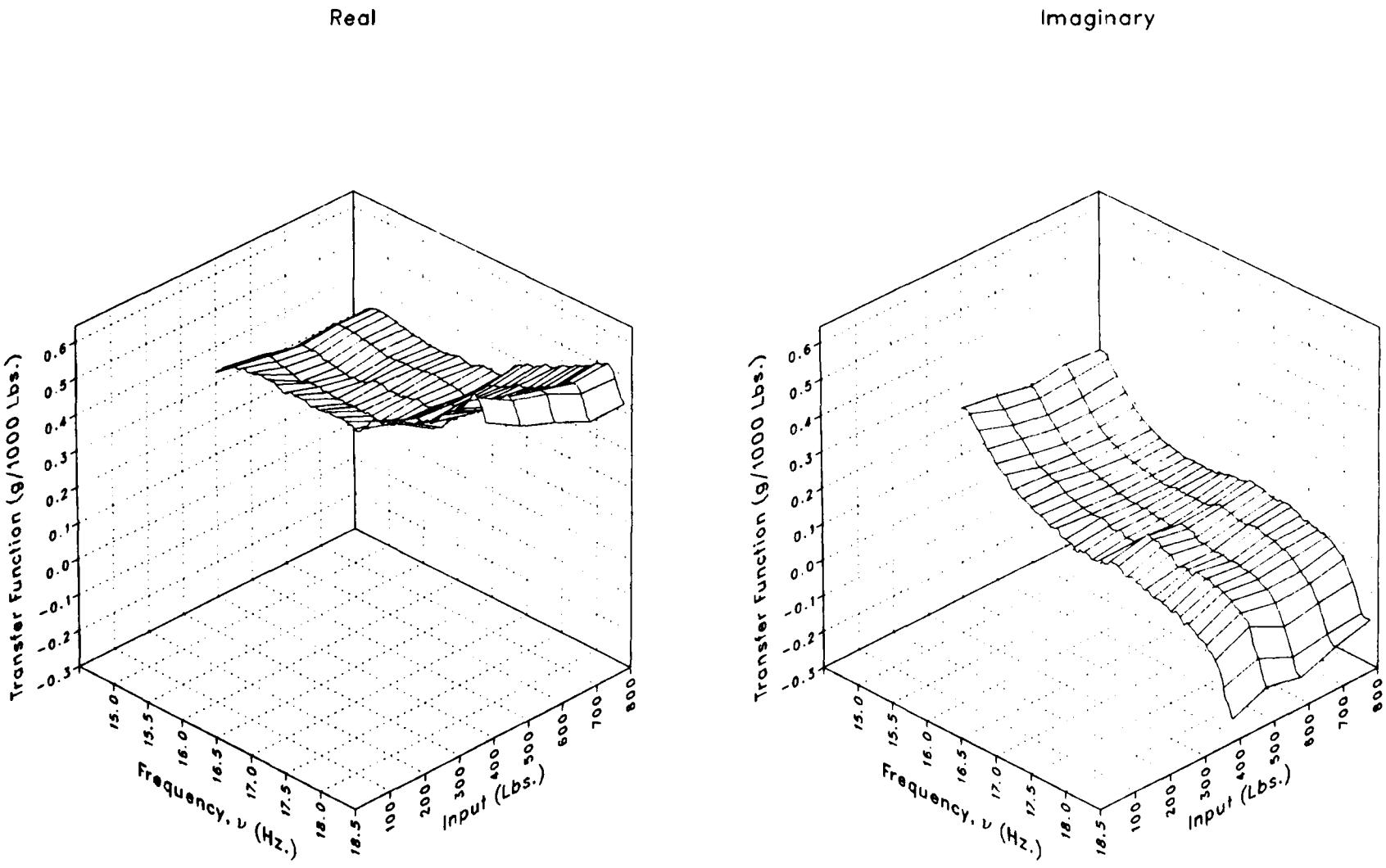

(n) STA56NV

Figure 4.– Continued.

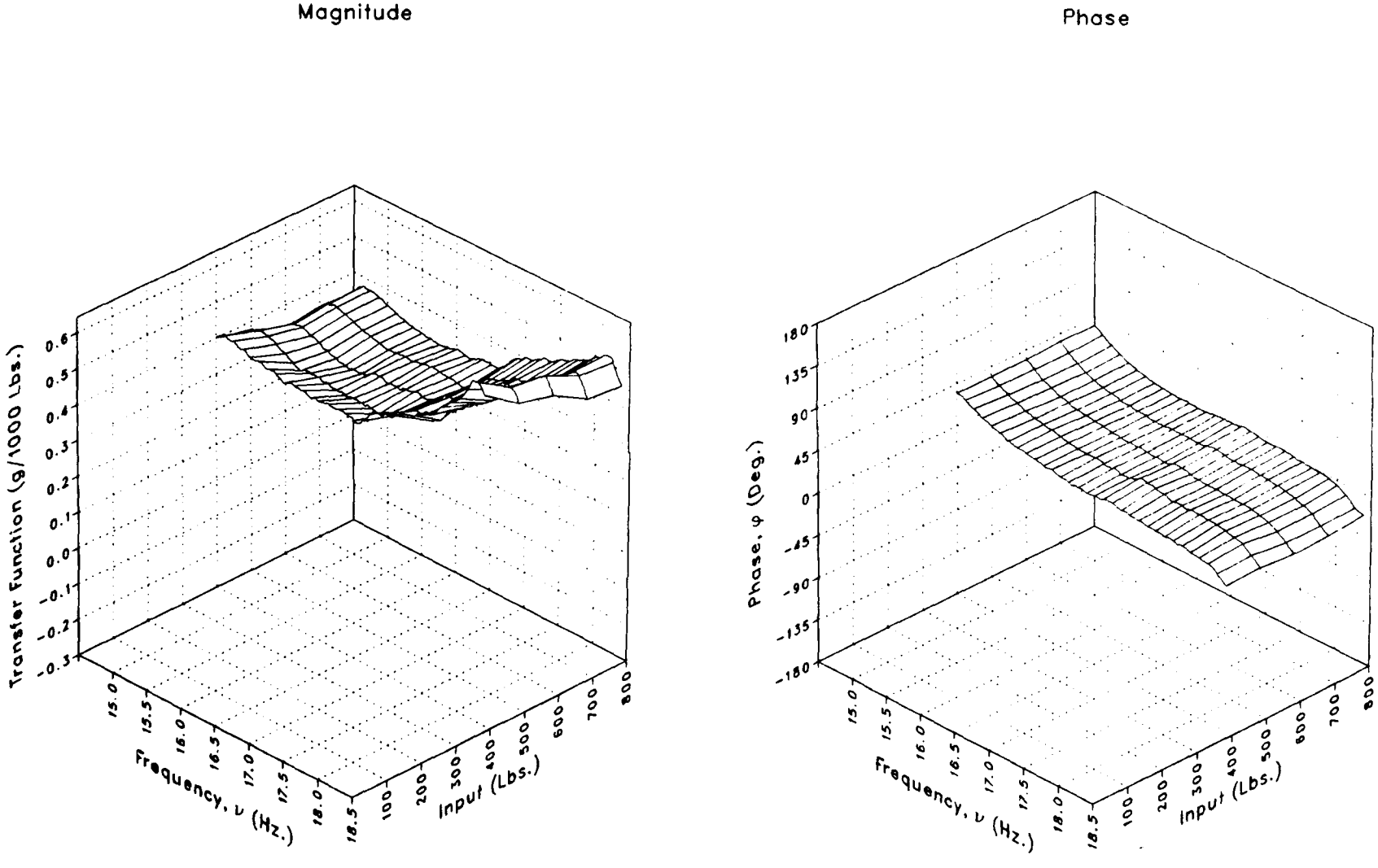

(n) STA56NV Concluded.

Figure 4.– Continued.

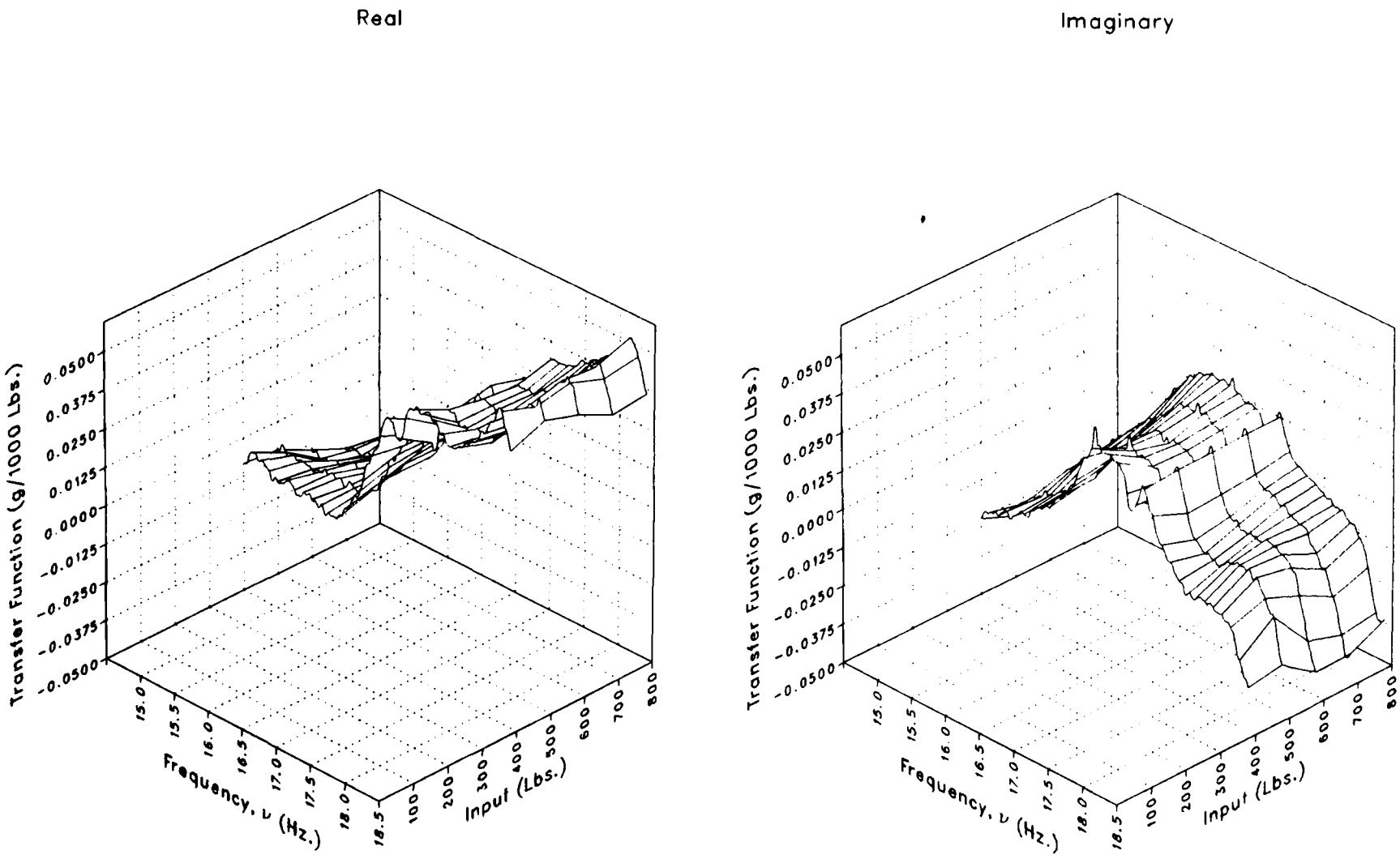

(o) STA56NL

Figure 4.– Continued.

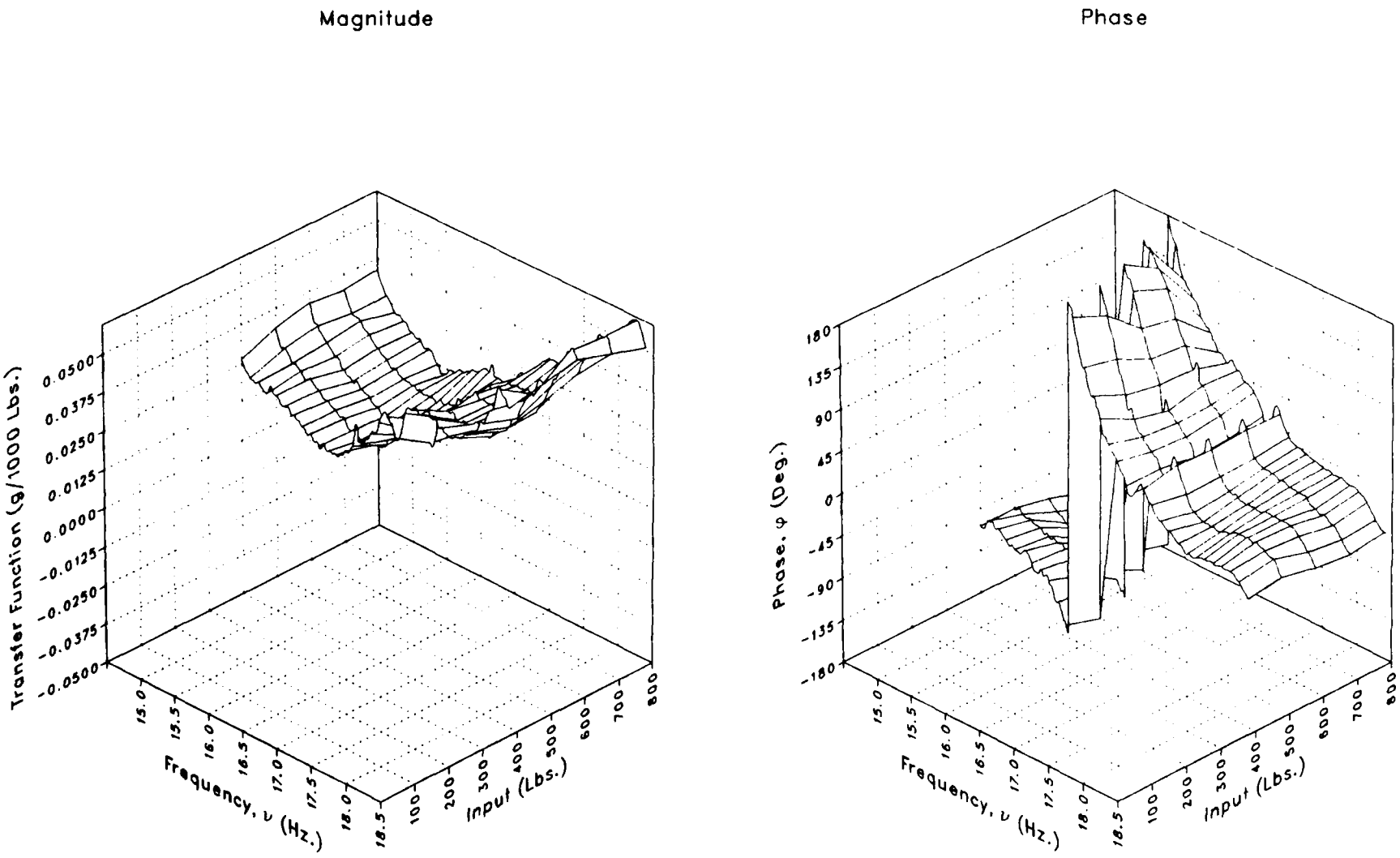

(o) STA56NL Concluded.

Figure 4.– Continued.

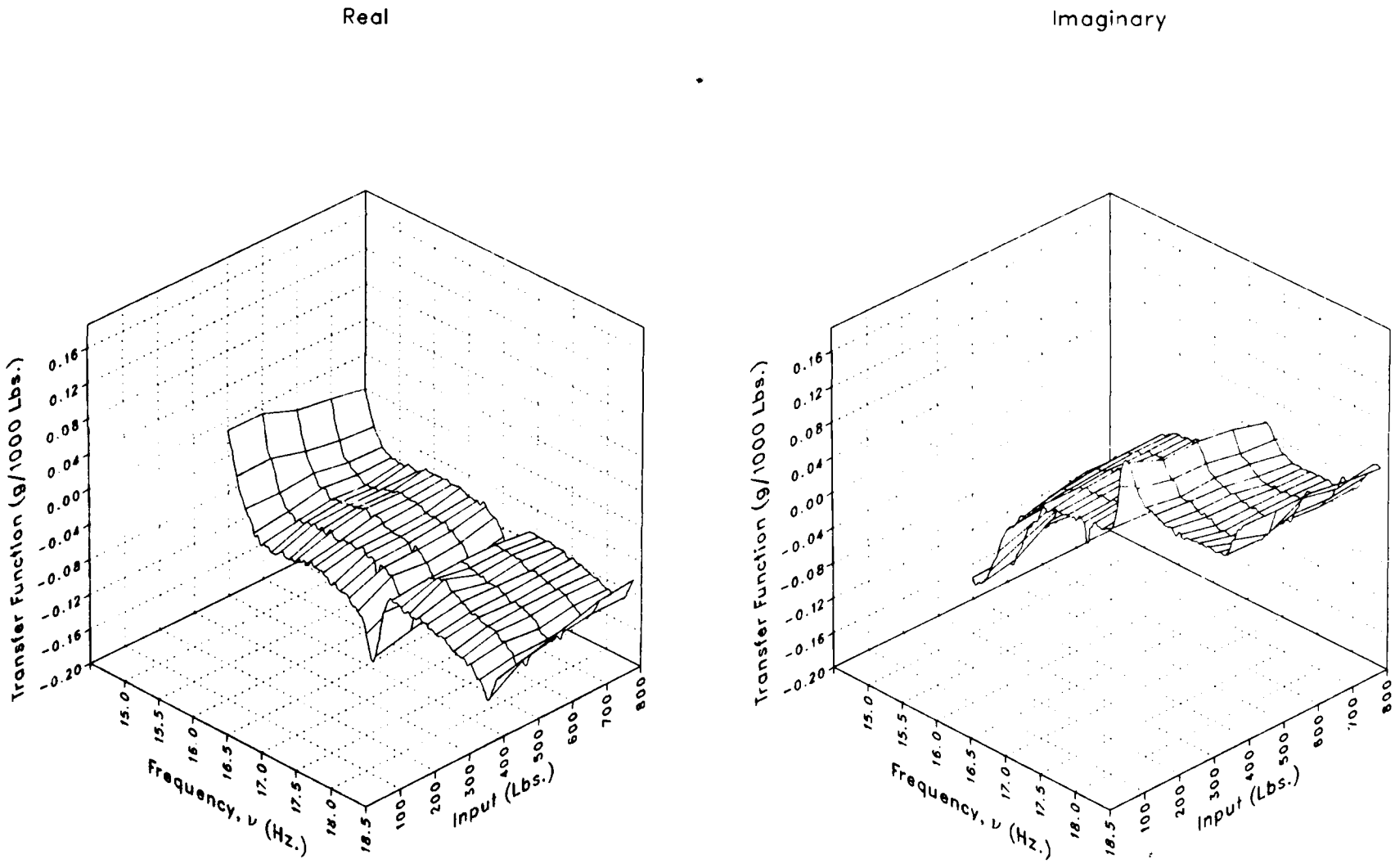

(p) VWGTPRT

Figure 4.– Continued.

Magnitude

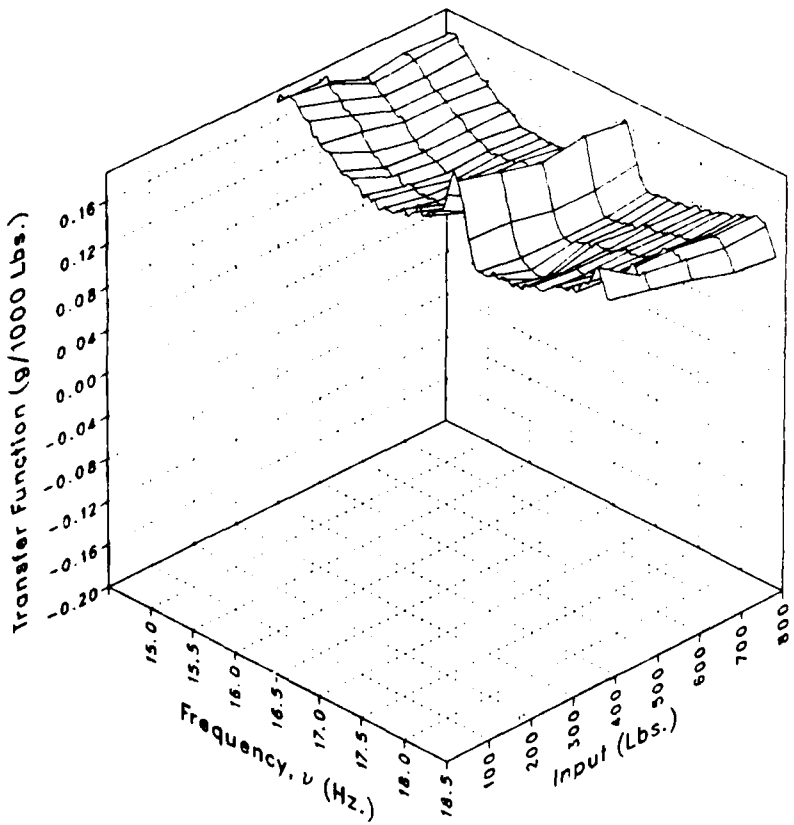

Phase

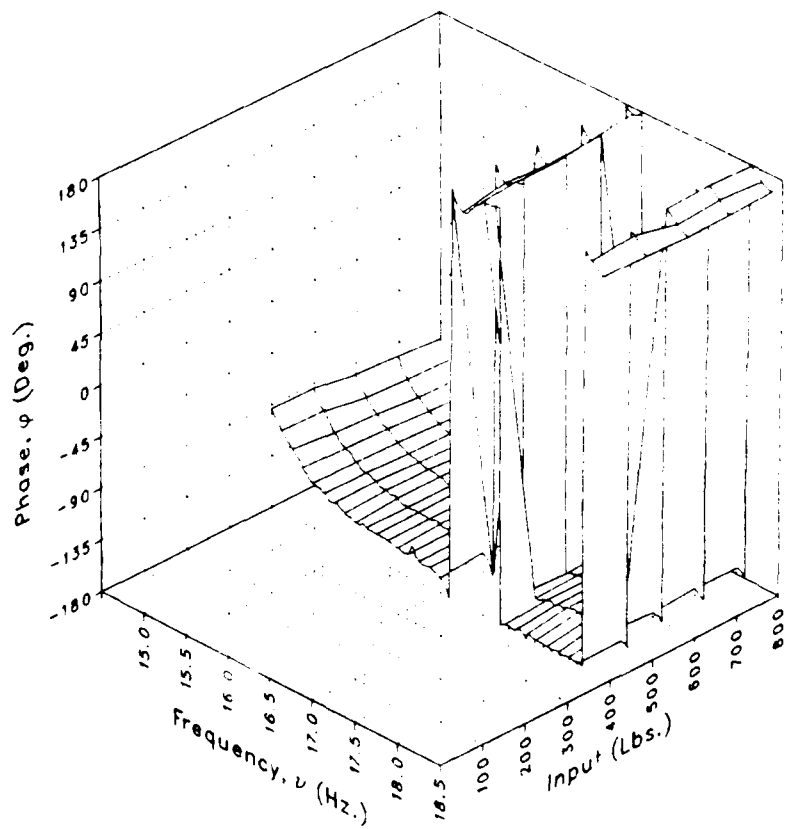

(p) VWGTPRT Concluded.

Figure 4.– Continued.

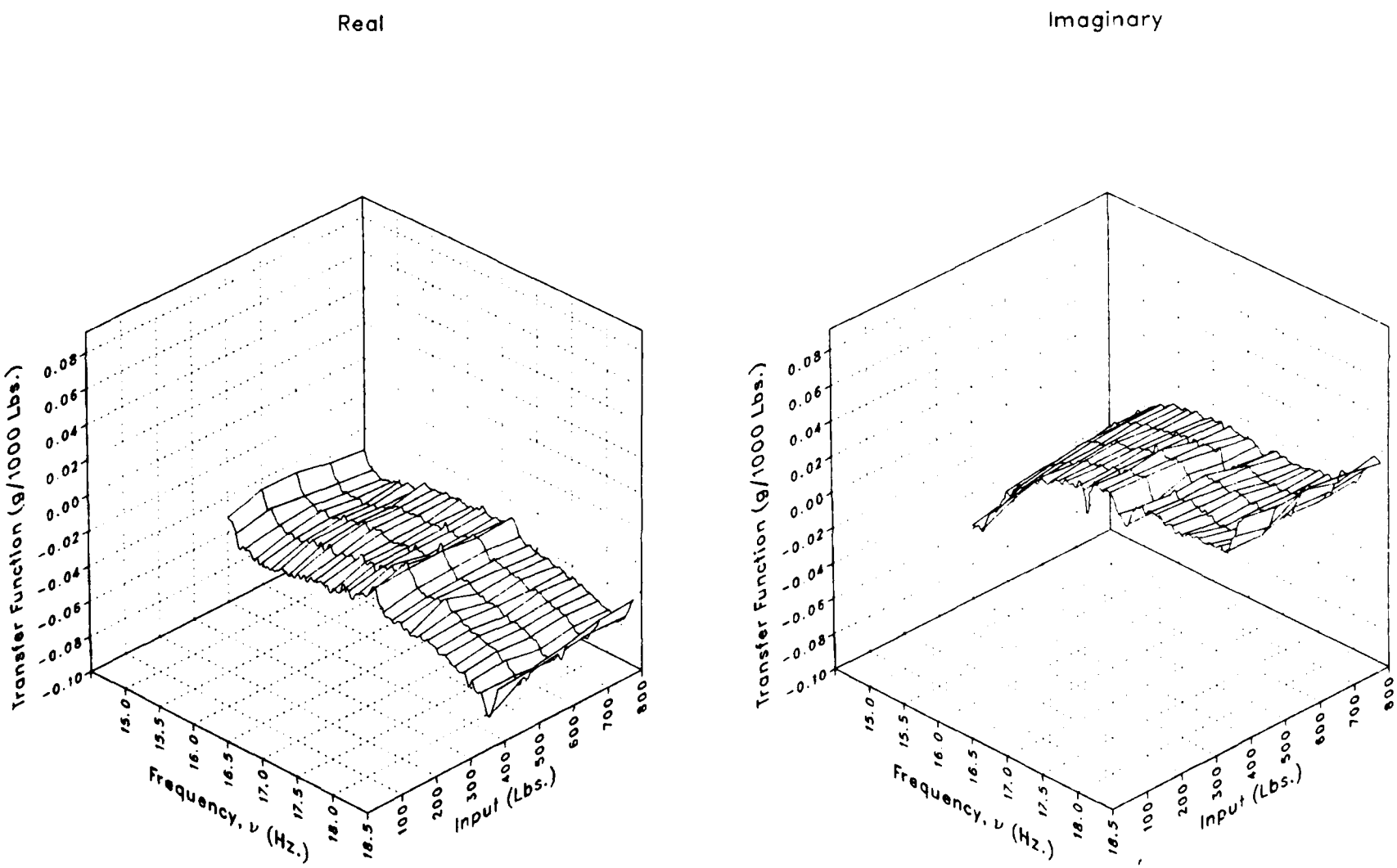

(q) VWGTPLT

Figure 4.– Continued.

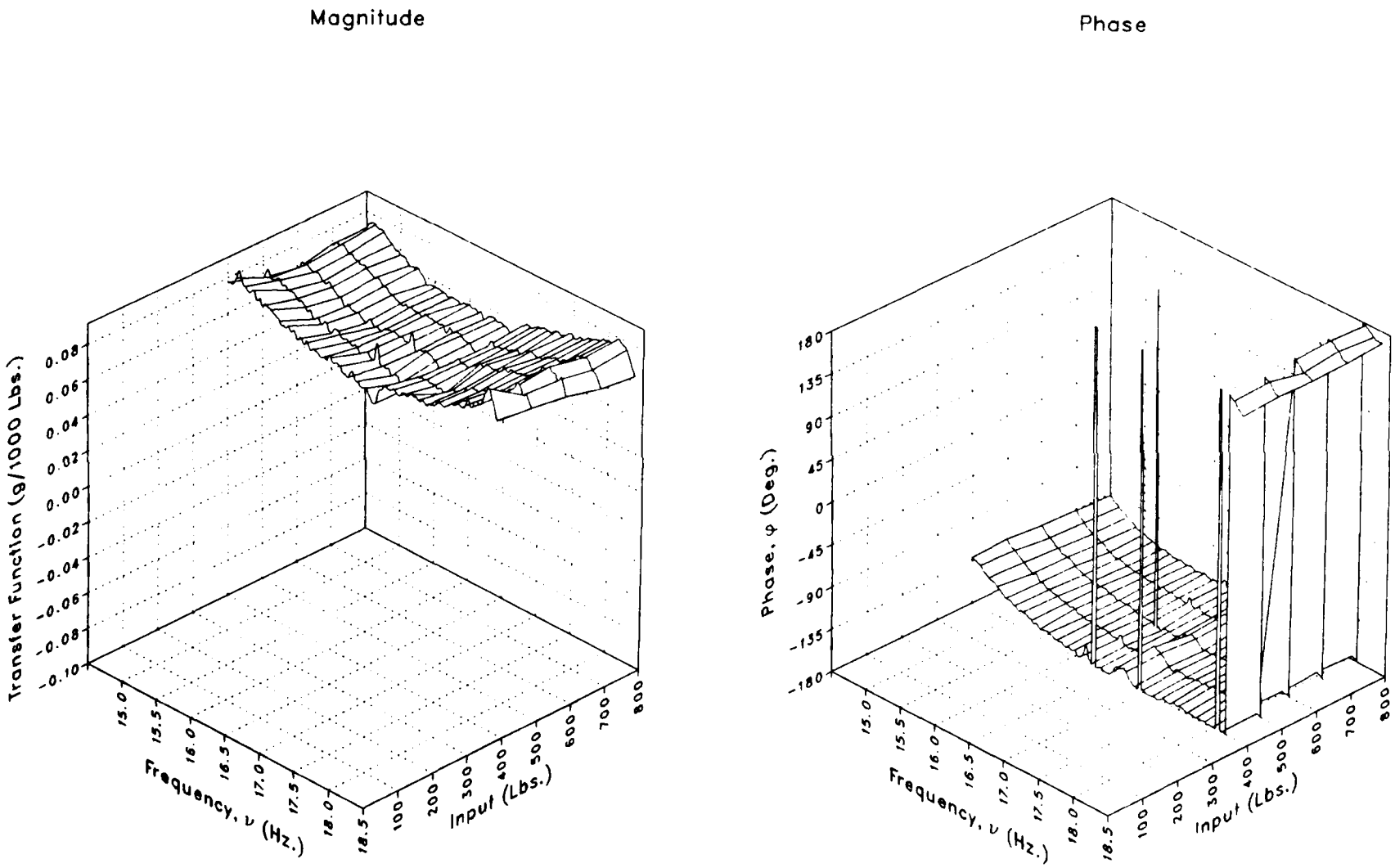

(q) VWGTPLT Concluded.

Figure 4.– Continued.

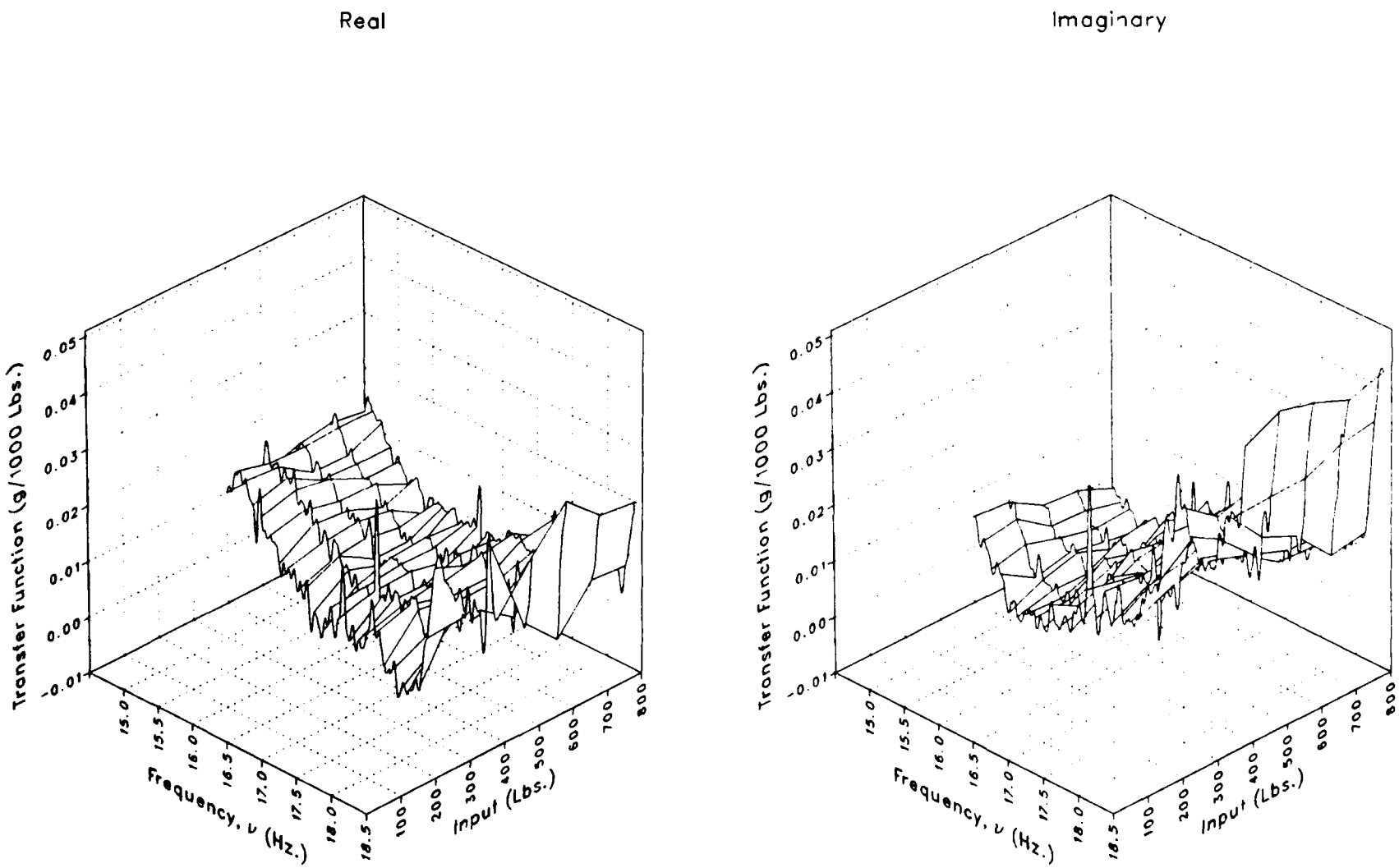

(r) LIGB

Figure 4.– Continued.

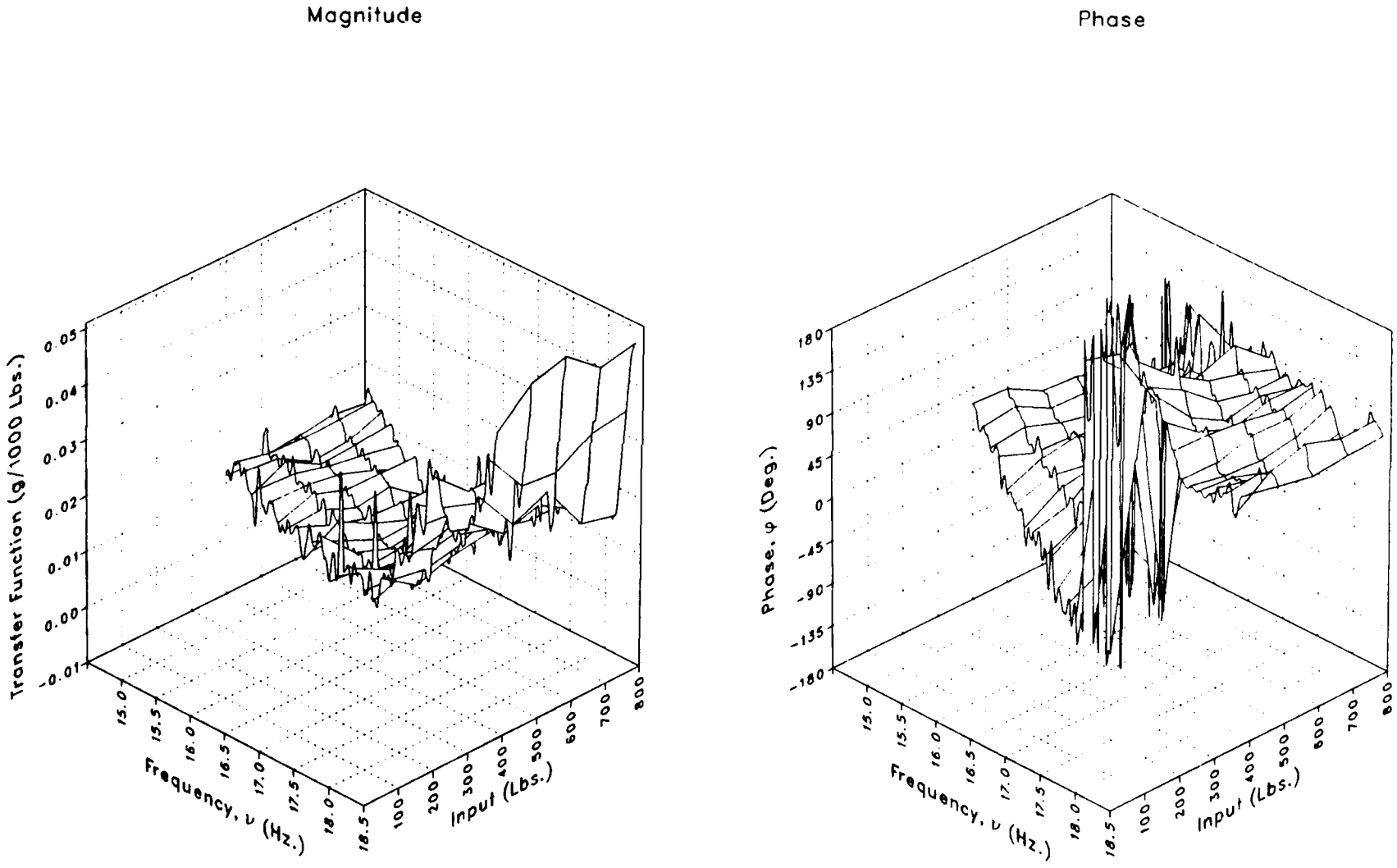

(r) LIGB Concluded.

Figure 4.– Continued.

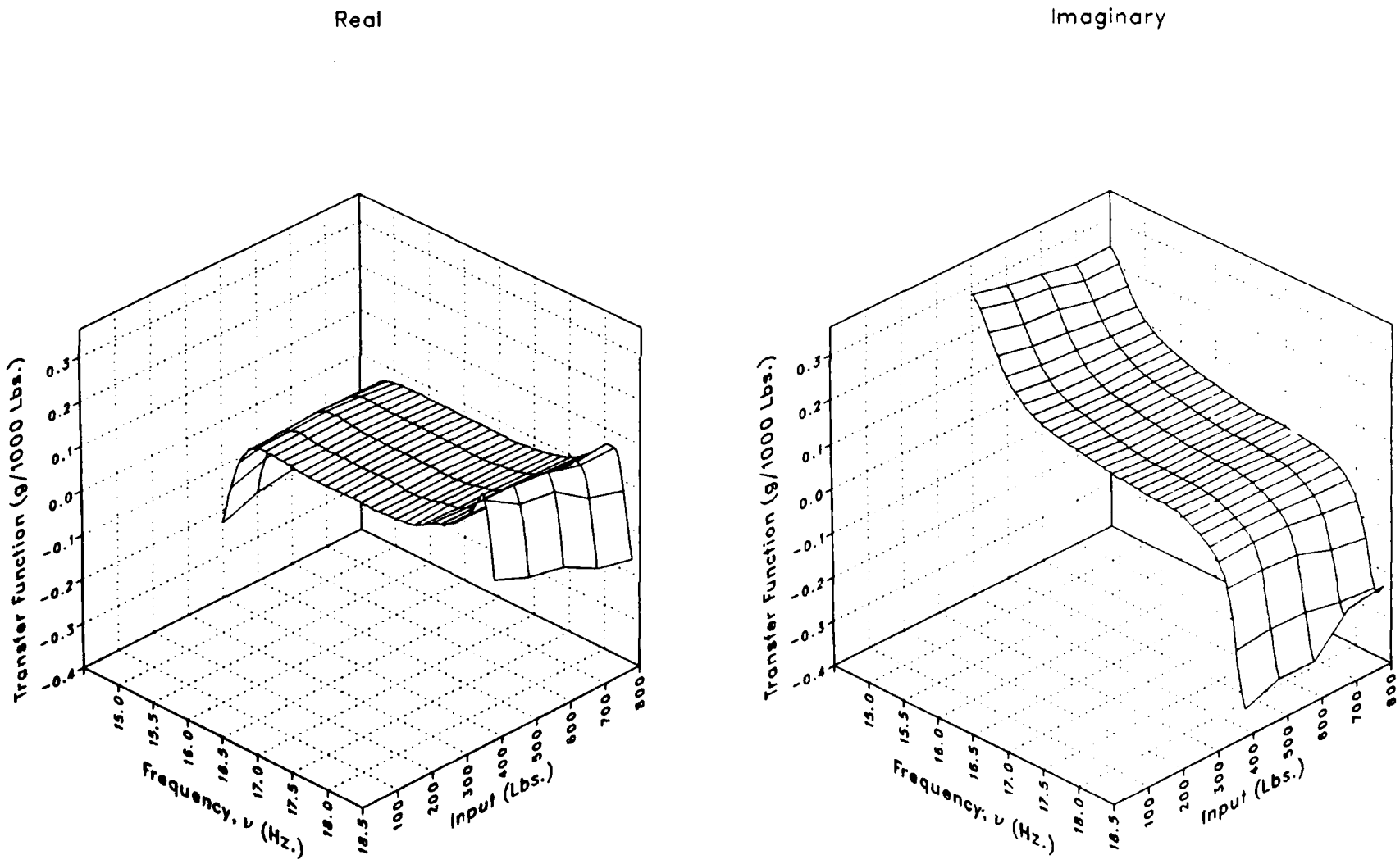

(s) VIGB

Figure 4.– Continued.

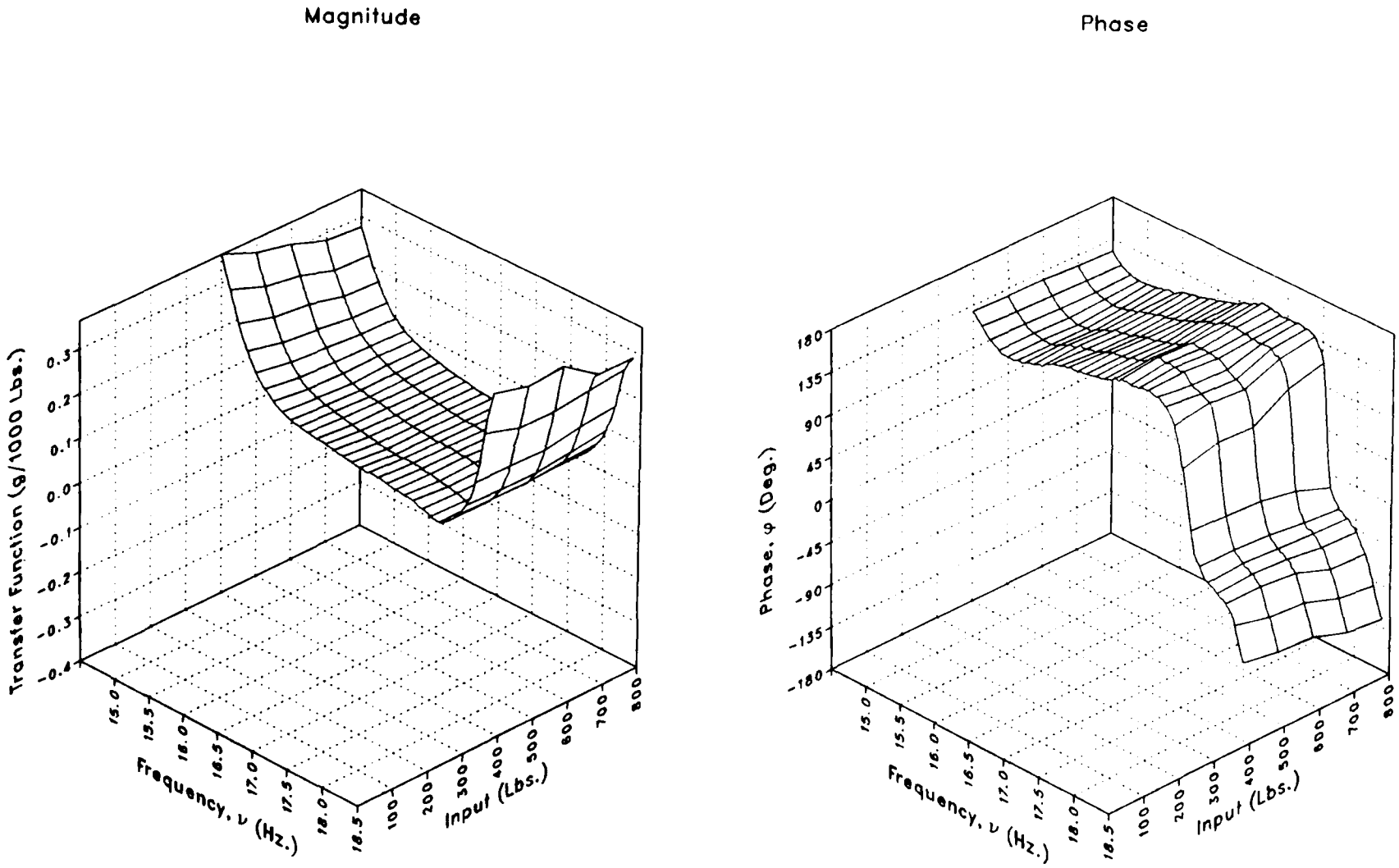

(s) VIGB Concluded.

Figure 4.– Continued.

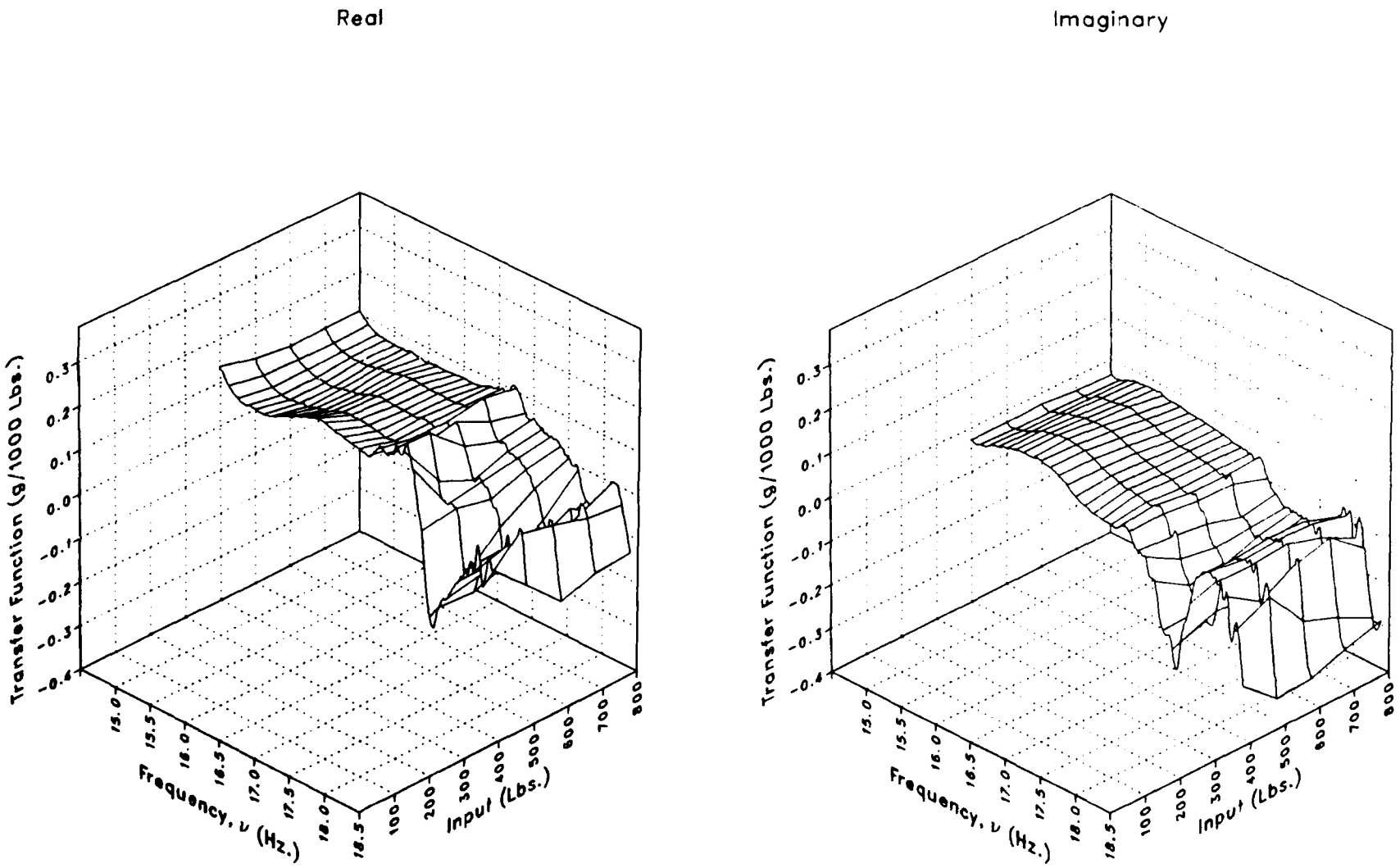

(t) LATTPYLN

Figure 4.– Continued.

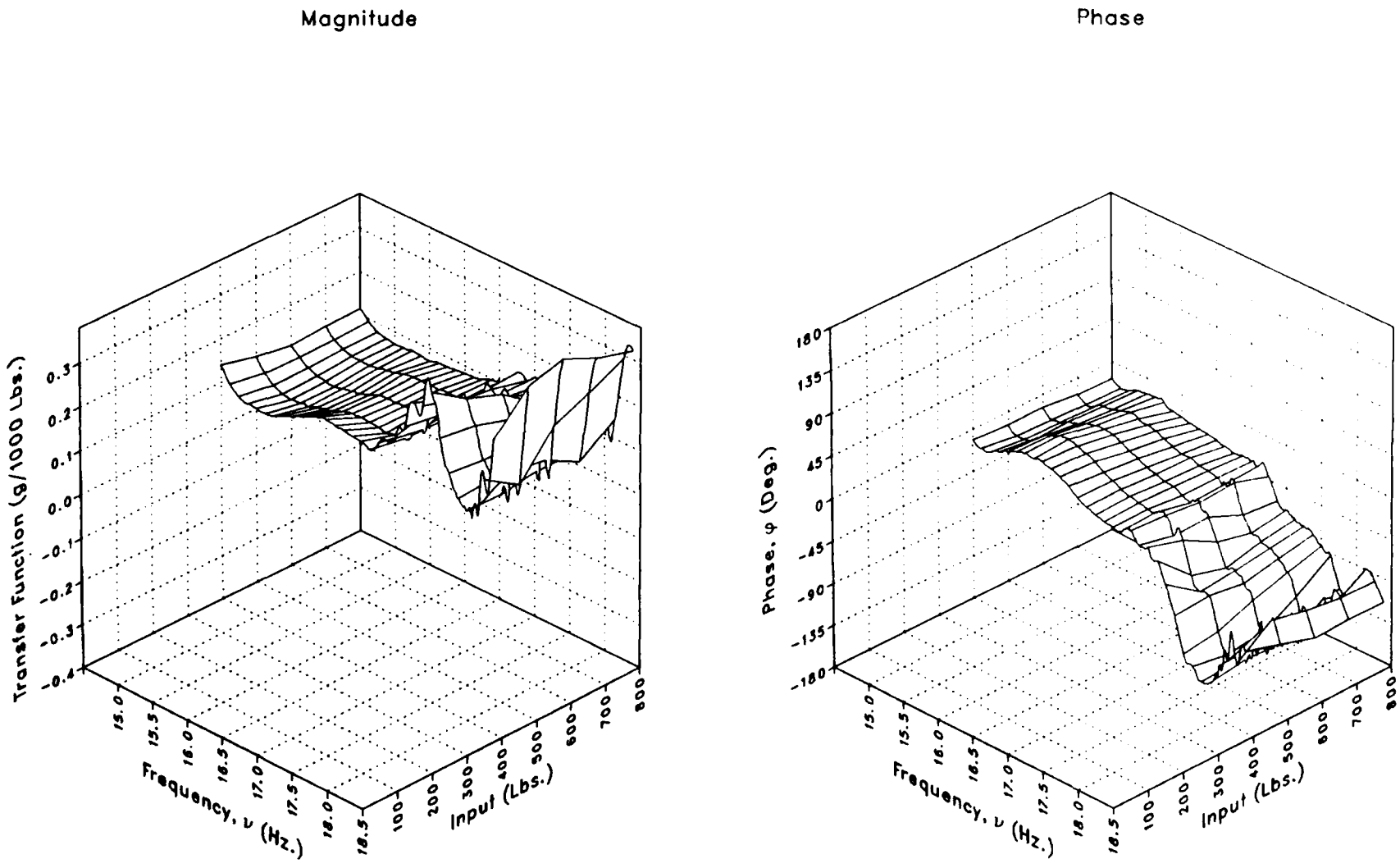

(t) LATTPYLN Concluded.

Figure 4.– Continued.

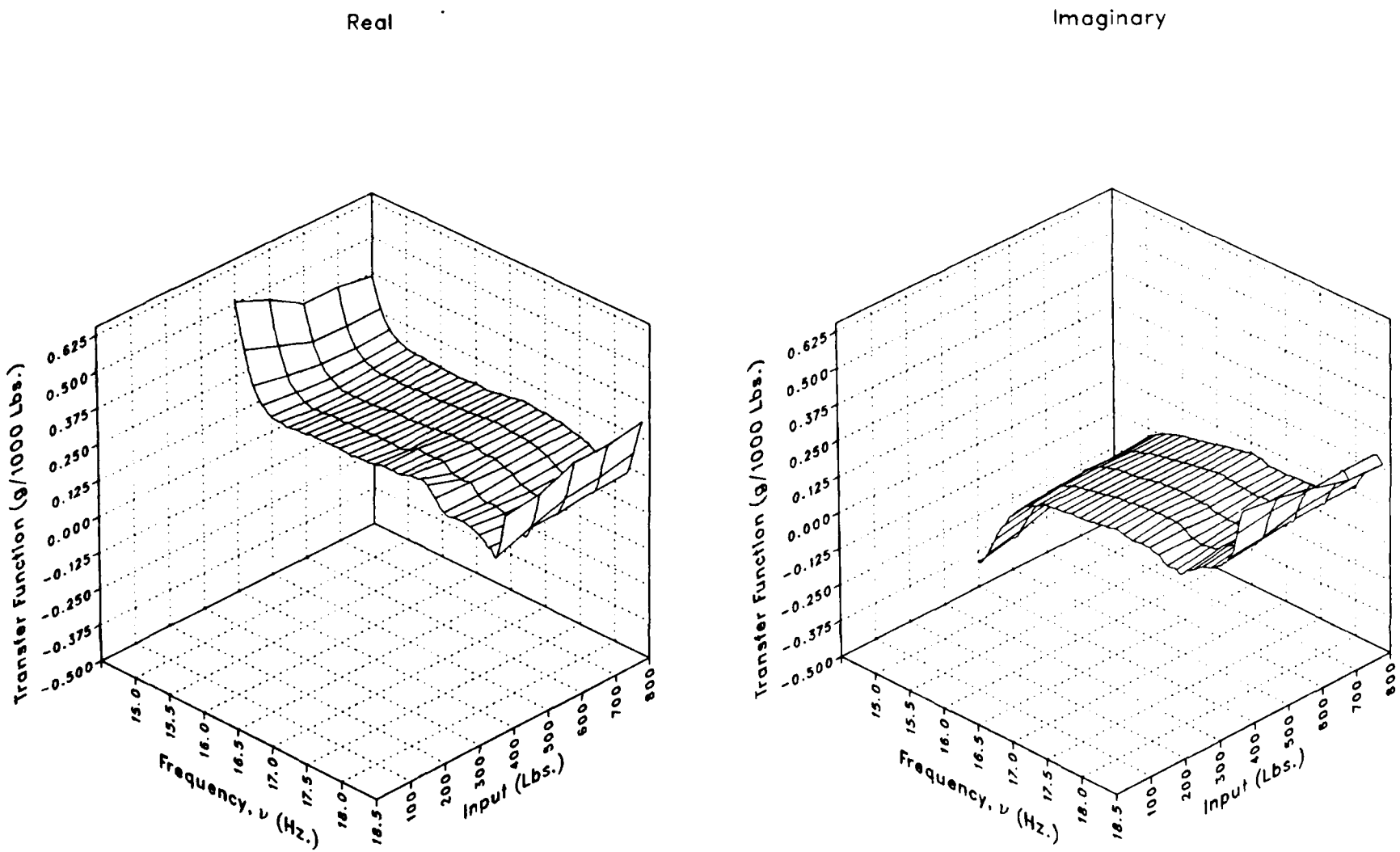

(u) VTTPYLON

Figure 4.– Continued.

Magnitude

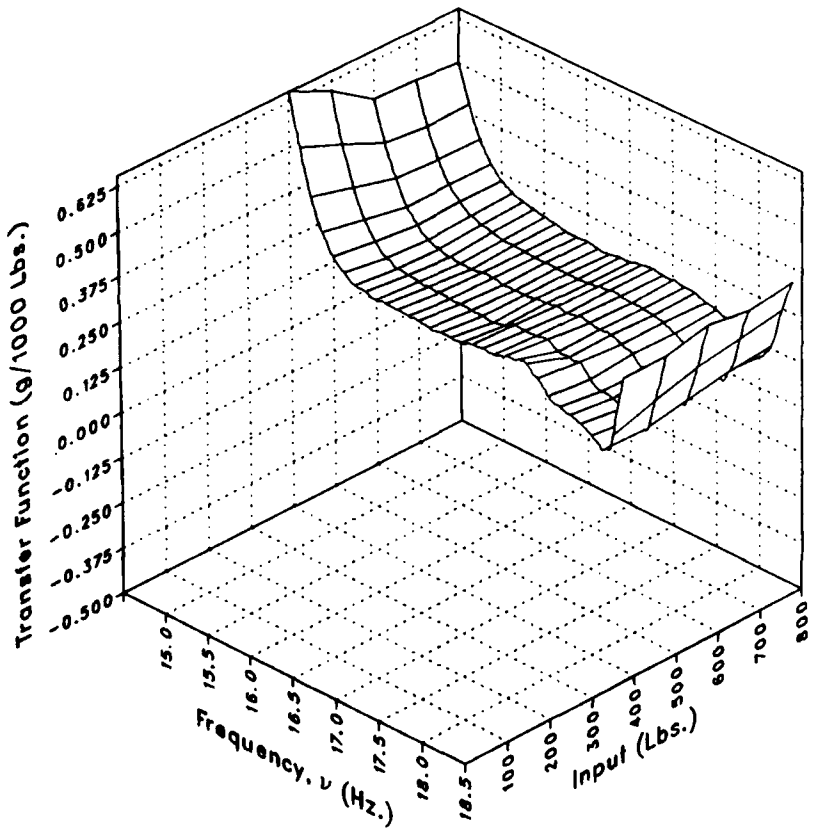

Phase

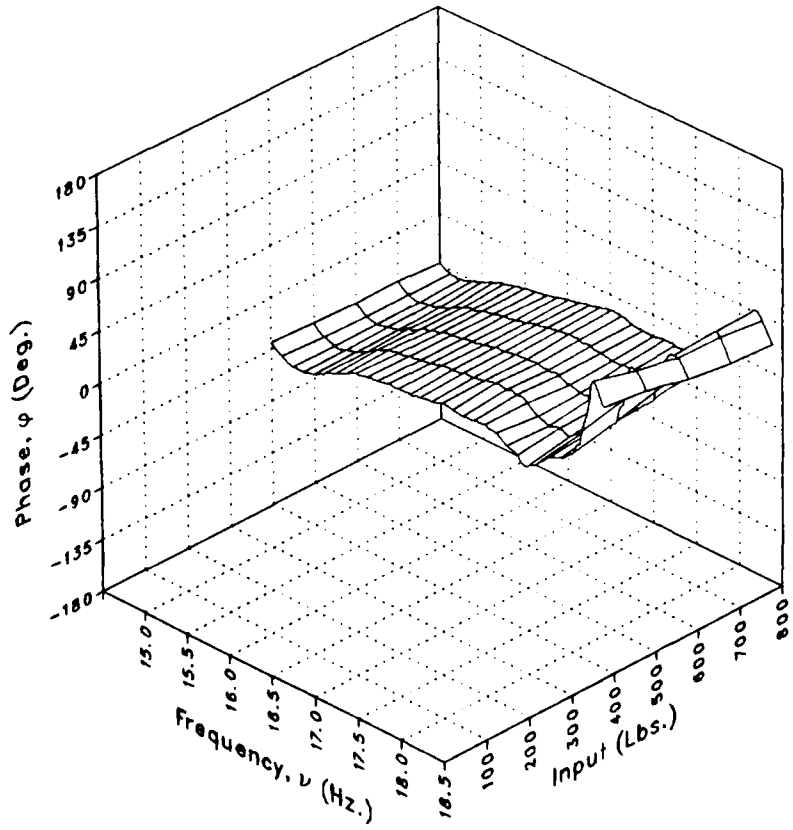

(u) VTTPYLON Concluded.

Figure 4.– Continued.

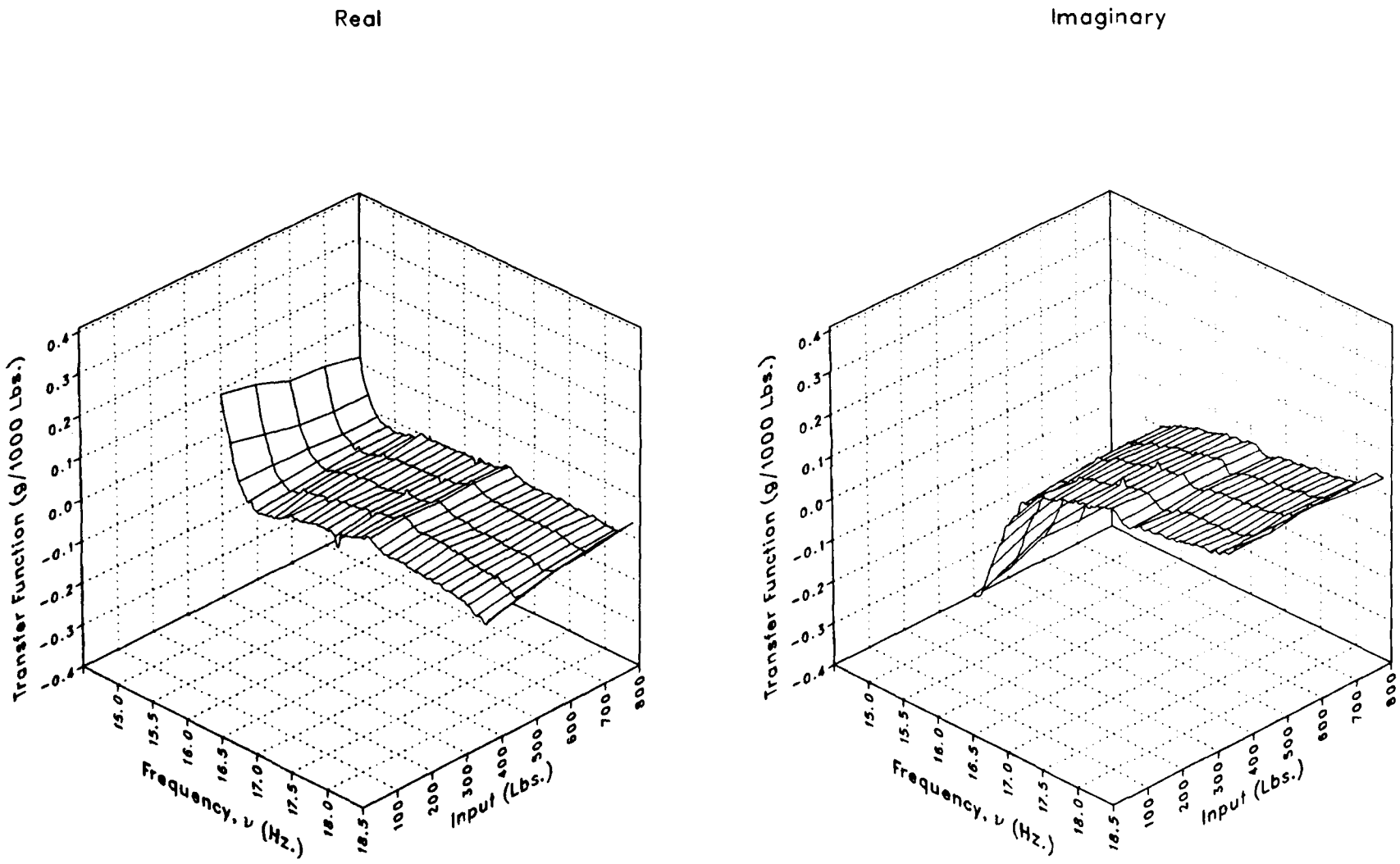

(v) XMRFLV

Figure 4.– Continued.

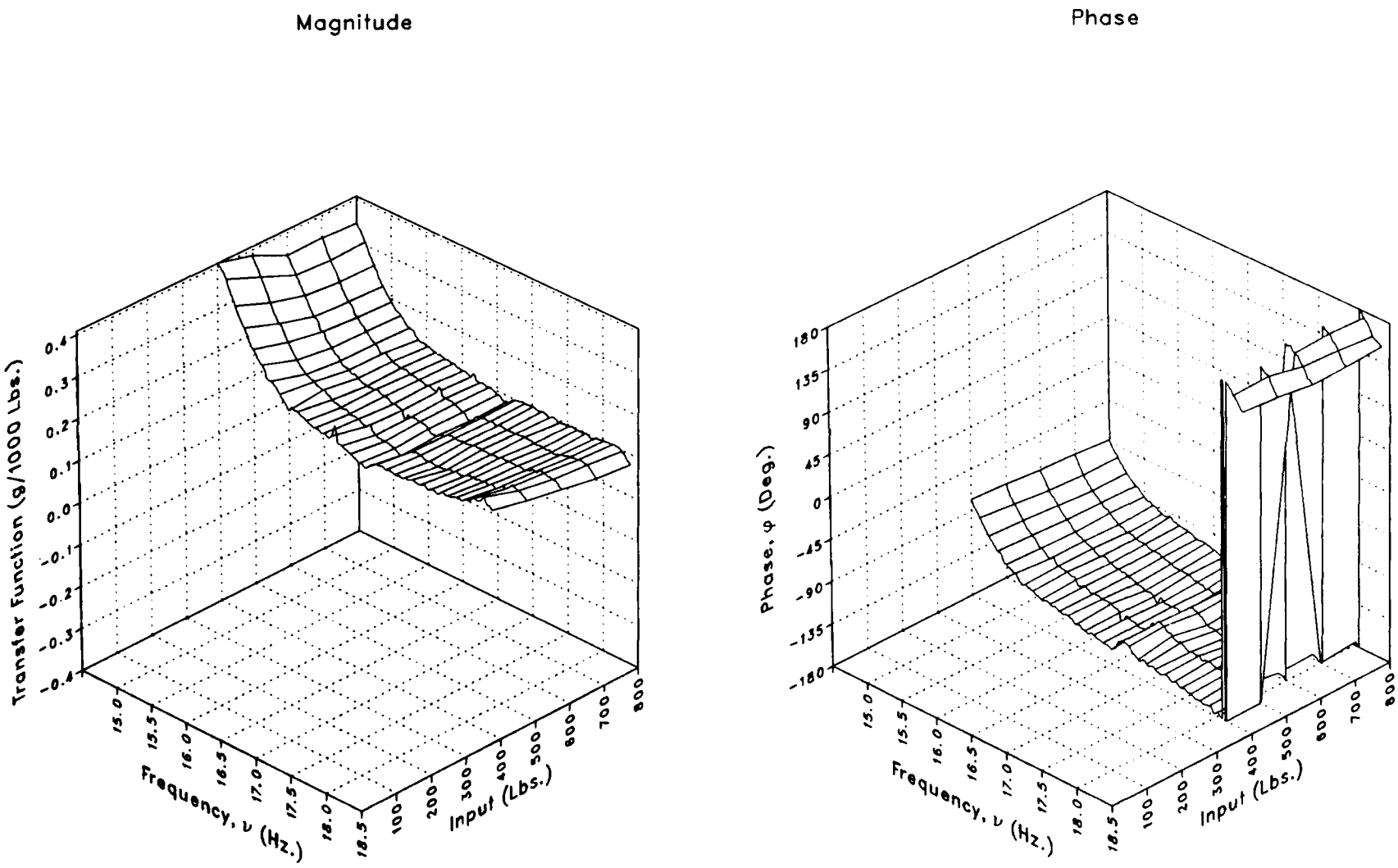

(v) XMRFLV Concluded.

Figure 4.– Continued.

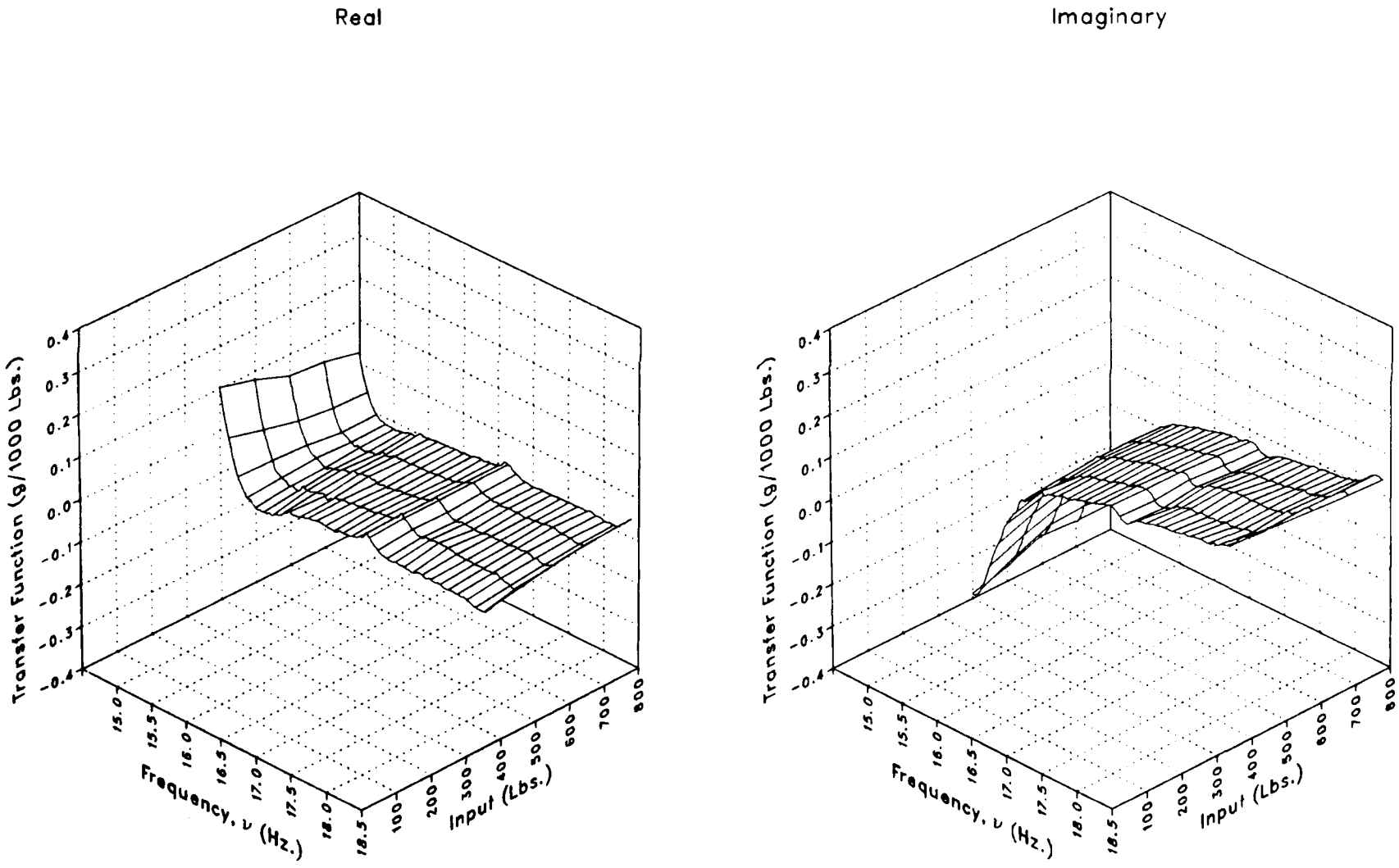

(w) XMRFRV

Figure 4.– Continued.

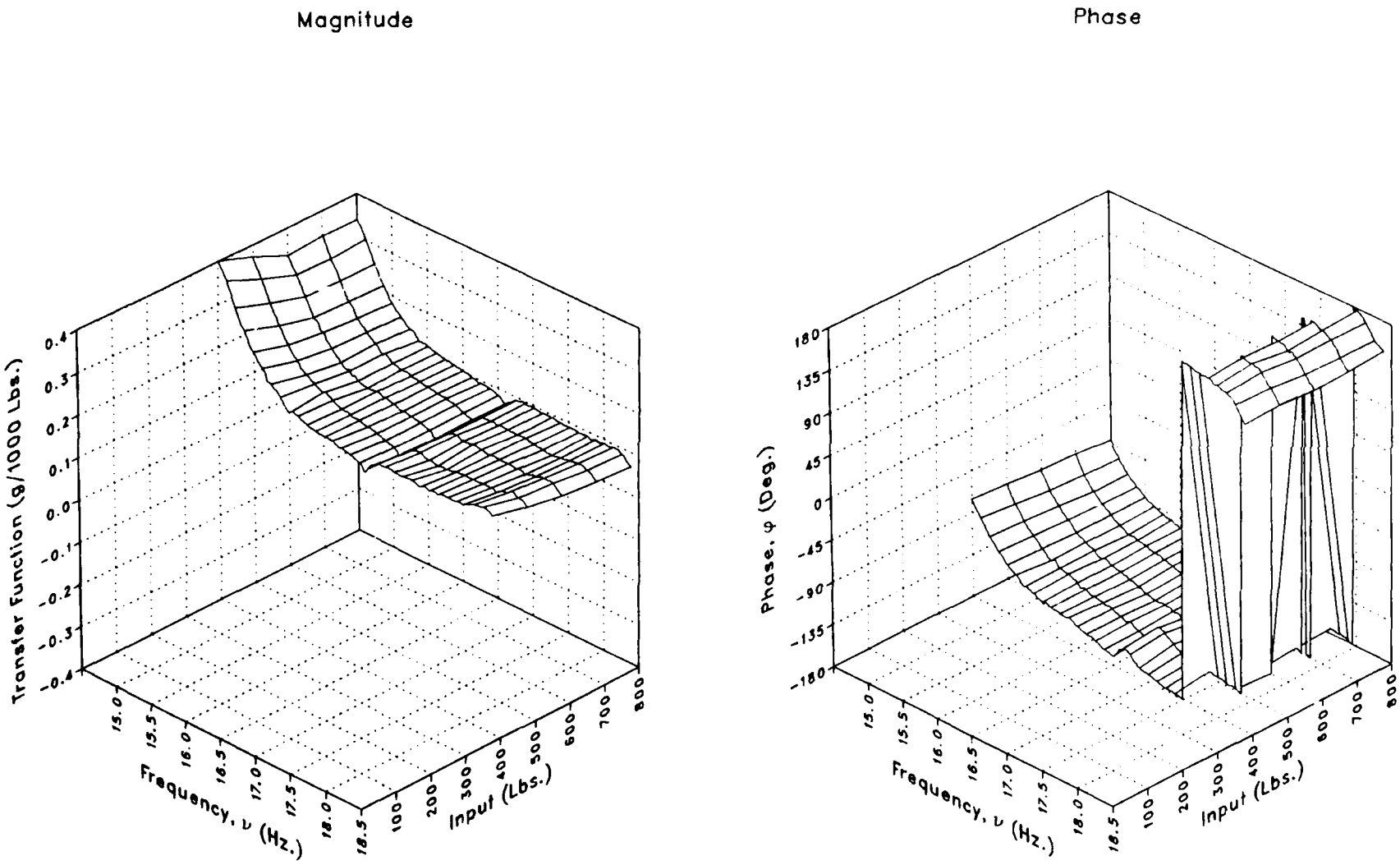

(w) XMRFRV Concluded.

Figure 4.– Continued.

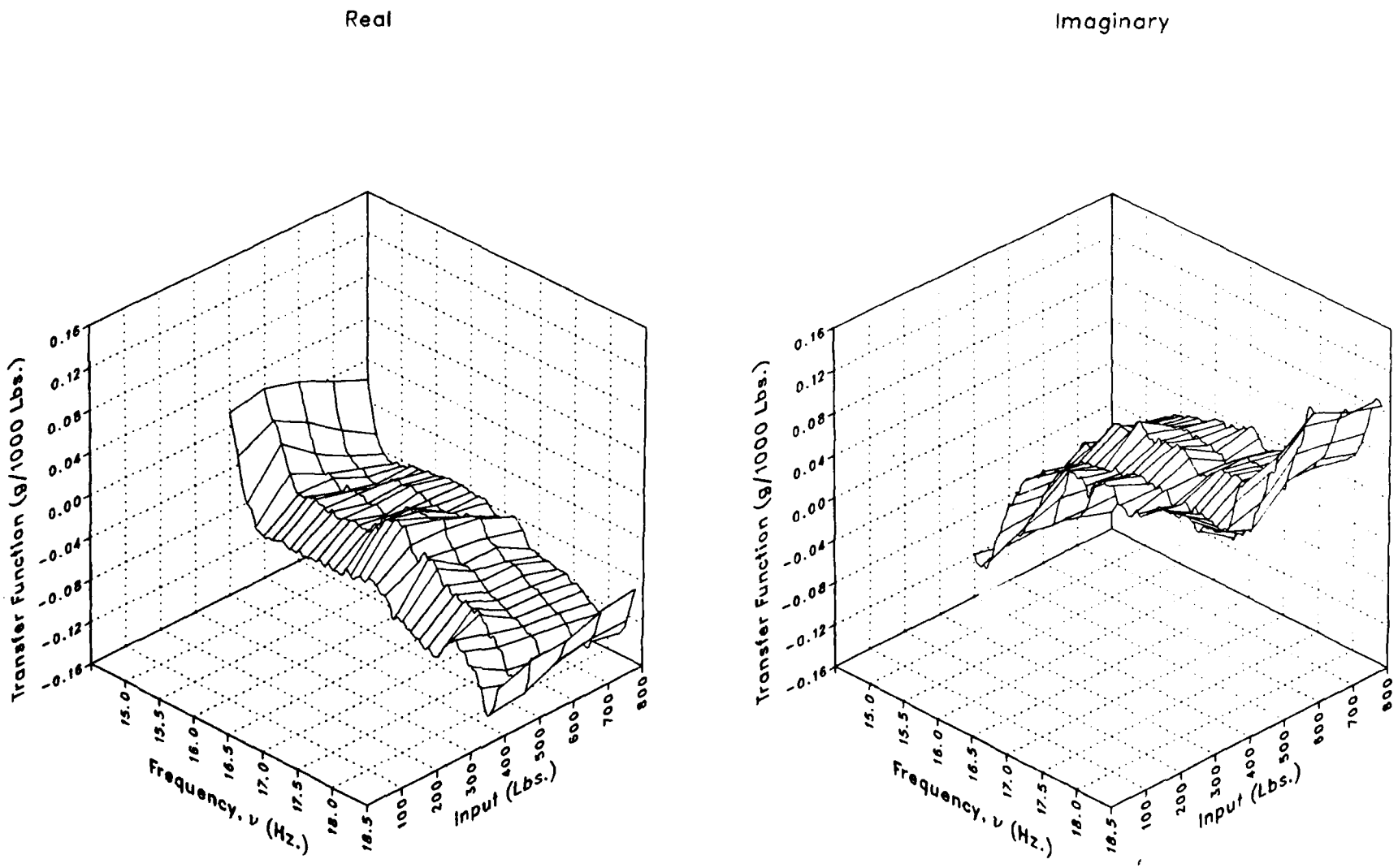

(x) S222FLRV

Figure 4.– Continued.

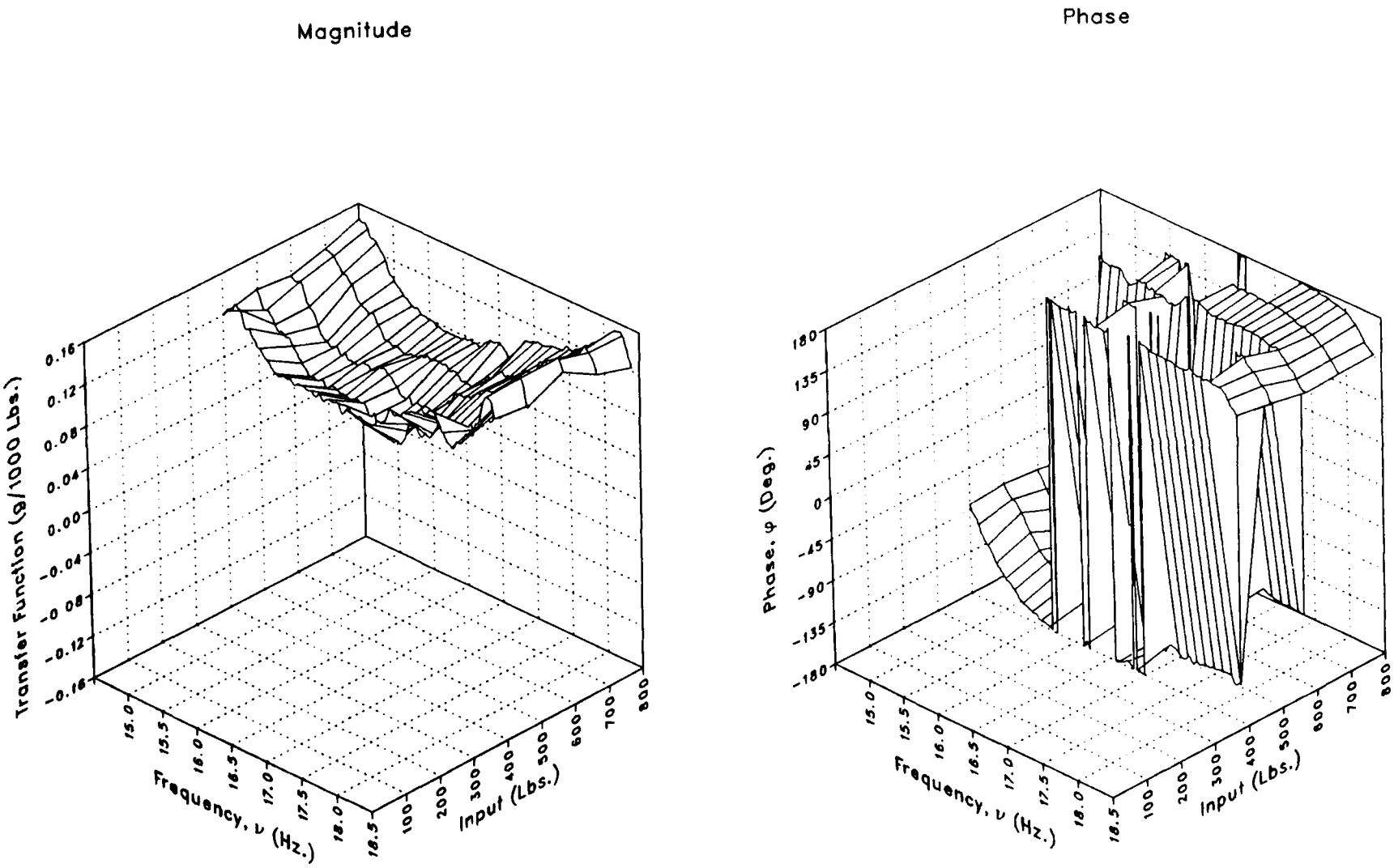

(x) S222FLRV Concluded.

Figure 4.– Continued.

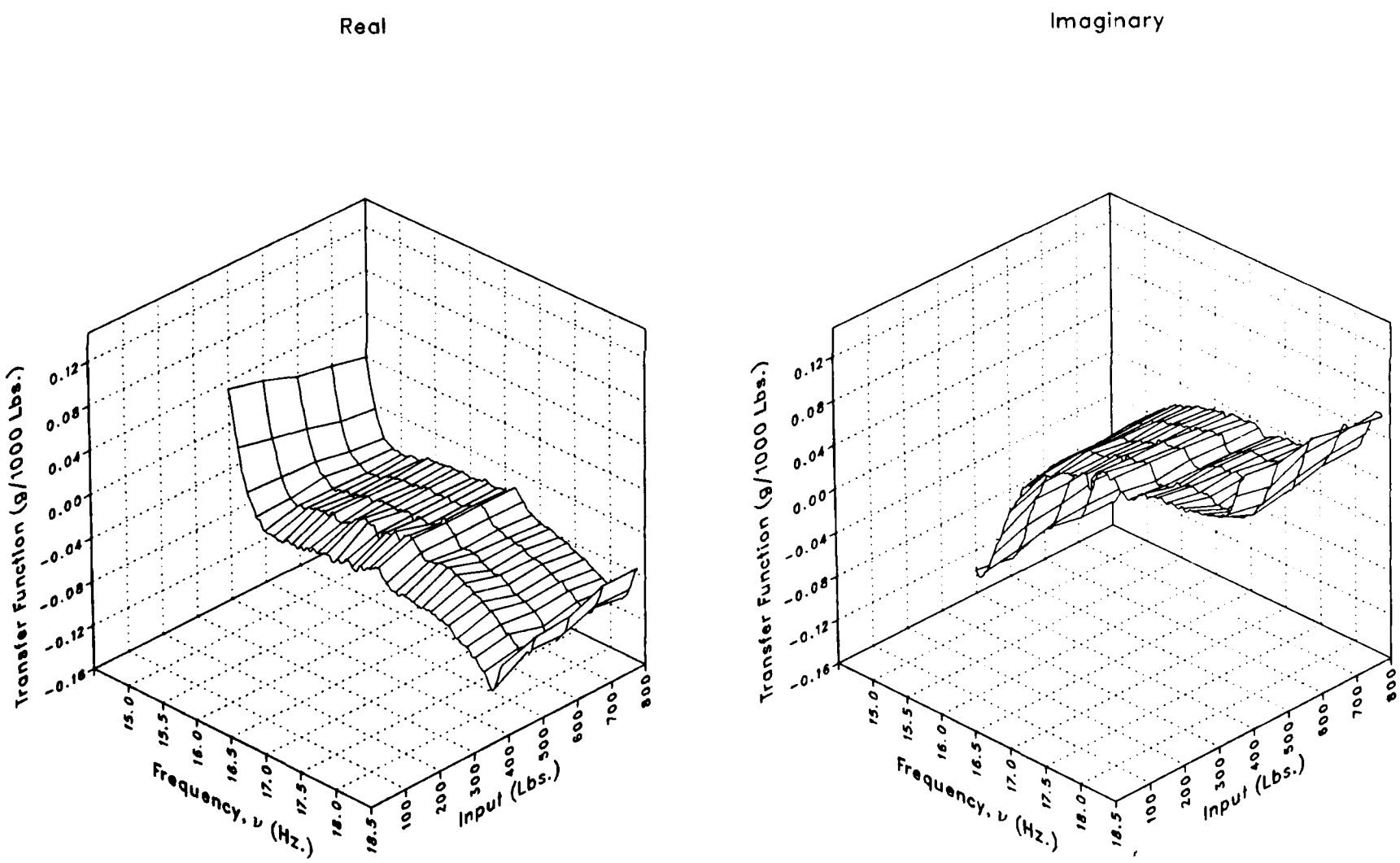

(y) S222FLLV

Figure 4.– Continued.

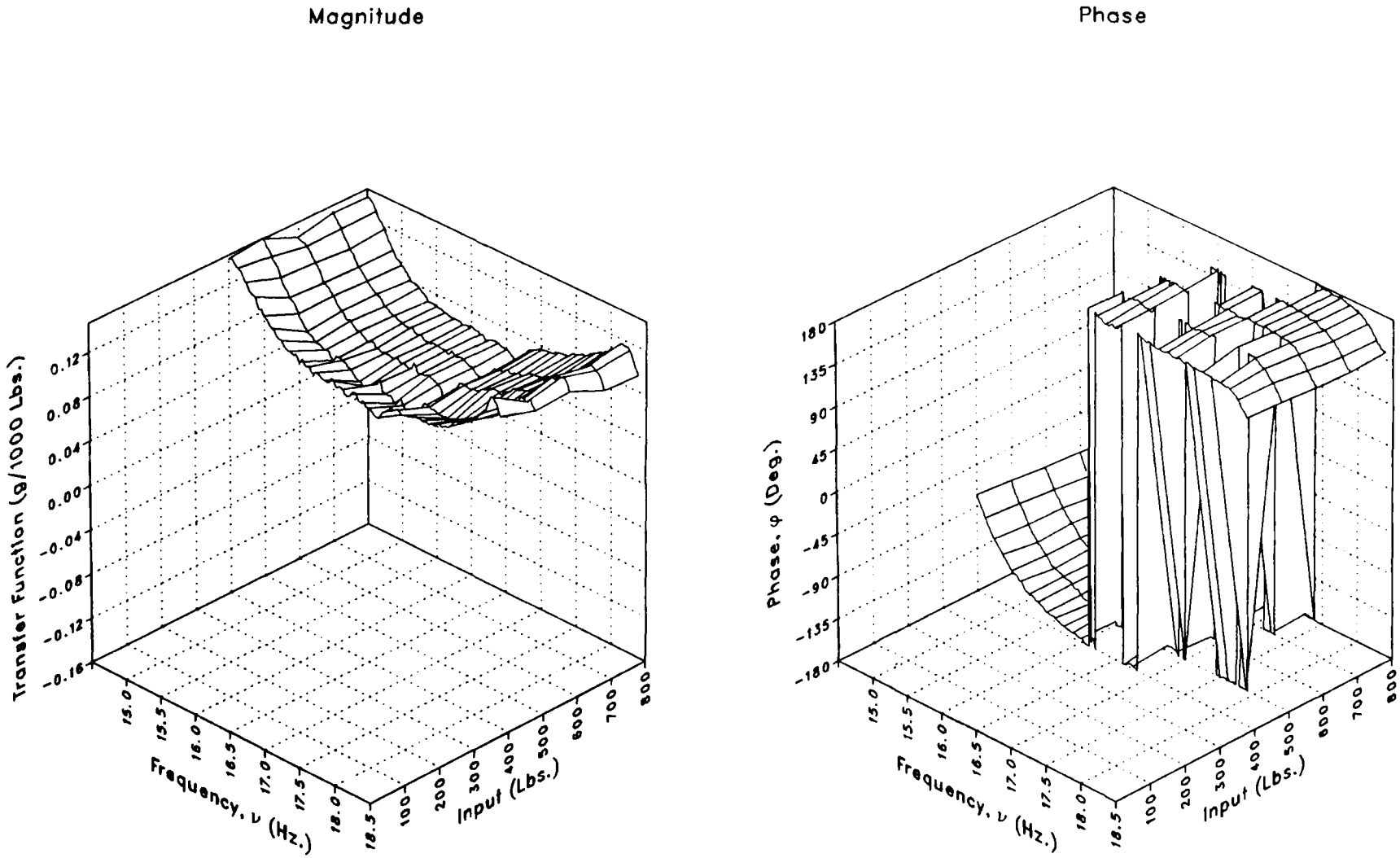

(y) S222FLLV Concluded.

Figure 4.– Continued.

Real

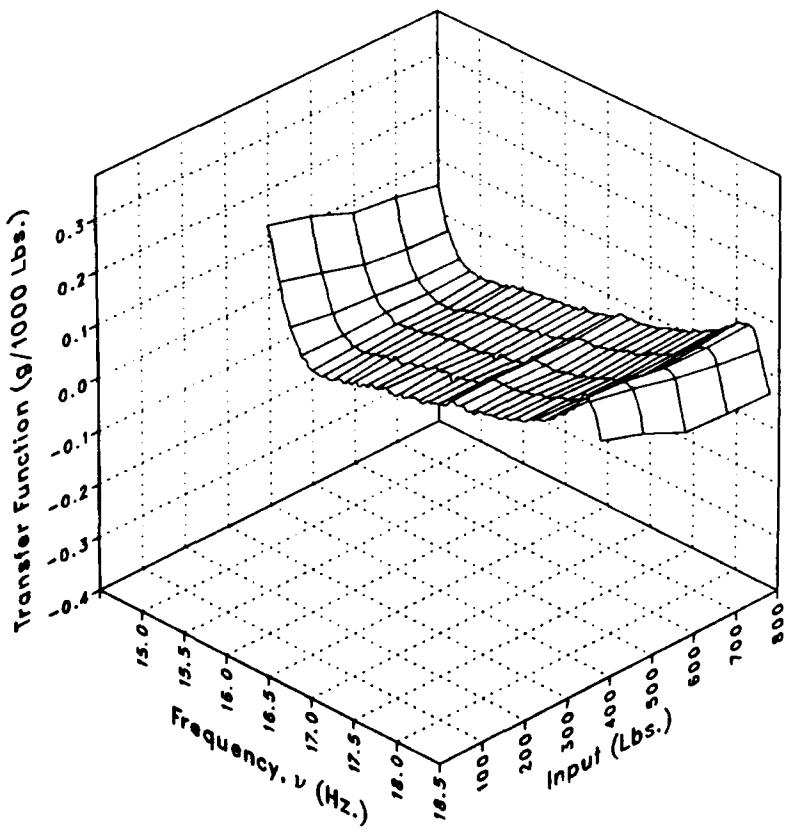

Imaginary

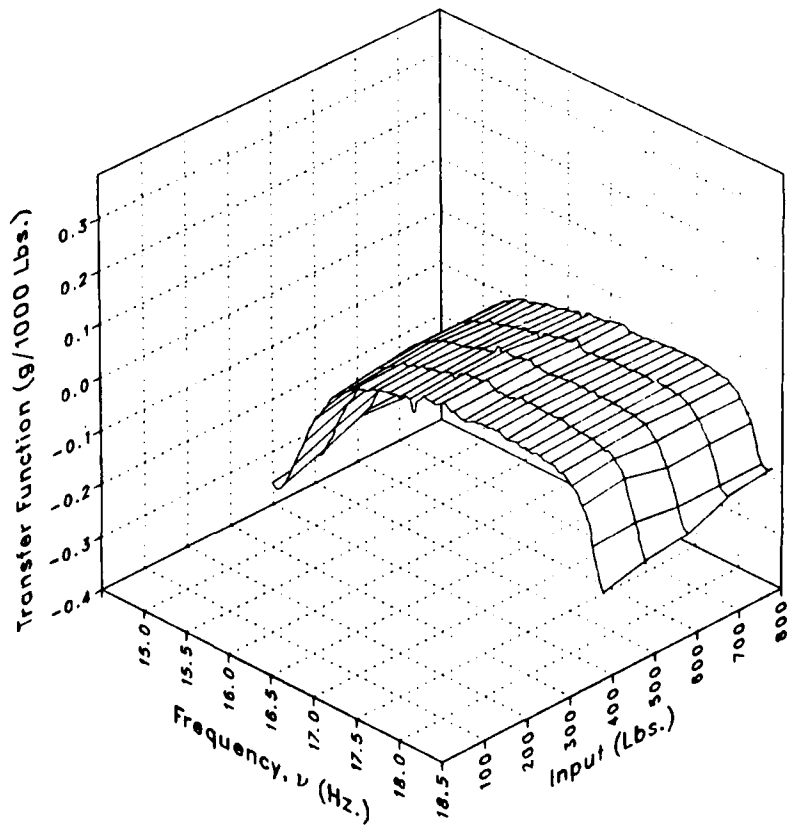

(z) S450FLV

Figure 4.– Continued.

Magnitude

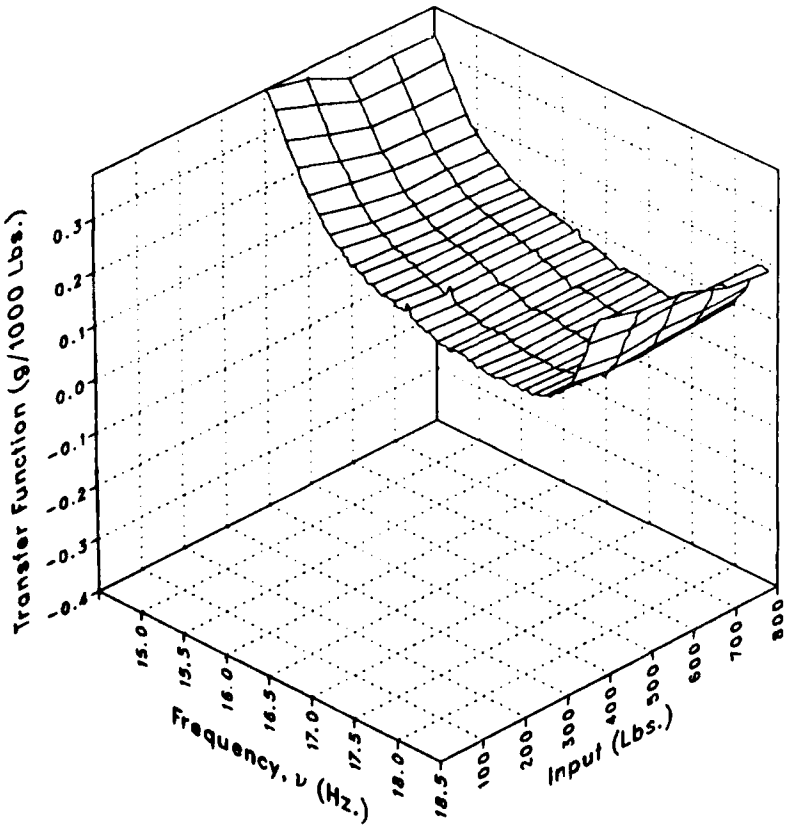

Phase

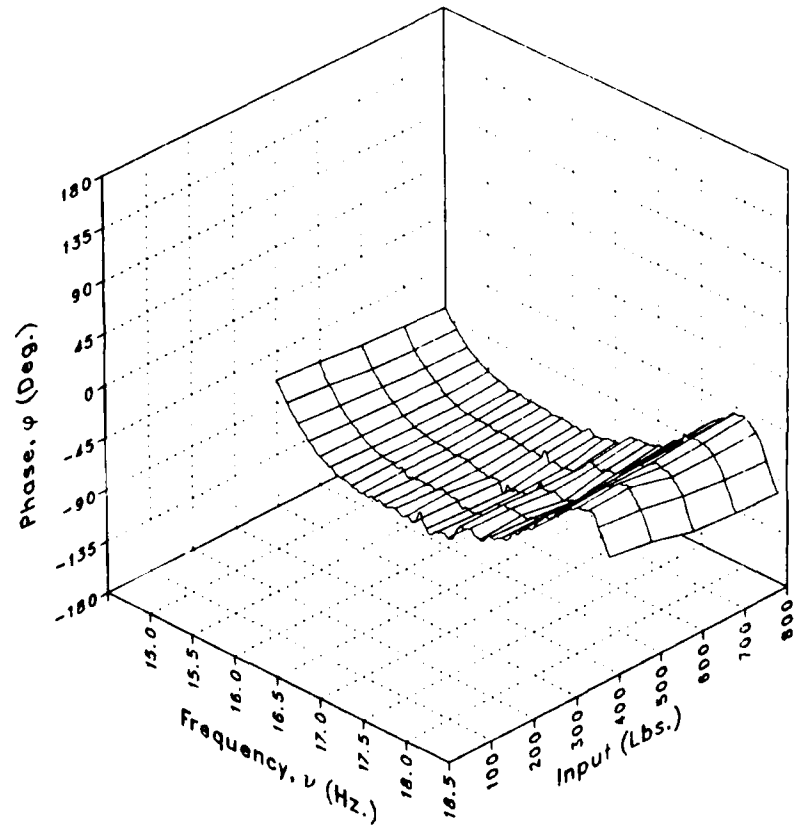

(z) S450FLV Concluded.

Figure 4.– Continued.

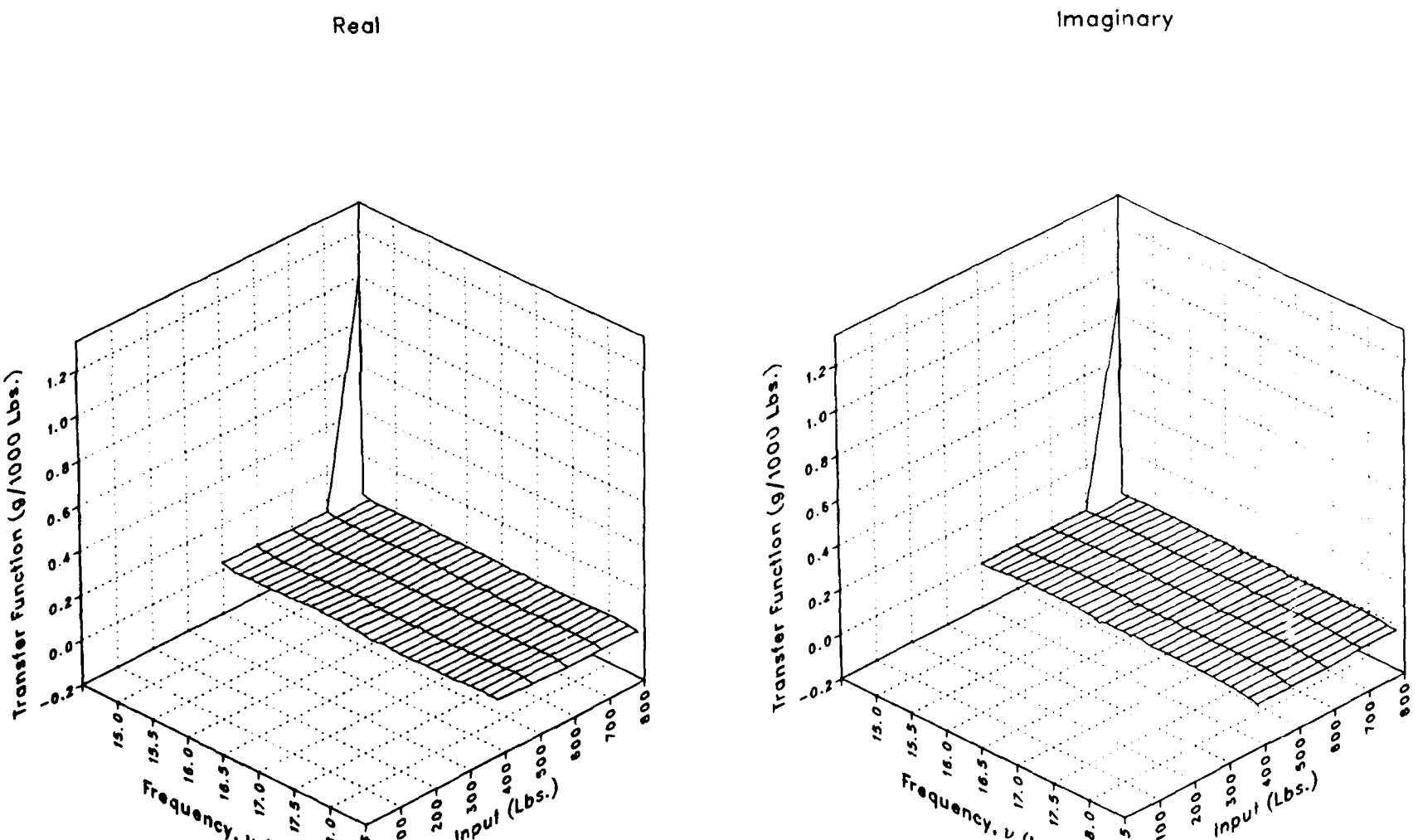

(aa) S450FLL

Figure 4.– Continued.

Magnitude

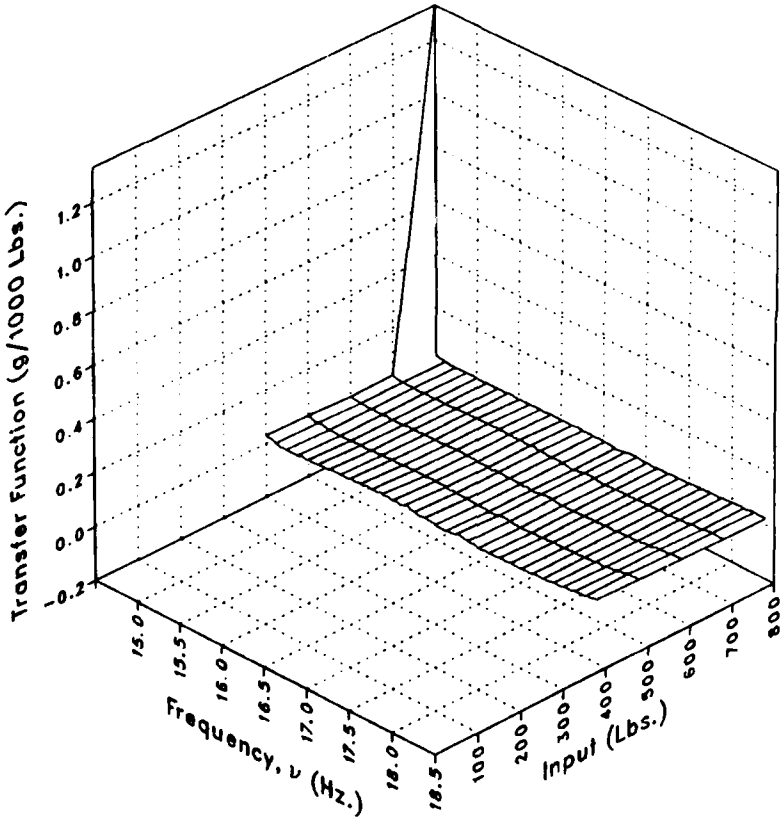

Phase

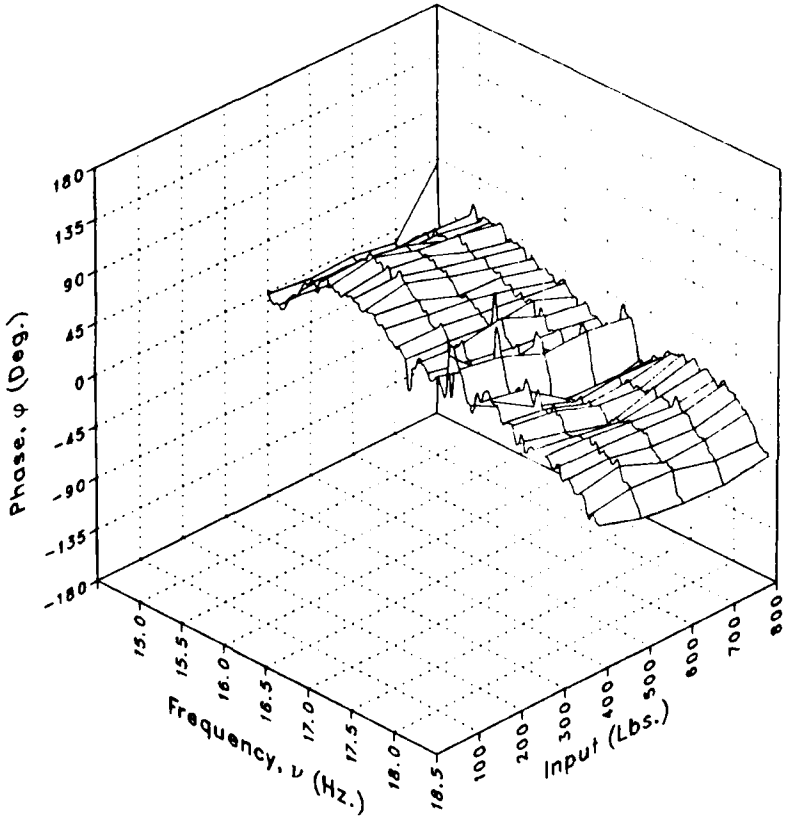

(aa) S450FLL Concluded.

Figure 4.– Continued.

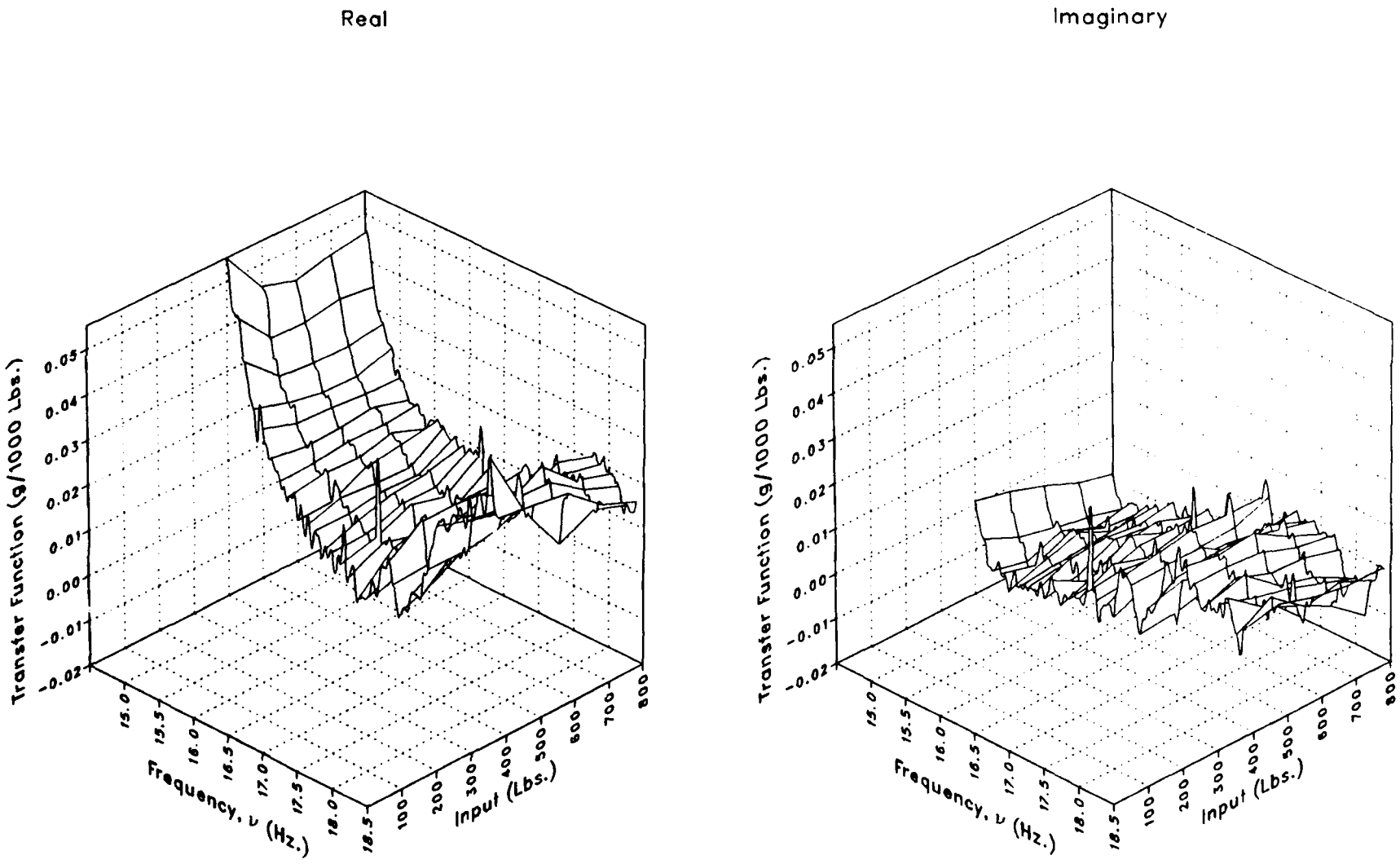

(bb) S450OVRL

Figure 4.– Continued.

Magnitude

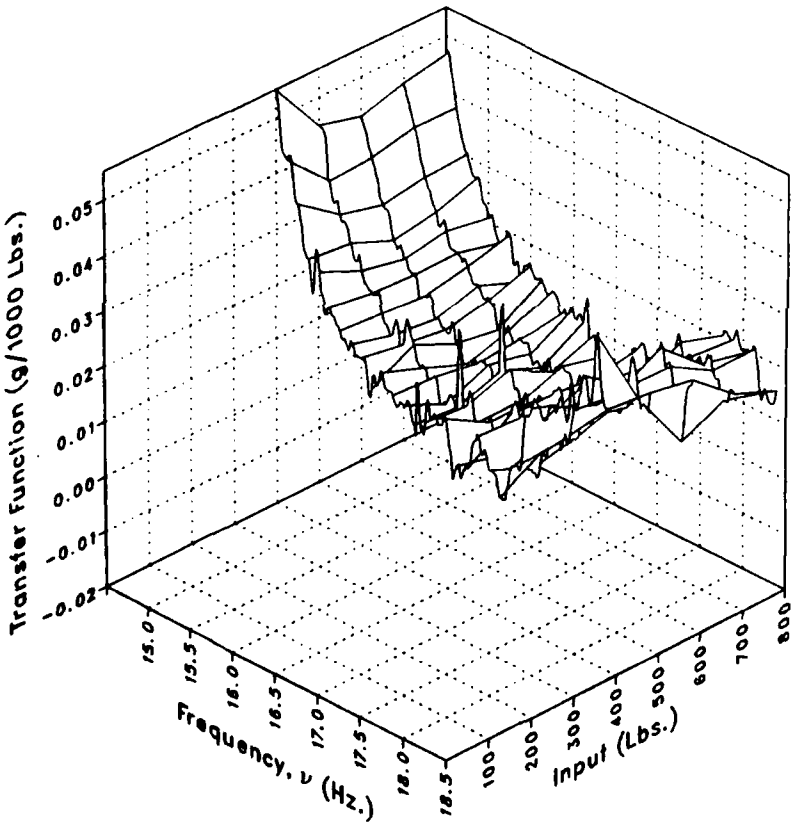

Phase

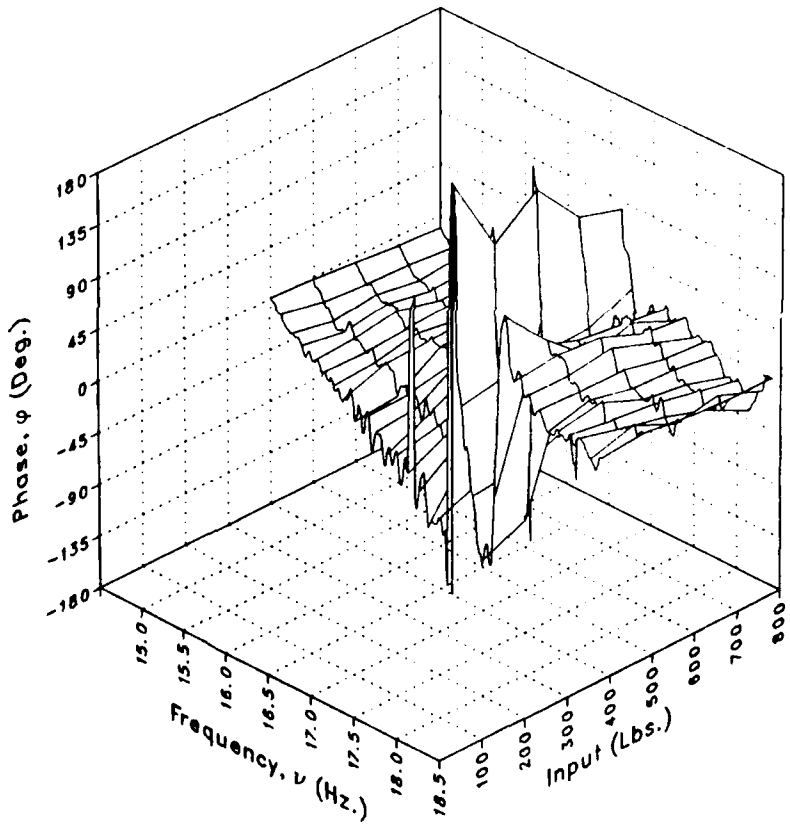

(bb) S450OVRL Concluded.

Figure 4.– Concluded.

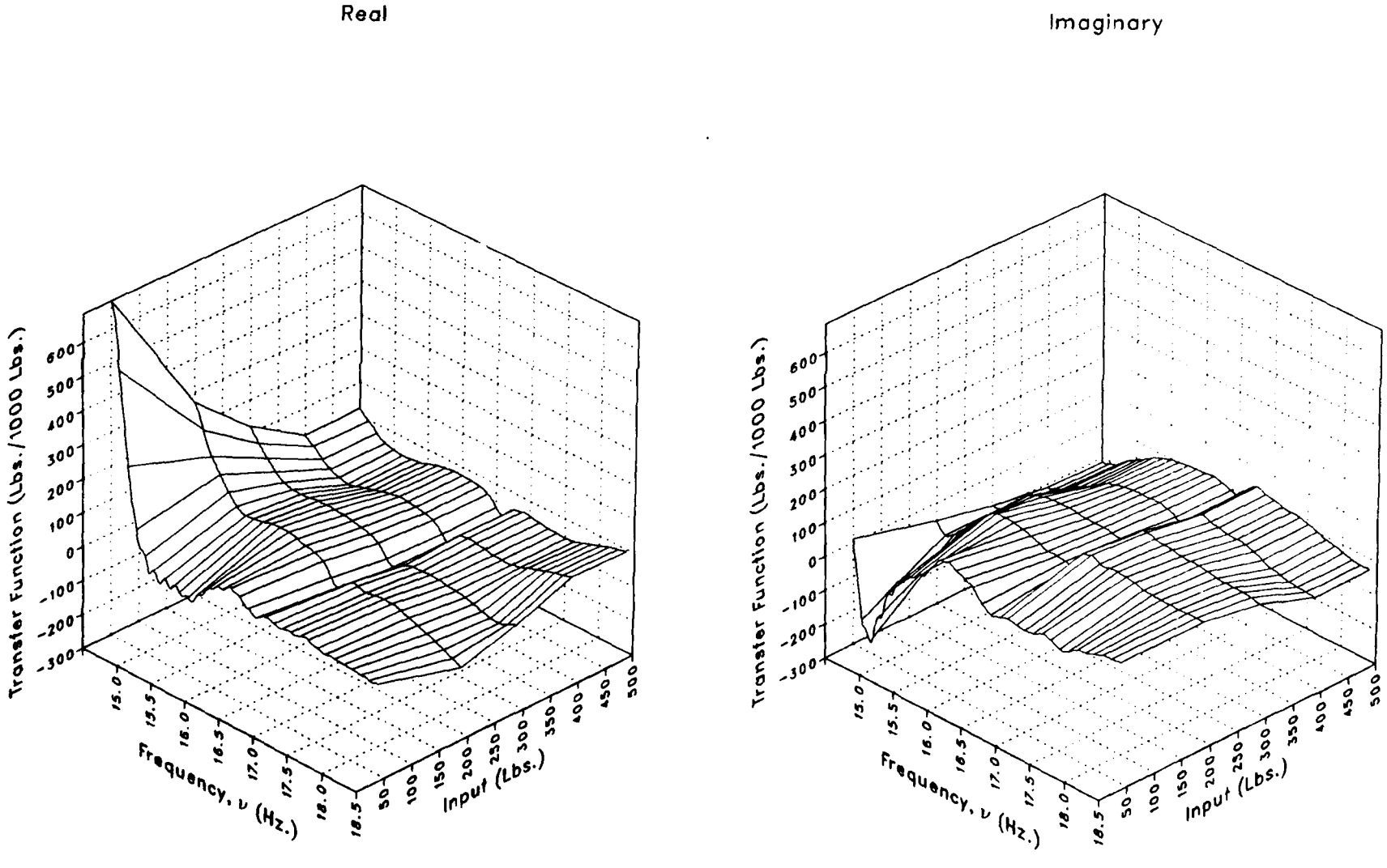

(a) MRDRAG

Figure 5.– Roll forcing.

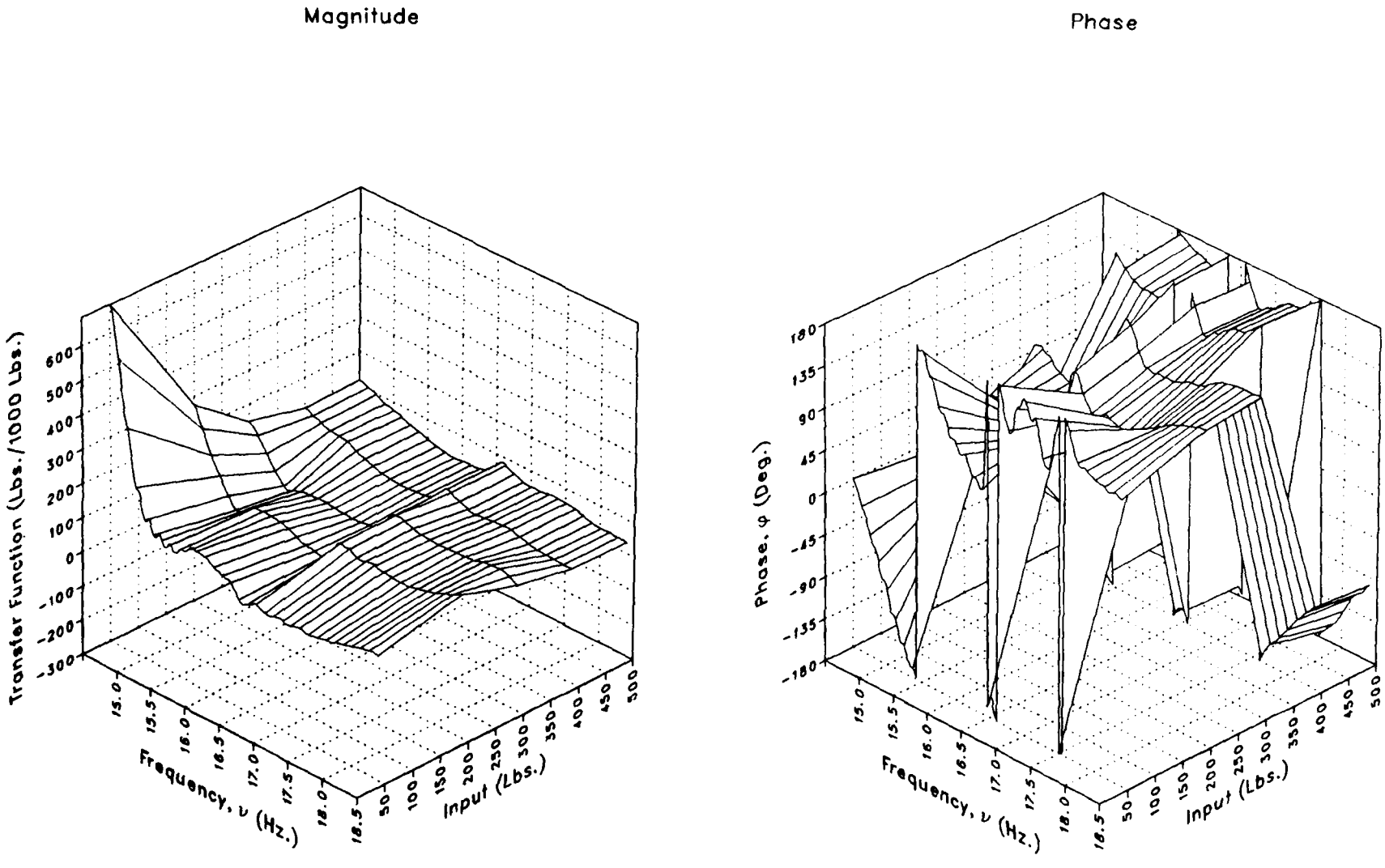

(a) MRDRAG Concluded.

Figure 5.– Continued.

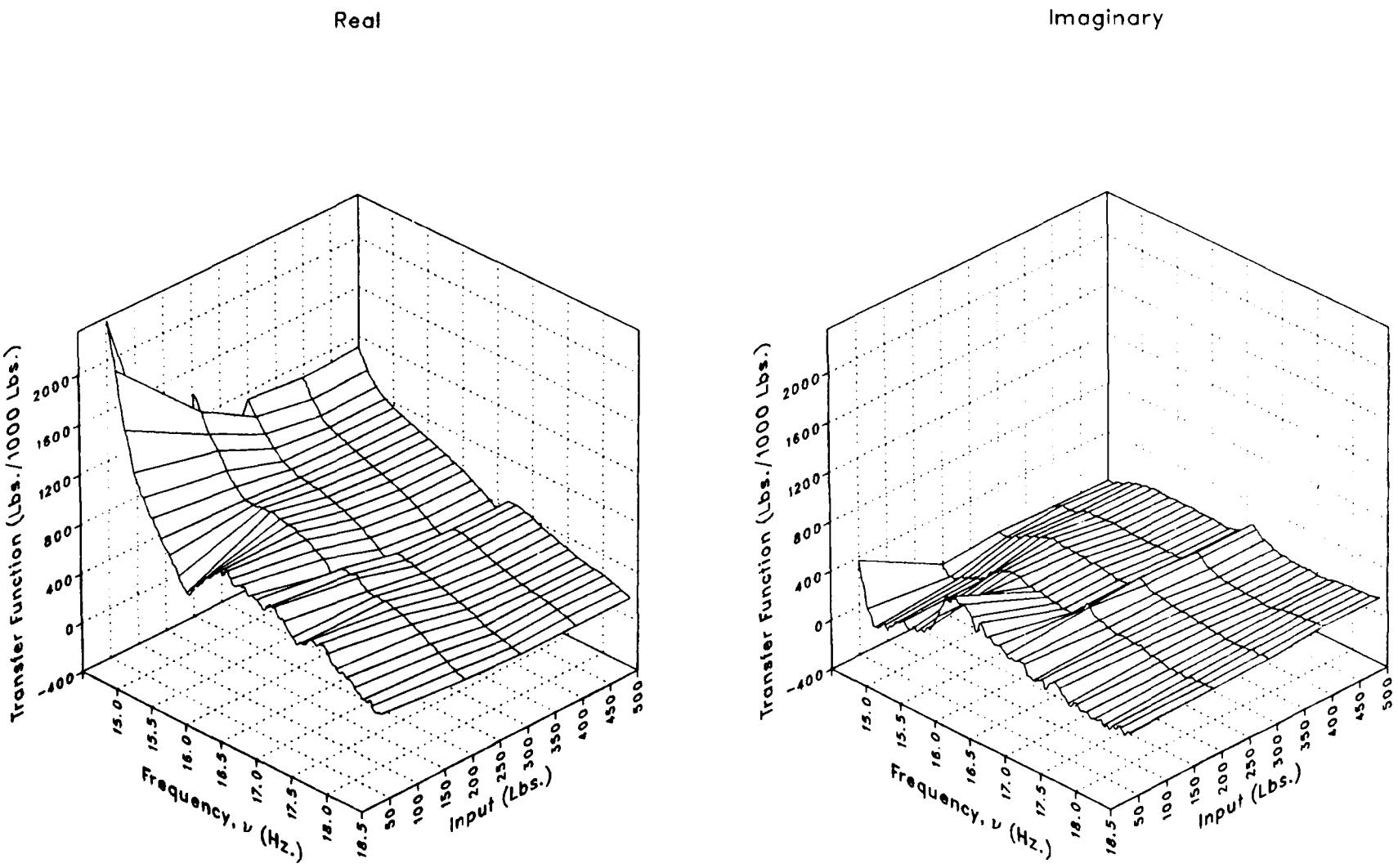

(b) MRLIFTA

Figure 5.– Continued.

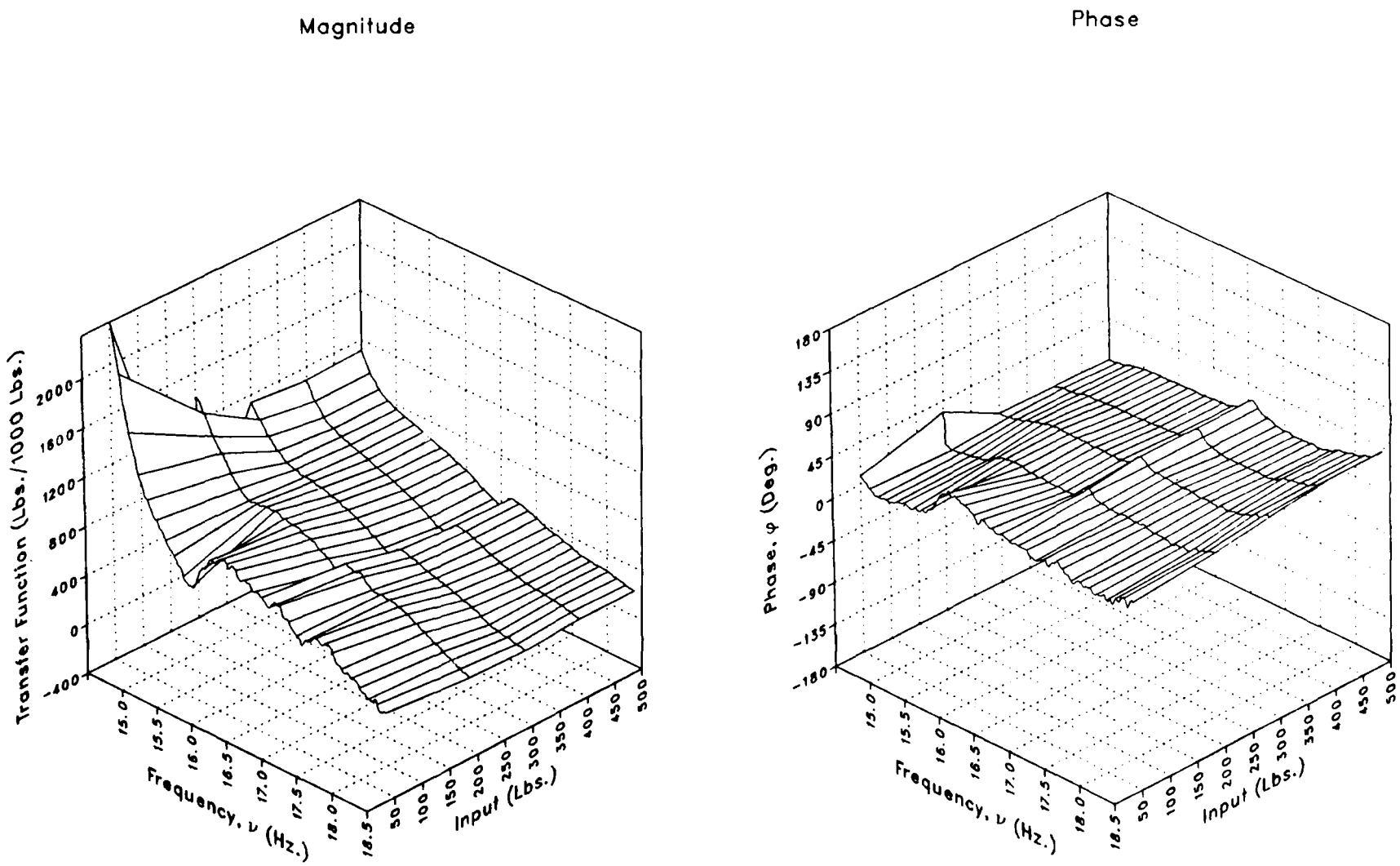

(b) MRLIFTA Concluded.

Figure 5.– Continued.

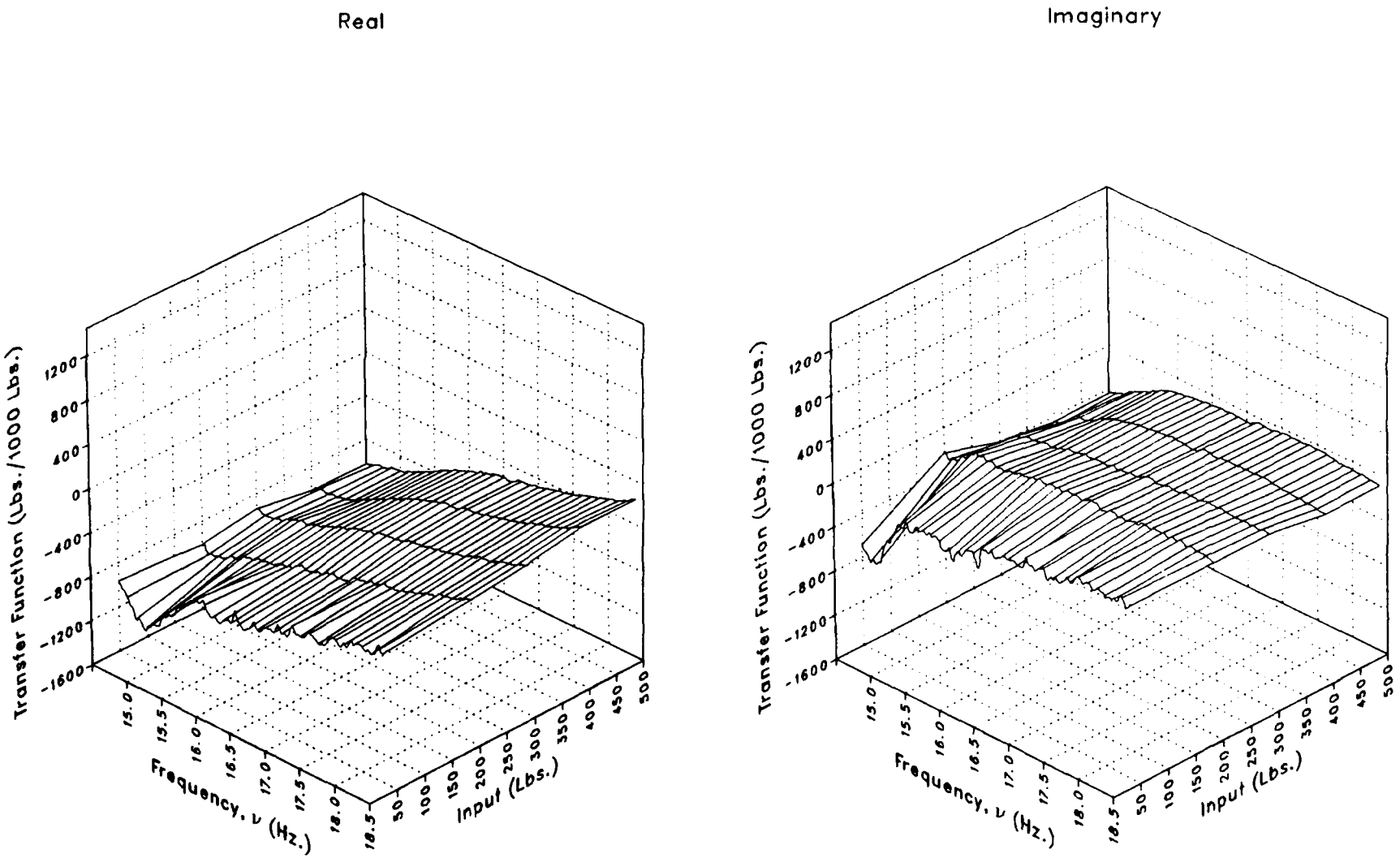

(c) MRLIFTB

Figure 5.– Continued.

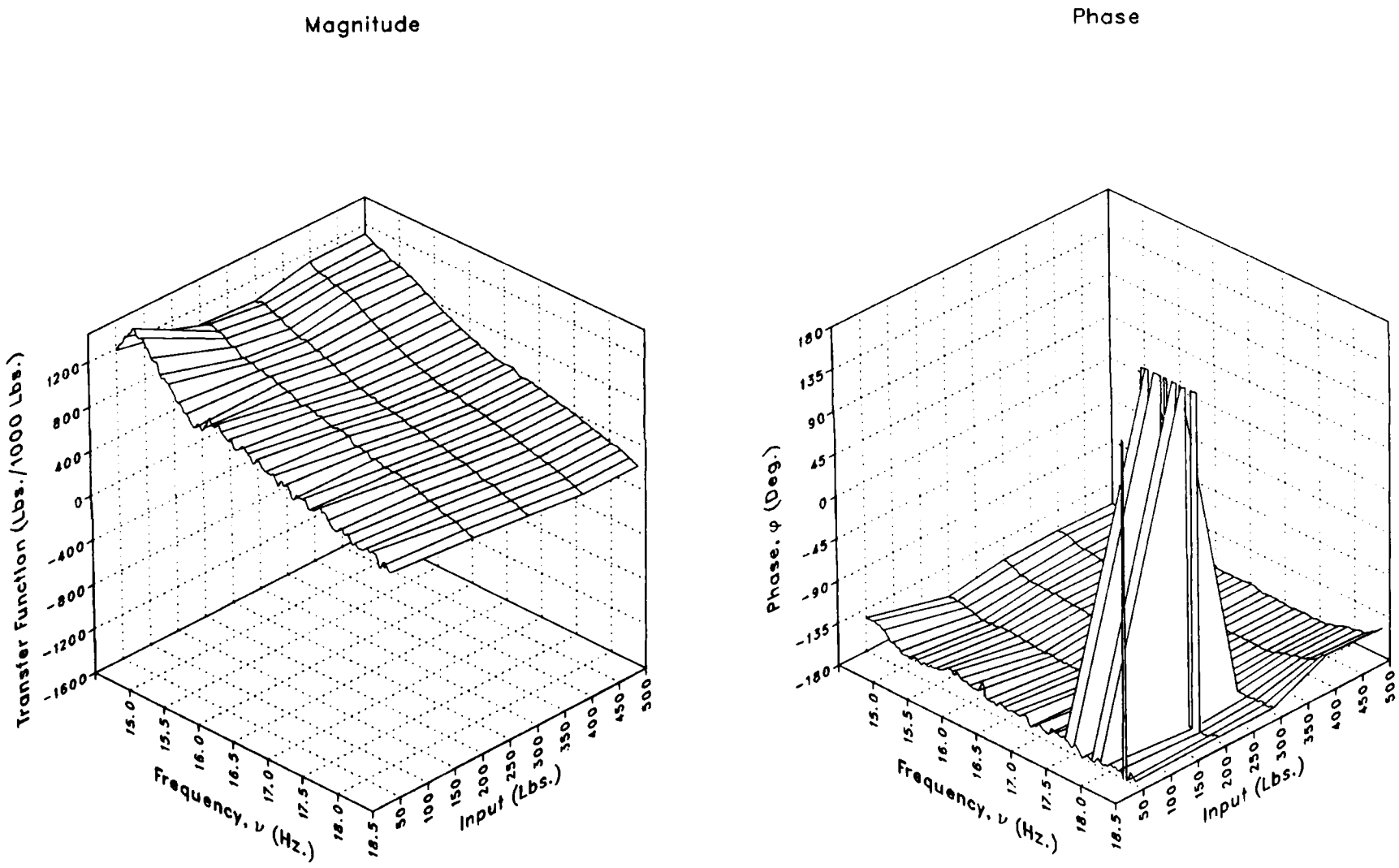

(c) MRLIFTB Concluded.

Figure 5.– Continued.

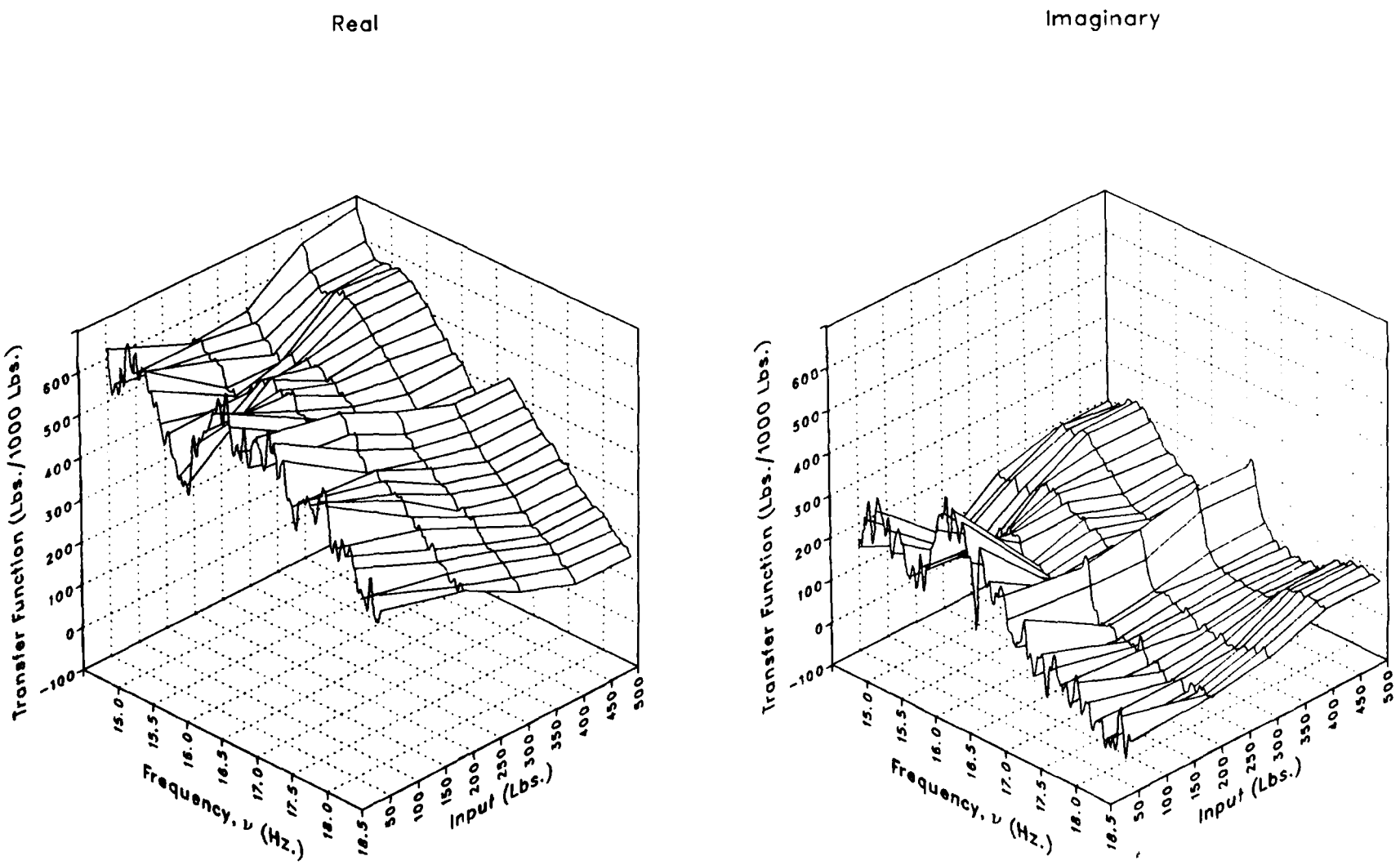

(d) MRLIFTC

Figure 5.– Continued.

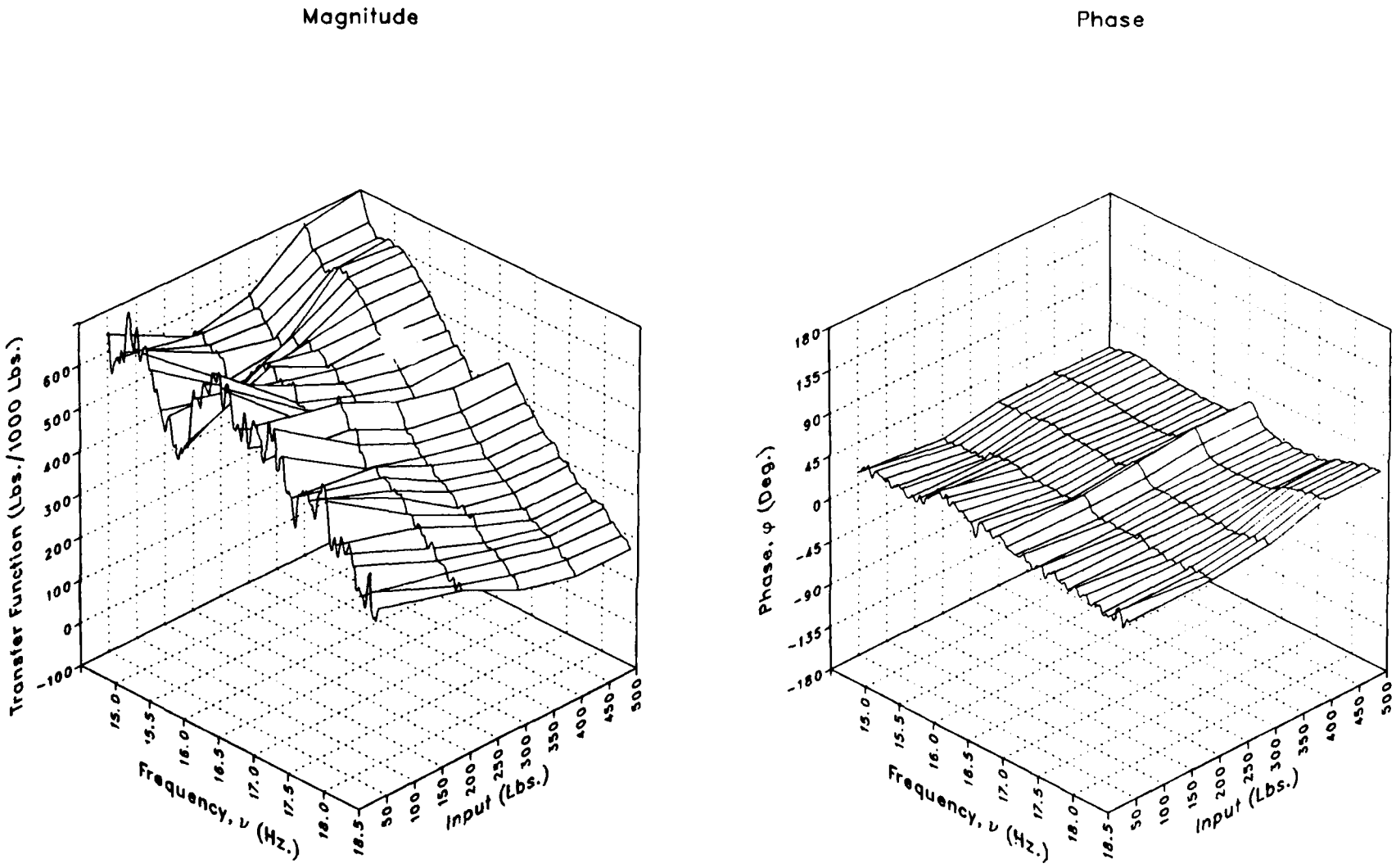

(d) MRLIFTC Concluded.

Figure 5.– Continued.

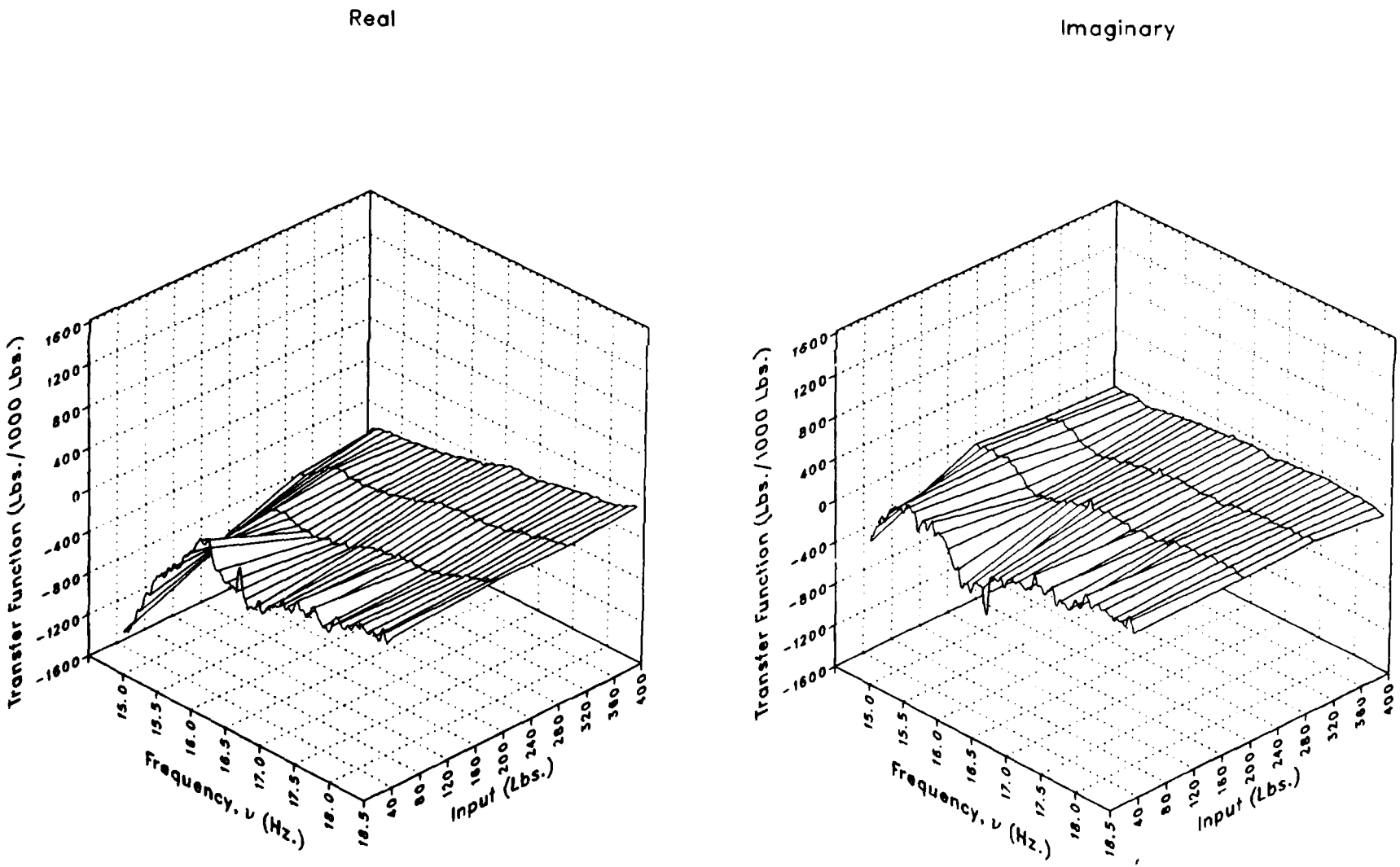

(e) MRLIFTD

Figure 5.– Continued.

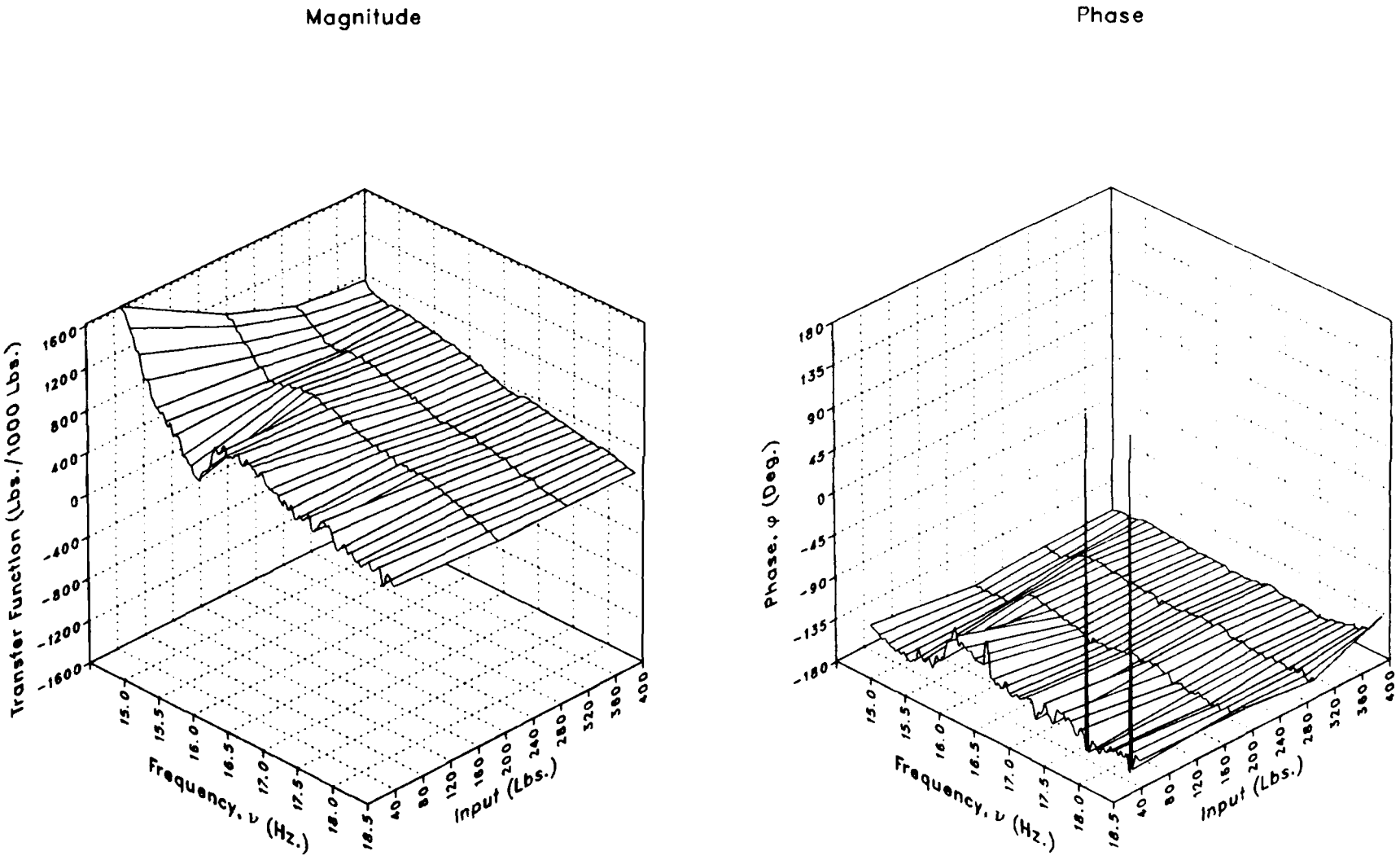

(e) MRLIFTD Concluded.

Figure 5.– Continued.

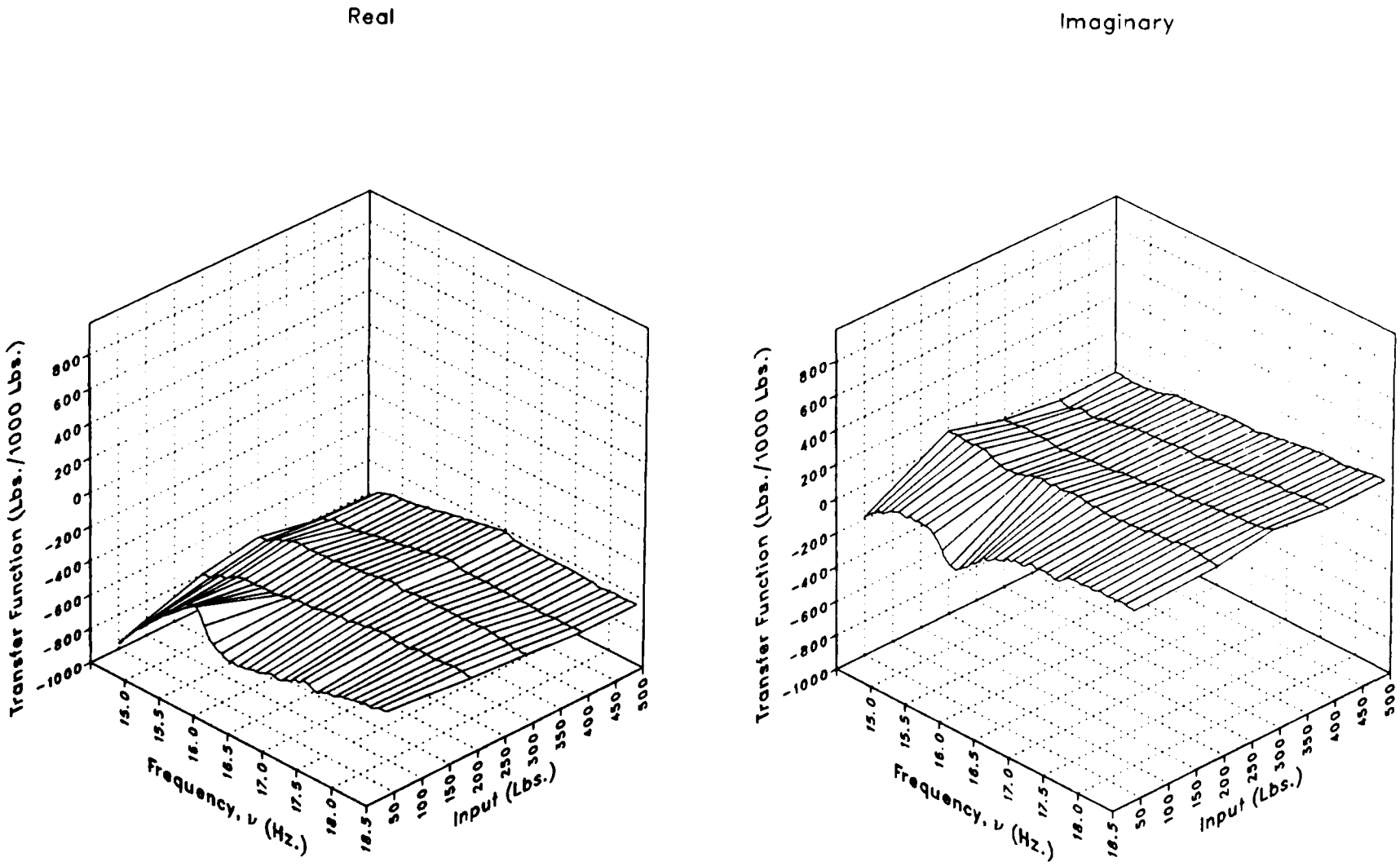

(f) MRGBQCE

Figure 5.– Continued.

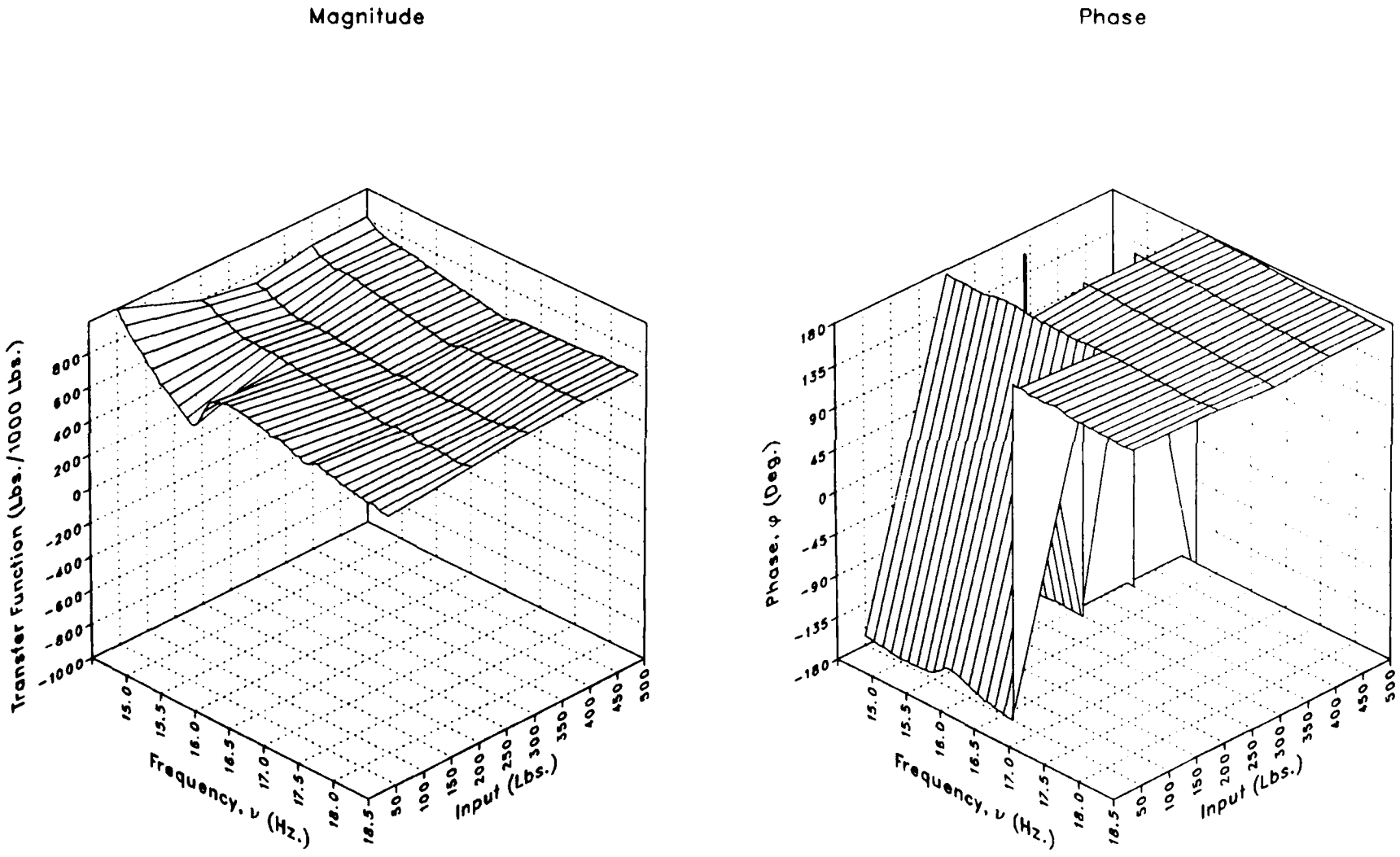

(f) MRGBQCE Concluded.

Figure 5.– Continued.

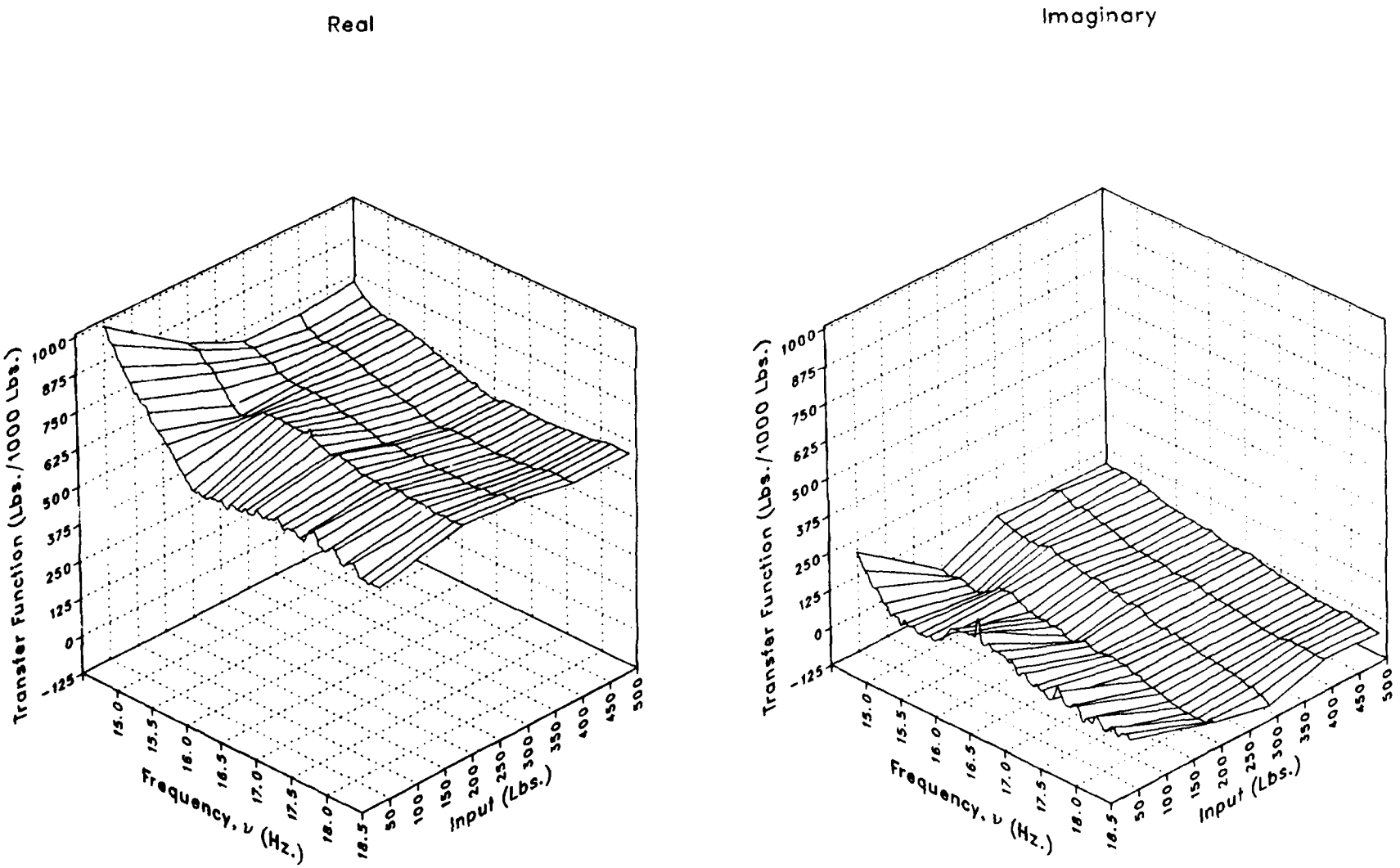

(g) MRGBQCF

Figure 5.– Continued.

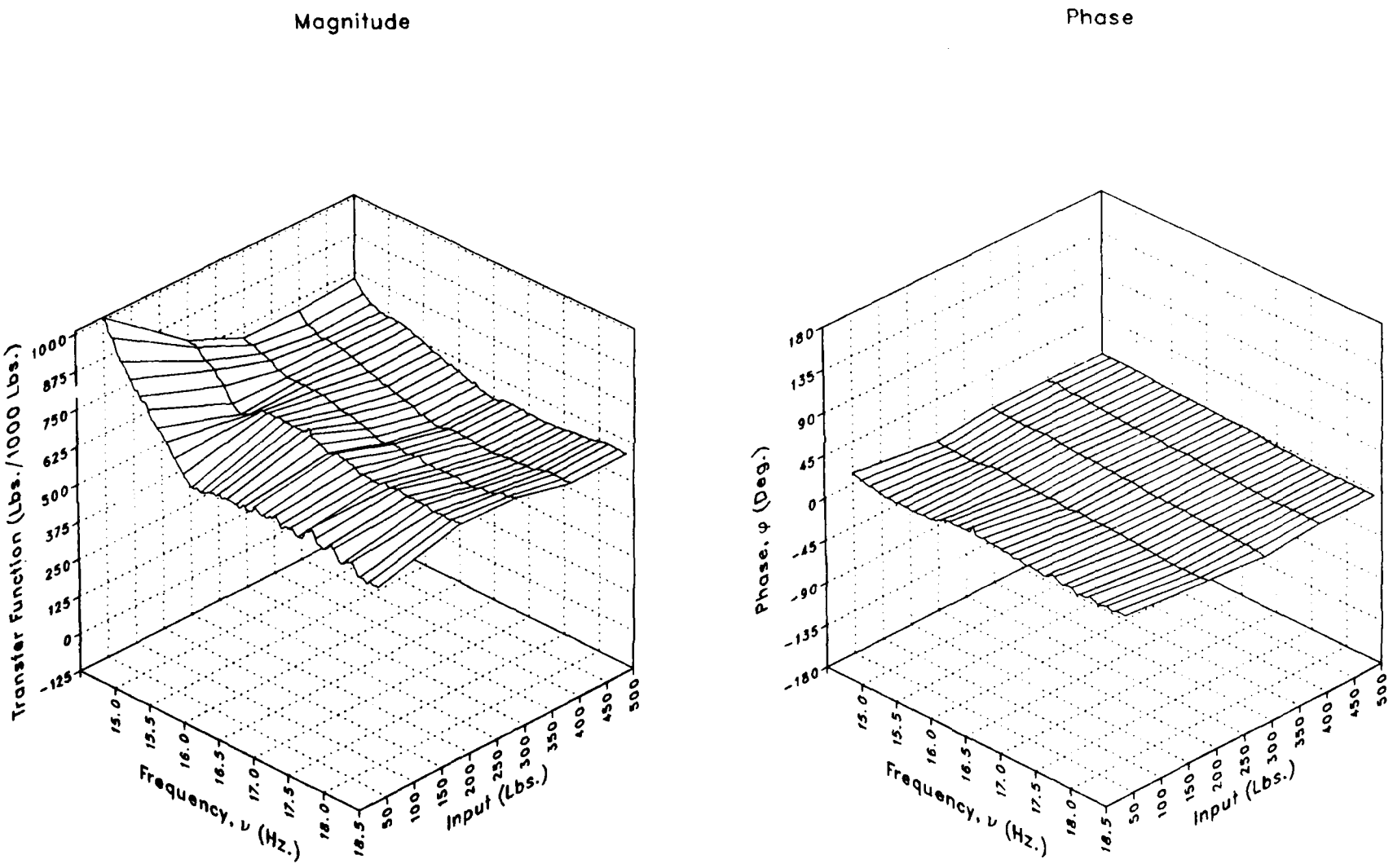

(g) MRGBQCF Concluded.

Figure 5.– Continued.

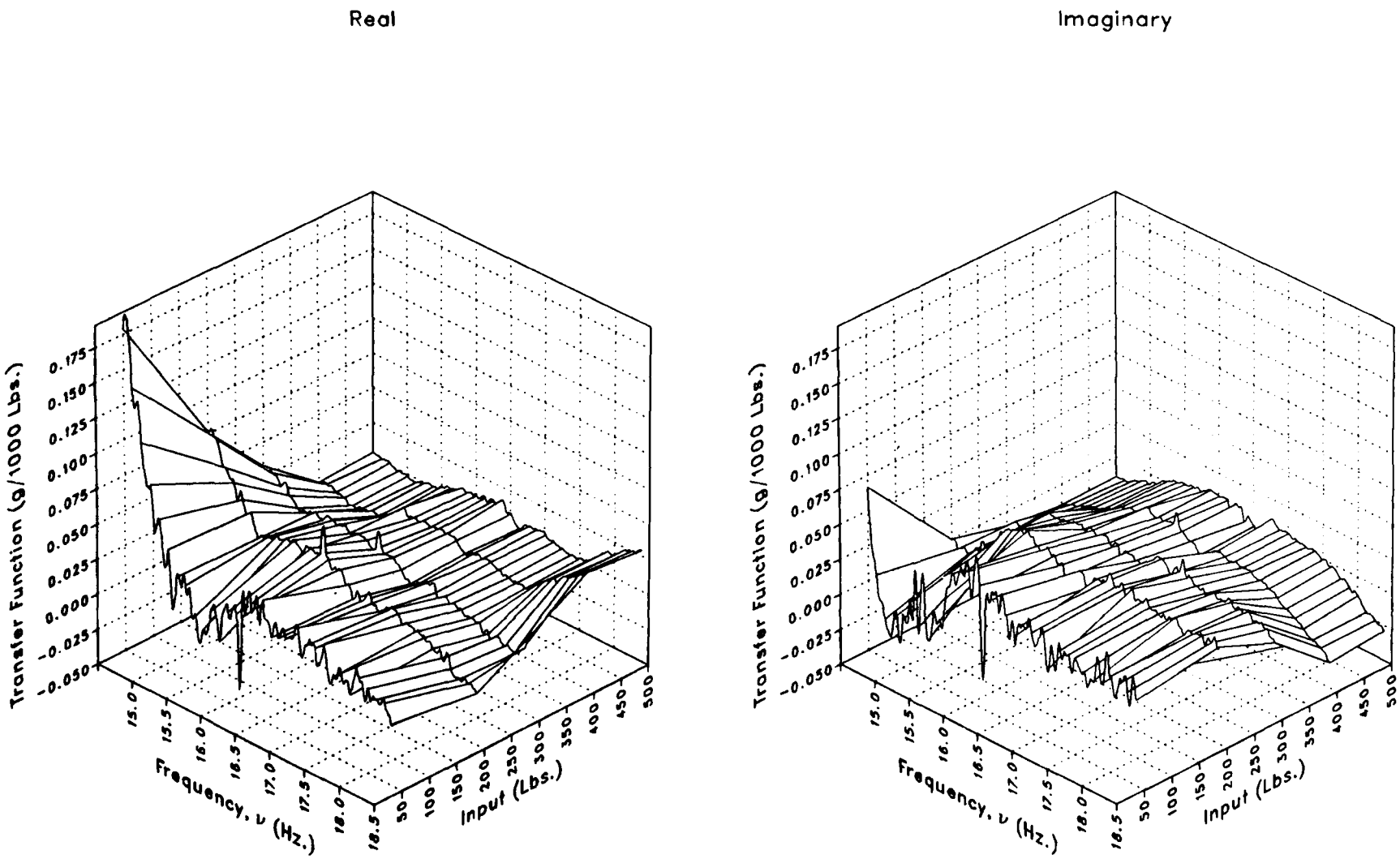

(h) LOMGB

Figure 5.– Continued.

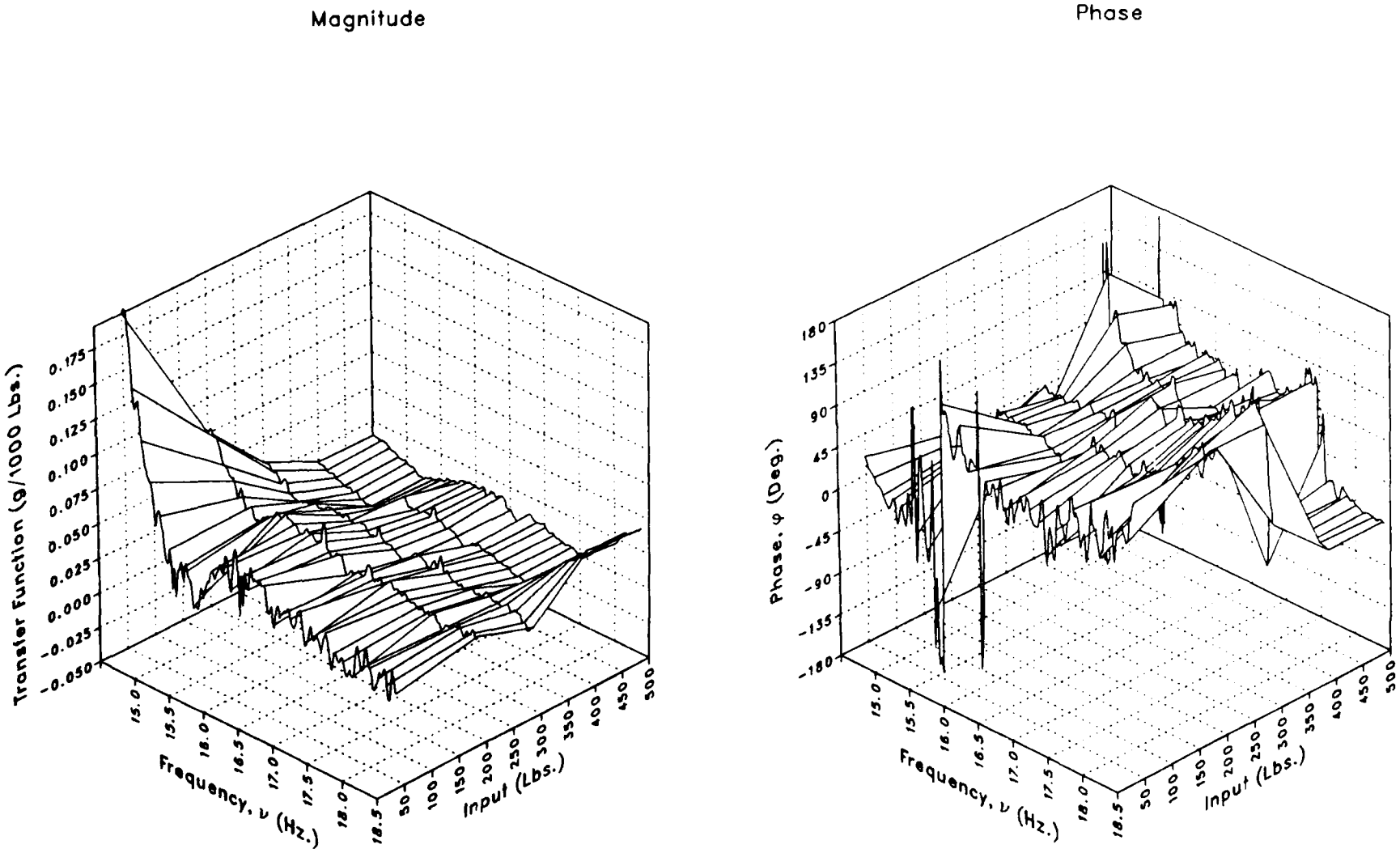

(h) LOMGB Concluded.

Figure 5.– Continued.

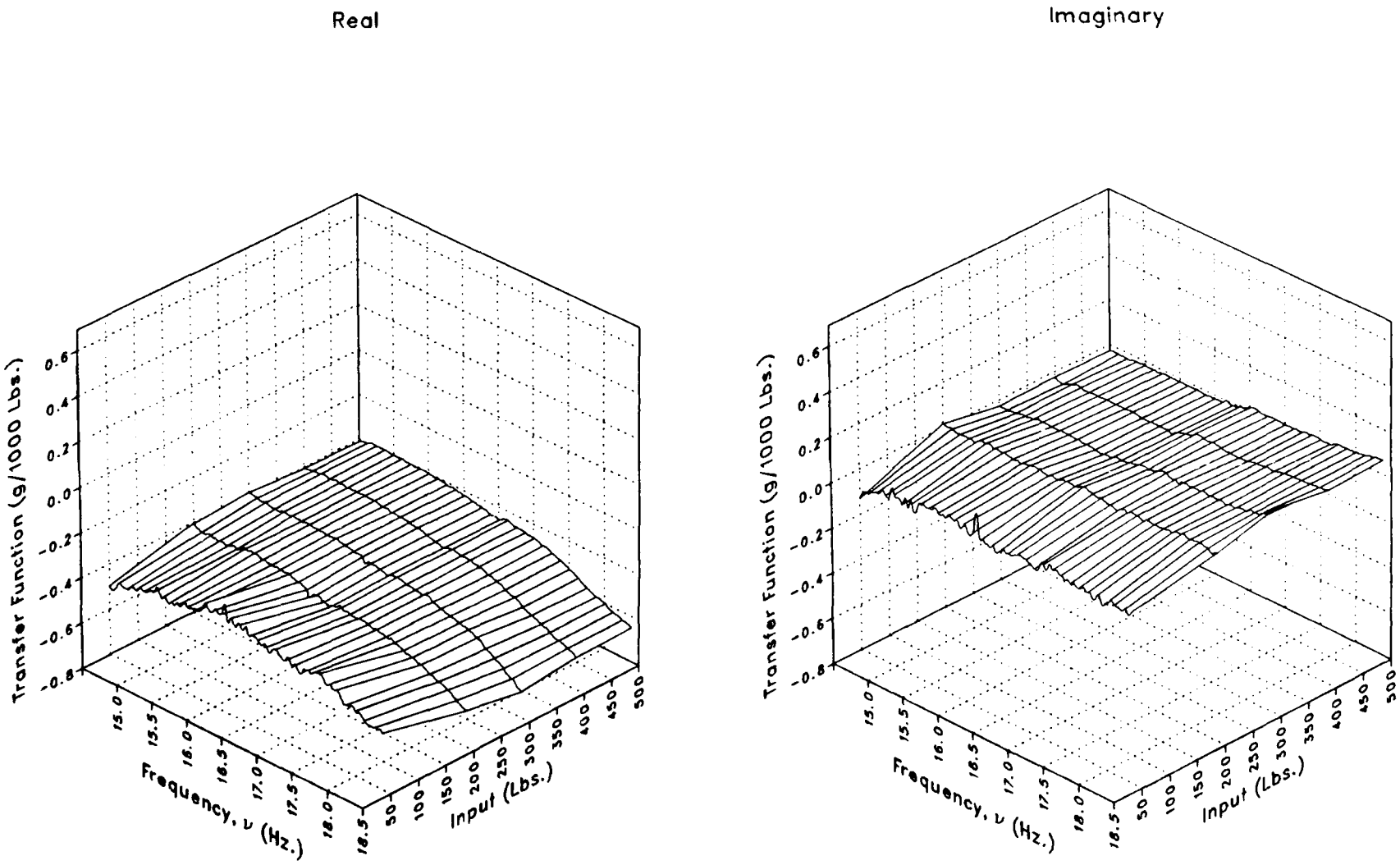

(i) LMGB

Figure 5.– Continued.

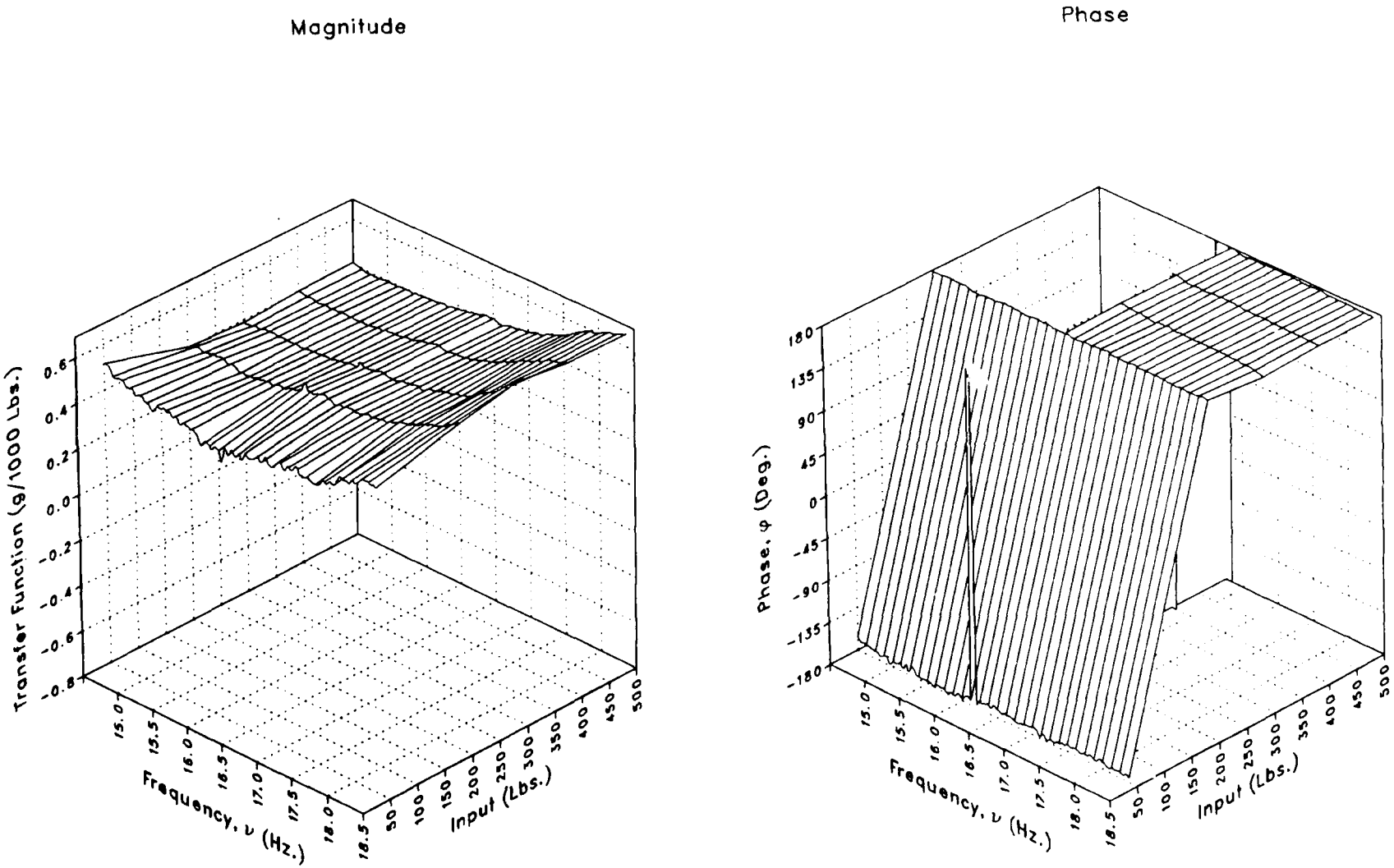

(i) LMGB Concluded.

Figure 5.– Continued.

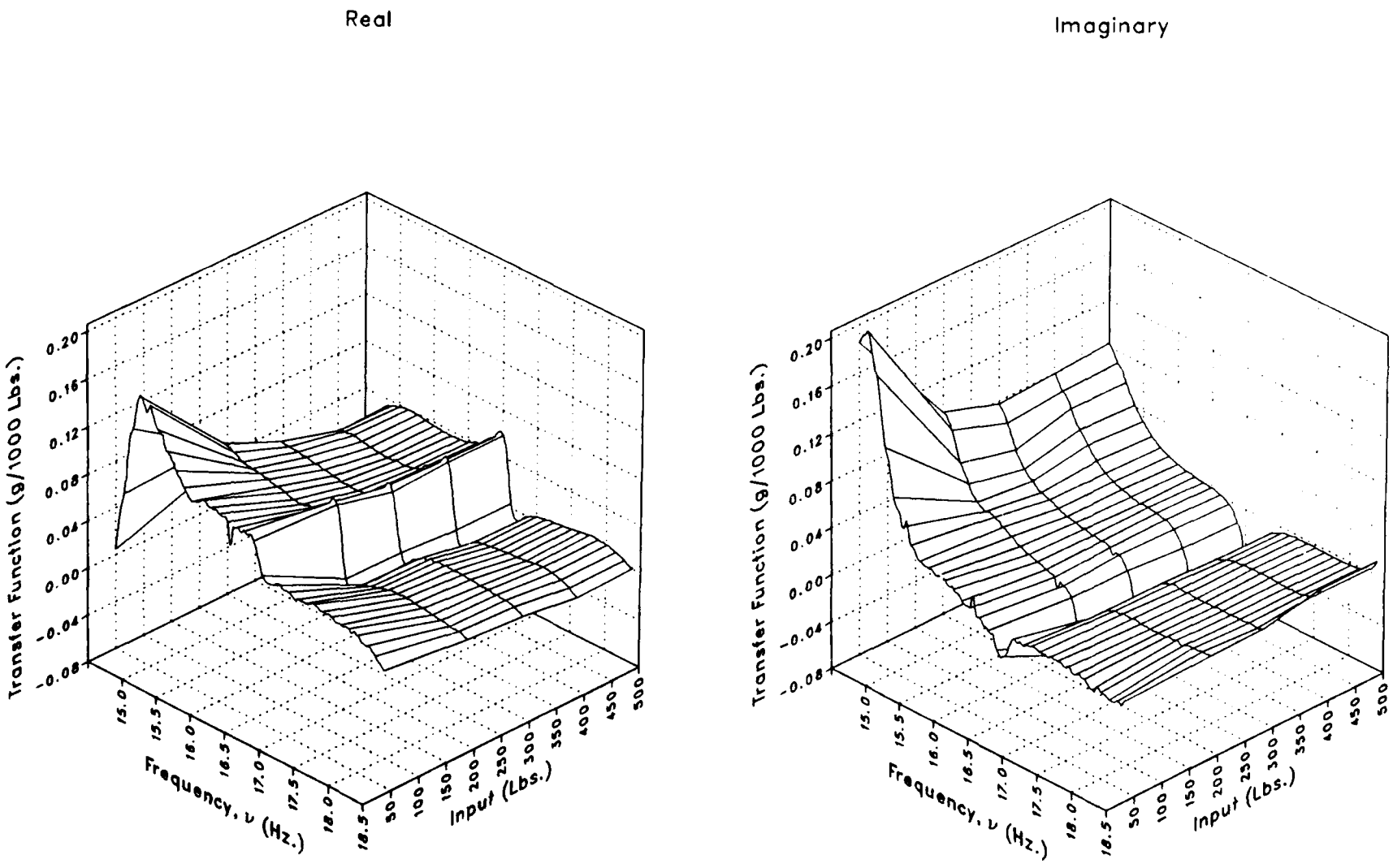

(j) VMGB

Figure 5.– Continued.

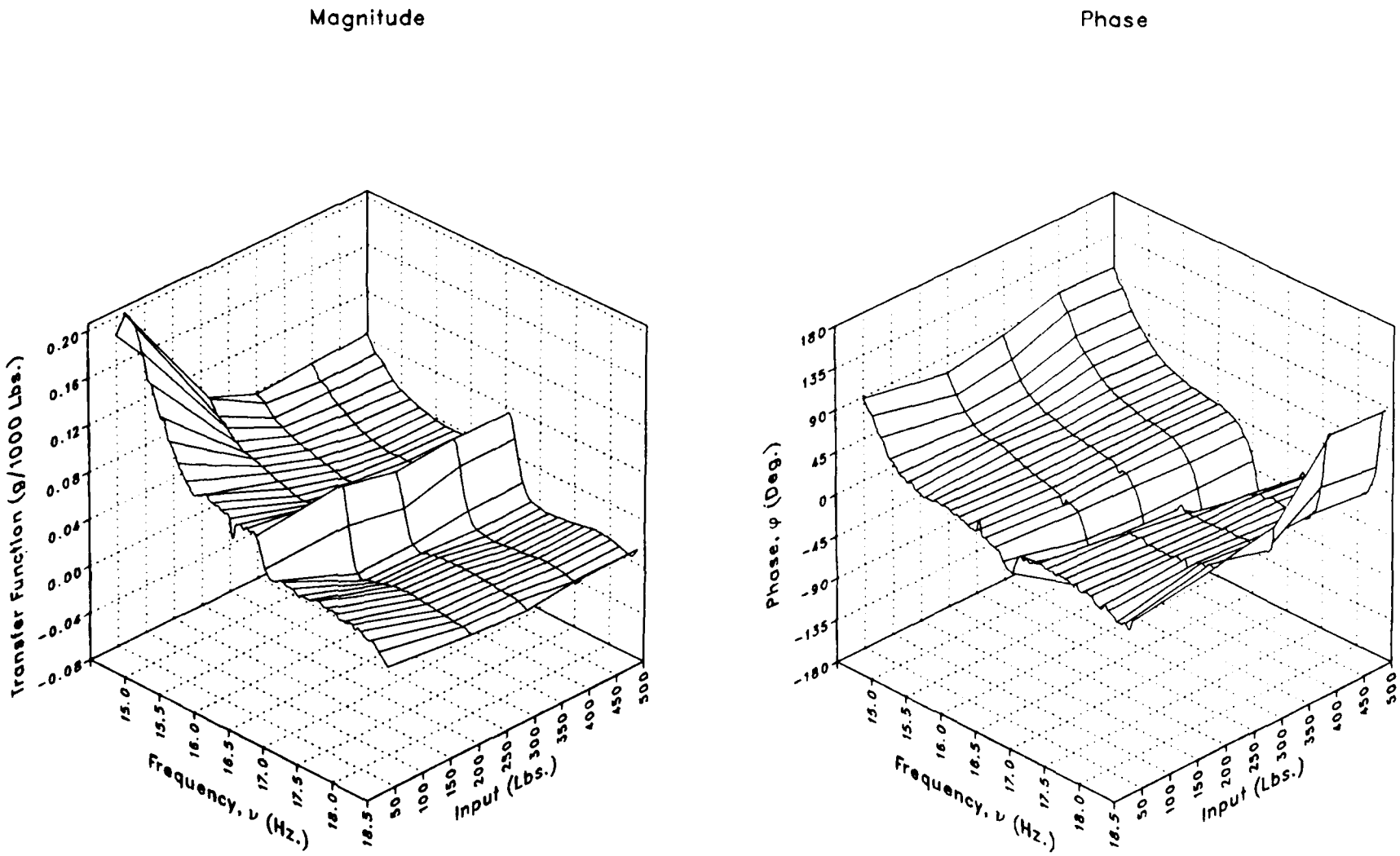

(j) VMGB Concluded.

Figure 5.– Continued.

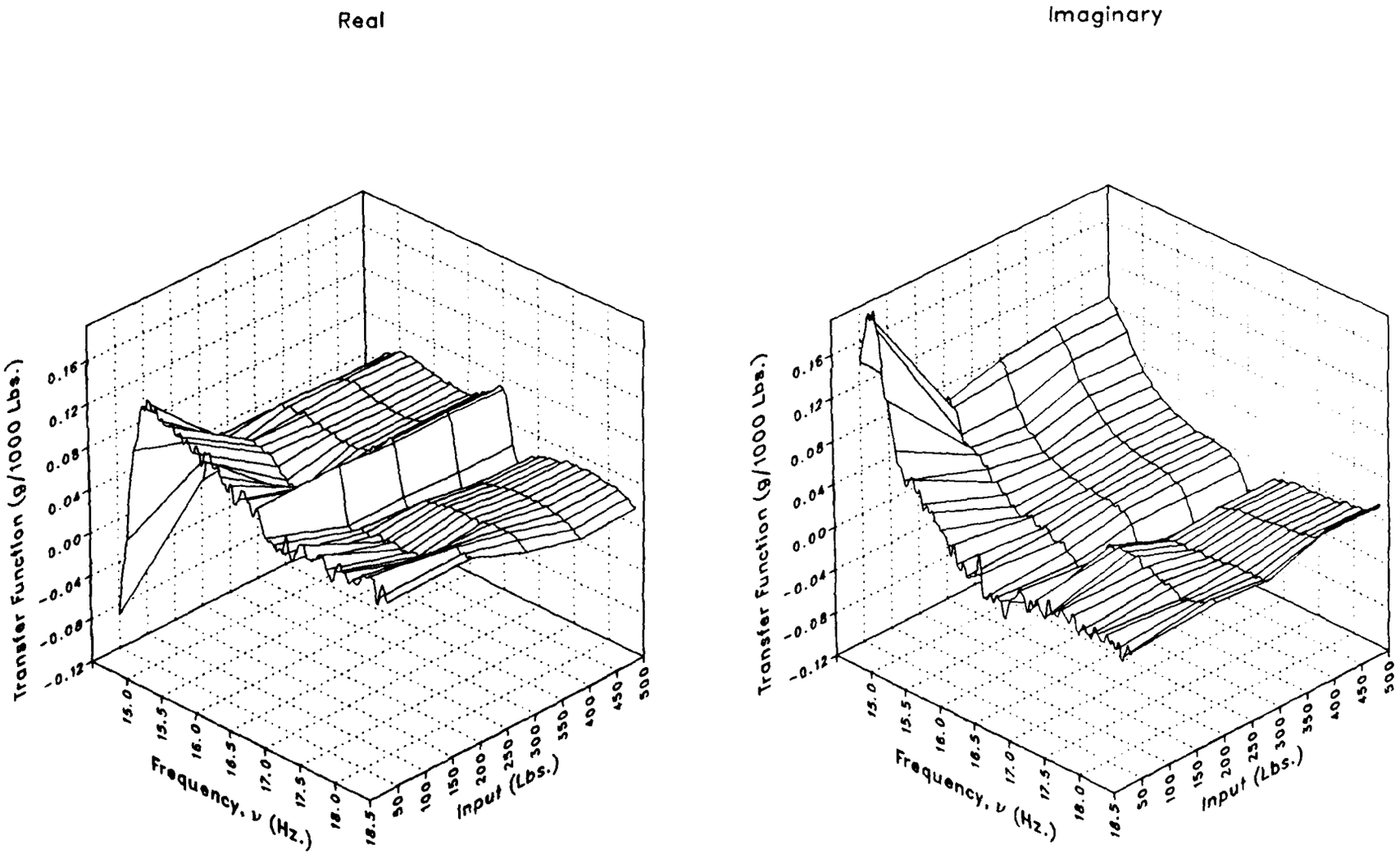

(k) XMRFBPV

Figure 5.– Continued.

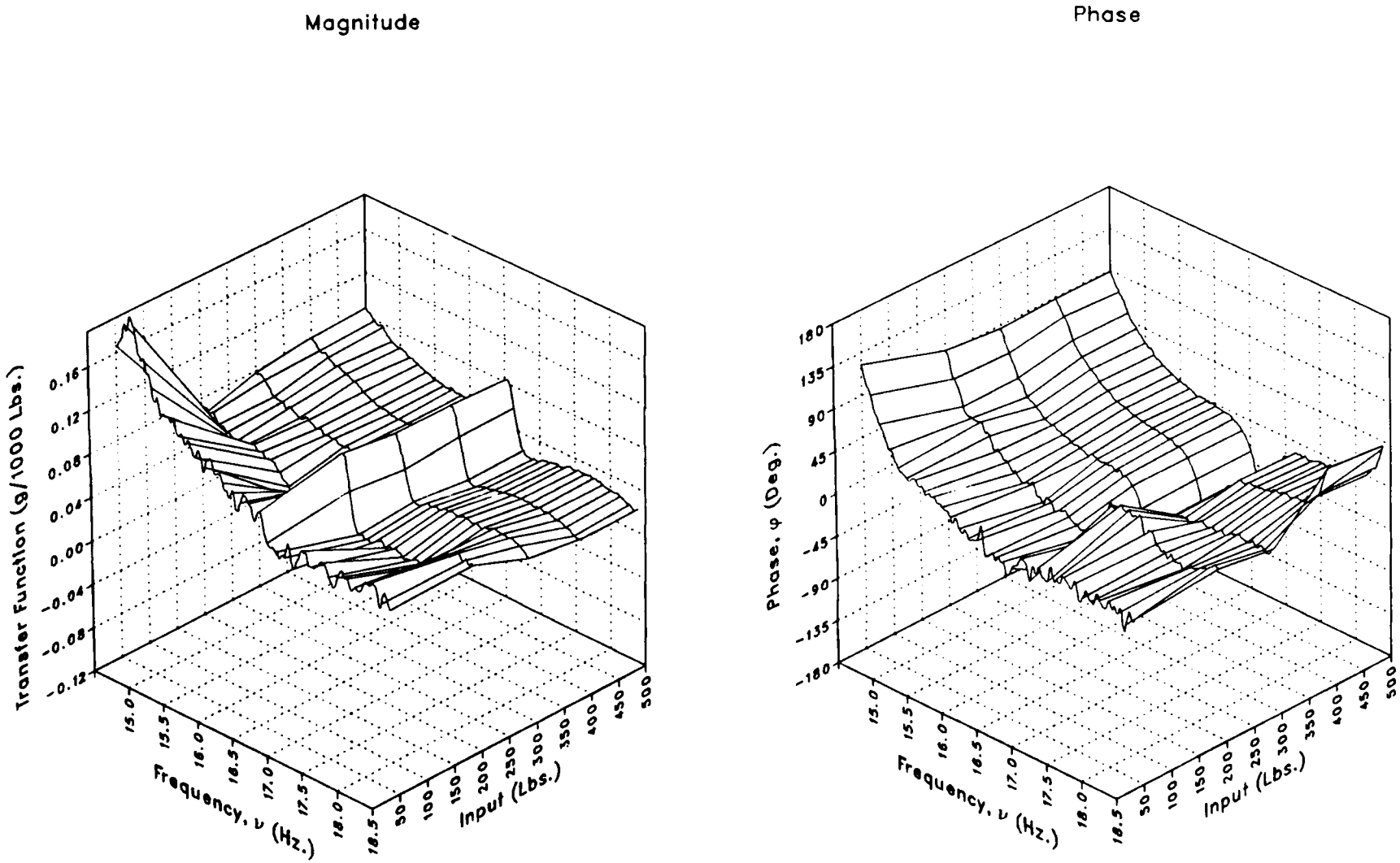

(k) XMRFBPV Concluded.

Figure 5.– Continued.

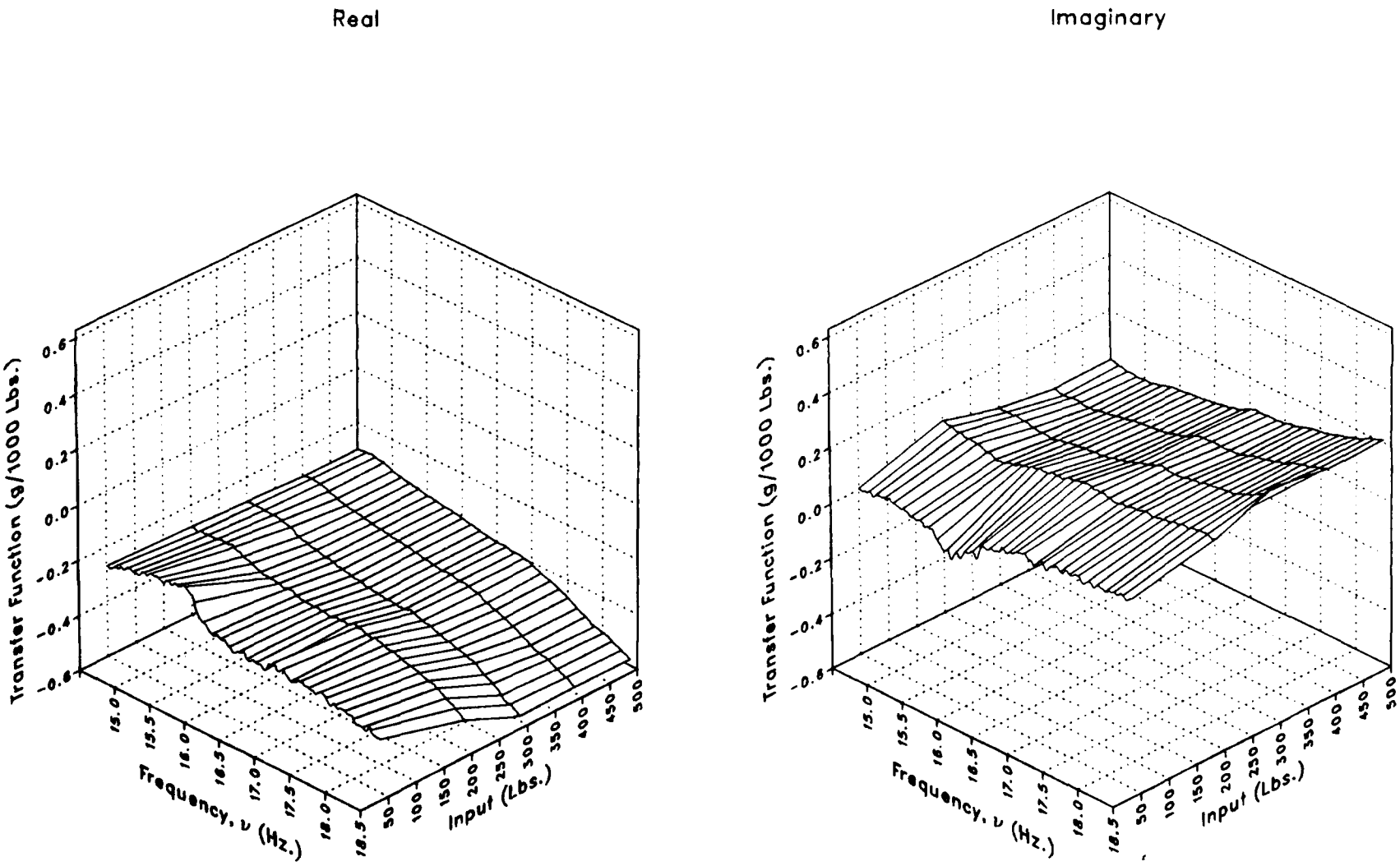

(l) XMRFBPL

Figure 5.– Continued.

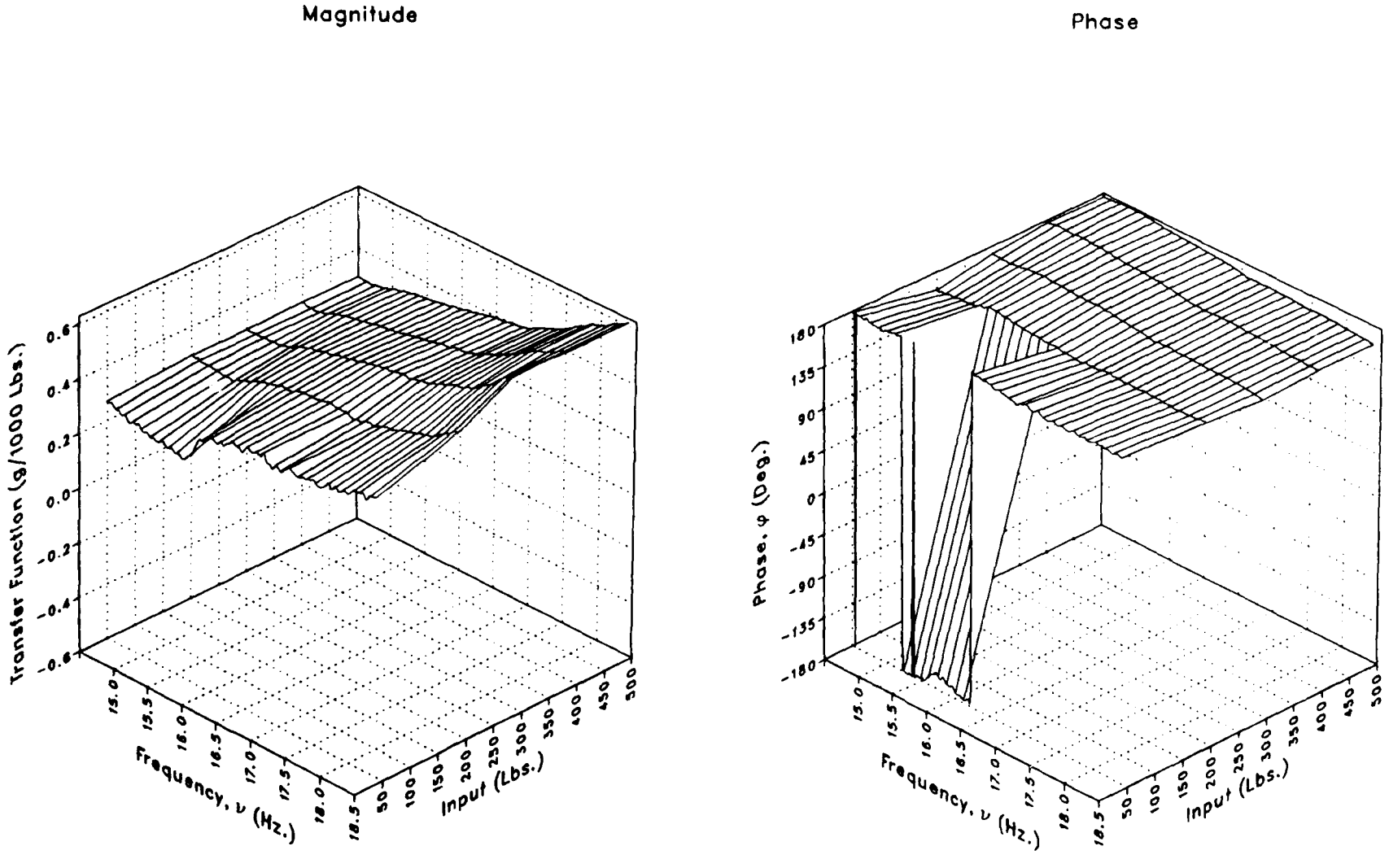

(l) XMRFBPL Concluded.

Figure 5.– Continued.

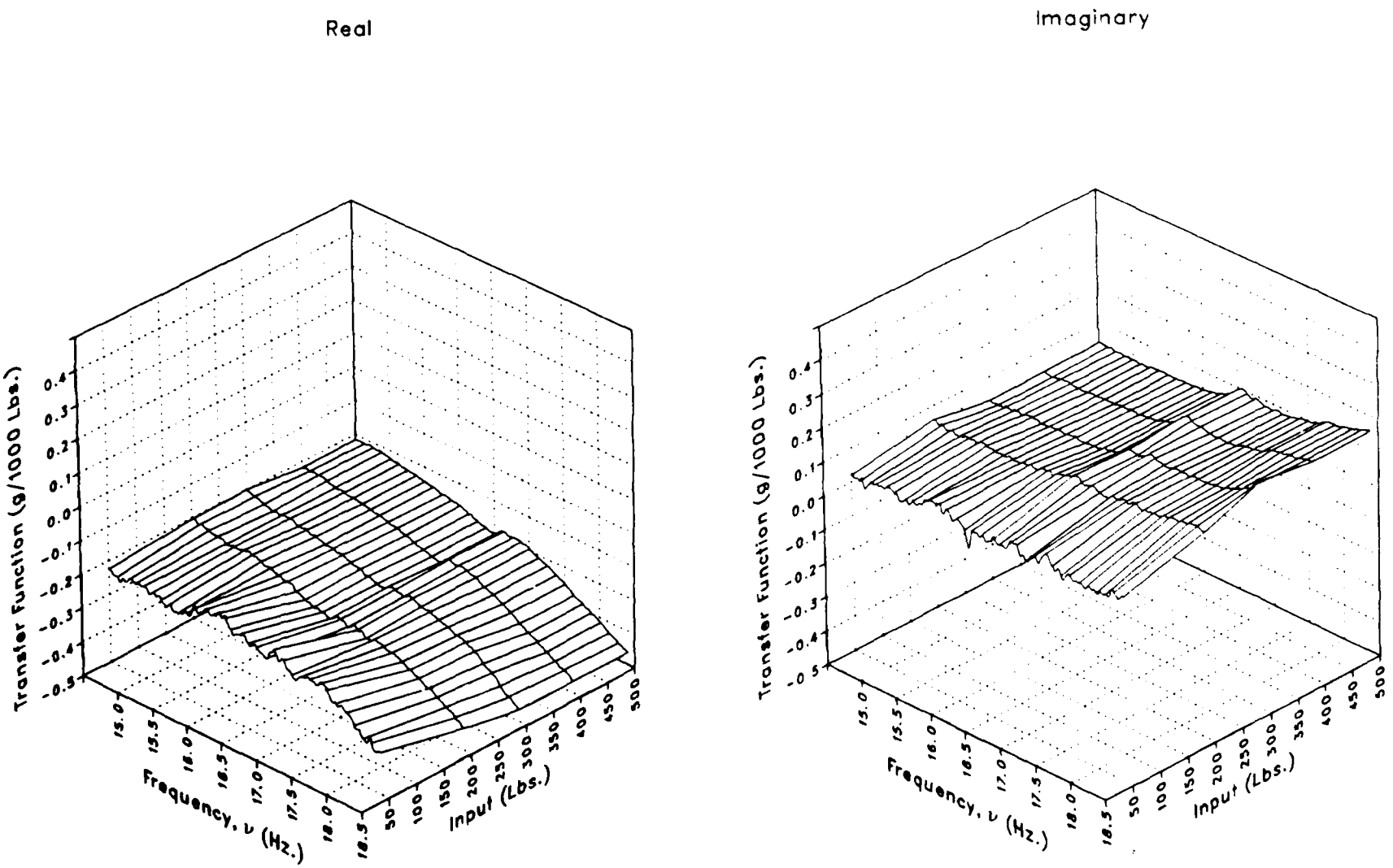

(m) XMRFBPLO

Figure 5.– Continued.

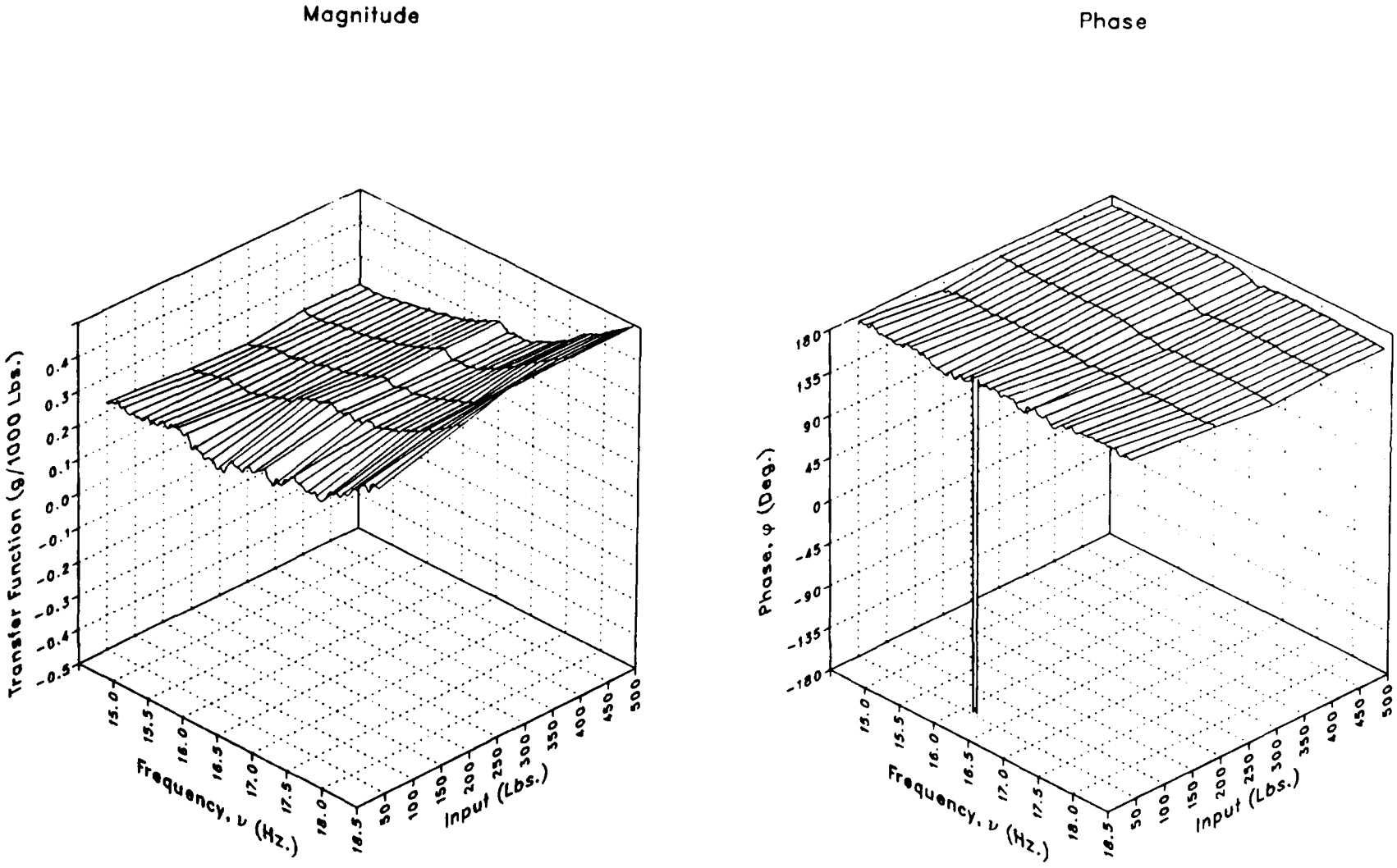

(m) XMRFBPLO Concluded.

Figure 5.– Continued.

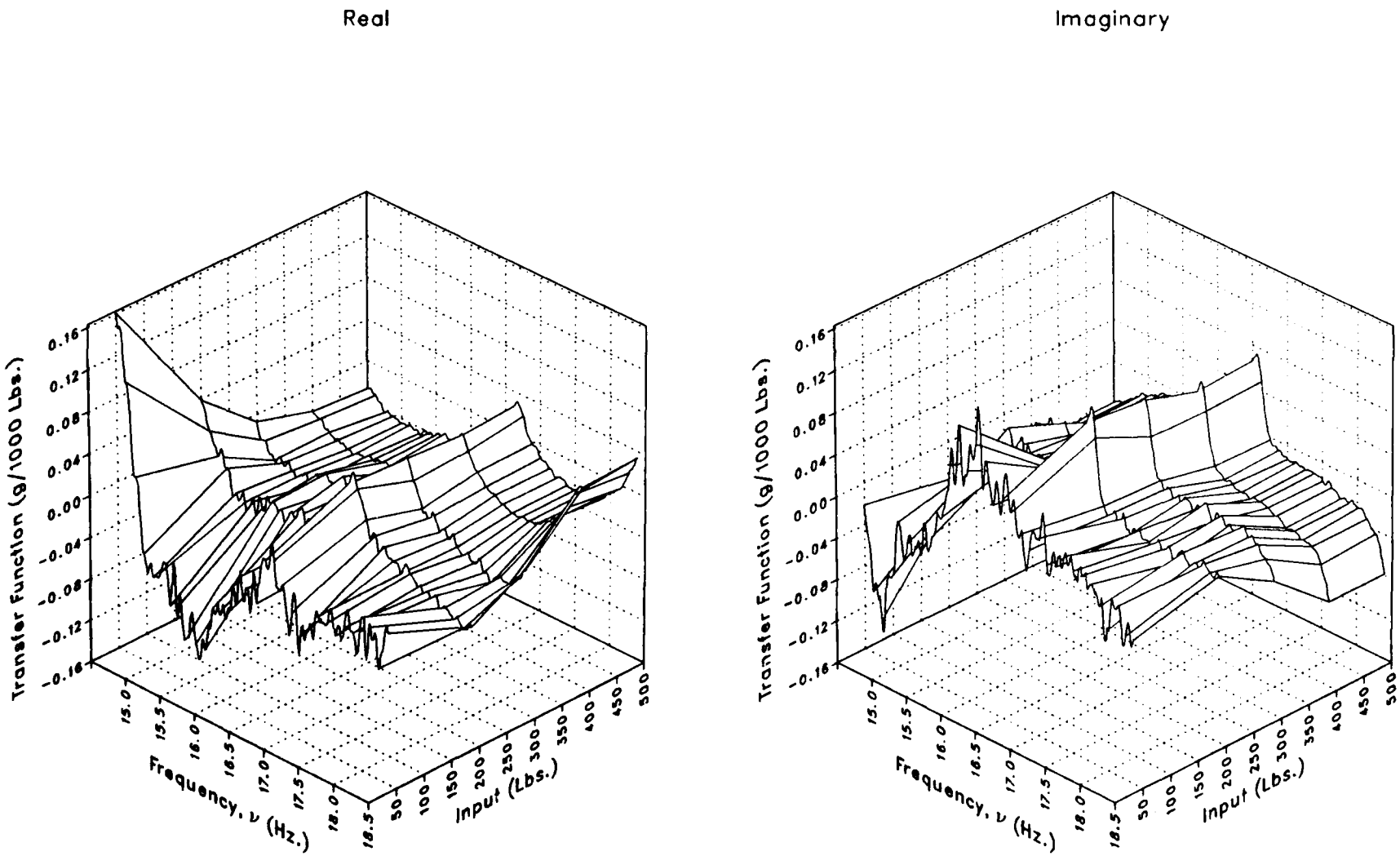

(n) STA56NV

Figure 5.– Continued.

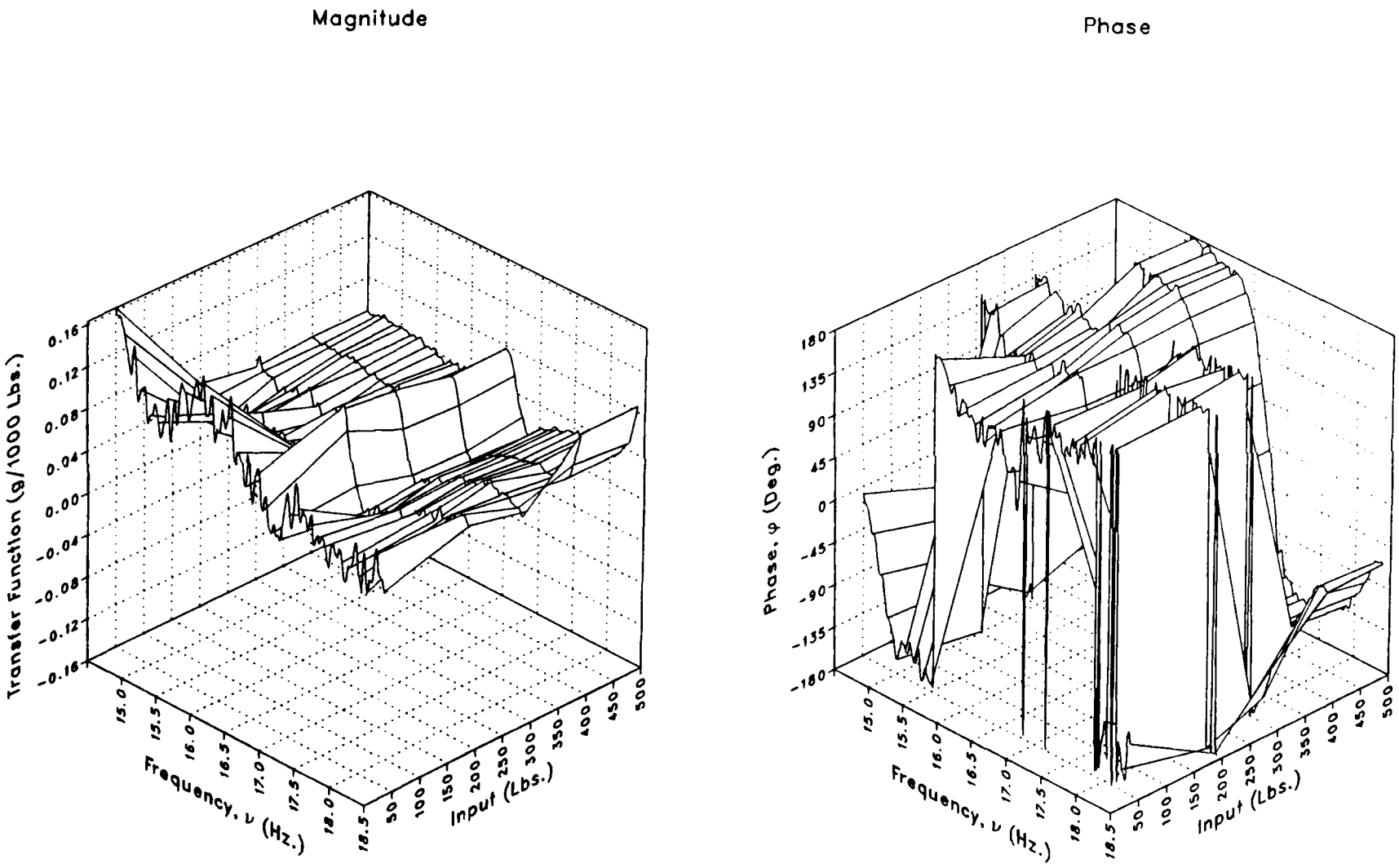

(n) STA56NV Concluded.

Figure 5.– Continued.

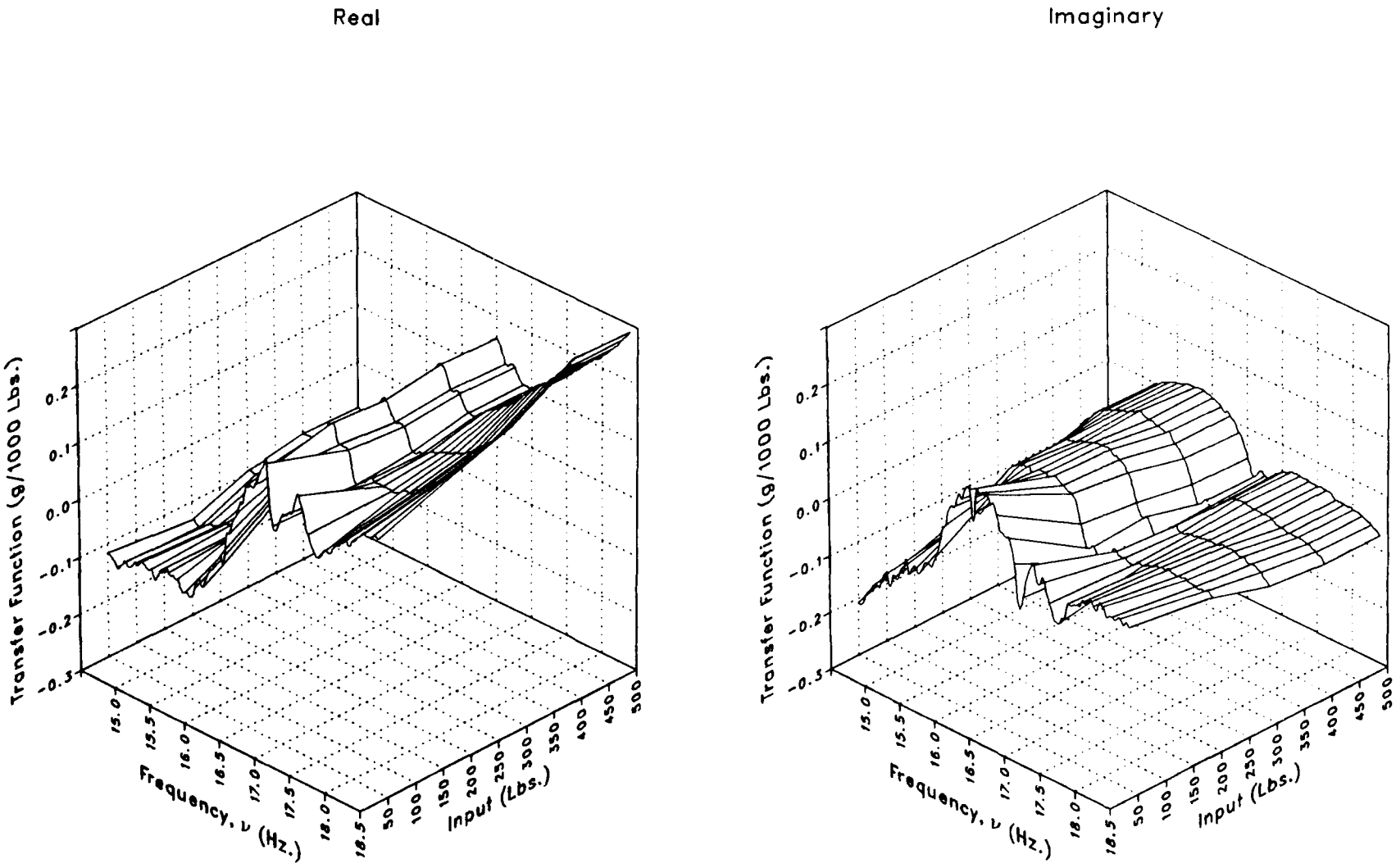

(o) STA56NL

Figure 5.– Continued.

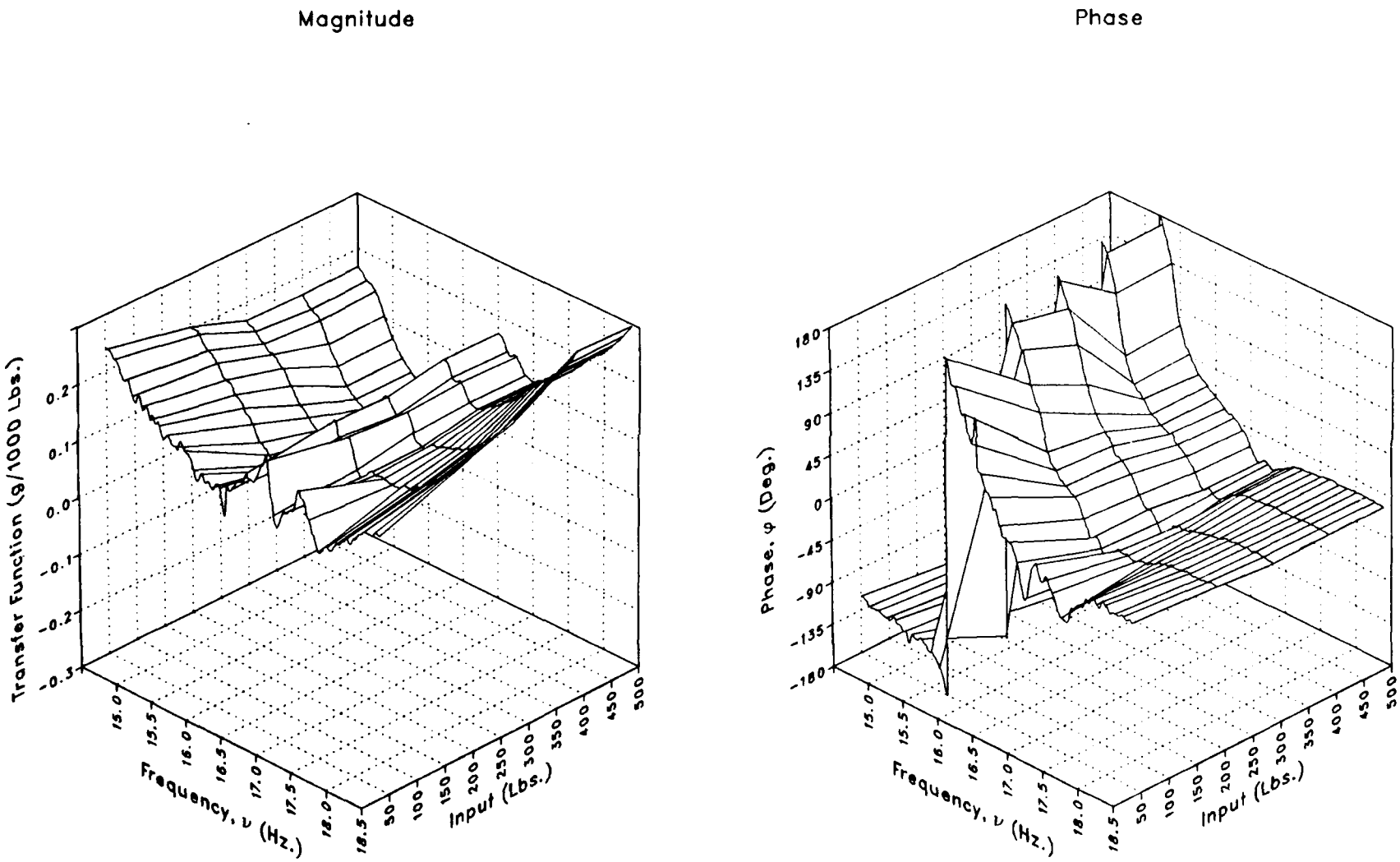

(o) STA56NL Concluded.

Figure 5.– Continued.

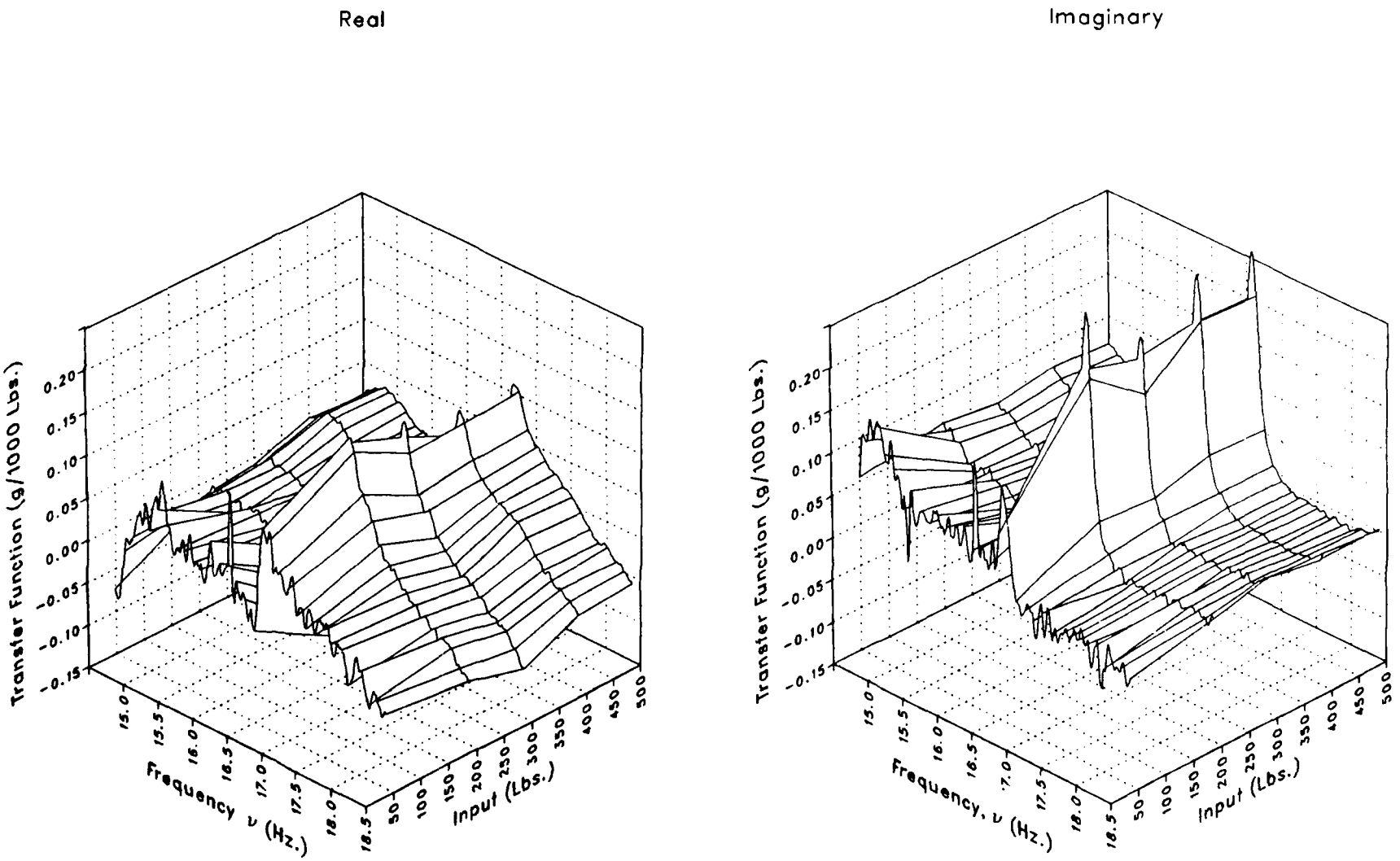

(p) VWGTPRT

Figure 5.– Continued.

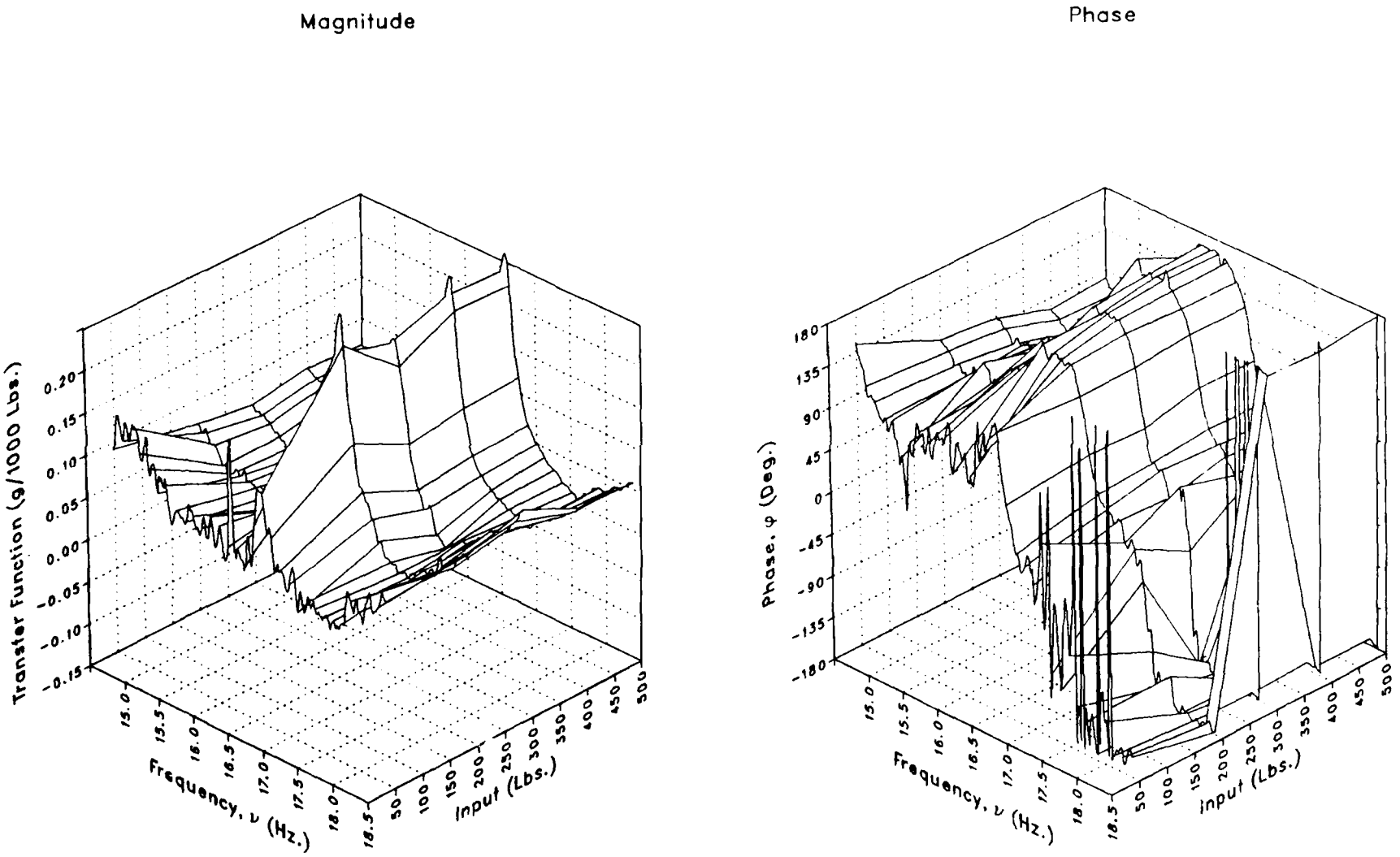

(p) VWGTPRT Concluded.

Figure 5.– Continued.

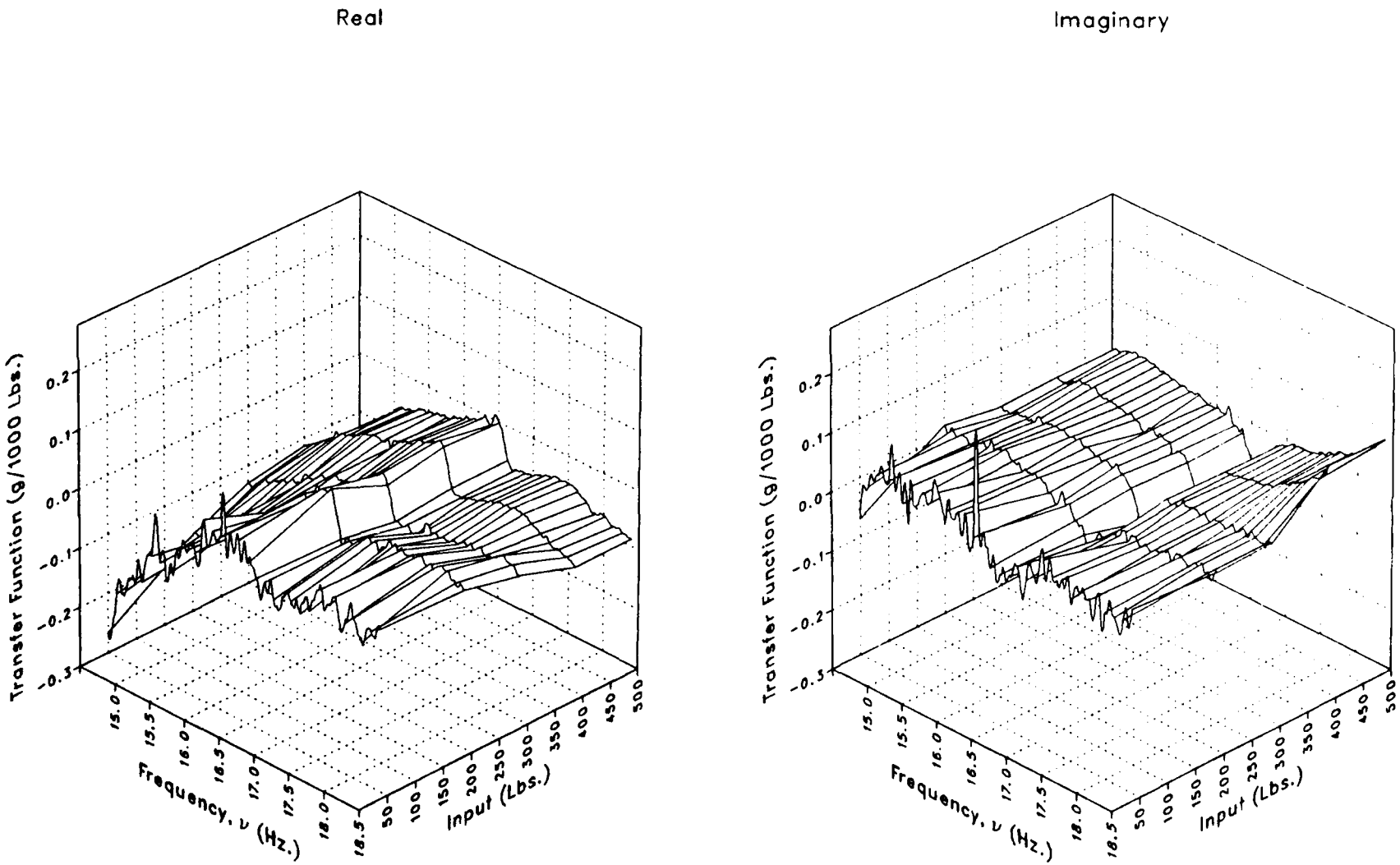

(q) VWGTPLT

Figure 5.– Continued.

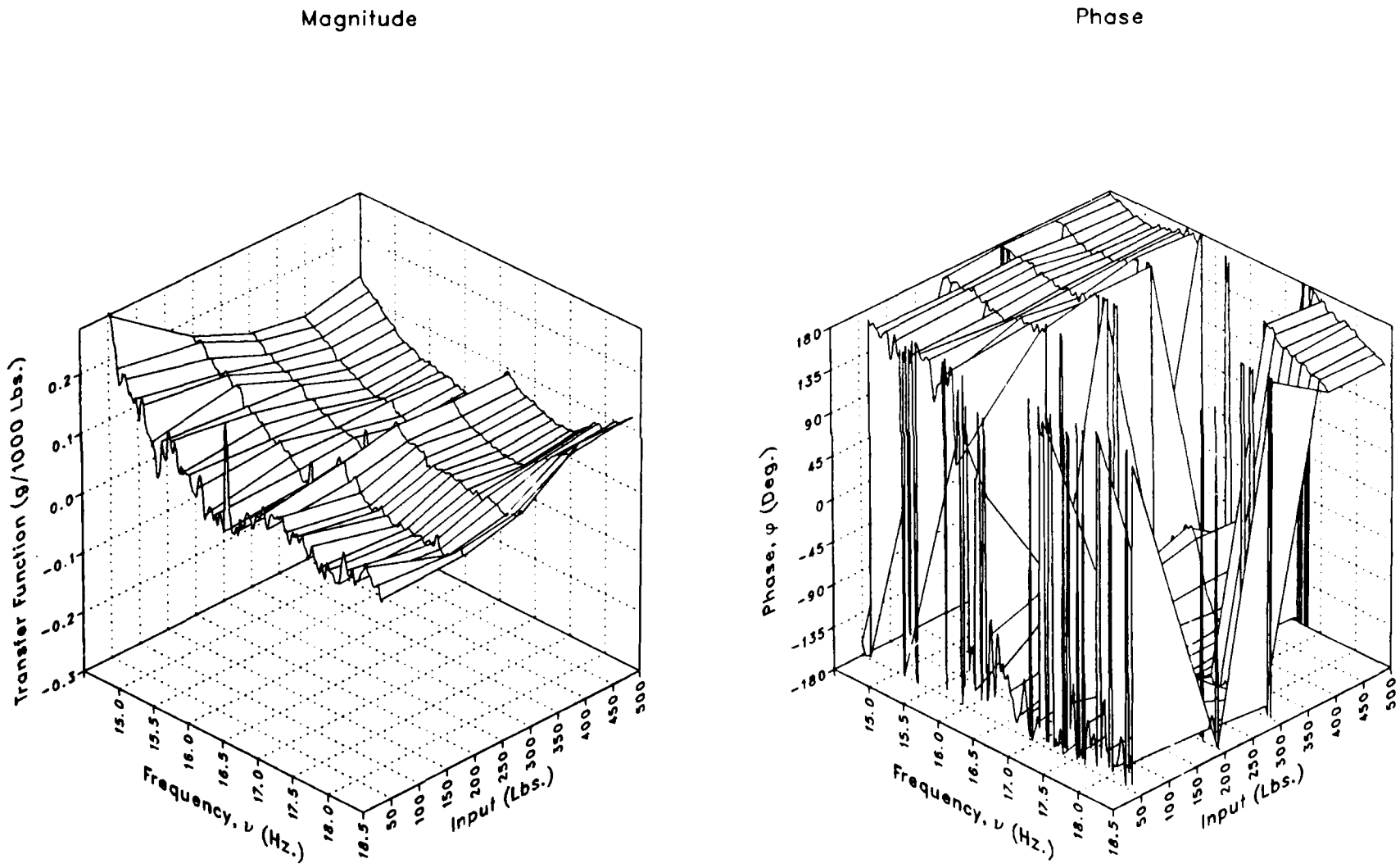

(q) VWGTPLT Concluded.

Figure 5.– Continued.

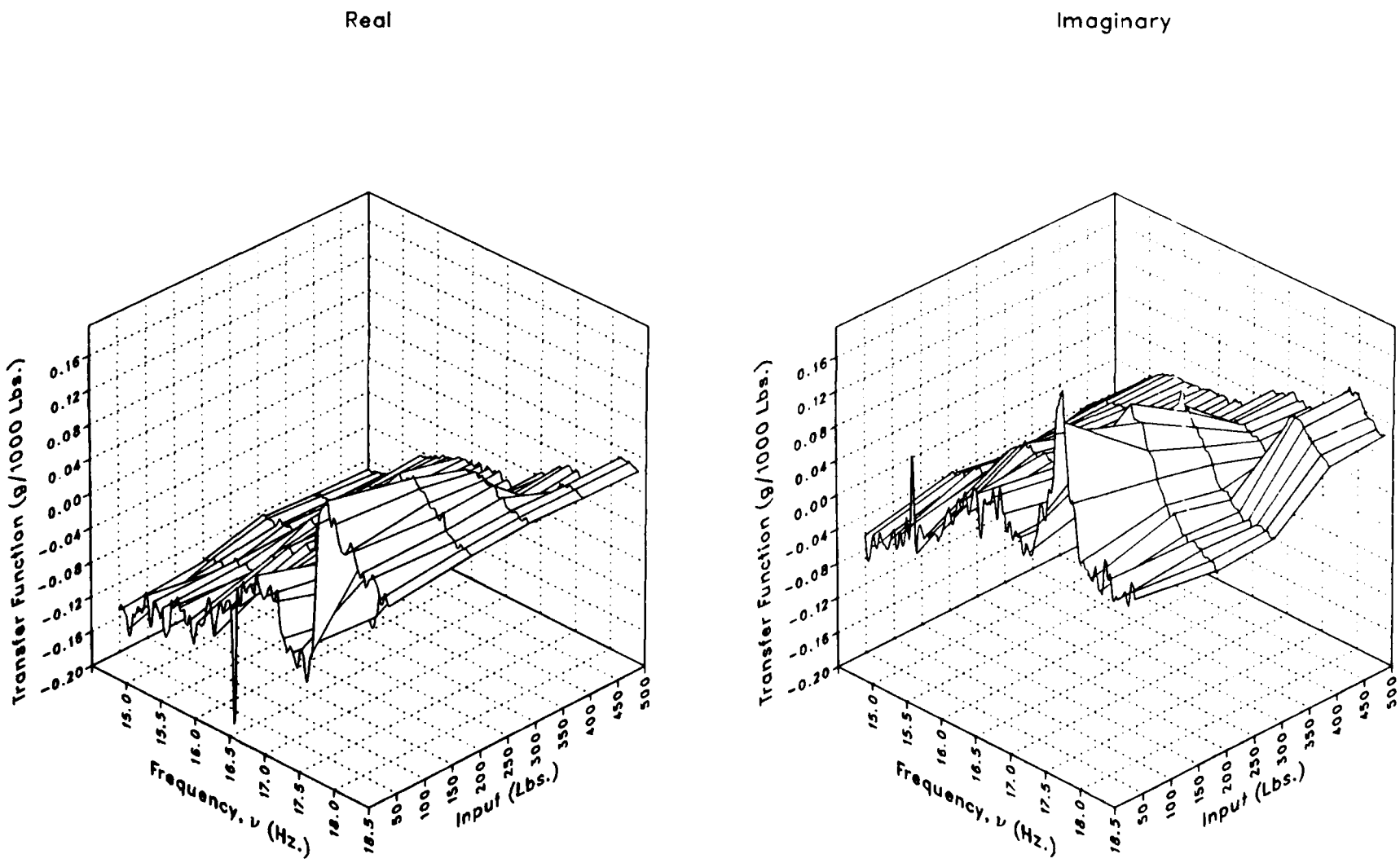

(r) LIGB

Figure 5.– Continued.

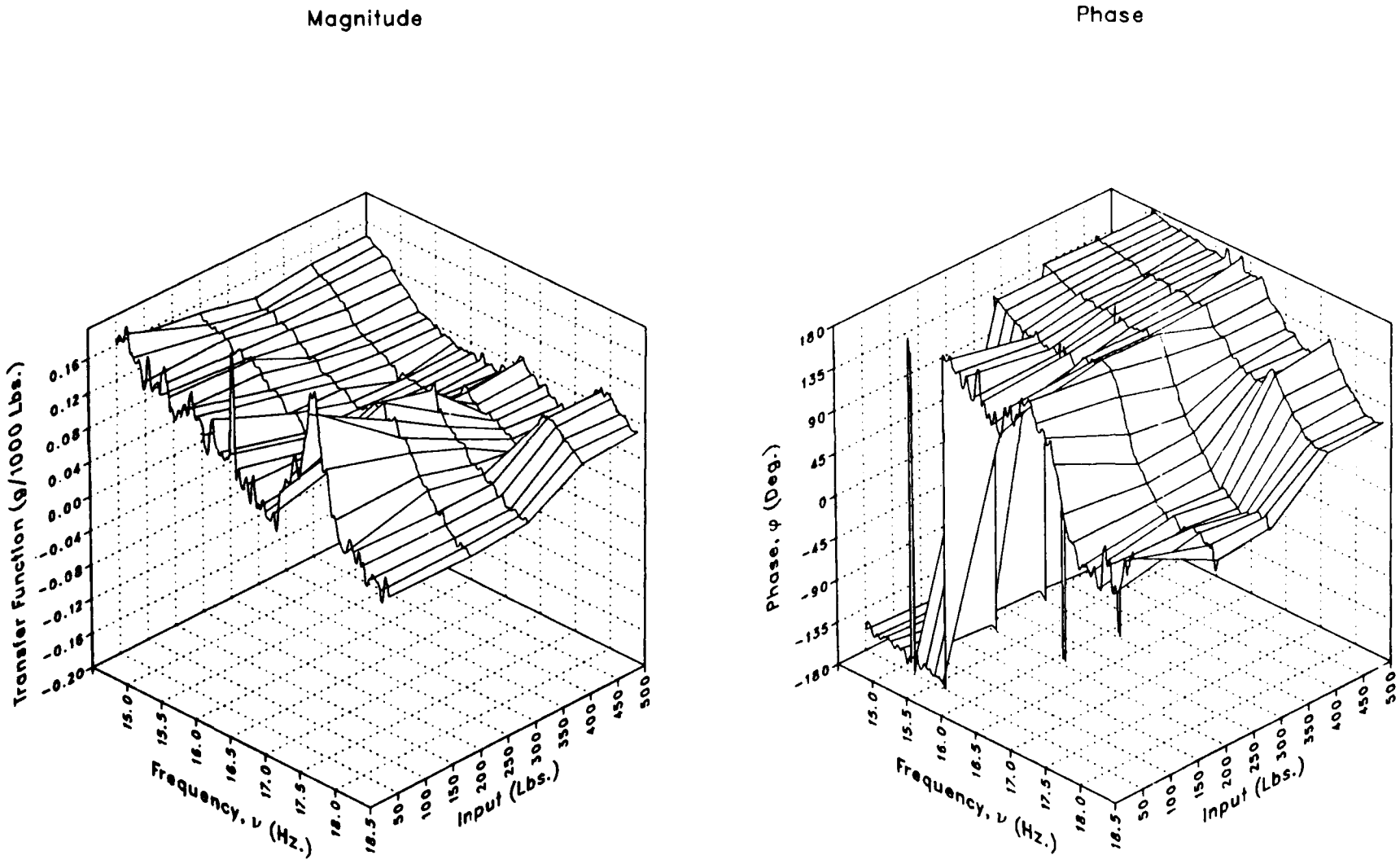

(r) LIGB Concluded.

Figure 5.– Continued.

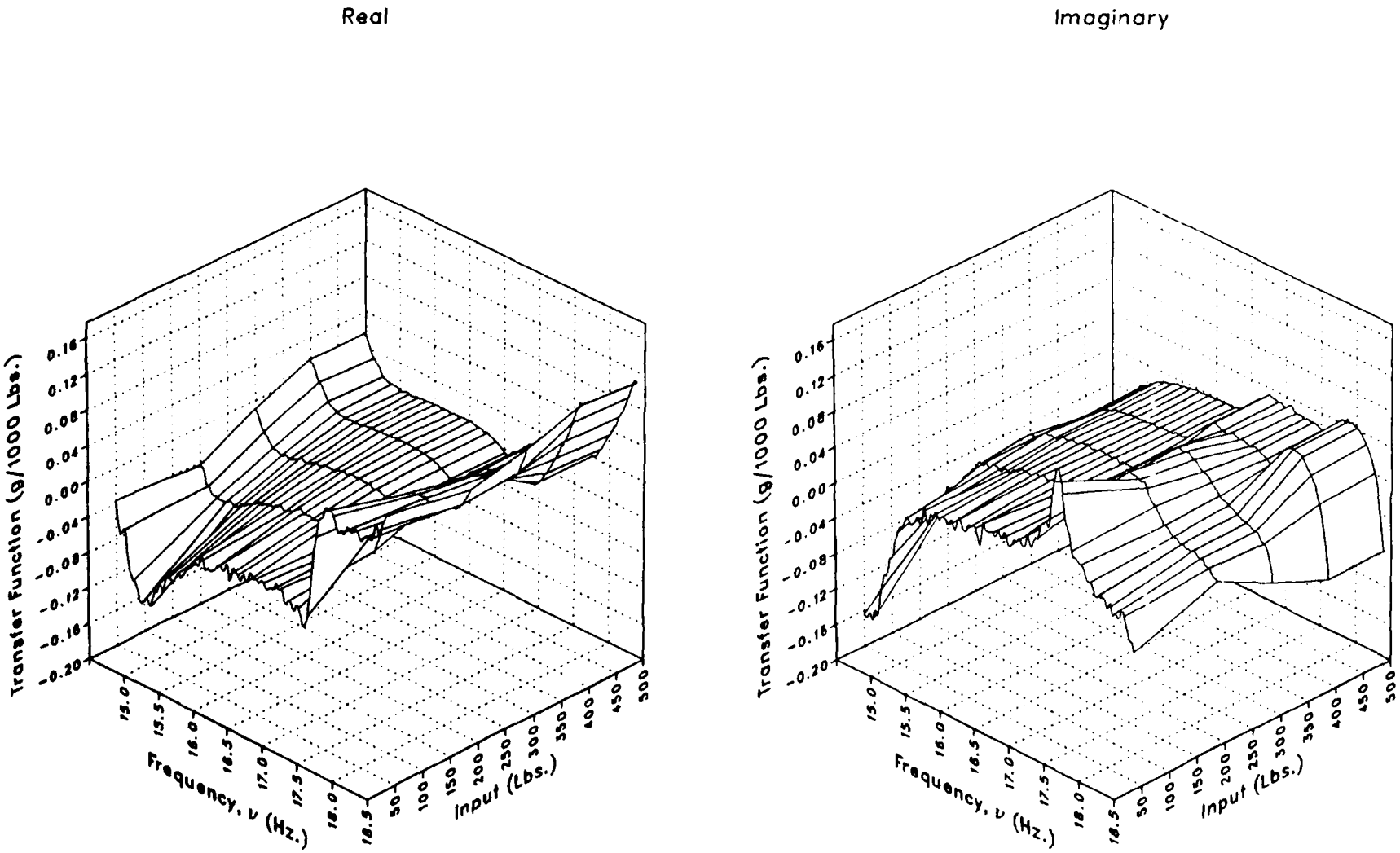

(s) VIGB

Figure 5.– Continued.

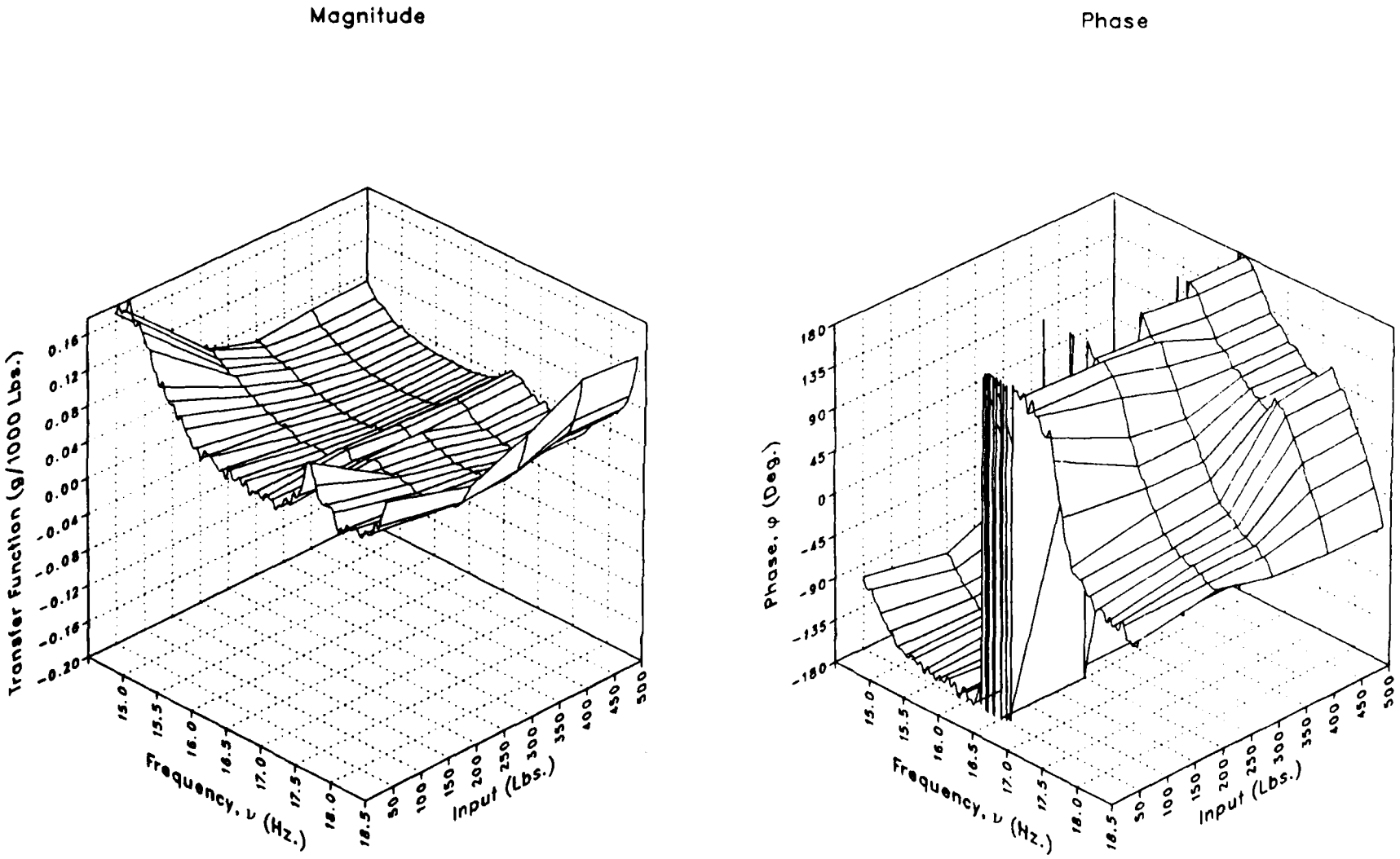

(s) VIGB Concluded.

Figure 5.– Continued.

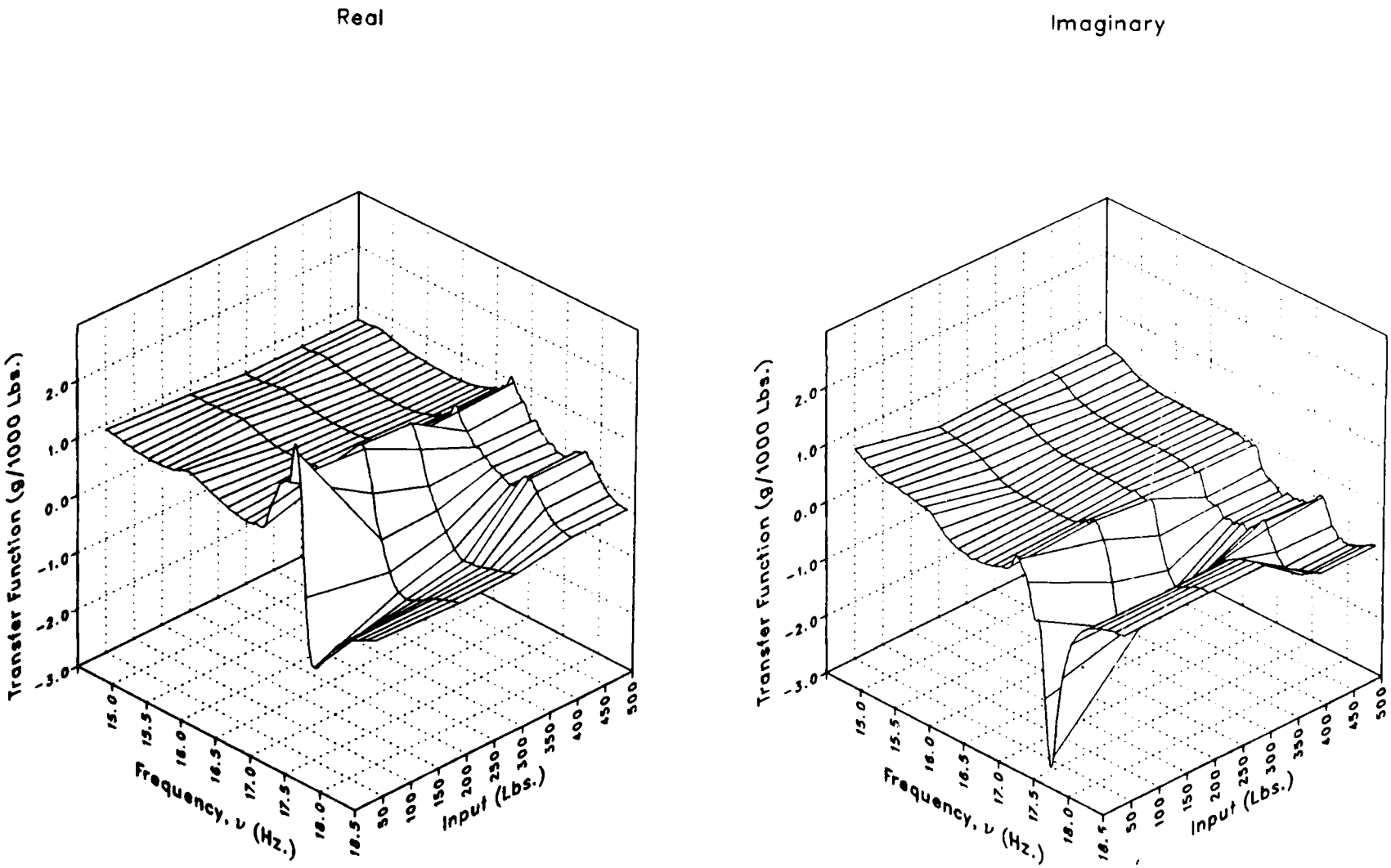

(t) LATTPYLN

Figure 5.– Continued.

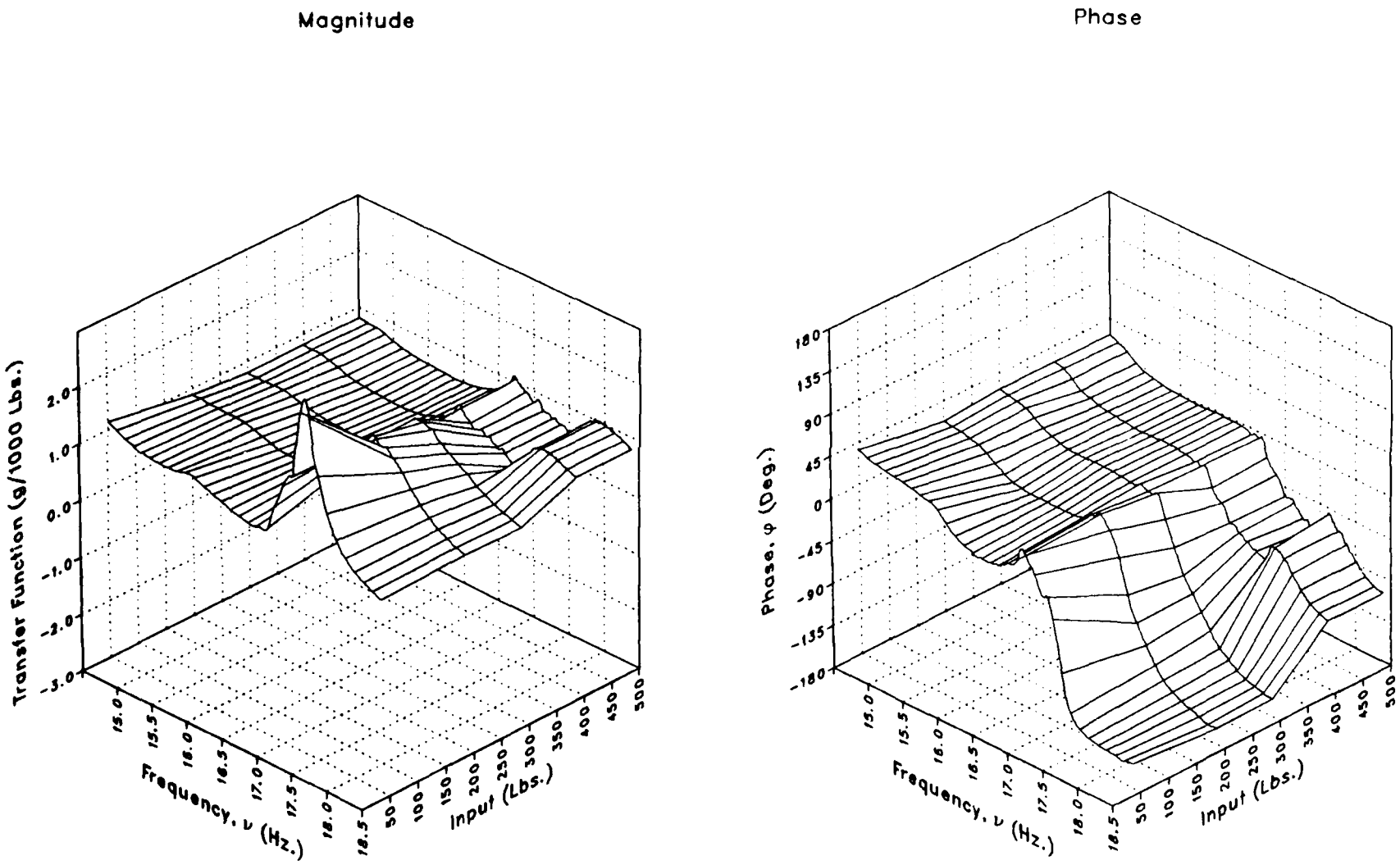

(t) LATTPYLN Concluded.

Figure 5.– Continued.

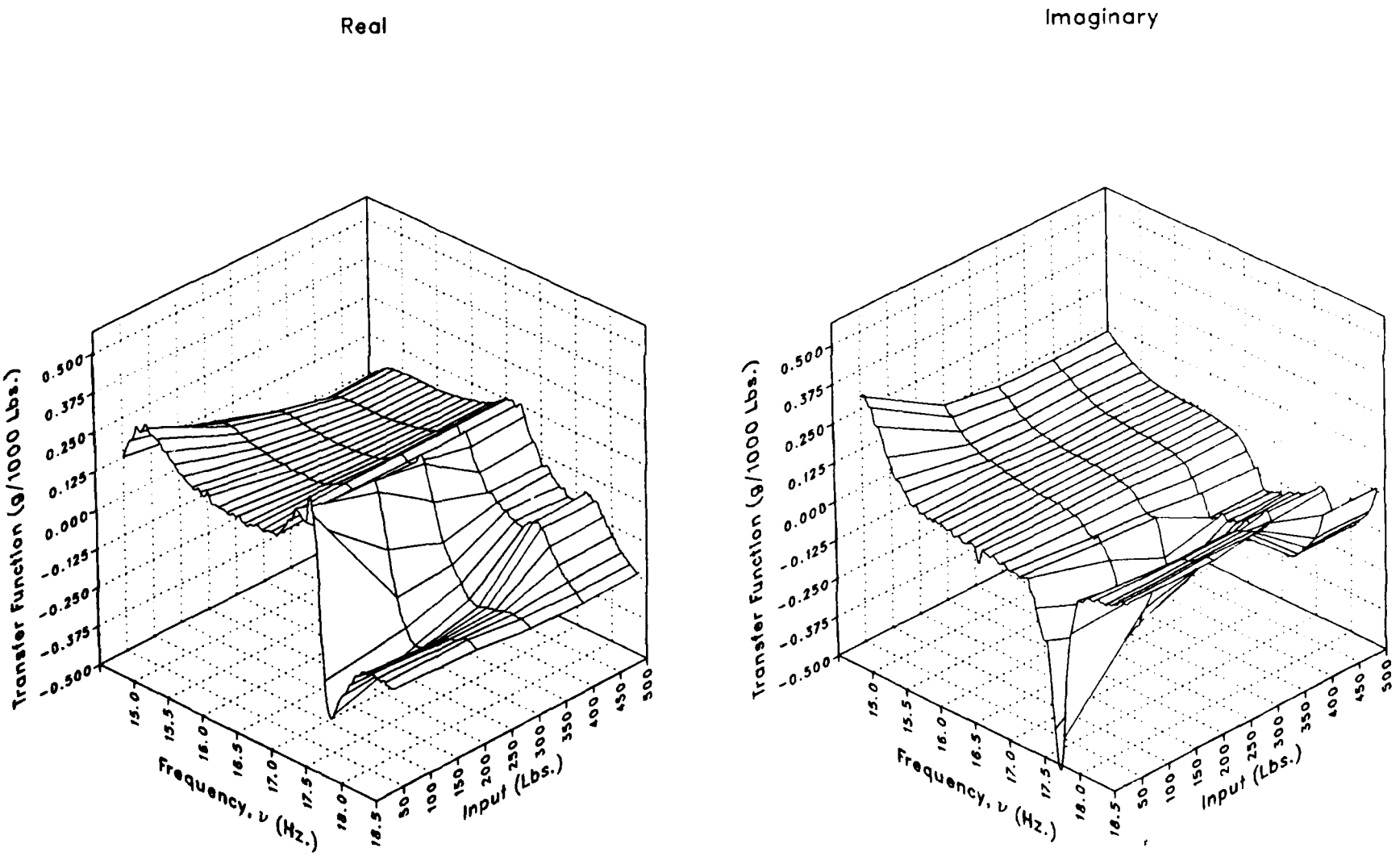

(u) VTTPYLON

Figure 5.– Continued.

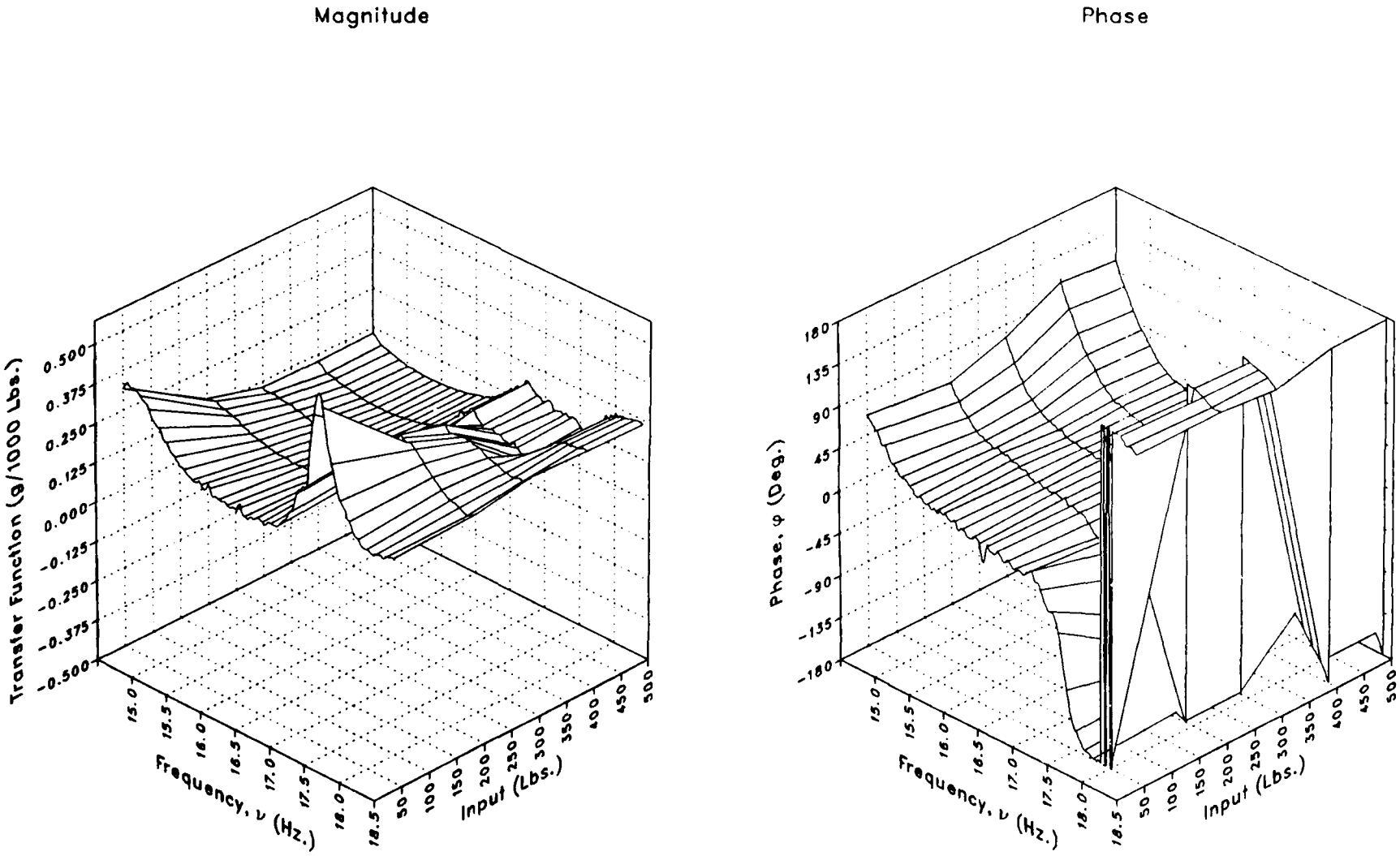

(u) VT fPYLON Concluded.

Figure 5.– Continued.

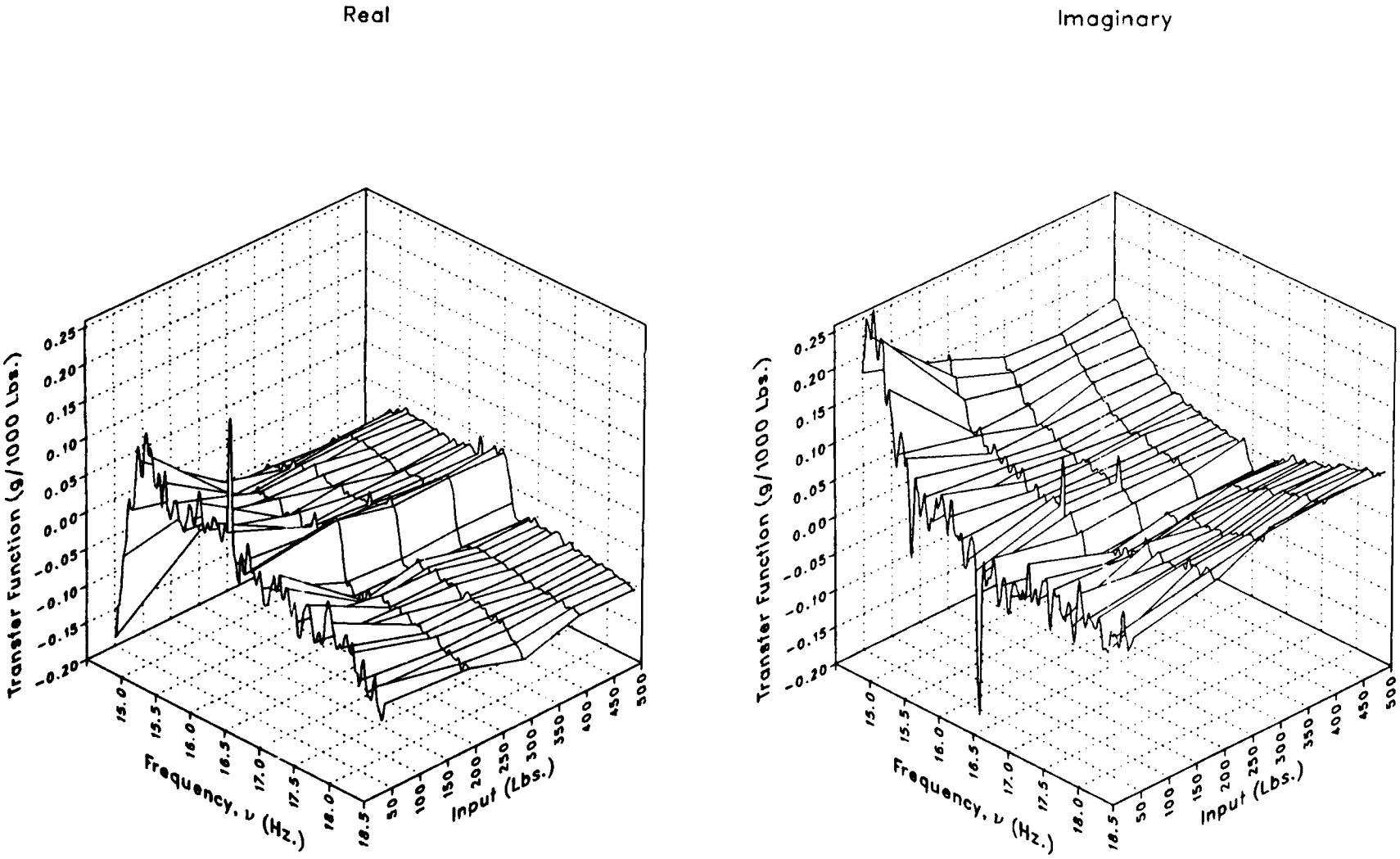

(v) XMRFLV

Figure 5.– Continued.

Magnitude

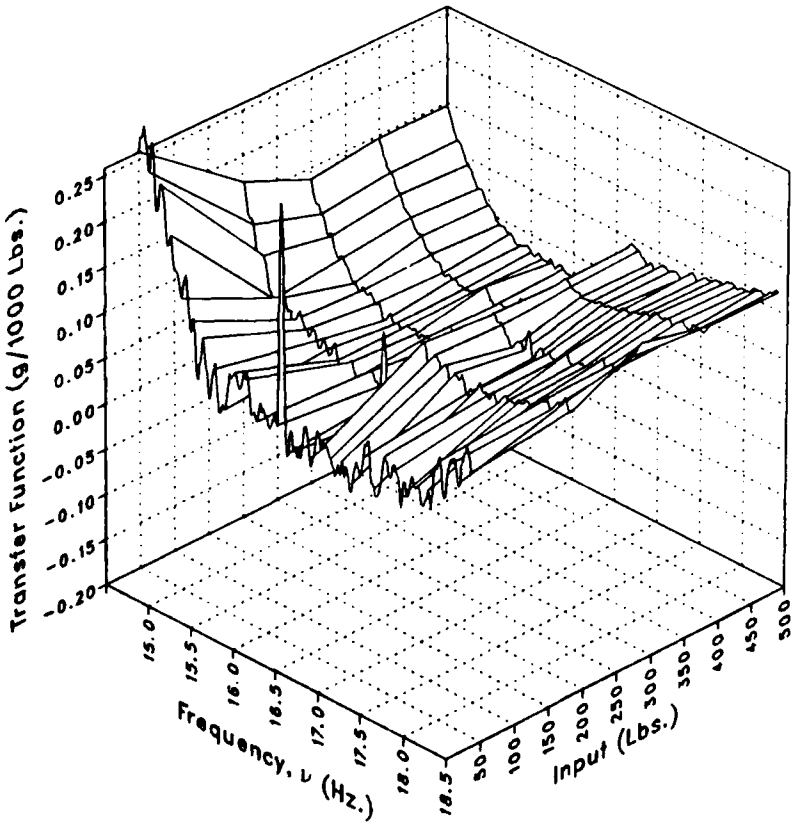

Phase

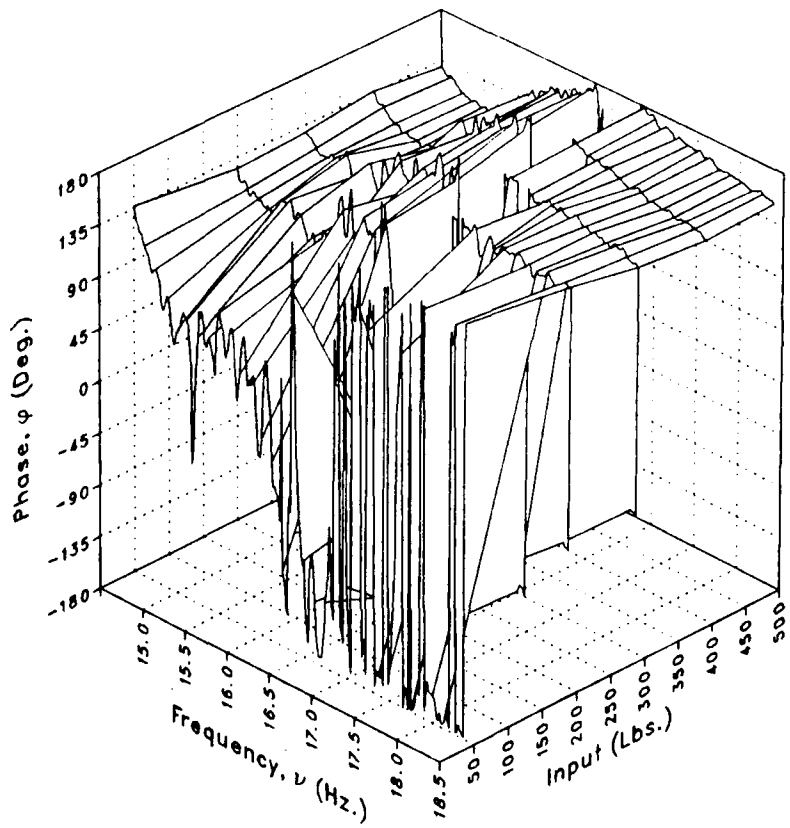

(v) XMRFLV Concluded.

Figure 5.– Continued.

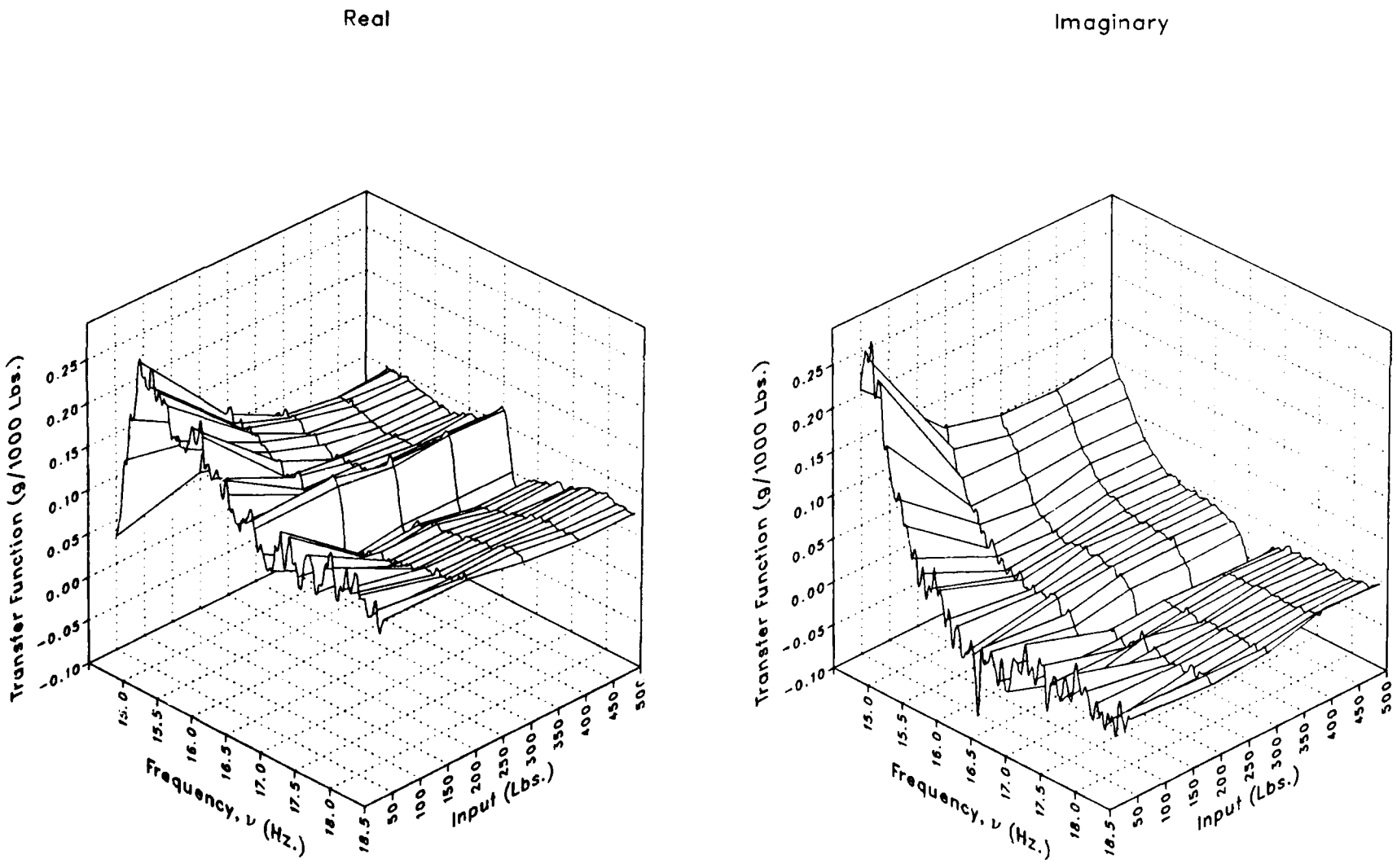

(w) XMRFRV

Figure 5.– Continued.

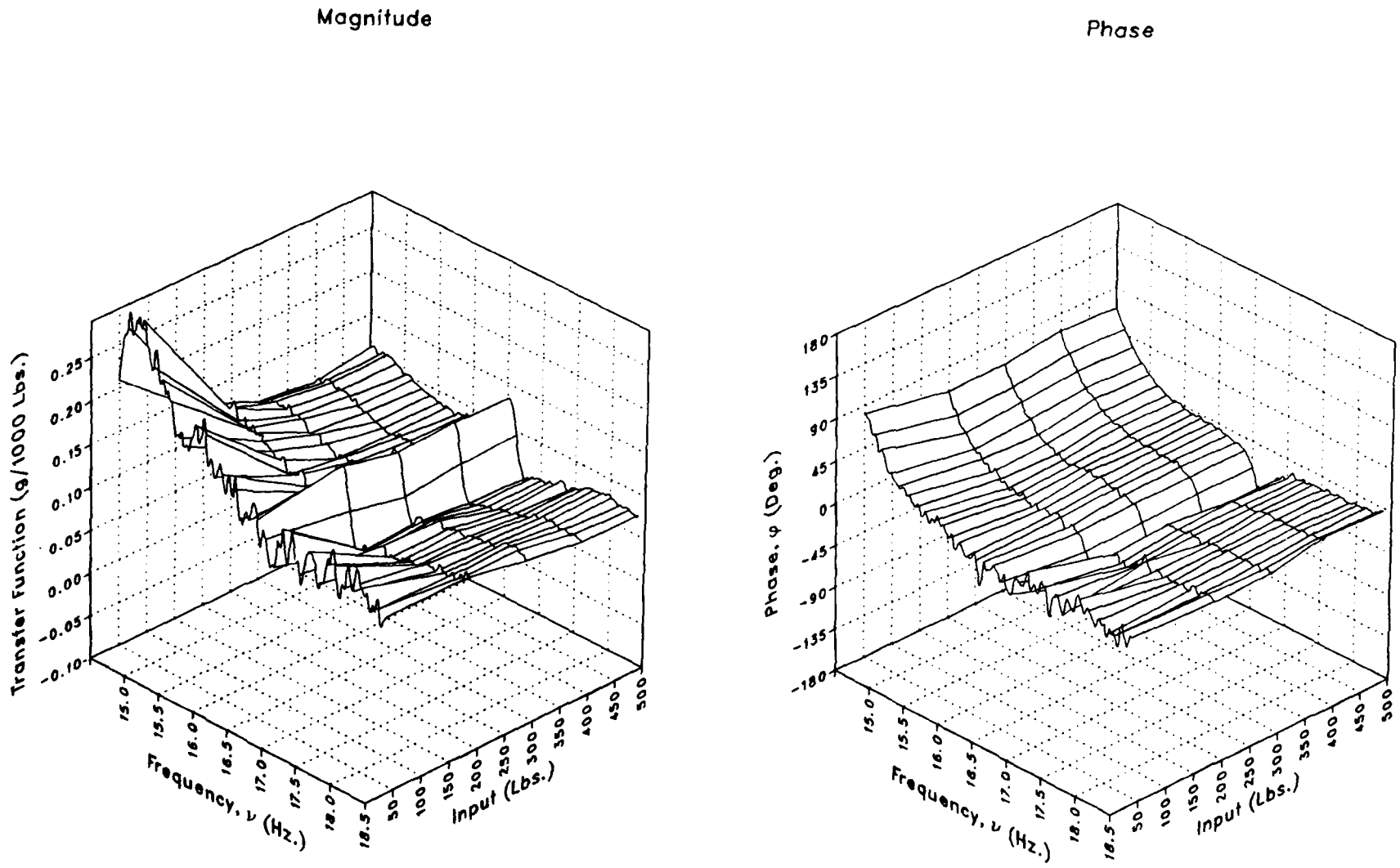

(w) XMRFRV Concluded.

Figure 5.– Continued.

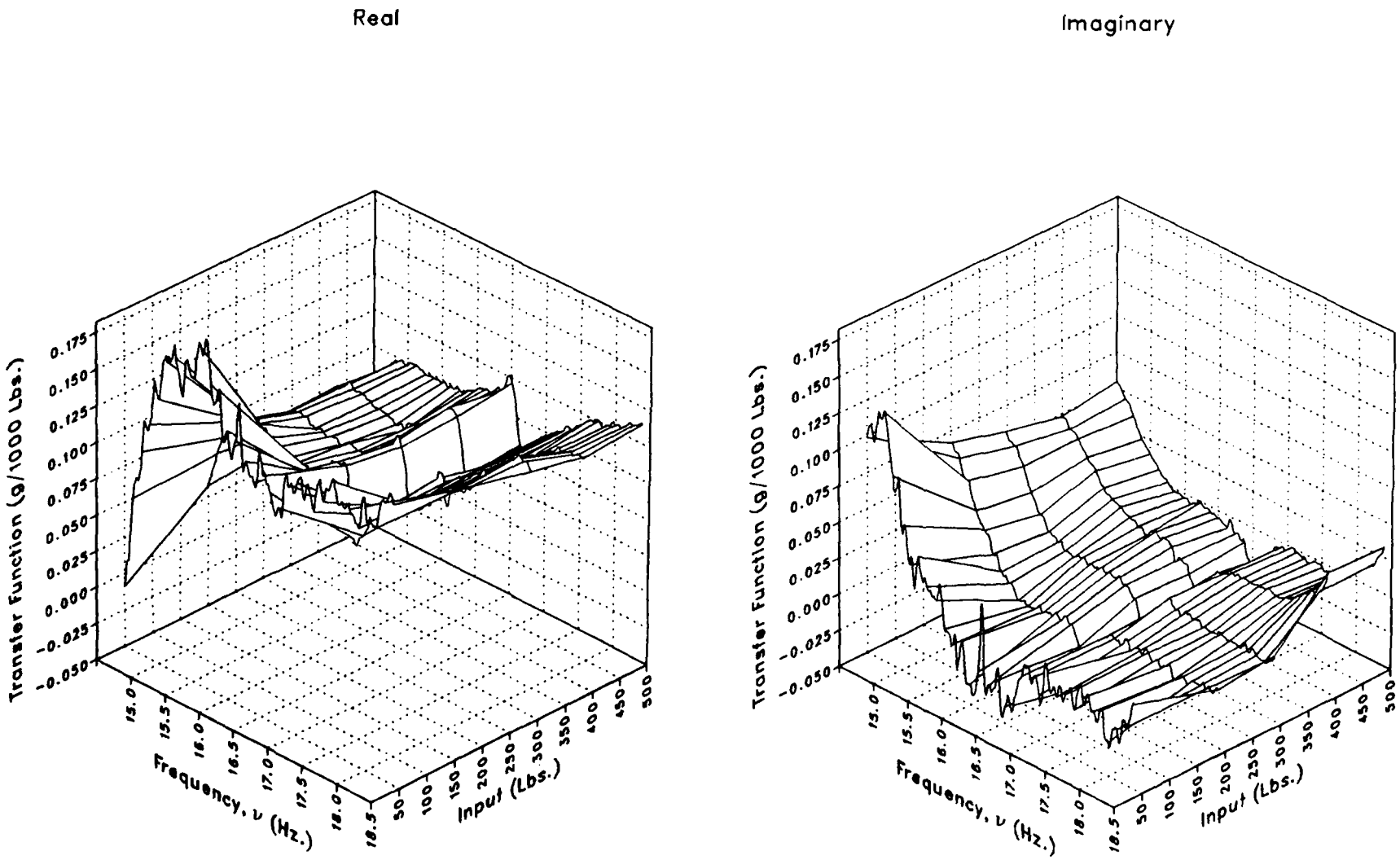

(x) S222FLRV

Figure 5.– Continued.

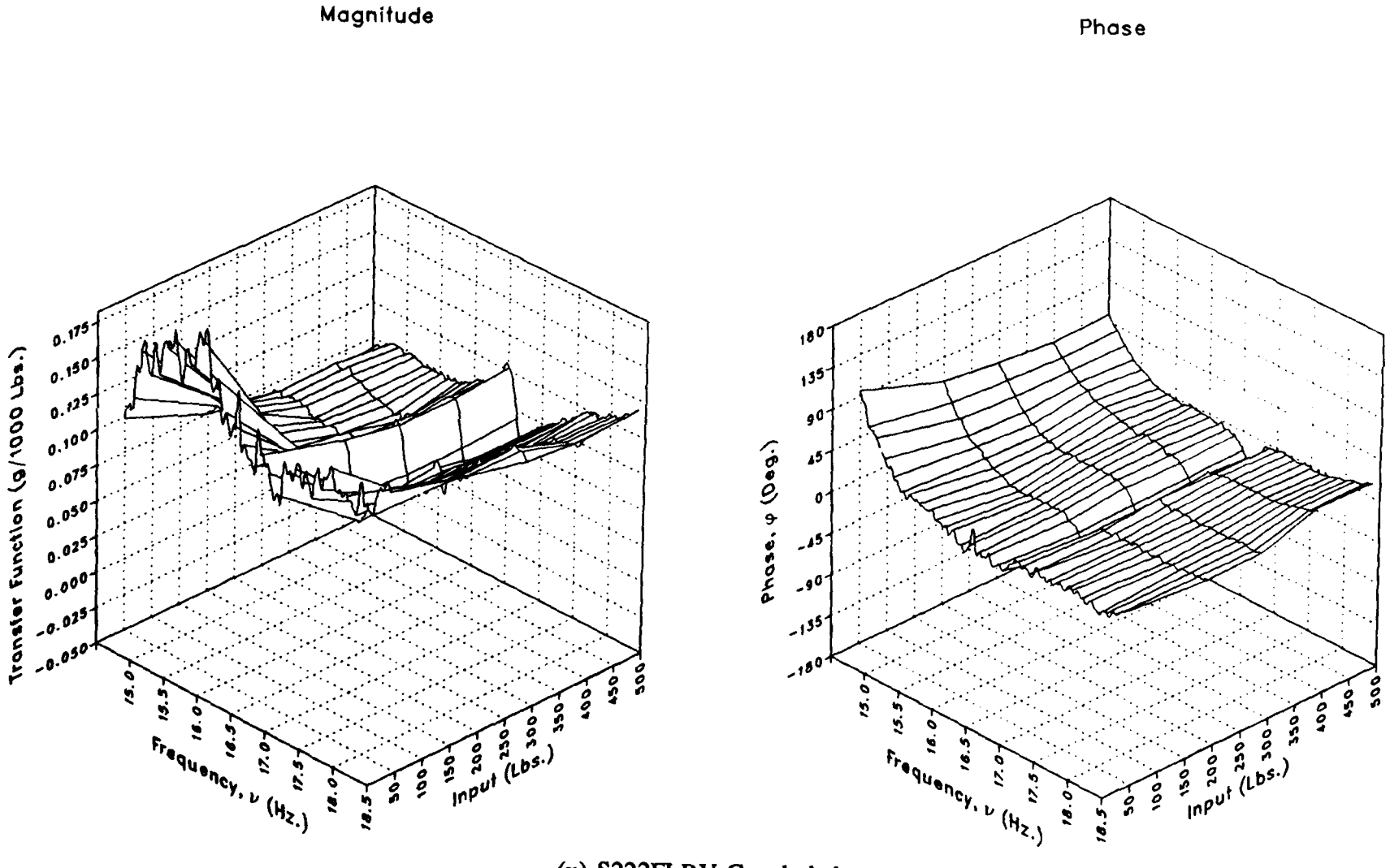

(x) S222FLRV Concluded.

Figure 5.– Continued.

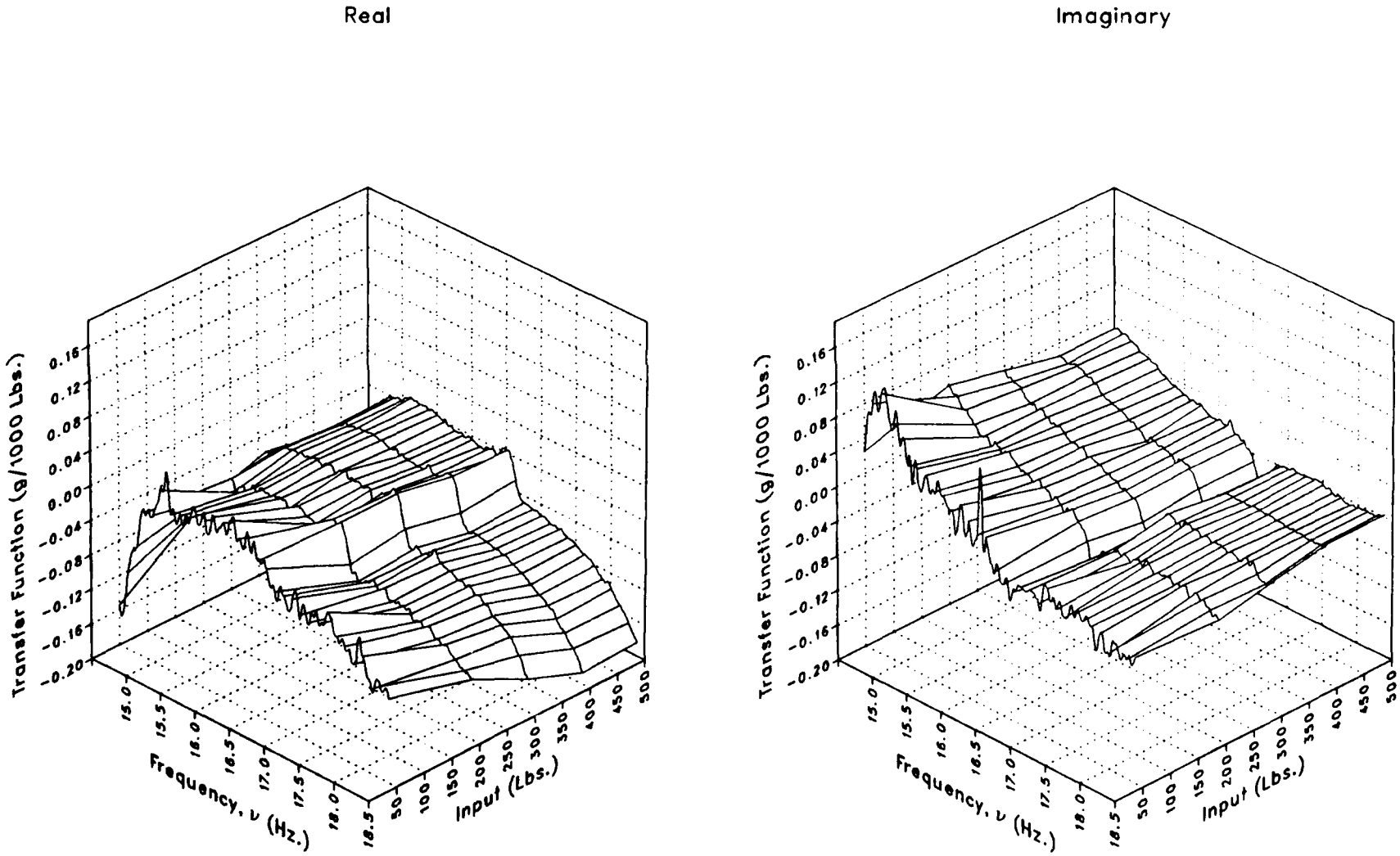

(y) S222FLLV

Figure 5.– Continued.

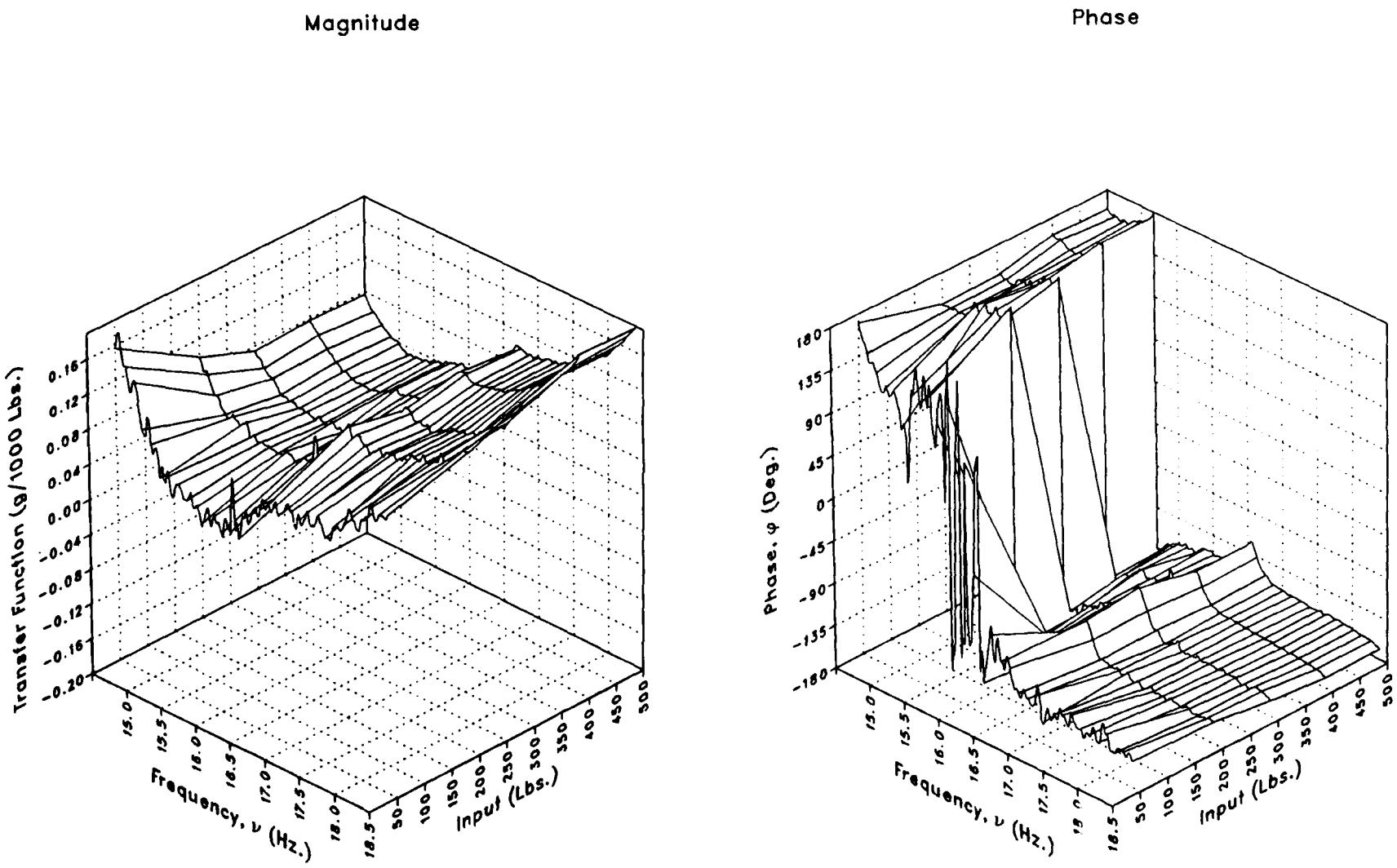

(y) S222FLLV Concluded.

Figure 5.– Continued.

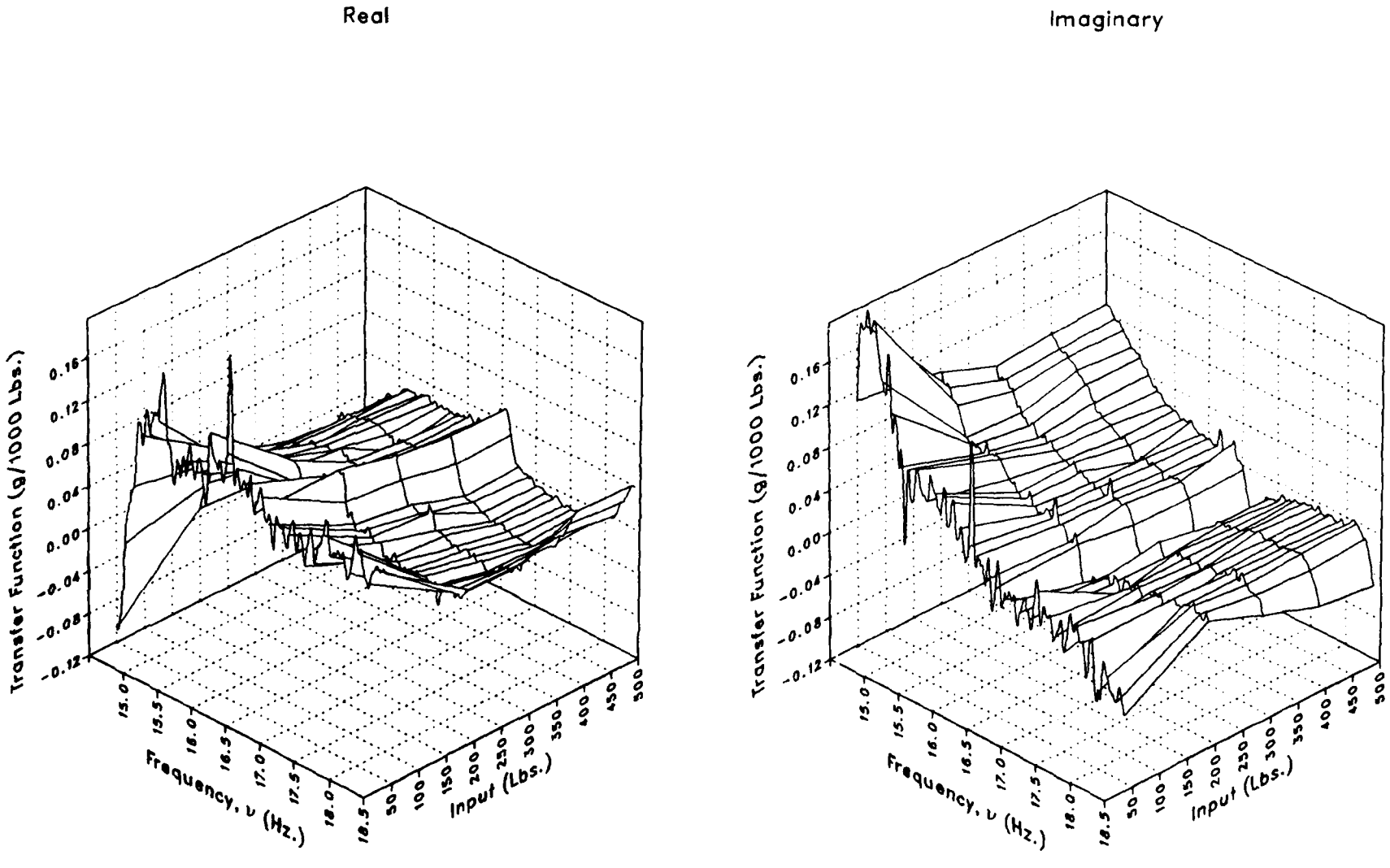

(z) S450FLV

Figure 5.– Continued.

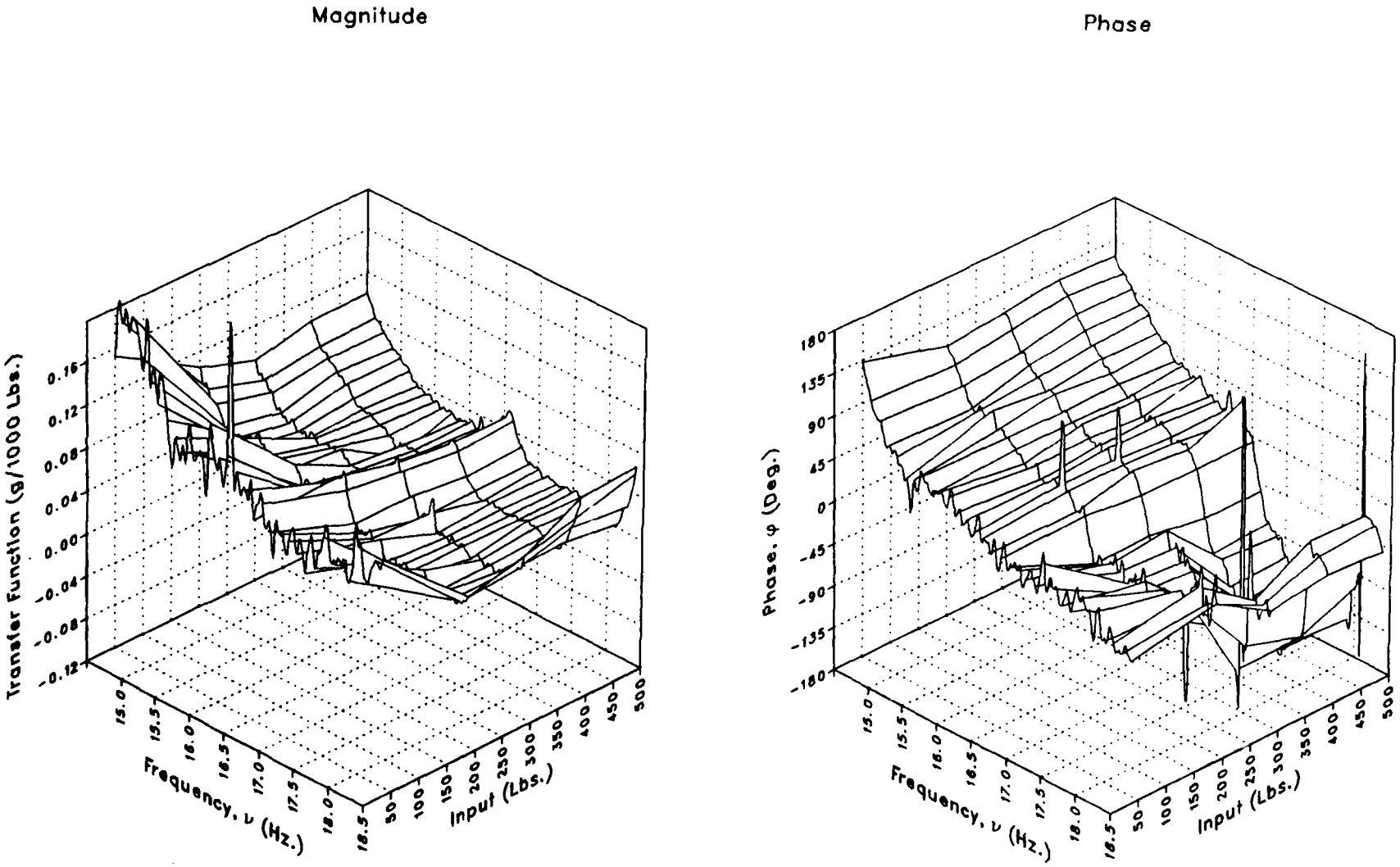

(z) S450FLV Concluded.

Figure 5.– Continued.

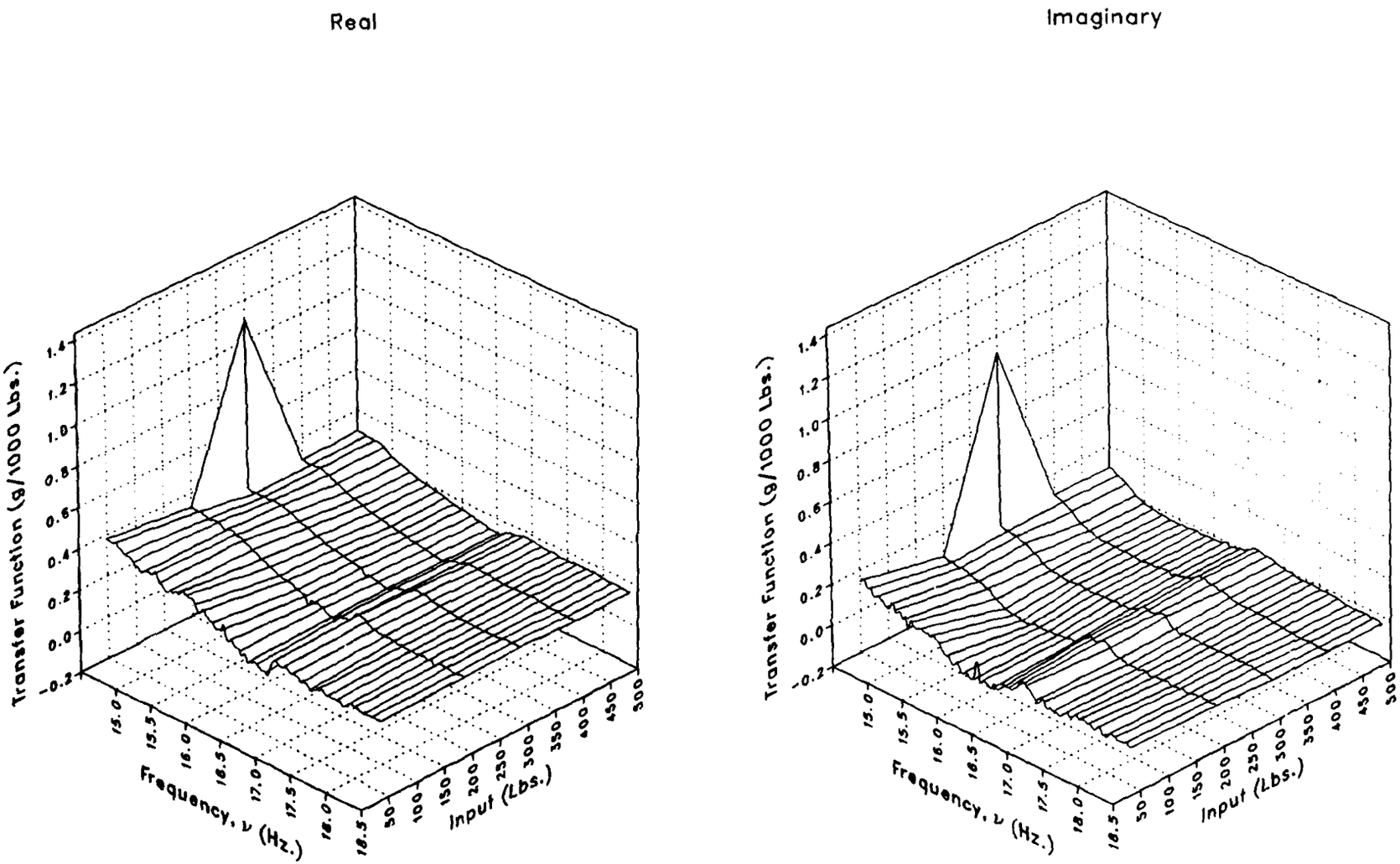

(aa) S450FLL

Figure 5.– Continued.

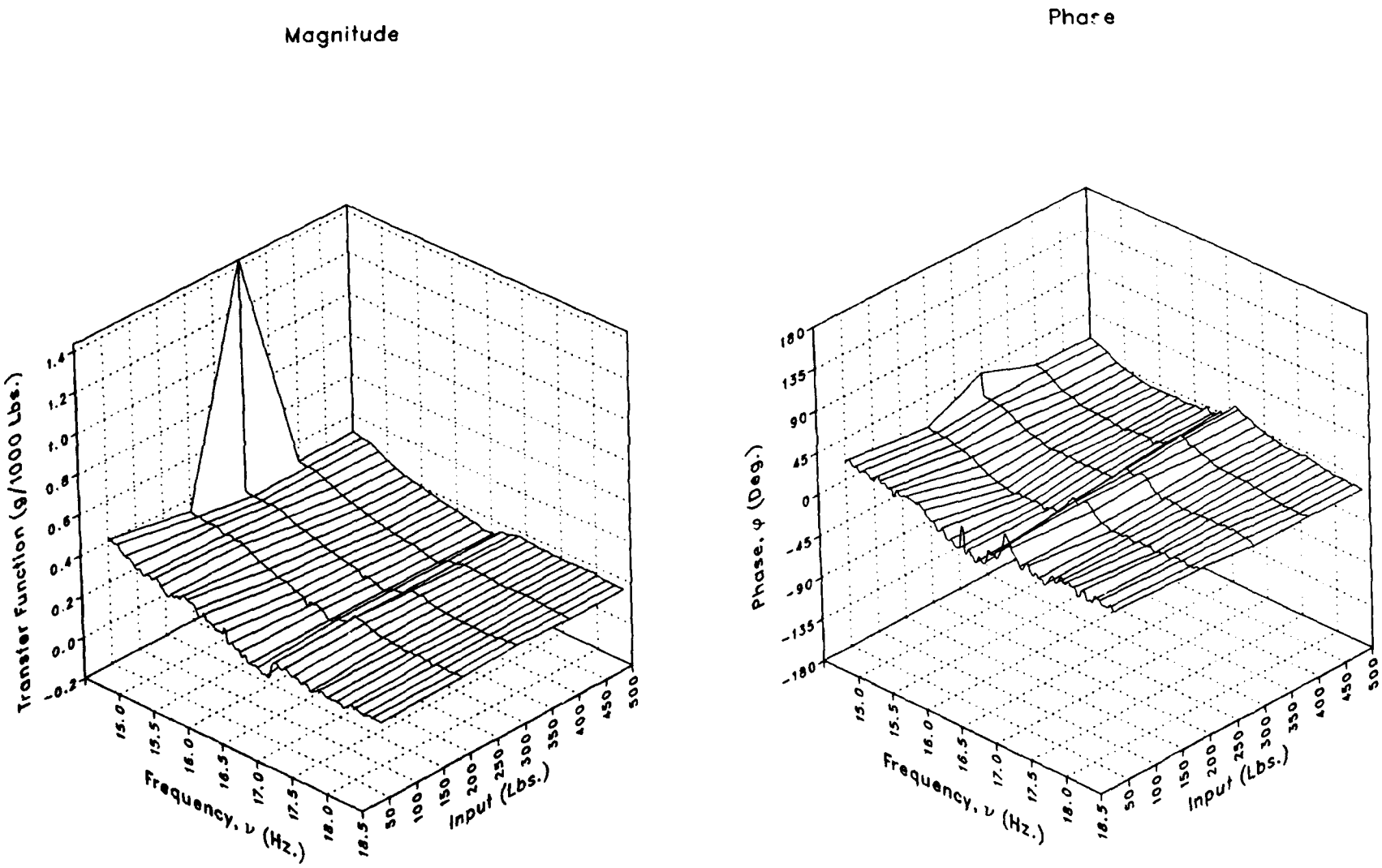

(aa) S450FLL Concluded.

Figure 5.– Continued.

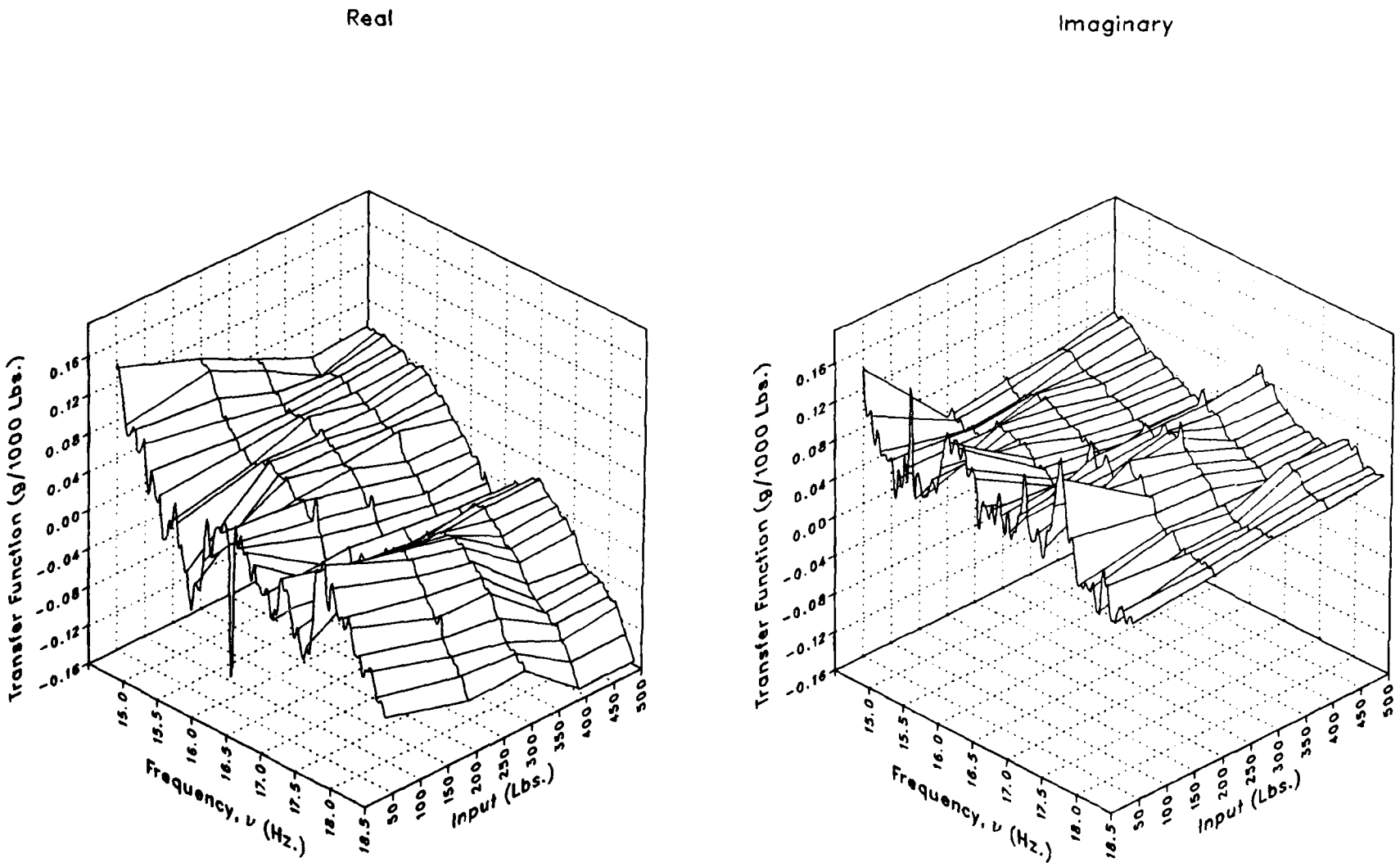

(bb) S450OVRL

Figure 5.– Continued.

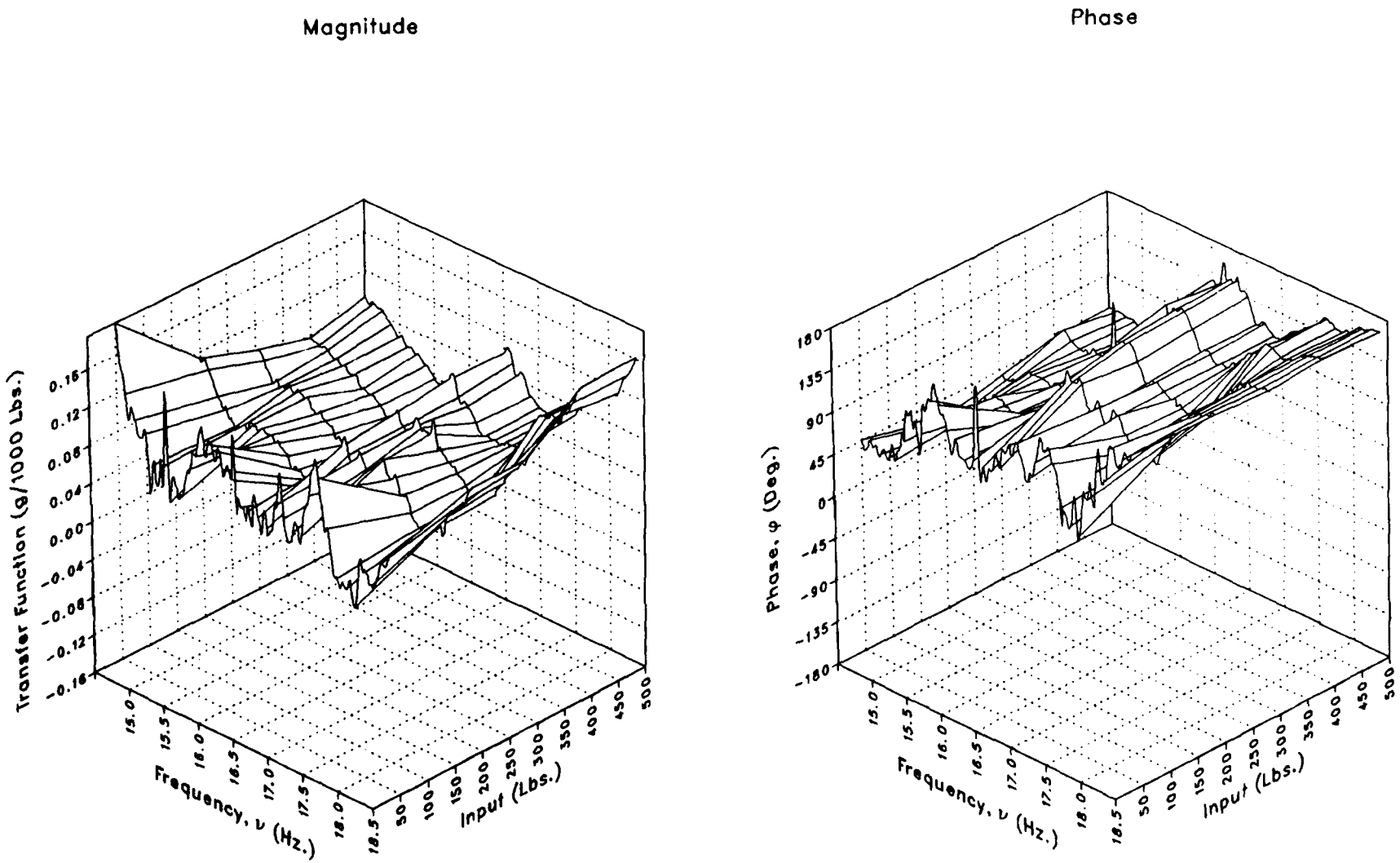

(bb) S450OVRL Concluded.

Figure 5.– Concluded.

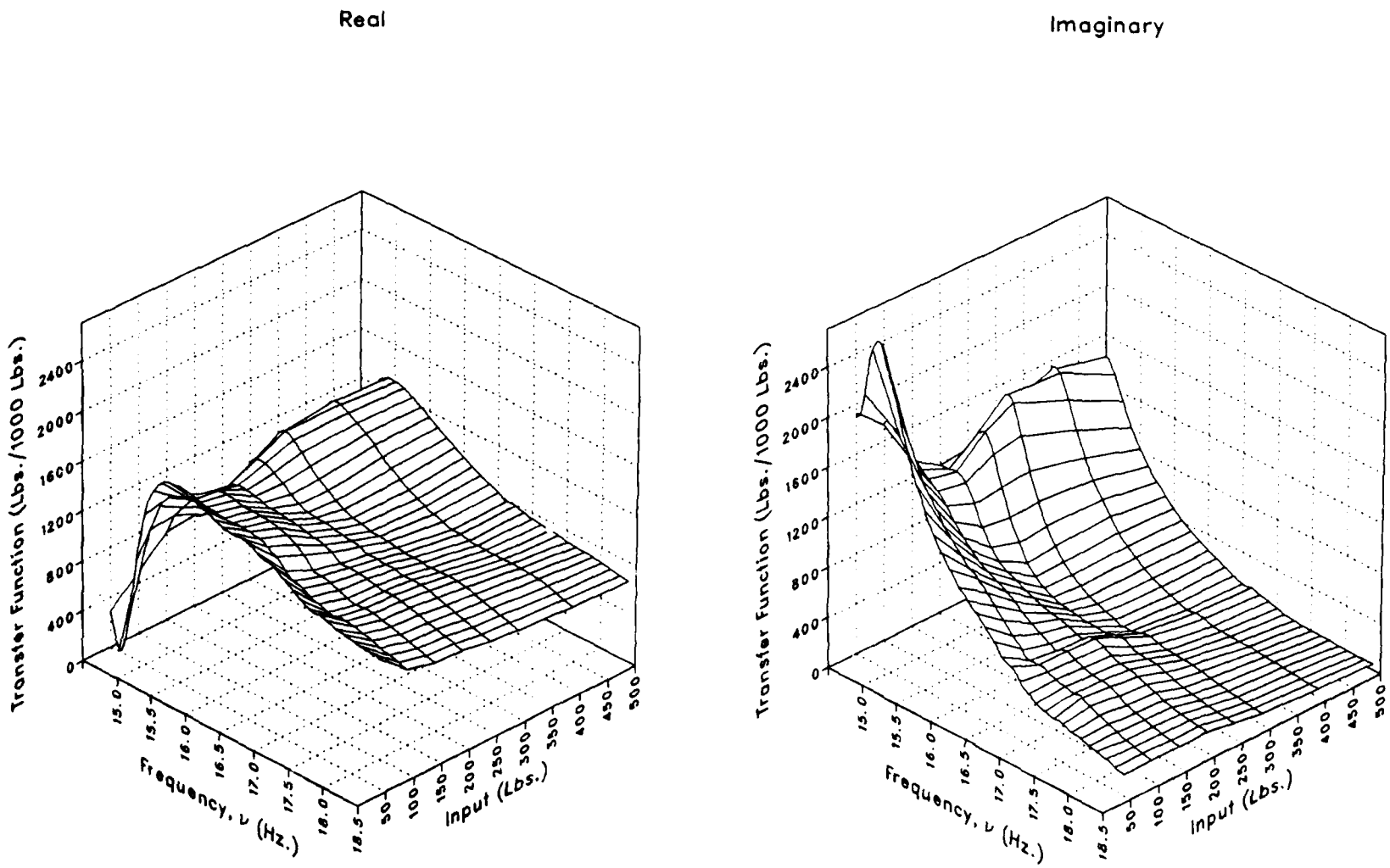

(a) MRDRAG

Figure 6.– Multi-axis forcing.

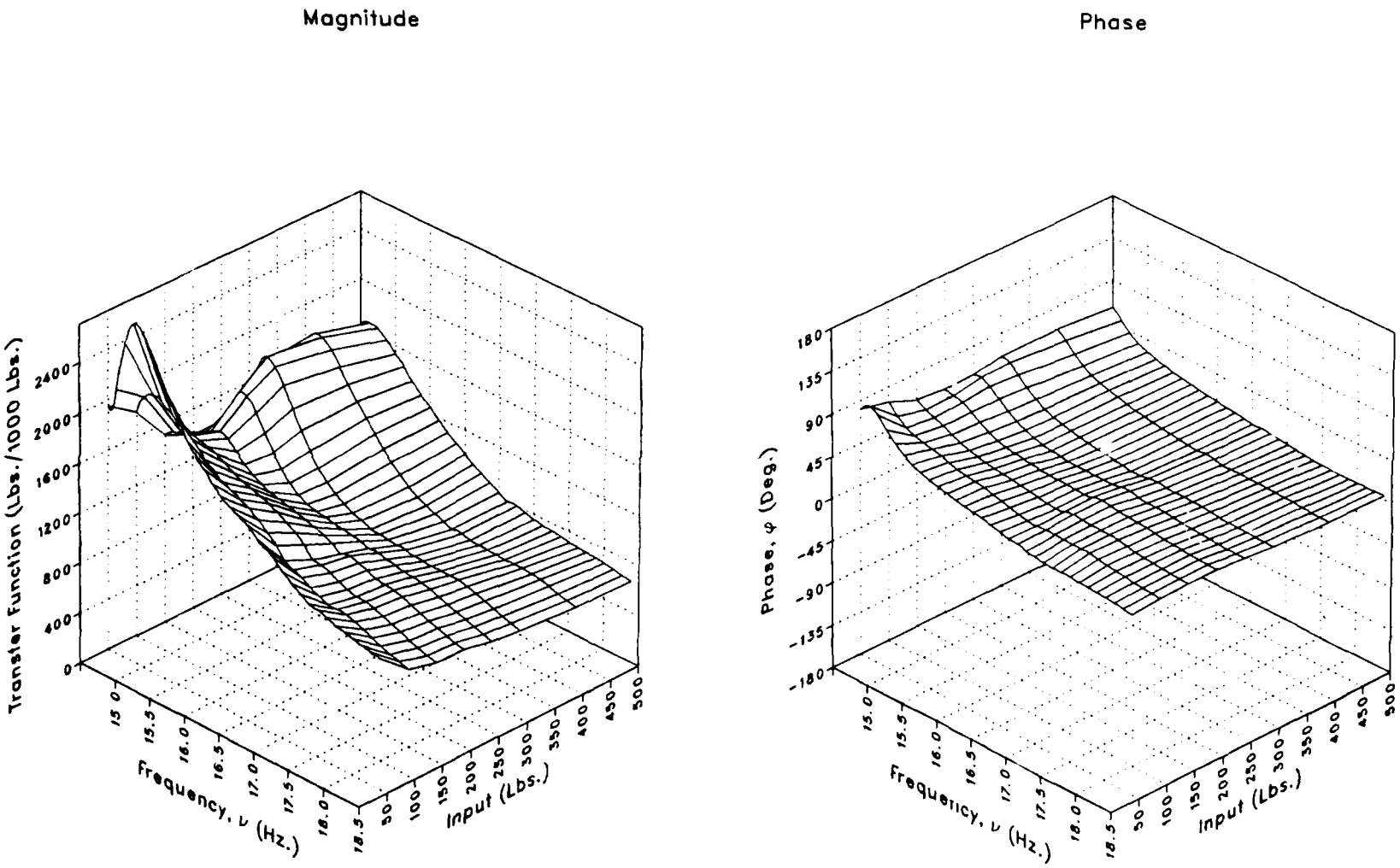

(a) MRDRAG Concluded.

Figure 6.– Continued.

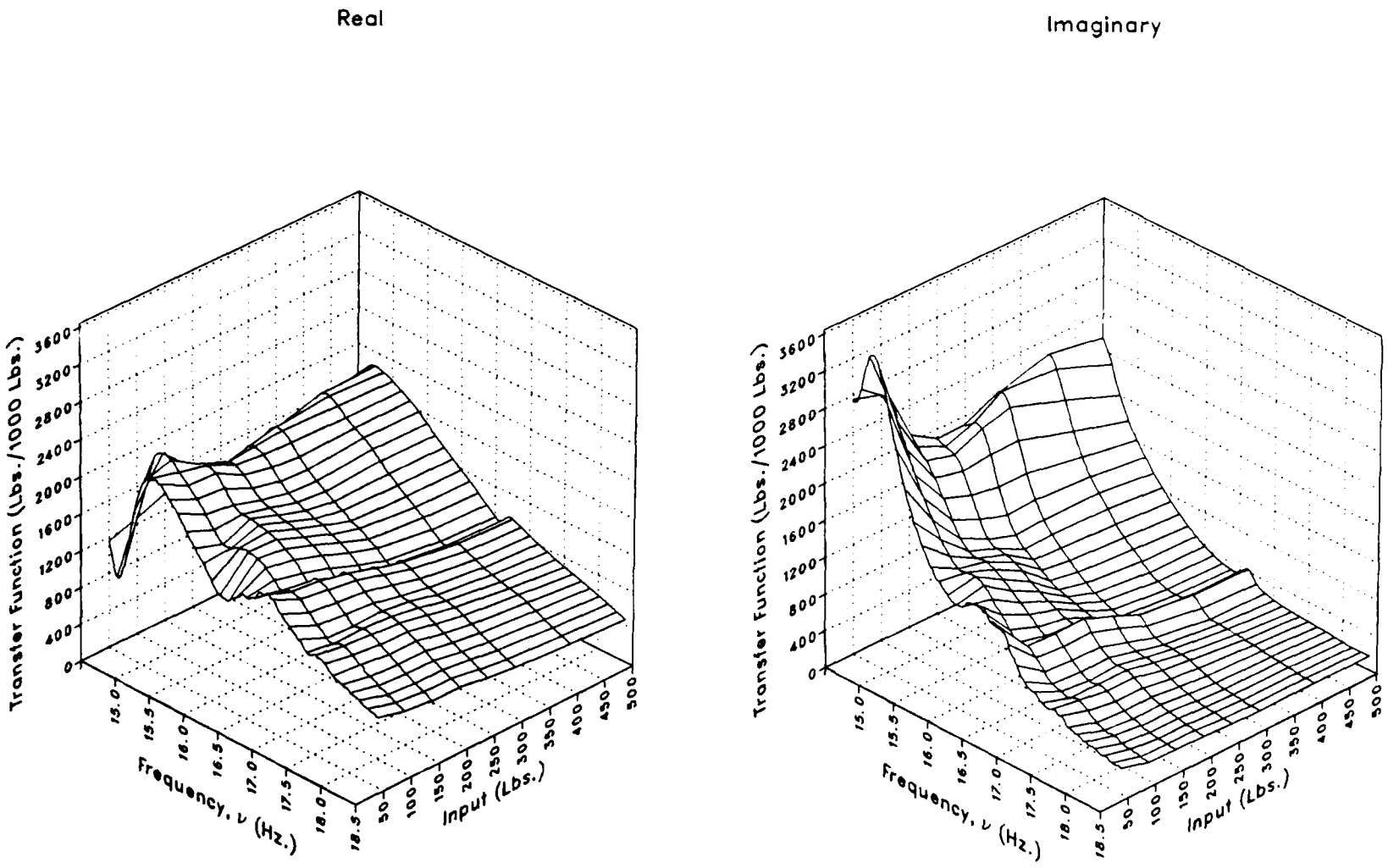

(b) MRLIFTA

Figure 6.– Continued.

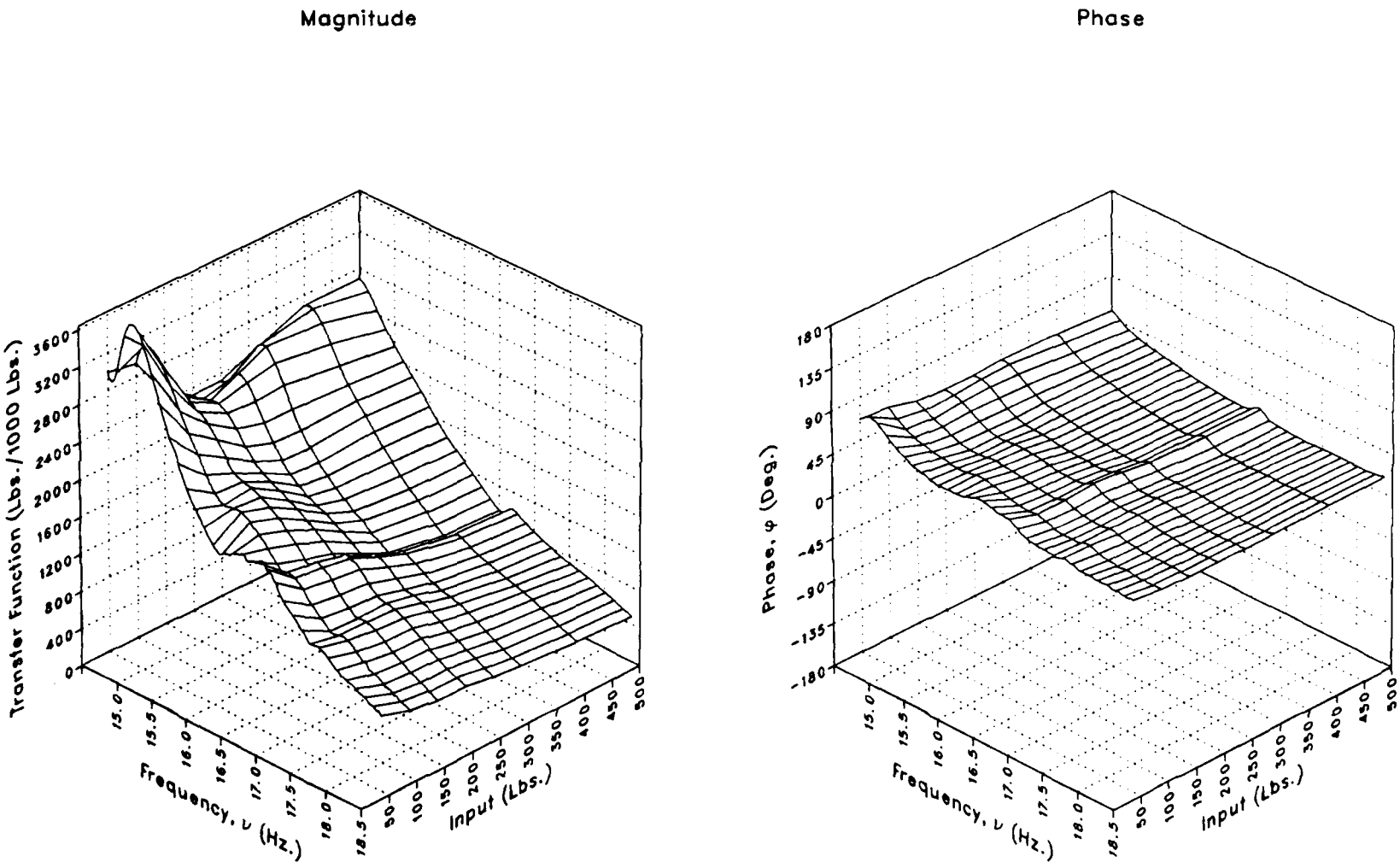

(b) MRLIFTA Concluded.

Figure 6.– Continued.

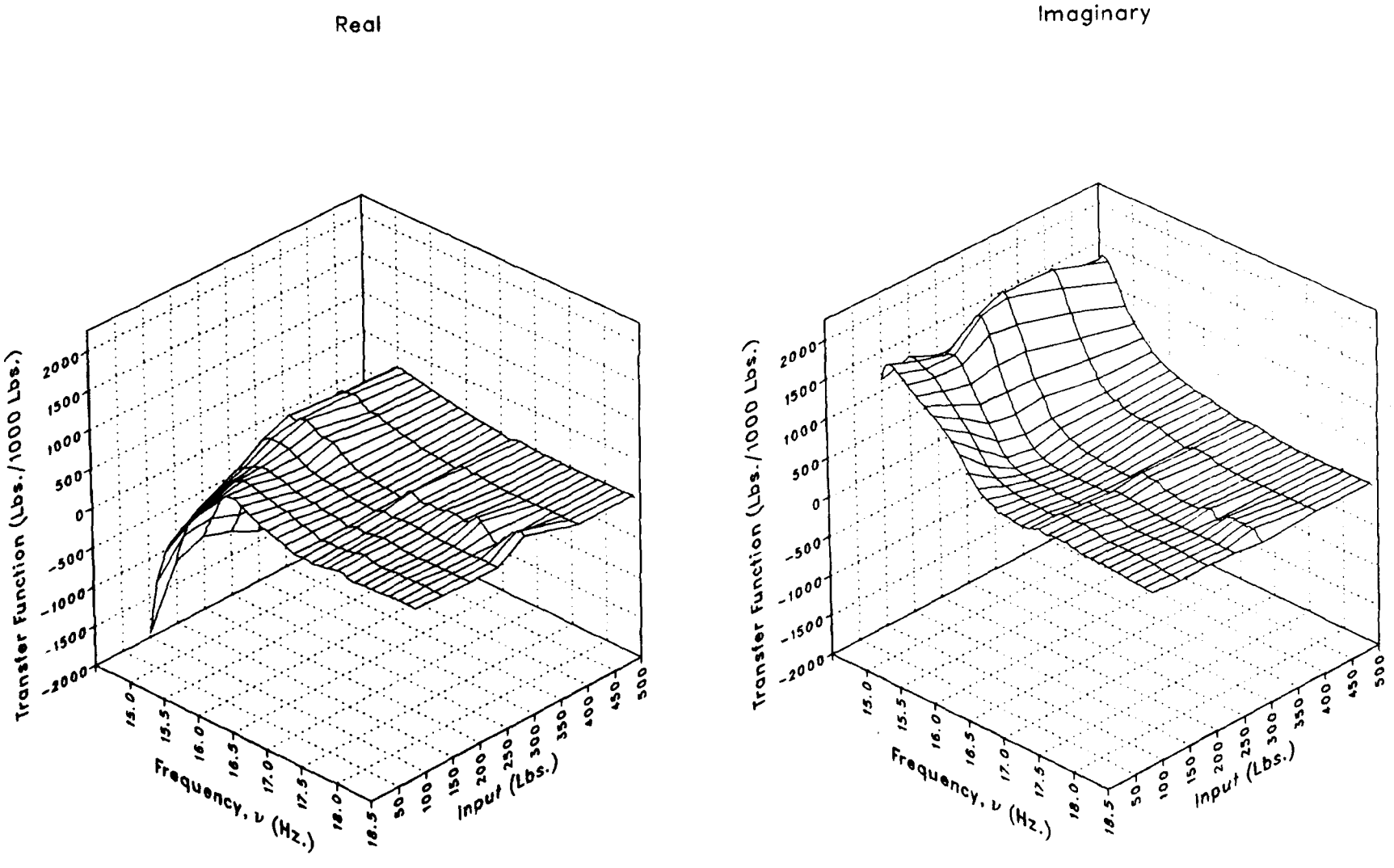

(c) MRLIFTB

Figure 6.– Continued.

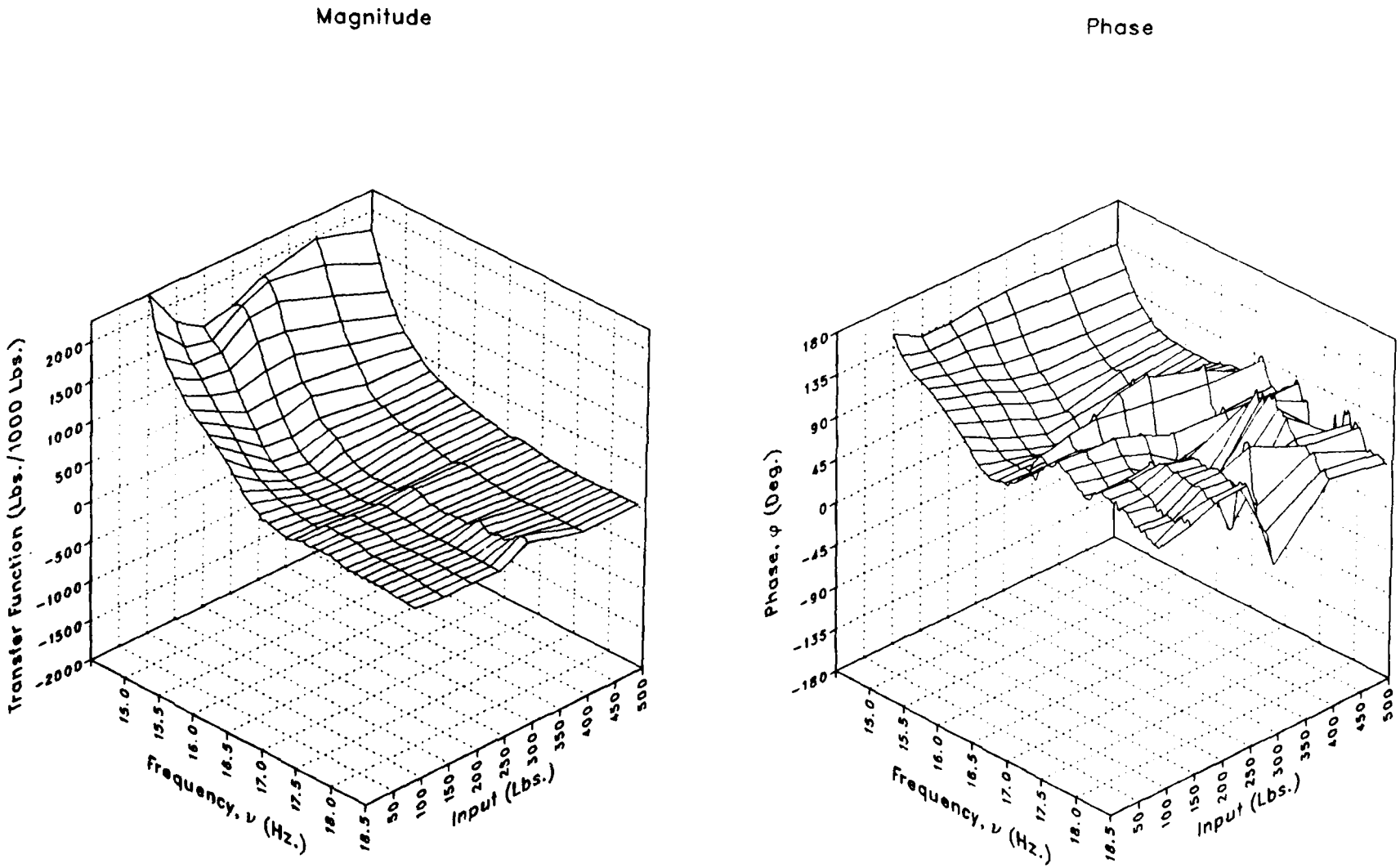

(c) MRLIFTB Concluded.

Figure 6.– Continued.

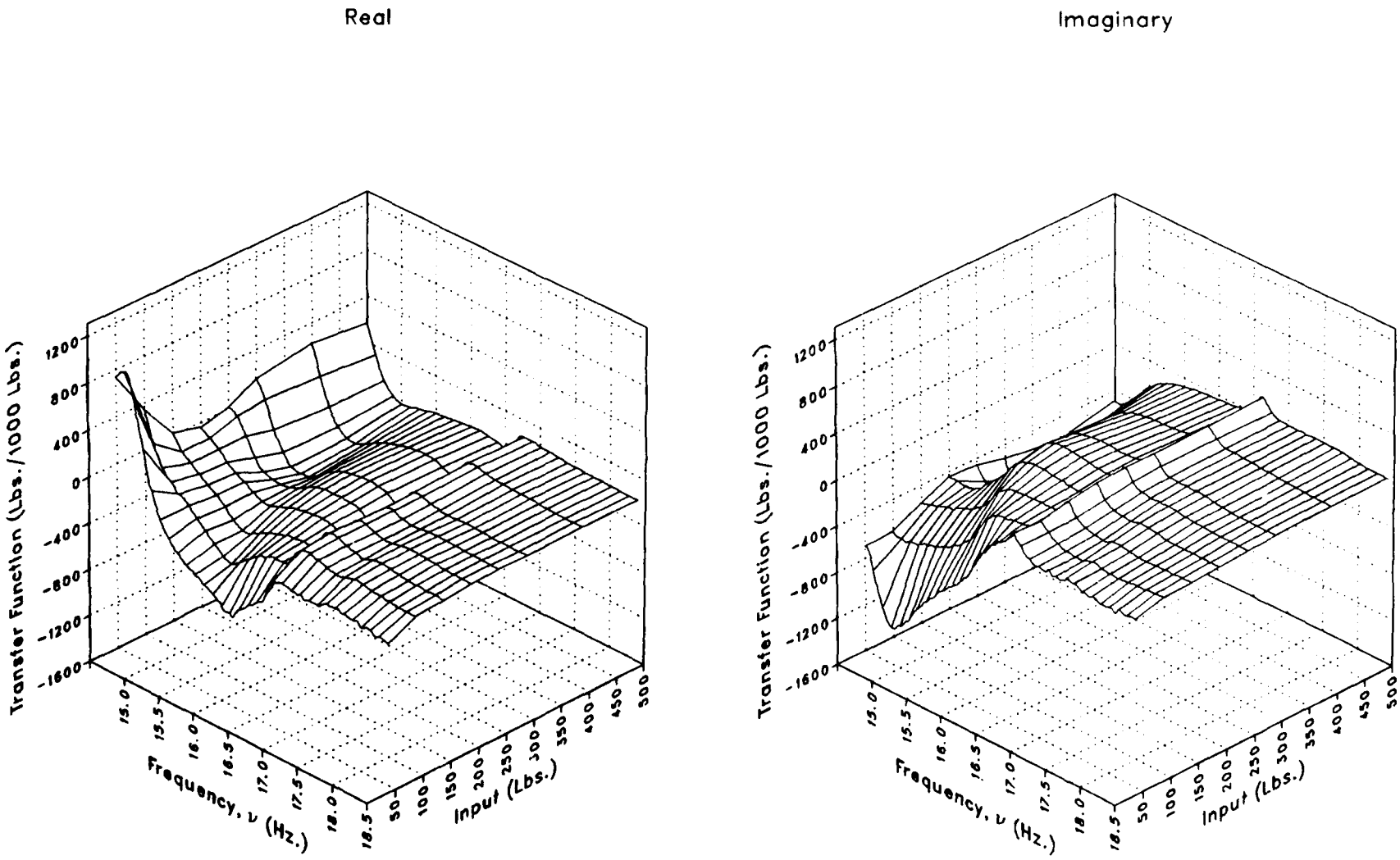

(d) MRLIFTC

Figure 6.– Continued.

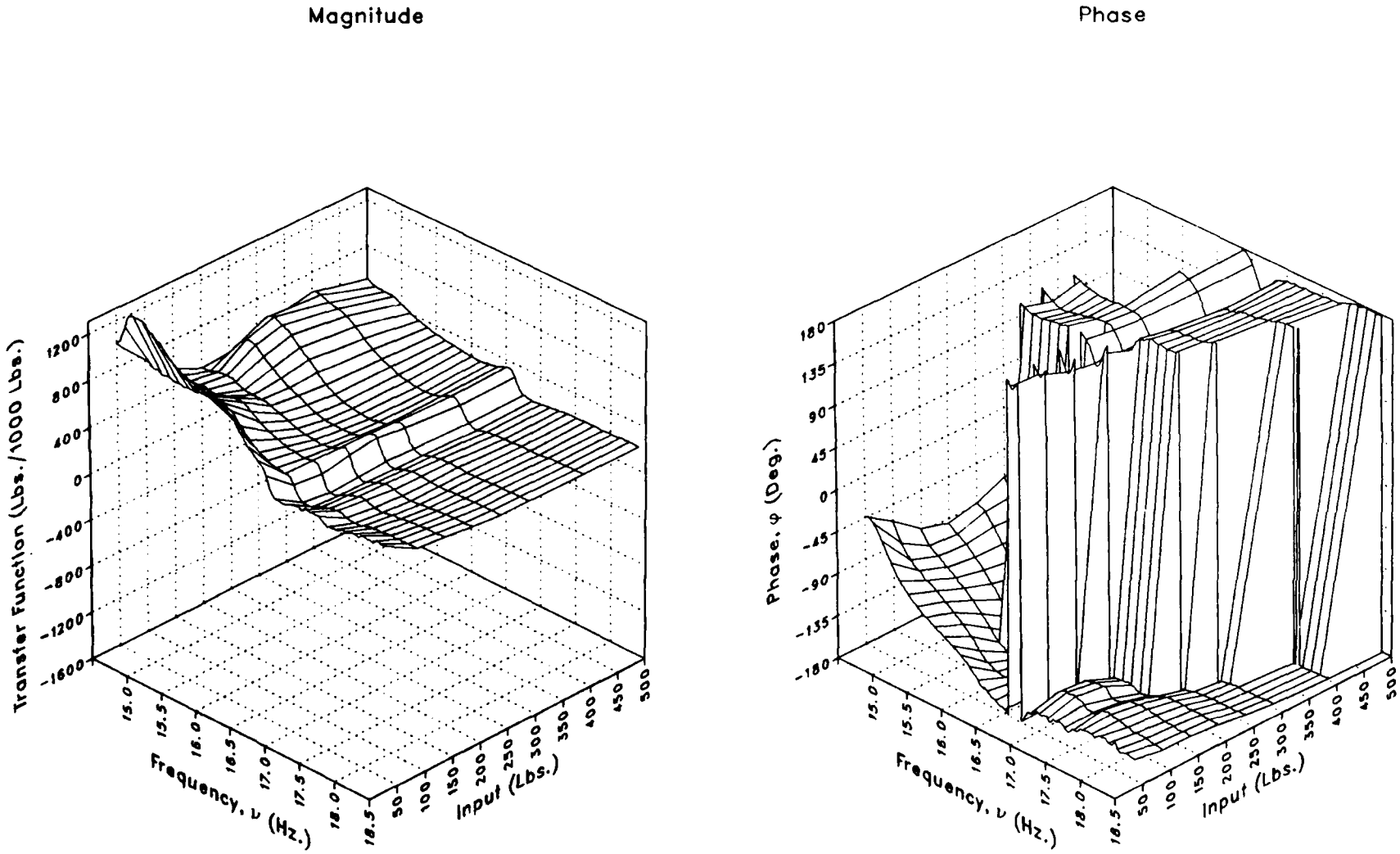

(d) MRLIFTC Concluded.

Figure 6.– Continued.

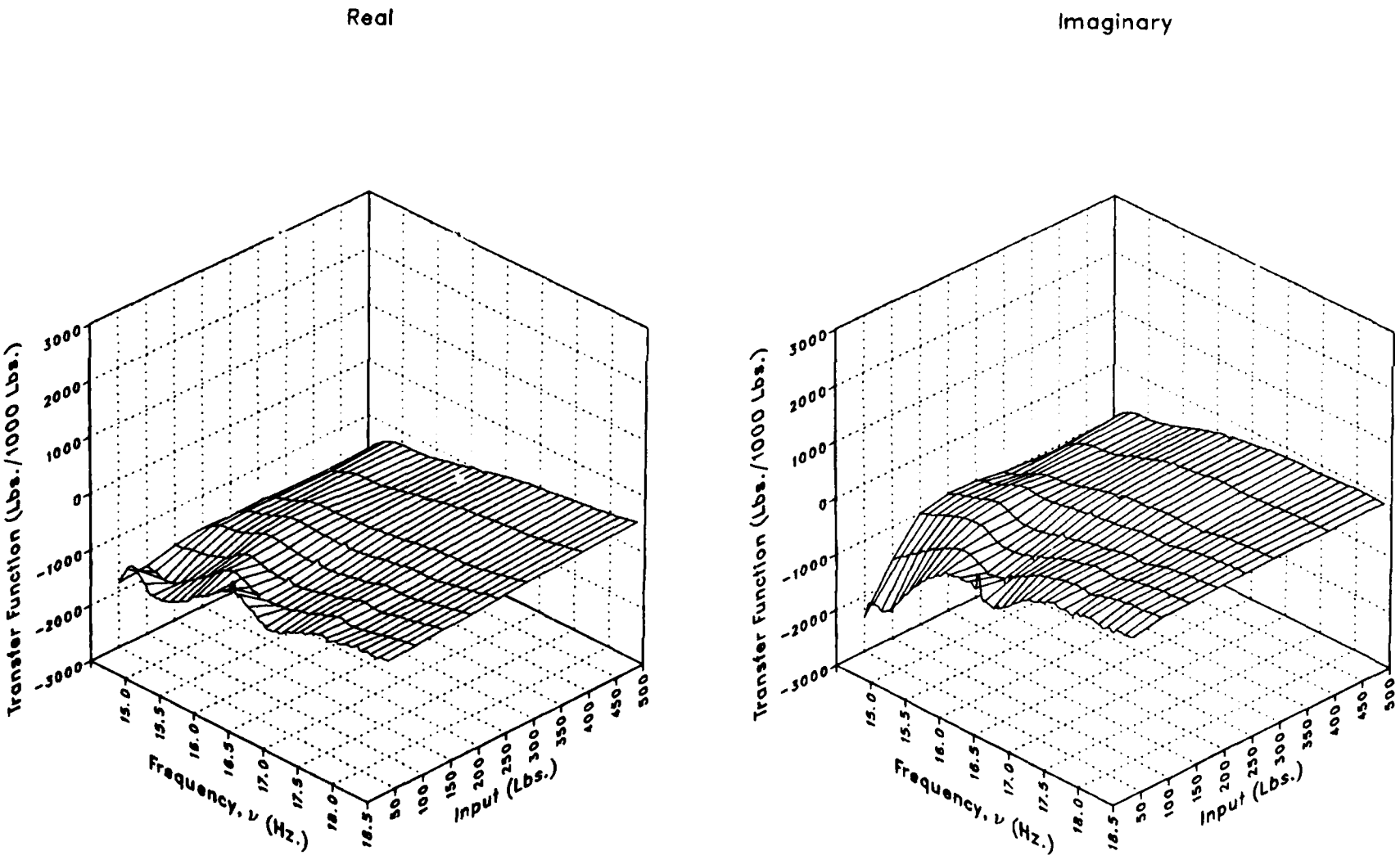

(e) MRLIFTD

Figure 6.– Continued.

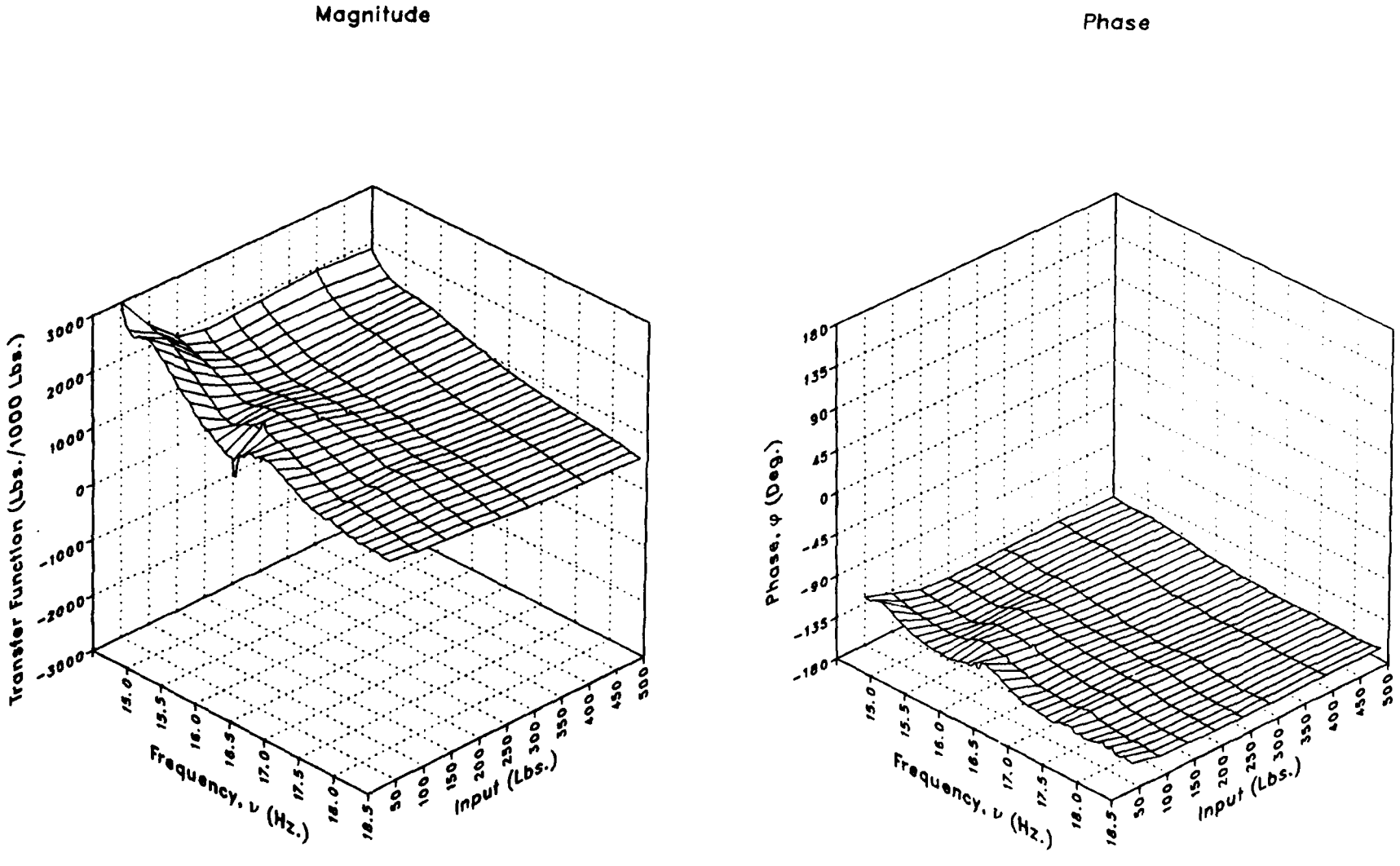

(e) MRLIFTD Concluded.

Figure 6.– Continued.

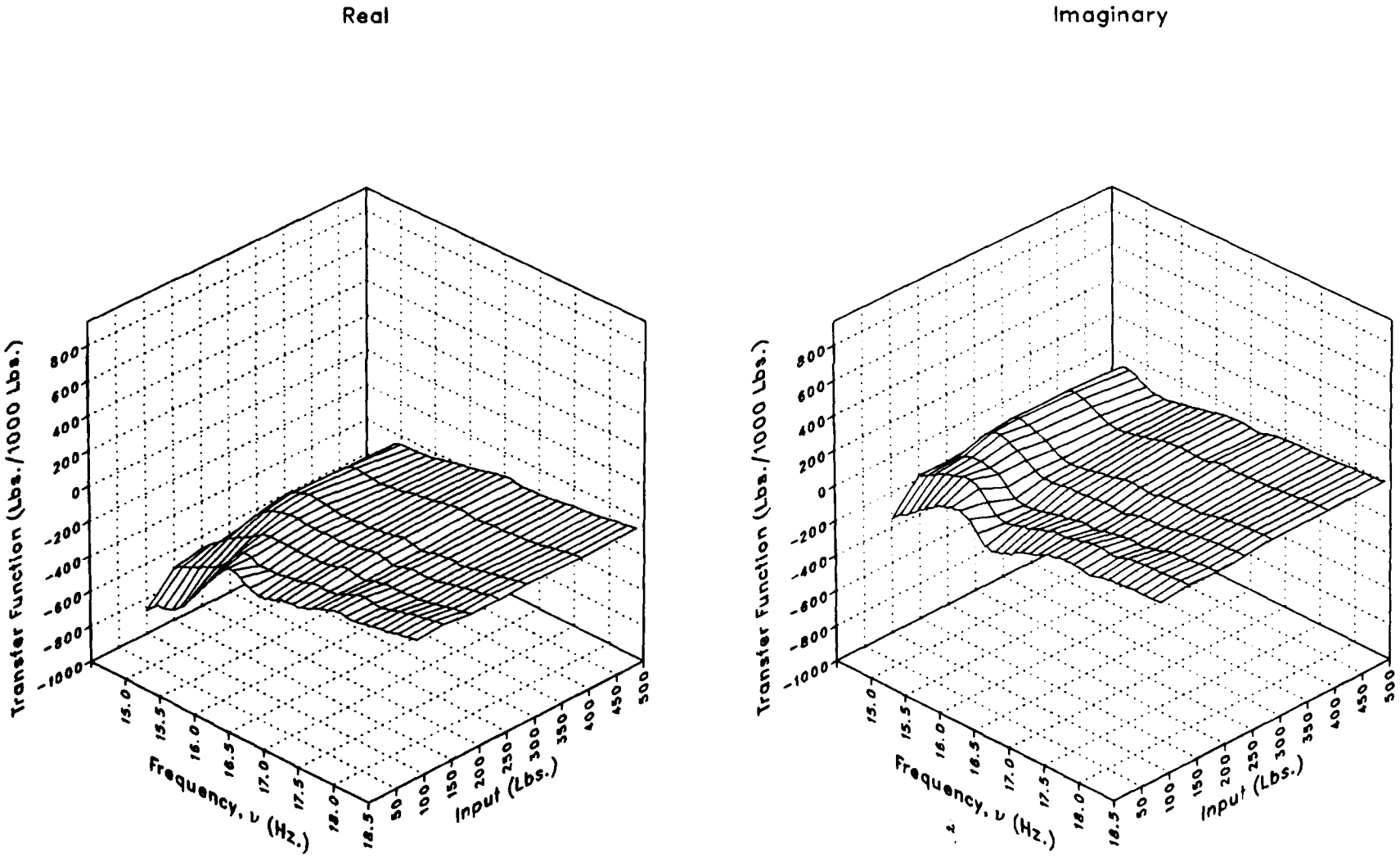

(f) MRGBQCE

Figure 6.– Continued.

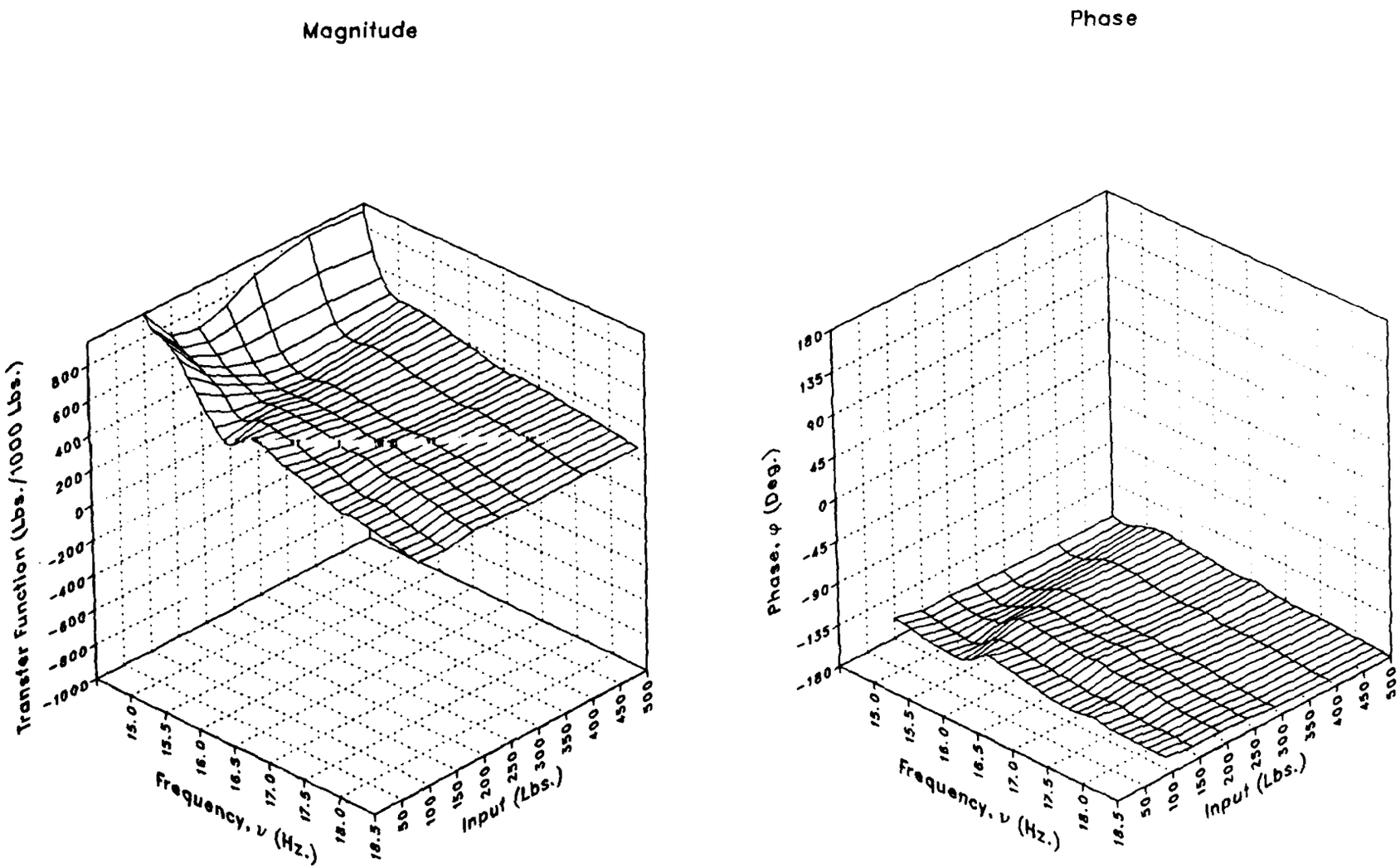

(f) MRGBQCE Concluded.

Figure 6.– Continued.

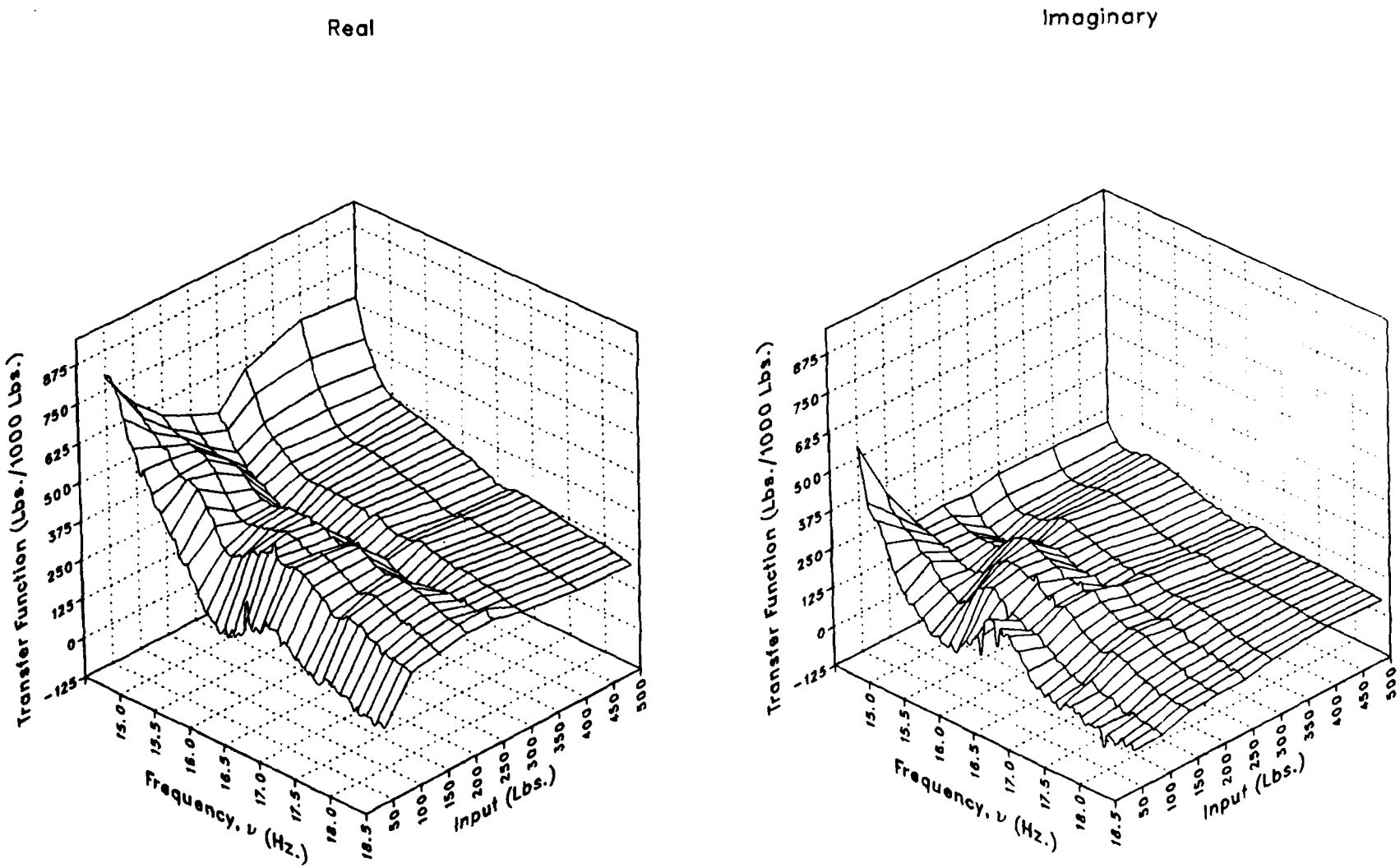

(g) MRGBQCF

Figure 6.– Continued.

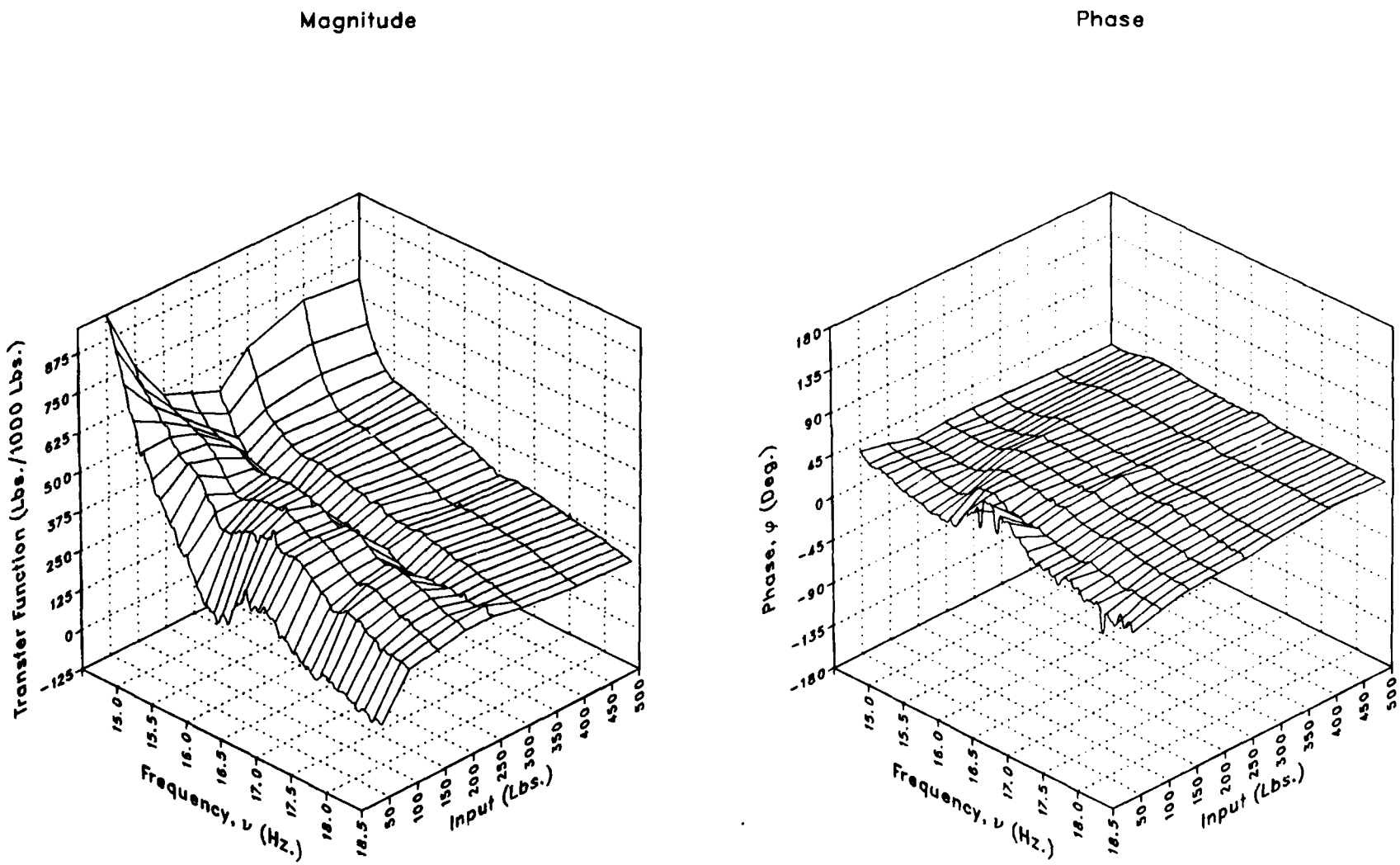

(g) MRGBQCF Concluded.

Figure 6.– Continued.

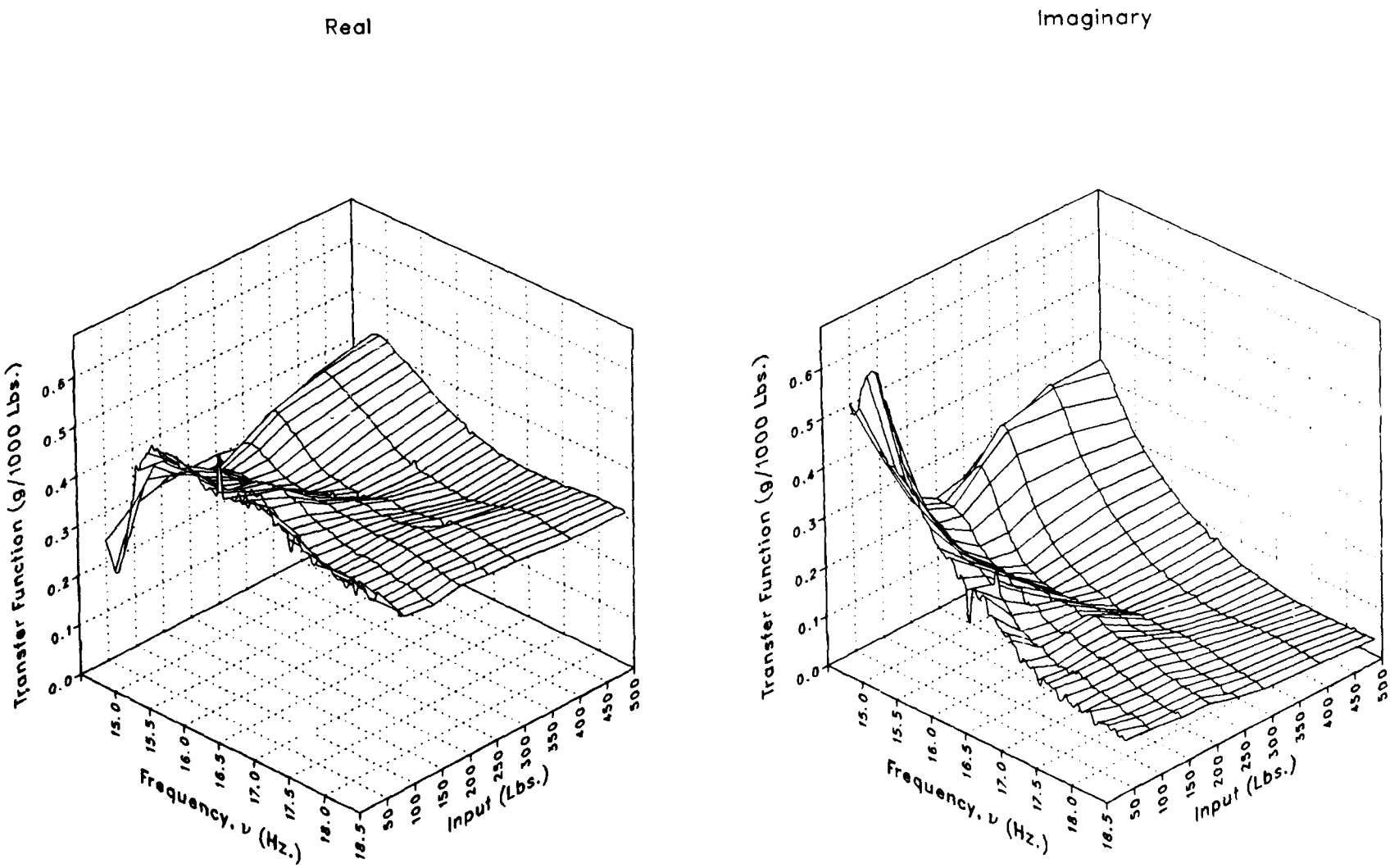

(h) LOMGB

Figure 6.– Continued.

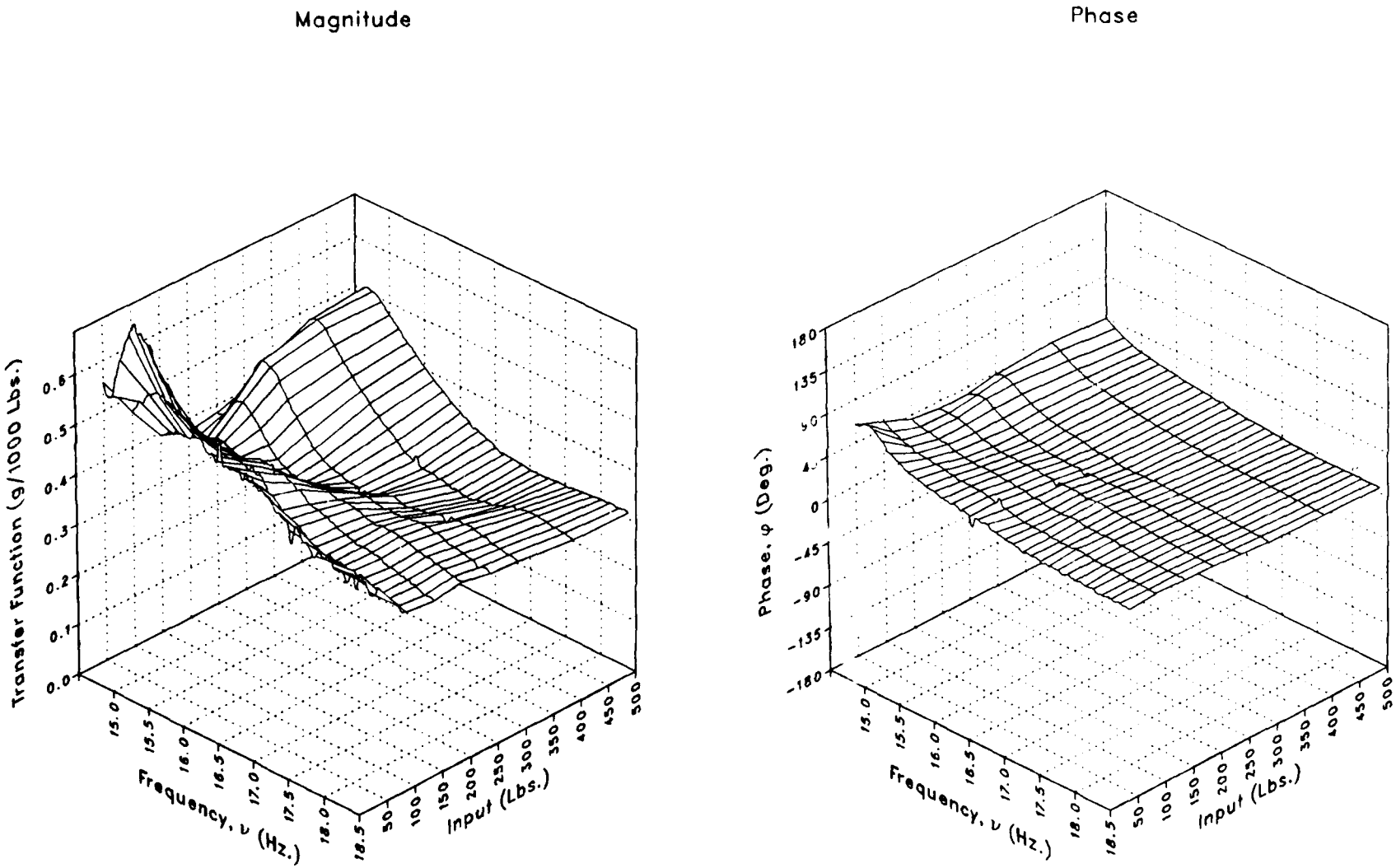

(h) LOMGB Concluded.

Figure 6.– Continued.

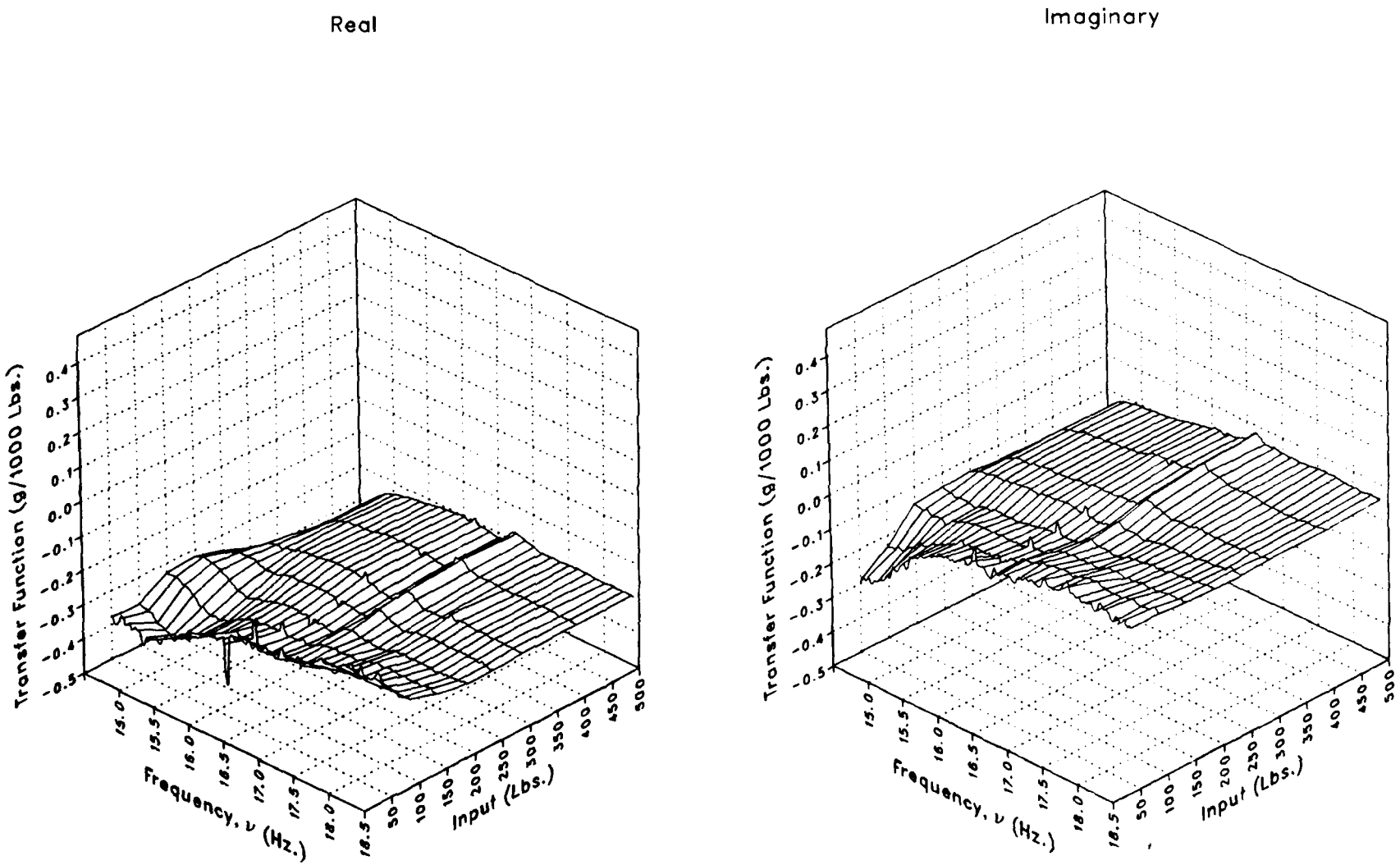

(i) LMGB

Figure 6.– Continued.

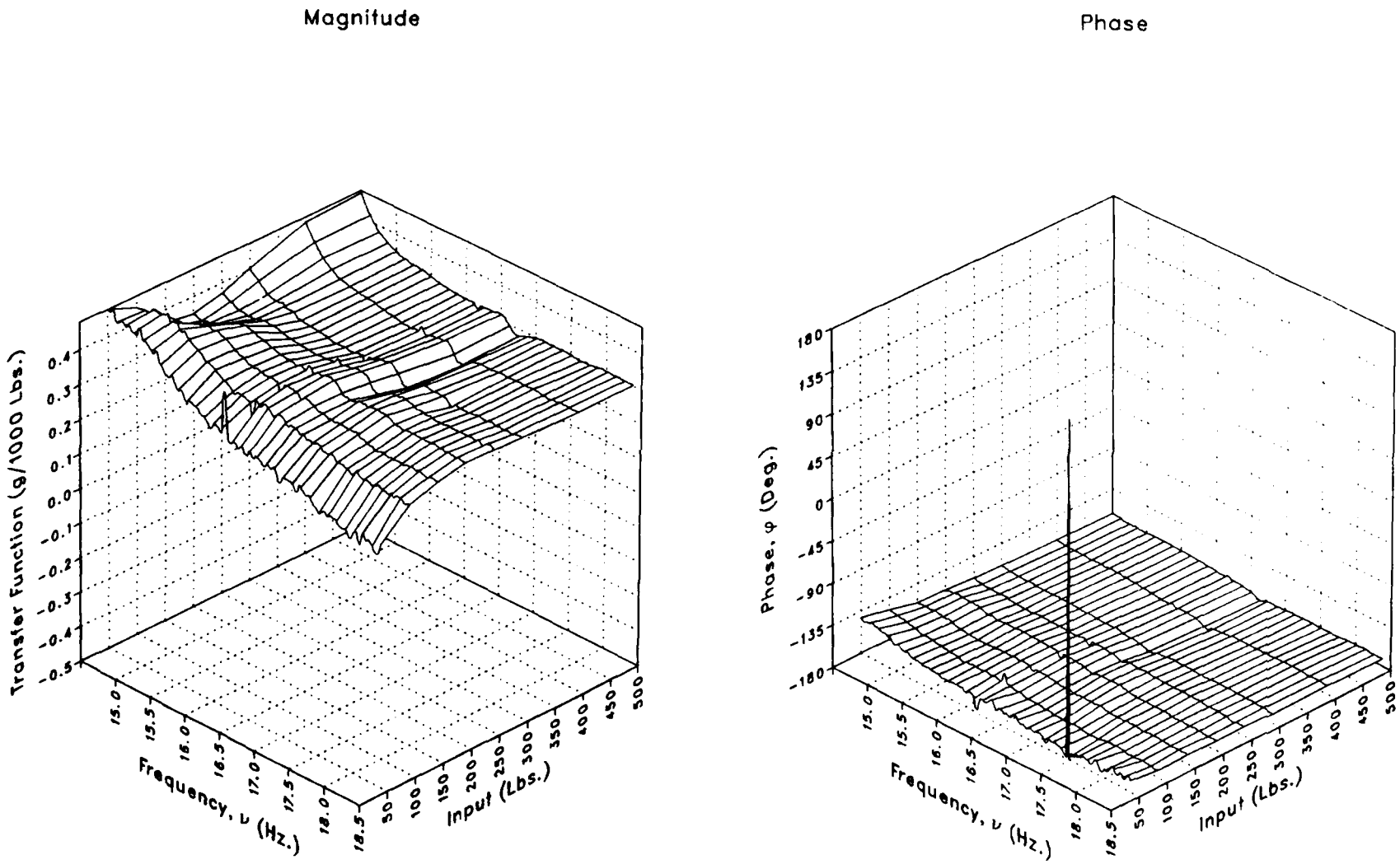

(i) LMGB Concluded.

Figure 6.– Continued.

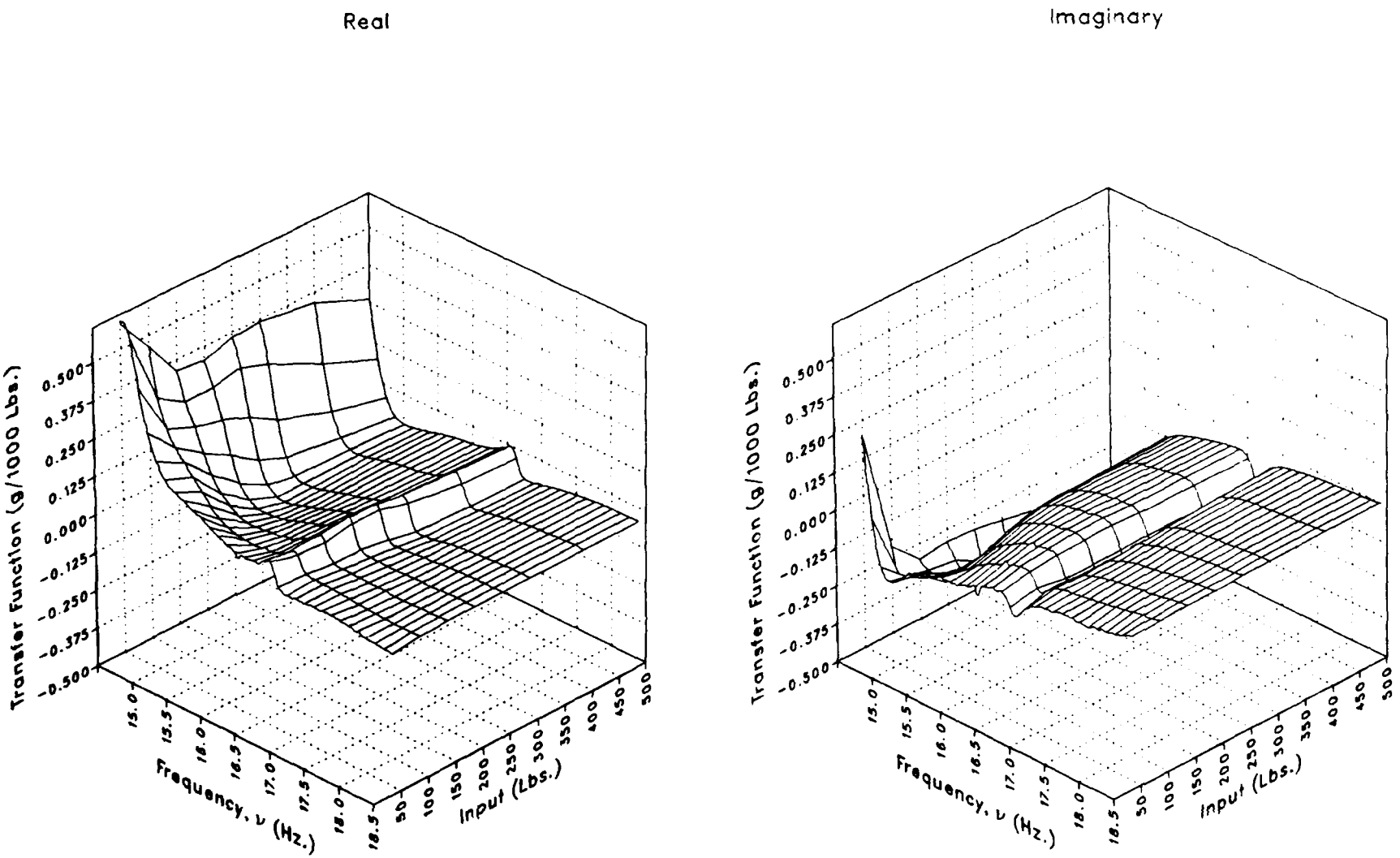

(j) VMGB

Figure 6.– Continued.

Magnitude

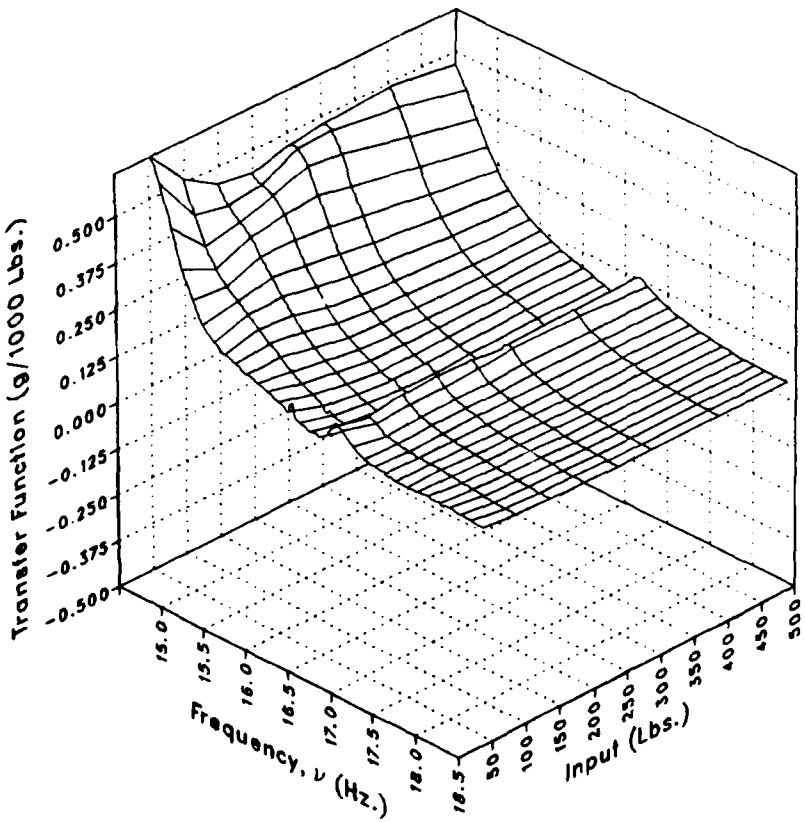

Phase

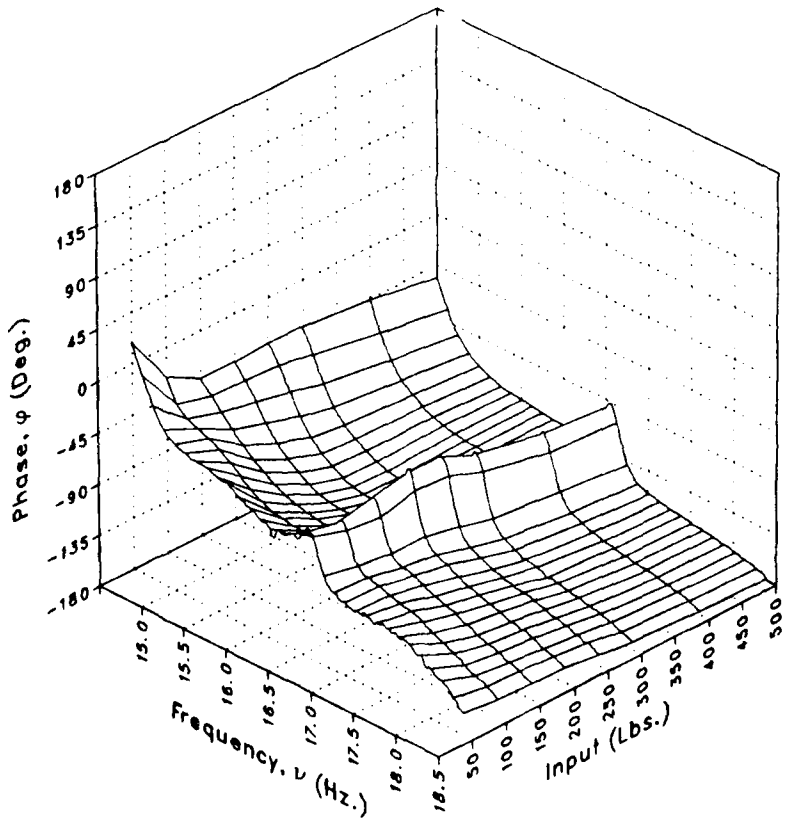

(j) VMGB Concluded.

Figure 6.– Continued.

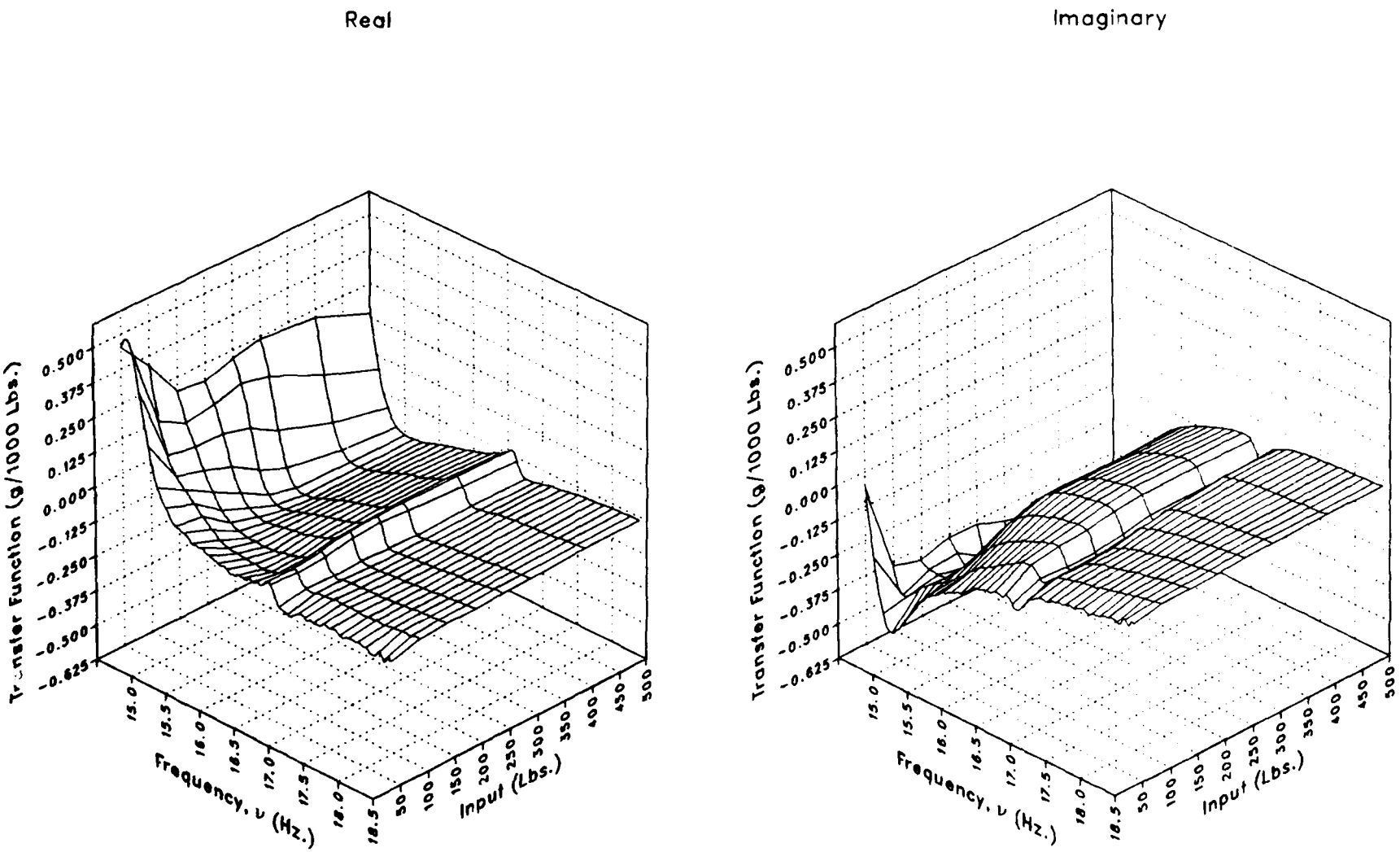

(k) XMRFBPV

Figure 6.– Continued.

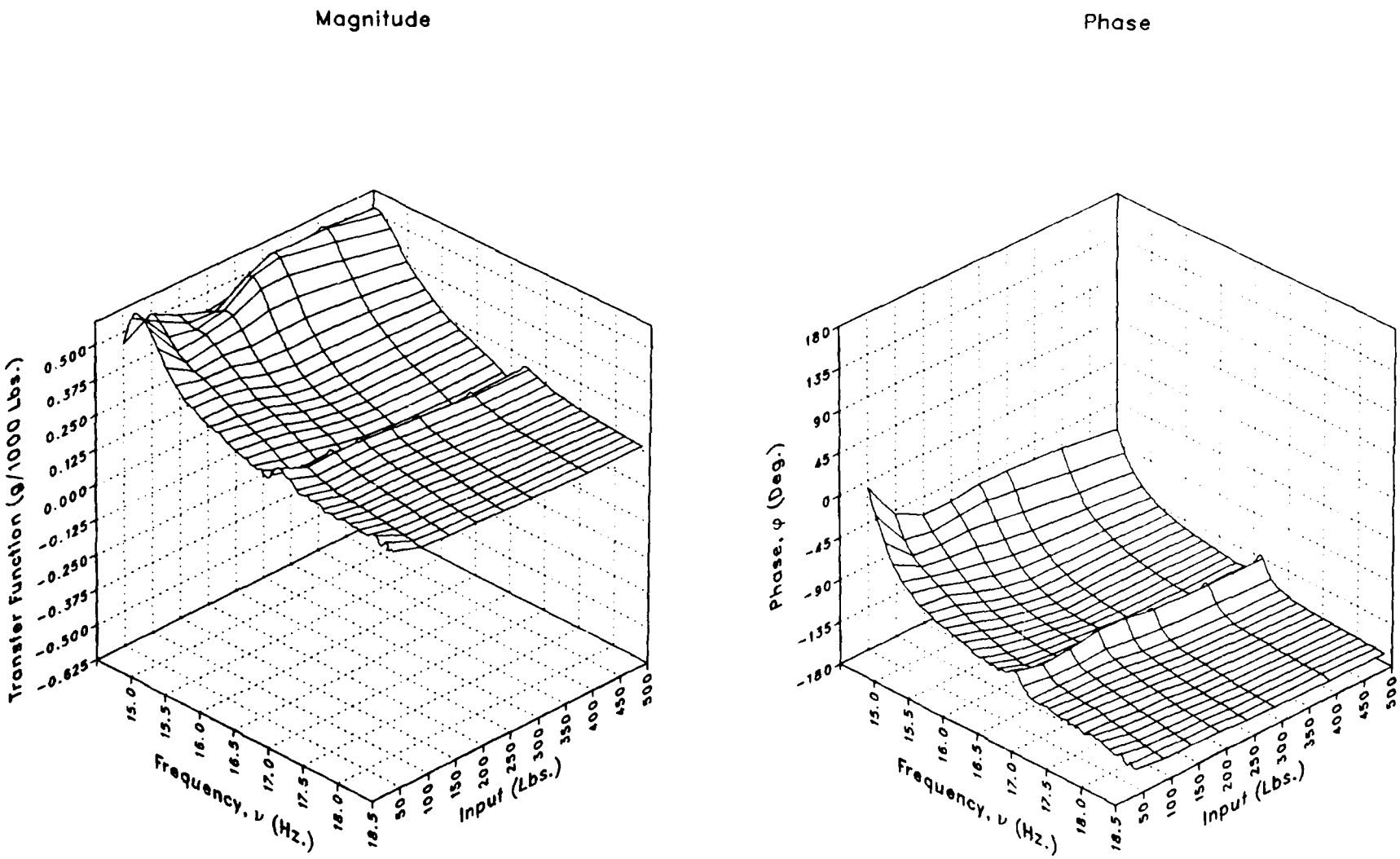

(k) XMRFBPV Concluded.

Figure 6.– Continued.

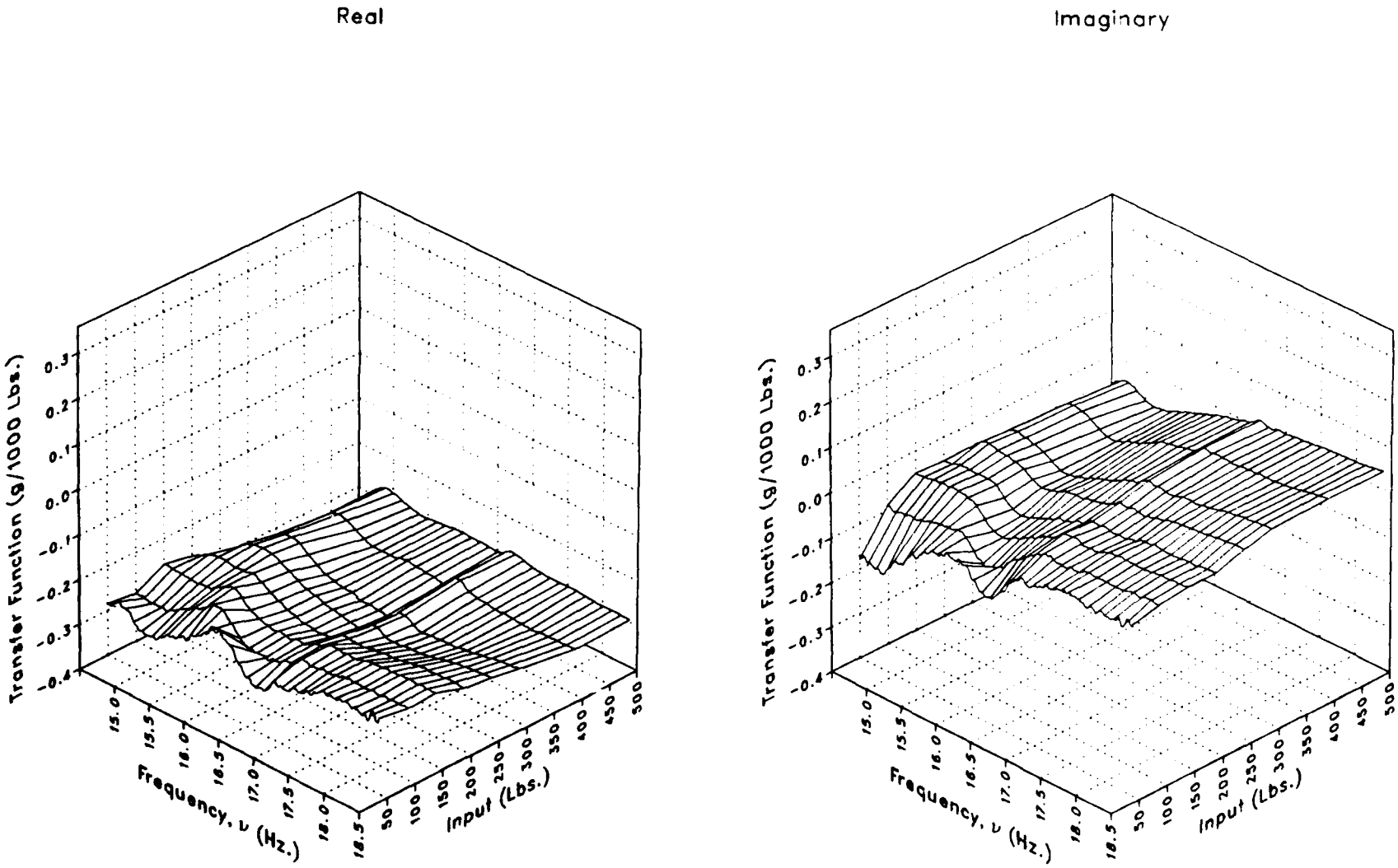

(l) XMRFBPL

Figure 6.– Continued.

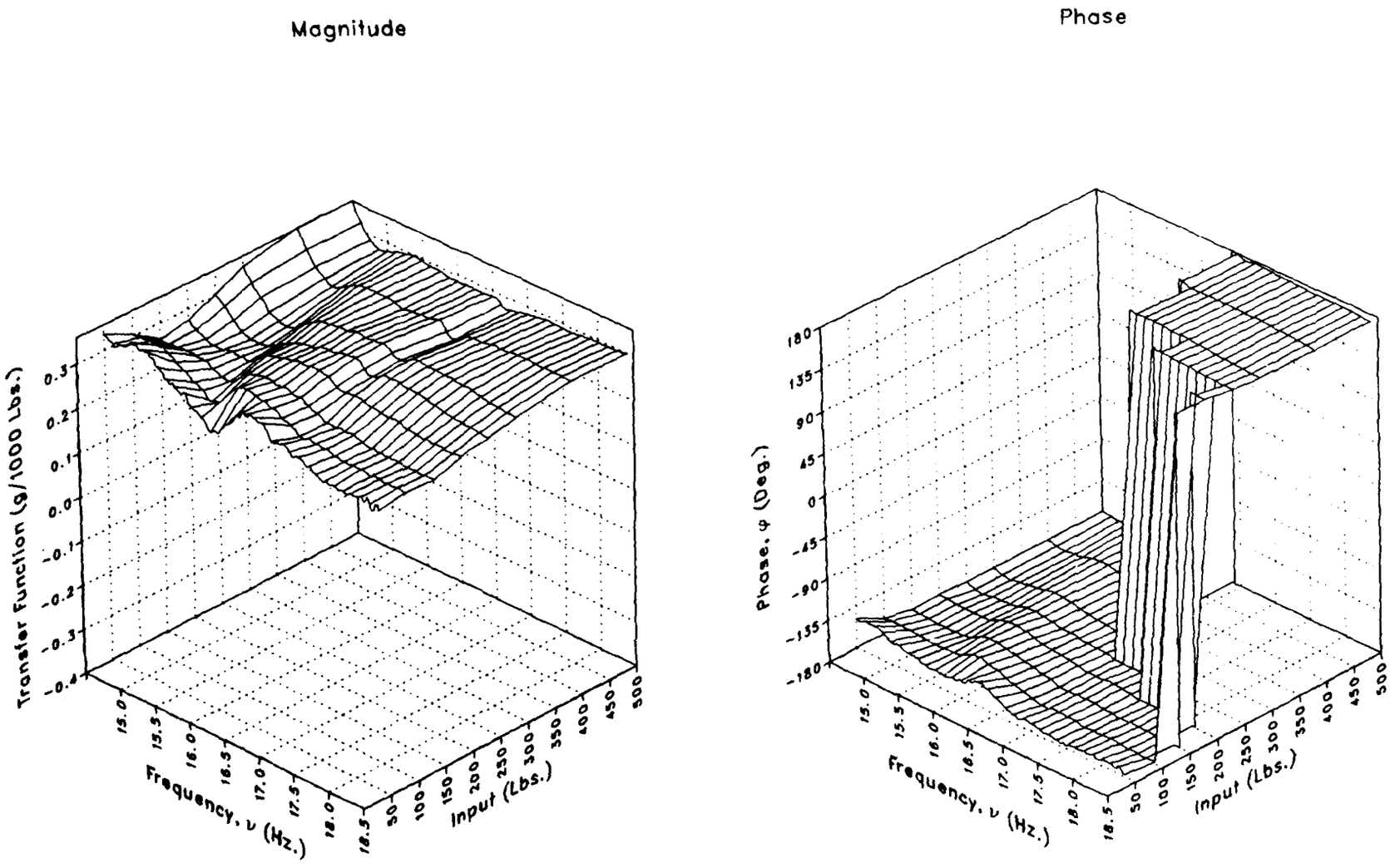

(l) XMRFBPL Concluded.

Figure 6.– Continued.

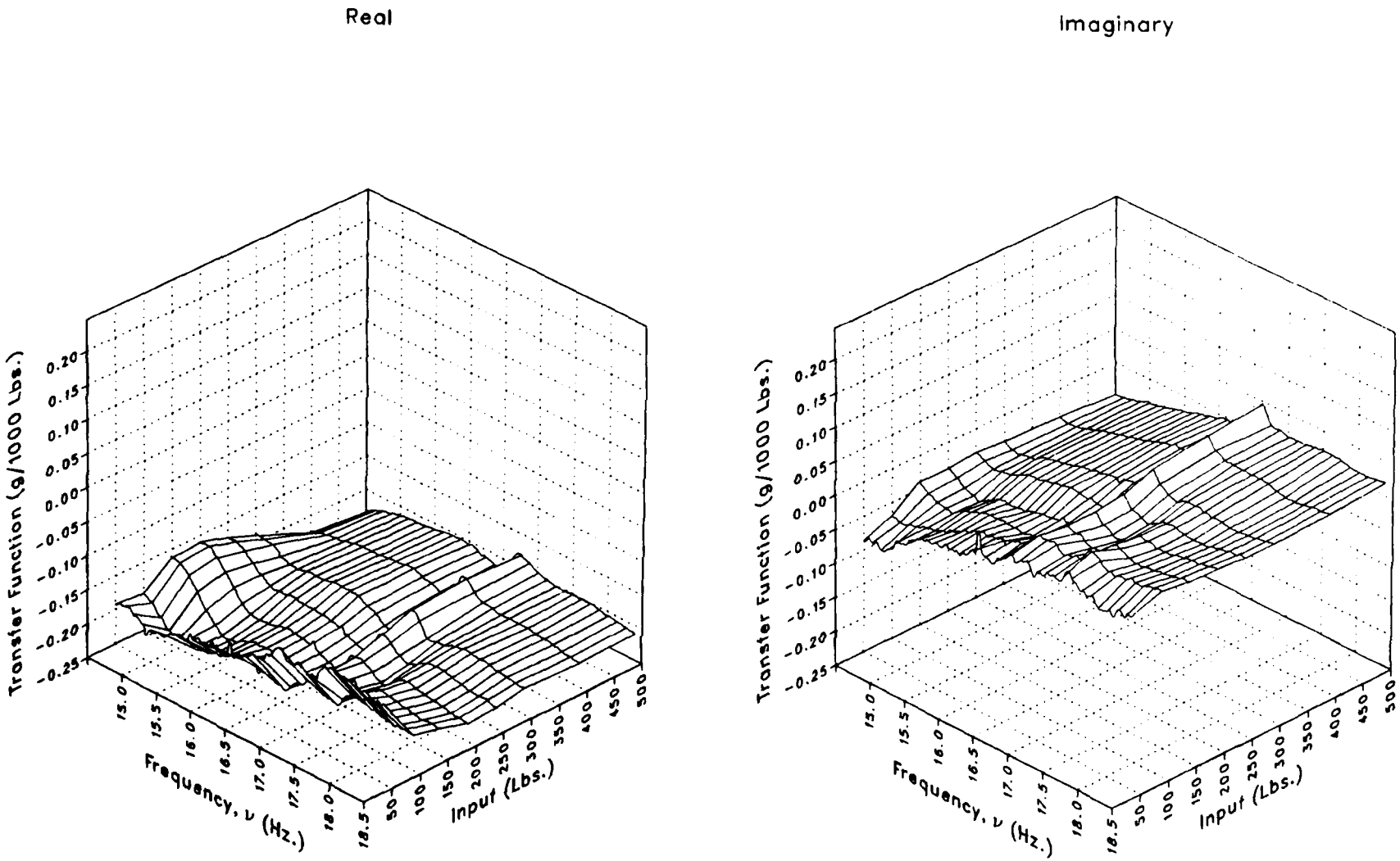

(m) XMRFBPLO

Figure 6.– Continued.

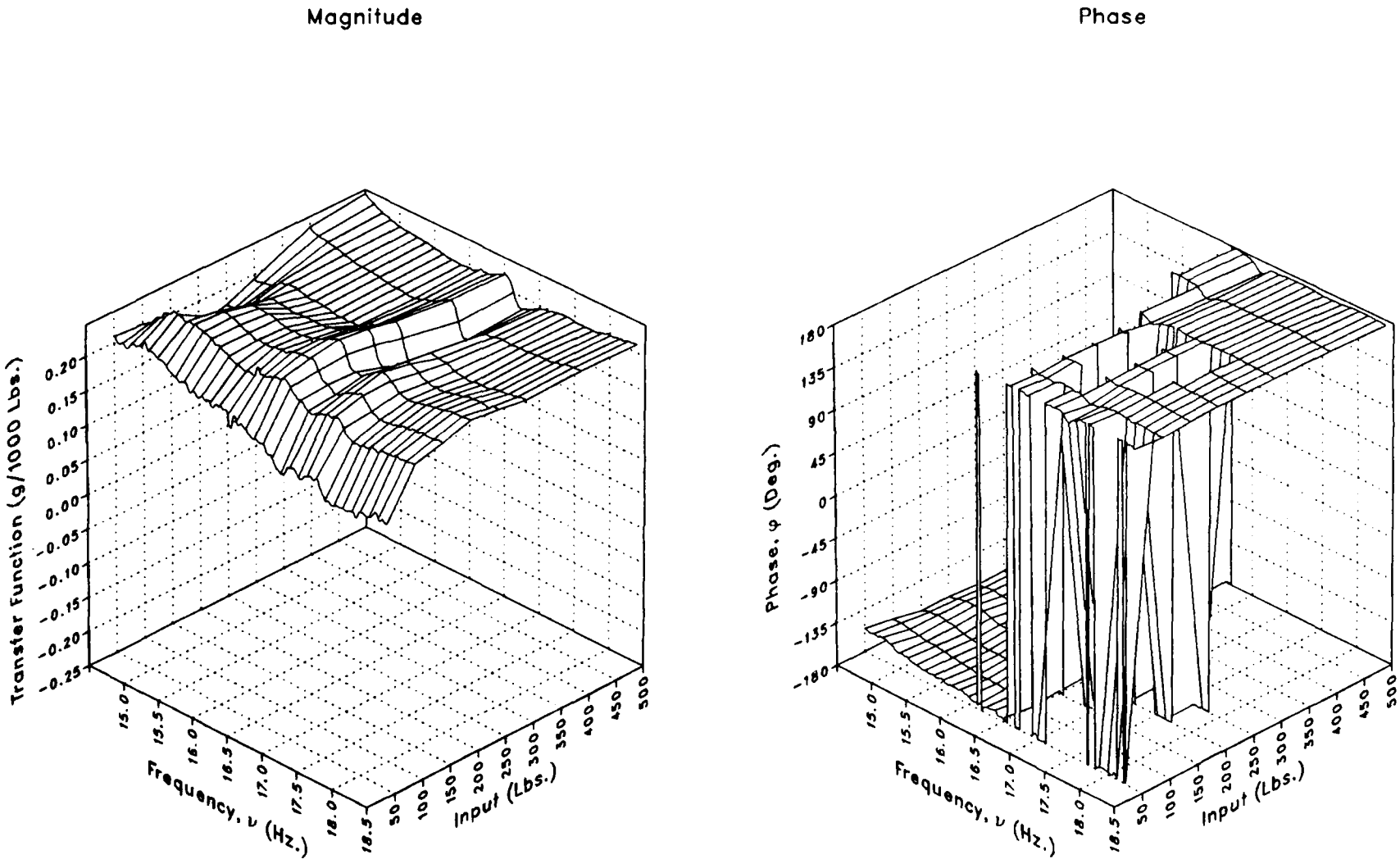

(m) XMRFBPLO Concluded.

Figure 6.– Continued.

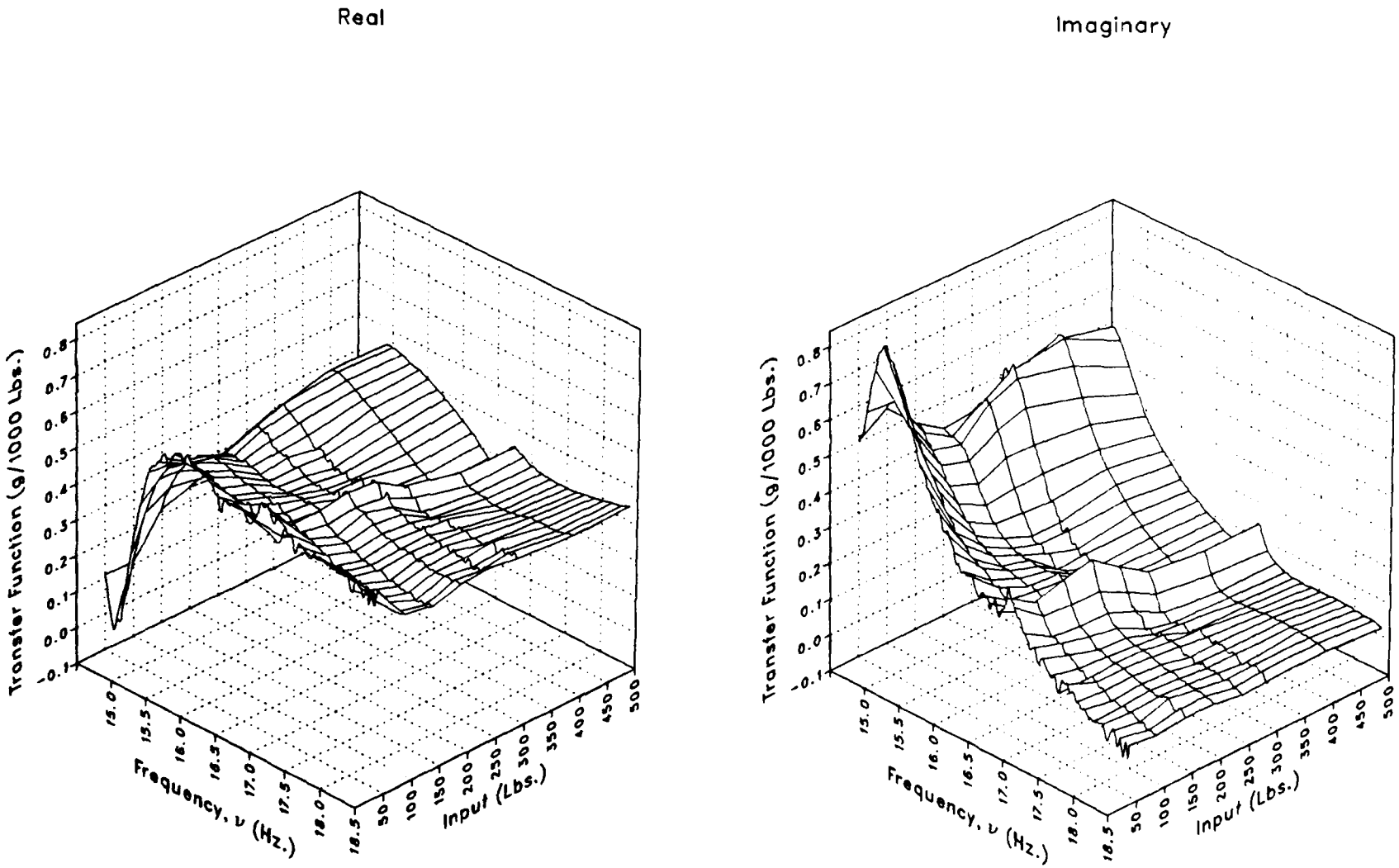

(n) STA56NV

Figure 6.– *Continued.*

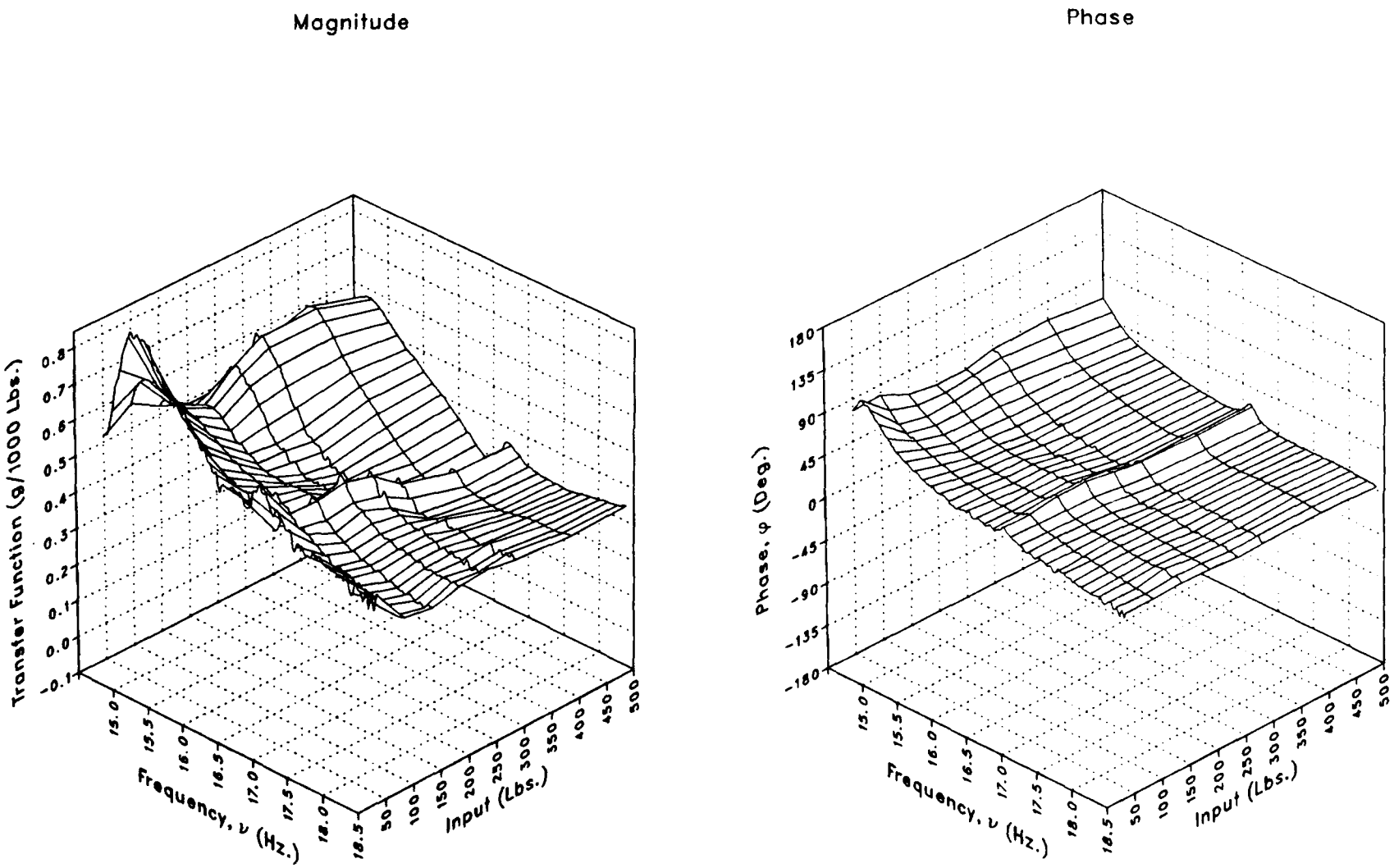

(n) STA56NV Concluded.

Figure 6.– Continued.

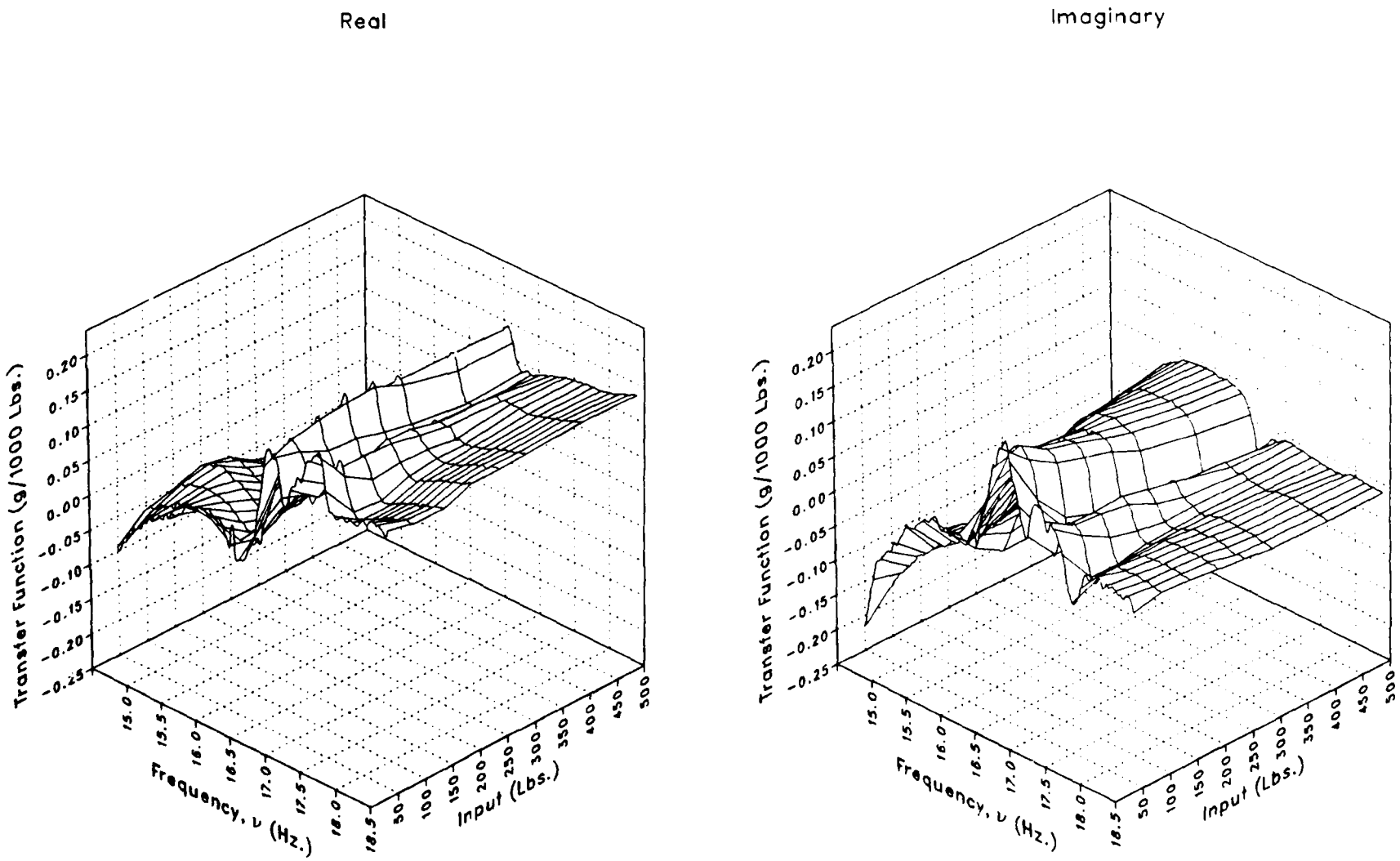

(o) STA56NL

Figure 6.– Continued.

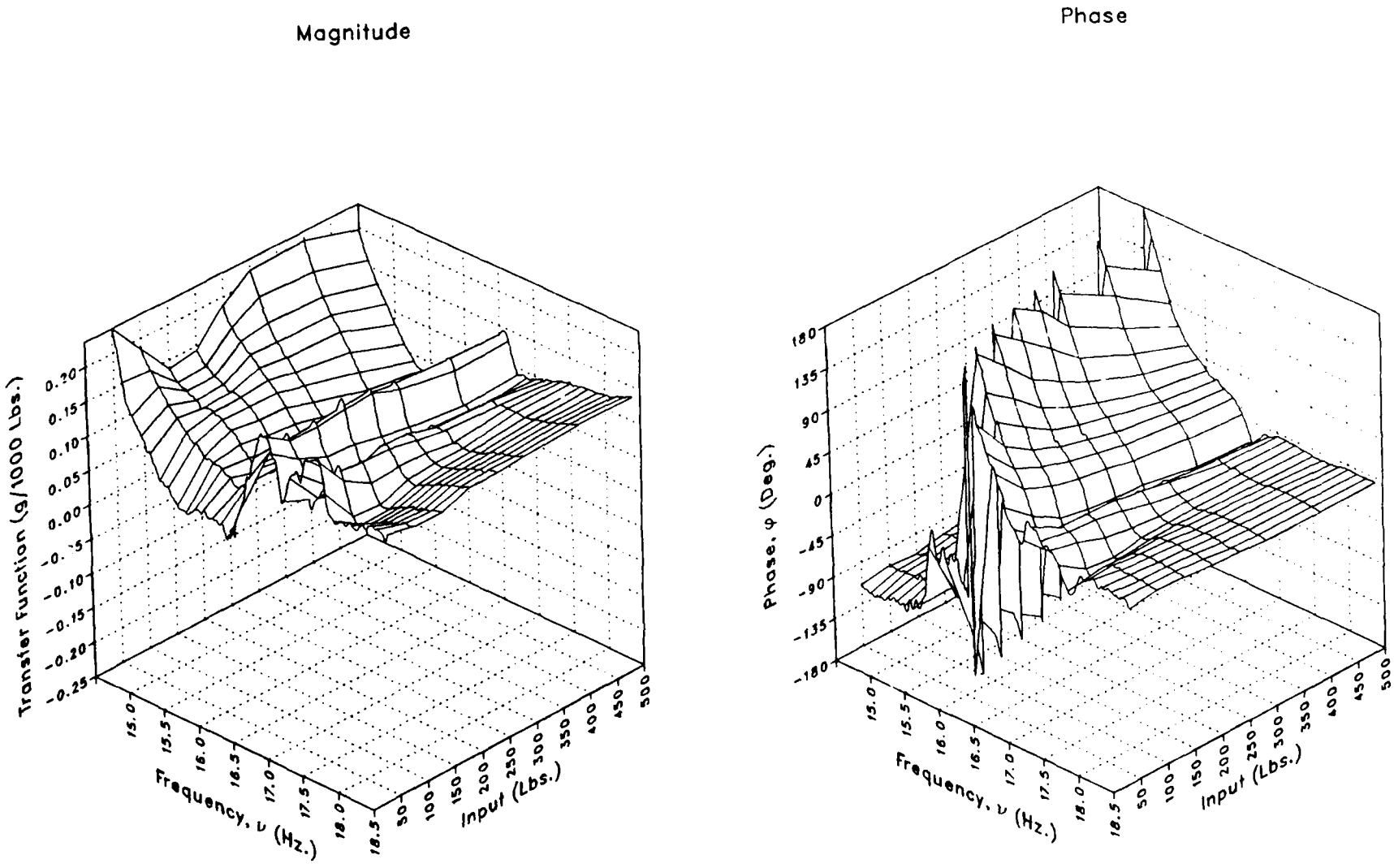

(o) STA56NL Concluded.

Figure 6.– Continued.

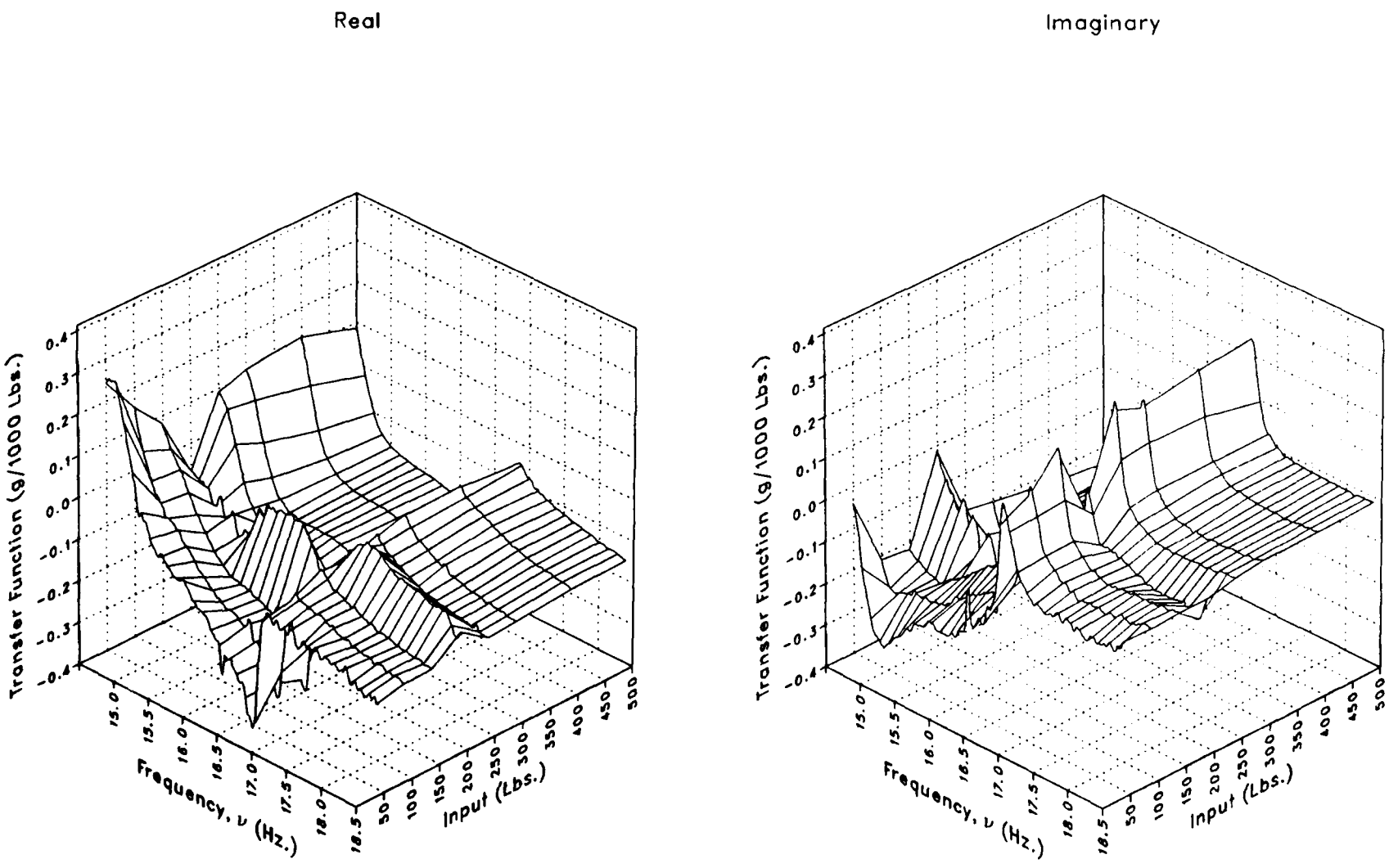

(p) VWGTPRT

Figure 6.– Continued.

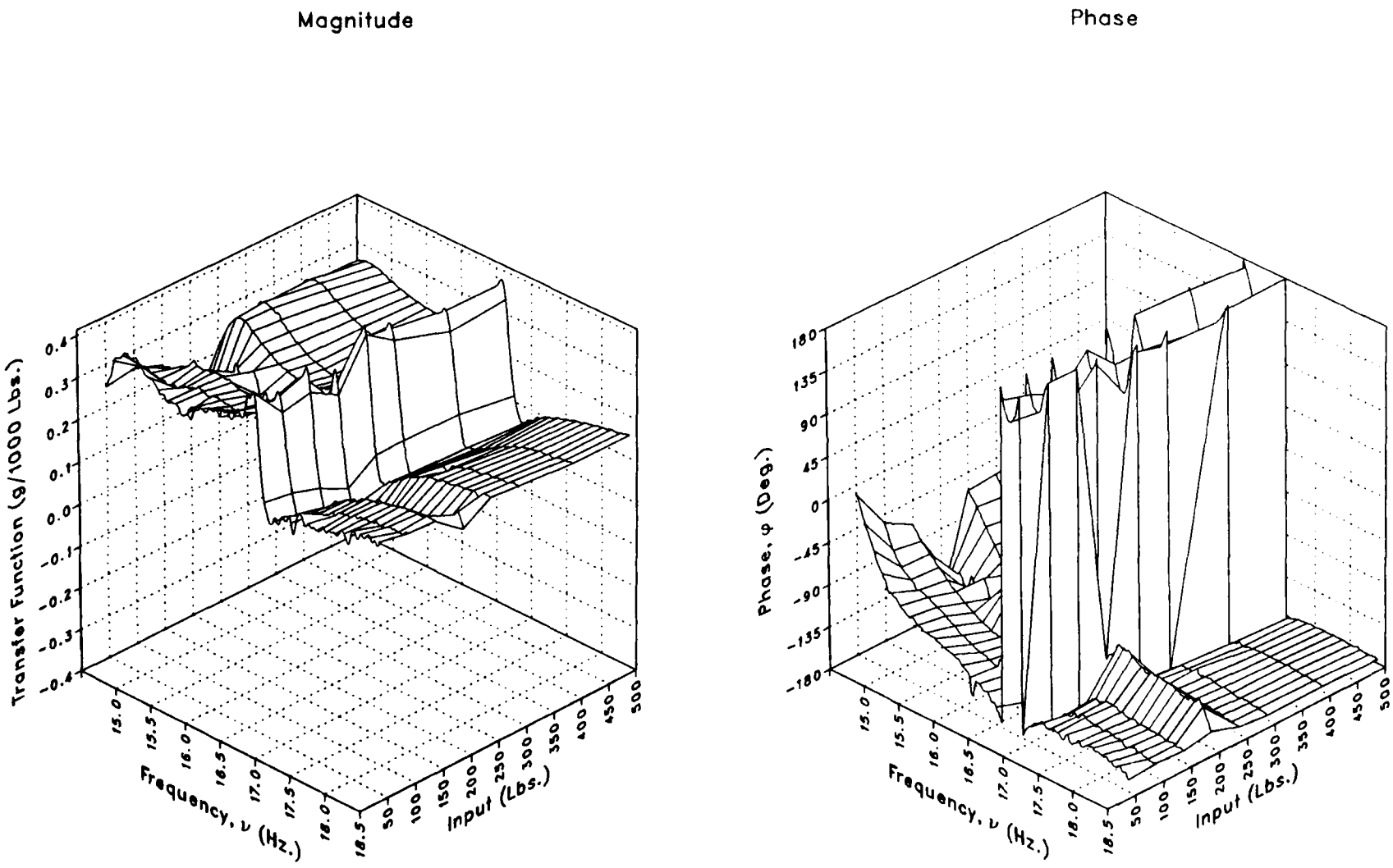

(p) VWGTPRT Concluded.

Figure 6.– Continued.

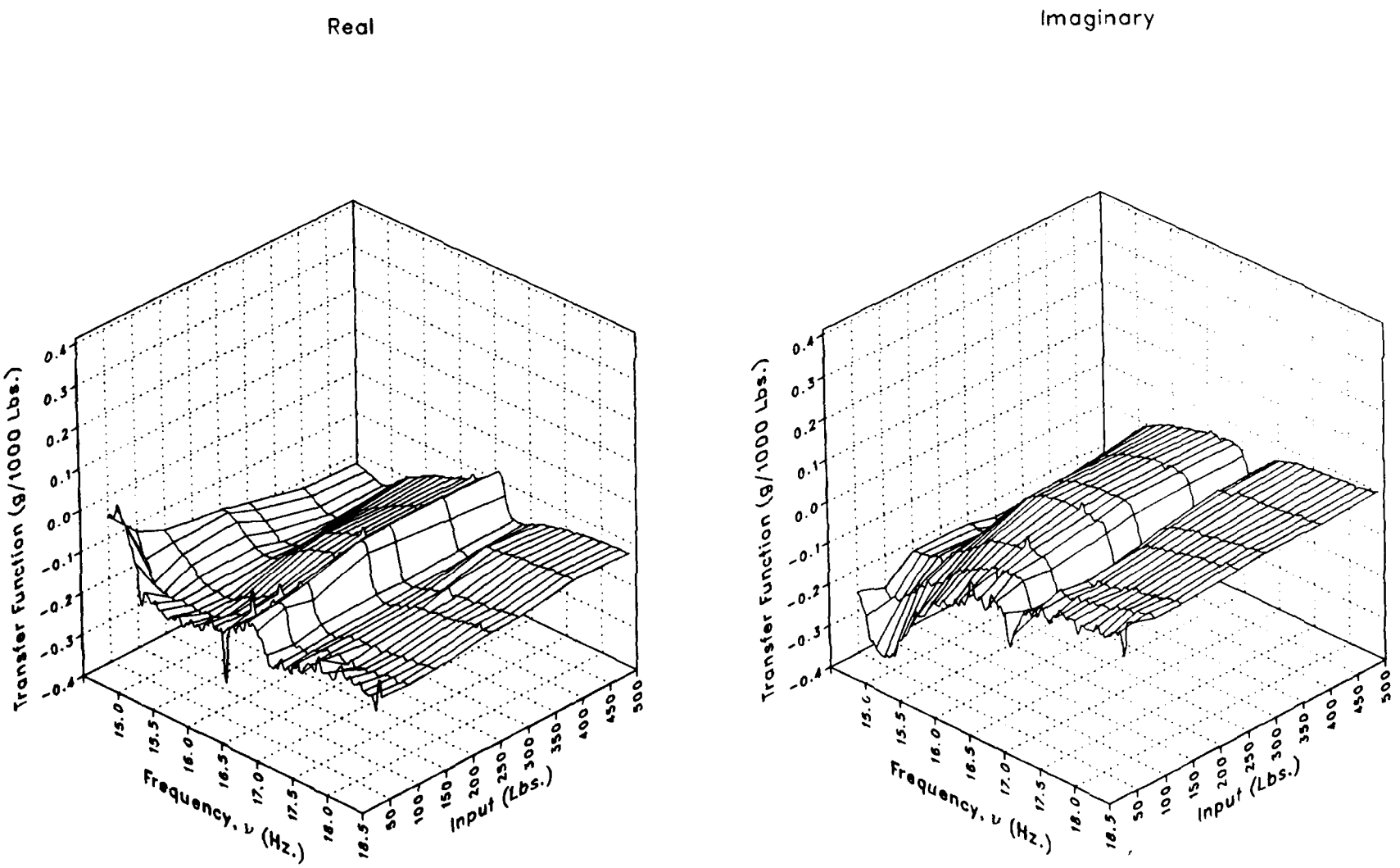

(q) VWGTPLT

Figure 6.– Continued.

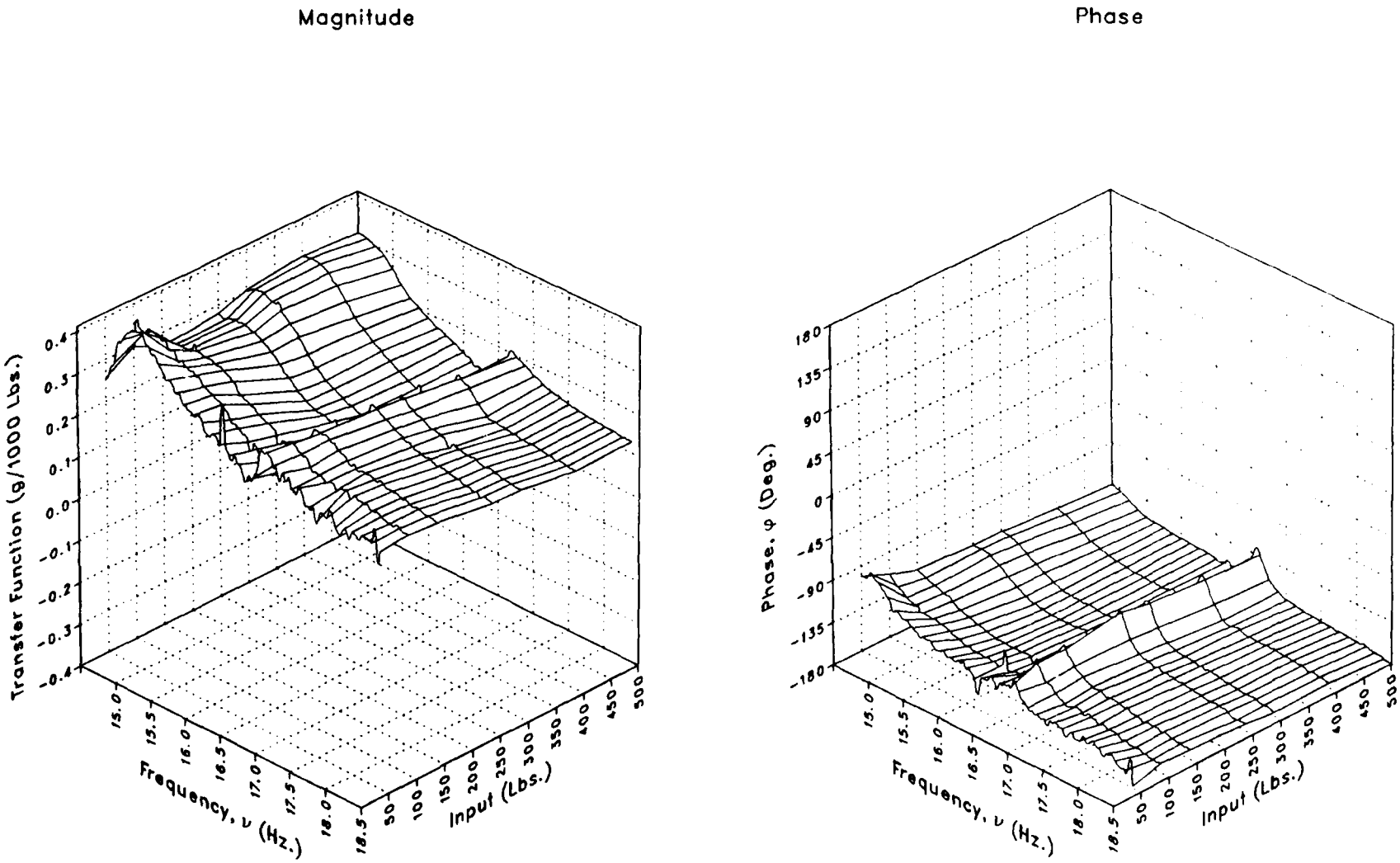

(q) VWGTPLT Concluded.

Figure 6.– Continued.

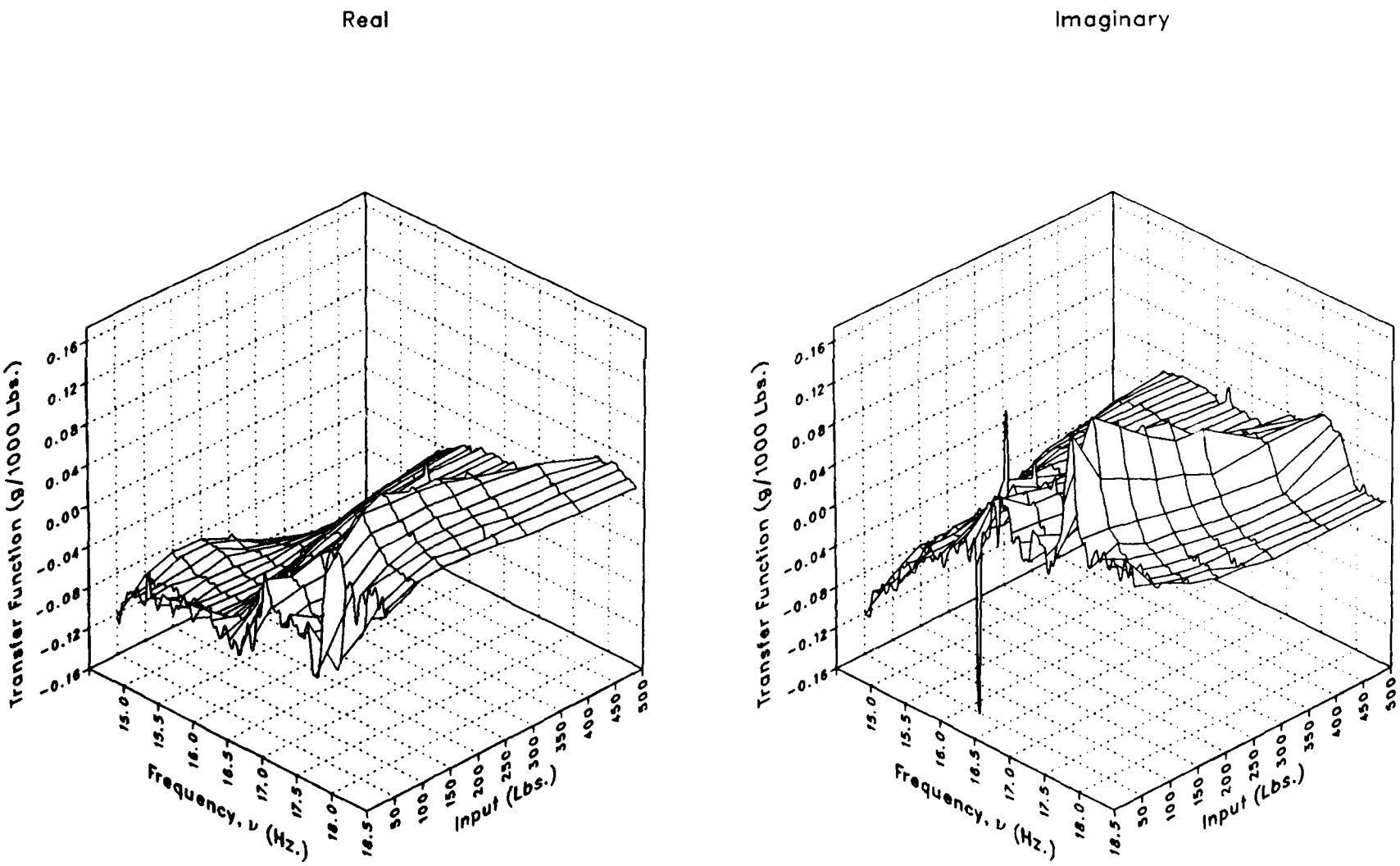

(r) LIGB

Figure 6.– Continued.

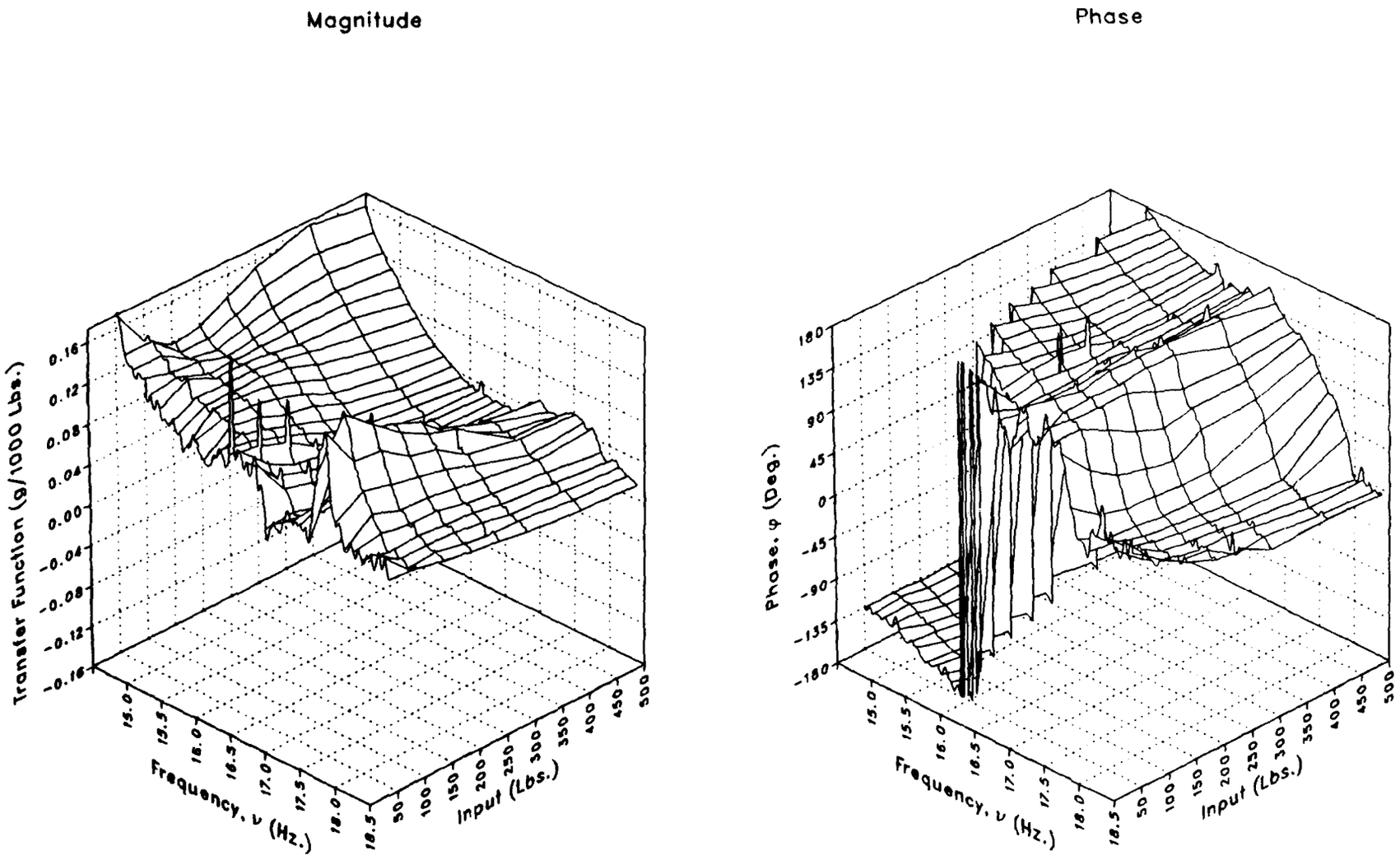

(r) LIGB Concluded.

Figure 6.– Continued.

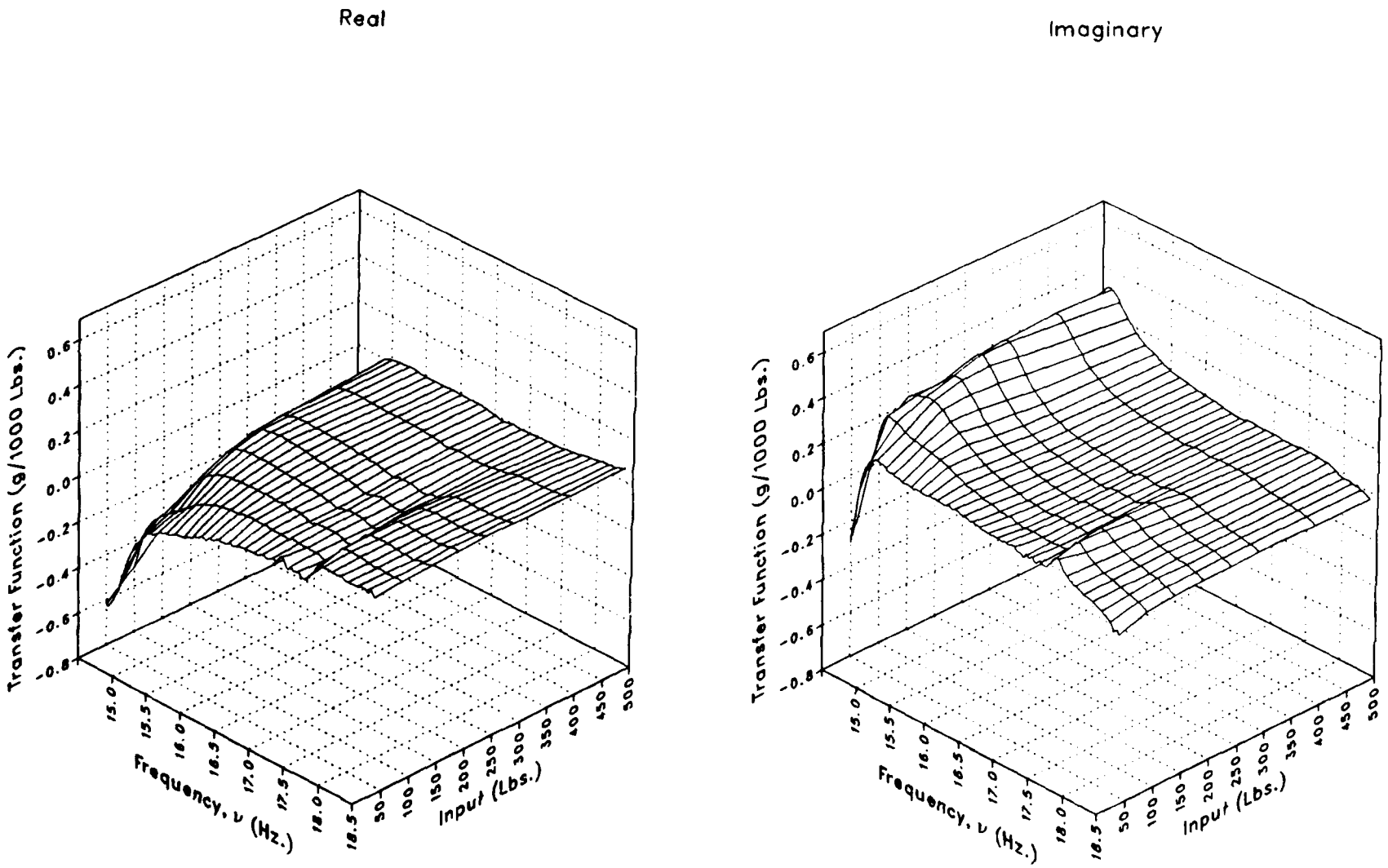

(s) VIGB

Figure 6.– Continued.

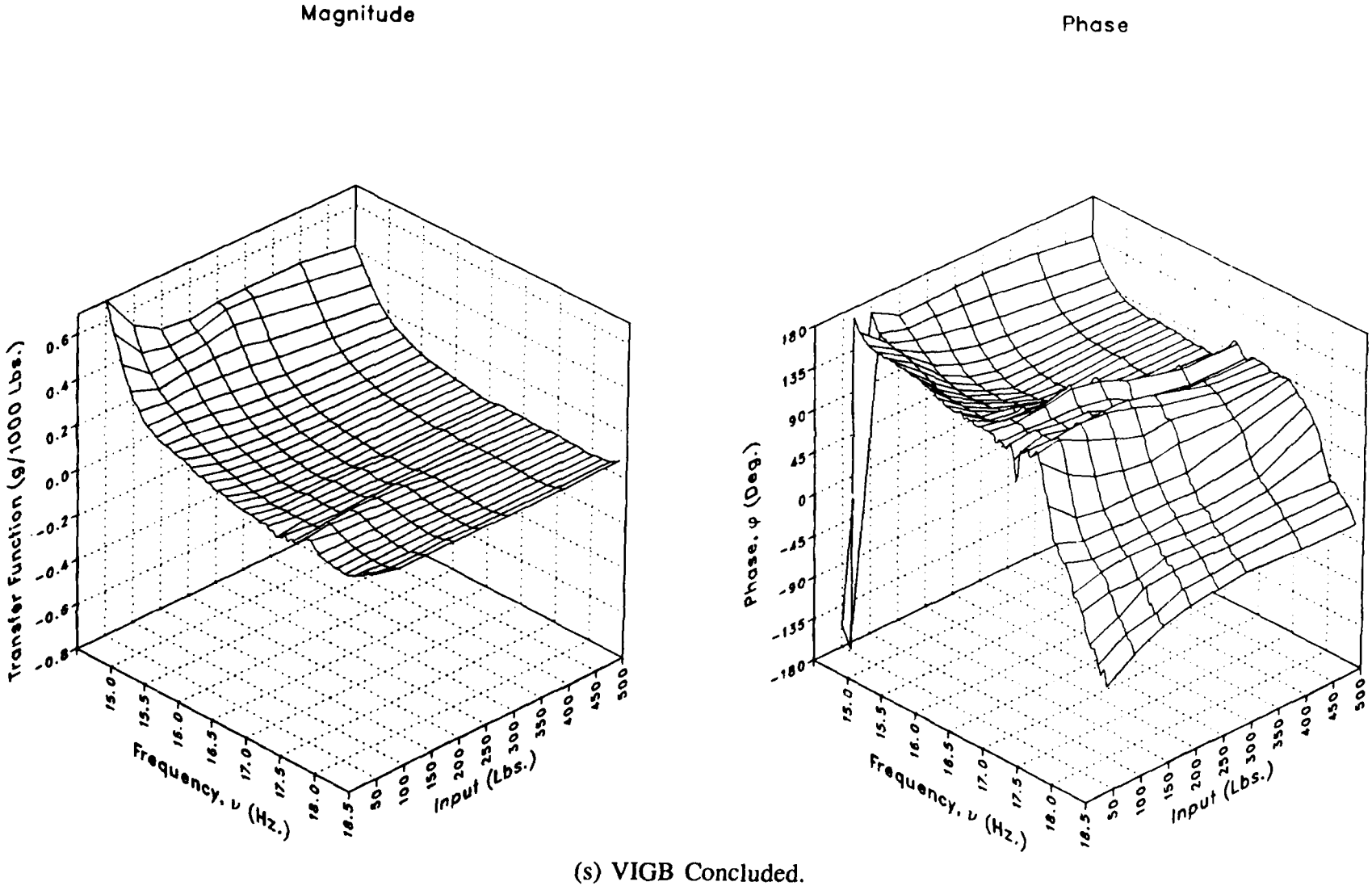

(s) VIGB Concluded.

Figure 6.– Continued.

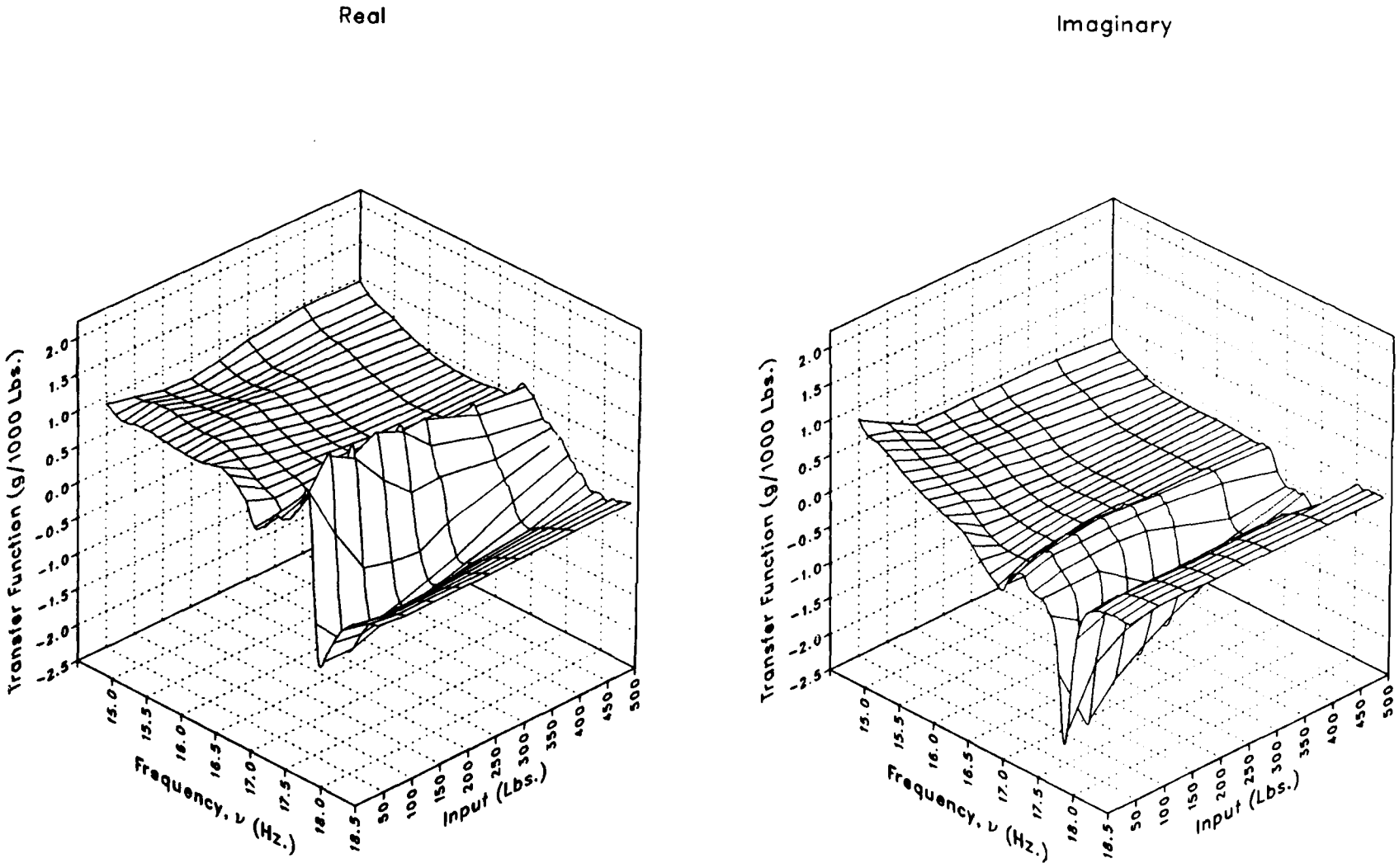

(t) LATTPYLN

Figure 6.– Continued.

Magnitude

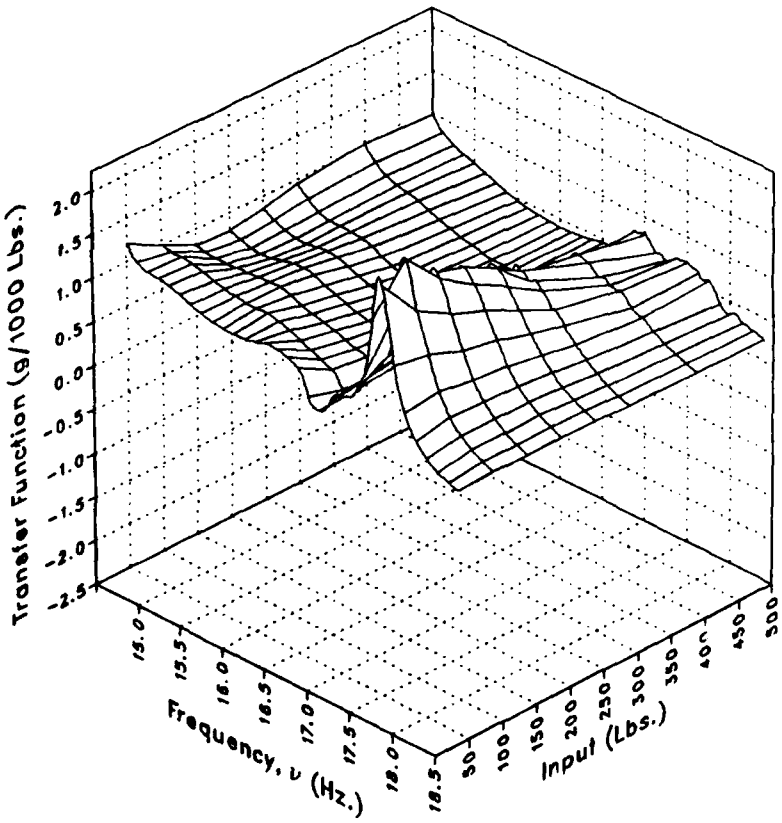

Phase

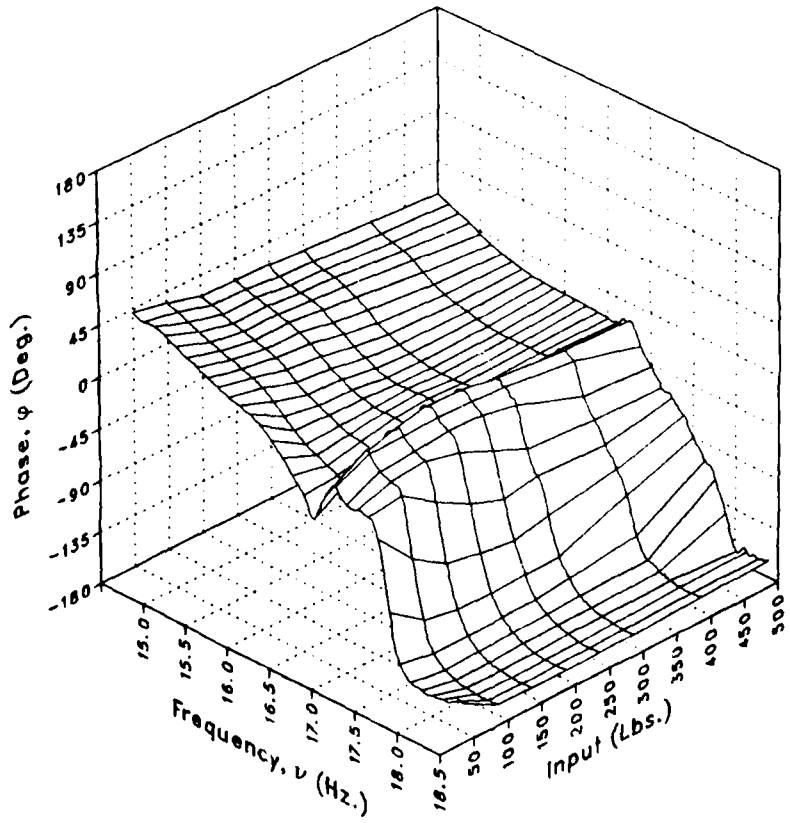

(t) LATTPYLN Concluded.

Figure 6.– Continued.

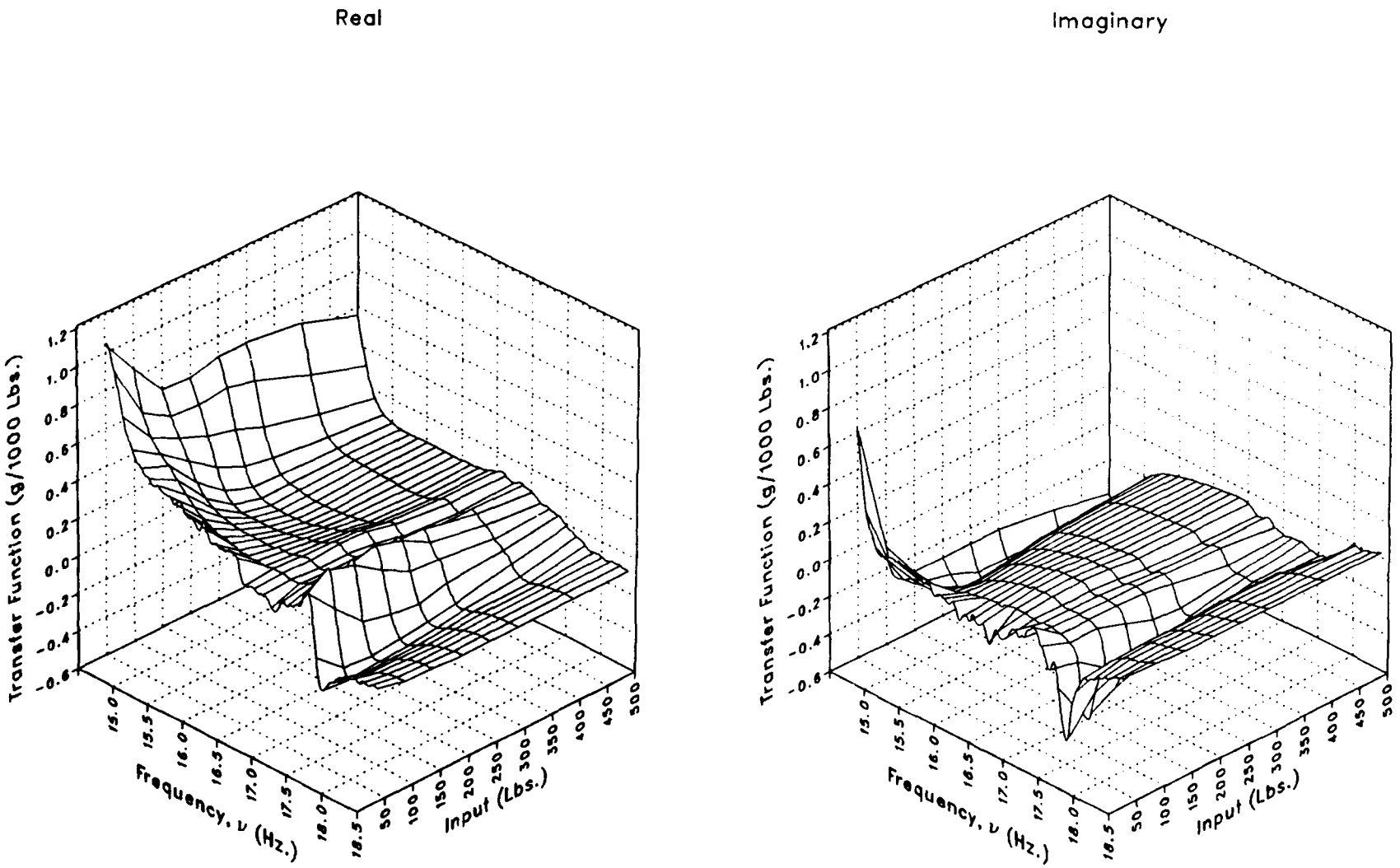

(u) VTTPYLON

Figure 6.– Continued.

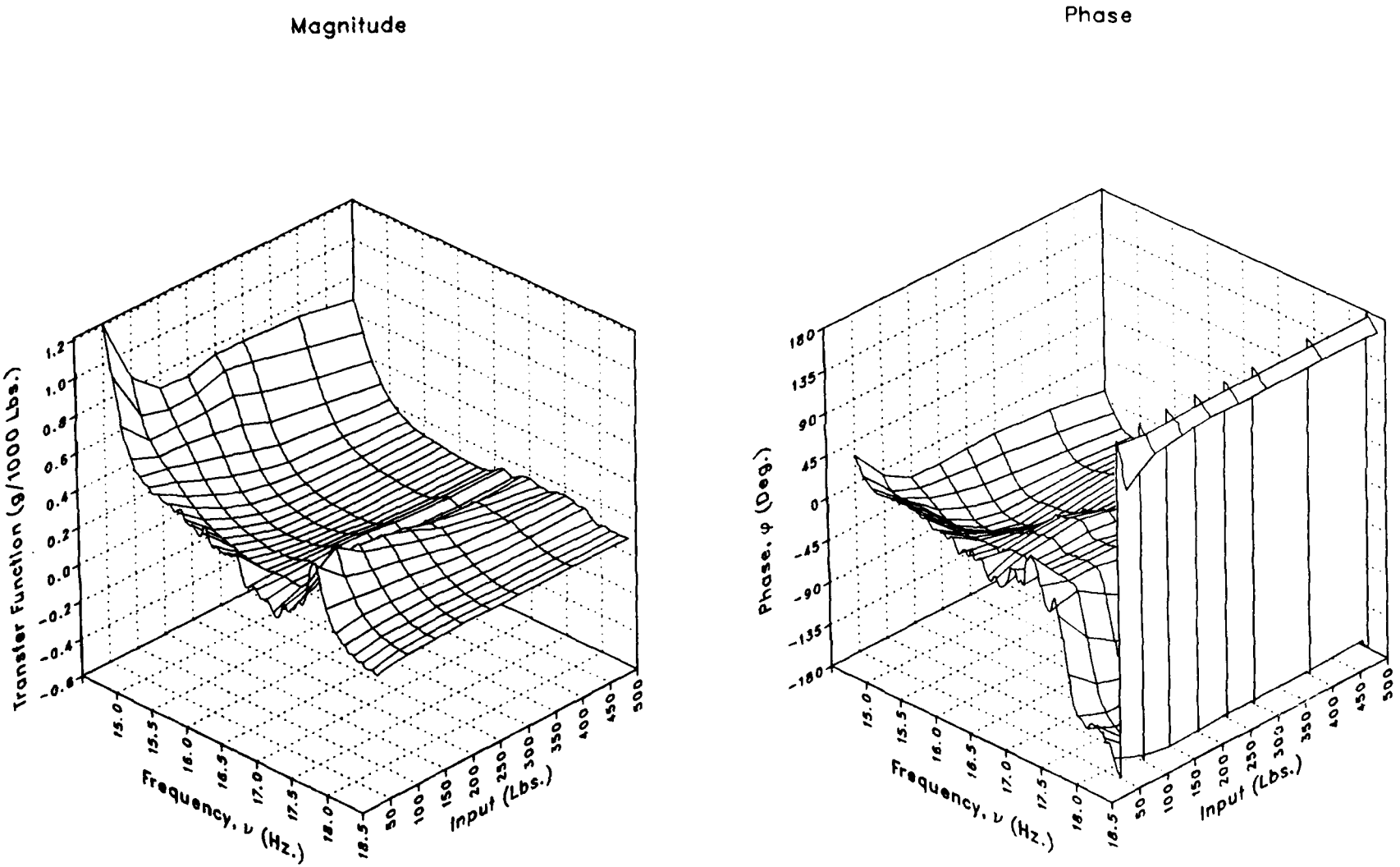

(u) VTTPYLON Concluded.

Figure 6.– Continued.

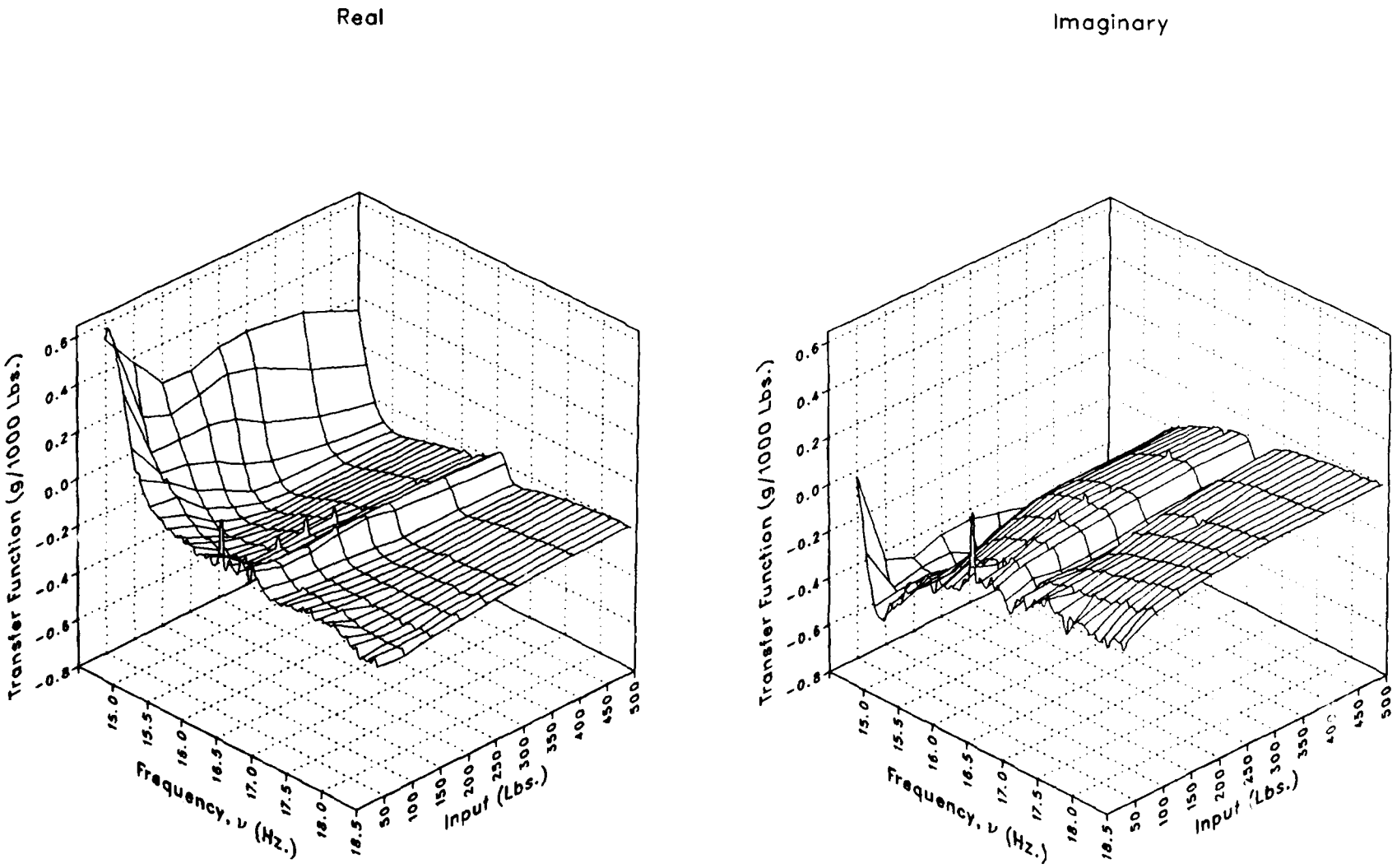

(v) XMRFLV

Figure 6.– Continued.

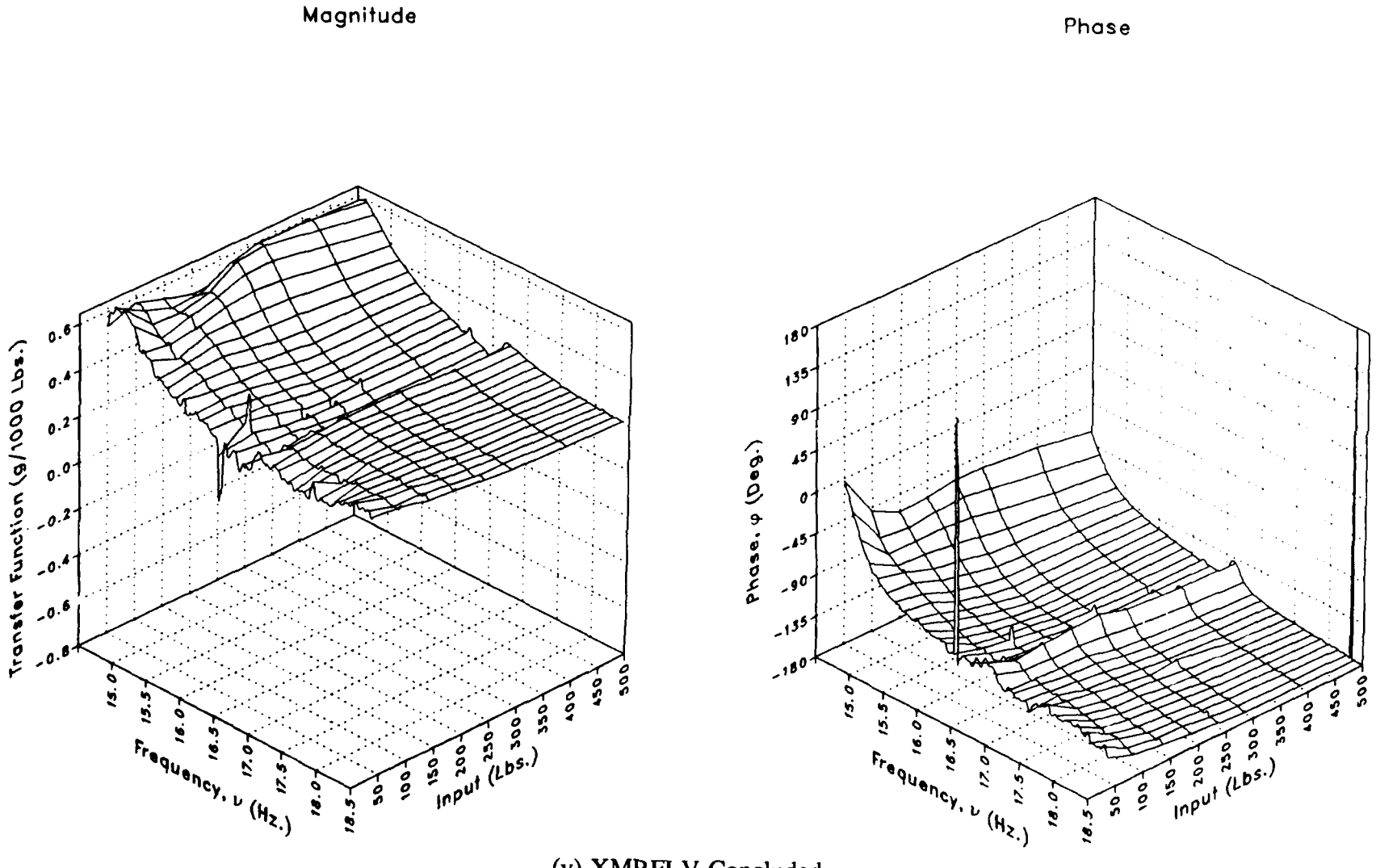

(v) XMRFLV Concluded.

Figure 6.– Continued.

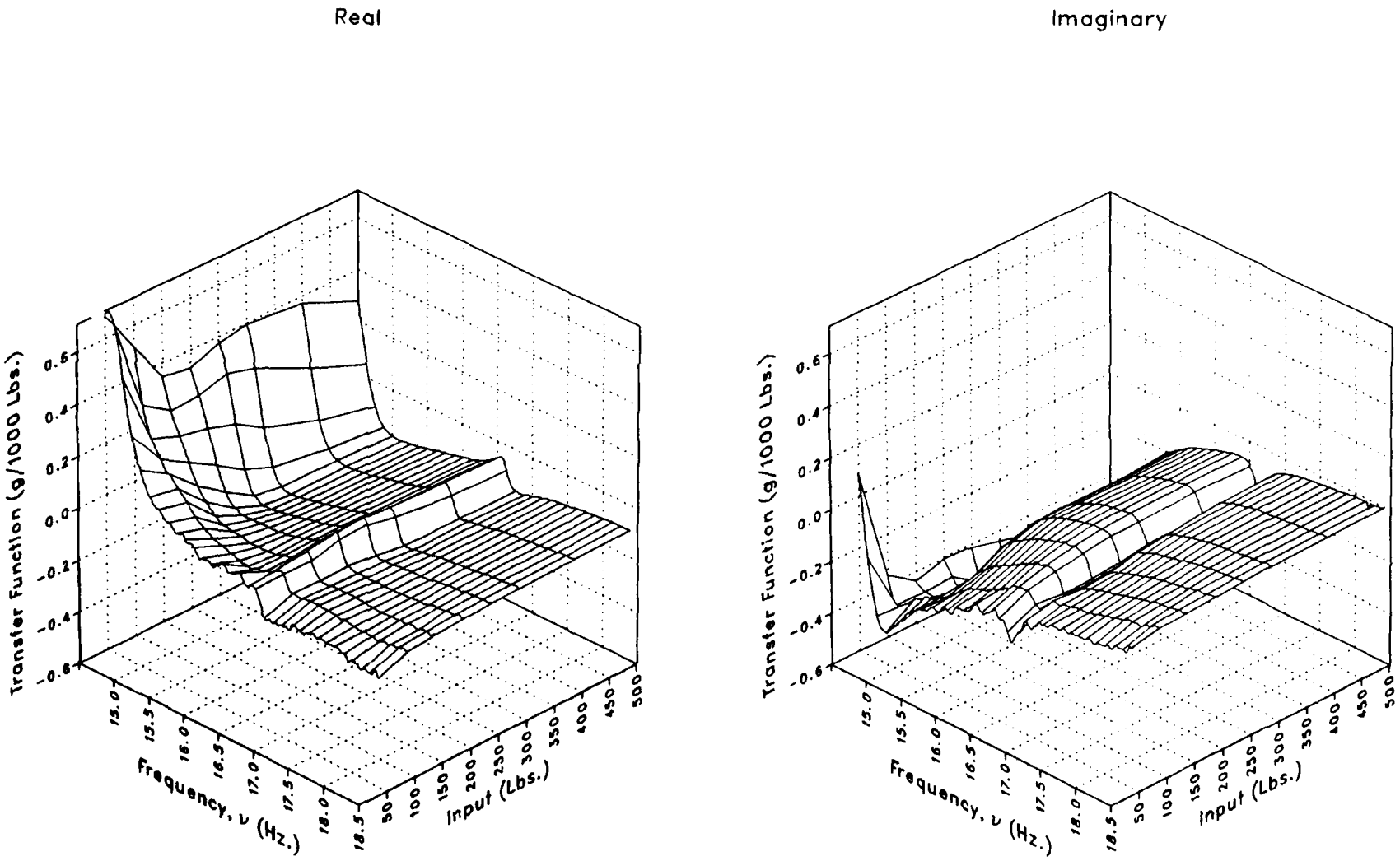

(w) XMRFRV

Figure 6.– Continued.

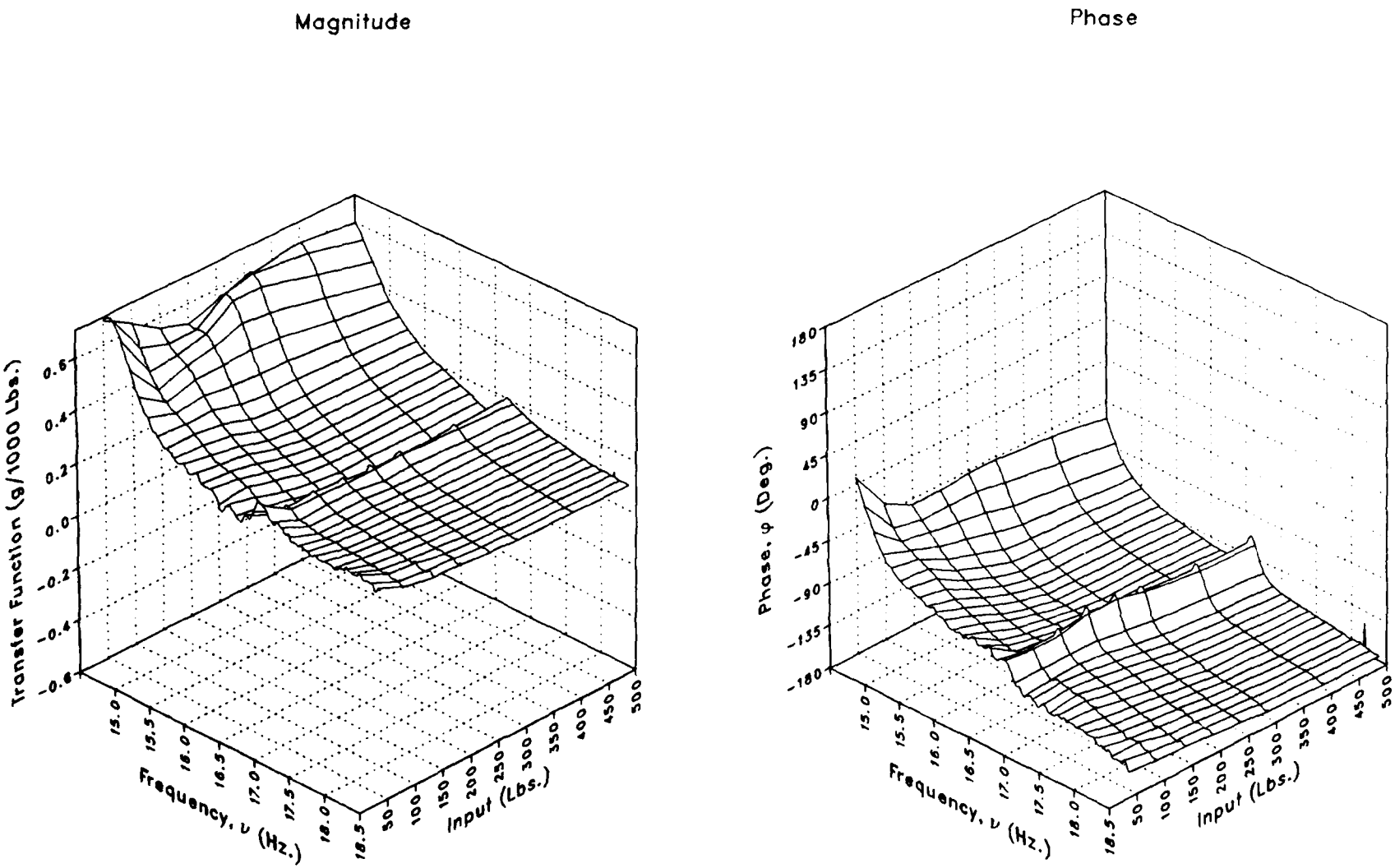

(w) XMRFRV Concluded.

Figure 6.– Continued.

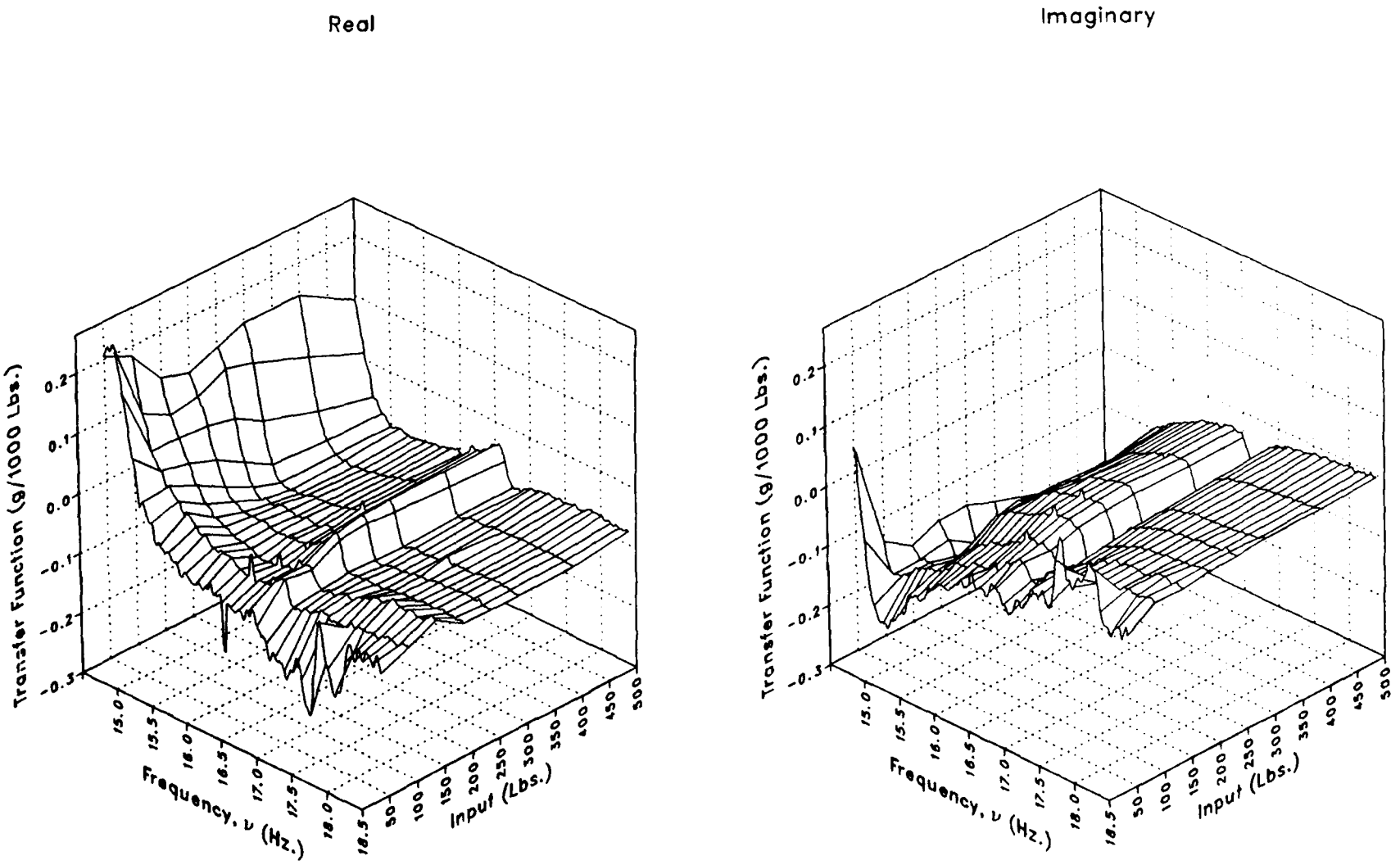

(x) S222FLRV

Figure 6.– Continued.

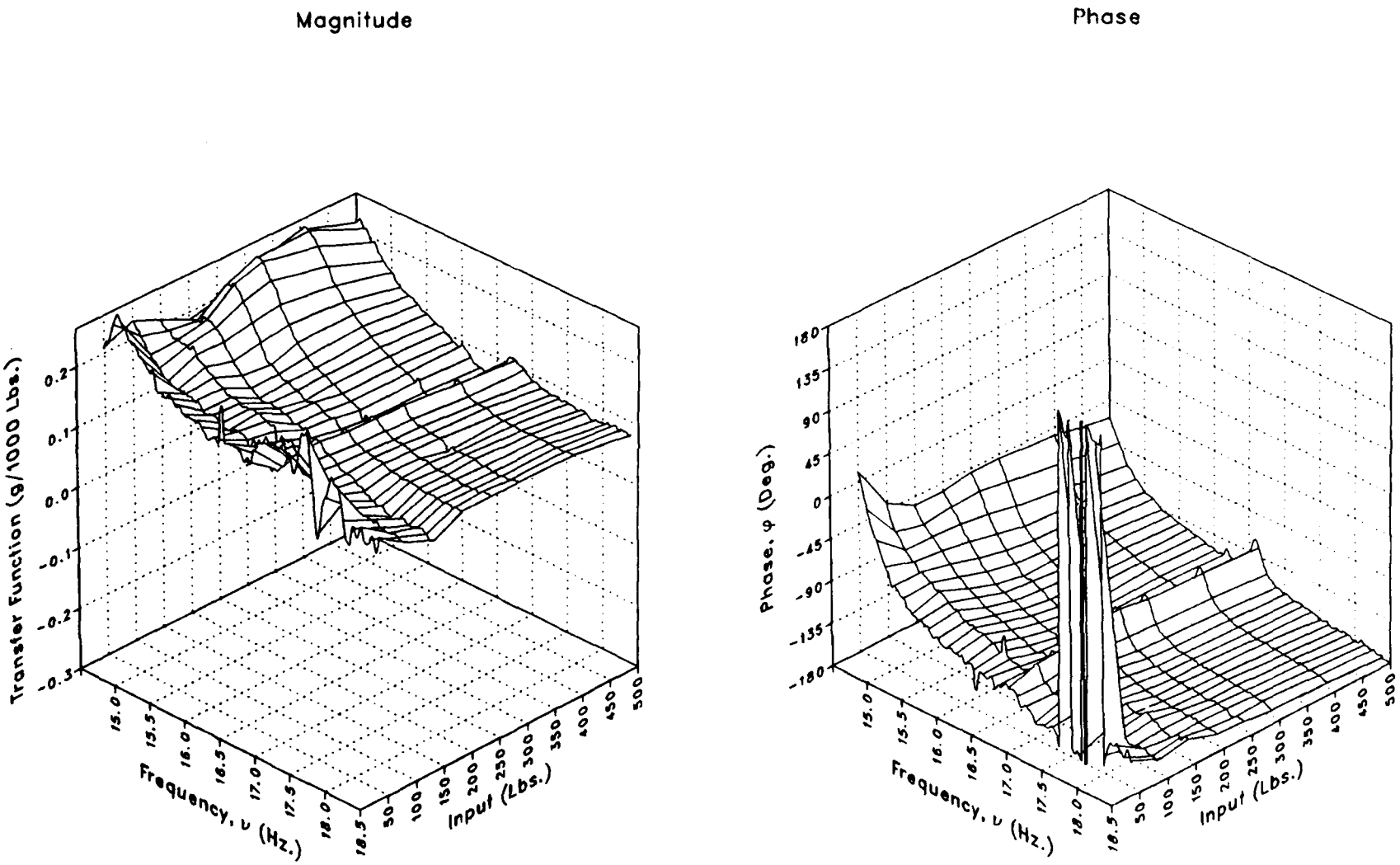

(x) S222FLRV Concluded.

Figure 6.– Continued.

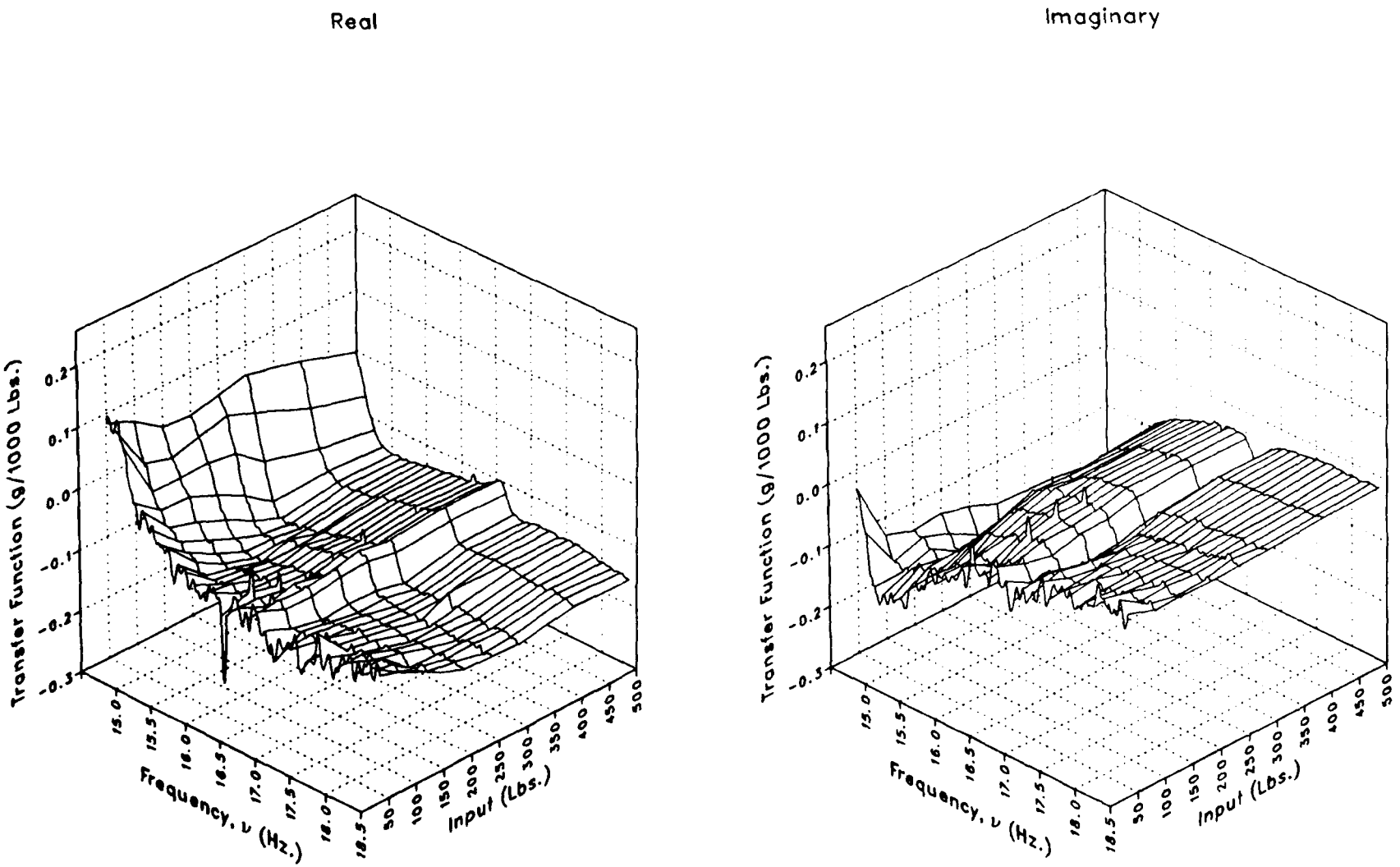

(y) S222FLLV

Figure 6.– Continued.

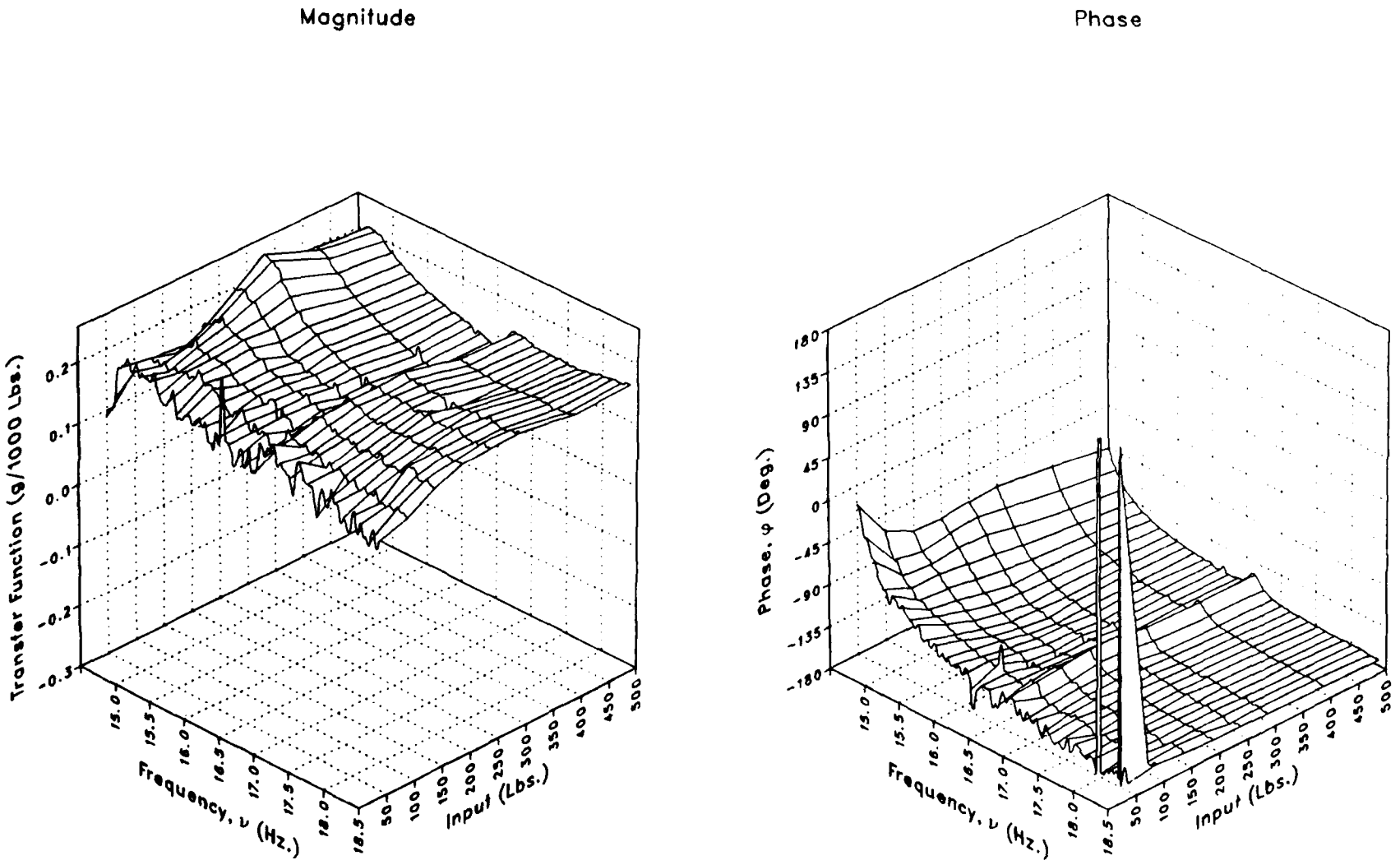

(y) S222FLLV Concluded.

Figure 6.– Continued.

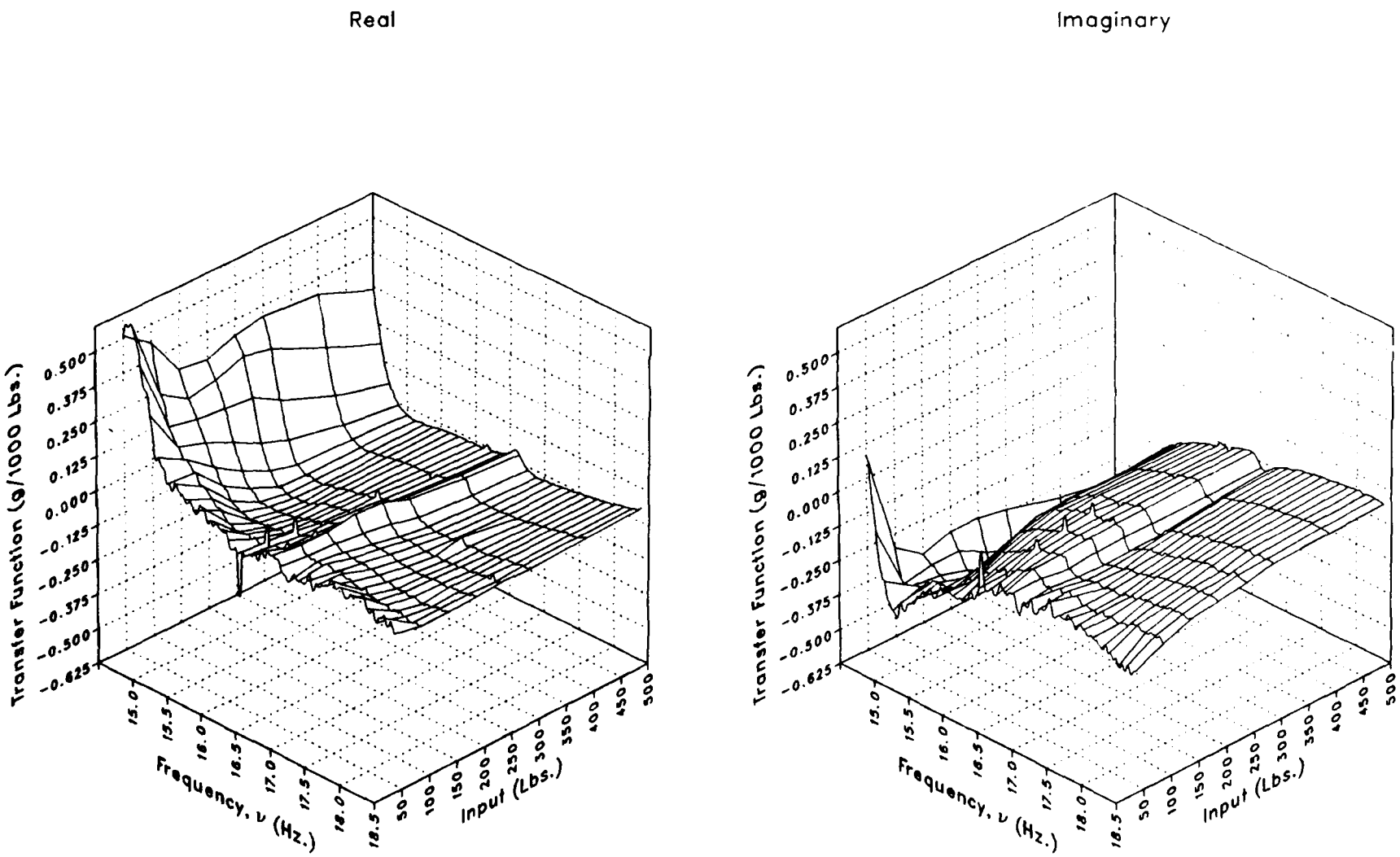

(z) S450FLV

Figure 6.– Continued.

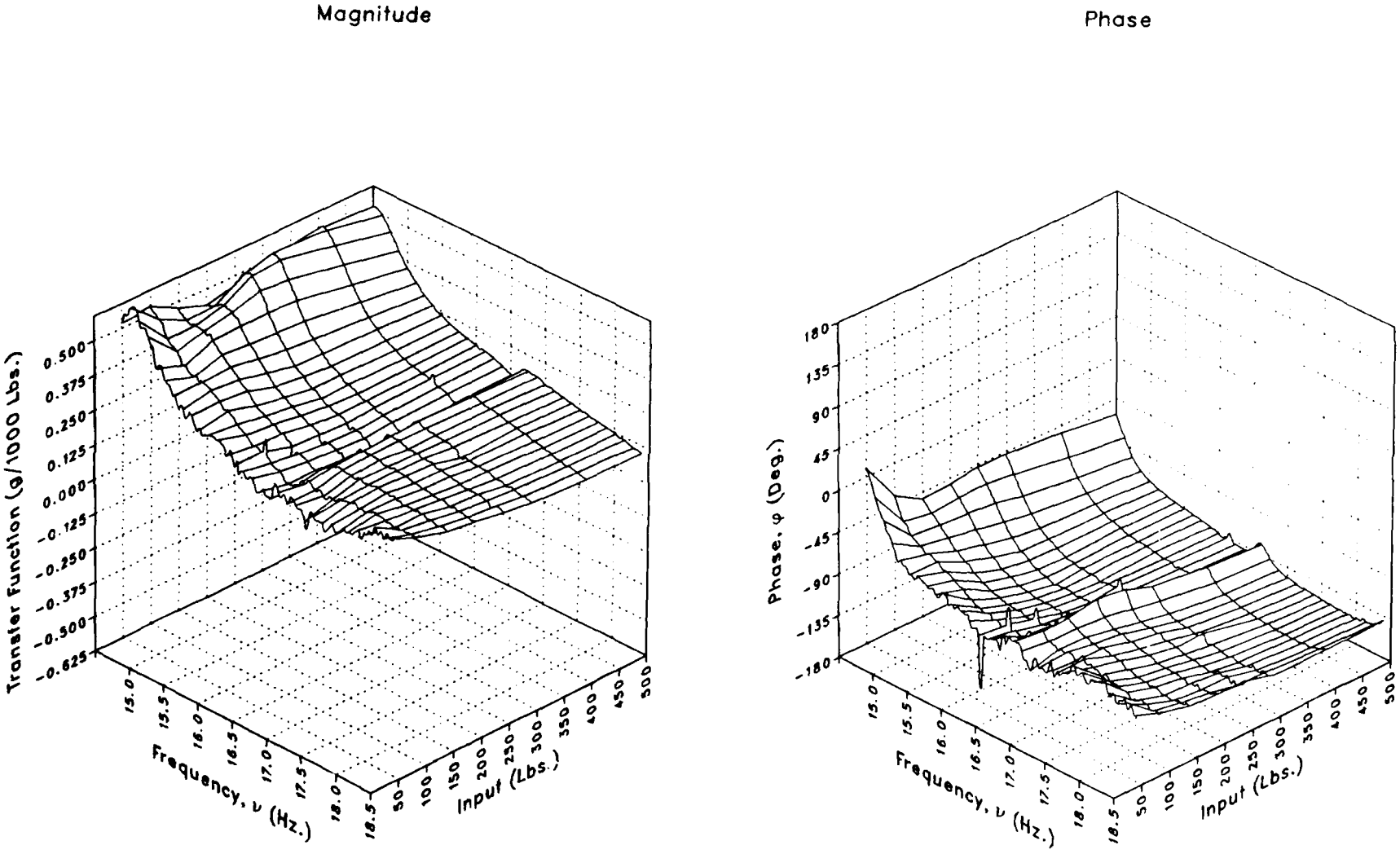

(z) S450FLV Concluded.

Figure 6.– Continued.

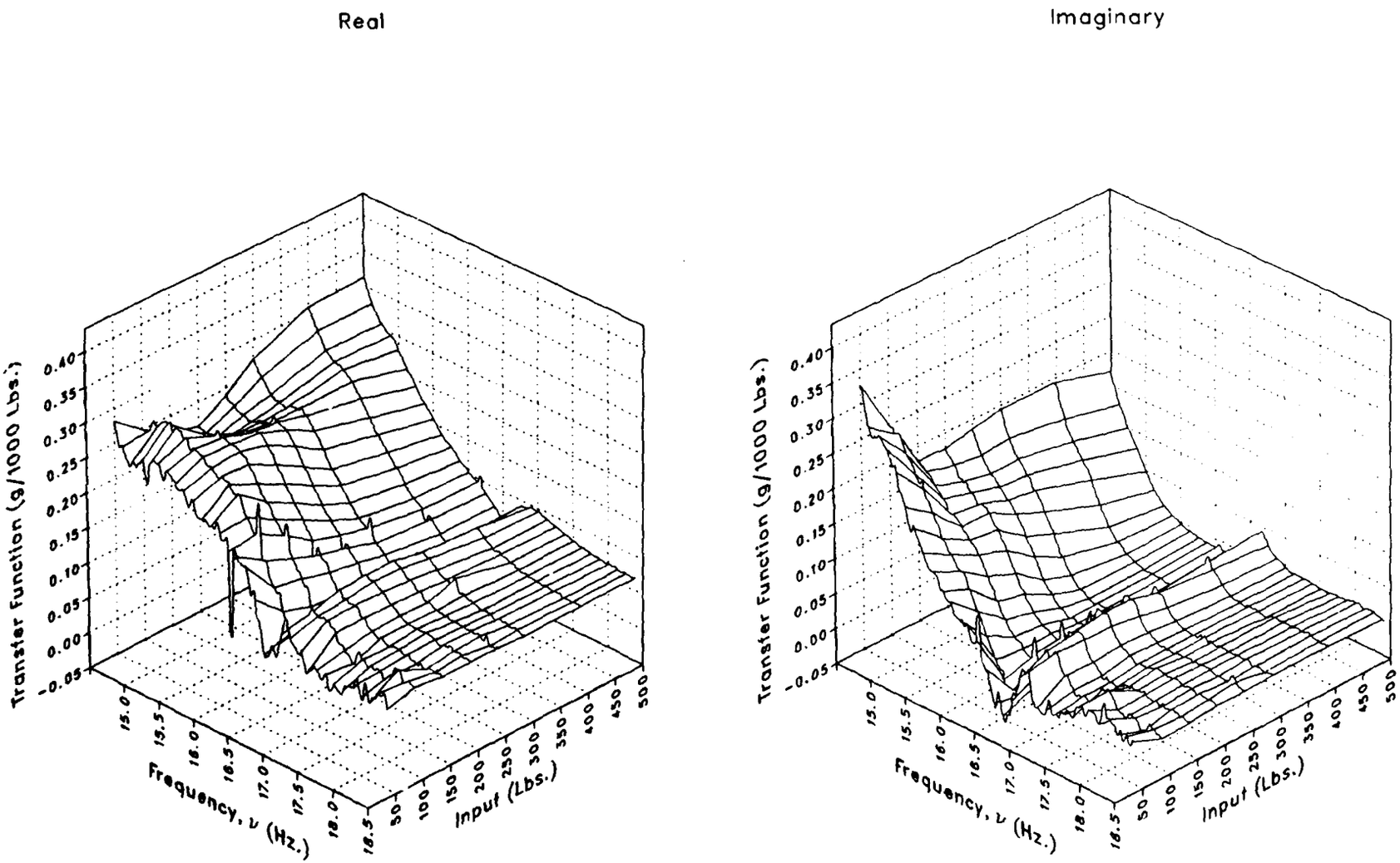

(aa) S450FLL

Figure 6.– Continued.

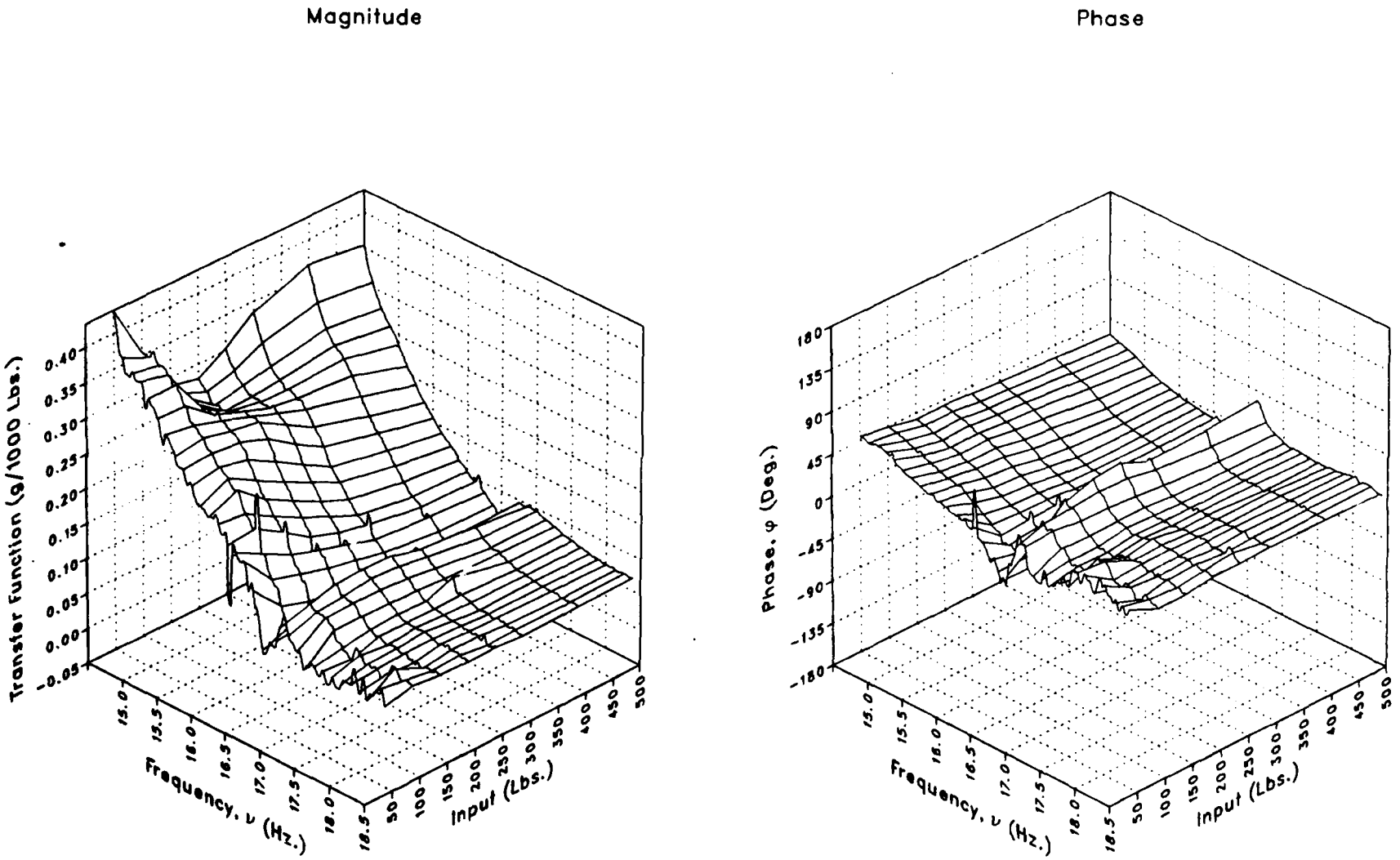

(aa) S450FLL Concluded.

Figure 6.– Continued.

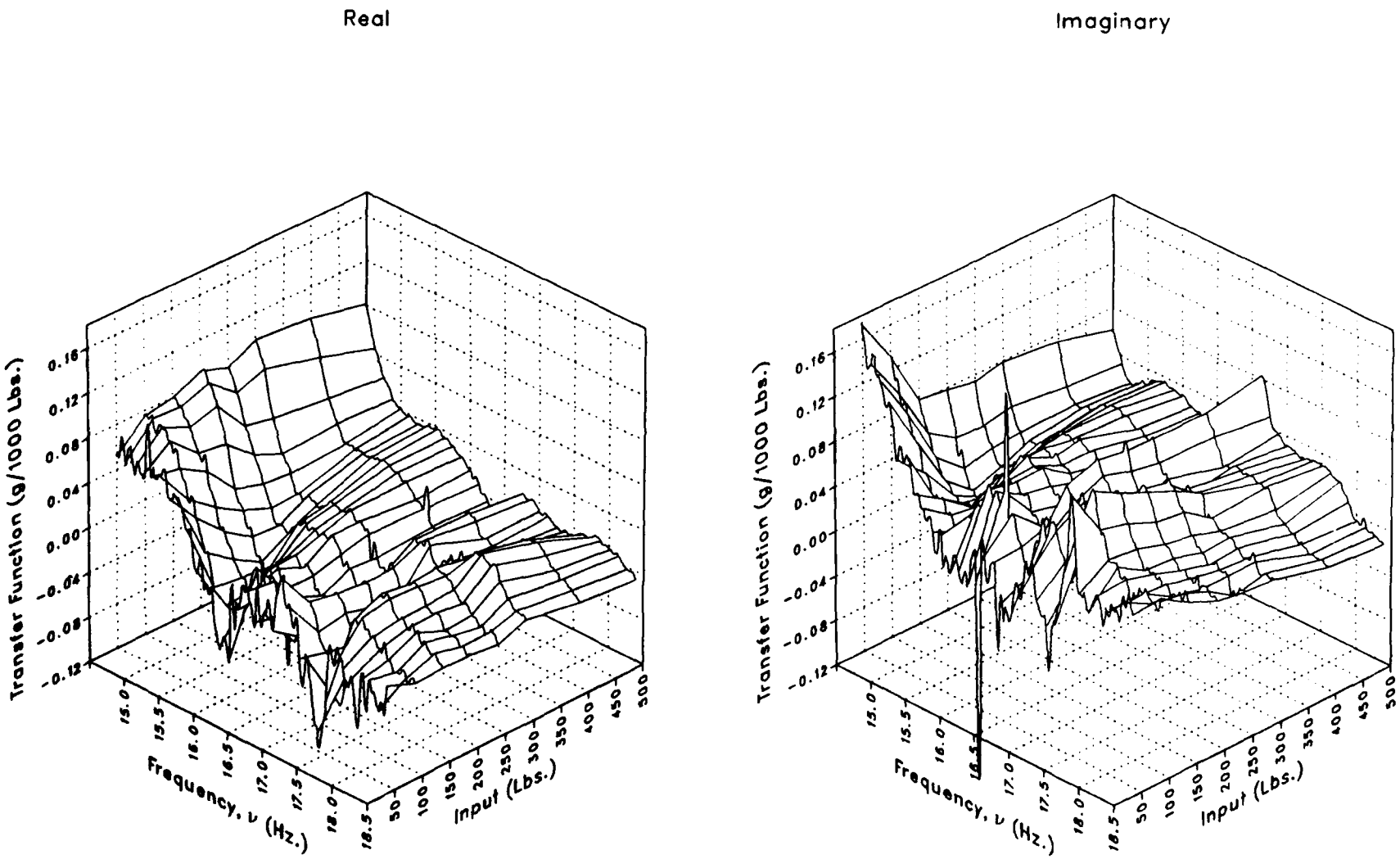

(bb) S450OVRL

Figure 6.– Continued.

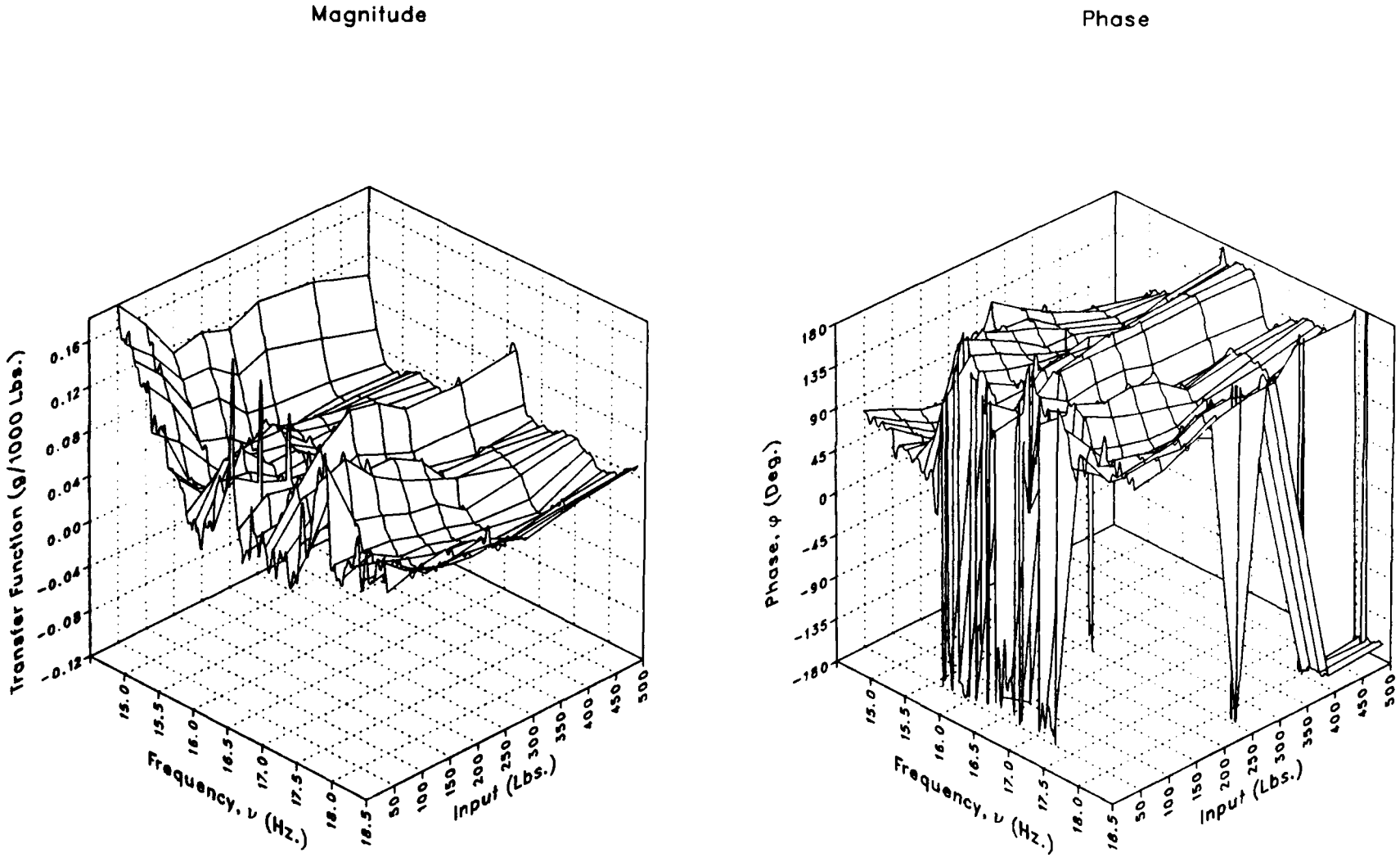

(bb) S450OVRL Concluded.

Figure 6.– Concluded.

NASA
National Aeronautics and Space Administration

Report Documentation Page

1. Report No. NASA TM-4186 AVSCOM TR-88-A-003	2. Government Accession No.	3. Recipient's Catalog No.
4. Title and Subtitle Rotor Systems Research Aircraft Risk-Reduction Shake Test		5. Report Date August 1990
		6. Performing Organization Code
7. Author(s) J. Brent Wellman		8. Performing Organization Report No. A-88316
		10. Work Unit No.
9. Performing Organization Name and Address Ames Research Center and Aeroflightdynamics Directorate, U.S. Army Aviation Research and Technology Activity, Ames Research Center, Moffett Field, CA 94035-1000		11. Contract or Grant No.
12. Sponsoring Agency Name and Address National Aeronautics and Space Administration Washington, DC 20546-0001 and U.S. Army Aviation Systems Command, St. Louis, MO 63120-1798		13. Type of Report and Period Covered Technical Memorandum
		14. Sponsoring Agency Code

15. Supplementary Notes

Point of Contact: J. Brent Wellman, Ames Research Center, MS 237-5,
Moffett Field, CA 94035-1000
(415) 604-6573 or FTS 464-6573

16. Abstract

A shake test and an extensive analysis of results were performed to evaluate the possibility of and the method for dynamically calibrating the Rotor Systems Research Aircraft (RSRA). The RSRA airframe was subjected to known vibratory loads in several degrees of freedom and the responses of many aircraft transducers were recorded. Analysis of the transducer responses using the technique of dynamic force determination showed that the RSRA, when used as a dynamic measurement system, could predict, a posteriori, an excitation force in a single axis to an accuracy of about 5% and sometimes better. As the analysis was broadened to include multiple degrees of freedom for the excitation force, the predictive ability of the measurement system degraded to about 20%, with the error occasionally reaching 100%. The poor performance of the measurement system is explained by the nonlinear response of the RSRA to vibratory forces and the inadequacy of the particular method used in accounting for this nonlinearity.

17. Key Words (Suggested by Author(s)) Force determination, Shake testing, Modal analysis, RSRA, Dynamic calibration	18. Distribution Statement Unclassified-Unlimited Subject Category - 05

19. Security Classif. (of this report) Unclassified	20. Security Classif. (of this page) Unclassified	21. No. of Pages 356	22. Price A16

NASA FORM 1626 OCT 86

For sale by the National Technical Information Service, Springfield, Virginia 22161

NASA-Langley, 1990